UNIVERSIDAD COMPLUTENSE DE MADRID
FACULTAD DE CIENCIAS FÍSICAS

TESIS DOCTORAL

Características hidrodinámicas del medio producido en colisiones Pb-Pb a√sNN=2.76 TeV y 5.02 TeV en el LHC utilizando el detector ALICE

Hydrodynamic characteristics of the medium produced in Pb-Pb collisions at √sNN=2.76 TeV and 5.02 Tev at the LHC using the ALICE setup

MEMORIA PARA OPTAR AL GRADO DE DOCTOR

PRESENTADA POR

Víctor González Sebastián

Directores

Ana María Marín García
Pedro Ladrón de Guevara Montero

Madrid

UNIVERSIDAD
COMPLUTENSE
MADRID

TESIS DOCTORAL

Características hidrodinámicas del medio producido en colisiones Pb–Pb a $\sqrt{s_{\mathrm{NN}}} = 2.76$ TeV y 5.02 TeV en el LHC utilizando el detector ALICE

Hydrodynamic characteristics of the medium produced in Pb–Pb collisions at $\sqrt{s_{\mathrm{NN}}} = 2.76$ TeV and 5.02 TeV at the LHC using the ALICE setup

---

Autor:
Víctor González Sebastián

Directores:
Dr. Ana María Marín García
Dr. Pedro Ladrón de Guevara Montero

Tesis presentada en la
Universidad Complutense de Madrid
para la obtención del grado de Doctor en Física

en el

Departamento de Física Teórica
Facultad de Ciencias Físicas

Septiembre 12, 2019

UNIVERSIDAD COMPLUTENSE MADRID

DECLARACIÓN DE AUTORÍA Y ORIGINALIDAD DE LA TESIS PRESENTADA PARA OBTENER EL TÍTULO DE DOCTOR

D./Dña. VICTOR GONZALEZ SEBASTIAN,
estudiante en el Programa de Doctorado D9AD - DOCTORADO EN FÍSICA,
de la Facultad de Ciencias Físicas de la Universidad Complutense de Madrid, como autor/a de la tesis presentada para la obtención del título de Doctor y titulada:

CARACTERÍSTICAS HIDRODINÁMICAS DEL MEDIO PRODUCIDO EN COLISIONES PB-PB SQRT{S_{NN}} = 2.76 TEV Y 5.02 TEV EN EL LHC UTILIZANDO EL DETECTOR ALICE

y dirigida por:
ANA MARÍA MARÍN GARCÍA
PEDRO LADRON DE GUEVARA MONTERO

DECLARO QUE:

La tesis es una obra original que no infringe los derechos de propiedad intelectual ni los derechos de propiedad industrial u otros, de acuerdo con el ordenamiento jurídico vigente, en particular, la Ley de Propiedad Intelectual (R.D. legislativo 1/1996, de 12 de abril, por el que se aprueba el texto refundido de la Ley de Propiedad Intelectual, modificado por la Ley 2/2019, de 1 de marzo, regularizando, aclarando y armonizando las disposiciones legales vigentes sobre la materia), en particular, las disposiciones referidas al derecho de cita.

Del mismo modo, asumo frente a la Universidad cualquier responsabilidad que pudiera derivarse de la autoría o falta de originalidad del contenido de la tesis presentada de conformidad con el ordenamiento jurídico vigente.

En Madrid, a 10 de septiembre de 2019

Fdo.: Víctor González Sebastián

Esta DECLARACIÓN DE AUTORÍA Y ORIGINALIDAD debe ser insertada en la primera página de la tesis presentada para la obtención del título de Doctor.

"*I love those who yearn for the impossible.*"

Goethe

Resumen

Características hidrodinámicas del medio producido en colisiones Pb–Pb a $\sqrt{s_{\mathrm{NN}}}$ = 2.76 TeV y 5.02 TeV en el LHC utilizando el detector ALICE

Víctor González Sebastián

La constatación de que el medio producido en colisiones relativistas de iones-pesados, denominado plasma de quarks y gluones (QGP por sus siglas en inglés), se comporta casi como un fluido ideal originó un aluvión de iniciativas para intentar determinar sus características. Aparte de la ecuación de estado y del diagrama de fases, las características más relevantes de un fluido son sus coeficientes de transporte. Los coeficientes de trasporte conducen la evolución del fluido en su retorno al estado de equilibrio. El éxito de los modelos hidrodinámicos en reproducir valores medidos experimentalmente llevó a la proliferación de métodos que extraían los coeficientes de transporte del QGP a partir de simulaciones hidrodinámicas. Utilizar modelos para inferir los coeficientes de transporte incorpora una incertidumbre inherente al modelo que se elije y a las condiciones iniciales con las que se inicia la simulación. El objetivo de esta tesis es el de extraer los coeficientes de transporte del QGP directamente, desde medidas experimentales, utilizando correlaciones de las componentes del momento de pares de partículas.

Las correlaciones de dos partículas se han convertido en una de las mejores herramientas para caracterizar su producción y estudiar la dinámica de las colisiones de iones pesados. Las correlaciones de dos partículas que habitualmente aparecen en las medidas experimentales son las correlaciones de número de partículas. Sin embargo, cuando se trata de caracterizar las propiedades de transporte del QGP son las correlaciones de las componentes del momento las que son relevantes, aunque su presencia experimental es aún escasa. Gavin et al. propusieron un correlador del momento transverso de dos-partículas para extraer la viscosidad específica de cizalla, η/s, del QGP y, posteriormente, para extraer su tiempo de relajación. Dobado et al. propusieron un correlador de energía / momento transverso de dos-partículas para extraer la viscosidad específica de volumen, ζ/s, del QGP.

Esta tesis se enfoca en la extracción del correlador de momento transverso de dos partículas en función de la separación angular relativa. La medida del correlador independiente de la carga en colisiones plomo-plomo, Pb–Pb, se realiza por primera vez a energías del LHC. La medida del correlador dependiente de la carga en colisiones Pb–Pb, y de ambas versiones, independiente y dependiente de la carga, en colisiones protón-protón, pp, y en colisiones protón-Plomo, p–Pb, es la primera vez que se realiza. El correlador se parametriza utilizando un modelo multicomponente bidimensional, novedoso para este correlador, para capturar sus principales características. El comportamiento del correlador independiente de la carga se compara con resultados a energías RHIC y con resultados del comportamiento de otros correladores de dos partículas medidos a energías del LHC. Así mismo, la evolución con las características de la colisión de ambas versiones del correlador se comparan con predicciones de modelos teóricos implementados en generadores de eventos. Ninguno de los modelos utilizados reproduce la riqueza de matices que presenta el correlador medido experimentalmente, lo que permite poner restricciones a los modelos utilizados por dichos generadores.

Las características del medio afectan al alcance de los efectos de sus fluctuaciones, es decir, al alcance de las transferencias de esas fluctuaciones entre celdas de fluido vecinas. Los efectos de la transferencia de las fluctuaciones del momento transverso se ponen de manifiesto en la forma del correlador del momento transverso de dos partículas, y su alcance, en su anchura. Utilizando la evolución con las características de la colisión de la anchura longitudinal del correlador del momento transverso de dos partículas se ha extraído un valor $\eta/s = 0.066 \pm 0.012$. El valor se encuentra en el rango de los extraídos comparando distintas medidas experimentales con los valores esperados por modelos teóricos y próximo al límite $1/4\pi$. Por otro lado, el análisis del correlador en sistemas pequeños, pp y p–Pb, ha permitido extraer una anchura longitudinal que no varía con la multiplicidad de partículas cargadas producidas en la colisión lo que permite cualificar al correlador como sensible a la formación del QGP.

El extenso análisis del correlador del momento transverso de dos partículas ha permitido constatar su sensibilidad a procesos de transferencia de las fluctuaciones del momento transverso diferenciándose de la de otros correladores de dos partículas. Se ha constatado como esta sensibilidad permite poner restricciones a cómo la física de los procesos de las colisiones de iones pesados está implementada en los generadores de eventos. Asimismo, la sensibilidad del correlador ha permitido establecer diferencias entre los sistemas de iones pesados y los sistemas pequeños, en un momento en el que está en cuestión cuál es el tamaño mínimo de una gota de QGP. El comportamiento longitudinal del correlador ha permitido la extracción de un valor de η/s que, aunque por la naturaleza del método implica la convolución a lo largo de la vida completa del sistema, proviene, por primera vez a energías LHC, directamente de los datos medidos. La medida experimental de los correladores del momento transverso está en sus albores y los resultados de esta tesis contribuirán a darle un empuje considerable.

Abstract

Hydrodynamic characteristics of the medium produced in Pb–Pb collisions at $\sqrt{s_{\mathrm{NN}}} = 2.76$ TeV and 5.02 TeV at the LHC using the ALICE setup

by Víctor González Sebastián

The finding that the medium produced in relativistic heavy-ion collisions, denominated as quark gluon plasma (QGP), behaves almost like an ideal fluid caused a flood of initiatives to try to determine their characteristics. Apart from the equation of state and the phase diagram, the most relevant characteristics of a fluid are its transport coefficients. The transport coefficients drive the evolution of the fluid in its return to equilibrium. The success of hydrodynamic models in reproducing experimentally measured values led to the proliferation of methods that extracted the transport coefficients of QGP from hydrodynamic simulations. Using models to infer transport coefficients incorporates an uncertainty inherent in the model chosen and the initial conditions with which the simulation begins. The objective of this thesis is to extract the transport coefficients of the QGP directly, from experimental measures, using two-particle momentum components correlations.

Two-particle correlations have emerged as one of the best tools to characterize particle production and to study the dynamics of heavy-ion collisions. Two-particle correlations that usually appear in the experimental measures are two-particle number correlations. However, when it comes to characterizing the transport properties of QGP, it is the correlations of the components of the momentum that are relevant, although their experimental presence is still scarce. Gavin et al. proposed a two-particle transverse momentum correlator to extract the specific shear viscosity, η/s, of QGP and, latter, to extract its relaxation time. Dobado et al. proposed a two-particle transverse momentum energy correlator to extract the specific bulk viscosity, ζ/s, of QGP.

This thesis focuses on the extraction of the two-particle transverse momentum correlator as a function of the relative angular separation. The measurement of the charge independent correlator in lead–lead, Pb–Pb, collisions is made for the first time at LHC energies. The measure of the charge dependent correlator in Pb–Pb collisions, and of both correlator versions, charge independent and charge dependent, in proton–proton, pp, collisions and in proton-lead, p–Pb, collisions is the first being made. The correlator is parameterized using a bidimensional multi-component model, new for this correlator, to capture its main characteristics. The charge independent correlator behavior is compared with results at RHIC energies and with results from other two-particle correlators measured at LHC energies. Likewise, the evolution with the collision characteristics of both versions of the correlator are compared with predictions from theoretical models implemented in event generators. None of the models reproduce the richness of nuances presented by the correlator, which allows to set constrains on the theoretical models used by these generators.

The characteristics of the medium affect the scope of the effects of its fluctuations, i.e. the extent of the transfer of these fluctuations between neighbor fluid cells. The effects of the transfer of the transverse momentum fluctuations are manifested in the shape of the two-particle transverse momentum correlator, and their extent, in its width. Using the evolution with the characteristics of the collision of the two-particle transverse momentum correlation longitudinal width, a value $\eta/s = 0.066 \pm 0.012$ has been extracted. The value is in the scope of those extracted by using model simulations although somewhat lower than the theoretical limit $1/4\pi$. On the other hand, the analysis of the correlator in small systems, pp and p–Pb, has allowed the extraction of a longitudinal width that does not vary with the characteristics of the collision, which allows the correlator to be qualified as sensitive to the formation of the QGP.

The extensive analysis of the two-particle transverse momentum correlator has allowed to verify its sensitivity to the transverse momentum fluctuations transfer processes, differing from that of other two-particle correlators. It has been found how this sensitivity allows to set constrains on how the physics of heavy-ion collisions processes are implemented in event generators. Likewise, the sensitivity of the correlator has allowed to establish differences between heavy-ion systems and small systems, at a time when the minimum size of a drop of QGP is in question. The longitudinal behavior of the correlator has allowed the extraction of a value of η/s which, although due to the nature of the method, implies convolution throughout the entire life of the system, it comes, for the first time at LHC energies, directly from measured data. The experimental measure of the transverse momentum correlators is in its dawn and the results of this thesis will contribute to give it a considerable boost.

Acknowledgements

I would like to dedicate some lines to express my gratitude to all those people who have somehow contributed to complete this thesis during the last years.

First of all, I want to thank my supervisors, Dr. Ana Marín and Dr. Pedro Ladrón de Guevara, for their continued orientation, push, availability and willingness. Their always successful questions have taken this work along unexpected but tremendously productive and exciting paths.

I will never have enough words to thank Prof. Claude Pruneau for his generosity in offering me his friendship and sharing his vision on the physical nature of reality and especially on two-particle correlations. His innate ability to act as a mentor has greatly enriched the quality of my own physics insights.

Probably, nothing I have done would have concluded in the way it did if it had not been for Prof. Silvia Masciocchi, who kindly affiliated me to the GSI Helmoltzzentrum für Schwerionenforschung GmbH when Spain left the ALICE Collaboration. This gave me the opportunity of continue my work in ALICE and also the possibility to show the results of that work at conferences.

I want to thank Dr. Alice Ohlson and Dr. Anthony Timmins for agreeing to be external evaluators of my thesis. To my tutor Dr. Felipe Llanes for being able to count on him whenever necessary.

My thanks also to David Cinabro and Sergei Voloshin, who supported Prof. Pruneau's initiative and made possible my stay at Wayne State University as Visiting Scholar. I also want to thank Sean Gavin and George Moschelli for fruitful discussions and the good times shared.

I am indebted to Ilya Selyuzenkov for offer me his friendship and for unveiling to me the principles that govern the big collaborations. Thanks to Ilya and Jaap Onderwaater for introducing me to the world of flow vectors, during my service task of developing the QnVectorCorrection Framework, and for the good times in Darmstadt. Thanks to Sumit Basu and Jinjing Pan for all the shared meetings, for the shared work and for the good times in Detroit.

Finally I will always be indebted to my beloved family who have silently endured an important part of this work, the least visible, the company, the closeness and the unconditional love.

List of publications, conferences and research visits

Publications

1. Víctor González, Ana Marín, Pedro Ladrón de Guevara, Jinjin Pan, Sumit Basu, Claude Pruneau, "Effect of centrality bin width corrections on two-particle number and transverse momentum differential correlation functions"

   Phys. Rev. C 99, 034907 (2019)
   arXiv:1909.04962v2

2. Monika Kofarago for the ALICE Collaboration (co-autor), "The evolution of the near-side peak in two-particle number and transverse momentum correlations in Pb–Pb collisions from ALICE"

   QM18 Proceedings. Nucl. Phys. 982 (2019)

3. Víctor González, J. Onderwaater, I. Selyuzhenkov, "Detector non-uniformity corrections for collision symmetry plane estimates"

   GSI Scientific Report 2015 / 2016-1

Papers in preparation

1. ALICE Collaboration, "Longitudinal and azimuthal evolution of two-particle transverse momentum correlations in Pb–Pb collisions at $\sqrt{s_{\mathrm{NN}}}$ = 2.76 TeV in ALICE"

   Finalized internal review and editorial board review. In whole collaboration review phase previous to Physics Letters B submission.

Conferences

1. XIV Workshop on Particle Correlations and Femtoscopy, Dubna. Russia

   From 2019/06/03 to 2019/06/07

2. Quark Matter 2018, Venice. Italy

   From 2018/05/13 to 2018/05/19

Talks and contributions

1. Talk - XIV Workshop on Particle Correlations and Femtoscopy, Dubna. Russia

   "Two-particle transverse momentum correlations in Pb–Pb collisions at $\sqrt{s_{\mathrm{NN}}}$ = 2.76 TeV". June 06, 2019

2. Parallel talk - Quark Matter 2018 (co-author)

   "The evolution of the near-side peak in two-particle number and transverse momentum correlations in Pb–Pb collisions from ALICE". May 16, 2018

3. Poster - Quark Matter 2018

   "Two-particle transverse momentum correlations in Pb–Pb collisions al ALICE". May 15, 2018

4. Seminar - Lawrence Technological University, Southfield, Michigan. USA

   "Correlation measurements at the LHC using the ALICE detector". September 29, 2017

5. Seminar - Wayne State University, Detroit, Michigan. USA

   "Determination of η/s with p_{T} correlations from Pb–Pb collisions at $\sqrt{s_{\mathrm{NN}}}$ = 2.76 and 5.04 TeV". September 15, 2017

Research visits

1. Heavy-ion Group, Department of Physics and Astronomy, Wayne State University. Detroit, Michigan. USA

   From 2017/07/14 to 2017/10/10

2. Event plane service task. GSI Darmstadt. Germany

   From 2016/08/15 to 2016/08/19
   From 2016/04/04 to 2016/04/08
   From 2015/11/23 to 2015/11/27

3. Shift leader at ALICE (P2) experiment in CERN LHC. Geneva. Switzerland

   From 2015/09/01 to 2015/09/30

Software

1. Framework for two-particle transverse momentum correlation analysis in ALICE at the LHC

   Transverse momentum correlations framework
   @https://github.com/alisw/AliPhysics/tree/master/PWGCF/Correlations/DPhi/Unfoldedhistos

2. QnVectorCorrection Framework as used by ALICE at the LHC

   ALICE QnVectorCorrecton framework
   @https://github.com/alisw/AliPhysics/tree/master/PWGPP/EVCHAR/FlowVectorCorrections

3. QnVectorCorrection Framework as used by NA49 and NA61/SHINE at SPS, and the future CBM at FAIR

   Portable QnVectorCorrection framework
   @https://github.com/FlowCorrections/FlowVectorCorrections/tree/master/QnCorrections

Contents

List of Figures

List of Tables

List of Abbreviations

ACORDE	**A**LICE **C**osmic **R**ay **De**tector
AdS/CFT	**A**nti-**d**e **S**itter/**C**onformal **F**ield **T**heory
ALICE	**A** **L**arge **I**on **C**ollider **E**xperiment
BNL	**B**rookhaven **N**ational **L**aboratory
CD	**C**harge **D**ependent track combination
CERN	European Organization for Nuclear Research **C**onseil **E**uropéen pour la **R**echerche **N**ucléaire
CFT	**C**onformal **F**ield **T**heory
CGC	**C**olor **G**lass **C**ondensate
CI	**C**harge **I**ndependent track combination
CL1	**C**entral **L**ayer one(**1**)
CTP	**C**entral **T**rigger **P**rocessor
DCA	**D**istance of **C**losest **A**pproach
EbyE	**E**vent-**by**-**E**vent
EMCal	**E**lectro**m**agnetic **Cal**orimeter
EoS	**E**quation **o**f **S**tate
FMD	**F**orward **M**ultiplicity **D**etector
HBT	**H**anbury **B**rown and **T**wiss
HIC	**H**eavy-**I**on **C**ollisions
HMPID	**H**igh **M**omentum **P**article **I**dentification **D**etector
HRG	**H**adron **R**esonance **G**as model
HW	**H**ard**W**are
IP	**I**nteraction **P**oint
ITS	**I**nner **T**racking **S**ystem
L0	**L**evel zero (**0**) trigger
L1	**L**evel one (**1**) trigger
L2	**L**evel two (**2**) trigger
LHS	**L**eft-**H**and **S**ide
LHC	**L**arge **H**adron **C**ollider
LS	**L**ike **S**ign track combination
MB	**M**inimum **B**ias
MC	**M**onte **C**arlo
MCMC	**M**arkov **C**hain **M**onte **C**arlo
MCH	**M**uon **C**hamber
MRPC	**M**ulti-gap **R**esistive-**P**late **C**hamber
MTR	**M**uon **T**rigger
MWPC	**M**ulti-**W**ire **P**roportional **C**hamber
NBD	**N**egative **B**inomial **D**istribution
PDF	**P**robability **D**ensity **F**unction
PHOS	**Pho**ton **S**pectrometer
PHSD	**P**arton-**H**adron-**S**tring **D**ynamics model
PMD	**P**hoton **M**ultiplicity **D**etector

QA	**Q**uality **A**ssurance
rHIC	**r**elativistic **H**eavy-**I**on **C**ollisions
RHIC	**R**elativistic **H**eavy-**I**on **C**ollider
RHS	**R**ight-**H**and **S**ide
RICH	**R**ing **I**maging **Ch**erenkov
RMS	**R**oot **M**ean **S**quare
SC	**S**ymmetric **C**umulants
SDD	**S**ilicon **D**rift **D**etector
SPD	**S**ilicon **P**ixel **D**etector
SSD	**S**ilicon **S**trip **D**etector
SW	**S**oft**W**are
TOF	**T**ime-**O**f-**F**light detector
TPC	**T**ime **P**rojection **C**hamber
TRD	**T**ransition **R**adiation **D**etector
UrQMD	**U**ltra-**r**elativistic **Q**uantum **M**olecular **D**ynamic model
US	**U**nlike **S**ign track combination
VISH	**V**iscous **I**srael-**S**tewart **H**ydrodynamics model
ZDC	**Z**ero **D**egree **C**alorimeter
ZEM	**Z**ero degree **E**lectro**m**agnetic calorimeter
(ZPC)	**Z**hang's **P**arton **C**ascade model

List of Symbols

β	relativistic velocity	v/c	
γ	Lorentz factor	$1/\sqrt{1-\beta^2}$	
$\Delta\eta$	relative pseudorapidity	$\eta_i - \eta_j$	
$\Delta\varphi$	relative azimuthal angle	$\varphi_i - \varphi_j$	rad
ζ/s	specific bulk viscosity		
η	pseudorapidity	$-\log\left[\tan\left(\theta/2\right)\right]$ $\log\left[\left(p + p_z\right)/\left(p - p_z\right)\right]/2$	
η/s	specific shear viscosity		
φ	azimuthal angle		rad
θ	polar angle		rad
E	energy		GeV
m	mass	$\sqrt{E^2 - (p\,c)^2}/c^2$	GeV$/c^2$
p	momentum	$p_\mathrm{T}\cosh\eta$	GeV$/c$
p_T	transverse momentum		GeV$/c$
p_z	longitudinal momentum	$p_\mathrm{T}\sinh\eta$	GeV$/c$
y	rapidity	$\log\left[\left(E + p_z c\right)/\left(E - p_z c\right)\right]/2$	
$\mathrm{d}N_\mathrm{ch}/\mathrm{d}\eta$	charged-particle density		
N_coll	number of binary nucleon collisions		
N_part	number of participant nucleons		

Dedicated to
Luis, Valentina, Lucía, Eduardo e Irene

Chapter 1

Introduction

According to the current knowledge of the early and present Universe, about 13,800 million years ago, just within the first microseconds after the Big Bang, Nature was a primordial extremely hot and dense soup of quark and gluons [1]. It took Nature 13,800 million years to revisit that state in the ephemeral drops produced at the heart of the huge relativistic heavy-ion colliders.

In the presence of high temperatures and/or energy densities, Quantum Chromo Dynamics (QCD) predicts [2] the existence of a new state of the matter in which the degrees of freedom are quarks and gluons, with their behavior described by the QCD asymptotic freedom regime. This state of matter is in contrast to the usual state described by hadronic degrees of freedom and in which quarks and gluons are confined inside the hadrons. The study of this new state of matter, known as Quark–Gluon Plasma (QGP), is the main focus of the heavy-ion collision (HIC) programs at the two large collider complexes, the Relativistic Heavy-Ion Collider (RHIC) at Brookhaven National Laboratory (BNL), in New York, and the Large Hadron Collider (LHC) at the European Organization for Nuclear Research (CERN) near Geneva.

The study of the heavy-ion collisions involves many objectives. The first and main goal is to confirm that QGP is actually produced in heavy-ion collisions. A secondary but also very important goal of heavy-ion collision research at the LHC and RHIC involves understanding the QGP characteristics, including its Equation of state (EoS), identifying the location of the critical point in the phase diagram of nuclear matter, figuring out the temperature and the order of the phase transitions, the extraction of the transport coefficients, and so on. Figure 1.1 presents a schematic of the state of the art in understanding the phase diagram of nuclear matter. It also illustrates the huge efforts set forth, around the world, in understanding the nature and properties of the QGP. These efforts include the current facilities at BNL and CERN, as well as new undertakings at Darmstadt (FAIR) and Dubna (NICA).

This thesis is within the scope of understanding the QGP. Specifically this PhD thesis is focused on the extraction of the QGP transport parameters. Transport parameters drive the medium towards its equilibrium. They allow the propagation of the initial conditions, initial fluctuations and medium fluctuations to the final showers of particles which reach the detectors. The transport parameter footprints are imparted on these measured particles. The cosmology perspective could give additional reach to this approach and to the impact of the QGP transport parameters footprints.

As will be described in Chapter 2, different initiatives have been carried out to extract the values of the QGP transport parameters. Most of these are based on modeling the behavior of the medium created in heavy-ion collisions, usually by hydrodynamics evolution, and then constraining transport parameters by comparing the model predictions to measured data. The relevance of the QGP transport parameters can be probably measured just by the amount of different strategies used to constrain their values. In practice, these approaches always involve uncertainties on the different ingredients which conform each of the used models. Indeed, the choice of a concrete model instead of some other models introduce a certain degree of uncertainty. All this will be covered.

The main goal of this PhD thesis is to extract the QGP transport parameters directly from measured data based on two-particle momentum correlations. The aim is that data will drive the transport parameters extraction and as such their uncertainties. Two-particle correlations are powerful tools not

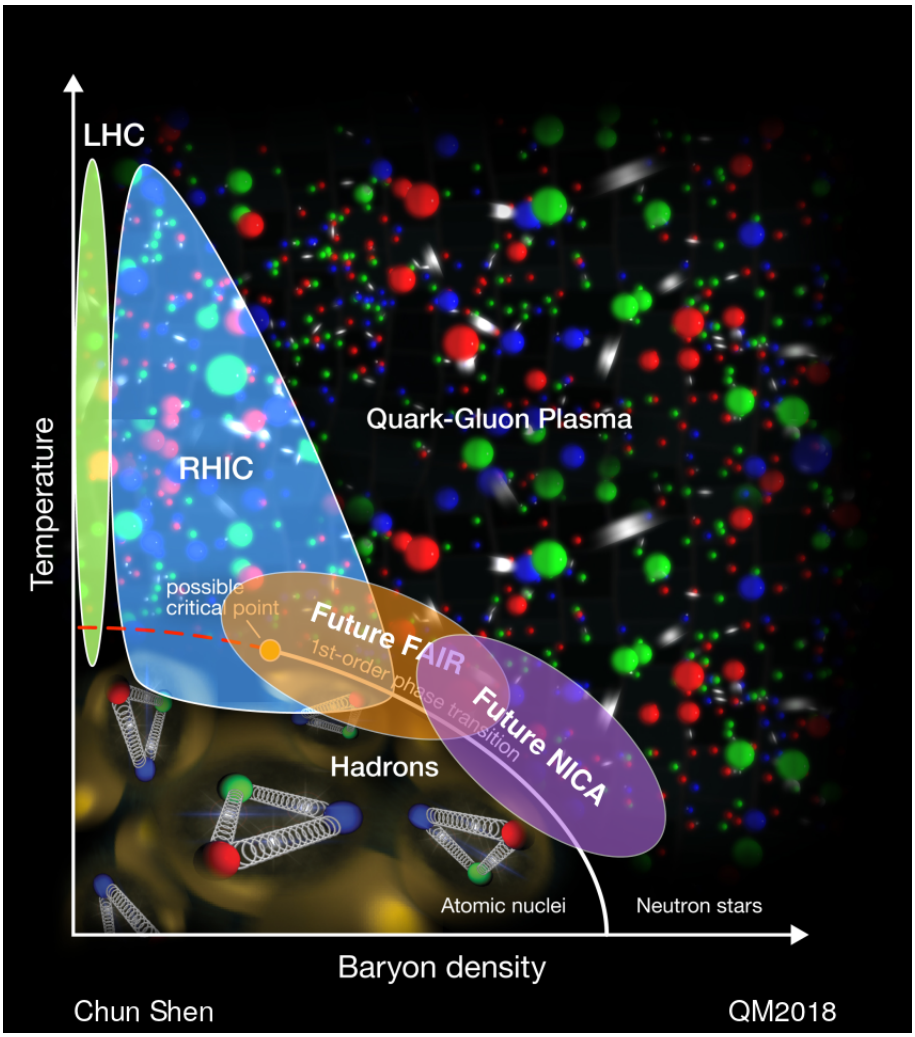

FIGURE 1.1: Phase diagram of hot nuclear matter as a function of baryon density and temperature [3].

just to describe quantitatively detailed aspects of the particle production mechanisms and the underlying system dynamics but also to visualize them and get qualitative insights on these processes. In particular, two-particle momentum correlations with their sensitivity to momentum fluctuations open the door for accessing to the transport dynamics and its connection to QGP transport coefficients. The ultimate goal of this PhD thesis is to extract the transport parameters η/s and ζ/s directly from experimental data by using methods based on two-particle transverse momentum correlations. This method is completely unexplored at LHC energies as well as for small systems as it has only been pursued in one system at RHIC energies, Au–Au collisions at $\sqrt{s_{\mathrm{NN}}} = 200$ GeV. The analysis in "small" systems is quite relevant, given that the question whether QGP is or not produced in pp or in p–Pb collisions is still a matter of active research.

In this introductory chapter, a short description of the current understanding of the evolution of the medium created in heavy-ion collisions is given. Next brief descriptions of the main stages of the models are presented. The effects of shear and bulk viscosity on the evolution of the medium towards its potential equilibrium conclude the description. The structure of this thesis is then briefly introduced.

1.1 The evolution of a heavy-ion collision

This section gives a brief qualitative description of the phases a single nucleus-nucleus collision traverses until it is finally detected as a multitude of tracks within a detector.

In a heavy-ion collision, both nuclei approach each other as two disks, due to Lorentz contraction, of not uniformly distributed set of QGP primordial components nodes. The energy density achieved when these colliding primordial nodes merge creates the conditions for a transition to the QGP phase in a pre-thermalization scenario. In these early stages of the collision, the momentum is predominantly in the beam direction and there are spatial anisotropies linked to the shape of the overlapping area. The medium thermalizes very quickly and the anisotropies build up pressure gradients which drive the medium towards its expansion and eventual cooling. The medium starts to flow. Initially the expansion starts longitudinally, driven by the momentum anisotropy, but the transverse pressure gradients, due to the spatial anisotropy, immediately builds up the transverse expansion. The interplay between the viscous evolution and pressure gradients drives the expansion and cooling in both the longitudinal and the transverse dimensions.

As the system expands, it becomes gradually more dilute and cold, and at some point, can no longer be described as a flowing medium. Neither the temperature nor the energy density are any longer able to keep the system in a de-confined state and the transition to the hadronic, confined state, suddenly happens. The system is still interacting but its chemical composition has settled down. The chemical freeze-out occurs. The system is now an hadron gas, which expands and cools while its components still interact. At some point during this expansion, interaction cease, the kinetic freeze-out occurs, and hadrons freely stream out to eventually reach the active parts of the detector.

The fact that the medium thermalizes makes it possible to use hydrodynamics to model the evolution of the collision system. Ideally, a description from first principles would be the preferred approach. The QCD Lagrangian density is given by [4]

$$\mathcal{L} = \bar{\psi}(i\,\gamma \not{D}_{ij} - m\,\delta_{ij})\,\psi_j - \frac{1}{4}\,G^{\alpha}_{\mu\nu}G^{\mu\nu}_{\alpha} \tag{1.1}$$

where ψ is a quark field, $\not{D} = \gamma_\mu D^\mu$ where γ^μ are the Dirac matrices and D^μ a covariant derivative, m is a quark mass, δ is a Kronecker delta, and $G^{\mu\nu}_{\alpha}$ are the gluon fields, with $\alpha = 1, \ldots, 8$. Although looking simple, it is hard to make any prediction directly from QCD in HIC. Instead, hydrodynamics as a phenomenological theory, has demonstrated its ability to reproduce measurable observables.

1.2 Modeling the collision system evolution

Modeling the evolution of the medium produced in relativistic heavy-ion collisions (rHIC) requires a quantitative description of the different stages mentioned in the previous section. The complete model framework can be divided into four parts: pre-equilibrium dynamics, viscous hydrodynamic evolution, transition from fluid to particles, and final hadronic transport [5].

The pre-equilibrium stage is the initial stage of the system from instants before the nuclei collide and until the medium can be considered thermalized and the viscous hydrodynamic evolution stage starts. Modeling of the pre-equilibrium stage generally involves a quantitative description, but usually somewhat ad hoc, of the initial distributions of QCD matter in both colliding nuclei. It also involves modeling of the subsequent evolution of the colliding QCD matter according to QCD physics. The description of the distribution of matter is usually based on models of nuclear density distributions and considers the nuclear thickness in order to distribute the nucleons. The introduction of event-by-event (EbyE) fluctuations in the initial distributions makes each event unique and emulates the actual experimental conditions where collisions with apparently isotropic overlap areas show collective behavior. The model might then go down to a deeper description of the colliding matter. From the simplest models, describing

collisions as sets of individual nucleon–nucleon collisions determined by the nucleon–nucleon cross section, to the more detailed one involving individual color charge/fields distributions and interactions. Depending on the level of detail, there will be a more or less complex evolution from the instant at which the collision actually happens, $\tau = 0$, and the time at which the expanding system is considered thermalized, $\tau = \tau_0$. The initial conditions set the stage for the hydrodynamic evolution. In general, they depend on the complexity of the pre-equilibrium stage modeling but they should include, at time $\tau = \tau_0$ when the system is assumed to have thermalized, the energy/entropy density distribution, the fluid flow velocity, the shear–stress tensor and the bulk viscous pressure, although few of these quantities may set to zero for simplicity's sake in some models.

The viscous hydrodynamic evolution usually involves solving causal second order viscous hydrodynamic equations. In the simplest viscous models, the system evolution is described in terms of equations of 1+1 dimensions, where the first 1 represents the radial (spatial) dimension, and the second 1 represents the temporal dimension. In such cases, only shear viscous effects are included and the complexity of 3D evolution is neglected. More comprehensive models include 2 or 3 spatial dimensions. The latter are denoted as 3+1 models. They include terms that couple the shear–stress tensor and the bulk viscous pressure. Apart from the initial conditions provided by the previous stage, a key ingredient of the hydrodynamic evolution is the equation of state (EoS), which establishes the dependence of the energy density on the pressure. Models vary in their handling of the EoS. The simplest models describe the system as an ideal gas but more sophisticated calculations include various parametrizations of the lattice QCD EoS. In the most advanced models, the evolution of η/s and ζ/s with the temperature is also parametrized. Hydrodynamic models evolve the system from initial conditions untill the chemical freeze-out. The chemical freeze-out is defined as a switching condition which depends on the model. It is usually chosen to correspond to a specific temperature, $T_{\rm sw}$, but it can also be implemented in terms of a specific value of the energy or entropy densities, or a specific elapsed system-evolution time. At this point, a chemical freeze-out takes place.

The transition from fluid to particles, often called **particlization**, emulates the smooth crossover transition where quarks and gluons combine into hadrons when the diluted system cools down below the critical temperature. The process is modeled with the Cooper-Frye prescription [6], which scans the energy density on a hypersurface and converts it into hadron momentum distributions. At this point, the hydrodynamic description of the system is switched to an hadronic and kinetic description. Such a transition has to be performed in a space–time region in which both are within their domain of applicability. Some of the latest models also incorporate viscous corrections into the particlization process at this point.

The last modeling stage involves the microscopic hadronic cascade simulation of the interaction and propagation of hadrons produced at chemical freeze-out. This evolution carries the system from chemical freeze-out towards a stage known as kinetic freeze-out, where all interactions cease and all unstable and short lived resonances have decayed. There are models in which the hadronic evolution has its own EoS, which should then match with the one used in the viscous hydrodynamic stage at the crossover temperature. Some models also incorporate viscous effects corrections with their own η/s and ζ/s parametrizations.

1.3 Effects of shear viscosity and bulk viscosity

The shear viscosity acts against the deformation or non isotropic expansion of a fluid element while the bulk viscosity acts against the expansion or compression of the fluid. Bulk viscosity causes locally isotropic deviations from equilibrium. In an isotropically expanding fireball, bulk viscosity counteracts the expansion reducing the radial flow acceleration and thus inhibiting the build-up of radial flow. Shear viscosity causes locally anisotropic deviations from equilibrium. Shear viscosity tries to equalize the expansion rates along different directions by building up a shear viscous pressure in the local rest frame.

In relativistic heavy-ion collisions, the initial expansion rate is highly anisotropic and much larger along the beam direction than in the transverse plane. In this initial phase, the shear viscous pressure reduces the longitudinal and increases the transverse pressure. QGP cools less rapidly in its longitudinal expansion but the build-up of transverse flow is increased. Transverse anisotropies in the initial fireball geometry, reflected in anisotropic transverse pressure gradients, generate anisotropies in the developing transverse flow; the shear viscous pressure reduces these flow anisotropies, i.e. it degrades the medium's ability to convert initial transverse pressure anisotropies into final transverse flow anisotropies [7]. The combination of low specific shear viscosity of the QGP with system's lifetime allows traces of the initial fluctuations to survive the dissipative evolution and appear as anisotropies in the final state measured magnitudes.

1.4 The structure of this thesis

In addition to this introductory chapter this thesis is organized as follows. The methods to extract the transport properties of the QGP are described in Chapter 2. A basic description of the ideal and viscous hydrodynamics is given at the beginning. Then, a brief introduction to the terminology and main applicable variables used experimentally in relativistic heavy-ion collisions, gives place to an overview of the different attempts of constraining the medium transport parameters by comparing model predictions to measured data. The method of extracting the values of those transport parameters directly from measured data, i.e. those used in this PhD thesis, based on two-particle transverse momentum correlations, is then described. First, a brief introduction to two-particle correlations is given and then the description of the actual methods concludes the chapter.

The apparatus used for collecting the data utilized to elaborate the results presented in this thesis, the ALICE detector, is briefly introduced in Chapter 3. A short description of the main detector components is followed by a brief synthesis of how collision events are selected, reconstructed and characterized. To finalize, the main components of the software (SW) framework are shortly described. Chapter 4 describes the data sets and the Monte Carlo (MC) simulations utilized and the criteria for selecting events and tracks within them.

The full methodology to measure two-particle transverse momentum correlation is elaborated in Chapter 5 where the detailed description of the procedures followed to extract the results presented in this thesis is described. Special attention is given there to the extraction of the systematic uncertainties. Chapter 6 and Chapter 7 cover the main results for Pb–Pb collisions and for small systems, p–Pb and pp. The discussions of the results and their further elaboration are presented in Chapter 8. To finally give place to the conclusions and outlook in Chapter 9.

Chapter 2

Transport properties of the QGP

As the QGP behaves as a fluid, the hydrodynamic description is fundamental for the interpretation of the measured results. This chapter starts with a brief description of the modeling of a relativistic fluid by means of relativistic hydrodynamic equations. First, ideal hydrodynamics is introduced, and then, viscous hydrodynamics is elaborated. The equations defining fluid properties like shear and bulk viscosity are also presented. Then a brief introduction to the main terminology and observables used on the field of relativistic heavy-ion collisions is given. The different ways of extracting the QGP transport parameters are then exposed. Namely, a brief survey of the different attempts for extracting the fluid properties, by comparing model predictions with actual measured data, is presented. Finally, the proposed methods for directly extracting fluid properties directly from two-particle correlations measurements are described. First a brief introduction on two-particle correlations is given and then, the actual methods are explained.

2.1 Basic relativistic hydrodynamics

2.1.1 Ideal hydrodynamics

The energy–momentum tensor and projection operators

The energy–momentum tensor, $T^{\mu\nu}$, of an ideal relativistic fluid has to be built out of the hydrodynamic degrees of freedom, namely two Lorentz scalars, the energy density, ϵ, and the hydrostatic pressure, p, and one vector, the fluid four–velocity, u^μ, as well as the metric tensor g [8]. $T^{\mu\nu}$ describes the distribution of energy and momentum in the system. $T^{\mu\nu}$ is symmetric and transforms as a tensor under Lorentz transformations. The time–time component T^{00} is the energy density. The time–space component, $T^{0i} = T^{i0}$ is the momentum density. The space–space component, $T^{ij} = T^{ji}$, is the momentum flux density. The momentum flux through a surface element $\mathrm{d}\vec{s}$ is just the force acting on this surface element then, $T^{ij}\mathrm{d}s_j$ is the force acting on the surface element $\mathrm{d}\vec{s}$. In the local rest frame of an ideal fluid volume element, T^{00} is the proper energy density, ϵ, the momentum density should be vanishing $T^{0i} = T^{i0} = 0$ and the pressure exerted by a given portion of the fluid is the same in all directions and everywhere perpendicular to the surface on which acts so, $T^{ij}\mathrm{d}s_j = p\mathrm{d}s_i \rightarrow T^{ij} = p\delta^{ij}$ [9]. Then, in an arbitrary reference frame the stress energy tensor for an ideal relativistic fluid reads as

$$T^{\mu\nu} = (\epsilon + p)\, u^\mu u^\nu - p\, g^{\mu\nu} \tag{2.1}$$

with p the isotropic pressure in the rest frame and $g^{\mu\nu} = \mathrm{diag}\,(1, -1, -1, -1)$ the metric tensor.

In the local rest frame the fluid four–velocity

$$u^\mu = (1, 0, 0, 0) \tag{2.2}$$

then, on any reference frame

$$u^\mu u_\mu = 1 \tag{2.3}$$

It is useful to define two projection operators, one along the fluid four–vector, which is the own u^μ, and another along the space–time surface orthogonal to the fluid four vector

$$\Delta^{\mu\nu} = (g^{\mu\nu} - u^\mu u^\nu) \tag{2.4}$$

where trivially, both operators behave accordingly to projection operators

$$u^\mu u_\mu = 1 \tag{2.5}$$

$$\begin{aligned}\Delta^{\mu\nu}\Delta^\alpha_\nu &= (g^{\mu\nu} - u^\mu u^\nu)(g^\alpha_\nu - u_\nu u^\alpha) \\ &= (g^{\mu\nu} g^\alpha_\nu - u^\mu u^\nu g^\alpha_\nu - u^\alpha u_\nu g^{\mu\nu} + u^\mu u^\nu u^\alpha u_\nu) \\ &= (g^{\mu\alpha} - u^\mu u^\alpha) \\ &= \Delta^{\mu\alpha}\end{aligned} \tag{2.6}$$

so, for any tensor $A^{\mu\nu}$,

$$A^{\mu\nu} u_\mu u^\mu u_\mu = A^{\mu\nu} u_\mu \tag{2.7}$$

$$\begin{aligned}A^{\mu\nu}\Delta^\alpha_\nu\Delta^\beta_\alpha &= (A^{\mu\alpha} - A^{\mu\nu}u^\alpha u_\nu)(g^\beta_\alpha - u^\beta u_\alpha) \\ &= A^{\mu\beta} - A^{\mu\nu}u^\beta u_\nu - A^{\mu\alpha}u^\beta u_\alpha + A^{\mu\nu}u^\alpha u_\nu u^\beta u_\alpha \\ &= A^{\mu\beta} - A^{\mu\nu}u^\beta u_\nu \\ &= A^{\mu\nu}\Delta^\beta_\nu,\end{aligned} \tag{2.8}$$

and are, as expected, orthogonal

$$\Delta^{\mu\nu} u_\nu = (g^{\mu\nu} - u^\mu u^\nu) u_\nu = u^\mu - u^\mu u^\nu u_\nu = \Delta^{\mu\nu} u_\mu = 0. \tag{2.9}$$

With the projection operators the ideal fluid energy momentum tensor stays as

$$T^{\mu\nu} = \epsilon u^\mu u^\nu - p\Delta^{\mu\nu}. \tag{2.10}$$

The fundamental equations

The basic hydrodynamic equations, in the absence of external sources, are extracted from the conservation of the energy–momentum

$$\partial_\mu T^{\mu\nu} = 0 \tag{2.11}$$

and from the current conservation

$$\partial_\mu j^\mu_Q = 0 \tag{2.12}$$

where j^μ_Q is the conserved current of the conserved quantity Q which could be the electric charge, the strangeness, the baryon number, etc.

Making use of the projection operators

$$u_\nu \partial_\mu T^{\mu\nu} = 0 \rightarrow (\epsilon + p)\partial_\mu u^\mu + u^\mu \partial_\mu \epsilon = 0 \tag{2.13}$$

$$\Delta^\alpha_\nu \, \partial_\mu T^{\mu\nu} = 0 \rightarrow (\epsilon + p) u^\mu \partial_\mu u^\alpha - \Delta^{\mu\alpha}\partial_\mu p = 0 \tag{2.14}$$

where the result $0 = \partial_\nu u_\mu u^\mu = 2u^\mu \partial_\nu u_\mu = 2u_\mu \partial_\nu u^\mu \rightarrow u_\mu \partial_\nu u^\mu = u^\mu \partial_\nu u_\mu = 0$ has been used.

By defining the conserved current

$$j^\mu_Q = n_Q u^\mu \tag{2.15}$$

where n_Q is the charge Q density, introducing the first law of thermodynamics

$$\epsilon + p = Ts + \mu n_Q \tag{2.16}$$

where T is the temperature, s the entropy density, and μ_Q is the chemical potential of the species with charge Q, and using the Gibbs-Duhem relation

$$n_Q \partial_\nu \mu_Q = -s\partial_\nu T + \partial_\nu p, \tag{2.17}$$

Eq. (2.13) gives

$$\begin{aligned}
0 &= u_\mu \partial_\nu T^{\nu\mu} \\
&= (\epsilon + p)\partial_\nu u^\nu + u^\nu \partial_\nu \epsilon \\
&= (Ts + \mu n_Q)\partial_\nu u^\nu + u^\nu \partial_\nu (Ts + \mu n_Q - p) \\
&= T(s\partial_\nu u^\nu + u^\nu \partial_\nu s) + \mu (n_Q \partial_\nu u^\nu + u^\nu \partial_\nu n_Q) + s u^\nu \partial_\nu T + n_Q u^\nu \partial_\nu \mu - u^\nu \partial_\nu p \\
&= T\partial_\nu (s u^\nu) + \mu \partial_\nu (n_Q u^\nu) + u^\nu (n_Q \partial_\nu \mu_Q + s\partial_\nu T - \partial_\nu p) \\
&= T\partial_\nu (s u^\nu)
\end{aligned} \tag{2.18}$$

where in the third line Eq. (2.16) has been used, and in the fifth one the Eqs. (2.15), (2.12), and (2.17) have been used. Introducing the entropy current as

$$S^\mu = s u^\mu \tag{2.19}$$

Eq. (2.18) reads

$$\partial_\mu S^\mu = 0. \tag{2.20}$$

Hence, in ideal relativistic hydrodynamic, the entropy is conserved.

By introducing the projection derivatives, along the fluid flow

$$D = u^\mu \partial_\mu, \tag{2.21}$$

and orthogonal to the fluid flow

$$\nabla^\alpha = \Delta^{\mu\alpha} \partial_\mu \tag{2.22}$$

so that

$$\partial_\mu = u_\mu D + \nabla_\mu, \tag{2.23}$$

the fundamental equations for ideal relativistic hydrodynamic, Eqs. (2.13) and (2.14), take the compact form

$$D\epsilon + (\epsilon + p)\partial_\mu u^\mu = 0 \tag{2.24}$$

$$(\epsilon + p) D u^\alpha - \nabla^\alpha p = 0 \tag{2.25}$$

where Eqs. (2.24) and (2.25) are the relativistic versions of the continuity equation and of the Euler equation, respectively.

2.1.2 Viscous hydrodynamics

Landau and Eckart frames

The ideal relativistic hydrodynamic flow is uniquely determined since the local fluxes of the energy and the charge densities are in the same direction. According to Eqs. (2.10) and (2.15)

$$T^{\mu\nu}u_\nu = \epsilon u^\mu \tag{2.26}$$

$$j^\mu_Q = n_Q u^\mu, \tag{2.27}$$

the energy density is an eigenvalue of the energy–momentum tensor with u^μ, the flow vector, as its eigenvector, pointing in the same direction that the conserved current. The presence of viscous effects leads to the separation of the two local fluxes. As will be seen, additional terms are incorporated to both, Eqs. (2.26) and (2.27). The denominated Landau frame [9] is chosen in the direction of the total energy flux in a way that the viscous effects are manifested on the orthogonal space, $T^\mu_\nu u^\nu_{\rm L} = \epsilon u^\mu_{\rm L}$. The Eckart frame is chosen in the direction in which the total conserved charge flux is not affected by viscous effects, $j^\mu_Q = n_{Q\rm E}u^\mu_{\rm E}$ [10]. These choices reflect the freedom of defining the local rest frame either as the frame where the energy density (Landau) or the charge density (Eckart) is at rest [8]. In what follows the Landau frame is assumed.

The relativistic Navier-Stokes equation

The presence of dissipative processes incorporates additional, dissipative, terms in the energy-momentum tensor and in the conserved current [9]

$$T^{\mu\nu} = \epsilon u^\mu u^\nu - p\Delta^{\mu\nu} + \Pi^{\mu\nu} \tag{2.28}$$

$$j^\mu_Q = n_Q u^\mu + \nu^\mu_Q \tag{2.29}$$

with $\Pi^{\mu\nu}$ the viscous stress tensor, which incorporates the viscous dissipation effects, and ν^μ incorporating the dissipative effects in the particle flow. Taking the same approach as before, i.e. projecting the conservation of the energy–momentum tensor equations $\partial_\mu T^{\mu\nu} = 0$ along the flow vector and its orthogonal space, gives

$$u_\nu \partial_\mu T^{\mu\nu} = (\epsilon + p)\partial_\mu u^\mu + D\epsilon + u_\nu \partial_\mu \Pi^{\mu\nu} = 0 \tag{2.30}$$

$$\Delta^\alpha_\nu \partial_\mu T^{\mu\nu} = (\epsilon + p)Du^\alpha - \nabla^\alpha p + \Delta^\alpha_\nu \partial_\mu \Pi^{\mu\nu} = 0 \tag{2.31}$$

where the definitions of the derivatives along the flow, Eq. (2.21), and orthogonal to it, Eq. (2.22), have been used. Eqs. (2.30) and (2.31) are the relativistic versions of the Navier-Stokes equation.

The shape of the energy–momentum tensor and of the conserved current are imposed by the second law of thermodynamics which states that entropy must always locally increase. In Landau frame all viscous contributions are orthogonal to the flow vector, then,

$$u_\mu T^{\mu\nu} = \epsilon u^\nu \rightarrow u_\mu \Pi^{\mu\nu} = 0. \tag{2.32}$$

Using the symmetrization notation

$$A_{(\mu}B_{\nu)} = \frac{1}{2}\left(A_\mu B_\nu + A_\nu B_\mu\right), \tag{2.33}$$

Eq. (2.32) gives

$$\begin{aligned} u_\nu \partial_\mu \Pi^{\mu\nu} &= -\Pi^{\mu\nu} \partial_{(\mu} u_{\nu)} \\ &= -\Pi^{\mu\nu} \nabla_{(\mu} u_{\nu)} \end{aligned} \tag{2.34}$$

where the Landau frame and the symmetry of $\Pi^{\mu\nu}$ have been used.

Following then the same treatment as in the ideal case considering the expression of the first law of thermodynamics (Eq. (2.16)) and the Gibbs-Duhem relation (Eq. (2.17)), the conservation of the energy–momentum tensor along the flow vector (in Eq. (2.30)) gives

$$\begin{aligned} 0 &= (Ts + \mu n_Q)\, \partial_\mu u^\mu + D\,(Ts + \mu n_Q - p) - \Pi^{\mu\nu} \nabla_{(\mu} u_{\nu)} \\ &= T(s \partial_\mu u^\mu + Ds) + \mu\,(n_Q \partial_\mu u^\mu + D n_Q) + sDT + n_Q D\mu - Dp - \Pi^{\mu\nu} \nabla_{(\mu} u_{\nu)} \\ &= T \partial_\mu\,(s u^\mu) + \mu\, \partial_\mu \left(n_Q u^\mu\right) - \Pi^{\mu\nu} \nabla_{(\mu} u_{\nu)} \\ &= \partial_\mu\,(s u^\mu) - \frac{1}{T}\,\mu\, \partial_\mu \nu_Q^\mu - \frac{1}{T}\,\Pi^{\mu\nu} \nabla_{(\mu} u_{\nu)} \\ &= \partial_\mu \left(s u^\mu - \frac{1}{T} \mu\, \nu_Q^\mu\right) + \nu_Q^\mu \nabla_\mu \left(\frac{\mu}{T}\right) - \frac{1}{T}\,\Pi^{\mu\nu} \nabla_{(\mu} u_{\nu)} \end{aligned} \tag{2.35}$$

where Eqs. (2.16) and (2.34) have been used in the first line, Eq. (2.17) in the third line and the conservation of the current in Eq. (2.29), $\partial_\mu j_Q^\mu = 0$, has been used in the last line.

From Eq. (2.35)

$$\partial_\mu \left(s u^\mu - \frac{1}{T} \mu\, \nu_Q^\mu\right) = \frac{1}{T}\,\Pi^{\mu\nu} \nabla_{(\mu} u_{\nu)} - \nu_Q^\mu \nabla_\mu \left(\frac{\mu}{T}\right) \tag{2.36}$$

where the left-hand side (LHS) is interpreted as the change in the entropy flux so that the right-hand side (RHS) must be the increase in entropy owing to dissipative processes [9]. It has to be strictly positive, conditioning the shape of the dissipative parts of the energy–momentum tensor, $\Pi^{\mu\nu}$, and of the four-current, ν^μ.

The viscous stress tensor $\Pi^{\mu\nu}$ is usually decomposed into the sum of the shear stress tensor, $\pi^{\mu\nu}$, traceless, plus a remainder, with non-vanishing trace, which incorporates the bulk pressure, Π

$$\Pi_\mu^\mu = \pi_\mu^\mu + \Delta_\mu^\mu \Pi \rightarrow \Pi = \frac{1}{3} \Pi_\mu^\mu \tag{2.37}$$

then

$$\Pi^{\mu\nu} = \pi^{\mu\nu} + \Delta^{\mu\nu} \Pi. \tag{2.38}$$

The Landau frame condition Eq. (2.32) then reads

$$0 = u_\mu \Pi^{\mu\nu} = u_\mu \pi^{\mu\nu}. \tag{2.39}$$

Analogously the tensor $\nabla_{(\mu} u_{\nu)}$ is separated in a traceless part, $\nabla_{<\mu} u_{\nu>}$, and a non vanishing trace part, trivially,

$$\nabla_{(\mu} u_{\nu)} = \nabla_{<\mu} u_{\nu>} + \frac{1}{3} \Delta_{\mu\nu} \nabla_\alpha u^\alpha. \tag{2.40}$$

With these decompositions Eq. (2.36) gives

$$\begin{aligned}\partial_\mu \left(s u^\mu - \frac{1}{T}\mu\, v_Q^\mu \right) &= \frac{1}{T}\,(\pi^{\mu\nu} + \Delta^{\mu\nu}\Pi)\left(\nabla_{<\mu} u_{\nu>} + \frac{1}{3}\Delta_{\mu\nu}\nabla_\alpha u^\alpha\right) - v_Q^\mu \nabla_\mu \left(\frac{\mu}{T}\right) \\ &= \frac{1}{T}\,\pi^{\mu\nu}\nabla_{<\mu} u_{\nu>} + \frac{\Pi}{T}\,\nabla_\alpha u^\alpha - v_Q^\mu \nabla_\mu \left(\frac{\mu}{T}\right) \end{aligned} \tag{2.41}$$

where the $\pi^{\mu\nu}\Delta_{\mu\nu}\nabla_\alpha u^\alpha$ term vanishes due to the traceless nature of $\pi^{\mu\nu}$ and to the Landau frame condition (Eq. 2.39), the term $\Delta^{\mu\nu}\Pi\nabla_{<\mu} u_{\nu>}$ vanishes due to orthogonality, and, trivially, $\Delta^{\mu\nu}\Delta_{\mu\nu} = 3$. Then, introducing the phenomenological definitions, so-called *constitutive equations*, for the shear stress tensor, $\pi^{\mu\nu}$, the bulk pressure, Π, and the diffusive part of the four-current, v^ν,

$$\pi^{\mu\nu} = \eta \nabla^{<\mu} u^{\nu>} \tag{2.42}$$

$$\Pi = \zeta \nabla_\alpha u^\alpha \tag{2.43}$$

$$v_Q^\mu = -\kappa \left(\frac{n_Q T}{\epsilon + p}\right) \nabla^\mu \left(\frac{\mu}{T}\right) \tag{2.44}$$

where $\eta \geq 0$ is the shear viscosity, $\zeta \geq 0$ is the bulk viscosity, and $\kappa \geq 0$ is the thermal conductivity, the positiveness of the change of the entropy flux in Eq. (2.36) is guaranteed. As it will be seen now, the relativistic Navier-Stokes equation violates causality.

Acausality of Navier-Stokes equation

Considering a charge free system and considering small perturbation which, in principle, only depend on one space coordinate and time[1]

$$\epsilon = \epsilon_0 + \delta\epsilon(t, x) \tag{2.45}$$
$$u^\mu = u_0^\mu + \delta u^\mu(t, x) \tag{2.46}$$
$$p = p_0 + \delta p(t, x), \tag{2.47}$$

the constitutive equations, Eqs. (2.42) and (2.43), give

$$\Pi = -\zeta_0\, \partial_x\, \delta u^x \tag{2.48}$$
$$\pi^{\mu\nu} = -\eta_0 \left(\delta^{x\mu}\, \partial_x\, \delta u^\nu + \delta^{x\nu}\, \partial_x\, \delta u^\mu + \frac{2}{3} g^{\mu\nu}(1 - \delta^{t\mu}\delta^{t\nu})\partial_x\, \delta u^x \right) \tag{2.49}$$
$$\tag{2.50}$$

to first order in δu. Then, the Navier-Stokes equation along the y dimension,

$$(\epsilon_0 + p_0)\, \partial_t \delta u^y - \eta_0 \partial_x^2 \delta u^y = 0, \tag{2.51}$$

to first order in δu, is a diffusion-type evolution equation for the perturbation δu^y. Considering a $\delta u \propto e^{-\omega t + ikx}$ wave *ansatz* in Eq. (2.51) to investigate the individual modes of this diffusion process [8], the dispersion relation

$$\omega = \frac{\eta_0}{\epsilon_0 + p_0} k^2 \tag{2.52}$$

of the diffusion equation is obtained. Eq. (2.52) can be used to estimate the speed of diffusion of a mode with wavenumber k

$$v(k) = \frac{\mathrm{d}\omega}{\mathrm{d}k} = 2\, \frac{\eta_0}{\epsilon_0 + p_0} k \tag{2.53}$$

[1] Following relations are trivial but useful. In the fluid element rest frame where $u_0^\mu = (1, 0, 0, 0)$

$$\partial_\nu u^\mu = \partial_\nu (u_0^\mu + \delta u^\mu) = \delta_\nu^t\, \partial_t\, \delta u^\mu + \delta_\nu^x\, \partial_x\, \delta u^\mu$$

in particular

$$\partial_\mu u^\mu = \partial_t\, \delta u^t + \partial_x\, \delta u^x$$

and

$$D\, u^\mu = u^\nu\, \partial_\nu\, u^\mu = \partial_t\, \delta u^\mu + O(\delta^2).$$

The orthogonal projector

$$\begin{aligned} \Delta^{\mu\nu} &= g^{\mu\nu} - (u_0 + \delta u)^\mu (u_0 + \delta u)^\nu) \\ &= g^{\mu\nu}(1 - \delta^{t\mu}\delta^{t\nu}) + (\delta^{t\mu} - 1)\, \delta^{t\nu}\, \delta u^\mu + (\delta^{t\nu} - 1)\, \delta^{t\mu}\, \delta u^\nu + O(\delta^2) \end{aligned}$$

Then, for any magnitude p

$$\nabla^\mu p = \Delta^{\mu\nu} \partial_\nu\, (p_0 + \delta p) = -\delta^{\mu x} \partial_x\, \delta p + O(\delta^2)$$

(remember, $\delta = \delta(t, x)$ only), and in particular

$$\nabla_\mu u_\nu = \delta_\mu^x\, \partial_x\, \delta u_\nu + O(\delta^2)$$

and then

$$\Delta^{\mu\nu} \nabla_\alpha u^\alpha = g^{\mu\nu}(1 - \delta^{t\mu}\delta^{t\nu})\partial_x\, \delta u^x + O(\delta^2)$$

therefore

$$\nabla_{<\mu} u_{\nu>} = \frac{1}{2} \left(\delta_\mu^x\, \partial_x\, \delta u_\nu + \delta_\nu^x\, \partial_x\, \delta u_\mu \right) - \frac{2}{3} g_{\mu\nu}(1 - \delta_{t\mu}\delta_{t\nu})\partial_x\, \delta u^x + O(\delta^2).$$

which grows with k without limit. Therefore the relativistic Navier-Stokes equation does not constitute a causal theory because exhibits unphysical behavior for the short wavelength ($k \gg 1$) modes. The actual issue is not the causal violation, which could be overcome by restricting the modeling to the long wavelength modes, but in the instabilities in the numerical solutions for the short wavelength models which are usually needed when dealing with complicated flow profiles [8].

One way to regulate this behavior is to introduce a second order in the gradients correction for the viscous stress tensor

$$\tau_\pi \partial_t \Pi^{xy} + \Pi^{xy} = -\eta_0 \partial_x \delta u^y \tag{2.54}$$

where τ_π is a new transport coefficient referred as relaxation time. With Eq. (2.54), referred as the Maxwell-Cattaneo law [11], the Navier-Stokes equation now reads

$$(\epsilon_0 + p_0)\partial_t^2 \, \delta u^y + \frac{\epsilon_0 + p_0}{\tau_\pi} \partial_t \, \delta u^y - \frac{\eta_0}{\tau_\pi} \partial_x^2 \, \delta u^y = 0 \tag{2.55}$$

to first order in δu, and, by using the same wave *ansatz*, the obtained dispersion relation reads

$$\omega = \frac{\eta_0}{\epsilon_0 + p_0} \frac{k^2}{1 - \omega \tau_\pi}. \tag{2.56}$$

It is interesting to highlight that for large frequency $\omega \gg 1$ Eq. (2.56) does not describe diffusive behavior, but instead propagating waves with a propagation speed that is finite in the limit of $k \gg 1$,

$$v^{\max} \equiv \lim_{k \to \inf} \frac{\mathrm{d}|\omega|}{\mathrm{d}k} = \sqrt{\frac{\eta_0}{(\epsilon_0 + p_0)\, \tau_\pi}} \tag{2.57}$$

Müller-Israel-Stewart theory

The shape of the viscous stress tensor and of the viscous correction to the conserved current were obtained by considering the system in equilibrium. By using the first law of thermodynamics and the Gibbs-Duhem relation, the form of the entropy density current was extracted. By enforcing its increase according to the second law of thermodynamics the phenomenological constitutive equations were inferred and the viscous terms gained their shape. This procedure which only considers first order in the gradients in the expression of the entropy density current is valid in circumstances where space-time gradients and viscous stress are negligible, i.e., under quasistationary conditions. To infer the correct linear phenomenological laws from the expression for the entropy production, the latter is required to second order [12, 13].

Incorporating second order in gradients terms to the expression of the entropy current, assuming that deviations from equilibrium are not too large so that high order terms can be neglected, the entropy current for a charge free system adopts the form [8]

$$s^\mu = s u^\mu - \frac{\beta_0}{2T} u^\mu \Pi^2 - \frac{\beta_2}{2T} u^\mu \pi_{\alpha\beta} \pi^{\alpha\beta} + O\left(\Pi^3\right) \tag{2.58}$$

with β_0 and β_2 quantifying the contribution of the second order terms. Following a similar procedure using again the relativistic Navier-Stokes equation Eq. (2.30), the first law of thermodynamics Eq. (2.16), and the Gibbs-Duhem relation Eq. (2.17), the condition of increase of the entropy current allows to extract the new shape of the viscous stress tensor [8]

$$\pi^{\mu\nu} = \eta \left(\nabla^{<\mu} u^{\nu>} - \pi^{\mu\nu} \, TD\left(\frac{\beta_2}{T}\right) - 2\beta_2 D \, \pi^{\mu\nu} - \beta_2 \pi^{\mu\nu} \, \partial_\alpha u^\alpha \right), \qquad \eta \geq 0 \tag{2.59}$$

$$\Pi = \zeta \left(\nabla_\alpha u^\alpha - \frac{1}{2} \Pi TD\left(\frac{\beta_0}{T}\right) - \beta_0 D\Pi - \frac{1}{2}\beta_0 \Pi \partial_\alpha u^\alpha \right), \qquad \zeta \geq 0 \tag{2.60}$$

Length scales and validity of hydrodynamic approximation

In kinetic theory the evolution of a medium is microscopically described following the evolution of the single particle distribution function $f(x,p)$ which gives the probability of finding a particle with four momentum p^μ at space-time position x^ν. Classical kinetic theory is valid if the interaction among the constituents is weak, or equivalently, if the mean free path, $\lambda_{\rm mfp}$, the mean distance between two consecutive particle interactions, is sufficiently large. Hydrodynamics works best for systems made of strongly interaction constituents [14].

A relativistic system of (almost) massless degrees of freedom can be characterized by two microscopic length scales, the thermal wavelength $\lambda_{\rm th} \sim 1/T$ and the above mean free path, whose ratio characterizes the magnitude of the transport coefficients [14]

$$\frac{\lambda_{\rm mfp}}{\lambda_{th}} \sim \frac{\eta}{s}, \frac{\zeta}{s}, \frac{T\kappa}{s}. \tag{2.61}$$

In terms of this ratio three regimes of microscopic dynamics can be defined [14]

1. Dilute gas regime
$$\frac{\lambda_{\rm mfp}}{\lambda_{th}} \sim \frac{\eta}{s} \gg 1 \tag{2.62}$$
or weak coupling regime, where the microscopic kinetic theory can be applied.

2. Dense gas regime
$$\frac{\lambda_{\rm mfp}}{\lambda_{th}} \sim \frac{\eta}{s} \sim 1 \tag{2.63}$$
or moderate coupling regime, where the interactions happen on the $\lambda_{\rm th}$ scale and the microscopic kinetic theory must be replaced by a quantum kinetic approach.

3. Liquid regime
$$\frac{\lambda_{\rm mfp}}{\lambda_{th}} \sim \frac{\eta}{s} \ll 1 \tag{2.64}$$
or strong coupling regime where the system has no well-defined quasi-particles and no valid kinetic theory description.

Therefore, η/s, ζ/s, and $T\kappa/s$, not only provide dimensionless values for the shear and bulk viscosity and the heat conductivity, also allow their comparison among different systems of diverse entropy density, and give a measure of the validity of the hydrodynamic description. These are the values that will be addressed in this thesis.

Now that the hydrodynamic basis has been established the next section will give a brief introduction to the main terminology and observables on the field of relativistic heavy-ion collisions which are used along this thesis.

2.2 Relativistic heavy-ion collisions

2.2.1 Kinematic variables

What is ultimately measured by a detector as ALICE, described in Chapter 3, from a relativistic heavy-ion collision, is a set of charged tracks each of a given momentum, $\vec{p}$, in GeV/c units. The number of measured tracks can easily reach the few thousand figure. The momentum, $\vec{p}$, is assigned to the track in its DCA to the interaction vertex (or to the secondary vertex if applicable). Particle identification techniques, as described in sect. 3.10, allow to assign a concrete mass, m, in GeV/c^2 units, to each track and then its energy according to $E = \sqrt{m^2 + p^2}$, in GeV units and with p the $\vec{p}$ module, $p = |\vec{p}|$.

The track momentum, $\vec{p}$, can be represented by its Cartesian coordinates, $\vec{p} \equiv (p_x, p_y, p_z)$, according to ALICE coordinate system described in sect. 3.6. The track transverse momentum, p_{T}, is then defined as the track momentum component along the plane perpendicular to the beam direction, the xy plane,

$$p_{\mathrm{T}} = \sqrt{p_x^2 + p_y^2}. \tag{2.65}$$

The track azimuthal angle, φ, is defined as the angle which separates the track momentum $\vec{p}$ projection on the transverse plane, $\vec{p}_{\mathrm{T}}$, from the x axis. Then

$$\varphi = \arctan\left(\frac{p_y}{p_x}\right) = \arcsin\left(\frac{p_y}{p_{\mathrm{T}}}\right). \tag{2.66}$$

The track polar angle, θ, is defined as the angle which separates the track momentum $\vec{p}$ from the z axis along the beam direction. Then

$$\theta = \arctan\left(\frac{p_{\mathrm{T}}}{p_z}\right) = \arccos\left(\frac{p_z}{|\vec{p}|}\right). \tag{2.67}$$

The track polar angle is not a convenient measure in collider detectors as ALICE where for symmetric systems, i.e. Pb–Pb, the activity is expected to be symmetric with respect to the transverse plane at $\theta = \pi/2$. A more convenient measure is the so denominated pseudorapidity, η. The track pseudorapidity is defined as

$$\eta = \frac{1}{2}\log\left(\frac{|\vec{p}| + p_z}{|\vec{p}| - p_z}\right) = \log\left(\cot\left(\frac{\theta}{2}\right)\right) \tag{2.68}$$

so, it is a pure geometrical magnitude which does not require particle identification. For completeness, although not used along this thesis, the track rapidity is also introduced because it actually was the precursor of track pseudorapidity. When the track is identified and got an associated mass, track rapidity is defined as

$$y = \frac{1}{2}\log\left(\frac{E + p_z}{E - p_z}\right). \tag{2.69}$$

In the nonrelativistic limit rapidity and velocity along the longitudinal axis coincide. In the ultrarelativistic limit rapidity and pseudorapidity coincide.

2.2.2 Initial conditions

The variables described in this section cannot be directly measured but they can be inferred by using models tuned to measured data. The distance which separates the center of both colliding nuclei on the transverse plane to the beam direction is denominated the impact parameter, b. By using a Glauber model as described in sect. 3.9 for extracting the centrality of the collision is also possible to extract the associated impact parameter [15]. The plane defined by the beam direction and by the line which connects both colliding nuclei on the transverse plane is denominated the reaction plane. The angle which separates the reaction plane from the xz plane is known as the reaction plane angle, Ψ_{R}.

If the energy density distribution on the transverse plane of the overlapping area of the colliding nuclei is described by $\rho_e(x, y)$ at collision time, the spatial eccentricity of the collision is defined as

$$\begin{aligned}\varepsilon &= \frac{\int \mathrm{d}x\,\mathrm{d}y\,\rho_e(x,y)\,(x^2 - y^2)}{\int \mathrm{d}x\,\mathrm{d}y\,\rho_e(x,y)\,(x^2 + y^2)} \\ &= \frac{\langle x^2 - y^2\rangle}{\langle x^2 + y^2\rangle}.\end{aligned} \tag{2.70}$$

The overlap area is defined as

$$S = \pi \sqrt{\frac{\int \mathrm{d}x\,\mathrm{d}y\,\rho_e(x,y)\,x^2}{\int \mathrm{d}x\,\mathrm{d}y\,\rho_e(x,y)} \frac{\int \mathrm{d}x\,\mathrm{d}y\,\rho_e(x,y)\,y^2}{\int \mathrm{d}x\,\mathrm{d}y\,\rho_e(x,y)}} = \pi \sqrt{\langle x^2 \rangle \langle y^2 \rangle}. \tag{2.71}$$

2.2.3 Anisotropic flow

In the case of ideal hydrodynamics described in sect. 2.1.1 the fundamental transverse equation given in Eq. (2.25) in the fluid cell rest frame reads

$$\partial_t u^\mu = \frac{\nabla^\mu p}{e + p}, \tag{2.72}$$

i.e. in the presence of pressure gradients the fluid is accelerated. In non-central collisions the overlap area of the colliding nuclei has an almond shape, with non null eccentricity. This spatial anisotropy will give place to anisotropic pressure gradients which cause, not only the fluid elements to flow, but them to flow in an anisotropic way according to Eq. (2.72). The initial spatial anisotropy is then translated by means of anisotropic flow to an azimuthally anisotropic distribution on the final state particles which reach the detector. By using a Fourier expansion of the particle azimuthal distribution

$$\frac{\mathrm{d}N}{\mathrm{d}\varphi} \propto 1 + 2 \sum_{n=1}^{\infty} v_n \left[\cos(n(\varphi - \Psi_n)\right], \tag{2.73}$$

the anisotropic flow is quantified by means of the harmonic coefficients v_n and the corresponding symmetry plane angles Ψ_n. The different harmonic coefficients are then given by [16]

$$v_n = \langle \cos\left[n(\varphi - \Psi_n)\right] \rangle \tag{2.74}$$

where $\langle \dots \rangle$ is intended as the average over the event ensemble. Intuitively, the symmetry plane of order n is the one that makes the corresponding *sin* term of the ordinary Fourier expansion to vanish. The first harmonic coefficient corresponds to an overall shift of the distribution in the transverse plane. The corresponding flow is denominated directed flow, its magnitude is v_1 and its direction is given by the angle Ψ_1. The second harmonic describes the eccentricity of an ellipse like distribution as the one expected from the overlap region in non-central heavy-ion collisions. The second harmonic coefficient v_2 carries information on the magnitude of the ellipse eccentricity. The corresponding flow is denominated elliptic flow and the orientation of the ellipse major axis given by Ψ_2, lies roughly parallel to the reaction plane given by Ψ_R so, $\Psi_2 \sim \Psi_\mathrm{R}$. The harmonic coefficient v_3 describes the triangular flow, v_4 the quadrangular flow, and so on [16]. In principle, for symmetric systems as Pb–Pb and by pure geometric considerations it was expected that the odd harmonic coefficients should vanish. The consideration of initial state fluctuations on an event by event basis [17] revealed this fluctuations as the reason of not only the non-nullity of the odd harmonic coefficients but also of the even harmonic coefficients in perfectly central collisions where a hypothetical almond shape are not in place. Usually the harmonic coefficients are denominated as its corresponding flow so, v_1 is referred as direct flow, v_2 is referred as elliptic flow, v_3 as triangular flow, etc. Due to the almond-like geometry of the overlap area of the colliding nuclei on the transverse plane, elliptic flow, v_2, is the largest contributor to the azimuthal anisotropy in non-central collisions where it manifests as the characteristic $\cos(2\Delta\varphi)$ modulation.

Equations (2.73) and (2.74) contain the Ψ_n parameters which are experimentally inaccessible. An estimation of symmetry angles, Ψ_n, can be obtained, on an event basis, by means of the denominated

flow vector, or Q-vector,

$$Q_n = \sum_{k=0}^{M} e^{in\varphi_k} \tag{2.75}$$

where M is the event multiplicity, φ_k is the azimuthal angle of track k, and n corresponds to the harmonic of interest [18]. Q-vectors need to be corrected for detector effects [19]. The Q-vector measurements and the corrections needed can be done using the QnVectorCorrection Framework [20], that I developed during my ALICE service task. Then

$$\Psi_n \simeq \Psi_n^{\mathrm{EP}} = \frac{1}{n} \arg Q_n = \frac{1}{n} \arctan\left(\frac{\sum \sin(n\varphi_k)}{\sum \cos(n\varphi_k)}\right) \tag{2.76}$$

where Ψ_n^{EP} is the denominated event plane for the harmonic n which is used as an estimate of the n harmonic symmetry plane, Ψ_n.

2.2.4 Harmonic coefficients

Different methods have been devised to measure the harmonic coefficients v_n. A brief overview is given providing appropriate references for a better and deeper understanding if required. The initial and simplest method is known as the event plane method, EP, and is based on the event plane angle, Ψ_{EP}, extracted as an estimate of the reaction plane in Eq. (2.76). According to the event plane method [18], the harmonic coefficients are given by

$$\begin{aligned} v_n &= \langle \cos\left[n(\varphi - \Psi_n)\right] \rangle \\ &= \frac{1}{R_n} \langle \cos\left[n(\varphi - \Psi_n^{\mathrm{EP}})\right] \rangle \end{aligned} \tag{2.77}$$

where R_n is the resolution of the event plane angle for the harmonic n, Ψ_n^{EP} and which gives a measure of how much the estimated Ψ_n^{EP} separates from Ψ_n. The event plane resolution is given by [18]

$$R_n = \sqrt{\langle \cos\left[n(\Psi_n^{\mathrm{EP,a}} - \Psi_n^{\mathrm{EP,b}})\right] \rangle} \tag{2.78}$$

where $\Psi_n^{\mathrm{EP,ff}}$, for $\alpha = \mathrm{a}, \mathrm{b}$, represents the n harmonic event plane angle for two independent sub-events, a and b, which can be constructed by randomly assigning detected tracks into this two subsets. For suppressing non flow effects due to particles being correlated at production time, pseudorapidity gaps, $\Delta\eta$, can be introduced correlating particles from different acceptance regions.

A variant of the event plane method is the scalar product method, SP. In the construction of the event plane method the Q-vector is normalized to its module. Without this normalization the harmonic coefficients are obtained according to the scalar product method [19, 21] as

$$v_n = \frac{\langle \langle u_n Q_n^* \rangle \rangle}{2\sqrt{\langle Q_n^{\mathrm{a}} Q_n^{\mathrm{b}*} \rangle}} \tag{2.79}$$

where $u_n = \cos n\varphi + i \sin n\varphi$ is a unit vector for each single particle within an event, the inner $\langle \dots \rangle$ are intended as an event average and the outer and single ones are intended as an average over the whole event ensemble; and a and b are sub-events as above mentioned.

To improve the measurement of the harmonic coefficients, specially for removing contributions from non flow effects, new methods based on multi-particle azimuthal correlations have been developed. The 2- and 4-particle azimuthal correlations can be obtained according to a two steps procedure [22]. In the

first step the single event averages

$$\langle 2 \rangle \equiv \langle e^{in(\varphi_1 - \varphi_2)} \rangle \equiv \frac{1}{\binom{M}{2} 2!} \sum_{\substack{k,l=1 \\ k \neq l}}^{M} e^{in(\varphi_k - \varphi_l)}, \tag{2.80}$$

$$\langle 4 \rangle \equiv \langle e^{in(\varphi_1 + \varphi_2 - \varphi_3 - \varphi_4)} \rangle \equiv \frac{1}{\binom{M}{4} 4!} \sum_{\substack{j,k,l,m=1 \\ j \neq k \neq l \neq m}}^{M} e^{in(\varphi_j + \varphi_k - \varphi_l - \varphi_k)}, \tag{2.81}$$

are defined where M is the event multiplicity and φ_i is the azimuthal angle of track i. The second step involves the averaging over all events

$$\langle\langle 2 \rangle\rangle \equiv \langle\langle e^{in(\varphi_1 - \varphi_2)} \rangle\rangle \equiv \frac{\sum_{i=1}^{N} W_{\langle 2 \rangle, i} \langle 2 \rangle_i}{\sum_{i=1}^{N} W_{\langle 2 \rangle, i}}, \tag{2.82}$$

$$\langle\langle 4 \rangle\rangle \equiv \langle\langle e^{in(\varphi_1 + \varphi_2 - \varphi_3 - \varphi_4)} \rangle\rangle \equiv \frac{\sum_{i=1}^{N} W_{\langle 4 \rangle, i} \langle 4 \rangle_i}{\sum_{i=1}^{N} W_{\langle 4 \rangle, i}}, \tag{2.83}$$

where N is the total number of events, and $W_{\langle 2 \rangle, i}$ and $W_{\langle 4 \rangle, i}$ event i weights defined according to

$$W_{\langle 2 \rangle, i} \equiv M_i (M_i - 1) \tag{2.84}$$

$$W_{\langle 2 \rangle, i} \equiv M_i (M_i - 1)(M_i - 2)(M_i - 3), \tag{2.85}$$

i.e. the number of different 2- and 4-particle combinations in an event of multiplicity M_i and with v_n independent of multiplicity [22]. The second and fourth order cumulants [23], $c_n\{2\}$ and $c_n\{4\}$, respectively, are then extracted as [22]

$$c_n\{2\} = \langle\langle 2 \rangle\rangle \tag{2.86}$$

and

$$c_n\{4\} = \langle\langle 4 \rangle\rangle - 2\langle\langle 2 \rangle\rangle^2, \tag{2.87}$$

respectively. Equations 2.86 and 2.87 are applicable only for detectors with uniform acceptance. For a generalization to detectors with non-uniform acceptance and extensions to higher orders see [22].

The different order cumulants provide independent estimates for the same harmonic coefficient. For the above concrete case of second and fourth order cumulants [23],

$$v_n\{2\} = \sqrt{c_n\{2\}}, \tag{2.88}$$

$$v_n\{4\} = \sqrt[4]{-c_n\{4\}}, \tag{2.89}$$

respectively, where the notation $v_n\{a\}$ denotes the harmonic coefficient, flow, v_n estimated from the ath order cumulant $c_n\{a\}$ using a-particle azimuthal correlations. The cumulant method for removing non flow effects is rooted on the fact that non flow correlations usually involve a reduced number of tracks, as in the case of decays or of particles belonging to a jet. But the procedure is computationally intensive.

The experimental use of the multi-particle cumulants received a boost when a generic framework for extracting multi-particle azimuthal correlations was delivered [24]. It not only allowed the computationally efficient extraction of higher order cumulants but also the incorporation of the symmetric cumulants to the set of the anisotropic flow analysis tools. Symmetric cumulants are multi-particle correlations which involve two harmonics. For instance 4-particle symmetric cumulant which involves harmonics m and n, denominated as SC(m,n), will involve the four-particle correlations

$$\langle\langle e^{i(m\varphi_1 + n\varphi_2 - m\varphi_3 - n\varphi_4)} \rangle\rangle. \tag{2.90}$$

Symmetric cumulant SC(m,n) gives a measure of the correlation of the event-by-event fluctuations of the v_m and v_n flows [24].

2.2.5 Radial flow

Radial flow is the isotropic component of the transverse expansion of the medium. It gets reflected in the transverse momentum spectra. It is usually measured as the radial expansion velocity by fitting the spectra with a blast-wave function [25, 26]

$$\frac{1}{p_{\mathrm{T}}}\frac{\mathrm{d}N}{\mathrm{d}p_{\mathrm{T}}} \propto \int_0^R r\,\mathrm{d}r\, m_{\mathrm{T}} I_0\left(\frac{p_{\mathrm{T}}\sinh\rho}{T_{\mathrm{kin}}}\right) K_1\left(\frac{m_{\mathrm{T}}\cosh\rho}{T_{\mathrm{kin}}}\right) \tag{2.91}$$

where $m_{\mathrm{T}} = \sqrt{p_{\mathrm{T}}^2 + m^2}$ is the transverse mass, I_0 and K_1 the modified Bessel functions, r is the radial distance in the transverse plane, R is the radius of the fireball, T_{kin} is the freeze-out temperature, and the velocity profile ρ is described by

$$\rho = \tanh^{-1}\beta_{\mathrm{T}} = \tanh^{-1}\left(\left(\frac{r}{R}\right)^n \beta_{\mathrm{s}}\right) \tag{2.92}$$

where β_{T} is the transverse expansion velocity and β_{s} the expansion velocity at the surface. The free parameters in the fit are the kinetic freeze-out temperature, T_{kin}, the average transverse velocity, $\langle\beta_{\mathrm{T}}\rangle$, and the exponent of the velocity profile, n.

2.2.6 Viscous effects

Anisotropic transverse flow affects the shape of the transverse momentum spectra through a direction-dependent blue-shift factor. As was described in sect. 1.3 bulk viscosity reduces the radial flow acceleration which leads to steeper p_{T}-spectra and therefore suppression of the average transverse momentum of hadrons [5]. As also described in sect. 1.3 shear viscosity favors the build-up of radial flow which renders flatter the p_{T}-spectra [7]. Shear viscosity reduces the flow anisotropies and directly affects the flow coefficients. Therefore, large elliptic flow observed at RHIC and at the LCH points to a low η/s. The damping of the flow coefficients, v_n, due to the effects of η/s is stronger for larger n [7], becoming also sensitive to its magnitude.

2.3 Inference from model to data comparison

In this section a brief survey of the progress in the extraction of the QGP transport parameters, shear viscosity and bulk viscosity, by comparing measured data to models predictions is presented. It basically started when the ideal hydrodynamic simulations were not able to describe the p_{T}-differential evolution of elliptic flow. The viscous effects introduced by the shear viscosity immediately characterized the QGP as the most perfect fluid ever known. The realization from lattice QCD results that bulk viscosity could peak around the transition from QGP to a gas of hadrons [27] pushed for the incorporation of this transport parameter also into the viscous hydrodynamic simulations and in the process of constraining the values of these transport parameters. To help guide the reader through the different experimental observables used to infer the transport parameters, subsequent sections are subdivided with the help of subsection headings.

2.3.1 Shear viscosity

Transverse momentum spectrum and elliptic flow of charged particles

One of the main observables to gain information about the η/s of the QGP is the elliptic flow of charged particles. The incorporation of viscous hydrodynamic simulations was mainly forced by the limitations of ideal hydrodynamics in reproducing the p_T dependence of the elliptic flow. Initial efforts started using causal second order viscous hydrodynamic simulations, which discarded bulk viscosity and heat conductivity effects. For the equation of state (EoS) usually a lattice QCD EoS was used and for initial conditions a "boost-invariant" energy density distribution along the longitudinal direction was considered. The initial energy density distribution, e, in the transverse plane usually followed a Glauber-type energy density distribution assuming the distribution being proportional to the number of colliding nucleons, N_{coll}. A particlization step which involved the Cooper-Frye prescription [6] was used

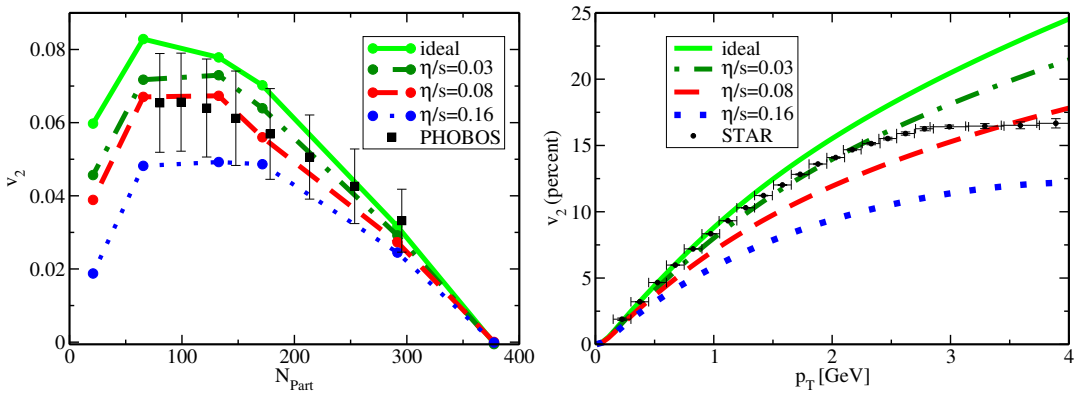

FIGURE 2.1: PHOBOS [28] data on p_T integrated v_2 (left panel) and STAR [29] data on minimum bias p_T-differential v_2 (right panel), for charged particles in Au–Au collisions at $\sqrt{s_{NN}}$ = 200 GeV, compared to hydrodynamic model for various viscosity ratios η/s. Error bars for PHOBOS data show 90% confidence level systematic uncertainties while for STAR only statistical uncertainties are shown [30].

as the mechanism for transforming hydrodynamic quantities, such as the energy density and the fluid velocity, into particle spectra, usually, at a single freeze-out temperature T_f. In [30], the normalization of the energy density, e, and the T_f value were chosen such that the measured total multiplicity and mean transverse momentum, $\langle p_T \rangle$, as a function of the total number of participants, N_{part}, were appropriately described. The η/s values were chosen to be constant throughout the evolution of the system. The effects of resonance decays with masses up to 2 GeV were incorporated into the particlization process. With these considerations, it was possible to associate the behavior of the elliptic flow reported by PHOBOS and STAR experiments at RHIC with the magnitude of η/s. As the left panel of Fig. 2.1 shows, data on integrated v_2 is fairly well reproduced by using a value of $\eta/s \sim 0.08$ and seems consistent, within systematic uncertainties, with the results using $\eta/s \sim 0.16$. This is not the case for the evolution of v_2 with transverse momentum as shown in the right panel of Fig. 2.1. While the influence of the shear viscosity managed to qualitatively explain why v_2 does not keep growing with p_T, quantitatively data seem to favor a ratio η/s smaller than the conjectured minimal bound [30].

Event-by-event (EbyE) fluctuations of the initial conditions in the density distribution on the transverse plane and also in its longitudinal profile, not any longer "boost invariant", were incorporated in the initial stage previous to the hydrodynamic evolution. EbyE fluctuations inclusion allowed to also describe experimental v_2 data for similar values of η/s. But most relevant, they showed that collectivity in central collisions is associated with EbyE initial conditions fluctuations and not only with geometrical anisotropies as is the case for semi-central collisions. They also were able to explain why odd flow

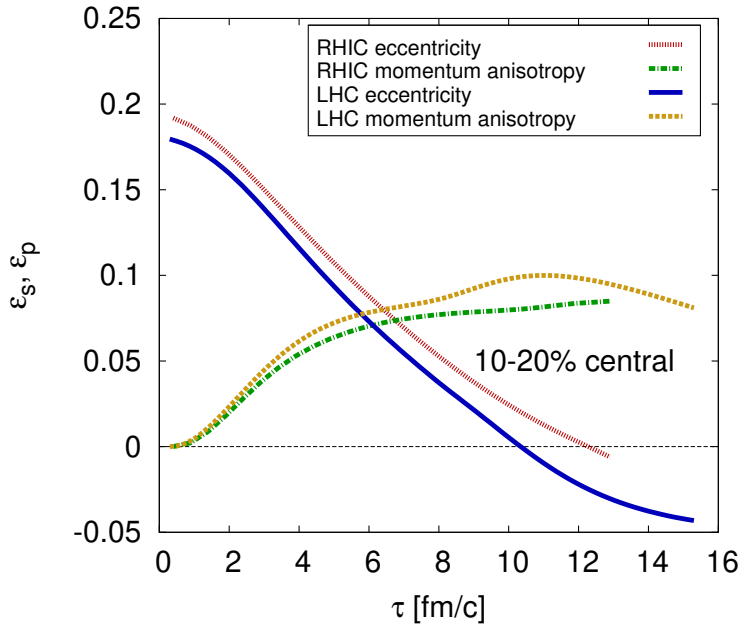

FIGURE 2.2: Time evolution of the eccentricity and momentum anisotropy in 10–20% central collisions at RHIC and the LHC. In both cases the maximal momentum anisotropy is built up almost entirely during the first $5-6$ fm/c [31].

coefficients don't vanish as would have been expected from pure geometrical criteria. Consequently the earlier time build up of the elliptic flow, also explained why the differences between v_2 evolution with p_T at RHIC and LHC were small contradicting the expectations. As Fig. 2.2 shows, although lifetime is longer at the LHC the evolution of the eccentricity and of the momentum anisotropy are similar for both scenarios [31].

Further improvements came from the separation of the pure (viscous) hydrodynamic evolution in the QGP phase from the late hadron resonance gas phase. The hydrodynamic description evolved the system from initial conditions till the switching temperature, where a chemical freeze-out takes place and the produced particle species get frozen. Then a microscopic hadronic cascade simulation evolves the system towards the final kinetic freeze-out. Model uncertainties came mainly from the initial conditions of the hydrodynamic phase, its starting time, τ_0, and the initial transverse flow velocity, among them.

In [35] different hydrodynamic evolution starting times were selected, which required the initial energy density to be normalized, for each of them, to reproduce the measured charged hadron multiplicity. The ratio η/s needed also to be adjusted, for each of the starting times, to reproduce the measured elliptic flow. The initial entropy distributions on the transverse plane were based on the MC Glauber model and the MC-KLN model, a Color Glass Condensate (CGC) which considers the inner nucleon constituents. They needed to be tuned to reproduce the measured collision centrality dependence of the charged hadrons rapidity density. EbyE fluctuations were incorporated in the initial conditions models to introduce eccentricity, ϵ, fluctuations. In Fig. 2.3 the measured v_2 scaled with the eccentricity, ϵ, extracted from the simulations, is presented versus the measured multiplicity density $\mathrm{d}N_{\mathrm{ch}}/\mathrm{d}y$ scaled with the overlap area, S, also extracted from the simulations, for both kinds of initial conditions. Data are compared with the same results from models for both initial conditions, and different values of η/s. The relation v_2/ϵ versus $(1/S)(\mathrm{d}N_{\mathrm{ch}}/\mathrm{d}y)$ was proposed as universal [35]. Data are best fitted with η/s values of 0.16 or 0.08 depending on whether the initial conditions are from CGC or MC-Glauber, respectively. The main source of uncertainty was the difference in magnitude of the source eccentricity and the overlap area from both initial conditions models.

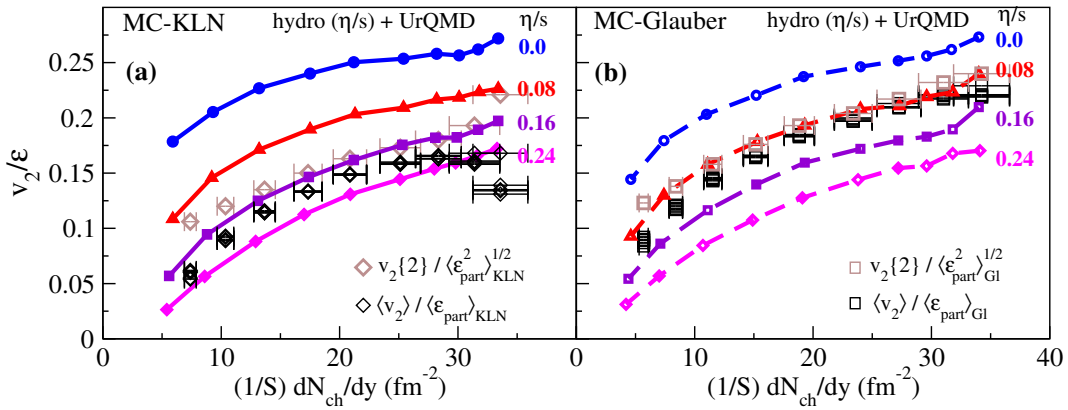

FIGURE 2.3: Comparison of $v_2(\eta/s)/\epsilon$ vs. $(1/S)(\mathrm{d}N_{\mathrm{ch}})/\mathrm{d}y$ with experimental data for $\langle v_2\rangle$ [32] and $v_2\{2\}$ [33] and $\mathrm{d}N_{\mathrm{ch}})/\mathrm{d}y$ [34] from STAR Collaboration. The experimental data used in (a) and (b) are identical, but the eccentricity, $\langle\epsilon_{\mathrm{part}}\rangle$, and overlap surfaces, S, normalization factors used in the vertical and horizontal axes are taken from the CGC based model (a) and from the Glauber based model (b). Theoretical curves are from simulations with CGC based initial conditions in (a) and with MC-Glauber based initial conditions in (b). As explained in the text each η/s value has associated a τ_0 starting time for the hydrodynamic evolution [35]. The different data values for $\langle v_2\rangle$ came from the different procedures for extracting the elliptic flow used in [33, 36].

Transverse momentum spectra and elliptic flow of identified particles

Focusing just on the hadronic phase and considering that at kinetic freeze-out the system is left with a set of flow fields for the different hadron species at a certain temperature, in [37] the different flows are modeled by using a viscous blast wave parametrization, assuming that at freeze-out the system of hadrons is close enough to kinetic equilibrium. The model is simultaneously fitted to the transverse momentum spectra and to the p_{T}-differential elliptic flow of pions, kaons and protons for different centrality ranges. From a Bayesian inference package, into which a parametrized dependence of η/s with temperature was incorporated, the preferred values for the viscous blast wave parametrization were obtained, among them the temperature and the associated η/s. Fig. 2.4 shows the results of viscous blast wave model compared to data from the ALICE collaboration [39, 38]. With this model it was possible to extract the evolution of η/s with temperature [37] as shown in Fig. 2.5.

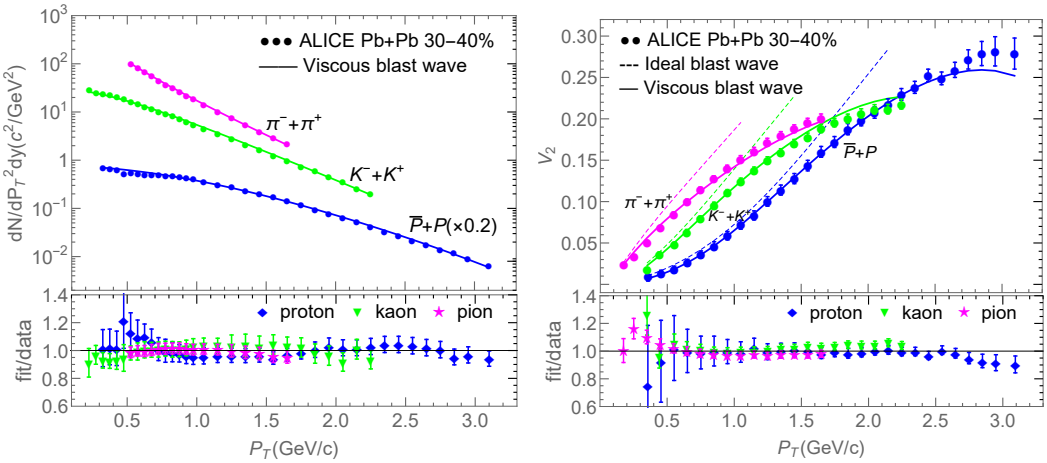

FIGURE 2.4: Left panel: transverse momentum spectra for pions, kaons and protons (solid lines), respectively, using a viscous blast wave model with the extracted, preferred fit parameters [37] for the ALICE 30–40% centrality data [38, 39] compared with the actual data (circles). Right panel: elliptic flow v_2 for pions, kaons, and protons (solid lines) for the same parameters [37], together with ALICE data (circles) [39].

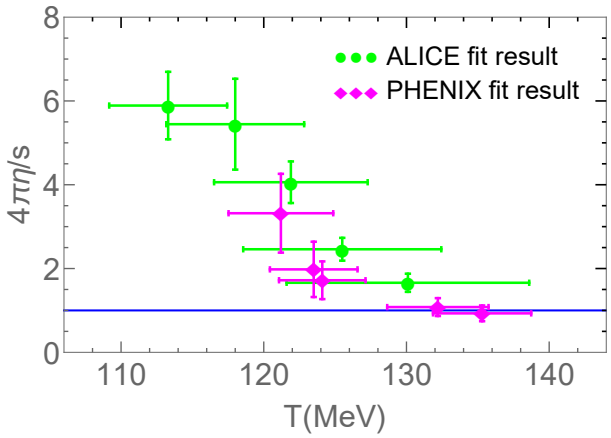

FIGURE 2.5: Specific shear viscosity η/s at corresponding kinetic freeze-out temperature T extracted from the available ALICE and PHENIX centrality bins. Shown uncertainties combine the Bayesian package uncertainties and the uncertainties extracted by systematically varying underlying assumptions needed to apply the model. The uncertainty of the model itself it is not assigned [37].

Higher order harmonic coefficients

The uncertainties in η/s still remained bounded to the hydrodynamic initial conditions and in some part to the applicability of the chosen model. In an attempt to reduce uncertainties, a parametrized EbyE generator model which interpolated different initial conditions descriptions, was introduced. Initial conditions were coupled to a second order boost invariant viscous hydrodynamic evolution, in which the temperature dependence of η/s and ζ/s was also parametrized. The value of η/s was made linearly dependent of the temperature, with the linear coefficients as model parameters, while ζ/s was given a profile like the one shown later in Fig. 2.11 from [40] scaled with an additional model parameter. The hydrodynamic evolution incorporated a lattice QCD based EoS blended to a hadron resonance gas EoS in

the hadronic temperature interval. After an isothermal freeze-out particlization an hadronic afterburner evolved the final shower of particles. In [41] a multivariate model with a set of reduced inputs, which corresponds to different values of the parameters within their variation ranges, was trained. The samples introduced for training were the measured observables extracted after the whole simulation and which will be compared with the actual data measured by PHENIX and ALICE collaborations.

In the top row of Fig. 2.6 the results of the simulated observables are compared with measured data from the ALICE collaboration [17, 26]. The simulated observables are extracted from 300 design points chosen within the parameters ranges. Measured $v_n\{2\}$ are extracted with the direct Q-cumulant method [22]. The goal was to be able to faithfully produce, emulate, a valid output for any combination

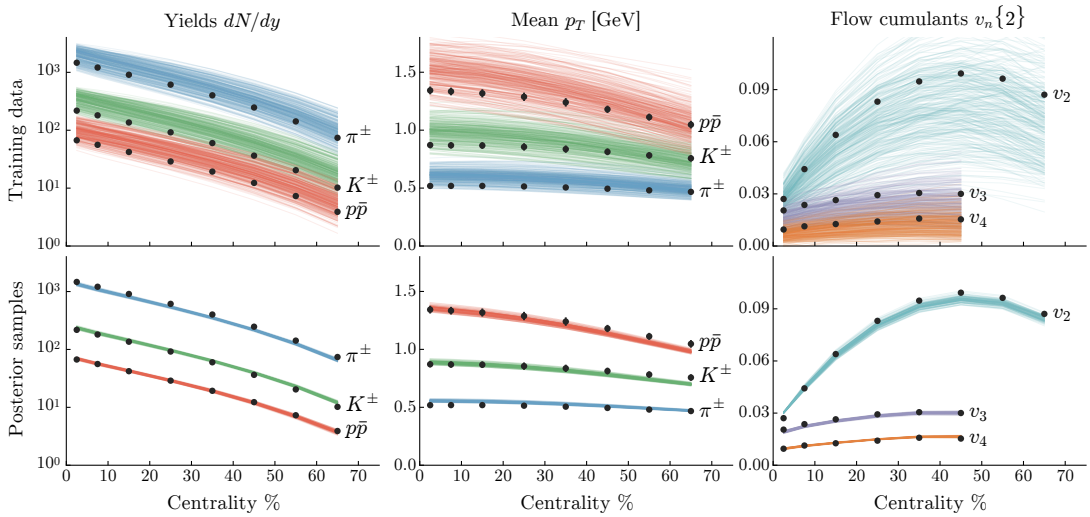

FIGURE 2.6: Simulated observables from a multivariate model [41] compared to experimental data from the ALICE experiment [17, 26]. Top row: explicit model calculations for each of the 300 design points, with parameter values selected within their variation ranges (training samples). Bottom row: emulator predictions of 100 random samples drawn from the posterior distribution (Fig. 2.7). Left column: identified particle yields $\mathrm{d}N/\mathrm{d}y$, central: mean transverse momentum $\langle p_{\mathrm{T}} \rangle$, right: flow coefficients for charged particles.

of the values of the parameters without the need of running the whole simulation for such a combination. The final step, which calibrates the model parameters to optimally reproduce the experimental data, is performed by Bayesian inference incorporating principal component analysis for minimizing the number of required input combinations. A final set of random walks through the parameter space generated using Markov chain Monte Carlo (MCMC) method permits the extraction of the posterior distribution of the model parameters [41].

Figure 2.7 shows the posterior parameters distributions for two different calibrations, to the identified particles yields $\mathrm{d}N/\mathrm{d}y$ and to the charged particle yields $\mathrm{d}N_{\mathrm{ch}}/\mathrm{d}y$. Bottom row of Fig. 2.6 shows the emulator predictions for 100 random samples of the parameters extracted from the diagonal distributions on Fig. 2.7. Finally, Fig. 2.8 shows model calculations using the high-probability parameters values from the posterior distributions on Fig. 2.7. In [41] the use of bulk viscous correction at particlization was neglected due to the variety of its proposed forms which predict significantly different behavior. Any quantitative conclusion on ζ/s was then precluded although the non nullity of ζ/s was determined.

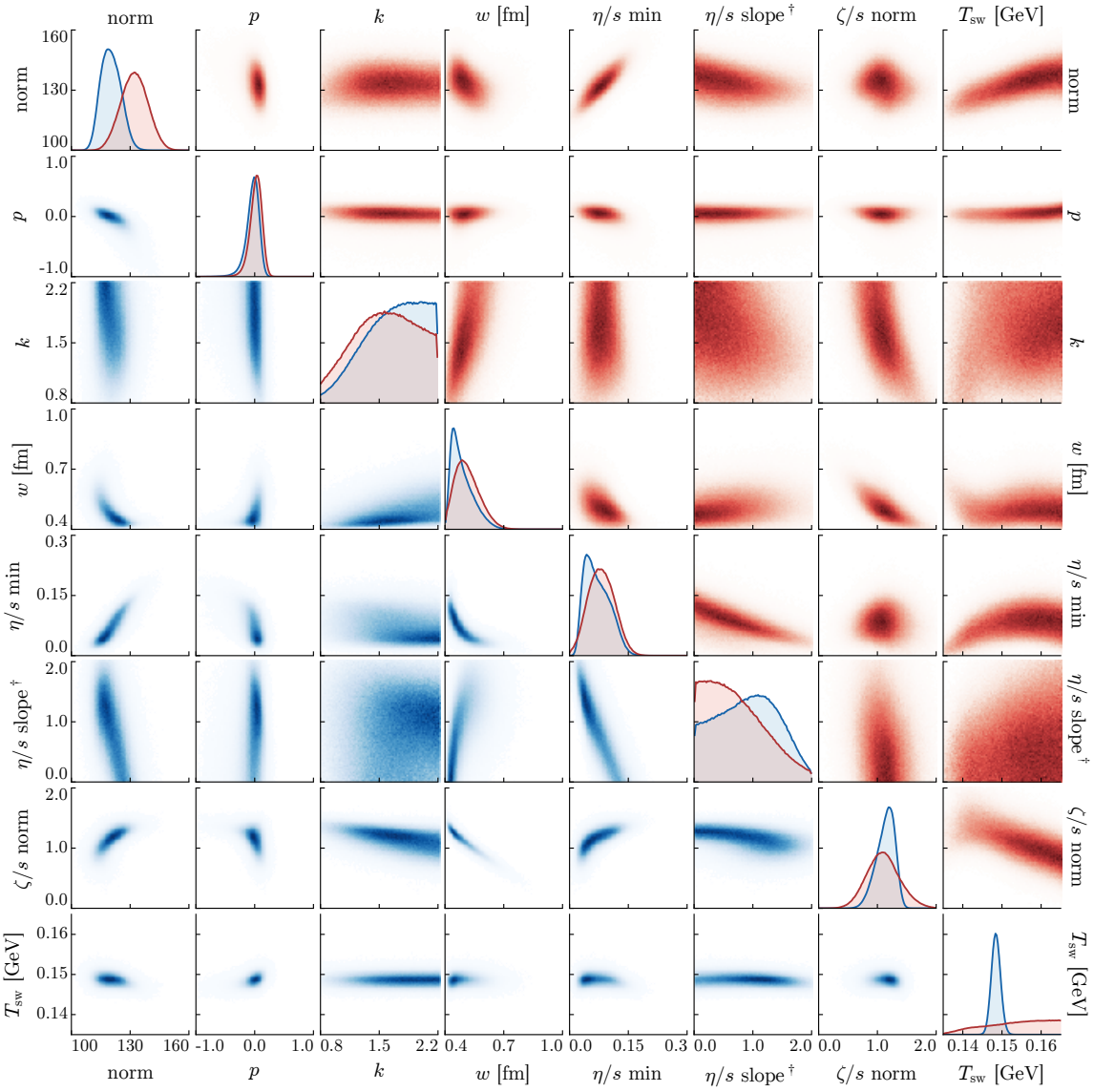

FIGURE 2.7: Posterior distribution for the model parameters from calibrating to identified particle yields $\mathrm{d}N/\mathrm{d}y$ (blue, lower triangle) and charged particle yields $\mathrm{d}N_{\mathrm{ch}}/\mathrm{d}y$ (red, upper triangle) from the ALICE collaboration [17, 26]. The diagonal has marginal distribution for each parameter, while the off-diagonal contains joint distributions showing correlation among pairs of parameters. †The units for η/s slope are [GeV^{-1}] [41].

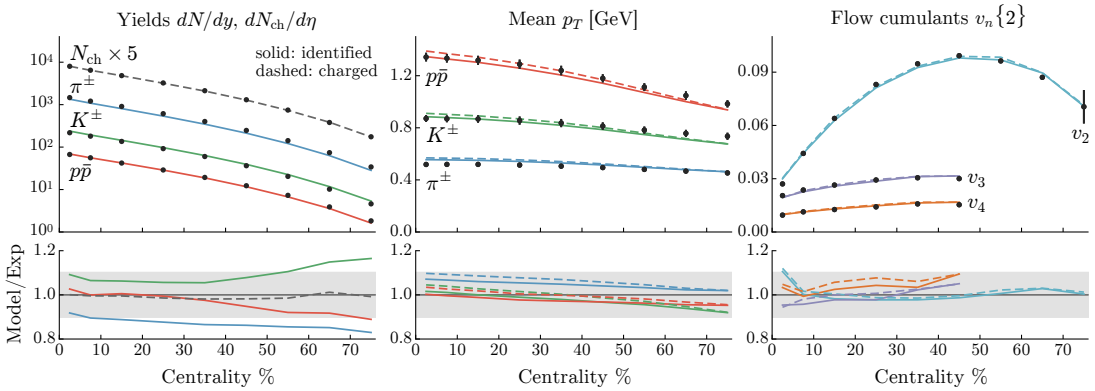

FIGURE 2.8: Model calculations using the high-probability parameters from the posterior distribution 2.7. Solid lines are calculations using parameters based on the identified particle posterior, dashed lines are based on the charged particle posterior, and points are data from the ALICE collaboration [17, 26]. Top row: calculations of identified or charged particle yields $\mathrm{d}N_{\rm ch}/\mathrm{d}y$ or $\mathrm{d}N_{\rm ch}/\mathrm{d}y$ (left), $\langle p_{\rm T} \rangle$ (central), and flow cumulants $v_n\{2\}$ (right) compared to data. Bottom: ratio of model calculations to data, where gray band indicates ±10% [41].

Symmetric cumulants

The recent steps on the way of extracting η/s involve the incorporation of new observables. Anisotropic flow is generated by the initial anisotropic geometry and its fluctuations coupled with an expansion of the produced medium. But azimuthal anisotropy can also be produced from other sources as minijets, resonances, etc... The extraction of the ordinary flow coefficients usually require of mechanisms to identify and suppress this non-flow contributions. Symmetric cumulants (SC) from multi-particle correlations which involve different order flow harmonics have been suggested as robust against non-flow effects and easy to correct for non uniform azimuthal acceptance and p_{T} dependent inefficiencies [24] . Relationship between event-by-event fluctuations of amplitudes of two different flow harmonics v_m and v_n can exist. Analyzing these relationships with SC has revealed them as sensitive to fluctuations of the initial conditions and to the transport properties of the QGP [42]. Symmetric 2-harmonic 4-particle cumulant SC(4,2) gives a measure of the correlations between EbyE fluctuations of the magnitudes of v_2 and v_4 harmonic coefficients while SC(3,2) gives a measure of the correlations between EbyE fluctuations of the magnitudes of v_2 and v_3. In Fig. 2.9, SC(4,2) and SC(3,2) measured by the ALICE

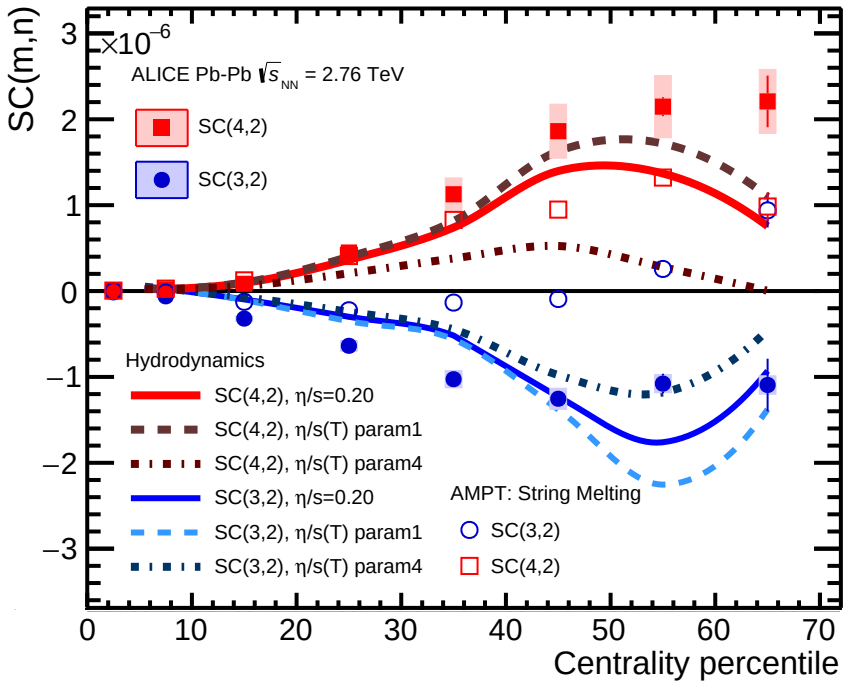

FIGURE 2.9: Comparison of observables SC(4,2) (red filled squares) and SC(3,2) (blue filled circles) to theoretical models from [43]. Solid lines indicate the predictions with constant η/s while the dashed lines indicate predictions for different parametrizations of η/s temperature dependence. AMPT predictions also shown [42].

collaboration [42] are compared with simulations from a model [43] where the initial conditions are calculated using a next-to-leading order (NLO) perturbative-QCD+saturation model coupled with a viscous hydrodynamic evolution [44, 45] where the temperature dependence of η/s was parametrized with different profiles as shown in Fig. 2.10.

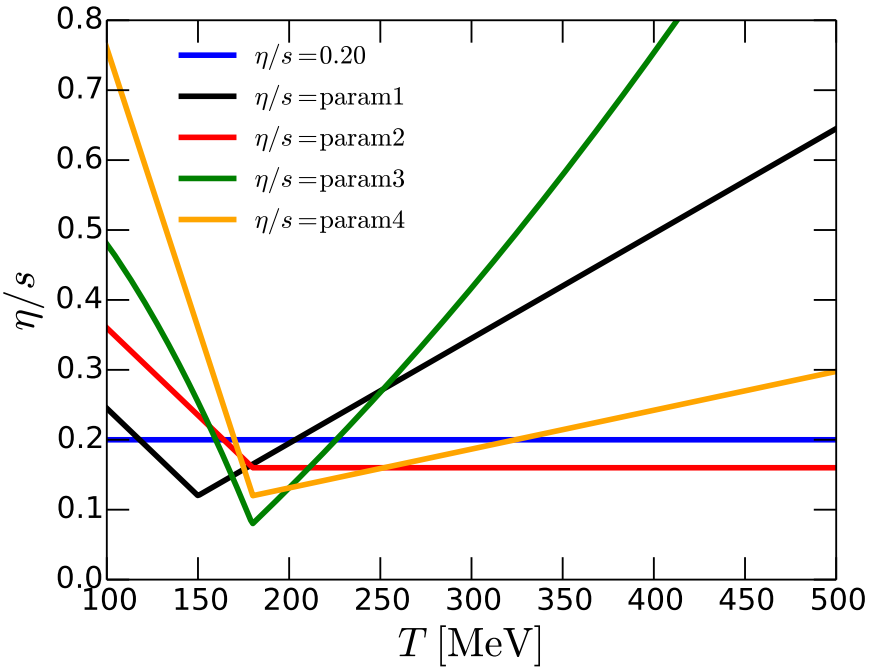

FIGURE 2.10: Parametrizations of the temperature dependence of η/s, labeled here in the order of increasing η/s at $T = 100$ MeV [43].

2.3.2 Bulk viscosity

Higher order harmonics of charged particles and multiplicity and average p_{T} of identified particles

The peaked, at the phase transition region (Fig. 2.11), bulk viscosity profile extracted from lattice QCD predictions motivated its incorporation into the viscous hydrodynamics models to evaluate its effects on an extended set of observables.

The impact of strongly peaked bulk viscosity at the phase transition region on different experimentally accessible quantities, integrated v_n, mid-rapidity multiplicity, and mean transverse momentum, was studied in [46, 5]. The early time description of the collision was provided by the IP-Glasma model, known to provide a good description of flow harmonic coefficients. The intermediate fluid-dynamical evolution is resolved using Israel-Stewart theory considering second order terms that couple the shear-stress tensor and bulk viscous pressure. After the hydrodynamic evolution an hadronic rescattering phase was incorporated by using UrQMD at a certain switch temperature, T_{sw}. This hybrid approach was found capable of describing simultaneously the multiplicity and average transverse momentum of pions, kaons, and protons, when a finite bulk viscosity, which follows the profile in Fig 2.11, is included near the QCD phase transition region. The introduction of bulk viscosity into the hydrodynamic evolution was found to have a large effect on the average transverse momentum of charged hadrons and on the elliptic flow coefficient. In fact, when using the IP-Glasma initial conditions, the bulk viscosity is essential to describe the p_{T} spectra of charged hadrons. Similar description with only shear viscosity could not be obtained. The introduction of bulk viscosity considerable reduces, by almost 50%, the value of the shear viscosity needed to describe the harmonic flow coefficients. The larger value of η/s compensates the reduction of momentum anisotropy due to the effect of the bulk viscosity [46].

The values of η/s are adjusted to provide a good agreement with the integrated flow harmonic coefficients, v_n, up to $n = 4$. The temperature T_{sw} is tuned to better reproduce the multiplicity and average transverse momentum of different hadron species. In [5] it was found that the T_{sw} at RHIC (=165 MeV) is larger than the one at the LHC (=145 MeV) giving as a potential explanation the fact that

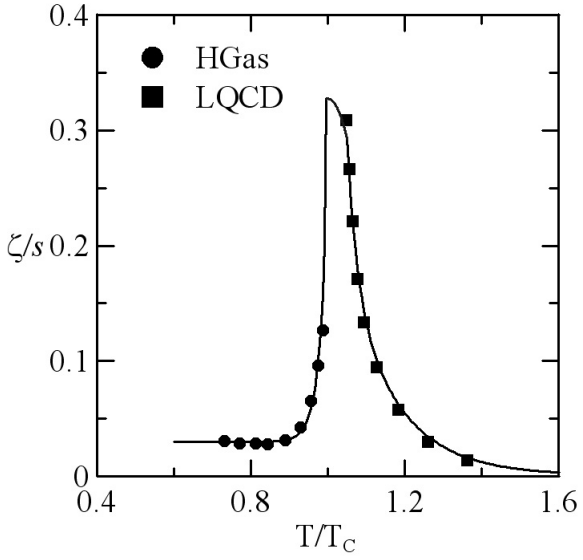

FIGURE 2.11: Bulk viscosity over entropy density near the the QCD phase transition. The profile combines the evolution of the QGP phase from lattice QCD [27] and of the hadronic phase from an hadron resonance gas (HRG) model [40, 47].

systems produced at LHC energies have more entropy and, consequently, are more long-lived than the ones produced at RHIC. Fig. 2.12 shows the multiplicity and average p_T for pions, kaons and protons, as well as the charged hadrons anisotropic flow coefficients $v_{2,3,4}$, from central to semi-peripheral collisions. Left panels curves are produced from simulations incorporating both, η/s and ζ/s while right panels curves are produced from simulations with $\zeta/s = 0$ [5]. The simulations without bulk viscosity are still able to well describe the centrality dependence of the flow harmonic coefficients. However, these calculations overestimate the $\langle p_T \rangle$ of the three species by almost 30%. This happens because the IP-Glasma model gives rise to an initial state with large gradients of pressure and the subsequent fluid-dynamic expansion accordingly produces a significant radial flow. Therefore, in order to describe the data the transverse momentum of produced particles must be considerably reduced. Including ζ/s leads to a suppression of $\langle p_T \rangle$ and improve the description of data. This is because ζ/s acts as a resistance to the expansion or compression of the fluid [46].

Higher order harmonics and p_T spectra of identified particles

The p_T differential observables are more sensitive to out-of-equilibrium corrections of the hadronic momentum distribution because of shear viscosity [5]. Fig. 2.13 shows the p_T differential $v_n\{2\}$ of $n = 2, 3, 4$ of charged hadrons compared with the ALICE [17] and the CMS [48, 49] collaborations data. Fig. 2.14 shows the p_T spectra for pions, kaons and protons, for four centrality classes, with and without hadronic interaction in the hadronic phase. For the full hadronic rescattering, the simulations describe data for the most central collisions but tension appears when moving towards peripheral ones, especially for kaons and protons but also for pions with $p_T > 1.5$ GeV/c. Finally Fig. 2.15 shows identified particle harmonic flow coefficients as measured by the ALICE collaboration [39, 50] compared with simulations results with and without hadronic interactions in the hadronic rescattering phase. The value of the flow coefficients are generally overestimated for pion and kaon at high p_T.

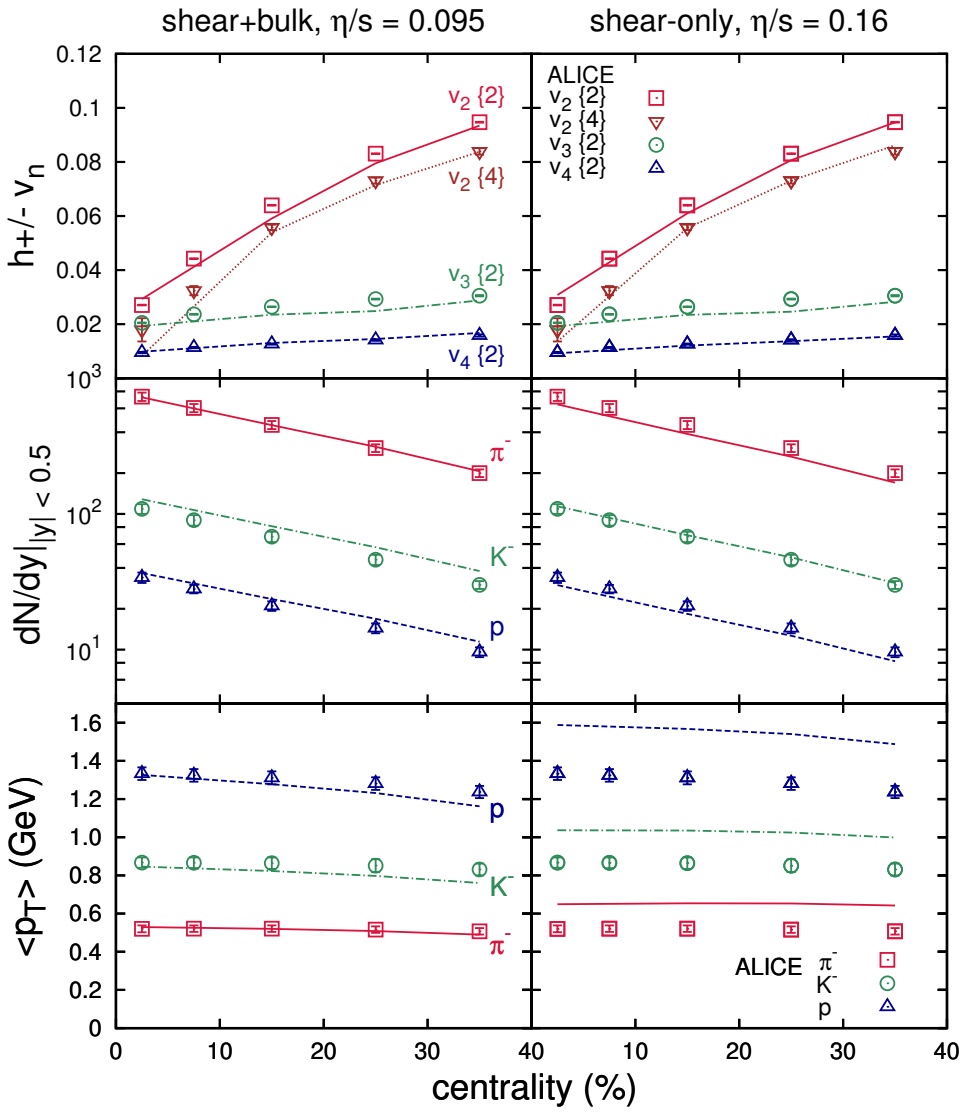

FIGURE 2.12: Integrated harmonic coefficients v_n (upper), and mid-rapidity multiplicity (middle) and average p_T (lower) for pion, kaon and proton, as functions of collision centrality. η/s is determined to fit the ALICE data on v_n [17]. ALICE data for multiplicity and $\langle p_T \rangle$ taken from [15]. Left panels curves were obtained from simulations including bulk viscosity as shown in Fig. 2.11 while right panels curves were obtained from simulations with $\zeta/s = 0$ [5].

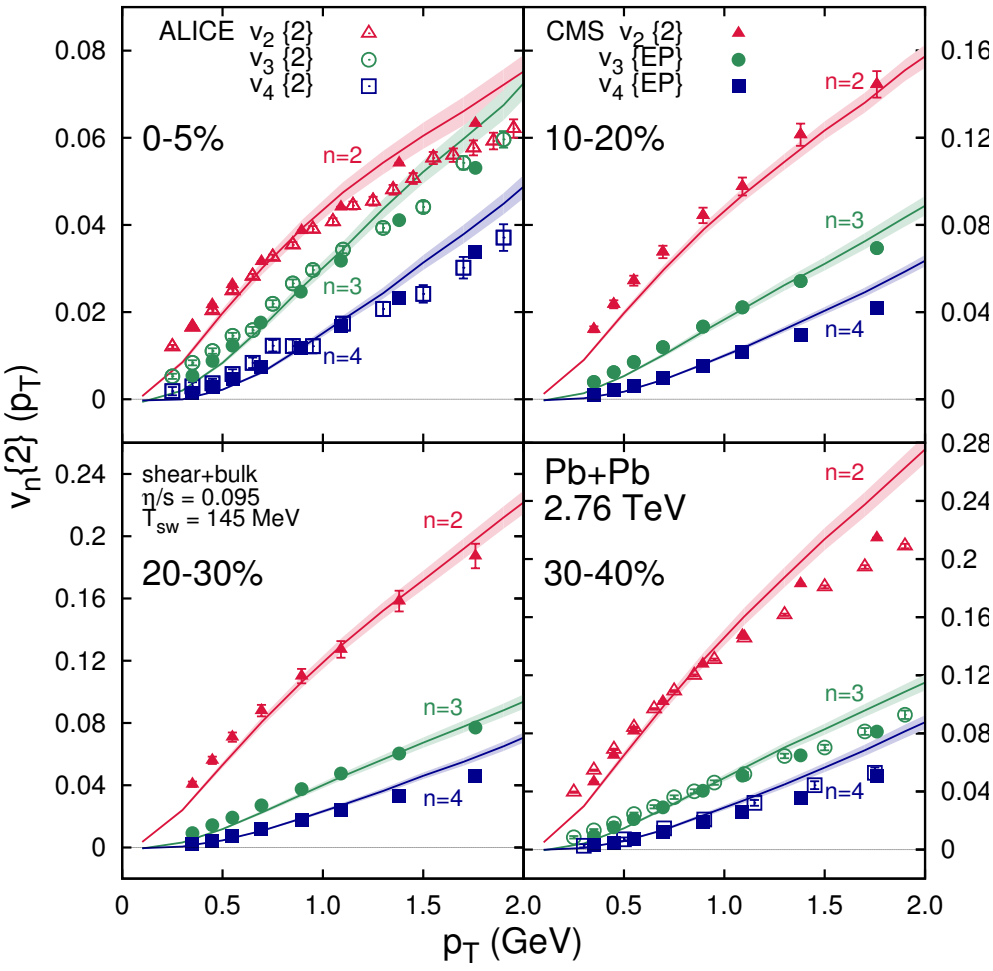

FIGURE 2.13: p_T differential $v_n\{2\}$ ($n = 2, 3, 4$) of charged hadrons for centrality classes 0–5%, 10–20%, 20–30%, and 30–40% in Pb–Pb collisions at $\sqrt{s_{NN}}$ = 2.76 TeV compared to results from ALICE [17] and CMS [48, 49] collaborations. Statistical errors are shown as bands around the curves [5].

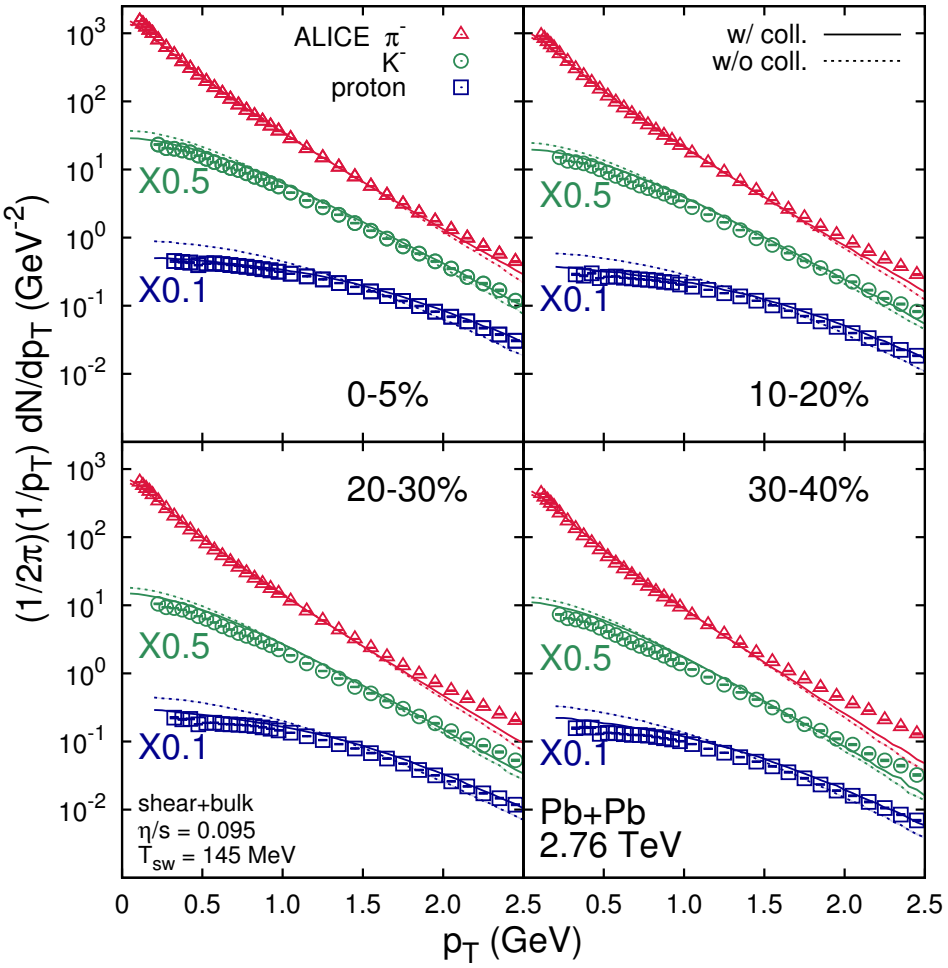

FIGURE 2.14: p_T spectra of identified hadrons for centrality classes 0–5%, 10–20%, 20–30%, and 30–40% of Pb–Pb collisions with $\sqrt{s_{NN}}$ = 2.76 TeV compared to results from the ALICE collaboration [15]. The solid curves correspond to full hadronic rescattering phase with UrQMD while the dashed curves correspond to only hadronic decays from UrQMD but not further hadronic interactions. The statistical errors are shown as bands around the curves [5].

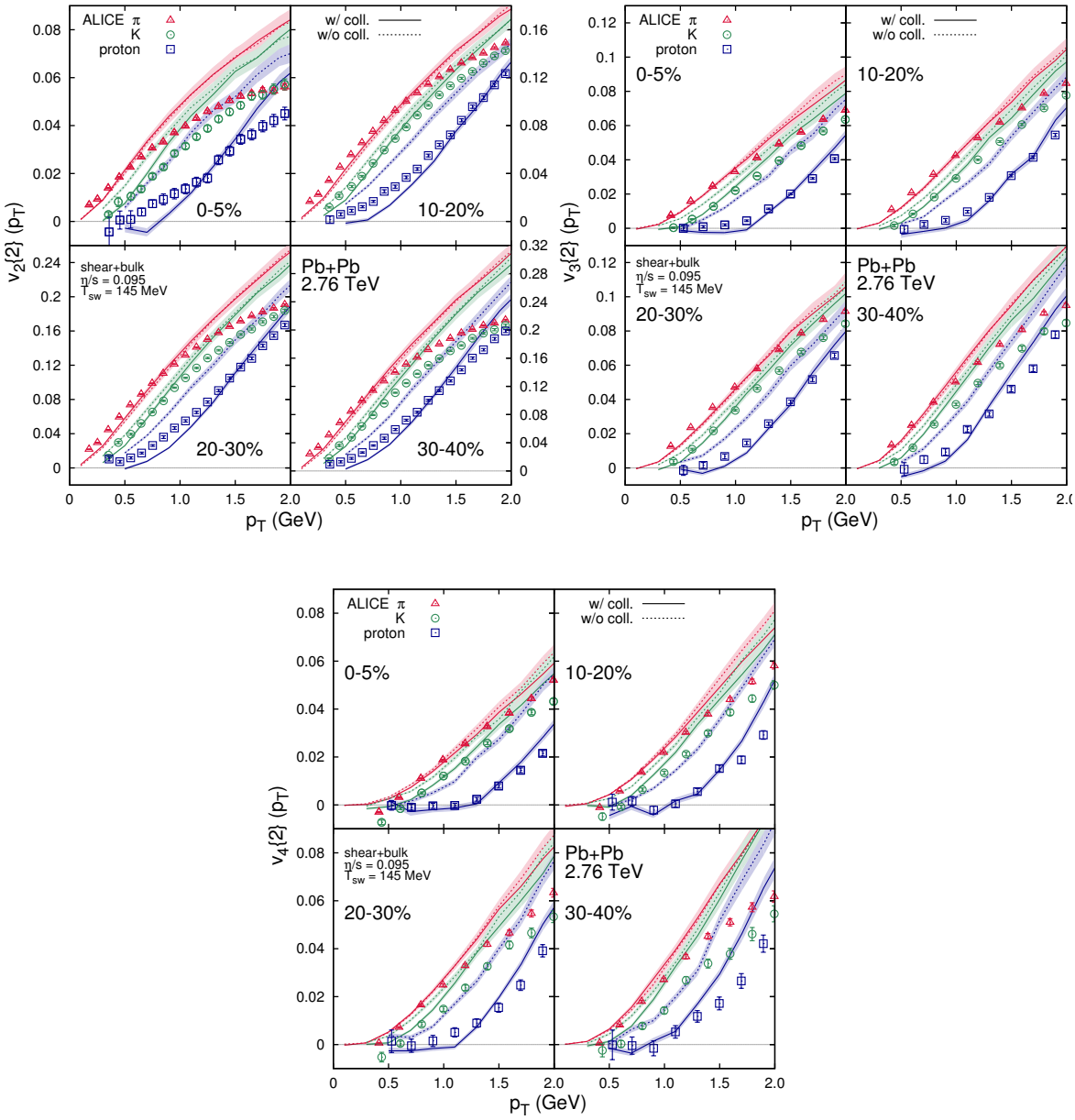

FIGURE 2.15: p_T differential $v_2\{2\}$ (top left), $v_3\{2\}$ (top right), and $v_4\{2\}$ (bottom) of identified hadrons for centrality classes 0–5%, 10–20%, 20–30%, and 30–40% in Pb–Pb collisions at $\sqrt{s_{NN}}$ = 2.76 TeV compared to results from the ALICE collaboration [39, 50]. The solid curves correspond to full hadronic rescattering phase with UrQMD while the dashed curves correspond to only hadronic decays from UrQMD but not further hadronic interactions. The statistical errors are shown as bands around the curves [5].

Due to the sensitivity of the heavy hadrons to the transition between the hydrodynamic and the hadronic rescattering phases[5], the extension of the comparison to strange baryons data additionally constrains the potential ζ/s effects. Fig. 2.16 shows p_T spectra and elliptic flow coefficient v_2 of strange baryons as measured by the ALICE collaboration [15, 51, 52]. The p_T spectra are relatively well

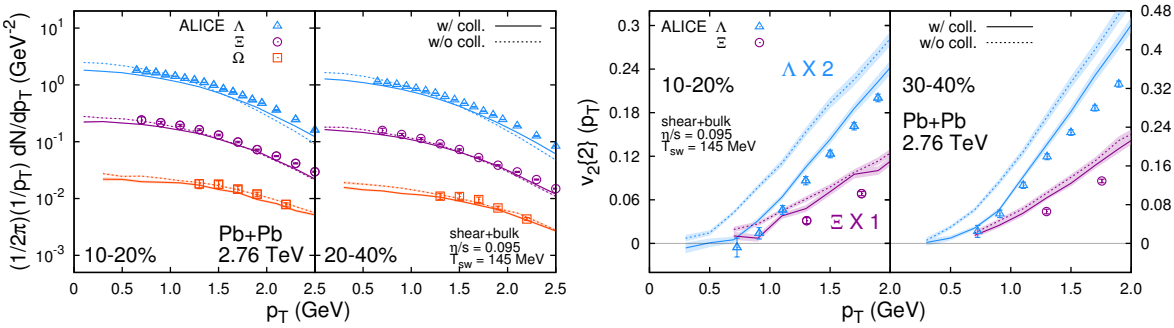

FIGURE 2.16: p_T spectra (two left panels) and p_T differential v_2 (two right panels) of strange baryons for centrality classes 10–20% and 20–30% (10–20% and 30–40% for v_2) in Pb–Pb collisions at $\sqrt{s_{NN}}$ = 2.76 TeV compared to results from the ALICE collaboration [15, 51, 52]. The solid curves correspond to full hadronic rescattering phase with UrQMD while the dashed curves correspond to only hadronic decays from UrQMD but not further hadronic interactions. The statistical errors are shown as bands around the curves [5].

described while the v_2 is overestimated by the simulations in line with expectations about the above sensitivity.

Direct-photon spectra and direct-photon elliptic flow

Additional observables as the direct-photon p_T spectrum and direct-photon elliptic flow have been also incorporated to constrain the value ζ/s of the QGP. Direct photons, defined as photons not originating from hadron decays, are a valuable tool to study details of the QGP evolution. Unlike hadrons, direct photons are produced at all stages of the collision and traverse the QGP basically unaffected, delivering direct information on the conditions at the time of the production. Different p_T regions are dominated by photons emitted at different stages of the collision [53]. The state-of-the-art measurement of direct-photon spectrum in Pb–Pb collisions at $\sqrt{s_{NN}}$ = 2.76 TeV from the ALICE collaboration is shown in Fig. 2.17 compared with expectations from models which assume the formation of a QGP [53]. The van Hees et al. model [54] and the Chatterjee et al. model [55, 58] are based on ideal hydrodynamic evolution. The parton-hadron-string dynamics (PHSD) model from Linnyk et al. [56], a relativistic transport approach in which the full evolution of the collision is described microscopically, incorporate shear viscous effects. Paquet et al. calculations [57] which involve full viscous hydrodynamics will be discussed afterwards.

Direct-photons provide the possibility to investigate the development of flow during the QGP evolution. Consistent reproduction of both the direct-photon spectra and direct-photon elliptic flow is a challenge for the current models. The state-of-the-art measurement of direct-photon elliptic flow in Pb–Pb collisions at $\sqrt{s_{NN}}$ = 2.76 TeV from the ALICE collaboration is shown in Fig. 2.18 compared to the estimated decay-photon elliptic flow from ALICE simulations, and to the predictions of several theoretical models [59]. Chatterjee et al. model [60] is based on EbyE ideal hydrodynamics with fluctuating initial conditions. Paquet et al. [57] and PHSD [56] models were already mentioned.

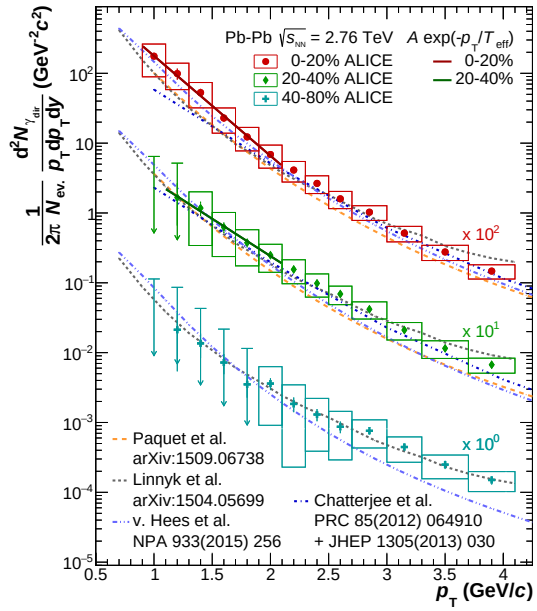

FIGURE 2.17: Comparison of model calculations from Refs. [54, 55, 56, 57] with the direct-photon spectra in Pb–Pb collisions at $\sqrt{s_{\rm NN}}$ = 2.76 TeV for the 0–20% (scaled by a factor 100), the 20–40% (scaled by a factor 10) and 40–80% centrality classes. All models include a contribution from pQCD photons. For the 0–20% and 20-40% classes the fit with an exponential function is show in addition [53].

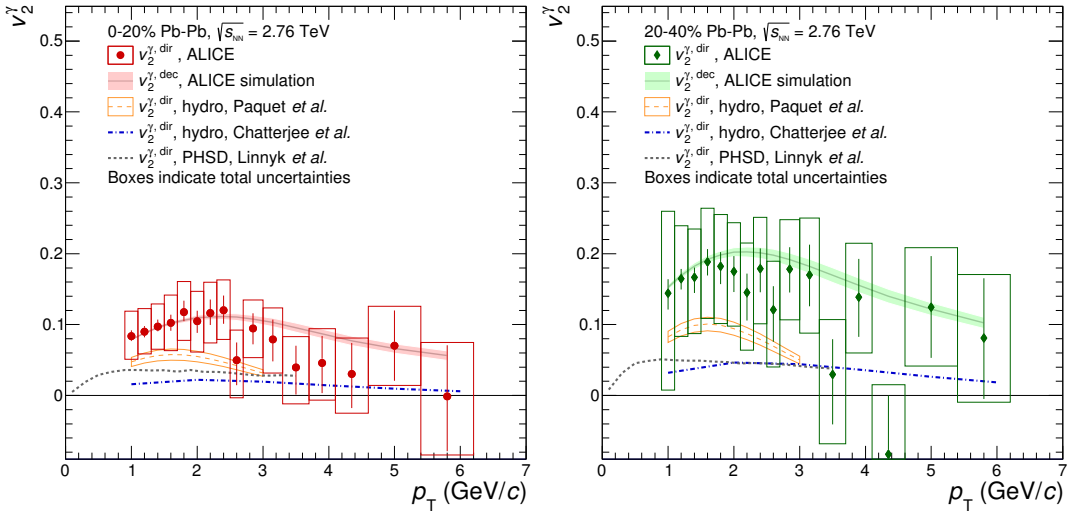

FIGURE 2.18: Elliptic flow of direct photons compared to model calculations from Refs. [56, 57, 60] in the 0–20% (left) and 20–40% (right) centrality classes. The vertical bars on each data point indicate the statistical uncertainties and the boxes the total uncertainty [59].

Modeling initial conditions using IP-Glasma [61], using a viscous hydrodynamic evolution, and an hadronic rescattering phase based on UrQMD, the direct-photon spectrum and the direct-photon v_2 have been studied in [57]. The viscous hydrodynamic evolution was configured with the parameters as obtained in [46] and the theoretical latest photon production rates were incorporated into the simulation. Fig. 2.19 presents the direct-photon spectrum and direct-photon v_2 in Pb–Pb collisions at $\sqrt{s_{\rm NN}}$ = 2.76 TeV as measured by the ALICE detector at the LHC [53, 62, 63] compared with hydrodynamic simulations. The simulations were run without incorporating ζ/s in the hydrodynamic evolution, using two different values for η/s, and incorporating ζ/s according to Fig. 2.11 profile. The ζ/s effect is

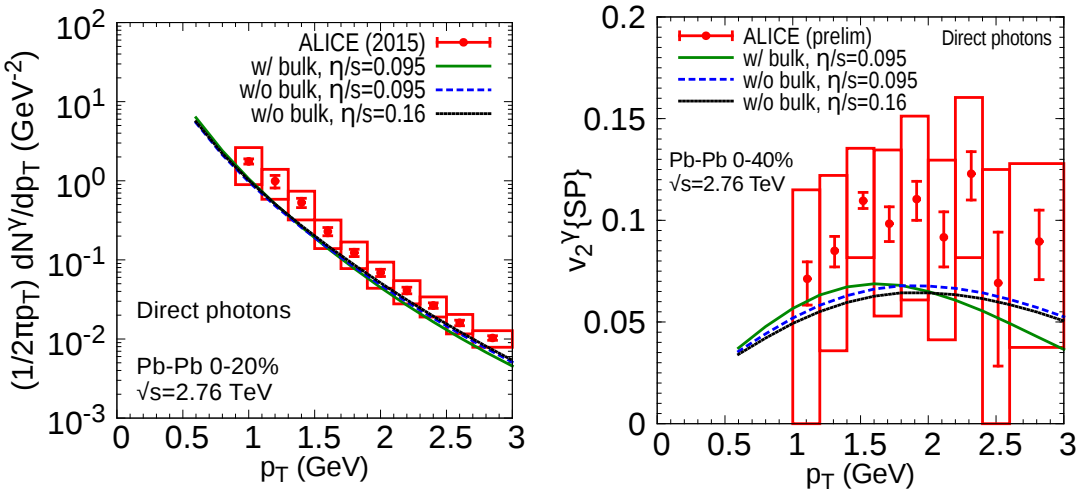

FIGURE 2.19: Effects of bulk viscosity on the direct photon spectrum (left panel) and v_2 (right panel) in Pb–Pb collisions at $\sqrt{s_{\rm NN}}$ = 2.76 TeV compared with ALICE measurements [53, 62, 63]. Bars and rectangles on ALICE data show statistical and systematic uncertainties, respectively. The two values of η/s are the ones required to properly describe hadronic v_n in the absence, $\eta/s = 0.16$, or presence, $\eta/s = 0.095$, of ζ/s with Fig. 2.11 profile [57].

small. The spectrum is slightly soften and the v_2 maximum value shifted toward lower $p_{\rm T}$, potentially signaling this as the effect of a finite bulk viscosity [57].

There are two main ζ/s contributions on the direct-photon observables. The effects on the overall spacetime evolution of the system and the effects on the photon emission rates [57]. Fig. 2.20 shows the effects, on the direct-photon spectrum and direct-photon v_2, of incorporating or not viscous corrections to the photon emission rates. There is a small effect on the direct photon spectrum interpreted from the fact that viscous corrections are larger at higher $p_{\rm T}$ where prompt photons dominate over thermal ones. The effect on v_2 is relevant at high $p_{\rm T}$ where is suppressed by both viscous corrections. Not all kind of photon emission rates are corrected for viscous effects. Consequently shown results most likely underestimate the effects of viscosity [57].

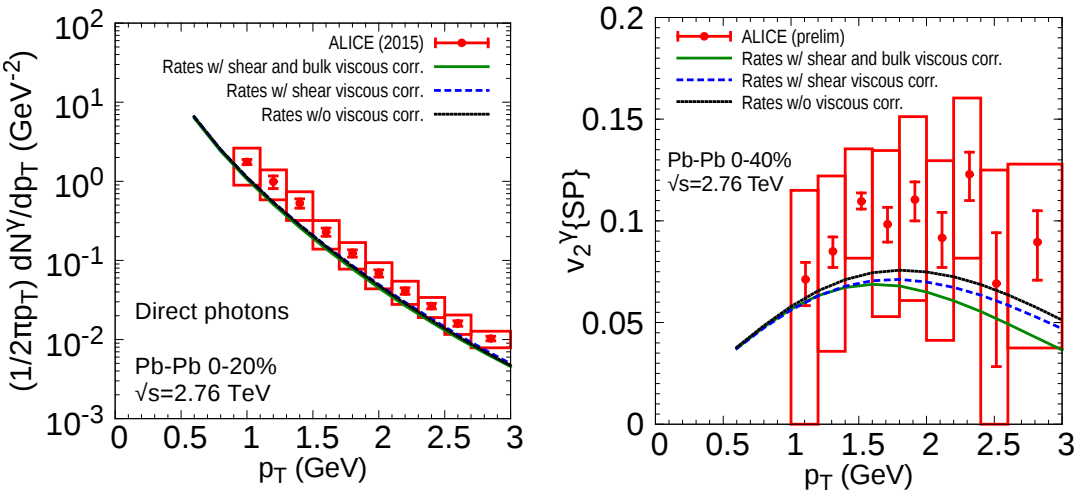

FIGURE 2.20: Effects of viscosity corrections to the photons emission rates for the direct photon spectrum (left panel) and v_2 (right panel) in Pb–Pb collisions at $\sqrt{s_{\rm NN}} = 2.76$ TeV compared with ALICE measurements [53, 62, 63]. Bars and rectangles on ALICE data show statistical and systematic uncertainties, respectively. The curves represent full viscous corrections, η/s only viscous corrections, and no viscous corrections on the photon emission rates [57].

HBT radii

The effects of bulk viscosity on the interferometry correlations were explored in [64]. Bulk viscosity was incorporated with two different profiles based on the one shown in Fig. 2.11. The first profile, denoted as $\zeta/s = 0.35$, is the same profile as in Fig. 2.11, which at the transition temperature peaks at the value $\zeta/s = 0.35$. The second profile, denoted as $\zeta/s = 0.02$, has the same profile at low temperature, below the transition, as in Fig. 2.11 but instead of peaking, decreases quickly having a value $\zeta/s = 0.02$ at the transition temperature. The value of η/s was fixed at $\eta/s = 0.08$, and a Glauber MC model was used for generating fluctuating initial condition. Fig. 2.21 shows the comparison of the Hanbury Brown and Twiss (HBT) radii with and without ζ/s effects. Although the differences are small, the presence of ζ/s reduces the ratio $R_{\rm out}/R_{\rm side}$, better describing the measured data.

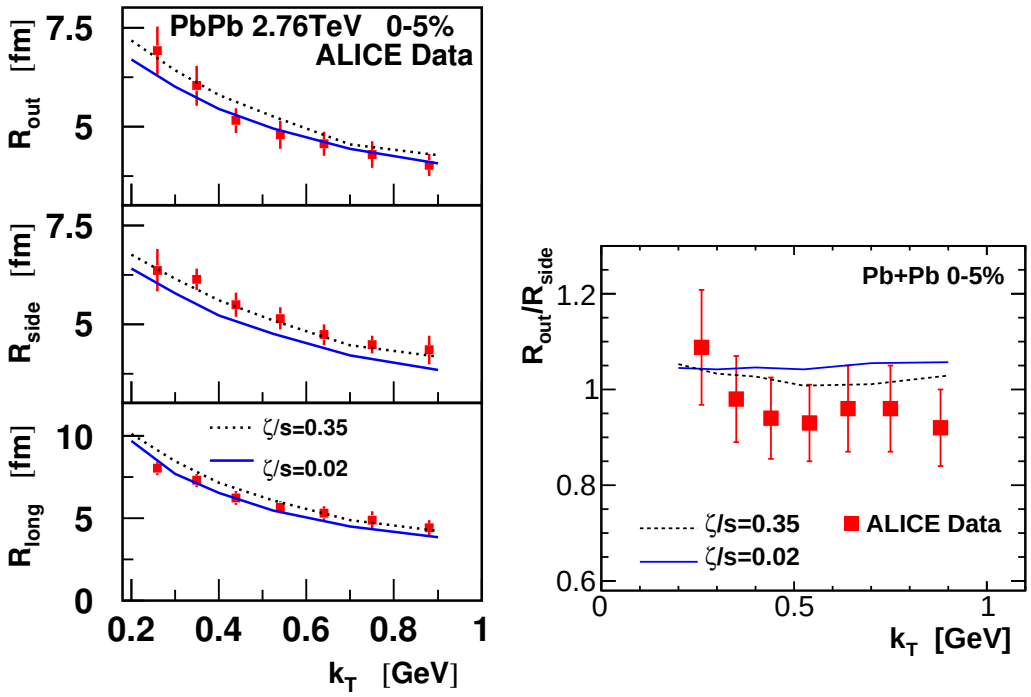

FIGURE 2.21: The HBT radii for most central Pb–Pb collisions at $\sqrt{s_{\mathrm{NN}}}$ = 2.76 TeV compared with ALICE measurements [65]. Bars on ALICE data show total uncertainties. The curves represent calculations with fluctuating initial conditions from a Glauber Monte Carlo model using a Fig. 2.11 ζ/s profile (dotted lines) and a comparable very low value which does not peak at the transition (solid lines) [64].

2.4 Two-particle correlations

Different methods for constraining η/s and ζ/s values based on comparison of measured data to expectations from models which incorporated viscous hydrodynamics have been presented in the previous section. In this section, the methods for extracting those values directly from data by using two-particle correlations are briefly described. The section begins with few basic definitions to proceed with the introduction of the two main areas of two-particle correlations, the one focused in number of particles correlations, and the one focused in momentum components correlations. Concrete two-particle correlation functions are then introduced to further describe the basis of the transport parameter extraction by using two particle correlations. Finally few available previous results are introduced.

2.4.1 Basic definitions

Correlation functions have emerged as one of the best tools to characterize particle production and to study the dynamics of HIC. The concept of particle correlation is rooted in the notion that if a particle is observed at a given point in the phase space, then there is a finite probability to observe one (or several other particles) at a different phase space point (several different phase space points). In the context of HIC there are different particle production mechanisms involved and there are few dynamics also in place. The way of inferring as much information as possible about these particle production mechanisms and system dynamics, begins by modeling the number of particles emitted in a phase space bin centered at $\vec{p}_i$, $N(\vec{p}_i)$, by a probability density function (PDF) $\mathbb{P}_1(N(\vec{p}_i))$. The average of this number, $\langle N(\vec{p}_i)\rangle$,

is then given by [66]

$$\langle N(\vec{p}_i)\rangle = \mathbb{E}\left[N(\vec{p}_i)\right] = \int N(\vec{p}_i)\,\mathbb{P}_1(N(\vec{p}_i))\,\mathrm{d}N(\vec{p}_i). \tag{2.93}$$

Likewise, the number of particles jointly emitted in two phase space bins centered at $\vec{p}_i$ and $\vec{p}_j$, can be modeled by a joint PDF $\mathbb{P}_2(N(\vec{p}_i), N(\vec{p}_j))$ where then

$$\langle N(\vec{p}_i)\,N(\vec{p}_j)\rangle = \mathbb{E}\left[N(\vec{p}_i)\,N(\vec{p}_j)\right] = \int N(\vec{p}_i)\,N(\vec{p}_j)\,\mathbb{P}_2(N(\vec{p}_i), N(\vec{p}_j))\,\mathrm{d}N(\vec{p}_i)\,\mathrm{d}N(\vec{p}_j). \tag{2.94}$$

The number of particles produced at $\vec{p}_i$ and $\vec{p}_j$ can be considered uncorrelated if and only if the joint probability can be factorized [66]

$$\mathbb{P}_{2,\mathrm{uncor}}(N(\vec{p}_i), N(\vec{p}_j)) = \mathbb{P}_1(N(\vec{p}_i)) \times \mathbb{P}_1(N(\vec{p}_j)) \tag{2.95}$$

A measure of the degree of correlation is then given by the covariance of $N(\vec{p}_i)$ and $N(\vec{p}_j)$

$$\mathbb{C}[N(i), N(j)] = \mathbb{E}[N(i)\,N(j)] - \mathbb{E}[N(i)]\,\mathbb{E}[N(j)] \tag{2.96}$$

where, for convenience, the substitution $N(\vec{p}_i) \to N(i)$ has been taken.

Defining the single- and two-particle density distributions as

$$\rho_1(\vec{p}_i) = \langle N(i)\rangle\,\mathbb{P}_1(N(\vec{p}_i)) = \frac{\mathrm{d}^3N}{\mathrm{d}\vec{p}_i} \tag{2.97}$$

$$\rho_2(\vec{p}_i, \vec{p}_j) = \langle N(i)\,N(j)\rangle\,\mathbb{P}_2(N(\vec{p}_i), N(\vec{p}_j)) = \frac{\mathrm{d}^6N}{\mathrm{d}\vec{p}_i\,\mathrm{d}\vec{p}_j}, \tag{2.98}$$

the covariance in Eq. (2.96) as a function of the single- and two-particle densities in Eqs. (2.97) and (2.98) stays as

$$r(\vec{p}_i, \vec{p}_j) = \rho_2(\vec{p}_i, \vec{p}_j) - \rho_1(\vec{p}_i)\rho_1(\vec{p}_j) \tag{2.99}$$

where, consequently, when particles produced at $\vec{p}_i$ and $\vec{p}_j$ are uncorrelated r vanishes.

2.4.2 Two-particle number correlations

The normalized two-particle number correlation function R_2 reads as

$$\begin{aligned} R_2(\vec{p}_i, \vec{p}_j) &= \frac{\mathbb{C}[N(i), N(j)]}{\mathbb{E}[N(i)]\,\mathbb{E}[N(j)]} \\ &= \frac{\mathbb{E}[N(i)\,N(j)]}{\mathbb{E}[N(i)]\,\mathbb{E}[N(j)]} - 1 \\ &= \frac{\langle N(i)\,N(j)\rangle}{\langle N(i)\rangle\,\langle N(j)\rangle} - 1. \end{aligned} \tag{2.100}$$

When both i and j match, i.e when both bins are the same, and there is only one set of indistinguishable particles then

$$R_2(\vec{p}_i, \vec{p}_i) = \frac{\langle N(i)\,(N(i)-1)\rangle}{\langle N(i)\rangle^2} - 1. \tag{2.101}$$

The one set of indistinguishable particles condition also happens when there are distinguishable particles but all of them are included, without distinction, in the process of extracting the correlation function.

The two-particle number correlation function R_2 is encountered defined with different expressions in the literature, although all of them represent the same principle. When the single- and two-particle densities in Eqs. (2.97) and (2.98) are used, the two-particle number correlation function R_2 adopts the form

$$R_2(\vec{p}_i, \vec{p}_j) = \frac{\int_{i,j} \rho_2(\vec{p}_i, \vec{p}_j)\, \mathrm{d}\vec{p}_i\, \mathrm{d}\vec{p}_j}{\int_i \rho_1(\vec{p}_i)\, \mathrm{d}\vec{p}_i \int_j \rho_1(\vec{p}_j)\, \mathrm{d}\vec{p}_j} - 1 \tag{2.102}$$

where the integrals are intended over the phase space spanned by bin i, by bin j, or by both i and j.

In some cases ρ_1 and ρ_2 are directly associated with the average of the number of particles emitted in a finite size bin centered at $\vec{p}_i$ and to the average of the number of pairs emitted in two finite size bins centered at $\vec{p}_i$ and $\vec{p}_j$, respectively

$$\rho_1(\vec{p}_i) = \langle N(i) \rangle = \int_i \frac{\mathrm{d}^3 N}{\mathrm{d}\vec{p}_i}\, \mathrm{d}\vec{p}_i \tag{2.103}$$

$$\rho_2(\vec{p}_i, \vec{p}_j) = \langle N(i)\, N(j) \rangle = \int_{i,j} \frac{\mathrm{d}^6 N}{\mathrm{d}\vec{p}_i\, \mathrm{d}\vec{p}_j}\, \mathrm{d}\vec{p}_i\, \mathrm{d}\vec{p}_j \tag{2.104}$$

in which case the two-particle number correlator adopts the form

$$R_2(\vec{p}_i, \vec{p}_j) = \frac{\rho_2(\vec{p}_i, \vec{p}_j)}{\rho_1(\vec{p}_i)\, \rho_1(\vec{p}_j)} - 1. \tag{2.105}$$

When there are no correlations between the number of particles emitted in the bin centered at $\vec{p}_i$ and the number of particles emitted in the bin centered at $\vec{p}_j$ the value of the correlator $R_2(\vec{p}_i, \vec{p}_j)$ vanishes. This also happens during local equilibrium where the system behaves according to Poisson statistics and the pair distribution factors $\rho_2(\vec{p}_i, \vec{p}_j) \to \rho_1(\vec{p}_i)\, \rho_1(\vec{p}_j)$. Therefore R_2 is a measure of the dynamical fluctuations of the density of the number of emitted particles. A relevant feature of the R_2 correlators is that they are 'robust' in the sense that they are independent of the experimental efficiency, provided that the efficiency is independent of the multiplicity [67].

For correcting limited detector acceptance, what is, usually, experimentally measured is the quantity

$$R_2(\vec{p}_i, \vec{p}_j) = \frac{\rho_2^{\mathrm{same}}(\vec{p}_i, \vec{p}_j)}{\rho_2^{\mathrm{mixed}}(\vec{p}_i, \vec{p}_j)} \tag{2.106}$$

where ρ_2^{same} and ρ_2^{mixed} stand for the two-particle density extracted from a single event and from a set of events with the same characteristics, respectively. For concreteness, in ρ_2^{same} both indexes, i and j 'pick' tracks from the same event. In ρ_2^{mixed} the index i 'picks' tracks from one event while index j 'picks' tracks from a set of events with similar characteristics to the previous one. Apart from the obvious simplification of removing the 'ones' from Eq. (2.105), Eq. (2.106), which synthesizes the mixed events technique, relays on the assumption that the single-particle density is approximately the same across events and then it cancels out in the actual ratio $R_2^{\mathrm{same}}/R_2^{\mathrm{mixed}}$. The aim is that the denominator cancels all detector limited acceptance effects and does not introduce any alteration in the correlation function because it is, by construction, uncorrelated[2].

In general, and this applies also to the next section on two-particle momentum correlations, correlators can be measured for identified particles. The most basic identification is the particle charge sign.

[2]Of course, the number of events used for the mixing and the granularity of the classes used for select them could have its impact on the degree of correlation introduced by the denominator in Eq. (2.106).

It is then immediate to define the R_2^{++}, R_2^{+-}, R_2^{-+} and R_2^{--}, correlation functions

$$R_2^{\alpha\beta}(\vec{p}_i^{\,\alpha}, \vec{p}_j^{\,\beta}) = \frac{\rho_2^{\alpha\beta}(\vec{p}_i^{\,\alpha}, \vec{p}_j^{\,\beta})}{\rho_1^{\alpha}(\vec{p}_i^{\,\alpha})\, \rho_1^{\beta}(\vec{p}_j^{\,\beta})} - 1 \tag{2.107}$$

with $\alpha, \beta = +, -$, the like sign (LS) and unlike sign (US) correlation functions, R_2^{LS} and R_2^{US}, respectively,

$$R_2^{\mathrm{LS}} = \frac{1}{2}\left(R_2^{++} + R_2^{--}\right) \tag{2.108}$$

$$R_2^{\mathrm{US}} = \frac{1}{2}\left(R_2^{+-} + R_2^{-+}\right), \tag{2.109}$$

and, from them, the charge independent (CI) and charge dependent (CD) correlation functions

$$R_2^{\mathrm{CI}} = \frac{1}{2}\left(R_2^{US} + R_2^{LS}\right) \tag{2.110}$$

$$R_2^{\mathrm{CD}} = \frac{1}{2}\left(R_2^{US} - R_2^{LS}\right). \tag{2.111}$$

CI correlators give a measure of the average strength of the correlations between all charged particles. CD correlators give a measure of the difference in the strength of the correlations between US pairs and LS pairs. A key example of this characteristic is the absence of charge independent azimuthal collectivity in these correlators. The charge independent azimuthal collectivity affects in the same way to US pairs as to LS pairs then, by construction, it cancels out. Another example are momentum conservation effects. At LHC energies similar number of positively and negatively charged particles are produced and they show very similar p_{T} spectra [68]. Consequently, the impact of energy-momentum conservation is expected to be of about the same magnitude for US pairs as for LS pairs therefore, again by construction, the effects cancel out. The CD correlator is then left sensitive to charge pair creation, and transport processes [69]. R_2 two-particle number correlator has been reported by the ALICE collaboration in [69].

The scope of the two-particle number correlations is considerably enlarged when instead of electric charges the generic charge concept is incorporated in a straightforward manner by assigning to α and β in Eq. (2.107) the corresponding values of the conserved generic charges, e.g. strangeness, charm, etc, directly or by the actual particles which carry them.

2.4.3 Two-particle momentum components correlations

By incorporating to the single- and two-particle density distributions from Eqs. (2.97) and (2.98) the different momentum components as weights, different two-particle correlations can be defined.

Correlations denominated as $\langle \Delta p\, \Delta p \rangle$ are defined as

$$\langle \Delta p_\sigma(\vec{p}_i)\, \Delta p_\lambda(\vec{p}_j) \rangle = \frac{\int \rho_2(\vec{p}_i, \vec{p}_j)\, \Delta p_\sigma(\vec{p}_i)\, \Delta p_\lambda(\vec{p}_j)\, \mathrm{d}\vec{p}_i\, \mathrm{d}\vec{p}_j}{\int \rho_2(\vec{p}_i, \vec{p}_j)\, \mathrm{d}\vec{p}_i\, \mathrm{d}\vec{p}_j} \tag{2.112}$$

where $\sigma, \lambda = x, y, z, \mathrm{T}$, denote the particle momentum component of interest, and $\Delta p_\gamma(\vec{p}_\alpha) = p_{\alpha\gamma} - \langle p_{\alpha\gamma} \rangle$, what the γ component of a particle emitted in a bin centered at $\vec{x}_\alpha$ deviates from the average of that component on this bin, for $\gamma = \sigma, \lambda$, and $\alpha = i, j$. The correlation in Eq. (2.112) vanishes in equilibrium, when there are not fluctuations, or when the momentum fluctuations in particles emitted in the bin centered at $\vec{p}_i$ are not correlated with momentum fluctuation in particles emitted in the bin centered at $\vec{p}_j$, so $\langle \Delta p\, \Delta p \rangle$ correlations are sensitive to momentum components fluctuations. They give a measure of the expected deviations of the momentum component σ with respect to its mean in a bin

centered at $\vec{p}_i$ knowing the deviations of the momentum component λ with respect to its mean in a bin centered at $\vec{p}_i$. As will be later described, the most common $\langle \Delta p\, \Delta p \rangle$ correlation function is $\langle \Delta p_{\mathrm{T}}\, \Delta p_{\mathrm{T}} \rangle$ where both, σ and λ, denote the transverse component.

By incorporating to the two-particle covariance from Eq. (2.99) the different momentum components as weights, a different set of two-particle momentum components correlations is defined as

$$\begin{aligned} C_{\sigma\lambda}(\vec{p}_i, \vec{p}_j) &\equiv \frac{1}{\langle N(i)\rangle\langle N(j)\rangle} \int p_{i\sigma} p_{j\lambda}\, r(\vec{p}_i, \vec{p}_j)\, \mathrm{d}\vec{p}_i\, \mathrm{d}\vec{p}_j \\ &= \frac{1}{\langle N(i)\rangle\langle N(j)\rangle} \left\langle \sum_{k\neq l} p_{k\sigma} p_{l\lambda} \right\rangle - \langle p_{i\sigma}\rangle\langle p_{j\lambda}\rangle \end{aligned} \tag{2.113}$$

where $\sigma, \lambda = x, y, z, \mathrm{T}$, denote the momentum component of interest, and the sum is a double sum over particle pairs k and l where k runs over the number of particles emitted in the bin centered at $\vec{x}_i$ and l runs over the number of particles emitted in the bin centered at $\vec{x}_i$, with the condition $k \neq l$ applying only when $i = j$, i.e. correlations on the same bin. As r vanishes in equilibrium the same happens with C. As will be described in sect. 2.4.5, the correlations defined by Eq.(2.113) are built to be sensitive to momentum components currents and as such to the fluctuations of the momentum component of the particles as well as to those of their number density [70]. Again, as in the previous case, the transverse component of the momentum is the one usually utilized. As such the next section will focus on two-particle transverse momentum correlations.

2.4.4 Two-particle transverse momentum correlations

Dimensionless two-particle transverse momentum correlation P_2 is defined from Eq. (2.112) as

$$P_2(\vec{p}_i, \vec{p}_j) = \frac{\langle \Delta p_{\mathrm{T}}(\vec{p}_i)\, \Delta p_{\mathrm{T}}(\vec{p}_j)\rangle}{\langle p_{\mathrm{T}}\rangle^2} = \frac{1}{\langle p_{\mathrm{T}}\rangle^2} \frac{\int \rho_2(\vec{p}_i, \vec{p}_j)\, \Delta p_{\mathrm{T}}(\vec{p}_i)\, \Delta p_{\mathrm{T}}(\vec{p}_j)\, \mathrm{d}\vec{p}_i\, \mathrm{d}\vec{p}_j}{\int \rho_2(\vec{p}_i, \vec{p}_j)\, \mathrm{d}\vec{p}_i\, \mathrm{d}\vec{p}_j} \tag{2.114}$$

where, as described before, $\Delta p_{\mathrm{T}}(\vec{p}_\alpha) = p_{\alpha\mathrm{T}} - \langle p_{\alpha\mathrm{T}}\rangle$, is what the p_{T} of a particle emitted in a bin centered at $\vec{p}_\alpha$ deviates from its average, $\langle p_{\alpha\mathrm{T}}\rangle$, in this bin, for $\alpha = i, j$, and $\langle p_{\mathrm{T}}\rangle = \int \rho_1\, p_{\mathrm{T}}\, \mathrm{d}p_{\mathrm{T}} \,/ \int \rho_1\, \mathrm{d}p_{\mathrm{T}}$, the inclusive average momentum of produced particles in an event ensemble [69]. The same said above for the $\langle \Delta p\, \Delta p \rangle$ correlations apply for P_2 , specifically, P_2 gives a measure of the expected deviations of the p_{T} with respect to its average in a bin centered at $\vec{p}_i$ knowing the deviations of the p_{T} with respect to its average in a bin centered at $\vec{p}_i$. Deviations can be positive or negative and the same applies to P_2. Two-particle transverse momentum correlator P_2 has been measured by the ALICE collaboration in [69].

Two particle transverse momentum correlator G_2, the focus of this thesis, is defined from Eq. (2.113) as

$$G_2(\vec{p}_i, \vec{p}_j) = \frac{1}{\langle N(i)\rangle\langle N(j)\rangle} \left\langle \sum_{k\neq l} p_{k\mathrm{T}} p_{l\mathrm{T}} \right\rangle - \langle p_{i\mathrm{T}}\rangle\langle p_{j\mathrm{T}}\rangle \tag{2.115}$$

where, as before, the sum is a double sum over particle pairs k and l where k runs over the number of particles emitted in the bin centered at $\vec{p}_i$ and l runs over the number of particles emitted in the bin centered at $\vec{p}_j$, with the condition $k \neq l$ applying only when $i = j$, i.e. correlations on the same bin. The same said above for $C_{\sigma\lambda}$ correlations apply for G_2, specifically, G_2 is built to be sensitive to transverse momentum currents and as such to p_{T} fluctuations and to number density fluctuations. The rationale for introducing G_2 will be described in the next section, where the links to the transverse momentum current fluctuations dissipation and to the effects of η/s are briefly introduced, which will give pass to its extraction in the section after the next.

2.4.5 Momentum fluctuations

Long range correlations are causally disconnected from any hydrodynamic evolution of fluctuations. Of course hydrodynamic evolution is in the origin of the collective behavior measured as long range correlations, but the role of the hydrodynamic evolution there is to transfer anisotropic initial conditions to the final state where they are measured. The focus here is on short range correlations, actually, in correlations of transverse momentum fluctuations which will develop during the hydrodynamic evolution and, therefore, will have a limited reach. Fluctuations in transverse momentum are different from fluctuations in particle number. While transverse momentum is a conserved quantity particle number is not. For extracting the way transverse momentum currents evolve within a relativistic near of equilibrium fluid, the momentum density current of a single fluid element is expressed as

$$T^{0i} = \gamma(\epsilon + p)u^i \tag{2.116}$$

and, then, in the fluid co-moving frame (where $u^\mu = (1, 0, 0, 0)$) the fluctuations in the momentum current are given by

$$\delta T^{0i} = (\epsilon + p)\delta u^i \tag{2.117}$$

When studying the causality violation of the Navier-Stokes equation in section 2.1.2 it was shown that for small perturbations, excluding bulk viscous effects and in absence of charge currents, the linearized transverse equation was, Eq. (2.51),

$$\partial_t \delta u^y - \nu \nabla^2 \delta u^y = 0 \tag{2.118}$$

with $\nu = \eta/(\epsilon + p) = \eta/(Ts)$, i.e the transverse flow fluctuations propagate via diffusion. A similar procedure gives the linearized transverse equation within the second order in gradients Müller-Israel-Stewart theory as [71]

$$\tau_\pi \partial_t^2 \delta u^y + \partial_t \delta u^y - \nu \nabla^2 \delta u^y = 0, \tag{2.119}$$

i.e. in second order in gradients theory the transverse flow fluctuations propagate via waves and via diffusion. Fluctuations in the transverse flow give rise to fluctuations in the transverse momentum. Using (2.117) in Eqs. (2.118) and (2.119) gives

$$\partial_t \delta T^{0y} = \nu \nabla^2 \delta T^{0y} \tag{2.120}$$

$$\tau_\pi \partial_t^2 \delta T^{0y} + \partial_t \delta T^{0y} = \nu \nabla^2 \delta T^{0y} \tag{2.121}$$

for the first and second order in gradients transverse momentum fluctuations propagation equations.

Eqs. (2.120) and (2.121) show that viscosity tends to reduce transverse momentum fluctuations distributing, by diffusion or by wave propagation, the excess of momentum density over the collision volume. This effect broadens the rapidity profile of fluctuations. To compute this broadening in first order of gradients approximation, Eq.(2.120) is written in terms of the spatial rapidity, ξ, and proper time, τ, as[3]

$$\partial_\tau \delta T^{0\xi} = \frac{\nu}{\tau^2} \partial_{\xi\xi}^2 \delta T^{0\xi}. \tag{2.124}$$

[3] The use of spatial rapidity and proper time as coordinates is justified by considering longitudinal boost invariant Bjorken flow whose four-velocity, with these coordinates, is

$$u^\mu = \left(\frac{t}{\tau}, 0, 0, \frac{z}{\tau}\right). \tag{2.122}$$

The boost invariant Bjorken flow is based on the observation of a plateau structure, flatness, of the charged particle multiplicity $\mathrm{d}N_{\mathrm{ch}}/\mathrm{d}y$ in the mean rapidity region. This "central-plateau" structure can be interpreted as the invariance under longitudinal Lorentz boosts of the mean rapidity region [72]. In Milne coordinates (τ, x, y, ξ)

$$u^\xi = \frac{\partial \xi}{\partial \tau} = \frac{\partial t}{\partial \tau}\frac{\partial \xi}{\partial t} + \frac{\partial z}{\partial \tau}\frac{\partial \xi}{\partial z} = u^t\left(-\frac{z}{\tau^2}\right) + u^z\left(\frac{t}{\tau^2}\right) = 0, \tag{2.123}$$

Multiplying Eq. (2.124) by the squared spatial rapidity ξ^2, integrating and expressing the variance of the transverse momentum fluctuations as

$$\mathrm{Var}_{\delta T} \equiv \langle (\xi - \langle \xi \rangle)^2 \rangle = \frac{\int \xi^2 \delta T^{0\xi} \mathrm{d}\xi}{\int \delta T^{0\xi} \mathrm{d}\xi} \tag{2.125}$$

as a measure of their reach, Eq. (2.124) gives [73, 74, 75]

$$\mathrm{Var}_{\delta T}(\tau) - \mathrm{Var}_{\delta T}(\tau_0) = 2\nu \left(\frac{1}{\tau_0} - \frac{1}{\tau} \right) \tag{2.126}$$

where τ_0 refers to the formation time where the hydrodynamic evolution starts.

This variance of the momentum fluctuations needs to be linked to actual HIC observables. On this purpose, transverse momentum fluctuations δT^{0y} are used to construct a transverse momentum correlation function between fluid cells. Tagging with i and j two of such fluid cells, a transverse momentum correlation function can be defined as

$$r = \langle T^{0y}(\vec{x}_i) T^{0y}(\vec{x}_j) \rangle - \langle T^{0y}(\vec{x}_i) \rangle \langle T^{0y}(\vec{x}_j) \rangle \tag{2.127}$$

where $\vec{x}_i$ and $\vec{x}_j$ represent the location of the fluid cells, the correlations are equal time correlations, and $\langle \cdots \rangle$ represent average over events ensembles. In Eq. (2.127) r represents the spatial correlations of the momentum currents. Considering small perturbations on T^{0y}

$$\delta T^{0y} = T^{0y} - \langle T^{0y} \rangle, \tag{2.128}$$

treating perturbations as stochastic in nature, and using stochastic methods, the displacement from equilibrium of the correlation function in Eq. (2.127), $\Delta r = r - r_{\mathrm{eq}}$, is expressed in terms of the transverse momentum fluctuations as [71]

$$\Delta r = \langle \delta T_i^{0y} \bar{T}_j^{0y} \rangle + \langle \bar{T}_i^{0y} \delta T_j^{0y} \rangle + \langle \delta T_i^{0y} \delta T_j^{0y} \rangle \tag{2.129}$$

where, for convenience, $T^{0y}(\vec{x}_\alpha)$ has been substituted by T_α^{0y} for $\alpha = i, j$, and $\langle T_\alpha^{0y} \rangle$ has been substituted by $\bar{T}_\alpha^{0y}$ also for $\alpha = i, j$. Applying now the transverse momentum fluctuations propagation equations, Eqs. (2.120) and (2.121) on the correlation function Eq. (2.129), the propagation of the differences from equilibrium of the transverse momentum fluctuations correlation function gives [71]

$$\partial_t \Delta r = \nu \left(\nabla_i^2 + \nabla_j^2 \right) \Delta r \tag{2.130}$$

$$\tau_\pi \partial_t^2 \Delta r + \partial_t \Delta r = \nu \left(\nabla_i^2 + \nabla_j^2 \right) \Delta r \tag{2.131}$$

where $\nabla_\alpha^2 f$ stands for the value of $\nabla^2 f$ at the fluid cell situated at $\vec{x}_\alpha$ for $\alpha = i, j$. Similar results were also derived for the propagation of net charge fluctuations in [73].

Expressing now Eqs. (2.130) and (2.131) in terms of proper time and spatial rapidity, as before, gives

$$\partial_\tau \Delta r = \frac{\nu}{\tau^2} \left(\nabla_i^2 + \nabla_j^2 \right) \Delta r \tag{2.132}$$

$$\tau_\pi \partial_\tau^2 \Delta r + \partial_\tau \Delta r = \frac{\nu}{\tau^2} \left(\nabla_i^2 + \nabla_j^2 \right) \Delta r \tag{2.133}$$

using u^t and u^z from Eq. (2.122). Since the velocity on the ξ-axis vanishes all initially independent of ξ magnitudes are invariant under Lorentz boosts along the ξ-axis.

For first order in gradients theory, Eq. (2.132), transverse momentum fluctuations propagate by means of diffusion governed by η/s. For second order in gradients theory, Eq. (2.133), transverse momentum fluctuations propagate by means of waves with diffusion getting relevance when the relaxation time τ_π is reached. For first order in gradients the spatial rapidity dependence of Δr is broadened by momentum diffusion. If the rapidity width for the transverse momentum fluctuations follows Eq. (2.126) then the width of Δr, σ, in the relative rapidity, $\Delta\xi = \xi_i - \xi_j$, grows from an initial value σ_0 following [74, 75]

$$\sigma^2 = \sigma_0^2 + 2(\mathrm{Var}_{\delta T}(\tau) - \mathrm{Var}_{\delta T}(\tau_0)) = \sigma_0 + \frac{4}{T}\frac{\eta}{s}\left(\frac{1}{\tau_0} - \frac{1}{\tau}\right). \tag{2.134}$$

In this expression, Eq. (2.134), the rapidity width at proper time τ, σ_τ, of the deviations from the equilibrium value of the transverse momentum correlation function r defined in Eq. (2.127), is expressed in terms of its width at formation time, σ_0, the system temperature, T, and the η/s value.

2.4.6 Extraction of the shear viscosity over entropy density ratio

Considering now the single particle phase space distribution

$$f(\vec{x}, \vec{p}) = \frac{\mathrm{d}n}{\mathrm{d}\vec{x}\,\mathrm{d}\vec{p}} \tag{2.135}$$

which gives the number of particles of momentum $\vec{p}$ in a cell at position $\vec{x}$, observing [74]

$$\begin{aligned}
\sum p_\mathrm{T} &= \int p_\mathrm{T}\,\mathrm{d}n \\
&= \int p_\mathrm{T} f(\vec{x}, \vec{p})\,\mathrm{d}\vec{x}\,\mathrm{d}\vec{p} \\
&= \int T^{0y}\,\mathrm{d}\vec{x}
\end{aligned} \tag{2.136}$$

$$\begin{aligned}
\sum p_{\mathrm{T}i} p_{\mathrm{T}j} &= \int p_{\mathrm{T}i} p_{\mathrm{T}j}\,\mathrm{d}n_i\,\mathrm{d}n_j \\
&= \int p_{\mathrm{T}i} p_{\mathrm{T}j} f(\vec{x}_i, \vec{p}_i)\, f(\vec{x}_j, \vec{p}_j)\,\mathrm{d}\vec{x}_i\,\mathrm{d}\vec{p}_i\,\mathrm{d}\vec{x}_j\,\mathrm{d}\vec{p}_j \\
&= \int T_i^{0y} T_j^{0y}\,\mathrm{d}\vec{x}_i\,\mathrm{d}\vec{x}_j
\end{aligned} \tag{2.137}$$

where

$$T^{0y} = \int p_\mathrm{T} f(\vec{x}, \vec{p})\,\mathrm{d}\vec{p} \tag{2.138}$$

has been used, and noting that in Eq. 2.137, the sum is unrestricted so

$$\sum p_{\mathrm{T}i} p_{\mathrm{T}j} = \sum_{i \neq j} p_{\mathrm{T}i} p_{\mathrm{T}j} + \sum p_{\mathrm{T}i}^2, \tag{2.139}$$

the spatial correlations of the momentum currents in Eq. (2.127) can be expressed as

$$\begin{aligned}
\int r\,\mathrm{d}\vec{x}_i\,\mathrm{d}\vec{x}_j &= \left\langle \sum p_{\mathrm{T}i} p_{\mathrm{T}j} \right\rangle - \langle N \rangle^2 \langle p_\mathrm{T} \rangle^2 \\
&= \langle N \rangle^2 G_2 + \sum p_{\mathrm{T}i}^2
\end{aligned} \tag{2.140}$$

where G_2 from Eq. (2.115) as defined in sect. 2.4.4 has been used. As described in sect. 2.4.4, in equilibrium G_2 vanishes so, finally,

$$G_2 = \frac{1}{\langle N \rangle^2} \int \Delta r(\vec{x}_i, \vec{x}_j)\, \mathrm{d}\vec{x}_i\, \mathrm{d}\vec{x}_j \tag{2.141}$$

by using $\int r_{\mathrm{eq}}\, \mathrm{d}\vec{x}_i\, \mathrm{d}\vec{x}_j = \sum p_{\mathrm{T}_i}^2$ from Eq. (2.140).

Viscosity information can then be obtained from G_2 as follows. The broadening in rapidity of deviations from equilibrium of the spatial correlations of the momentum current, Δr, depends on η/s via Eq. (2.134)

$$\sigma_c^2 - \sigma_0^2 = \frac{4}{T_c}\frac{\eta}{s}\left(\frac{1}{\tau_0} - \frac{1}{\tau_{\mathrm{c,f}}}\right) \tag{2.142}$$

with σ_c and σ_0 the longitudinal widths for most central and most peripheral collisions, respectively, τ_0 the formation time, $\tau_{\mathrm{c,f}}$ the freeze out time for the most central collisions, and T_c the critical temperature. Equation (2.140) implies that the rapidity dependence of Δr, and as such its longitudinal broadening, can be measured by studying the dependence of G_2 (Eq. (2.115)) on the rapidity window in which particles are measured [74]. Taking $\tau_0 = 1$ fm as the formation time, $\tau_c = 20$ fm as the freeze out time for central collisions, and $T_c = 170$ MeV, as the critical temperature, the value of η/s was estimated in [74]. The potential broadening of G_2^{CI} was inferred from the broadening of the transverse momentum differential correlations reported by STAR collaboration, which in its turn was inferred from event-wise mean transverse momentum fluctuations, [76]. Due to this uncertainty in the extraction of the broadening of G_2^{CI} the value for η/s reported in [74] is in the range $0.08 < \eta/s < 0.3$.

STAR collaboration measured the two-particle transverse momentum correlator[4] G_2^{CI} in Au–Au collisions at $\sqrt{s_{\mathrm{NN}}} = 200$ GeV [77]. The near side longitudinal projection of G_2^{CI} for three centrality classes is shown in Fig. 2.22 while its longitudinal width as a function of the number of participant nucleons, N_{part}, is shown in Fig. 2.23.

The width of the near side longitudinal projections of the correlator was extracted by calculating their RMS above a long range baseline, b, determined using the ansatz

$$g(b, a_{\mathrm{w}}, \sigma_{\mathrm{w}}, a_{\mathrm{n}}, \sigma_{\mathrm{n}}) = b + a_{\mathrm{w}} e^{-\frac{\Delta\eta^2}{2\sigma_{\mathrm{w}}^2}} + a_{\mathrm{n}} e^{-\frac{\Delta\eta^2}{2\sigma_{\mathrm{n}}^2}} \tag{2.143}$$

to fit the projections, where a_{w} and a_{n} stand for the amplitude of wide and narrow Gaussian with widths σ_{w} and σ_{n}, respectively. A lower bound of the RMS values, shown as dotted line in Fig. 2.23, was estimated by setting the value of the baseline equal to the values of the correlation at $\Delta\eta = 2.0$.

This section described a method for extracting the η/s values by means of two-particle transverse momentum correlations directly from measured data. This will be the method that will be used in this thesis.

[4] At that time, and also in the original work from Gavin et al. [74], G_2 correlator was denominated C. As that denomination is quite generic, during the development of this thesis work S. Voloshin suggested the G_2 denomination which, from one side, refers to its two-particle nature, paralleling that of R_2 and P_2, and from the other recognizes the inventor as the promoter of the idea.

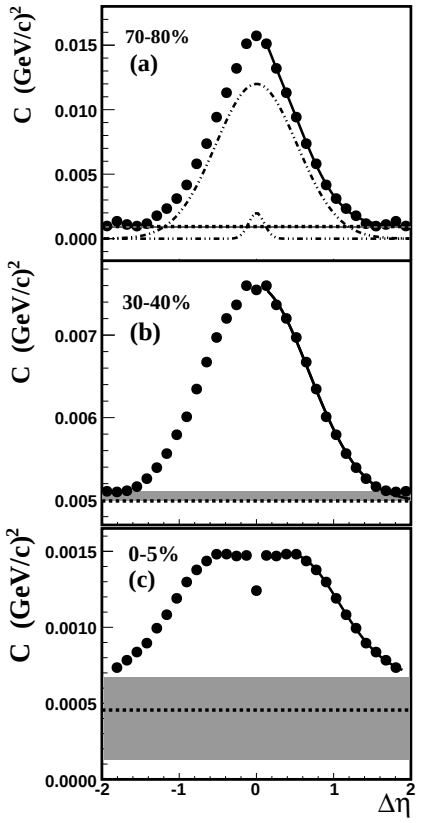

FIGURE 2.22: (a) Projection of the correlation function C, for $|\Delta\varphi| < 1.0$ (rad) on the $\Delta\eta$ axis for 70–80% centrality, (b) 30–40% centrality, and (c) 0–5% centrality in Au–Au collisions at $\sqrt{s_{\mathrm{NN}}} = 200$ GeV. The correlation function C is plotted in units of $(\mathrm{GeV}/c)^2$. The solid line shows the fit obtained with Eq. (2.143). The dotted line corresponds to the baseline b, obtained in the fit and shaded band shows uncertainty in determining b [77].

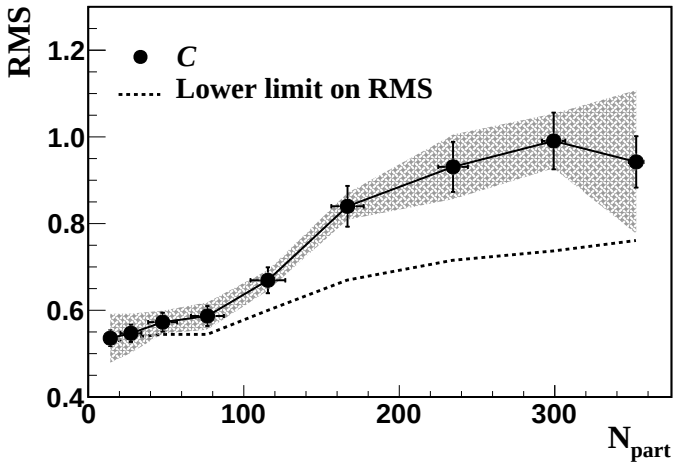

FIGURE 2.23: RMS as function of the number of participating nucleons for the correlation function C, for nine centrality classes in Au–Au collisions at $\sqrt{s_{\mathrm{NN}}} = 200$ GeV. The dotted line represents a lower limit estimate of the RMS explained in the text and the shaded band represents systematic uncertainties on the RMS [77].

2.4.7 Bulk viscosity extraction

This section will briefly describe a method for extracting the values of ζ using two-particle momentum correlations. This section is an extract of my master thesis [78] where the derivation of the suggested method for extracting the bulk viscosity by using two-particle momentum correlations is described.

According to the Landau and Lifschitz treatment of fluctuations in fluid dynamics [9], the viscous stress tensor $\Pi^{\mu\nu}$ (Eq. (2.38)) for a real fluid without charged currents in first order in gradients theory (Eqs. (2.42) and (2.43)) can be expressed as the sum of a term, τ^{hyd}, containing the hydrodynamic contribution, proportional to the fluid velocity (u^ν) gradients, and also a term, t, with pure statistical origin, that incorporates fluctuations not connected with such velocity gradients

$$\Pi_{\mu\nu} = \tau^{\text{hyd}}_{\mu\nu} + t_{\mu\nu} = -\eta\left(\partial_\mu u_\nu + \partial_\nu u_\mu - \frac{2}{3}\delta_{\mu\nu}\partial_\alpha u_\alpha\right) - \zeta\,\partial_\alpha u_\alpha \delta_{\mu\nu} + t_{\mu\nu} \tag{2.144}$$

with η and ζ, the shear and bulk viscosities respectively. The two point correlation function of this fluctuating term, at $(\vec{x}_1, t_1)$ and $(\vec{x}_2, t_2)$, being given as

$$\begin{aligned}\langle t_{\mu\nu}(\vec{x}_1, t_1)\, t_{\rho\sigma}(\vec{x}_2, t_2)\rangle = {} & \delta(\vec{x}_1 - \vec{x}_2)\,\delta(t_1 - t_2) \\ & \times 2T\left[\eta(\delta_{\mu\rho}\delta_{\nu\sigma} + \delta_{\mu\sigma}\delta_{\nu\rho})\right. \\ & \left. + \left(\zeta - \frac{2}{3}\eta\right)\delta_{\mu\nu}\delta_{\rho\sigma}\right].\end{aligned} \tag{2.145}$$

Taking the trace over the spatial indexes allows access to the bulk viscosity [79]

$$\langle t_{ll}(\vec{x}_1, t_1)\, t_{kk}(\vec{x}_2, t_2)\rangle = 18\,T\,\zeta\,\delta(\vec{x}_1 - \vec{x}_2)\,\delta(t_1 - t_2) \tag{2.146}$$

with T the temperature of the fluid.

Considering perfectly central collisions, where azimuthal symmetry can be relatively safely assumed, the trace of the viscous stress tensor in cylindrical coordinates reads

$$\begin{aligned}&\langle \Pi_{ll}(\vec{x}_1, t_1)\,\Pi_{kk}(\vec{x}_2, t_2)\rangle \\ &\quad = \langle (\Pi_{\text{TT}} + \Pi_{zz})(\vec{x}_1, t_1)\,(\Pi_{\text{TT}} + \Pi_{zz})(\vec{x}_2, t_2)\rangle.\end{aligned} \tag{2.147}$$

Requiring now that the average taken over all central collisions coincides with the equilibrium state, i.e., the average of the out-of-equilibrium part of the stress-energy tensor vanishes (referred as Average equilibrium hypothesis in [79] and [80]), will exclude potential systematic deviations from equilibrium that may affect all collisions and will attribute deviations from equilibrium to event-by-event fluctuations.

Under these assumptions, following [79], the radial component of the two-particle momentum correlation

$$C_{\text{TT}} = \left\langle \sum_{\text{all } i,j} \frac{(p_{\text{T},i})^2}{E_i}\,\frac{(p_{\text{T},j})^2}{E_j} \right\rangle, \tag{2.148}$$

where the sum over i, j extends over all pairs of particles within a given event and the average is taken over the whole set of most central events, is shown to be expressed as

$$\begin{aligned} C_{\mathrm{TT}} = &\left\langle \sum_i \frac{(p_{\mathrm{T},i})^2}{E_i} \right\rangle^2 \\ &+ \int \mathrm{d}\vec{x}_1 \, \mathrm{d}\vec{x}_2 \langle \tau_{\mathrm{TT}}^{\mathrm{hyd}}(\vec{x}_1) \, \tau_{\mathrm{TT}}^{\mathrm{hyd}}(\vec{x}_2) \rangle \\ &+ \int \mathrm{d}\vec{x}_1 \, \mathrm{d}\vec{x}_2 \langle t_{\mathrm{TT}}(\vec{x}_1) \, t_{\mathrm{TT}}(\vec{x}_2) \rangle \end{aligned} \tag{2.149}$$

The third term of the right hand side, i.e., the left hand side of Eq. (2.146), is of first order in $\Delta\mathcal{T}$ under a double integration over a small $\Delta\mathcal{T}$, while the second term, as argued in [80], features a time dependence that under such a double integration is of second order in $\Delta\mathcal{T}$. Integrating twice over a small fluid element ΔV, and twice over a small time interval $\Delta\mathcal{T}$ and using Eqs. (2.148) and (2.149) to first order and the corresponding ones for zz and Tz, Eq. (2.146) gives

$$\begin{aligned} &18T\,\zeta\,\frac{\Delta V}{\Delta\mathcal{T}} \\ &= \left\langle \sum_{\text{all } i,j} \frac{(p_{\mathrm{T},i})^2}{E_i} \frac{(p_{\mathrm{T},j})^2}{E_j} \right\rangle - \left\langle \sum_i \frac{(p_{\mathrm{T},i})^2}{E_i} \right\rangle^2 \\ &+ 2 \left\langle \sum_{\text{all } i,j} \frac{(p_{\mathrm{T},i})^2}{E_i} \frac{(p_{z,j})^2}{E_j} \right\rangle - 2 \langle N \rangle^2 \left\langle \frac{p_{\mathrm{T}}^2}{E} \right\rangle \left\langle \frac{p_z^2}{E} \right\rangle \\ &+ \left\langle \sum_{\text{all } i,j} \frac{(p_{z,i})^2}{E_i} \frac{(p_{z,j})^2}{E_j} \right\rangle - \langle N \rangle^2 \left\langle \frac{p_z^2}{E} \right\rangle \end{aligned} \tag{2.150}$$

or, considering that $p_{\mathrm{T}}^2 + p_z^2 = E^2 - m^2$,

$$\begin{aligned} &18T\,\zeta\,\frac{\Delta V}{\Delta\mathcal{T}} \\ &= \left\langle \sum_{\text{all } i,j} \frac{(E_i^2 - m_i^2)}{E_i} \frac{(E_j^2 - m_j^2)}{E_j} \right\rangle - \left\langle \sum_i \frac{E_i^2 - m_i^2}{E_i} \right\rangle^2 \\ &\equiv \Delta \left(\frac{(E^2 - m^2)}{E} \right) \end{aligned} \tag{2.151}$$

So far, the analysis has been carried out on the fluid's volume element rest frame, but all measures are taken on the laboratory frame so, boosting Eq. (2.151) with the fluid element four velocity $u = \gamma(1, \vec{\beta})$

and noting that $E_i = p_i \cdot u$ gives

$$\begin{aligned} & 18T\,\zeta\,\gamma^2\,\frac{\Delta V_{\rm lab}}{\Delta\mathcal{T}_{\rm lab}} \\ &= \left\langle \sum_{\text{all } i,j} \frac{((p_i\cdot u)^2 - m_i^2)}{p_i\cdot u}\,\frac{((p_j\cdot u)^2 - m_j^2)}{p_j\cdot u} \right\rangle \\ &\quad - \left\langle \sum_{i} \frac{(p_i\cdot u)^2 - m_i^2}{p_i\cdot u} \right\rangle^2 \\ &\equiv \Delta\left(\frac{((p\cdot u)^2 - m^2)}{p\cdot u}\right) \end{aligned} \tag{2.152}$$

To finally extract the bulk viscosity it is needed to express $\Delta V_{\rm lab}$ and $\Delta\mathcal{T}_{\rm lab}$ in terms of measurable magnitudes. Following [80], a set of kinematic cuts centered around energy E, transverse momentum $p_{\rm T}$, pseudorapidity η and azimuthal angle φ, presumably selects a swarm composed of those particles coming from the fluid element $\Delta V_{\rm lab}$ during the time interval $\Delta\mathcal{T}_{\rm lab}$. By the time of kinetic freeze-out τ_f a particle will have traveled a transverse distance $r = \tau_f\beta_{\rm T}$ while a particle arriving that far a time $\Delta\mathcal{T}_{\rm lab}$ latter would have been delayed $r/\Delta\beta_{\rm T}$ so,

$$\Delta\mathcal{T}_{\rm lab} = \tau_f\,\frac{\Delta\beta_{\rm T}}{\beta_{\rm T}}. \tag{2.153}$$

For the fluid volume element

$$\Delta V_{\rm lab} = r\Delta\varphi\,\Delta r\,\Delta z. \tag{2.154}$$

Considering $\Delta z = \tau_f\Delta\beta_z$, $\Delta r = \tau_f\Delta\beta_{\rm T}$ and $\vec{\beta} = \vec{p}/E$, from Eqs. (2.153) and (2.154)

$$\frac{\Delta\mathcal{T}_{\rm lab}}{\Delta V_{\rm lab}} = \frac{1}{\tau_f^2\Delta\varphi}\,\frac{E^4}{p_{\rm T}^2\,(E\Delta p_z - p_z\Delta E)} \tag{2.155}$$

so, finally, departing a bit from the expressions in [79] and [80], the bulk viscosity is given by

$$\begin{aligned} \zeta = & \frac{1}{18T_f\,\gamma^2\,\tau_f^2\Delta\varphi} \\ & \times \Delta\left(\frac{((p\cdot u)^2 - m^2)}{p\cdot u}\right) \\ & \times \frac{E^4}{p_{\rm T}^2\,(E\Delta p_z - p_z\Delta E)} \end{aligned} \tag{2.156}$$

where now T_f is the kinetic freeze-out temperature, and γ is the average Lorentz factor of the particle swarm.

The core of Eq. (2.156) is the correlator defined in Eq. (2.152)

$$\Delta\left(\frac{((p\cdot u)^2 - m^2)}{p\cdot u}\right) \equiv \left\langle \sum_{\text{all } i,j} \frac{((p_i\cdot u)^2 - m_i^2)}{p_i\cdot u}\,\frac{((p_j\cdot u)^2 - m_j^2)}{p_j\cdot u} \right\rangle - \left\langle \sum_{i} \frac{(p_i\cdot u)^2 - m_i^2}{p_i\cdot u} \right\rangle^2 \tag{2.157}$$

which has to be extracted from the set of tracks within a swarm centered at the selected values $p_{\rm T}$, E, η, and φ, and spanning $\Delta\varphi$ azimuthally, $\Delta\eta$ longitudinally, ΔE in energy, and $\Delta p_{\rm T}$ in transverse momentum.

2.4.8 Extraction of the relaxation time

As was described in sect. 2.4.5, for second order in gradients theory, imposed by causality requirements, diffusion broadens the rapidity distribution by wave-like propagation in addition to the usual diffusion. The signature role of τ_π is in determining the rate at which the system relaxes to Navier-Stokes hydrodynamics. With finite values of τ_π the profile of the correlation function changes from wavelike to diffusion-dominated [81]. This effect manifests as a valley developed at $\Delta\eta = 0$ with a shoulders structures on each side which get 'diffused' with time when the valley is filled due to the usual diffusion. By using the inspired by kinetic theory relationship

$$\tau_\pi = \beta \frac{\eta}{Ts}, \tag{2.158}$$

the value $\beta = 10$ was able to describe STAR data [81]. The longitudinal projection of the two-particle

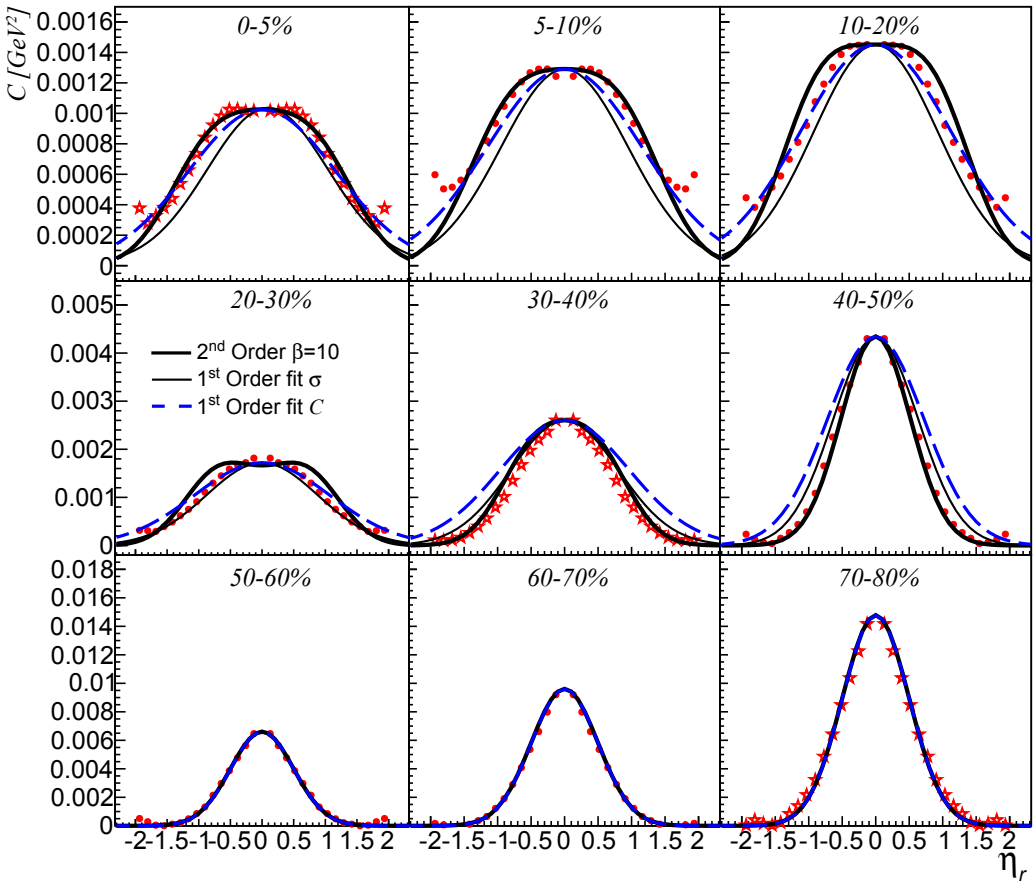

FIGURE 2.24: Longitudinal projection of the two-particle transverse momentum correlation $G_2^{\rm CI}$ in Au–Au collisions at $\sqrt{s_{\rm NN}}$ = 200 GeV compared with the characteristic evolution of second order diffusion from single peak to plateau. Data (open stars) are from [77] and (filled circles) from [81]. First order calculations are also compared for best fit to these data (dashed) and best fit to σ in Fig. 2.23 ($\eta_{\rm r}$ stands for $\Delta\eta$ while, as mentioned, C, which is inclusive, is referred as $G_2^{\rm CI}$) [81].

transverse momentum correlation $G_2^{\rm CI}$ in Au–Au collisions at $\sqrt{s_{\rm NN}}$ = 200 GeV is shown in Fig. 2.24 compared with results from evolution of second order diffusion. The characteristic profile of second order evolution presents a single peak at peripheral collisions which evolves towards a plateau structure from semi-central to most central collisions. This is in contraposition with first order diffusion which

stays single peaked along all centrality classes. Nevertheless, the characteristic shoulders, remainders of the wave mode propagation of fluctuations, which appear in second order evolution at semi-central collisions, with the valley structure at $\Delta\eta$ seem to reveal in data at more central collisions.

Chapter 3

The ALICE detector

3.1 Introduction

A Large Ion Collider Experiment (ALICE) (Fig 3.1), one of the main four LHC experiments together with CMS, ATLAS and LHCb, is a general purpose heavy-ion detector specifically designed to cope with collision scenario densities of up to $\mathrm{d}N_{\mathrm{ch}}/\mathrm{d}y = 8{,}000$ charged particles and focused on the characterization of the medium created in ultra-relativistic Pb–Pb collisions. ALICE experiment also studies lower multiplicity scenarios, pp and pA, which provide reference measurements for the AA interaction but also genuine small systems physics studies. The overall set of ALICE detectors can be grouped in three main sections: the central barrel detectors, the forward detectors and the muon spectrometer. Additionally ALICE is equipped in with a cosmic ray detector on the top of its central barrel. For a complete description of the detector and its performance see [82, 83].

This chapter gives a brief descriptions of the detectors which conform ALICE, the main source of data for elaborating the results presented in this thesis. Then, the way the events of physics interest are selected, reconstructed, and classified according to the centrality of their collisions are introduced. The capabilities for identifying the different particles of interest are briefly described to finalize with an overview of the ALICE software (SW) framework which support the reconstruction, simulation, and analysis processes.

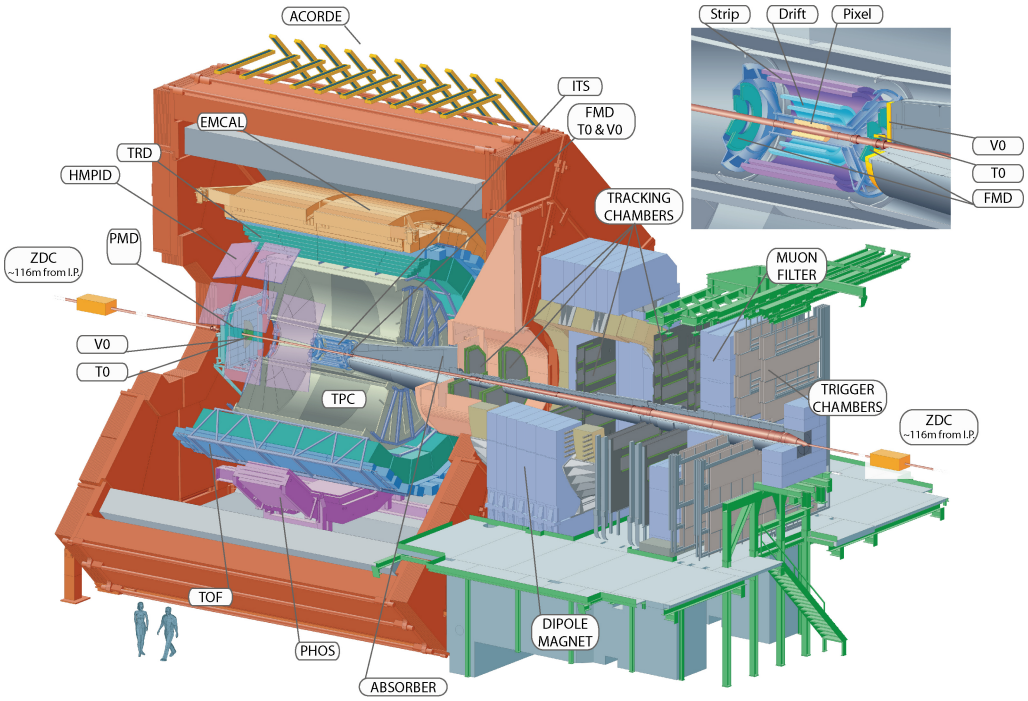

FIGURE 3.1: Schematic view of the ALICE experiment at the CERN LHC. The central barrel detectors (ITS, TPC, TRD, TOF, PHOS, EMCal and HMPID) are embedded in a solenoid with magnetic field $B = 0.5$ T and address particle production at mid rapidity. The cosmic-ray trigger detector ACORDE is positioned on top of the magnet. Forward detectors (PMD, FMD, V0, T0 and ZDC) are used for triggering, event characterization and multiplicity studies. The forward muon spectrometer, with tracking and triggering chambers, expands the detector capabilities to the muon sector [83].

3.2 Central barrel detectors

The Inner Tracking System (ITS), the Time Projection Chamber (TPC), the Transition Radiation Detector (TRD), the Time of Flight (TOF) detector, the Photon Spectrometer (PHOS), the Electromagnetic Calorimeter (EMCal) and the High Momentum Particle Identification Detector (HMPID) are all disposed within the inner region of the large L3 solenoid magnet which provides a magnetic field of up to 0.5 T. The ITS and the TPC are the ALICE main charged-particle tracking detectors.

3.2.1 Inner tracking system

The ITS consists of six cylindrical silicon detector layers concentric with the LHC beam pipe surrounding it at a distance between 4 and 43 cm. They are made with three different technologies [84, 85]

- Silicon Pixel Detector (SPD) in the two most inner layers where the charged-particle density reaches $50/\mathrm{cm}^2$ in Pb–Pb collisions. The SPD covers an extended pseudo-rapidity range ($|\eta| < 1.98$ in its inner layer and $|\eta| < 1.4$ in the next) for full charged-particle multiplicity coverage together with the FMD. The SPD is fundamental in the primary vertex position determination and on the measurement of its distance to secondary tracks originating from weak decays of strange, charm and beauty particles.

- Silicon Drift Detector (SDD) and Silicon Strip Detector (SSD) are used in the two central and the two outer layers, respectively. The SDD and the SSD are designed to measure ionization densities, and provide, additionally to the spatial resolution, analog output with $\mathrm{d}E/\mathrm{d}x$ information for particle identification in the low momentum range. The SDD information is key for TPC track matching. Their sensor strips are arranged parallel to the magnetic field for resolution optimization in the deflection plane.

The full ITS covers an $|\eta| < 0.9$ pseudo-rapidity range. Primary vertex determination with a resolution better than 100 μm, secondary vertexes reconstruction and tracking and identification of low p_{T} ($<$ 200 MeV/c) particles are among its primary functions.

3.2.2 Time projection chamber

The TPC, a cylinder with a length of 500 cm along the beam pipe, is the main ALICE tracking device [86]. Covers the whole azimuthal acceptance and a pseudo-rapidity range $|\eta| < 0.9$ for a full radial track coverage. The TPC inner radius, around 85 cm, is determined by the highest acceptable track density while its outer radius, around 250 cm, is determined by the needed length for reaching a $\mathrm{d}E/\mathrm{d}x$ resolution better than 5–7%. The TPC is able to reach an acceptance multiplicity of 20,000 primary and secondary charged-tracks.

The cylinder is filled with a gas mixture (Ne, CO_2) within an uniform electric field parallel to the z axis. The central electrode, at $z = 0$ cm, at 100 kV potential, creates an electric field with a gradient of about 400 V/cm which results in a maximum drift time of about 90 μs. Both end caps, are azimuthally segmented in 18 sectors. Each sector is radially segmented in two chambers, inner and outer. Each sector is equipped with two trapezoidal multi-wire proportional chamber (MWPC). A total of 557,568 channels for an active area of 32 m^2. The active channel provides the r and φ coordinates while z coordinate is provided by the drift time triggered by T0.

The main functions of the TPC are track reconstruction, transverse momentum determination in the 100 MeV/c $< p_{\mathrm{T}} <$ 100 GeV/c range based on the trajectory curvature and particle identification by measuring the energy loss ($\mathrm{d}E/\mathrm{d}x$) in the gas.

3.2.3 Transition radiation detector

The TRD consists of 522 chambers arranged in 6 layers at a radial distance from 2.90 m to 3.68 m from the beam axis. Each chamber comprises a radiator, a gas filled drift section and a MWPC. It is designed to improve the tracking at high p_{T} and to provide electron identification in the 1 GeV/c < p_{T} < 100 GeV/c range and triggering. The radiators are built to favor the emission of transition radiation in the presence of ultra-relativistic electrons. The TRD covers the whole azimuthal angle and a $|\eta| < 0.84$ pseudo-rapidity range except for the PHOS coverage zone to reduce the material budget towards the interaction point (IP). The TRD is azimuthally segmented in 18 sectors to match the TPC azimuthal segmentation. Longitudinally it consists of five sections. The 522 modules provide a total of 1.15×10^6 channels. The granularity in the transverse plane is based on the desired transverse momentum resolution while in the longitudinal direction is based on the need of track matching with the TPC even at the highest multiplicities [87].

The main functions of the TRD are identification of high momentum, > 1 GeV/c, electrons for mid rapidity quarkonia and heavy quark production studies and high p_{T} pion separation from electron.

3.2.4 Time-of-flight detector

Covers the central barrel over a 140 m^2 area with 160, 000 individual cells at a radius of about 4 m from the beam pipe on the whole azimuthal angle and a $|\eta| < 0.9$ pseudo-rapidity range except for the PHOS coverage zone to reduce the material budget towards the IP. The granularity is driven by the need of a high rate of particle identification even at the highest multiplicities. The TOF detector is segmented in 18 modules of 48 sensors blocks each in the transverse plane and in five modules of about 38 sensor blocks each in the longitudinal direction. The sensors blocks are disposed in strips transverse to the beam axis and tilted to be perpendicular to the direction towards the IP. Each double rows of 48 sensors constitutes a gas filled Multi-gap Resistive-Plate Chamber which, in the presence of a charged-particle, starts a gas avalanche which generates the observed signal [88].

The main functions of the TOF detector are pion and kaon separation in the 0.5 GeV/c < p_{T} < 3.0 GeV/c range, proton identification in the 0.5 GeV/c < p_{T} < 4.0 GeV/c range and electron identification in the 0.3 GeV/c < p_{T} < 0.5 GeV/c range, by measuring the time elapsed from the IP.

3.2.5 High momentum particle identification detector

Arm located around two o'clock with a $|\eta| < 0.6$ pseudo-rapidity range over a $1.2^{\mathrm{o}} < \varphi < 58.8^{\mathrm{o}}$ azimuthal angle. With an optimized geometry respect to the particle yields and two-particle correlations large opening angle requirements, the HMPID detector consists of seven Ring Imaging Cherenkov (RICH) counter modules with liquid radiator, a methane based MWPC and the photon counter electronics [89].

The main functions of the HMPID detector are the inclusive identified hadrons measures at p_{T} > 1 GeV/c, particle identification capabilities enhancement above the ranges reached by ITS, TPC and TOF and expansion of the π/K and K/p discrimination range to 3 and 5 GeV/c, respectively.

3.2.6 Photon spectrometer

Located in the lower part of the central barrel at 4.6 m radial distance of the IP, covers a $|\eta| < 0.125$ pseudo-rapidity range over a $\Delta\varphi = 70^{\mathrm{o}}$ azimuthal angle range. The PHOS is a single arm, high-resolution electromagnetic calorimeter which detects and identifies photons and electrons in a wide p_{T} range from ~ 100 MeV/c to ~ 100 GeV/c and additionally provides a trigger in case of a large energy deposition by an energetic particle. The PHOS calorimeter is designed to measure spectra, collective flow and correlations of thermal and prompt direct photons, and of neutral mesons via their decay into photon pairs. This requires high granularity as well as excellent energy and position resolution. Three

of the PHOS modules are segmented in 56 rows of 64 elements while the fourth is segmented in 56 rows 32 elements. Each element is made of a scintillator crystal cell coupled to avalanche photo-diodes providing 2 ns response time over a 0.010–80 GeV/c dynamic range. Each module is complemented with a MWPC which provides a precise charged-particles veto signal. Resulting energy resolution reaches $\sigma_E/E = (1.8\%/E) \oplus (3.3\%/\sqrt{E}) \oplus 1.1\%$ [90, 91].

The main functions of PHOS are low p_{T} direct, carrying information about the thermal and dynamic properties of the collision early phase, and secondary photon and π^0 measurements and rare events triggering.

3.2.7 Electromagnetic calorimeter

Located on the central barrel at 4.5 m radial distance of the beam pipe, covers a $|\eta| < 0.7$ pseudo-rapidity range over a $80^{\mathrm{o}} < \varphi < 187^{\mathrm{o}}$ azimuthal angle, larger than PHOS but with lower granularity and energy resolution. Optimized for jet rate production and fragmentation function measurements is segmented in 12, 228 layered Pb-scintillator towers, tilted towards the IP, deployed in 12 super-modules each arranged as 24 strips of 12 2×2 towers [92].

The main functions of EMCal are fast and efficient triggering for hard jets, photon and electron and neutral energy jet components measurement enabling full jet reconstruction.

3.3 ALICE cosmic ray detector

Consists of a set of 60 plastic scintillator modules located on top of the L3 solenoid which conforms the central barrel, at a radial distance of 8.5 m of the beam pipe, and covering a $|\eta| < 1.3$ pseudo-rapidity range over a $-60^{\mathrm{o}} < \varphi < 60^{\mathrm{o}}$ azimuthal angle.

The main functions of the ACORDE detector are fast triggering signal for commissioning, calibration and alignment and atmospheric muon and multi-muon detection.

3.4 Muon spectrometer

Located at high pseudo-rapidity, $-4 < \eta < -2.4$, for providing good acceptance down to zero p_{T} under a manageable hadron decays background, the muon spectrometer covers the whole azimuthal range, and expands from a position at 90 cm of the IP. It consists of a passive conic section front absorber, 4.13 m long, followed by five detector tracking stations (double-plane cathode pad chambers), the Muon Chambers (MCH), a passive muon-filter wall and two detector trigger stations (double-plane resistive plate chambers) at 16 and 17 m of the IP, the Muon Trigger (MTR). A magnetic dipole surrounding the central tracking stations at a distance of 7 m of the interaction point provides a magnetic field of 0.67 T [93]. Muon identification is feasible starting from 4 GeV/c, due to the large absorption required for proper hadron flow rejection, while a 100 MeV/c^2 resolution at 10 GeV/c^2 invariant mass is provided by the magnetic field intensity and the spatial resolution of the tracking system, being the high granularity of the tracking and trigger stations determined by the high multiplicity environment.

The main functions of the muon spectrometer are to provide support for the complete spectrum of heavy-quark vector-mesons resonances, as well as the ϕ meson, measurements in the $\mu^+\mu^-$ channel, the unlike-sign dimuon continuum up to masses around 10 GeV/c^2 measurements and the measurements of muons from semi-leptonic decays and from $e - \mu$ decays.

3.5 Forward and trigger detectors

3.5.1 T0 detector

It consists of two sets of twelve photomultiplier based Cherenkov counters located at 72.7 cm of the IP, T0C, with $-3.28 < \eta < -2.97$ pseudo-rapidity range, and at 375 cm of the IP, T0A, with $4.61 < \eta < 4.92$ pseudo-rapidity range, both at 6.5 cm radial distance of the beam pipe [94].

The main functions of the T0 detector are triggering signal for TOF time counting, vertex position measure, V0 redundancy, and minimum bias (MB) and multiplicity triggers generation.

3.5.2 V0 detector

It consists of two set of scintillator counters located at 90 cm of the IP, V0C, 48 counters in two inner rings of eight counter each and two outer rings of 16 counters each, with $-3.7 < \eta < -1.7$ pseudo-rapidity range, and at 340 cm of the IP, V0A, 32 counters in four rings of eight sectors each, with $2.8 < \eta < 5.1$ pseudo-rapidity range [95, 94].

The main functions of the V0 detector are MB triggering for the central barrel detectors, collision centrality estimation based on the registered multiplicity and reaction plane estimation.

3.5.3 Forward multiplicity detector

It is deployed in two configurations of silicon detector rings, inner (i), which consists of 20 sectors with 512 silicon strips each, and outer (o), which consists of 40 sectors with 256 silicon strips each, with 4.2 cm and 15.4 cm inner (17.2 cm and 28.4 cm outer) radius, respectively, located at 320 (i), 83.4 (i), 75.2 (o), −62.8 (i) and −75.2 cm (o) z positions along the beam axis [94].

The main functions of the FMD are charged-particle multiplicity measurement, multiplicity fluctuations estimation and reaction plane determination.

3.5.4 Photon multiplicity detector

It is located at 3.64 m of the IP, with full azimuthal coverage and $2.3 < \eta < 3.7$ pseudo-rapidity range. The expected large particle multiplicity in the forward direction conditioned its architecture. The PMD consists of a thick lead converter sandwiched between two planes, and a large set arrays of gas proportional counters in a honeycomb cellular structure. The two planes on the lead converter behave as the charged particle veto and as the photon identification pre-shower. The combined thickness and granularity is optimized for photon showers overlap minimization. 24 modules with to different arrangements of 48×96 honeycomb cells configure each active plane [96].

The main functions of the PMD are photon multiplicity and spatial distribution measurements and reaction plane estimation.

3.5.5 Zero degree calorimeter

The Neutron (ZN) and Proton (ZP) Cherenkov hadronic calorimeters are located at 116 m on either sides of the IP, ZN between the beam pipes and ZP externally on the side where positive particles are deflected [97].

The main functions of the ZDC are collision centrality estimation based on the number of spectators measurement and reaction plane estimation.

3.5.6 Zero degree electromagnetic calorimeter

Cherenkov electromagnetic calorimeters located at 7 m of the IP, opposite to the muon arm, and on both sides of the beam pipe.

The main function of the zero degree electromagnetic calorimeter (ZEM) calorimeters is the measurement of the energy of particles emitted at forward rapidity, $4.8 < \eta < 6.7$, for discriminating peripheral from central collisions which give the same pattern on the ZDC.

3.6 ALICE coordinate system

ALICE coordinate system is a right handed orthogonal Cartesian system which has its origin at the LHC Interaction Point 2 (IP2), at the center of the ALICE detector. Its z axis is along the LHC beam and anticlockwise, its x axis horizontal points towards the center of the LHC ring and its y axis vertical pointing upwards.

3.7 Physics selection

Not all collisions that happen at the ALICE coverage can be registered and not all those that can be registered are of physics interest. A complete set of triggers hierarchically distributed in three layers is an intimate component of the ALICE detector complex. The trigger system provides control for event acceptance during online data taking and further provides physics selection criteria during offline data analysis.

The trigger decision is generated by the ALICE Central Trigger Processor (CTP) based on trigger detectors signals and information about the LHC bunch filling scheme [83]. The Level 0 (L0) trigger decision is made $\sim$ 0.9 μs after the collision using inputs from V0, T0, EMCal, PHOS and MTR. The events accepted at L0 are evaluated, after allowing computation time for the TRD and the EMCal and propagation time for the ZDC ($\sim$ 6.5 μs), by the Level 1 (L1) trigger logic in the CTP. L0 and L1 decisions delivered to the detectors trigger the buffering of the event data on them. After allowing enough drift time for the TPC ($\sim$ 100 μs) the Level 2 (L2) trigger decision activates the sending of the event data to the Data Acquisition System (DAQ). Table 3.1 summarizes the most important trigger configurations used by ALICE. The trigger information is used as was said to select events of interest during online data taking but also the trigger information is also stored as part of the event data which eases the task of selecting events of interest during offline data analysis.

The minimum bias (MB) trigger is configured to minimized the machine induced effects which could bias the data sample selected for the analysis. The MB trigger has different configuration for the different collision systems used in the analyses of this thesis. In pp collisions the MB trigger configuration ($\mathrm{MB_{OR}}$) requires a hit in the SPD and in either V0-A or V0-C detectors. In p–Pb and in Pb–Pb collisions the MB trigger configuration ($\mathrm{MB_{AND}}$) requires a hit in both, V0-A and V0-C detectors.

TABLE 3.1: Major ALICE triggers [83].

Trigger	Description	Condition
MB-type triggers		
MBor	minimum bias	signals in V0 and SPD
MBand	minimum bias	signals in V0A and V0C
MBZ	minimum bias	MB and signals in both ZDC
SPI	multiplicity trigger	n hits in SPD
Centrality triggers		
CENT	central	V0 based centrality trigger for Pb–Pb (0–10%)
SEMI	semi-central	V0 based semi-central trigger for Pb–Pb (0–50%)
EMCal rare triggers		
E0	EMCal L0	EMCal L0 shower trigger in coincidence with MB
EJE	neutral jet	EMCal L1 jet algorithm following EMCal L0
EJE2	neutral jet	like EJE but with a lower threshold than EJE
EGA	photon/electron	EMCal L1 photon algorithm following EMCal L0
EGA2	photon/electron	like EGA but with a lower threshold than EGA
TRD rare triggers		
TJE	charged jet	n charged particles in TRD chamber in coincidence with MB
TQU	electron for quarkonia	electron with $p_{\mathrm{T}} > 2\mathrm{GeV}/c$ in TRD in coincidence with MB
TSE	electron for open beauty	electron with $p_{\mathrm{T}} > 3\mathrm{GeV}/c$ in TRD in coincidence with MB
MUON rare triggers		
MSL	single muon low	single muon in MTR in coincidence with MB
MSH	single muon high	like MSL but with a higher threshold
MUL	dimuon unlike sign	two muons above low threshold, unlike sign, in coinc. with MB
MLL	dimuon like sign	two muons above low threshold, same sign, in coinc. with MB
Miscellaneous triggers		
HM	high multiplicity	high multiplicity in SPD in coincidence with MB
PH	photon by PHOS	PHOS energy deposit in coincidence with MB
EE	single electron	electron signal in TRD (sector 6–8) and EMCal
DG	diffractive	charged particle in SPD and no signal in V0
CUP	barrel ultraperipheral	charged particle in SPD and no signal in V0, for Pb–Pb and p–Pb
MUP	muon ultraperipheral	(di-)muon in MTR and no signal in V0A, for Pb–Pb and p–Pb
ZED	electromagnetic dissociation	signal in any of the neutron ZDC
COS	cosmic trigger	signal in ACORDE

3.8 Event reconstruction

The event reconstruction, once accepted by the trigger system, takes as first step the collection of the data on each detector separately. This step, know as clusterization, converts such data in "clusters" characterized by positions, signal amplitudes, signal times, etc., and their associated errors. Then, based on the information from the two inner layers of the ITS (SPD), the preliminary vertex candidate is extracted. The track reconstruction starts on the TPC and proceeds inward towards the ITS and from there outward towards the TPC again and towards the external to TPC central barrel detectors. A final inward propagation towards the ITS allows the final interaction vertex extraction to proceed to the secondary vertex and cascade finding. The procedure is shown schematically in Fig 3.2.

3.8.1 Preliminary interaction vertex

Each pair of clusters, one in each SPD layer, defines a tracklet. The preliminary interaction vertex is extracted as the point to which the maximum number of tracklets converge. The procedure is repeated several times, discarding contributions to already found vertices, in order to identify multiple collisions which can happen in pile-up events.

3.8.2 Track reconstruction

Track reconstruction is performed following an inward-outward-inward scheme [98, 99] which extract the trajectory by using a Kalman filter technique. Track seeds are extracted from the two most external clusters of the TPC outer volume section and the preliminary interaction vertex. From them and based on the locality of the Kalman filter technique new clusters are incorporated to the track trajectory while progressing inward. At each step the track characteristics and its errors are updated with the new added cluster.

The track reconstruction proceeds, in the same way, inwards to the TPC inner volume until all potential clusters have been incorporated to the now reconstructed TPC track. The trajectory is now propagated to outermost layer of the ITS where it becomes the seed for the track finding in the ITS. The followed procedure is similar incorporating the potential clusters from each of the six ITS layers.

Quality criteria establish a limit in the number of shared clusters, a minimum number of track clusters and a minimum ratio of found versus expected number of clusters. Alternative track candidates for a concrete physic track in the TPC or for a concrete TPC track in the ITS are rejected on the base of

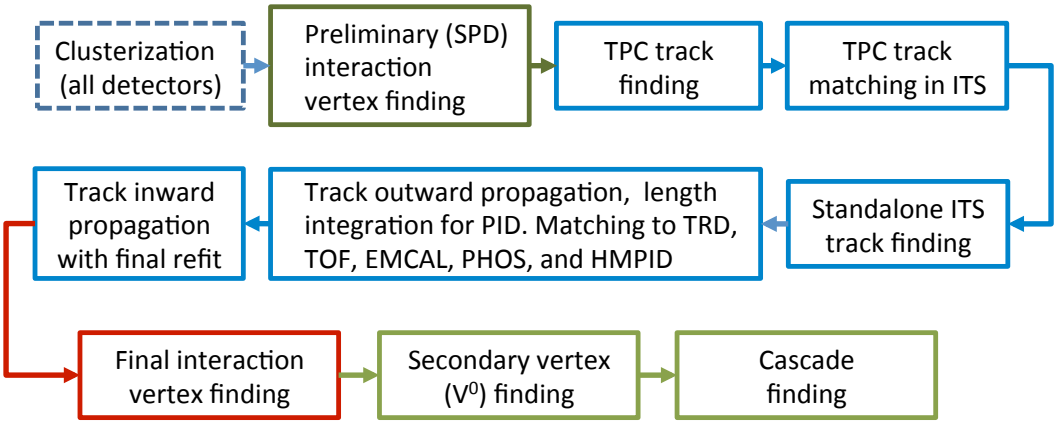

FIGURE 3.2: Event reconstruction flow [83].

these quality criteria being the highest quality track candidate the one incorporated to the reconstructed event.

Once the first inward process is finished with the list of ITS-TPC tracks candidates a standalone ITS reconstruction is performed over the remaining ITS clusters. The track seeds are taken from two clusters in the three innermost layers of the ITS and the preliminary interaction vertex. The successive clusters are incorporated from the local propagation of the seeds outwards to the next layer. Quality criteria decides over potential tracks candidates removing the final assigned clusters from further searches.

The outward propagation starts after propagating the tracks to their point of closest approach to the preliminary interaction vertex. At each outward step the quality of the track is updated and information about the behavior for the different particle species stored for further particle identification. The propagated track is matched with tracks candidates from the TRD on each of its layers and, once reached the TOF, to TOF clusters. Further track propagation potentially reaches EMCal, PHOS and HMPID, although contributions for external to the TPC detectors are not used to modify kinematic characteristics of the track.

In the final stage the tracks are propagated inwards refitting them with the previously found clusters on the TPC and the ITS. Track characterization and their corresponding uncertainties are re-evaluated and updated.

3.8.3 Interaction vertex determination

The reconstructed TPC-ITS tracks are used to find the interaction vertex with higher precision than the preliminary interaction vertex extracted from SPD tracklets. The tracks are propagated to the distance of closest approach to the beam line. The convergence point after removing outliers provide the interaction vertex position.

3.8.4 Secondary vertices (V^0)

The secondary vertex (V^0, for its topology) finding is based on selecting tracks with a distance of closest approach to the interaction vertex above a certain threshold. These tracks are in principle considered as produced from a secondary vertex. Unlike sign track pairs are selected as V^0 candidates based on its distance of closest approach, the distance of the point of closest approach and the interaction vertex, and the pointing angle towards the interaction vertex. A matching of the pointing angle towards the interaction vertex and the proper invariant mass reveal a K^0_s decay. Pointing angle unmatching and proper invariant mass reveal a potential Λ^0 decay.

Cascade (Ξ) decays finding involves an additional step after finding V^0 candidates which do not point towards the interaction vertex, above Λ^0, and which can be paired with an additional track to a new secondary vertex.

3.9 Centrality determination

Collision centrality is a measure of the initial overlap region of the colliding nuclei. It is customary to express the centrality of the collisions not in terms of the impact parameter b, the distance between the two nuclei on the transverse plane to the beams, but via a percentage of the total hadronic cross section, σ_{AA},

$$c(b) = \frac{1}{\sigma_{\mathrm{AA}}} \int_0^b \frac{\mathrm{d}\sigma}{\mathrm{d}\, b'} \,\mathrm{d}\, b' \tag{3.1}$$

where $c(b)$ is the centrality percentile of an AA collision with impact parameter b. Experimentally, the centrality is defined as the percentile of the hadronic cross section with detected charged particle multiplicity above a given threshold $N_{\mathrm{ch}}^{\mathrm{TH}}$ or with zero-degree energy below a given threshold $E_{\mathrm{ZDC}}^{\mathrm{TH}}$,

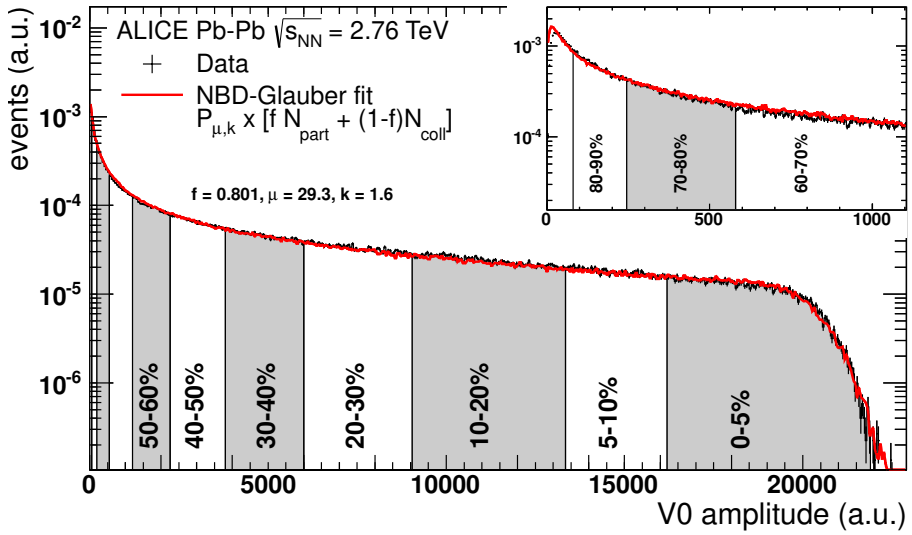

FIGURE 3.3: Distribution of the V0 amplitude (sum of V0A and V0C). The centrality bins are defined by integrating Eq. 3.2. The absolute scale is determined by fitting to a NBD-Glauber model (red line) whose parameters are also shown (see text). The inset shows a magnified version of the most peripheral region [15].

being the cross section replaced by the number of observed events n corrected for trigger efficiency and non-hadronic interaction background [15]

$$c \approx \frac{1}{N_{\text{ev}}} \int_{N_{\text{ch}}^{\text{TH}}}^{\text{inf}} \frac{\mathrm{d}\, n}{\mathrm{d}\, N'_{\text{ch}}} \mathrm{d}\, N'_{\text{ch}} \approx \frac{1}{N_{\text{ev}}} \int_{0}^{E_{\text{ZDC}}^{\text{TH}}} \frac{\mathrm{d}\, n}{\mathrm{d}\, E'_{\text{ZDC}}} \mathrm{d}\, E'_{\text{ZDC}}. \tag{3.2}$$

The centrality determination for Pb–Pb collisions at $\sqrt{s_{\text{NN}}}$ = 2.76 GeV using V0 multiplicity, after reducing electromagnetic dissociation and machine-induce backgrounds [15], is illustrated in Fig. 3.3 The scale on Fig. 3.3 is obtained by fitting a parameterized NBD-Glauber model to the multiplicity distribution. The Glauber model describes the collision geometry by initially distributing nucleons on each nucleus according to a Woods-Saxon potential distribution and then treating the collision as a sequence of independent binary nucleon-nucleon collisions, where nucleons follow straight line trajectories and the nucleon-nucleon cross section is the same for all successive collisions. Latest centrality estimation implementation assume $\sigma_{\text{NN}}^{\text{inel}} = 61.8 \pm 0.9$ mb for Pb–Pb collisions at $\sqrt{s_{\text{NN}}} =$ 2.76 GeV and $\sigma_{\text{NN}}^{\text{inel}} = 67.6 \pm 0.6$ mb for Pb–Pb collisions at $\sqrt{s_{\text{NN}}} = 5.02$ GeV [100]. The number of binary NN collisions N_{coll} and the number of participants N_{part} (nucleons which underwent a NN collision) are then extracted for a given impact parameter.

The particle multiplicity per nucleon-nucleon collision is parametrized by a negative binomial distribution[1](NBD) motivated by the fact that for MB pp and $\mathrm{p\bar{p}}$ collisions at high energy the charged particle multiplicity is well described by a NBD [15]. Inspired by two component models which decompose nucleus-nucleus collisions in soft and hard interactions, the number of particle sources is parameterized as [15]

$$N_{\text{sources}} = f\, N_{\text{part}} + (1 - f)\, N_{\text{coll}} \tag{3.3}$$

where the soft interactions part produce particles with multiplicity proportional to N_{part} and the probability for the hard interactions to occur is proportional to N_{coll}. The particle generation per interaction

proceeds then according to the NBD

$$P_{\mu,k}(n) = \frac{\Gamma(n+k)}{\Gamma(n+1)\,\Gamma(k)} \frac{(\mu/k)^n}{(1+\mu/k)^{n+k}} \tag{3.4}$$

obtaining the V0 amplitude for the considered event. The V0 amplitude distribution is simulated for an ensemble of events for each combination of the parameters f, μ and k having as goal the minimization of the χ^2 with respect to data. Once the process converges the number of events needed for the absolute centrality scale can be extracted. Centrality classes can then be defined by sharp cuts in the simulated V0 distribution and their associated mean number of participants, $\langle N_{\text{part}} \rangle$, and collisions, $\langle N_{\text{coll}} \rangle$, extracted [100].

3.10 Particle identification

Although the different detectors on the central barrel provide individual particle identification capabilities, what makes the ALICE experiment, in some way, unique is its overall particle identification power obtained combining those individual capabilities.

One of the paths for particle identification is by mean of the energy loss ($\mathrm{d}E/\mathrm{d}x$ deposits) along its trajectory. The Bethe-Bloch formula, describing energy loss [101], is parametrized according to [83]

$$f(\beta\gamma) = \frac{P_1}{\beta^{P_4}} \left(P_2 - \beta^{P_4} - \log\left(P_3 + \frac{1}{(\beta\gamma)^{P_5}} \right) \right), \tag{3.9}$$

where β is the particle velocity, γ is the Lorentz factor, and $P_{1\ldots5}$ are fit parameters. Expression (3.9) provides the expected $\mathrm{d}E/\mathrm{d}x$ for the different species at different momentum, the actual measured $\mathrm{d}E/\mathrm{d}x$ and momentum will provide a measure of the proximity to this expected value which can be then used to infer the probability for the measured track to belong to a determined species.

The outer four layers of the ITS provide a measurement of the ionization energy loss. Each type of charged particle have a different expected $\mathrm{d}E/\mathrm{d}x$ profile in crossing the ITS according to its momentum. Fig. 3.4 shows the distribution of $\mathrm{d}E/\mathrm{d}x$ for different charged-particle species.

At the TPC the momentum of charged-particles are extracted based on their trajectory deflection while the $\mathrm{d}E/\mathrm{d}x$ is extracted from the energy lost in the ionization of the gas. The profile of specific energy loss vs momentum for different particle species is shown in Fig. 3.5. At high momentum ($p > 1$ GeV/c) particles can still be separated on a statistical basis via multi-Gaussian fits as is shown

[1]The negative binomial distribution is defined as

$$P_{p,k}(n) = \binom{n+k-1}{n} (1-p)^k p^n. \tag{3.5}$$

It gives the probability for having accumulated n successes when getting the k failure in a sequence of independent Bernoulli trials being p the probability of success in each trial.

The mean of the NBD

$$\langle n \rangle = \frac{p\,k(1-p)}{p} \qquad \Rightarrow \qquad p = \frac{1}{1+\frac{\langle n \rangle}{k}} \tag{3.6}$$

so

$$P_{\langle n \rangle,k}(n) = \frac{(n+k-1)!}{n!\,(k-1)!} \left(\frac{\langle n \rangle}{1+\langle n \rangle} \right)^n \frac{1}{(1+\langle n \rangle)^k} \tag{3.7}$$

The variance of the NBD is given by

$$\sigma^2 = k\frac{1-p}{p^2} \qquad \Rightarrow \qquad k = \frac{\langle n \rangle^2}{\sigma^2 - \langle n \rangle} \tag{3.8}$$

so, k is a measure of the dispersion around the mean.

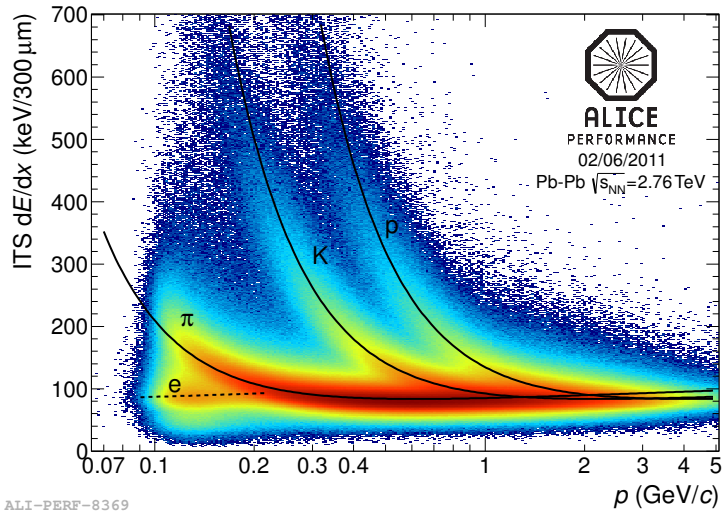

FIGURE 3.4: $\mathrm{d}E/\mathrm{d}x$ of charged particles vs their momentum, both measured by the ITS, in Pb–Pb collisions at 2.76 TeV. The lines are a parametrization of the detector response based on the Bethe-Bloch formula [83].

in Fig. 3.6 for pp and the 0–5% most central Pb–Pb collisions for a specific η range for best $\mathrm{d}E/\mathrm{d}x$ resolution.

Other technique for particle identification is based on measuring the time it takes a particle to follow a certain trajectory of known length. Based on the start time generated by the T0 detector, the TOF detector provides particle identification in the intermediate momentum range, up to 2.5 GeV/c for pions and kaons, and up to 4 GeV/c for protons. Figure 3.7 shows TOF inferred velocity β distribution vs track momentum (measured by the TPC) for different particle species.

The track-by-track charged hadron identification is extended to higher transverse momentum by the HMPID which base its discrimination on the Cherenkov angle of the ring produced by charged tracks as a proxy for their velocities.

Additionally the identification of electrons is enhanced by the electron identification capabilities of the TRD, based on their energy loss and transition radiation, and the EMCal and PHOS, measuring their energy deposition. The identification of photons is performed by reconstructing the electromagnetic shower developed in the PHOS and EMCal calorimeters. Muons are tracked and identified by the tracking stations on the muon spectrometer [83].

Figure 3.8 shows the pion-kaon (left panel) and kaon-proton (right panel) separation power of the ITS, TPC, TOF, and HMPID as a function of p_{T}. The separation is measured as the number of standard deviations, σ, between the kaon (proton) expectation value and the pion (kaon) expectation value for the different detectors. The momentum response is averaged over the range $|\eta| < 0.5$ and the separation is presented as a function of the transverse momentum [83]. The additional power of slicing either in momentum or in pseudorapidity is shown for the TPC over a forward pseudorapidity slice relevant for high-p_{T} PID analysis. At low p_{T} the ITS and the TPC provide the provide the main resolution while for intermediate p_{T} is the TOF which takes that role.

The individual separation power can be considerably improved by combining the separation power of several detectors. As an example Fig. 3.9 suggest a bidimensional selection procedure involving the TPC and TOF. While the TPC is almost blind on that transverse momentum window, as can be seen in Fig. 3.8, the combined resolution of both detectors considerably enhance the overall PID separation capabilities.

A further step is taken by using a Bayesian approach which makes use of the full ALICE PID

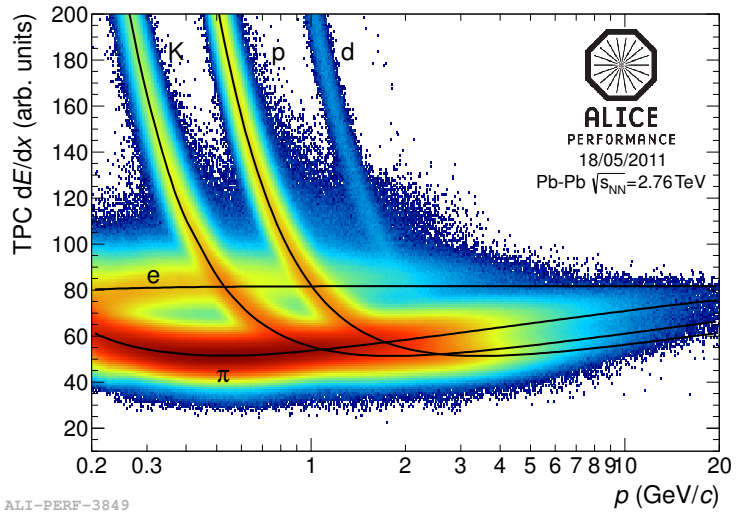

FIGURE 3.5: Specific energy loss in the TPC as a function of momentum with superimposed Bethe-Bloch lines for various particle species [83].

capabilities, expressing the signals on each of the independent detectors in terms of probabilities, and folding them with the expected abundances (priors) of each particle species [102].

The most common way of discriminating particle species on the different detectors is by using the n_σ variable implicitly used all above and defined as the deviation of the measured signal S_α from that expected for a species H_i, $\hat{S}(H_i)_\alpha$, in terms of the detector resolution for that species σ^i_α

$$n_{\sigma^i_\alpha} = \frac{S_\alpha - \hat{S}(H_i)_\alpha}{\sigma^i_\alpha} \tag{3.10}$$

where $\alpha = (\text{ITS, TPC, } \dots)$.

For a given detector α is then feasible to build the conditional probability $P_\alpha(S_\alpha|H_1)$ that a particle of species H_i will produce a signal S_α on that detector. For a detector with Gaussian response it will be a Gaussian centered in $\hat{S}(H_i)_\alpha$ with variance ${\sigma^i_\alpha}^2$ while for non-Gaussian response detectors they will be appropriate parametrization descriptions.

Combining them as the conditional probability of obtaining from a set of detectors a signal $\vec{S} = (S_{\text{ITS}}, S_{\text{TPC}}, \dots)$ for a given particle species H_i

$$P(\vec{S}\,|H_i) = \prod_{\alpha=\text{ITS,TPC, ...}} P_\alpha(S_\alpha|H_i), \tag{3.11}$$

Bayes' theorem allows to express the conditional probability of a particle of species H_i given some measured detectors signals, $P(H_i|\vec{S})$, as

$$P(H_i|\vec{S}) = \frac{P(\vec{S}\,|H_i)\; C(H_i)}{\sum\limits_{k=e,\mu,\pi,\ \dots} P(\vec{S}\,|H_k)\; C(H_k)} \tag{3.12}$$

where $C(H_i)$, an *a priori* probability of measuring the particle species known as the *prior*, is a 'best guess' of the true particle yield per event and the conditional probability $P(H_i|\vec{S})$ is known as the *posterior* probability.

The prior probabilities is usually extracted using an iterative process. An initial guess on the particles abundances for the considered system is used as $C_0(H_i)$. Bayesian posterior probabilities $P_n(H_i|\vec{S})$ are

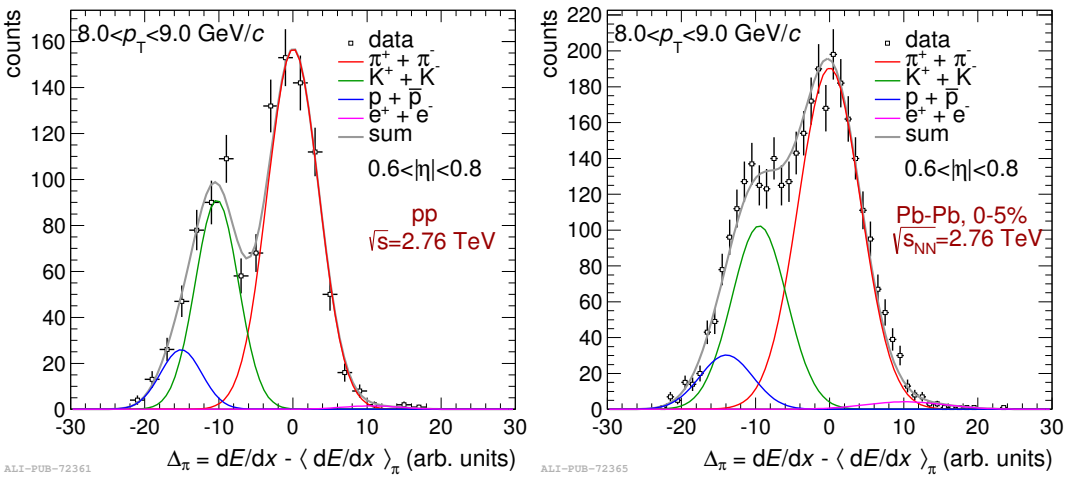

FIGURE 3.6: Ionization energy loss (dE/dx) distributions in the TPC for relatively high transverse momentum particles in pp (left) and Pb–Pb collisions (right) at $\sqrt{s_{\mathrm{NN}}}$ = 2.76 TeV. The lines represent a multi-Gaussian fit [83].

computed using the priors obtained in step $n-1$ by using Eq. 3.12. The yield at step n is extracted as

$$Y_n(H_i) = \sum_S P_n(H_i|\vec{S}) \tag{3.13}$$

and the subsequent prior distribution at step n as

$$C_n(H_i) = \frac{Y_n(H_i)}{\sum_k Y_n(H_k)}. \tag{3.14}$$

Usually, a satisfactory convergence in the value of the priors is obtained after 6–7 iterations [102]. Of course, the actual process is not only done based on the considered system but also on the concrete centrality or multiplicity range, under it the type of track selection used and under it on the concrete p_{T} range so, it is a full set of priors probabilities what is actually finally obtained.

Once the priors are made available for the system under consideration, on a per track analysis basis within a concrete event, its signals on the different involved detectors are extracted and with them, by using Eq. 3.12, the probability of being each of the different species considered. Then there three main criteria that could be followed to assign a species to the concerned track

- Fixed threshold. The track is accepted as of a certain species i if the probability of being of the species i is greater than some pre-defined value.
- Maximum probability. The track is assigned the species with highest probability.
- Weighted. The track is accepted but with a weight, equal to its Bayesian probability of being of the different species, applied on its yield.

When considering particle identification, due to the always limited nature of the process, it is needed to extract and apply a set of corrections which cope with such a limitation. A set of concepts are in place which basically require the use of Monte Carlo (MC) techniques to generate a, large enough, set of events of concrete and controlled characteristics and a simulation of the overall and detailed detector response being the intention of this last the replication of the actual detector measurements had its input been the events generated by the MC process (see sect. 3.11). The set of event characteristics produced by the MC process as such is generically denominated generator level characteristics while

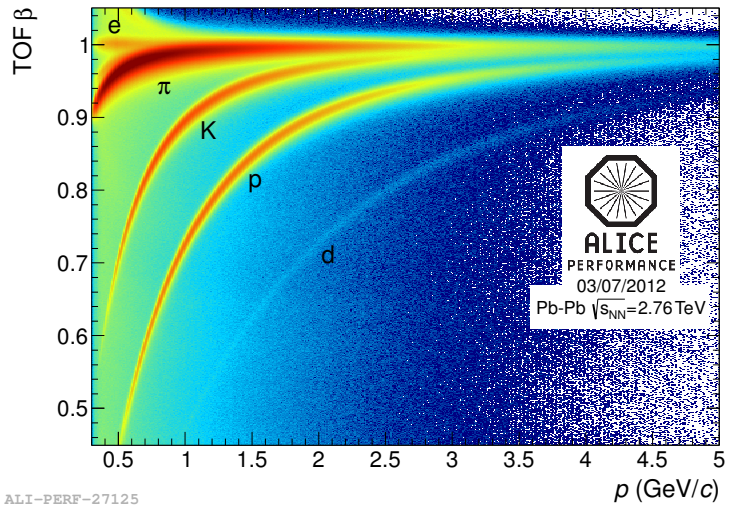

FIGURE 3.7: Distribution of β as measured by the TOF detector as a function of momentum for particles reaching TOF in Pb–Pb interactions [83].

the set of event characteristics obtained by the detector simulator is generically denominated detector level characteristics.

The efficiency of detecting a concrete species i, within a certain range of momentum centered at p, is defined as

$$\epsilon_{ii}(p) = \frac{N_{i_{\text{det}},\, i_{\text{gen}}}(p)}{N_{i_{\text{gen}}}(p)} \tag{3.15}$$

with $N_{i_{\text{det}},\, i_{\text{gen}}}(p)$ being the number of particles, within the range of momentum, identified as species i at the detector level which were actually of the species i at generator level, and $N_{i_{\text{gen}}}(p)$ the total number of particles, within the range of momentum, of species i at generator level.

The contamination of species i, within a certain range of momentum centered at p, due to a different species j is defined as

$$c_{ij}(p) = \frac{N_{i_{\text{det}},\, j_{\text{gen}}}(p)}{N_{i_{\text{det}}}(p)} \tag{3.16}$$

with $N_{i_{\text{det}},\, j_{\text{gen}}}(p)$ being the number of particles, within the range of momentum, identified as species i at the detector level which were actually of the species j at generator level and $N_{i_{\text{det}}}(p)$ the total number of particles, within the range of momentum, identified as species i at detector level.

The misidentification probability of species i, within a certain range of momentum centered at p, as a different species j is defined as

$$m_{ij}(p) = \frac{N_{j_{\text{det}},\, i_{\text{gen}}}(p)}{N_{i_{\text{gen}}}(p)}. \tag{3.17}$$

Then, trivially,

$$c_{ij}(p) = \frac{m_{ji}(p)\, N_{j_{\text{gen}}}(p)}{\epsilon_{ii}(p)\, N_{i_{\text{gen}}}(p) + \sum_{k\neq i} m_{ki}(p)\, N_{k_{\text{gen}}}(p)}. \tag{3.18}$$

For correcting for efficiency and contamination, within a certain range of momentum centered at p, a factor

$$w_i(p) = \frac{1 - \sum_{j\neq i} c_{ij}}{\epsilon_{ii}(p)} \tag{3.19}$$

is applied as a weight to each particle of species i within the range of momentum. Applying as a

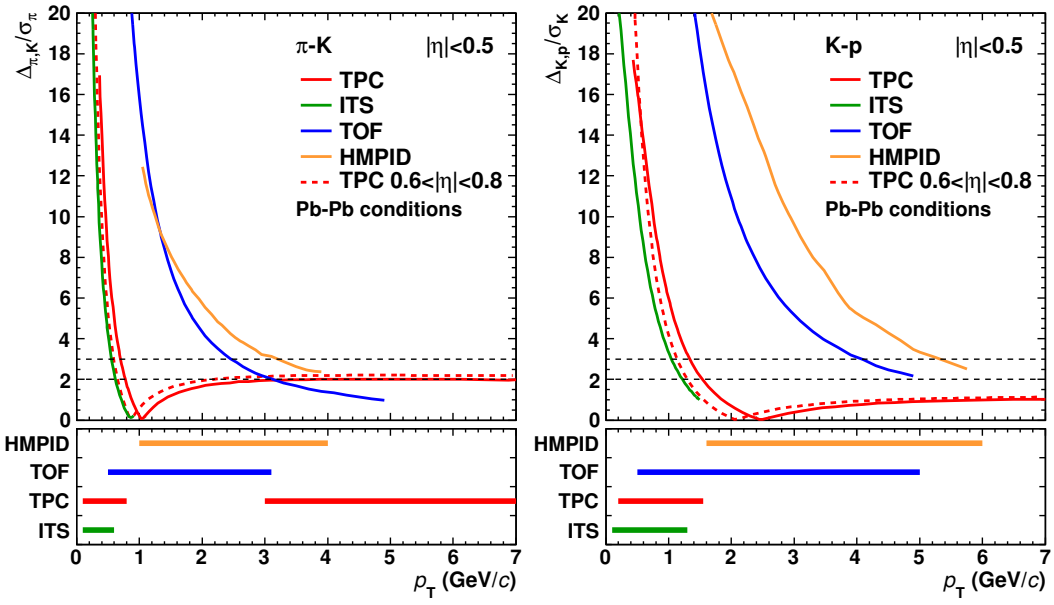

FIGURE 3.8: Separation power of hadron identification in the ITS, TPC, TOF, and HMPID as a function of p_{T} at midrapidity. The left (right) panel shows the separation of pions and kaons (kaons and protons), expressed as the distance between the expectation values divided by the resolution, σ for the pion and the kaon, respectively, averaged over $||eta| < 0.5$. For the TPC, an additional curve is shown in a narrower η region. The lower panels show the range over which the different ALICE detector systems have a separation power of more than 2σ [83].

weight means that if the particle has to be counted within an histogram, it has to be counted with weight w instead of with one, and the momentum of the particle, if it is q, it has to be considered as wq. Usually instead of correcting based on momentum ranges the p_{T} is used, and when dealing with inclusive primary particles, the only species considered as contaminating are secondary particles, but all the concepts described are immediately translated.

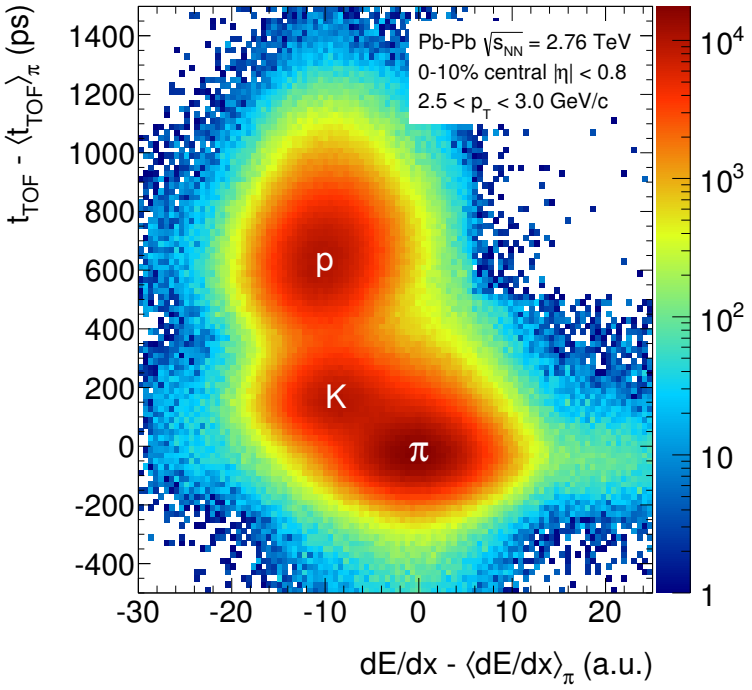

FIGURE 3.9: Combined pion identification with TOF and with dE/dx in the TPC [83].

3.11 ALICE SW framework

ALICE is quite complex experiment which is continuously being updated. The hardware (HW) updates usually takes place during the LHC long stop periods but SW updates is a daily task. The only way to cope with the complexity of the tasks involved and the need of a continuous update is to have a single, huge, SW framework which is used by all the agents involved in the main tasks of data collection, data simulation, data reconstruction and data analysis. The ALICE SW framework [103] consists of several tens of software packages each performing their own function in the framework. In this section the main components of the ALICE SW framework are described.

3.11.1 ALICE environment on the GRID, AliEn

Apart from the computer resources tightly tied to the data acquisition system directly from the detector components, the rest of the computer infrastructure utilized by ALICE is deployed as a worldwide grid of computing and file storage nodes. The task to make this distributed infrastructure transparent to the users and to the applications is performed by the AliEn middleware package.

There are two main tasks developed by AliEn [104] to maintain a distributed resilient file catalog and to efficiently allocate the distributed computing power to the different tasks which are required for execution. Neither the users nor the applications are aware of where the actual required data files are stored nor in which node of the grid are the actual tasks being executed. AliEn takes care of that. The user or the applications only specify, via a job description language, the task which has to be executed, denominated as a job in AliEn terminology, the files which has to take as inputs and the files expected to get as outputs. The files referred on the overall structure of the file catalog.

3.11.2 ROOT

ROOT [105] is a C++ based object oriented framework developed by CERN which is the base of all the SW developed within ALICE. Apart of providing the basic support for objects inheritance and persistence in the context of the physics of high energies and collider physics, ROOT is a modular scientific SW toolkit. It is specially designed to deal with big data processing for which, in the context of ALICE, relies on support from AliEn. It is mainly written in C++ but is also integrated with python and with R. It provides a full set of tools to handle histogramming, minimization, statistical analysis, data visualization and storage, multivariate analysis, and data modeling.

3.11.3 AliROOT

AliROOT [106] is the core of the ALICE SW framework. It describes the ALICE detector at the SW level for being used by the own AliROOT and by the rest of the components of the ALICE SW framework, including the users own physics analyses. AliROOT is in charge of the whole data collection and its format as raw data. At this level the raw data can come from two different sources, the actual data coming from the detector, or simulated data coming from the detector simulation packages as will be described latter. AliROOT is also in charge of the complete reconstruction of the data as entities able to be handled by other parts of the framework or the user analyses. These entities were described in previous sections of this chapter as events, interaction vertex, tracks, particles, decay vertexes, etc.

Quite relevant for the overall quality assurance (QA) of the reconstruction process is the fact that exactly the same SW is used for reconstructing those entities were the raw data coming from the actual detector or from the detector simulator.

3.11.4 Geometry and tracking, GEANT

The Geometry and tracking package GEANT [107] simulates the passage of elementary particles through the matter. Originally developed at CERN, its scope has reached areas such as medical and biological sciences, radio-protection and astronautics. The main application of GEANT within ALICE context its the transport of particles through an experimental setup for the simulation of detector response. To carry that, GEANT allows

(1) to describe the experimental setup, the ALICE detector in this context, by a structure of geometrical volumes each made of its own material. Each material is also described according to its propagation characteristics and its sensitivity characteristics applicable for volumes which describe sensitive detectors within the setup

(2) to accept events simulated by Monte Carlo generators

(3) to transport the particles of the accepted events trough the various volumes of the experimental setup taking into account the volumes boundaries, the nature of the particles, their interaction with the volume material and the defined present fields

(4) to record the particle trajectories and the response of the defined sensitive detectors

(5) to visualize the detectors and the particle trajectories.

Last two capabilities are usually not used in ALICE context. AliROOT takes care of GEANT output and its conversion to the same format that the raw data produce by the ALICE detector in actual collisions data taking. AliROOT also coordinates the output from the selected MC event generator and GEANT being possible of using a diversity of MC generators described next.

3.11.5 Monte Carlo generators

A wide set of MC generators are available under the ALICE SW framework. In this section the ones used in the development of this thesis are be described.

PYTHIA 6.4 Perugia-0

PYTHIA [108] is a general purpose event generator for high energy collisions of elementary particles. In the context of ALICE is used for generating pp collisions events. At the heart of PYTHIA is the Lund string fragmentation model [109, 110]. PYTHIA considers a wide range of physics processes. Hard and sub-processes, resonance decays, final- and initial-state parton showers, multiple parton-parton interaction and beam remnant with color connections which could conforms components of the underlying event, hadronization, decays, color rearrangement and Bose-Einstein effects as QCD interconnection effects.

HIJING 1.36

The heavy-ion jet interaction generator, HIJING, MC event generator [111] is based in a model for multiple jet production in hadronic interactions. Soft interactions leading to mini-jets are modeled along the lines of the Lund FRITIOF [112] and dual parton model (DPM) [113]. Interacting hadrons are considered under the context of multiple string phenomenology where multiple soft gluons exchanges between the constituent quarks or diquarks in hadrons can lead to longitudinal string-like excitations of those hadrons. The strings interact before fragmenting into particle showers. The multiple mini-jet production with initial and final state radiation is carried according to the PYTHIA model [108]. The extension to pA and A–A collisions is covered by decomposing the collision into binary hadron-hadron collisions determined by a Glauber geometry description for the given impact parameter.

HIJING implements two relevant features, jet quenching and nuclear shadowing. Jet quenching are final state interactions of high p_{T} partons which manifest as energy loss when traversing the dense nuclear matter. The jet quenching implementation is still very schematic. Shadowing describes the modification of the free nucleon parton density when nucleons are immerse within the nucleus. Nuclear shadowing reduces the number of minijets actually produced. HIJING does not incorporate final state interactions among low p_{T} produced particles which means that collective effects on that p_{T} range are not reproduced.

AMPT

The AMPT generator model [114] is used configured in three ‘flavors’, with hadronic rescattering, AMPT 1.25, with string melting, AMPT 2.25, and with hadronic rescattering and string melting, AMPT 2.25. AMPT consists of four main building blocks. The first block, which conforms the initial conditions, uses HIJING [111] to obtain the spatial and momentum distribution of mini-jet partons and soft string excitations. The second block implements a Zhang‘s parton cascade (ZPC) model [115] for parton scattering. The third constituent block performs the hadronization by two different mechanisms depending of the flavor, by using the Lund string fragmentation model [109] or by using a quark coalescence model [116] to combine partons into hadrons. The fourth constituent block incorporates an optional hadronic rescattering cascade based on a relativistic transport (ART) model [117]. In the flavor without string melting partons are recombined with their parent strings when they stop interacting and the resulting strings are then converted to hadron using the Lund fragmentation model. In the flavor with string melting the hadrons produced from the HIJING model are converted to their constituent partons which evolution is driven by ZPC. When they stop scattering are converted to hadrons by means of the quark coalescence model.

Chapter 4

Data sample and Monte Carlo simulations

4.1 Data sample

4.1.1 Data

Different data samples have been used in the development of this work. For the Pb–Pb analysis, Pb–Pb collisions data collected during LHC Run1 period in the year 2010 at $\sqrt{s_{\mathrm{NN}}}$ = 2.76 TeV, and Pb–Pb collisions data collected during LHC Run2 period in the year 2018 at $\sqrt{s_{\mathrm{NN}}}$ = 5.02 TeV, LHC10h and LHC18r, respectively, are used. For the p–Pb analysis, p–Pb collisions data collected during LHC Run1 period in the year 2013 at $\sqrt{s_{\mathrm{NN}}}$ = 5.02 TeV, LHC13b and LHC13c, are used. Finally, for the pp analysis, pp collisions data collected during LHC Run1 period in the year 2010 at $\sqrt{s_{\mathrm{NN}}}$ = 7 TeV, LHC10b and LHC10c, are used.

4.1.2 Simulations

There have been two main uses of the simulated data. As was described in the section 3.10 collected data usually require certain set of corrections due to the detector limited acceptance or to its potential non-linear response in the range required for the concrete analysis. As was there explained, correcting for these detector limitations requires simulating a set of events (generator level) and simulating the detector response to this events (detector level). For this purpose HIJING generated/reconstructed events have been used for extracting the corrections to apply to Pb–Pb collisions data. DPMJET generated/reconstructed events have been used for extracting the corrections to apply to p–Pb collisions data. Finally PYTHIA generated/reconstructed data have been used for extracting the corrections to apply to pp collisions data. The simulations are always configured with the same settings and detector conditions under which the actual data were taken. In all cases the simulation of the detector has been based on GEANT3. The production incorporated injected signals are ignored by the correlation analysis.

Following production datasets have been utilized for reconstructed simulated events

- HIJING Pb–Pb 2.76 LHC10h configured: LHC11a10a_bis, detector level
- HIJING Pb–Pb 2.76 LHC10h configured: LHC11a10b_bis, detector level
- DPMJET p–Pb 5.02 LHC13b and LHC13c configured: LHC13b2_efix, detector level
- PYTHIA pp 7 TeV LHC10b configured: LHC14j4b, detector level
- PYTHIA pp 7 TeV LHC10c configured: LHC14j4c, detector level

As both productions, LHC11a10a_bis and LHC11a10b_plus, were obtained with the same SW level they are merged and considered as a single one from now on. The same applies for LHC14j4b and LHC14j4c productions.

4.1.3 Model comparison

Following production dataset have been utilized for theory model comparisons

- HIJING Pb–Pb 2.76 LHC10h configured: LHC11a10a_bis, generator level
- HIJING Pb–Pb 2.76 LHC10h configured: LHC11a10b_bis, generator level
- AMPT Pb–Pb 2.76 TeV generator level, String melting ON, re-scattering ON: LHC13f3c
- AMPT Pb–Pb 2.76 TeV generator level, String melting OFF, re-scattering ON: LHC13f3b
- AMPT Pb–Pb 2.76 TeV generator level, String melting ON, re-scattering OFF: LHC13f3a

4.2 Event selection and track selection

4.2.1 Event selection

Physics selection

Physics selection as describe in section 3.7 is used to select minimum bias (MB) events. Events that fulfill all conditions from the physics selection are considered in the analysis.

An additional selection based on the z position of the reconstructed collision vertex is applied. Namely, only MB events with a valid reconstructed interaction vertex whose longitudinal coordinate lies within $|z_{\mathrm{vtx}}| < 7$ cm of the fiducial IP are considered for the analyses. The quality criteria used to validate a reconstructed vertex have been

- events whose vertex had not any track contribution are discarded
- events whose vertex have been extracted by means of the SPD detector, but which only have its z coordinate reconstructed with a resolution larger than 0.25 cm are discarded
- events whose vertex have been extracted by means of the SPD detector but which have a dispersion larger than 0.03 cm are discarded
- events whose distance between the vertex extracted from tracks and the vertex extracted by means of the SPD detector is larger than 0.2 mm are discarded

Pileup rejection

Pileup events are events which result from a superposition of two or more single events. Pileup events are detected in base of the different response times the different ALICE detectors have. As was described in section 3.7 the TPC detector, with its drift time requirement, drives the L2 trigger. The idea then is to correlate the activity in fast detectors, as V0, with the one in the TPC whose response time is considerable longer. The potential pileup affected events are then identified based on the relationship between the V0 total multiplicity and the total number of reconstructed tracks within the fiducial, 0.15 GeV/$c \leq p_{\mathrm{T}}$ and $|\eta| < 0.8$, acceptance which have reached the outer side of the TPC. Due to the larger read-out time of the TPC, in scenarios of out-of-bunch pileup, a fraction of events contain TPC tracks from these out-of-bunch pileup events. This is then reflected in a higher number of TPC tracks of what would be expected from just the event V0 multiplicity. Fig. 4.1 (left panel) shows V0 total multiplicity versus the number of tracks within the fiducial acceptance which have reached the outer side of the TPC before (left panel) and after (right panel) the complete event selection. The plots were produced to show the effect of the pileup events rejection so practically the whole centrality range, 0–90% has been considered. The

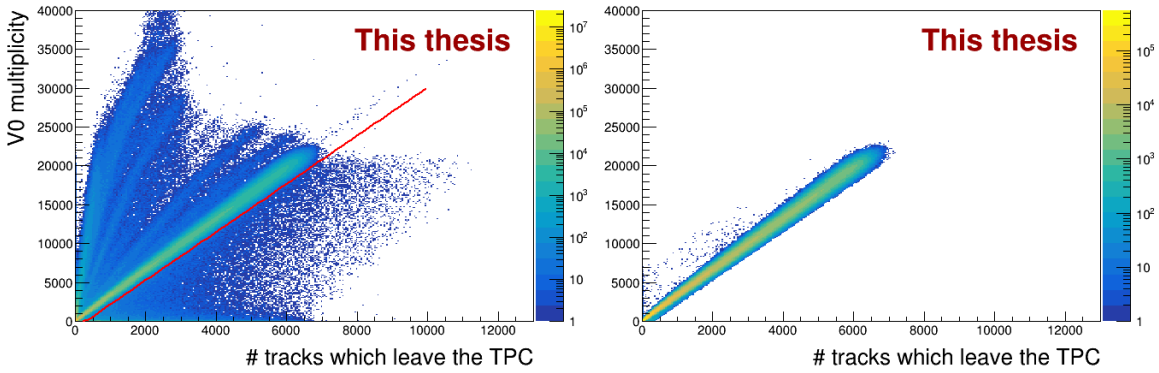

FIGURE 4.1: V0 total multiplicity versus the number of tracks within the 0.15 GeV $\leq p_T$ and $|\eta| < 0.8$ acceptance which leave the TPC, before event selection (left, all events are shown), and after event selection (right for 0–90% central events) in Pb–Pb collisions at $\sqrt{s_{NN}} = 2.76$ TeV.

condition is such that events for which

$$V0M < 3.1 \times N_{kTPCout} - 1,000 \tag{4.1}$$

are rejected. V0M refers to the total V0 multiplicity for the considered event while $N_{kTPCout}$ refers to the number of tracks within the fiducial acceptance which have reached the outer side of the TPC in that event.

For the Pb–Pb Run2 analysis the identification of events affected by pile up has been refined by using instead of the number of tracks leaving the TPC, the total number of TPC active clusters on the event. The effect of the refinement has been a slight decrease in the number of discarded events. The condition is now such that events for which

$$V0M < 1.3 \times 10^{-9} \times N^2_{TPC\ clusters} + 1.25 \times 10^{-2} \times N_{TPC\ clusters} - 4,000 \tag{4.2}$$

are rejected. $N_{TPC\ clusters}$ refers to the total number of TPC active cluster for the event considered. Fig. 4.2 shows V0 total multiplicity versus the number of total TPC active clusters before (left panel) and after (right panel) the complete event selection. The plots were produced to show the effect of the pileup events rejection so practically the whole centrality range, 0–90% has been considered.

Centrality or charged particle multiplicity selection

The centrality of the collision is determined in Pb–Pb events by using the V0 multiplicity as described in section 3.9. Nine centrality classes are used for classifying the Pb–Pb events and study the evolution of the two-particle transverse momentum correlation functions. They are presented in Table 4.1.

In analyzing p–Pb events and specially pp events the centrality concept could be a bit misleading. For these collision systems multiplicity classes are used instead in a concept totally parallel to that developed for the centrality in section 3.9. The V0 detector is again used for extracting the event charged particle multiplicity. For similitude they are presented in Table 4.2.

The number of analyzed events per centrality class are shown in Table 4.3:

4.2.2 Track selection

The tracks used for the analyses presented in this thesis are fully reconstructed by the TPC and complying with the following criteria

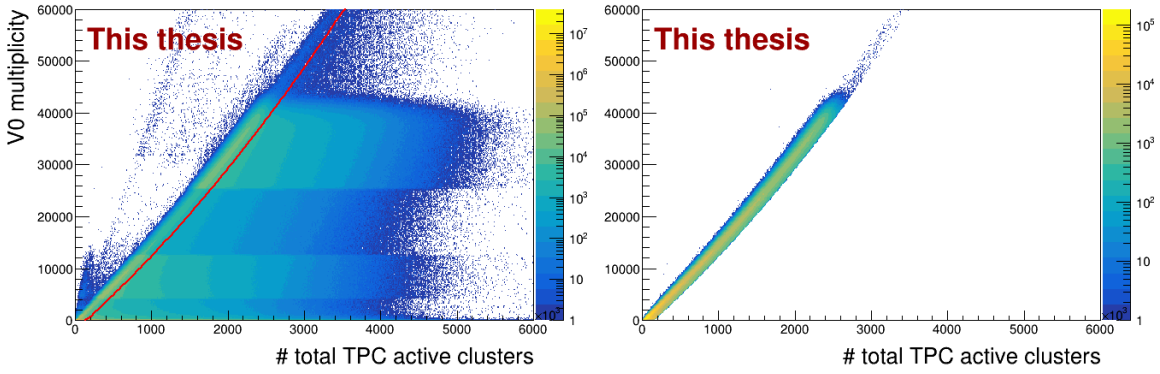

FIGURE 4.2: V0 total multiplicity versus the total number of TPC active clusters, before event selection (left, all events are shown), and after event selection (right for 0–90% central events) in Pb–Pb collisions at $\sqrt{s_{\mathrm{NN}}}$ = 5.02 TeV.

	Centrality range
most central	0-5%
	5-10%
	10-20%
	20-30%
	30-40%
	40-50%
	50-60%
	60-70%
more peripheral	70-80%

TABLE 4.1: The nine centrality ranges for classifying Pb–Pb events centrality.

	Multiplicity range
highest multiplicity	0-5%
	5-10%
	10-20%
	20-30%
	30-40%
	40-50%
	50-60%
	60-70%
Lower multiplicity	70-80%

TABLE 4.2: The nine multiplicity ranges for classifying pp and p–Pb events multiplicity.

	LHC10h	**LHC11a10**
0–5%	680,000	65,000
5–10%	682,000	75,000
10–20%	1,355,000	167,000
20–30%	1,358,000	189,000
30–40%	1,365,000	207,000
40–50%	1,359,000	221,000
50–60%	1,356,000	240,000
60–70%	1,360,000	260,000
70–80%	1,349,000	284,000

TABLE 4.3: Number of analyzed events per centrality class for the used productions, data and HIJING

- No hits in the ITS are required
- The refit stage towards the ITS is not required
- The track should have, at least, 50 active TPC clusters associated
- The track reconstructed quality should verify $\chi^2/N_{\text{TPC clusters}} < 4$ where $N_{\text{TPC clusters}}$ are the number of TPC active clusters associated to the track
- Tracks which show a kink, indication of a decay where only the charged particle can be detected, are discarded

To reduce the contamination from secondary particles an upper limit on the track distance of closest approach (DCA) to the interaction vertex is imposed. Accepted tracks require their DCA to comply with

$$\left(\frac{d_{xy}}{\text{DCA}_{xy}}\right)^2 + \left(\frac{d_z}{\text{DCA}_z}\right)^2 < 1, \tag{4.3}$$

where d_{xy} and d_z are the track DCA to the interaction vertex on the transverse plane and on the z axis, respectively, and with $\text{DCA}_{xy} = 2.4$ cm and $\text{DCA}_z = 3.2$ cm the limit values on both, respectively. Additionally the track is required to lay into the pseudo-rapidity range of the fiducial acceptance, $|\eta| < 0.8$, and in the transverse momentum range $0.2 < p_{\text{T}} < 2.0$ GeV$/s$. The transverse momentum range is motivated by the fact it captures the bulk of the collision produced matter.

Contamination from electrons (mainly from pair conversions) is limited by using the PID framework as described in the section 3.10. Tracks which are closer to the electron TPC line by more than 3σ and which are away from the pion, kaon and proton TPC lines by more than 5σ are discarded.

Chapter 5

Methodology for measuring two-particle transverse momentum correlations

5.1 Introduction

Two-particle transverse momentum differential correlations are not straightforward measuring observables. The right technique for properly measuring them is based on the use of flatten histograms in $(\eta_1, \varphi_1, \eta_2, \varphi_2)$ where η_α and φ_α refer to pseudo-rapidity and azimuthal angle, respectively, of the momentum of particle α within a pair, for $\alpha = 1, 2$. All needed magnitudes are collected into these kind of flattened histograms and the two-particle transverse momentum correlations are also built up in similar ones. A further reduction step provides the desired two-particle transverse momentum differential correlations in $(\Delta\eta, \Delta\varphi)$ being $\Delta\eta$ and $\Delta\varphi$ the relative angular separation in pseudo-rapidity and azimuthal angle of the two particles.

Without the use of this technique, STAR reported on two-particle transverse momentum differential correlations, for the first time, inferred from event-wise mean transverse momentum fluctuations [76], and on its energy dependence [118]. Already using the flatten histograms technique, STAR reported on the evolution of two-particle transverse momentum differential correlations with centrality [77] and extracted out of it an estimate for the ratio of the shear viscosity to entropy density η/s. Recently ALICE, also using the flatten histograms technique, reported on two-particle transverse momentum correlations, its flow dominance and further evidence support for flow coefficients factorization [119].

In this work the flatten histograms technique will be used to extract the evolution of the two-particle transverse momentum differential correlation

$$\mathrm{G}_2\left(\Delta\eta, \Delta\varphi\right) = \frac{\langle \sum_{\mathrm{i}}^{n_{1,1}} \sum_{\mathrm{j}\neq\mathrm{i}}^{n_{1,2}} p_{\mathrm{T,i}}\, p_{\mathrm{T,j}} \rangle}{\langle n_{1,1} \rangle \langle n_{1,2} \rangle} - \langle p_{\mathrm{T},1} \rangle \langle p_{\mathrm{T},2} \rangle \tag{5.1}$$

with collision centrality. $\Delta\eta$ and $\Delta\varphi$ refer to the two track separation both, longitudinally and azimuthally, respectively. The indexes, i and j, run over the event multiplicities of track one, $n_{1,1}$, and track two, $n_{1,2}$, respectively. G_2 can be extracted for two tracks of the same charge, like sign (LS) correlator, in which case both multiplicities match, or for two tracks of different charge, unlike sign (US) correlator, in which case both multiplicities differ. p_{T} stands for the transverse momentum of track one, $p_{\mathrm{T},1}$, or two, $p_{\mathrm{T},2}$. The averages are over the whole event ensemble.

G_2 is sensitive to momentum currents and as such provide information on the medium transport characteristics. The longer the system lives the wider the reach of the effects of such transport characteristics and the bigger the impact on the G_2 correlator. In order to study the evolution of G_2 with system lifetime, the correlator is measured in nine centrality intervals, from most central to most peripheral collisions, and its shape parametrized for better describing its evolution.

5.2 Correction procedures

5.2.1 Non-uniform acceptance (NUA) correction

As it is expected from a detector of the dimensions of the ALICE detector, its response along its fiducial acceptance is not fully uniform. The effects on two-particle correlations of the finite and non-uniform detector acceptance and of the non-perfect detector efficiency have been studied with great detail as reported in [66]. The main concern there, and in the actual experiments, is the potential dependence of the detector acceptance and the detector efficiency on the position of the interaction vertex along the longitudinal coordinate, $z_{\rm vtx}$. Differences on the detector response are observed within the $z_{\rm vtx}$ range used for the analysis(see section 4.2.1). The first suggested approach in [66] for correcting for these effects is to extract the correlation function in fine ranges of $z_{\rm vtx}$ and then obtain the final correlation function as a weighted average. This becomes prohibitively expensive in terms of memory and required volume of available data. As was described in the introduction of this chapter (5.1), the correlation function is extracted on each centrality range as an expression in $(\eta_1, \varphi_1, \eta_2, \varphi_2)$ where each of the magnitudes, $(\eta_1, \varphi_1, \eta_2, \varphi_2)$ are binned magnitudes. This puts high demands on memory requirements and compromises the limited available datasets. The weights technique, also suggested in [66], is used instead.

The rational behind of the weights technique is the flattening of the detector response on small $p_{\rm T}$ slices for each charged track polarity and on each centrality or multiplicity range. For a concrete $p_{\rm T}$ range, one small $p_{\rm T}$ slice, it is assumed that the detector response in detecting single tracks, of the considered charge and within the considered centrality/multiplicity range, should be flat in η, φ, and $z_{\rm vtx}$. While the variation of $\mathrm{d}N/\mathrm{d}\eta$ within $|\eta| < 0.9$ is very small for systems like Pb–Pb at LHC energies [120] and can be neglected, this is not the case for systems like p–Pb [121] (see Eq. (5.4)). The single track distribution on η, φ, and $z_{\rm vtx}$, for each $p_{\rm T}$ range, track polarity, and centrality range, is then corrected by the set of weights which produce the flattening of the detector response in such $p_{\rm T}$ range, track polarity, and centrality range.

The required weights are basically the inverse of the single track distribution and is extracted according to the following procedure. A pass over data is done filling histograms

$$N_C^{\pm}\left(z_{\rm vtx}, \eta, \varphi, p_{\rm T}\right) \tag{5.2}$$

separately, for positive and negative tracks and for each of the centrality or multiplicity ranges C considered in the analysis, and with η, φ and $p_{\rm T}$ the longitudinal and azimuthal coordinates and the transverse momentum of the tracks, respectively.

The binning for the histograms (5.2) is as follows (Table 5.1). For the whole 2π azimuthal acceptance, φ is divided in 72 bins. For the $|\eta| < 0.8$ pseudo rapidity acceptance, η bins have a width of 0.1 resulting in 16 bins. For few systematic analysis, the number of η bins varies accordingly keeping the bin width unchanged. For the transverse momentum acceptance, a width of 0.1 GeV/c is used so, for the whole analysis, done with a $0.2 < p_{\rm T} < 2.0$ GeV/c acceptance, 18 bins are used. Finally the range, $[-7.0, 7.0]$ cm, of the interaction vertex longitudinal coordinate, $z_{\rm vtx}$, is divided in 28 bins each 0.5 cm wide.

The set of weights is extracted by flattening the detector response on a per $p_{\rm T}$ bin basis

$$\omega_C^{\pm}\left(z_{\rm vtx}, \eta, \varphi, p_{\rm T}\right) = \frac{\langle N_C^{\pm}(p_{\rm T})\rangle}{N_C^{\pm}\left(z_{\rm vtx}, \eta, \varphi, p_{\rm T}\right)} \tag{5.3}$$

where $N_C^{\pm}\left(z_{\rm vtx}, \eta, \varphi, p_{\rm T}\right)$ given in (5.2) has been corrected for the $z_{\rm vtx}$ coordinate distribution (see below), and $\langle N_C^{\pm}(p_{\rm T})\rangle$ the average transverse momentum yield for the considered $p_{\rm T}$ bin. In the subsequent correlation data collection passes, each track is then weighted with the value given by

variable	# bins	bin width	range
z_{vtx}	28	0.5 cm	$[-7.0, 7.0]$ cm
p_{T}	18	0.1 GeV/c	$[0.2, 2.0]$ GeV/c
η	16	0.1	$[-0.8, 0.8]$
φ	72	$\pi/36$ rad	$[0.0, 2\pi]$

TABLE 5.1: Description of the bins structure for variables used in the two-particle transverse momentum correlation analyses.

Eq. (5.3) corresponding to its charge, η, φ and p_{T} magnitudes and the z_{vtx} coordinate and centrality class of the event the track belongs to.

The obtained weight coefficients will recover a flat detector response on a per p_{T} bin basis. The validity of this procedure requires that the (5.2) histograms were produced from a per p_{T} bin flat profile source. In this way the non-regularities in the single track distribution should be only produced due to the non uniform acceptance of the detector. This condition requires the previous flattening of (5.2) histograms according to the, z_{vtx} coordinate distribution. This aspect is further illustrated in Fig. 5.1 where the effect on the single track yield on an exterior and a central z_{vtx} bins can be compared before and after the flattening according to the z_{vtx} vertex coordinate distribution shown in Fig. 5.2.

An additional similar need was unveiled when extracting the NUA correction for simulated Pb–Pb MC data. MC tracks are not generated with a flat profile. In fact, the track generation profile is independent of the z_{vtx} coordinate but, for each p_{T} bin, it has a dependence on η which is far from flat and that changes when moving from one p_{T} bin to the next (see Fig. 5.3, left panel). In order to use the above procedure to extract NUA correction weights for MC reconstructed data, (5.2) histograms need to be previously flattened for track generation distribution. Fig. 5.3 illustrates this last point for HIJING events. The apparent connection of the different p_{T} bins is an artifact of the plotting machinery, they are handled in a completely independent manner and, in the plots, they are completely independent of each other. What the plots represent on a per p_{T} bin basis is the relative single track yield in pseudo-rapidity.

For Pb–Pb collisions data, the validity of using the weights extracted through expression (5.3) from (5.2) histograms flattened for the z_{vtx} distribution (Fig. 5.2), which implies that p_{T} spectra and $\langle p_{\text{T}} \rangle$ are independent of z_{vtx}, η as well as φ, is likely acceptable at the LHC in the context of the narrow η acceptance of the ALICE detector [66, 120]. On the other hand the weight extraction method needed to be further developed to be applicable for asymmetric systems like p–Pb. For these cases a variant of the procedure for extracting the weights has been proposed in this work. After extracting (5.2) histograms and flattening them for the z_{vtx} distribution (Fig. 5.2), the expression for extracting the weights proposed here is

$$\omega_C^{\pm}(z_{\text{vtx}}, \eta, \varphi, p_{\text{T}}) = \frac{\langle N_C^{\pm}(p_{\text{T}}, \eta) \rangle}{N_C^{\pm}(z_{\text{vtx}}, \eta, \varphi, p_{\text{T}})}, \tag{5.4}$$

with the same meaning than in (5.3), and which implicitly only assumes that p_{T} spectra and $\langle p_{\text{T}} \rangle$ are independent of z_{vtx} as well as φ, which is closest to the actual situation in asymmetric systems and applicable also to large η acceptance detector scenarios.

5.2.2 Non uniform efficiency (NUE) correction

As was mentioned in the previous section, NUA is corrected on a per p_{T} bin independent basis. In order to consider the fact that the detector response is not flat in p_{T} and to extract the p_{T} dependent efficiency of the detector, a procedure similar to the one described in section 3.10 is followed. For Pb–Pb collisions, reconstructed and generated data from a HIJING data sample are used to produce (5.2) histograms for both reconstructed and generated data. For the reconstructed data, weights are extracted following

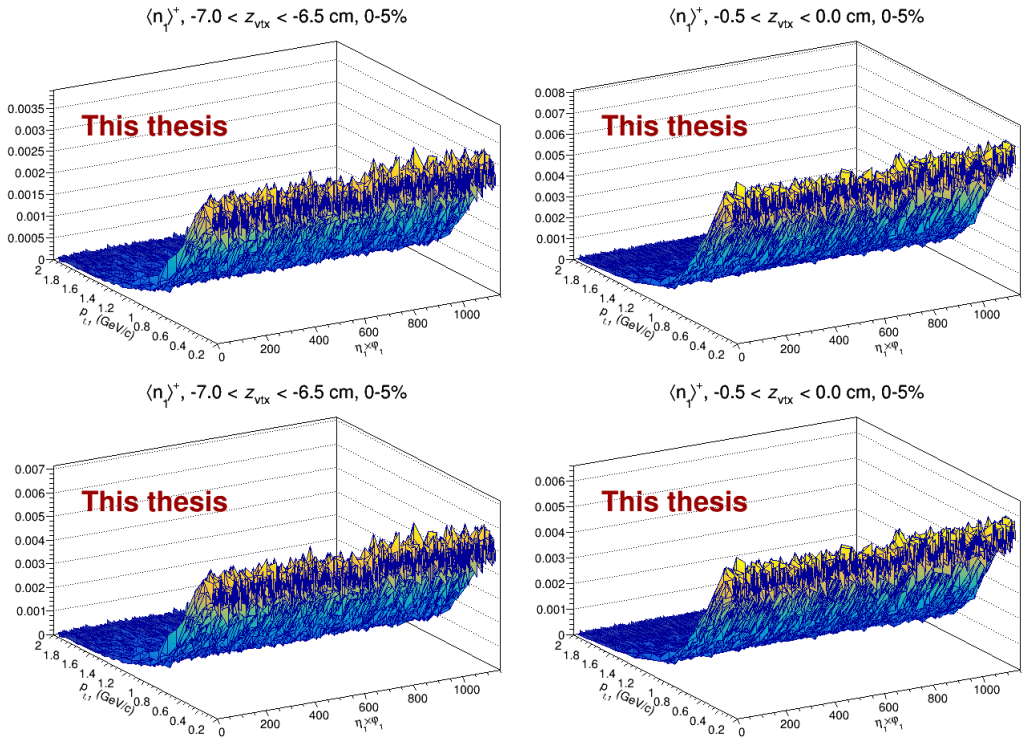

FIGURE 5.1: Single positive tracks density for most central HIJING events laying in an external z_{vtx} bin (left column) and in a central one (right column) before (top row) and after (bottom row) flattening, and normalizing, according to the z_{vtx} coordinate distribution (Fig. 5.2). NOTE: the x axis is in $\eta \times \varphi$ bins, each 72 consecutive bins (φ bins) add up one η bin; y axis is in p_{T} bins each 0.1 GeV/c width.

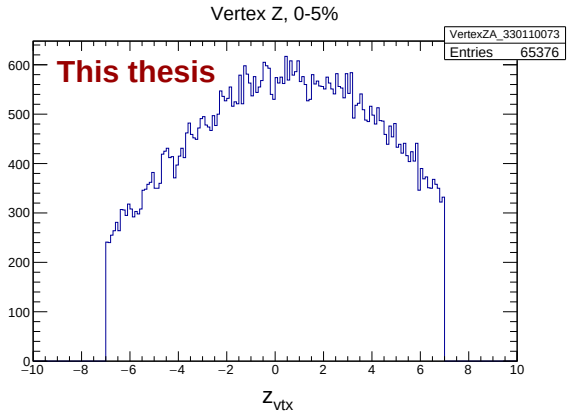

FIGURE 5.2: Distribution of the z_{vtx} coordinate for most central, 0-5%, HIJING events.

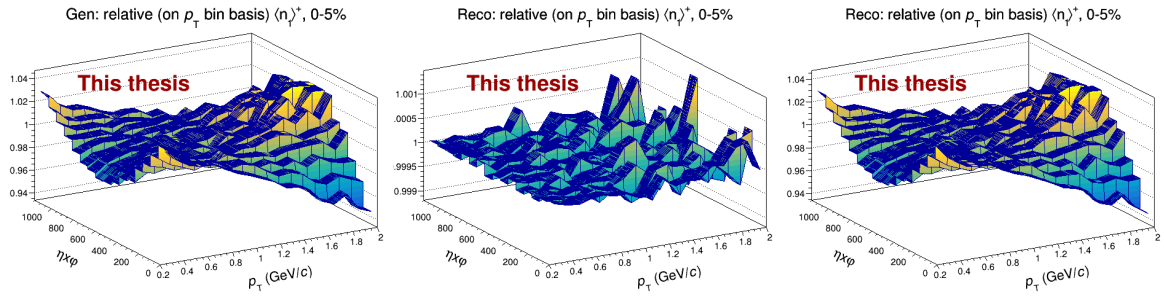

FIGURE 5.3: Relative single positive tracks yield on a per p_T bin basis for most central HIJING events as generated (left), reconstructed after applying NUA correction (central) built without considering the generation profile (the one on the left) and reconstructed after applying NUA correction (right) built considering the generation profile 5.1 (the one on the left). The relative yields are built on a per p_T bin basis so, on each p_T the relative yield in pseudo-rapidity is represented. The apparent relation between p_T bins is not representative of the true yield within such bins. NOTE: the y axis is in $\eta \times \varphi$ bins, each 72 consecutive bins (φ bins) constitute an η bin. The total acceptance used for these plots was the nominal for this analysis.

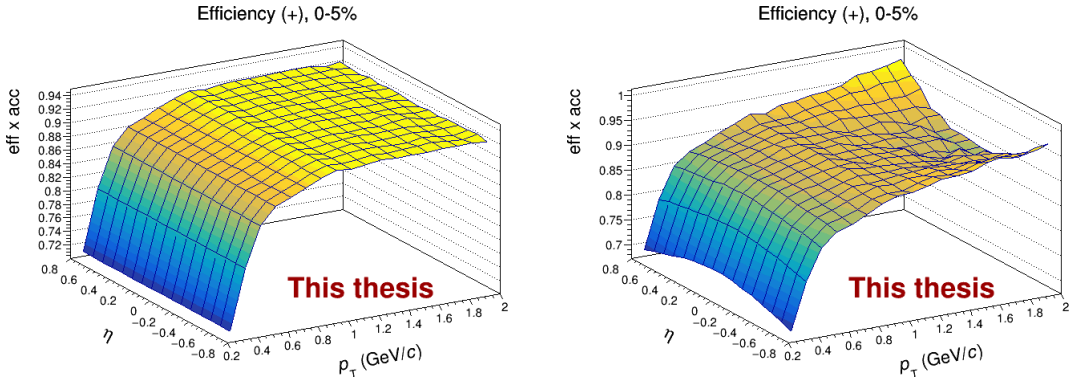

FIGURE 5.4: Single positive tracks efficiency for most central HIJING events when reconstructed after applying NUA correction built considering the generation profile (left) and when reconstructed after applying NUA correction built without considering the generation profile (right, see Fig. 5.3 left).

procedure described in the previous section Eq. (5.3). Then a subsequent pass over reconstructed MC data is carried out filling again (5.2) histograms but with the weighted yield per incorporated track.

The efficiency is then obtained as the ratio

$$\varepsilon_C^{\pm}(z_{\text{vtx}}, \eta, \varphi, p_T) = \frac{\omega_C^{\pm}(z_{\text{vtx}}, \eta, \varphi, p_T) \times N_{C\text{rec}}^{\pm}(z_{\text{vtx}}, \eta, \varphi, p_T)}{N_{C\text{gen}}^{\pm}(z_{\text{vtx}}, \eta, \varphi, p_T)} \tag{5.5}$$

with $N_{C\text{rec}}^{\pm}$ the (5.2) histograms for reconstructed tracks, $\omega_C^{\pm}$ the weights for the reconstructed tracks, and $N_{C\text{gen}}^{\pm}$ the (5.2) histograms for the generated tracks. The product $\omega_C^{\pm} \times N_{C\text{rec}}^{\pm}$ represents the (5.2) histograms filled with NUA corrected reconstructed tracks. It has been checked out that, after applying correctly built weights, the efficiency can be safely considered as flat on the azimuthal and z_{vtx} dimensions and, according to that, the ratio in Eq. (5.5) is only considered dependent on η and on p_T, $\varepsilon_C^{\pm}(\eta, p_T)$, as can be seen in Fig. 5.4 (left panel). Fig. 5.4 (right panel) shows the single positive track efficiency for the case of not properly built weights. By comparing left and right panels it is clearly seen

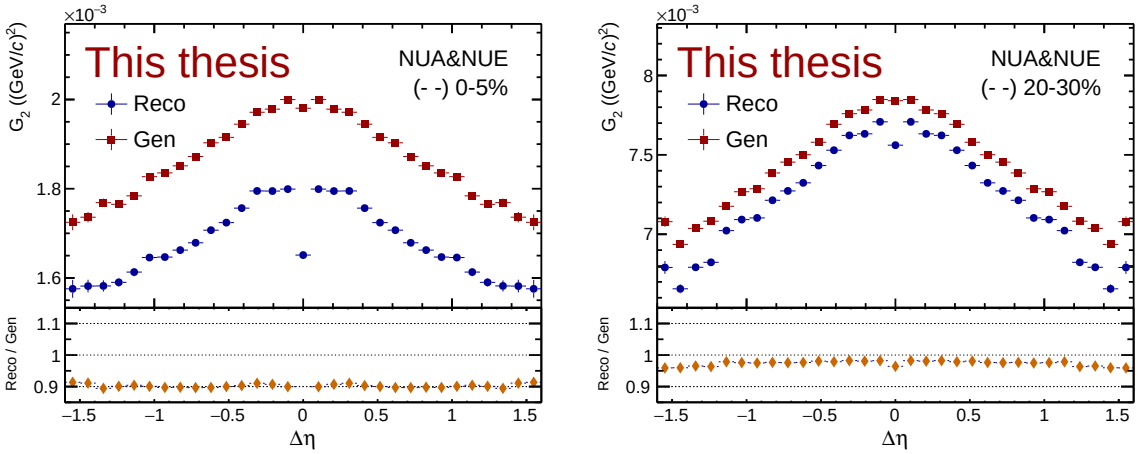

FIGURE 5.5: Longitudinal, $\Delta\eta$, projections of the correlation function from reconstructed (Reco) tracks, after applying NUA and NUE corrections, and from generated (Gen) tracks for most central events, 0–5%,(left) and for semi-central events, 20–30%,(right), for Pb–Pb collisions at $\sqrt{s_{NN}}$ = 2.76 TeV using HIJING as event generator.

that the efficiency is left completely untied to the profile with which particles are generated.

The actual NUE correction is obtained as the inverse of the values obtained in Eq. (5.5) and is applied multiplied by the NUA correction, extracted from data, as a per track single weight according to

$$\omega_{s_C^{\pm}}(z_{\text{vtx}}, \eta, \varphi, p_{\text{T}}) = \frac{\omega_C^{\pm}(z_{\text{vtx}}, \eta, \varphi, p_{\text{T}})}{\varepsilon_C^{\pm}(\eta, p_{\text{T}})} \tag{5.6}$$

where the NUA correction, $\omega_C^{\pm}$, is according to the centrality and the z_{vtx} coordinate of the considered event, and the charge, p_{T}, η and φ of the involved track, and the efficiency $\varepsilon_C^{\pm}$, according to the centrality of the considered event, and the charge, p_{T} and η of the involved track.

5.2.3 Pair efficiency correction and MC closure test

When NUA and NUE corrections, extracted according to the previous sections, are applied to the simulated HIJING data sample at the reconstructed level, the projection of the correlation function for reconstructed tracks along the $\Delta\eta$ dimension for the most central events, was lower by about 9% with respect to the one obtained from the generated tracks (Fig. 5.5). There were different approaches in trying to understand why this happened. The decisive one was to apply the single efficiency profile to the generated tracks in order to simulate the effect of the detector efficiency on the generated sample. What was obtained was an effect which was fully corrected by the NUE correction giving the confidence that the NUE procedure was correct. As the only effect not present then was the detector response to track pairs, the focus was addressed in that direction.

The effect of the pair detection efficiency manifests itself as single tracks which are split giving place to ghost pairs of similar tracks and also tracks which, similar in momentum and angle, cross and share clusters and get merged in a single track and the pair is lost. In principle this may seem a bit contradictory when observing Fig. 5.5. What would be expected would be to observe only effects at small relative angles. However, there is a set of ingredients that allow explaining the behavior shown in Fig. 5.5 in terms of the pair detection efficiency. On the one hand, as Eq. (5.1) shows, G_2 is constituted by the difference of two terms that turn out to be of about the same order, their difference being, and therefore G_2, two or three orders of magnitude inferior to any of them. On the other hand, as also Eq. (5.1) shows, only the first term of G_2 is sensitive to pair detection effects. Finally, when a pair of

tracks is lost, because one of them is masked by the other, or when a ghost pair appears, due to the split of one of the tracks, not only the combination at small angular separation is lost, or won, but the whole set of combinations with the rest of the tracks is as well lost, or won, and this appears as a contribution distributed throughout the whole available angular separation. This is expected to be a small effect but the fact that it only affects G_2 first term makes it relevant as Fig. 5.5 shows.

The usual method to cope with pair detection efficiency is to discard pairs based on the distance of closest approach of the two tracks within the detector fiducial volume (see for instance the method developed by the HBT group [122]). The method removes pairs which are potentially affected by the detector pair efficiency. In two particle correlation analysis it is usual to utilize the mixed events technique to correct for geometric acceptance and efficiency. This technique relies on the ratio of same magnitudes extracted from tracks from a single event as the numerator component and the ones extracted from tracks corresponding to a different number of events, the number of events to mix, as the denominator component. The fact that the pair inefficiency correction method is applied while building both, same event and mixed events, quantities, makes the effect of the method to cancel, explicitly correcting for detector pair inefficiencies. For the current work the mixed event technique is not used so, it cannot rely on similar methods to correct for pair detection efficiency.

In order to extract an estimation of the detector pair efficiency a process similar to the single efficiency extraction is carried out. Once the NUA and NUE efficiency corrections have been extracted, a pass on reconstructed data from the simulated data sample is carried out correcting each track for NUA and NUE and afterwards filling the histograms

$$N_2^{\mathrm{cc}}{}_C\left(\Delta\eta, \Delta\varphi, p_{\mathrm{T}1}, p_{\mathrm{T}2}\right) \tag{5.7}$$

for each charged tracks pair combination, where cc $= ++, +-, -+, --$, and $p_{\mathrm{T}1}$ and $p_{\mathrm{T}2}$, are the transverse momentum of each track on the pair, and are binned as explained above. $\Delta\varphi = \varphi_1 - \varphi_2$ is binned with the same number of bins as φ, while $\Delta\eta = \eta_1 - \eta_2$ is trivially binned in twice the number of bins of η minus one.

The same (5.7) histograms are filled but with the generated data from the simulated data sample. The pair efficiency is then obtained as the ratio

$$\varepsilon_2^{\mathrm{cc}}{}_C\left(\Delta\eta, \Delta\varphi, p_{\mathrm{T}1}, p_{\mathrm{T}2}\right) = \frac{\frac{\omega_C^{c_1}(z_{\mathrm{vtx}},\eta_1,\varphi_1,p_{\mathrm{T}1})\omega_C^{c_2}(z_{\mathrm{vtx}},\eta_2,\varphi_2,p_{\mathrm{T}2})}{\varepsilon_C^{c_1}(\eta_1,p_{\mathrm{T}1})\varepsilon_C^{c_2}(\eta_2,p_{\mathrm{T}2})} N_2^{\mathrm{cc}}{}_{C\ \mathrm{rec}}\left(\Delta\eta, \Delta\varphi, p_{\mathrm{T}1}, p_{\mathrm{T}2}\right)}{N_2^{\mathrm{cc}}{}_{C\ \mathrm{gen}}\left(\Delta\eta, \Delta\varphi, p_{\mathrm{T}1}, p_{\mathrm{T}2}\right)} \tag{5.8}$$

where each of the contributions to the reconstructed $N_2^{\mathrm{cc}}{}_{C\ \mathrm{rec}}$ histogram has been corrected for NUA, $\omega_C^{c_1}, \omega_C^{c_2}$, and NUE, $\varepsilon_C^{c_1}, \varepsilon_C^{c_2}$, according to each of their components. The actual pair efficiency correction is calculated as the inverse of the values obtained in Eq. (5.8) and is only applied when collecting pair magnitudes as a track pair weight

$$\omega_p^{\mathrm{cc}}{}_C = \frac{1}{\varepsilon_2^{\mathrm{cc}}{}_C\left(\Delta\eta, \Delta\varphi, p_{\mathrm{T}1}, p_{\mathrm{T}2}\right)} \tag{5.9}$$

according to the centrality of the event, C, the pair charge combination, cc, the p_{T} of the first track, the p_{T} of the second track, and the angular separation, $\Delta\eta$ and $\Delta\varphi$, of the pair. In the case of the two particle transverse momentum correlation G_2 given by Eq. (5.1) the pair efficiency correction only appears multiplying the terms of the summation on the numerator of the first term.

The effect on the HIJING data sample when the pair efficiency correction is extracted and applied as described above is as shown in Fig. 5.6. As it can be observed in the ratio plots, a perfect MC closure test is obtained for all centralities validating therefore the analysis technique and correction procedures applied.

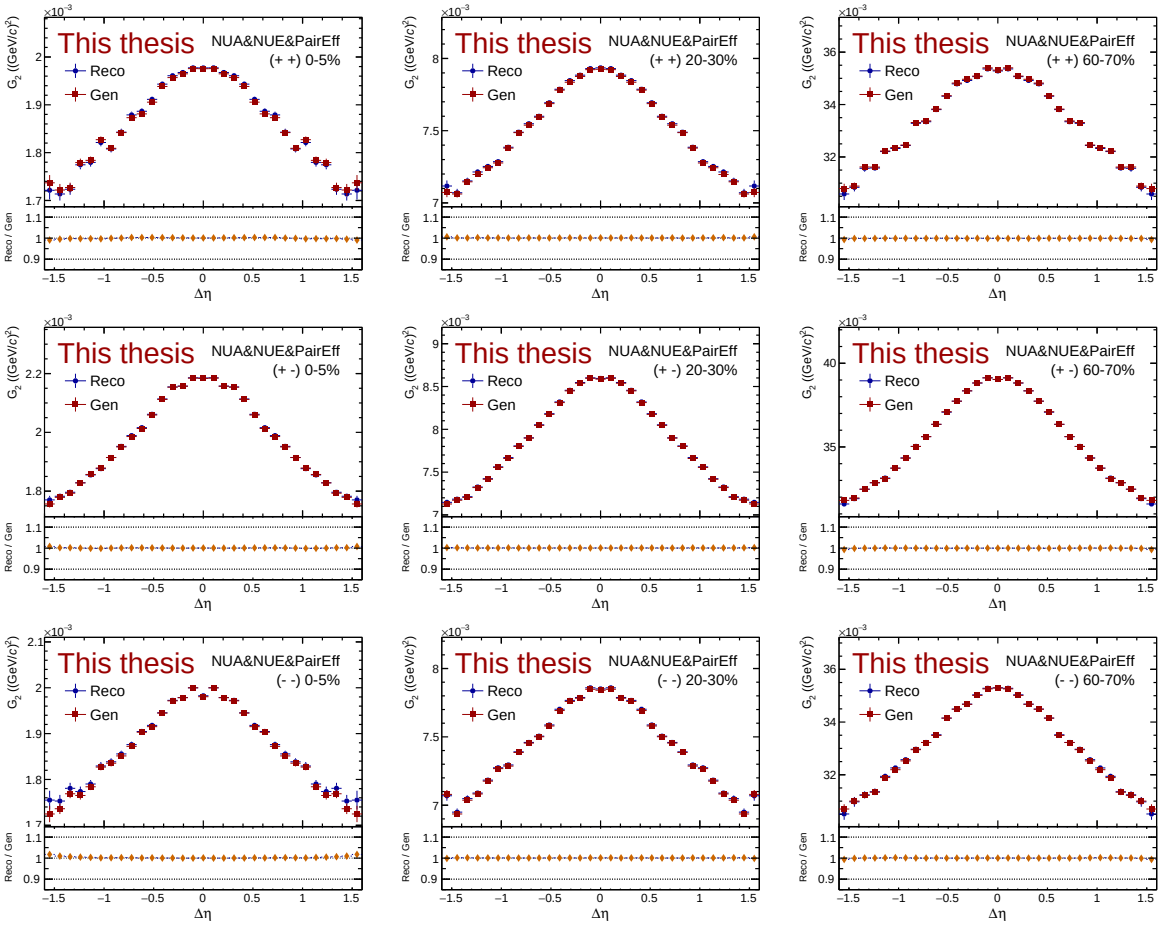

FIGURE 5.6: Longitudinal, $\Delta\eta$, projections of the correlation function from reconstructed (Reco) tracks, after applying NUA, NUE and pair efficiency corrections, compared to the correlation function calculated using generated (Gen) tracks, for ++ track pairs (top), +− track pairs (middle) and −− track pairs (bottom), for central 0–5% (left), semi-central 20–30% (center) and peripheral 60–70% (right) Pb–Pb collisions at $\sqrt{s_{NN}}$ = 2.76 TeV using HIJING as event generator.

5.2.4 Centrality bin width correction

Magnitudes involved in the extraction of G_2 given by Eq. (5.1) evolve in a different way along centrality bins. While one of the magnitudes can reach its average in the middle of a concrete centrality bin other might do it in its first or third quarter. At the end this means that the final extracted value of G_2 from Eq. (5.1) depends on the chosen centrality bin width.

The actual dependence of two-particle number and transverse momentum differential correlation functions on the collision centrality bin width was studied in great detail in [123]. A correction technique was there developed based on the hypothesis of a smooth behavior with collision centrality of the single- and pair- probability densities. The proper behavior of the correction technique was there shown on Pb–Pb simulations based on the HIJING and UrQMD models. The correction method developed for G_2 is briefly summarized. For details, the source [123] stands on.

The single- and two-particle conditional densities for a given multiplicity m are defined as

$$\rho_1(\eta, \varphi, p_{\mathrm{T}}|m) = \frac{1}{p_{\mathrm{T}}} \frac{dN}{d\varphi d\eta dp_{\mathrm{T}}}\bigg|_m, \tag{5.10}$$

$$\rho_2(\eta_1, \varphi_1, p_{\mathrm{T},1}, \eta_2, \varphi_2, p_{\mathrm{T},2}|m) = \frac{1}{p_{\mathrm{T},1}p_{\mathrm{T},2}} \frac{d^2N}{d\varphi_1 d\eta_1 dp_{\mathrm{T},1} d\varphi_2 d\eta_2 dp_{\mathrm{T},2}}\bigg|_m. \tag{5.11}$$

which typically are used integrated over the p_{T} range, applicable for the concrete analyses, as

$$\rho_1(\eta, \varphi|m) = \int \rho_1(\eta, \varphi, p_{\mathrm{T}}|m) dp_{\mathrm{T}}, \tag{5.12}$$

$$\rho_2(\eta_1, \varphi_1, \eta_2, \varphi_2|m) = \int \rho_2(\eta_1, \varphi_1, p_{\mathrm{T},1}, \eta_2, \varphi_2, p_{\mathrm{T},2}|m) dp_{\mathrm{T},1} dp_{\mathrm{T},2}, \tag{5.13}$$

and which can be written in terms of single- and two-particle probability densities, $\mathbb{P}_1(\eta, \varphi|m)$ and $\mathbb{P}_2(\eta_1, \varphi_1, \eta_2, \varphi_2|m)$, according to

$$\rho_1(\eta, \varphi|m) = \langle n \rangle_m \mathbb{P}_1(\eta, \varphi|m), \tag{5.14}$$

$$\rho_2(\eta_1, \varphi_1, \eta_2, \varphi_2|m) = \langle n(n-1) \rangle_m \mathbb{P}_2(\eta_1, \varphi_1, \eta_2, \varphi_2|m), \tag{5.15}$$

where, by definition, $\mathbb{P}_1$ and $\mathbb{P}_2$ respectively satisfy

$$\int d\varphi d\eta \, \mathbb{P}_1(\eta, \varphi|m) = 1, \tag{5.16}$$

$$\int d\varphi_1 d\eta_1 d\varphi_2 d\eta_2 \, \mathbb{P}_2(\eta_1, \varphi_1, \eta_2, \varphi_2|m) = 1, \tag{5.17}$$

as probability densities. The quantities $\langle n \rangle_m$ and $\langle n(n-1) \rangle_m$ are the mean number of particles and the mean number of pairs of particles in the acceptance of the measurement at a given reference multiplicity m; $\mathbb{P}_1(\eta, \varphi|m)$ is the probability of finding a particle at η, φ when the multiplicity is m, and $\mathbb{P}_2(\eta_1, \varphi_1, \eta_2, \varphi_2|m)$ is the joint probability of measuring particles at η_1, φ_1 and η_2, φ_2 when the multiplicity is m. In general, it is expected that $\langle n \rangle_m$ and $\langle n(n-1) \rangle_m$ will scale approximately linearly and quadratically, respectively, with m.

Measures of ρ_1 and ρ_2 cannot usually be done in arbitrary small multiplicity bins due to limitations associated with finite size datasets, CPU time, or storage considerations. In practice, densities are evaluated within finite width bins of multiplicity $[m_{\mathrm{min},k}, m_{\mathrm{max},k}]$ (where $k = 1, \ldots, K$, represents one of K "centrality" bins used in the analysis) as weighted average of the densities across the bins according

to

$$\bar{\rho}_1^{(k)}(\eta,\varphi) = \frac{1}{Q_k}\sum_{m=m_{\mathrm{min},k}}^{m_{\mathrm{max},k}} q(m)\rho_1(\eta,\varphi|m), \tag{5.18}$$

$$\bar{\rho}_2^{(k)}(\eta_1,\varphi_1,\eta_2,\varphi_2) = \frac{1}{Q_k}\sum_{m=m_{\mathrm{min},k}}^{m_{\mathrm{max},k}} q(m)\rho_2(\eta_1,\varphi_1,\eta_2,\varphi_2|m) \tag{5.19}$$

with

$$Q_k = \sum_{m=m_{\mathrm{min},k}}^{m_{\mathrm{max},k}} q(m) \tag{5.20}$$

and $q(m)$ representing the probability of events with multiplicity m in the reference acceptance.

At fixed reference multiplicity, m, the differential two-particle transverse momentum correlator G_2 can be written as [74]

$$\begin{aligned} G_2(\eta_1,\varphi_1,\eta_2,\varphi_2|m) = {} & \frac{\int dp_{\mathrm{T},1}\int dp_{\mathrm{T},2}\, p_{\mathrm{T},1}\, p_{\mathrm{T},2}\, \rho_2(\eta_1,\varphi_1,p_{\mathrm{T},1},\eta_2,\varphi_2,p_{\mathrm{T},2}|m)}{\rho_1(\eta_1,\varphi_1|m)\,\rho_1(\eta_2,\varphi_2|m)} \\ & - \langle p_{\mathrm{T}}(\eta_1,\varphi_1|m)\rangle\langle p_{\mathrm{T}}(\eta_2,\varphi_2|m)\rangle, \end{aligned} \tag{5.21}$$

where

$$\langle p_{\mathrm{T}}(\eta,\varphi|m)\rangle = \frac{\int dp_{\mathrm{T}} p_{\mathrm{T}}\,\rho_1(\eta,\varphi,p_{\mathrm{T}}|m)}{\rho_1(\eta,\varphi|m)} \tag{5.22}$$

is the event inclusive average particle transverse momentum at η, φ.

Introducing

$$\begin{aligned} S_1(\eta,\varphi|m) &= \int p_{\mathrm{T}}\, dp_{\mathrm{T}}\,\rho_1(\eta,\varphi,p_{\mathrm{T}}|m), \\ &= \langle n\rangle_m\, \mathbb{P}_1^{p_{\mathrm{T}}}(\eta,\varphi|m), \end{aligned} \tag{5.23}$$

$$\begin{aligned} S_2(\eta_1,\varphi_1,\eta_2,\varphi_2|m) &= \int p_{\mathrm{T},1}\, dp_{\mathrm{T},1}\int p_{\mathrm{T},2} dp_{\mathrm{T},2}\,\rho_2(\eta_1,\varphi_1,p_{\mathrm{T},1},\eta_2,\varphi_2,p_{\mathrm{T},2}|m), \\ &= \langle n(n-1)\rangle_m\, \mathbb{P}_2^{p_{\mathrm{T}}p_{\mathrm{T}}}(\eta_1,\varphi_1,\eta_2,\varphi_2|m) \end{aligned} \tag{5.24}$$

with

$$\mathbb{P}_1^{p_{\mathrm{T}}}(\eta,\varphi|m) = \int p_{\mathrm{T}}\, dp_{\mathrm{T}}\,\mathbb{P}_1(\eta,\varphi,p_{\mathrm{T}}|m), \tag{5.25}$$

$$\mathbb{P}_2^{p_{\mathrm{T}}p_{\mathrm{T}}}(\eta_1,\varphi_1,\eta_2,\varphi_2|m) = \int p_{\mathrm{T},1}\, dp_{\mathrm{T},1}\int p_{\mathrm{T},2}\, dp_{\mathrm{T},2}\,\mathbb{P}_2(\eta_1,\varphi_1,p_{\mathrm{T},1},\eta_2,\varphi_2,p_{\mathrm{T},2}|m), \tag{5.26}$$

and $\langle n\rangle_m$ and $\langle n(n-1)\rangle_m$, as above defined, the mean number of particles and the mean number of pairs of particles, respectively, at multiplicity m, Eq. (5.21) is written as

$$\begin{aligned} G_2(\eta_1,\varphi_1,\eta_2,\varphi_2|m) &= \frac{S_2(\eta_1,\varphi_1,\eta_2,\varphi_2|m)}{\rho_1(\eta_1,\varphi_1|m)\,\rho_1(\eta_2,\varphi_2|m)} - \frac{S_1(\eta_1,\varphi_1|m)}{\rho_1(\eta_1,\varphi_1|m)}\frac{S_1(\eta_2,\varphi_2|m)}{\rho_1(\eta_2,\varphi_2|m)} \\ &= \frac{\langle n(n-1)\rangle_m}{\langle n\rangle_m^2}\frac{\mathbb{P}_2^{p_{\mathrm{T}}p_{\mathrm{T}}}(\eta_1,\varphi_1,\eta_2,\varphi_2|m)}{\mathbb{P}_1(\eta_1,\varphi_1|m)\,\mathbb{P}_1(\eta_2,\varphi_2|m)} - \frac{\mathbb{P}_1^{p_{\mathrm{T}}}(\eta_1,\varphi_1|m)}{\mathbb{P}_1(\eta_1,\varphi_1|m)}\frac{\mathbb{P}_1^{p_{\mathrm{T}}}(\eta_2,\varphi_2|m)}{\mathbb{P}_1(\eta_2,\varphi_2|m)}. \end{aligned} \tag{5.27}$$

If the ratios $\mathbb{P}_1^{p_T}/\mathbb{P}_1$ and $\mathbb{P}_2^{p_T p_T}/\mathbb{P}_1\mathbb{P}_1$ have a modest dependence on the reference multiplicity (within a bin k), then it is legitimate to replace them by averages to obtain

$$G_2(\eta_1,\varphi_1,\eta_2,\varphi_2|m) = \frac{\langle n(n-1)\rangle_m}{\langle n\rangle_m^2}\frac{\bar{\mathbb{P}}_2^{p_T p_T(k)}(\eta_1,\varphi_1,\eta_2,\varphi_2)}{\bar{\mathbb{P}}_1^{(k)}(\eta_1,\varphi_1)\,\bar{\mathbb{P}}_1^{(k)}(\eta_2,\varphi_2)} - \frac{\bar{\mathbb{P}}_1^{p_T(k)}(\eta_1,\varphi_1)}{\bar{\mathbb{P}}_1^{(k)}(\eta_1,\varphi_1)}\frac{\bar{\mathbb{P}}_1^{p_T(k)}(\eta_2,\varphi_2)}{\bar{\mathbb{P}}_1^{(k)}(\eta_2,\varphi_2)}. \quad (5.28)$$

The centrality-bin averaged correlator $\bar{G}_2^{(k)}(\eta_1,\varphi_1,\eta_2,\varphi_2)$ may then be written as

$$\bar{G}_2^{(k)}(\eta_1,\varphi_1,\eta_2,\varphi_2) = \beta\frac{\bar{\mathbb{P}}_2^{p_T p_T(k)}(\eta_1,\varphi_1,\eta_2,\varphi_2)}{\bar{\mathbb{P}}_1^{(k)}(\eta_1,\varphi_1)\,\bar{\mathbb{P}}_1^{(k)}(\eta_2,\varphi_2)} - \frac{\bar{\mathbb{P}}_1^{p_T(k)}(\eta_1,\varphi_1)}{\bar{\mathbb{P}}_1^{(k)}(\eta_1,\varphi_1)}\frac{\bar{\mathbb{P}}_1^{p_T(k)}(\eta_2,\varphi_2)}{\bar{\mathbb{P}}_1^{(k)}(\eta_2,\varphi_2)} \quad (5.29)$$

with β defined as

$$\beta = \frac{1}{Q_k}\sum_{m=m_{\min,k}}^{m_{\max,k}} q(m)\frac{\langle n(n-1)\rangle_m}{\langle n\rangle_m^2}. \quad (5.30)$$

However, if it is not possible to carry out the analysis in fine (unit) bins of m, the numerators and denominators of G_2 must be separately averaged over the range $[m_{\min,k}, m_{\max,k}]$. With the same assumption on the behavior of the ratios $\mathbb{P}_1^{p_T}/\mathbb{P}_1$ and $\mathbb{P}_2^{p_T p_T}/\mathbb{P}_1\mathbb{P}_1$, it is obtained

$$G_2^{(\mathrm{Bin},k)}(\eta_1,\varphi_1,\eta_2,\varphi_2) = \alpha\frac{\bar{\mathbb{P}}_2^{p_T p_T(k)}(\eta_1,\varphi_1,\eta_2,\varphi_2)}{\bar{\mathbb{P}}_1^{(k)}(\eta_1,\varphi_1)\,\bar{\mathbb{P}}_1^{(k)}(\eta_2,\varphi_2)} - \frac{\bar{\mathbb{P}}_1^{p_T(k)}(\eta_1,\varphi_1)}{\bar{\mathbb{P}}_1^{(k)}(\eta_1,\varphi_1)}\frac{\bar{\mathbb{P}}_1^{p_T(k)}(\eta_2,\varphi_2)}{\bar{\mathbb{P}}_1^{(k)}(\eta_2,\varphi_2)} \quad (5.31)$$

with α defined as

$$\alpha = \frac{\frac{1}{Q_k}\sum_{m=m_{\min,k}}^{m_{\max,k}} q(m)\langle n(n-1)\rangle_m}{\left(\frac{1}{Q_k}\sum_{m=m_{\min,k}}^{m_{\max,k}} q(m)\langle n\rangle_m\right)^2} \quad (5.32)$$

Identifying $\langle p_T(\eta,\varphi)\rangle^{(\mathrm{Bin},k)} = \bar{\mathbb{P}}_1^{p_T(k)}(\eta,\varphi)/\bar{\mathbb{P}}_1^{(k)}(\eta,\varphi)$, the desired correlator $\bar{G}_2^{(k)}(\eta_1,\varphi_1,\eta_2,\varphi_2)$ may be determined as

$$\begin{aligned}
&\bar{G}_2^{(k)}(\eta_1,\varphi_1,\eta_2,\varphi_2)\\
&\quad= \beta\alpha^{-1}\left(G_2^{(\mathrm{Bin},k)}(\eta_1,\varphi_1,\eta_2,\varphi_2) + \langle p_T(\eta_1,\varphi_1)\rangle^{(\mathrm{Bin},k)}\langle p_T(\eta_2,\varphi_2)\rangle^{(\mathrm{Bin},k)}\right)\\
&\qquad - \langle p_T(\eta_1,\varphi_1)\rangle^{(\mathrm{Bin},k)}\langle p_T(\eta_2,\varphi_2)\rangle^{(\mathrm{Bin},k)}\\
&\quad= \beta\alpha^{-1}G_2^{(\mathrm{Bin},k)}(\eta_1,\varphi_1,\eta_2,\varphi_2) + \left(\beta\alpha^{-1}-1\right)\langle p_T(\eta_1,\varphi_1)\rangle^{(\mathrm{Bin},k)}\langle p_T(\eta_2,\varphi_2)\rangle^{(\mathrm{Bin},k)}.
\end{aligned} \quad (5.33)$$

Then the factor $\beta\alpha^{-1}$, which operates only over the first term of the G_2 correlator, is the correction which compensates for the centrality or multiplicity bin width effect

$$\omega_{\mathrm{bw}}{}_C^{\mathrm{cc}} = \frac{\beta_C^{\mathrm{cc}}}{\alpha_C^{\mathrm{cc}}} \quad (5.34)$$

with C the event centrality or multiplicity, and cc the pair charge combination.

From a procedural perspective the single track density, ρ_1, and the two-track density, ρ_2, are extracted in 1% centrality or multiplicity bins and the correction is then extracted as a factor which, as was said, affects only to the first term of the two-particle transverse momentum correlation G_2.

5.3 Correlator extraction procedure

As was described in the introduction to this chapter (section 5.1), the goal of the analysis work is to extract the evolution of the two particle transverse momentum correlation (5.1)

$$\mathrm{G}_2\left(\Delta\eta, \Delta\varphi\right) = \frac{\langle \sum_{i}^{n_{1,1}} \sum_{j\neq i}^{n_{1,2}} p_{\mathrm{T},i}\ p_{\mathrm{T},j} \rangle}{\langle n_{1,1} \rangle \langle n_{1,2} \rangle} - \langle p_{\mathrm{T},1} \rangle \langle p_{\mathrm{T},2} \rangle,$$

with the centrality of the collision. As was also suggested there, all magnitudes are collected on a per $(\eta_1, \varphi_1, \eta_2, \varphi_2)$ bin basis and what is actually computed is

$$\mathrm{G}_2\left(\eta_1, \varphi_1, \eta_2, \varphi_2\right) = \frac{\langle \sum_{i}^{n_{1,1}} \sum_{j\neq i}^{n_{1,2}} p_{\mathrm{T},i}\ p_{\mathrm{T},j} \rangle}{\langle n_{1,1} \rangle \langle n_{1,2} \rangle} - \langle p_{\mathrm{T},1} \rangle \langle p_{\mathrm{T},2} \rangle, \tag{5.35}$$

which in a further reduction step, is transformed, from a space on $(\eta_1, \varphi_1, \eta_2, \varphi_2)$, to one on $(\Delta\eta, \Delta\varphi)$, and obtained in its final differential way (5.1). The transformation is based on the idea that magnitudes are approximately invariant along the sum axes $\eta_1 + \eta_2$ and $\varphi_1 + \varphi_2$ so their averaging on the difference axes $\Delta\eta = \eta_1 - \eta_2$ and $\Delta\varphi = \varphi_1 - \varphi_2$ is a lossless projection [124].

The detailed definition for each of the terms of (5.35) is

$$\begin{aligned}
&\langle \sum_{i}^{n_{1,1}} \sum_{j\neq i}^{n_{1,2}} p_{\mathrm{T},i}\ p_{\mathrm{T},j} \rangle \left(\eta_1, \varphi_1, \eta_2, \varphi_2\right) \\
&\qquad = \frac{1}{N_{\mathrm{evt}}} \left[\sum_{N_{\mathrm{evt}}} \sum_{i}^{n_{1,1}} \sum_{j\neq i}^{n_{1,2}} \left[\omega_p \left(\Delta\eta, \Delta\varphi, p_{\mathrm{T},i_{\eta_1,\varphi_1}}, p_{\mathrm{T},j_{\eta_2,\varphi_2}} \right) \right.\right. \\
&\qquad \left.\left. \times \omega_s \left(z, p_{\mathrm{T},i_{\eta_1,\varphi_1}}, \eta_1, \varphi_1 \right) \times p_{\mathrm{T},i_{\eta_1,\varphi_1}} \times \omega_s \left(z, p_{\mathrm{T},j_{\eta_2,\varphi_2}}, \eta_2, \varphi_2 \right) \times p_{\mathrm{T},j_{\eta_2,\varphi_2}} \right] \right]
\end{aligned} \tag{5.36}$$

where ω_p denotes the pair efficiency correction, dependent on $\Delta\eta$, $\Delta\varphi$, $p_{\mathrm{T},1}$ and $p_{\mathrm{T},2}$, and ω_s denotes the combined NUA and NUE corrections, dependent both on p_{T} and η, and the first one, additionally, on φ and z_{vtx}, which for simplicity has been replaced by z.

$$\langle n_{1,\alpha} \rangle \left(\eta_\alpha, \varphi_\alpha\right) = \frac{\sum_{N_{\mathrm{evt}}} \sum_{i}^{n_{1,\alpha}} \omega_s \left(z, p_{\mathrm{T},i_{\eta_\alpha,\varphi_\alpha}}, \eta_\alpha, \varphi_\alpha \right)}{N_{\mathrm{evt}}} \tag{5.37}$$

where α enumerates the first and the second track in the pair and the component $p_{\mathrm{T},i_{\eta_\alpha,\varphi_\alpha}}$ expresses the fact that tracks whose η and φ match η_α and φ_α are the ones whose p_{T} contributes to the calculation for that concrete $(\eta_\alpha, \varphi_\alpha)$ bin, and

$$\langle p_{\mathrm{T},\alpha} \rangle \left(\eta_\alpha, \varphi_\alpha\right) = \frac{\sum_{N_{\mathrm{evt}}} \sum_{i}^{n_{1,\alpha}} \omega_s \left(z, p_{\mathrm{T},i_{\eta_\alpha,\varphi_\alpha}}, \eta_\alpha, \varphi_\alpha \right) \times p_{\mathrm{T},i_{\eta_\alpha,\varphi_\alpha}}}{\sum_{N_{\mathrm{evt}}} \sum_{i}^{n_{1,\alpha}} \omega_s \left(z, p_{\mathrm{T},i_{\eta_\alpha,\varphi_\alpha}}, \eta_\alpha, \varphi_\alpha \right)}. \tag{5.38}$$

The sum $\sum_{N_{\mathrm{evt}}}$ runs over the events ensemble while $\sum_{i}^{n_{1,1}}$ or $\sum_{j\neq i}^{n_{1,2}}$ run over the event track multiplicity.

To carry all this out, histograms, with the described binning (Table 5.1), are used to accumulate the following quantities

$H_{n_{1,1}}$	ω_{s1}	track one counts (in η_1, φ_1)
$H_{n_{1,2}}$	ω_{s2}	track two counts (in η_2, φ_2)
$H_{p_{\mathrm{T}1}}$	$\omega_{s1} \times p_{\mathrm{T}1}$	track one p_{T} (in η_1, φ_1)
$H_{p_{\mathrm{T}2}}$	$\omega_{s2} \times p_{\mathrm{T}2}$	track two p_{T} (in η_2, φ_2)
$H_{p_{\mathrm{T}1} \times p_{\mathrm{T}2}}$	$\omega_p \times \omega_{s1} \times p_{\mathrm{T}1} \times \omega_{s2} \times p_{\mathrm{T}2}$	pair p_{T} product (in $\eta_1, \varphi_1, \eta_2, \varphi_2$)

$H_{n_{1,1}}$ and $H_{n_{1,2}}$ are the usual single track distributions in η, φ. The histograms are actually filled on a per track basis, instead of with one, with the corresponding weight ω_{s1} or ω_{s2} according to Eq. (5.6). When collecting data for the LS analysis both histograms contain the same information, but that is not the case when collecting data for the US analysis.

$H_{p_{\mathrm{T}1}}$ and $H_{p_{\mathrm{T}2}}$ accumulate track transverse momentum in η, φ. The histograms are actually filled on a per track basis, instead with just the p_{T} of the track, with its product by the corresponding weight ω_{s1} or ω_{s2} according to Eq. (5.6). Here again, when collecting data for the LS analysis both histograms contain the same information but different in the case of the US analysis.

$H_{p_{\mathrm{T}1} \times p_{\mathrm{T}2}}$ is filled on a per pair basis at the end of each processed event, when the whole set of pairs can be produced. Apart from incorporating the product of the single weights corresponding to each of the component tracks according to Eq. (5.6), it also includes the product by the pair efficiency correction ω_p according to Eq. (5.9), as was described in section 5.2.3.

The numerator of the first term of the two particle transverse momentum correlation is obtained by just dividing $H_{p_{\mathrm{T}1} \times p_{\mathrm{T}2}}$ by the number of events and, of course, it is obtained in $\eta_1, \varphi_1, \eta_2, \varphi_2$. Both components of the denominator are also obtained by dividing $H_{n_{1,1}}$ and $H_{n_{1,2}}$ by the number of events. The whole denominator in $\eta_1, \varphi_1, \eta_2, \varphi_2$ is subsequently obtained as the external product of both downscaled histograms.

At this point, as explained in section 5.2.4, a factor is applied to the first term of the two-particle transverse momentum correlation to correct for centrality bin width impact according to [123]. The first term of G_2 finally has the shape

$$\frac{\langle \sum_{i}^{n_{1,1}} \sum_{j \neq i}^{n_{1,2}} p_{\mathrm{T},i}\ p_{\mathrm{T},j} \rangle}{\langle n_{1,1} \rangle \langle n_{1,2} \rangle} \omega_{\mathrm{bw}} {}^{\mathrm{cc}}_{C} \tag{5.39}$$

with ω_{bw} the centrality or multiplicity bin width effect correction according to Eq. (5.34).

Each of the components of the second term of the two particle transverse momentum correlation is obtained as the quotient of $H_{p_{\mathrm{T}}}$ and H_{n_1}. The whole second term in $\eta_1, \varphi_1, \eta_2, \varphi_2$ is again obtained as the external product of both components.

Once the two particle transverse momentum correlation is obtained in $\eta_1, \varphi_1, \eta_2, \varphi_2$ a reduction step is carried out for obtaining it in $\Delta\eta$ and $\Delta\varphi$. Due to the circular nature of the azimuthal angle no special care needs to be taken for reducing in the φ coordinates. But due to the limits in the longitudinal acceptance the proper scaling according to the different contributions is considered.

With above procedure, G_2 correlation function is obtained for basic track pair combinations, i.e. G_2^{++}, G_2^{+-}, G_2^{--}, and G_2^{-+}. From them, the LS, US, charge dependent (CD), and charge independent

(CI) track combinations are derived according to

$$G_2^{\mathrm{LS}} = \frac{1}{2}\left[G_2^{++} + G_2^{--}\right] \tag{5.40}$$

$$G_2^{\mathrm{US}} = \frac{1}{2}\left[G_2^{+-} + G_2^{-+}\right] \tag{5.41}$$

$$G_2^{\mathrm{CD}} = \frac{1}{2}\left[G_2^{\mathrm{US}} - G_2^{\mathrm{LS}}\right] \tag{5.42}$$

$$G_2^{\mathrm{CI}} = \frac{1}{2}\left[G_2^{\mathrm{US}} + G_2^{\mathrm{LS}}\right]. \tag{5.43}$$

Once the two-dimensional correlations functions have been extracted, the next step is to model them for extracting their main components and characteristics.

5.4 Parametrizing the two particle transverse momentum correlation

5.4.1 Fit model

The aim of the analysis described in this PhD thesis is to extract the evolution with collision centrality of the two particle transverse momentum correlation near side widths along the azimuthal and longitudinal dimensions beyond of the underlying collective behavior. The two-dimensional correlation function is therefore parametrized by a combination of different fit functions

- a base plane
- a Fourier expansion which will model the collective behavior
- a potential $\Delta\eta$ dependence of the Fourier expansion coefficients
- a two-dimensional generalized Gaussian which will capture the shape of interest

$$F(\Delta\eta, \Delta\varphi) =$$

$$B + \sum_{n=2}^{6} a_n \times \cos(n \cdot \Delta\varphi) \tag{5.44}$$

$$+ \left(a_{2_{\mathrm{lin}}} \times |\Delta\eta| + a_{2_{\mathrm{sq}}} \times (\Delta\eta)^2\right) \times \cos(2 \cdot \Delta\varphi) \tag{5.45}$$

$$+ \left(a_{3_{\mathrm{lin}}} \times |\Delta\eta| + a_{3_{\mathrm{sq}}} \times (\Delta\eta)^2)\right) \times \cos(3 \cdot \Delta\varphi) \tag{5.46}$$

$$+ A \times \frac{\gamma_{\Delta\eta}\gamma_{\Delta\varphi}}{4\,\omega_{\Delta\eta}\omega_{\Delta\varphi}\,\Gamma\left(\frac{1}{\gamma_{\Delta\eta}}\right)\Gamma\left(\frac{1}{\gamma_{\Delta\varphi}}\right)} \mathrm{e}^{-\left|\frac{\Delta\eta}{\omega_{\Delta\eta}}\right|^{\gamma_{\Delta\eta}} - \left|\frac{\Delta\varphi}{\omega_{\Delta\varphi}}\right|^{\gamma_{\Delta\varphi}}}. \tag{5.47}$$

The base plane B and the Fourier expansion up to sixth order is represented by the expression (5.44) where a_n represents its n order harmonic coefficient. The expressions (5.45) and (5.46) model the linear and quadratic dependence on pseudorapidity of the second and third order Fourier coefficients, respectively, where $a_{2_{\mathrm{lin}}}$ ($a_{3_{\mathrm{lin}}}$) and $a_{2_{\mathrm{sq}}}$ ($a_{3_{\mathrm{sq}}}$) represent the linear and quadratic dependence of the second (third) harmonic coefficient, respectively. The expression(5.47) contains an amplitude, A, and the two-dimensional generalized Gaussian where γ and ω parametrize the generalized Gaussian shape on each dimension, $\Delta\eta$ and $\Delta\varphi$. The generalized Gaussian behaves as a Gaussian when γ is two, and, when it is one, it behaves as a Laplace distribution.

The pseudorapidity dependence of the Fourier expansion coefficients has not been confirmed so far and the use of harmonic coefficients above fourth order has not provided improved χ^2 of the fit. Therefore, the fit model used is given by

$$F\left(\Delta\eta,\Delta\varphi\right) = B + \sum_{n=2}^{4} a_n \times \cos\left(n\cdot\Delta\varphi\right) + A \times \frac{\gamma_{\Delta\eta}\gamma_{\Delta\varphi}}{4\,\omega_{\Delta\eta}\omega_{\Delta\varphi}\,\Gamma\left(\frac{1}{\gamma_{\Delta\eta}}\right)\Gamma\left(\frac{1}{\gamma_{\Delta\varphi}}\right)}\,\mathrm{e}^{-\left|\frac{\Delta\eta}{\omega_{\Delta\eta}}\right|^{\gamma_{\Delta\eta}}-\left|\frac{\Delta\varphi}{\omega_{\Delta\varphi}}\right|^{\gamma_{\Delta\varphi}}}. \quad (5.48)$$

The longitudinal (azimuthal) width of the two particle transverse momentum correlation is calculated as the standard deviation in the $\Delta\eta$ ($\Delta\varphi$) dimension of the two-dimensional generalized Gaussian using

$$\sigma_{\Delta\eta(\Delta\varphi)} = \sqrt{\frac{\omega^2_{\Delta\eta(\Delta\varphi)}\Gamma(3/\gamma_{\Delta\eta(\Delta\varphi)})}{\Gamma(1/\gamma_{\Delta\eta(\Delta\varphi)})}}. \quad (5.49)$$

5.4.2 Exclusion zone

For Pb–Pb collisions the G_2^{CI} correlation function presents a depletion around $(\Delta\eta,\Delta\varphi) = (0,0)$ which, clearly, cannot be modeled by Eq. (5.48). A set of bins are therefore excluded from the fit in both dimensions, $\Delta\eta$ and $\Delta\varphi$, in the neighborhood of $(0,0)$. From the most central up to semi-peripheral collisions the number of excluded bins around $(0,0)$ is three while for peripheral collisions the exclusion of one bin is sufficient.

5.4.3 Fit procedure

The parametrization of the two-dimensional two-particle transverse momentum correlation with Eq. (5.48) is done in steps

1. a first approximation of the base plane B and the Fourier expansion parameters a_n, i.e. the collective behavior, is obtained from a fit to long range pseudo-rapidity correlations as follows
   (a) fixing the parameters γ and ω, for both $\Delta\eta$ and $\Delta\varphi$, to values whose impact do not appreciably reach the $|\Delta\eta| > 1.0$ slice
   (b) fixing the scale parameter A to the difference between the value of the correlation function on the border of the exclusion area and its mean value for the $|\Delta\eta| > 1.0$ slice
   (c) assigning as start value for B parameter the average of the correlation function over the near side azimuthal range $|\Delta\varphi| < 0.9\,\frac{\pi}{2}$, and over the long range pseudo-rapidity interval $\Delta\eta > 1.0$, and allowing it to vary only over positive values
   (d) assigning a small positive value (0.01) to the a_n parameters and allowing them to vary only over positive values
   (e) fitting the model to the two-dimensional correlation function over the near side azimuthal range $|\Delta\varphi| < 0.9\,\frac{\pi}{2}$, and over the long range pseudo-rapidity interval $\Delta\eta > 1.0$, that results on a first estimation of the collective behavior
2. a first estimation of the near side peak is obtained as follows
   (a) B and a_n are fixed to the values obtained in step one
   (b) the parameters A, and γ and ω, for both $\Delta\eta$ and $\Delta\varphi$, are allowed to vary within a broad range which allows the stability of the fit without limiting the parameters as such (it was checked that the final values are never close to this stability limits)
   (c) fitting the model to the two-dimensional correlation function over the near side azimuthal range $|\Delta\varphi| < 0.9\,\frac{\pi}{2}$, and over the whole relative pseudo-rapidity range $|\Delta\eta| < 1.6$

3. next a fine tune of the fit model parameters is obtained as follows

   (a) the obtained values for the parameters B and a_n, which were not allowed to vary in step two are now allowed to vary within a ±20% of their values

   (b) the values obtained for the parameters A, and γ and ω, for both $\Delta\eta$ and $\Delta\varphi$, are allowed to vary within ±20% of their values

   (c) fitting the model to the two-dimensional correlation function over the near side azimuthal range $|\Delta\varphi| < 0.9\,\frac{\pi}{2}$, and over the whole relative pseudo-rapidity range $|\Delta\eta| < 1.6$

4. the final step removes all parameter limits and is carried as follows

   (a) all model parameters limits are removed, only the fit stability ones (given in step two b) are left

   (b) fitting the model to the two-dimensional correlation function over the near side azimuthal range $|\Delta\varphi| < 0.9\,\frac{\pi}{2}$, and over the whole relativity pseudo-rapidity range $|\Delta\eta| < 1.6$

Once the fit has been completed the value of the width along $\Delta\eta$ and $\Delta\varphi$ are calculated from the resulting γ and ω parameters using Eq. (5.49)

5.5 Calculation of uncertainties

5.5.1 Statistical uncertainties

The complexity of the expression to evaluate, (5.35), and the correlated nature of the involved magnitudes make not viable to track the statistical uncertainties. In order to have an estimate, the sub-sample method [125] has been used. The whole set of collected data (in the order of 6000 data files depending of the collision system) has been randomly distributed in ten sub-sets. The bi-dimensional correlation function $G_2(\Delta\eta, \Delta\varphi)$ is then fully built for each track combination in each of the ten sub-sets and for each centrality range. The final value of the correlation function $G_2(\Delta\eta, \Delta\varphi)$ for each track combination and on each centrality range is then extracted as the mean of the ten sub-samples values and its statistical uncertainty as the standard error of that mean. In order to test that ten sub-samples was enough, the whole set of results has been obtained by using six sub-samples and 15 sub-samples instead without finding significant differences.

5.5.2 Systematic uncertainties

General procedure

For estimating the systematic uncertainties induced by detector effects, limitations, or bias induced by the criteria used for selecting tracks or events, the same analysis is fully carried out varying few of the conditions described in sections 4.2.1 and 4.2.2. Each full analysis, in which one of the conditions has been changed, is addressed as a systematic test while the original, with the criteria as described in sections 4.2.1 and 4.2.2, is addressed as the default analysis. The difference in the results obtained from the systematic test and the default analysis is the potential contribution of the systematic test to the systematic uncertainty of the default analysis. The significance of the contribution is estimated using the criteria [126]

$$\frac{|x_{\text{default}} - x_{\text{test}}|}{\sqrt{|\sigma^2_{\text{default}} - \sigma^2_{\text{test}}|}} > 1 \tag{5.50}$$

where x_{default} and x_{test} are the result values for the default analysis and for the systematic test, respectively, and σ_{default} and σ_{test} their respective statistical uncertainties. As it will be seen, x apply to any of the

obtained results. For example, when extracting the systematic uncertainties of the two-dimensional two-particle correlation function, x will be the value of the correlation function for each concrete $(\Delta\eta, \Delta\varphi)$. For the longitudinal projection of the two-particle correlation function x will be its value for each concrete $(\Delta\eta)$.

Magnetic field polarity

The whole Pb–Pb data sample at $\sqrt{s_{\mathrm{NN}}} = 2,76\,\mathrm{GeV}$ was taken, half of them with one magnetic field polarity, and half of them with the opposite one. This allowed to split the data sample into two sub-sets and to assess the impact of distortions of the own magnetic field, of the TPC electric field, and their impact on the efficiency.

The default analysis has been performed over the whole dataset without any consideration about the polarity of the magnetic field. Then two systematic tests have been analyzed. On the sub-set with positive magnetic field polarity in the L3 solenoid (section 3.2) and positive magnetic field in the muon spectrometer dipole (section 3.4). And on the sub-set with negative magnetic field polarity in the solenoid and negative magnetic field on muon spectrometer dipole.

For p–Pb and pp collisions the datasets used were produced with single magnetic field polarity so, these systematic tests have not been applied to extract the systematic uncertainties of the results of those analysis.

z_{vtx} range

To assess the effects of the proximity to the borders of the fiducial acceptance the range in which events are accepted according to the longitudinal position of the interaction vertex has been changed. As described in section 4.2.1, the z_{vtx} range for the default analysis is ±7cm of the nominal IP. A systematic test is performed by using as alternative range $|z_{\mathrm{vtx}}| < 3$ cm of the nominal IP.

Centrality estimation

In Pb–Pb collisions at both energies the event centrality is estimated by using the total V0 detector measured multiplicity as described in section 3.9. To assess the effects that this choice has on the correlation function, an alternative detector is used for the centrality estimation. The default analysis select events on centrality ranges based on the information provided by the V0 detector. A systematic test is performed by instead using the event multiplicity as measured in the second inner layer of the ITS, the central layer one (CL1), for estimating the centrality of the events.

For p–Pb and pp collisions the use of CL1 to estimate the event centrality is known to bias that estimation and for those collision systems this systematic test has not been carried on.

Track selection

To assess the potential bias introduced by the criteria used to select tracks within each event as well as to obtain an estimation of the effect of secondary tracks on the correlation function a different criteria for selecting tracks is applied. The default analysis has been performed selecting tracks according with the criteria described in section 4.2.2.

A systematic test is performed by using as alternative track selection criteria denominated

- tracks must have a successful refit towards the ITS
- any of the two exclusive (complementary) ITS hits requirements
  - a hit in any of the two internal layers of the ITS (the SPD)
  - no hit in the SPD but a hit in the third inner layer of the ITS (first layer of the SDD)

- a minimum of 70 active TPC clusters
- track distance of closest approach to the interaction vertex according to

$$d_z < \mathrm{DCA}_z \tag{5.51}$$
$$d_{xy} < \mathrm{DCA}_{xy} \tag{5.52}$$

where d_z and d_{xy} are the track DCA to the interaction vertex on the z axis and on the transverse plane, respectively, $\mathrm{DCA}_z = 2$ cm the threshold on the z axis, and DCA_{xy} a p_T dependent threshold on the transverse plane according to

$$\mathrm{DCA}_{xy} = 0.0182 + \frac{0.0350}{p_\mathrm{T}^{1.01}}, \tag{5.53}$$

which select tracks denominated as "Global".

Pair efficiency

As was described in section 5.2.3 the two track detector efficiency affects the correlation function mostly in its amplitude but not in its shape. There, a procedure for extracting a pair efficiency correction was described. The procedure obviously rely on having a proper simulation of the detector effects when two tracks have to be reconstructed. The process of extracting the pair efficiency correction showed almost a perfect MC closure test while when the extracted correction was applied to actual data it ended up introducing too much noise in the correlation function, specially for peripheral events. The main reason for this noise is the difference on the number of peripheral events available for the actual data analysis and for the simulated MC analysis. The pair efficiency correction was biased for correcting the simulated event densities.

A softer extraction of the pair efficiency correction was then introduced which, while showing still quite a good MC closure tests, did not introduced excessive noise in the correlation function. At the end, when the width of the correlation function was extracted, the values obtained from results without having applied the pair efficiency correction and the ones obtained from results having applied the pair efficiency correction match within statistical uncertainties for most of the centrality classes and the difference is relatively small for the rest.

The default analysis is carried out without correcting for detector pair efficiency. A systematic test is performed by introducing a further step which corrects for detector pair efficiency as described in section 5.2.3.

Fit exclusion zone

The dependence of the G_2^CI extracted widths with the size of the excluded region was assessed varying the size of the exclusion region. For Pb–Pb systems, the fit was performed after increasing by one bin each of the four directions of the excluded zone. The area was not decreased because the depletion around $(0, 0)$ cannot be modeled by the expression (5.48).

For the $\Delta\varphi$ dimension the impact on the G_2^CI width was found negligible for semi-central to peripheral events, shrinking by a 2% in the case of the most central events. However, the impact on the G_2^CI width on the $\Delta\eta$ dimension is significant for central and semi-central events. For semi-central events the width enlarges from 1.5% in the 30–40% centrality range up to 9% in the 5–10% centrality range while expanding up to 20% for the most central collisions. For the azimuthal dimension the effect has been considered within systematic uncertainties. For the longitudinal dimension the effect have been included as an asymmetric systematic contribution on the upper side of the width values.

	$\sigma_{\Delta\eta}$				$\sigma_{\Delta\varphi}$			
	CI (%)	**CD (%)**	**US (%)**	**LS (%)**	**CI (%)**	**CD (%)**	**US (%)**	**LS (%)**
Reduced vertex	2.1	0.7	1.5	2.0	0.5	0.5	0.4	1.0
Mag. field −−	2.2	0.7	1.4	2.2	0.6	1.0	0.5	1.3
Global tracks	1.8	3.2	4.7	5.1	2.0	2.6	2.4	7.8
Mag. field ++	1.3	0.9	1.4	1.7	0.4	1.1	0.4	0.6
Centrality	1.6	0.4	1.3	1.6	0.4	0.5	0.3	0.8
Pair efficiency	0.5	0.4	0.7	0.4	0.1	0.3	0.1	0.2

TABLE 5.2: Width systematic uncertainty contribution for each of the systematic tests for Pb–Pb collisions at $\sqrt{s_{\mathrm{NN}}}$ = 2.76 TeV.

5.5.3 Summary of systematic uncertainties on the projections of the correlation function

On the different systematic tests, the two-particle transverse momentum correlation projections along $\Delta\eta$ and $\Delta\varphi$ show an uncertainty on the overall origin for the amplitude measure (correlated along all bins) and an uncorrelated bin-by-bin uncertainty. The origin of the correlated uncertainty lies in the combinatorial nature of the correlation function background.

Therefore a baseline uncertainty, δB, is quoted in connection with the base plane parameter B used in the model expression (5.44). The maximum on the different test contributions for each centrality interval and pair charge combination is assigned. The contribution for each test is obtained by subtracting the projection along each dimension from the default analysis projection and fitting the result to a constant value. The constant value is the amplitude shift for the given test.

For the uncorrelated bin-by-bin contribution, each bin value, of the shifted correlation function, is evaluated following the procedure described in sect. 5.5.2 and its significance is estimated using Eq. 5.50.

The final projection bin systematic uncertainty is extracted as the quadratic sum of the individual contribution that were significant. Fig. 5.7 shows the systematic uncertainty contribution analysis for the $\Delta\eta$ projection of the charge independent (CI) two-particle transverse momentum correlation for the most central Pb–Pb events. This is a novel representation of the systematic analysis introduced during the elaboration of this work. Each panel shows each of the systematic tests. On them the correlated baseline uncertainty for the concrete test is quoted and the contribution on each bin after shifting to cancel the correlated amplitude origin uncertainty is shown together with its significance. After adding in quadrature the contribution on each significant bin, the final systematic uncertainty is incorporated into the final results presented in Chapter 6. Results of the systematic contribution analysis for the charge independent(CI) and charge dependent (CD) correlators, for both, longitudinal and azimuthal, projections are presented in Appendix A.

5.5.4 Summary of systematic uncertainties on the widths of the correlation function

For the different systematic tests, the widths of the two-particle transverse momentum correlations along $\Delta\eta$ and $\Delta\varphi$ dimensions are extracted according to the procedure described in section 5.4.3. Each individual test width and the default width, are then compared according to the criteria described in the introduction to this section 5.5.2, to estimate the systematic uncertainty.

For each of the tests, the contribution was found significant for most of the centrality classes and also not showing any concrete evolution pattern associated with them. Therefore all systematic uncertainty contributions were considered. In order to avoid "unphysical" fluctuations the final contribution for each systematic test was extracted as the average over all centrality classes. The analysis of the different contributions to the systematic uncertainties for the dependence of the width of the charge independent two-particle correlation function in the longitudinal dimension with centrality is shown in Fig. 5.8. Again this is a novel representation of the systematic analysis introduced during the elaboration of this

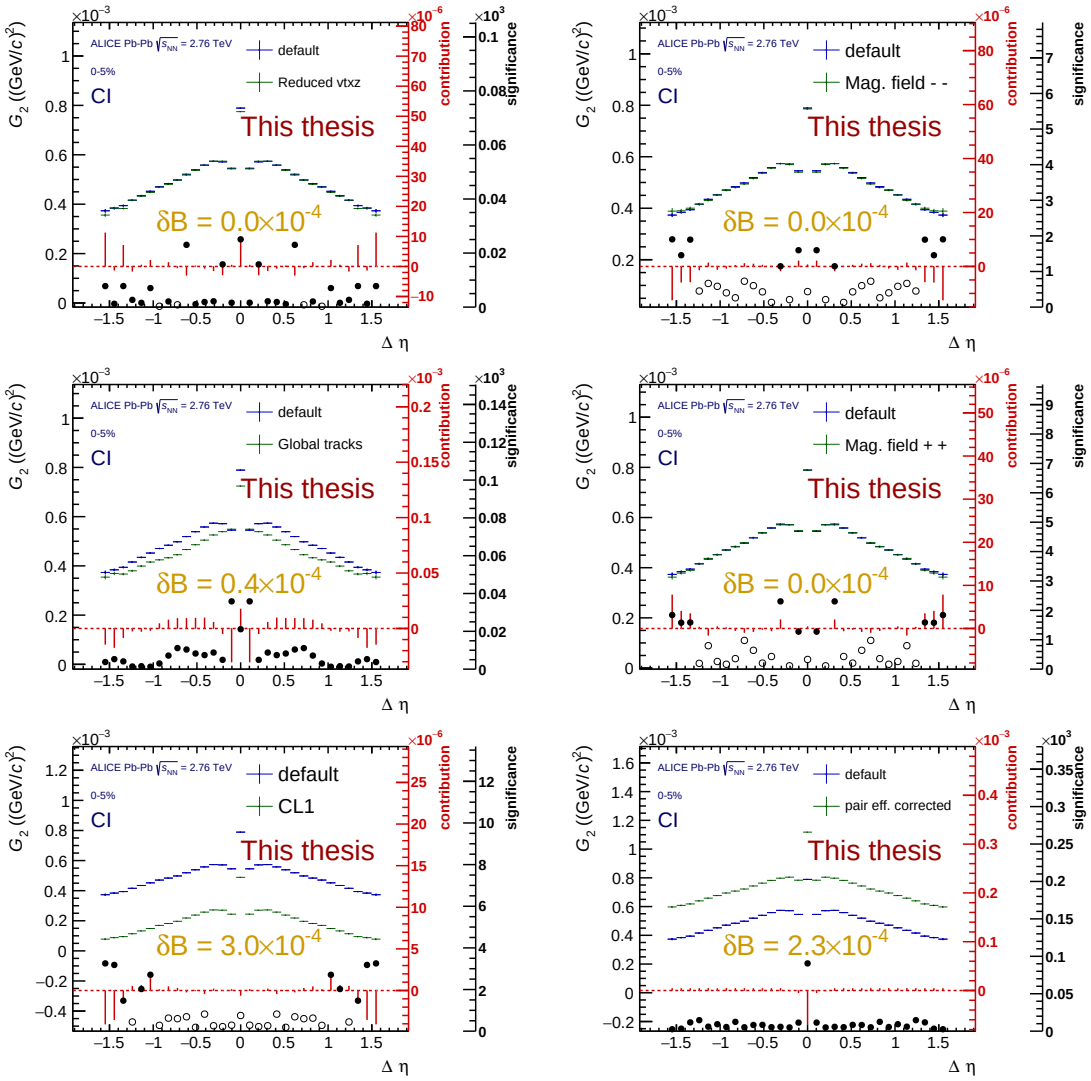

FIGURE 5.7: Analysis of the individual contribution to the systematic uncertainty for the $\Delta\eta$ projection of CI two-particle transverse momentum correlation function G_2 for the most central, 0–5%, Pb–Pb collisions at $\sqrt{s_{\mathrm{NN}}}$ = 2.76 TeV at ALICE. On the top row, reduced vertex acceptance (left) and magnetic field polarity −− tests; on the middle row, "Global" tracks (left) and magnetic field polarity ++ tests; on the bottom row, centrality estimation using CL1 information (left) and incorporation of the pair efficiency correction (right). On all panels the blue points are the results from the default analysis while the green are the ones from the corresponding test. Vertical bars represent statistical uncertainties. The red bars and red scale on the right side of the plots represent the contribution to the systematic uncertainty of the difference on each bin, after shifting to cancel the correlated amplitude origin uncertainty, according to the criteria described at the beginning of this section 5.5.2. The black circles and the black scale most right on each panel represent the significance of the concrete bin contribution according to that criteria. If the circle is empty the concrete contribution is not significant (< 1) and if it is full the contribution is significant (> 1). The orange figure shows the correlated baseline uncertainty.

work. Each panel shows each of systematic tests and the final systematic uncertainty contribution value. The final systematic uncertainties to the widths presented in the results Chapter 6 are obtained by adding in quadrature the different contributions on each centrality class. Results of the systematic contribution analysis for the four set of results, charge independent (CI), charge dependent (CD), unlike sign (US) and like sign (LS) in both, longitudinal and azimuthal, dimension are presented in Appendix A.

Table 5.2 is a summary of the considered systematic uncertainty contributions. To the uncertainties in G_2^{CI} the fit exclusion zone uncertainty was incorporated in quadrature as an asymmetric contribution as described in section 5.5.2.

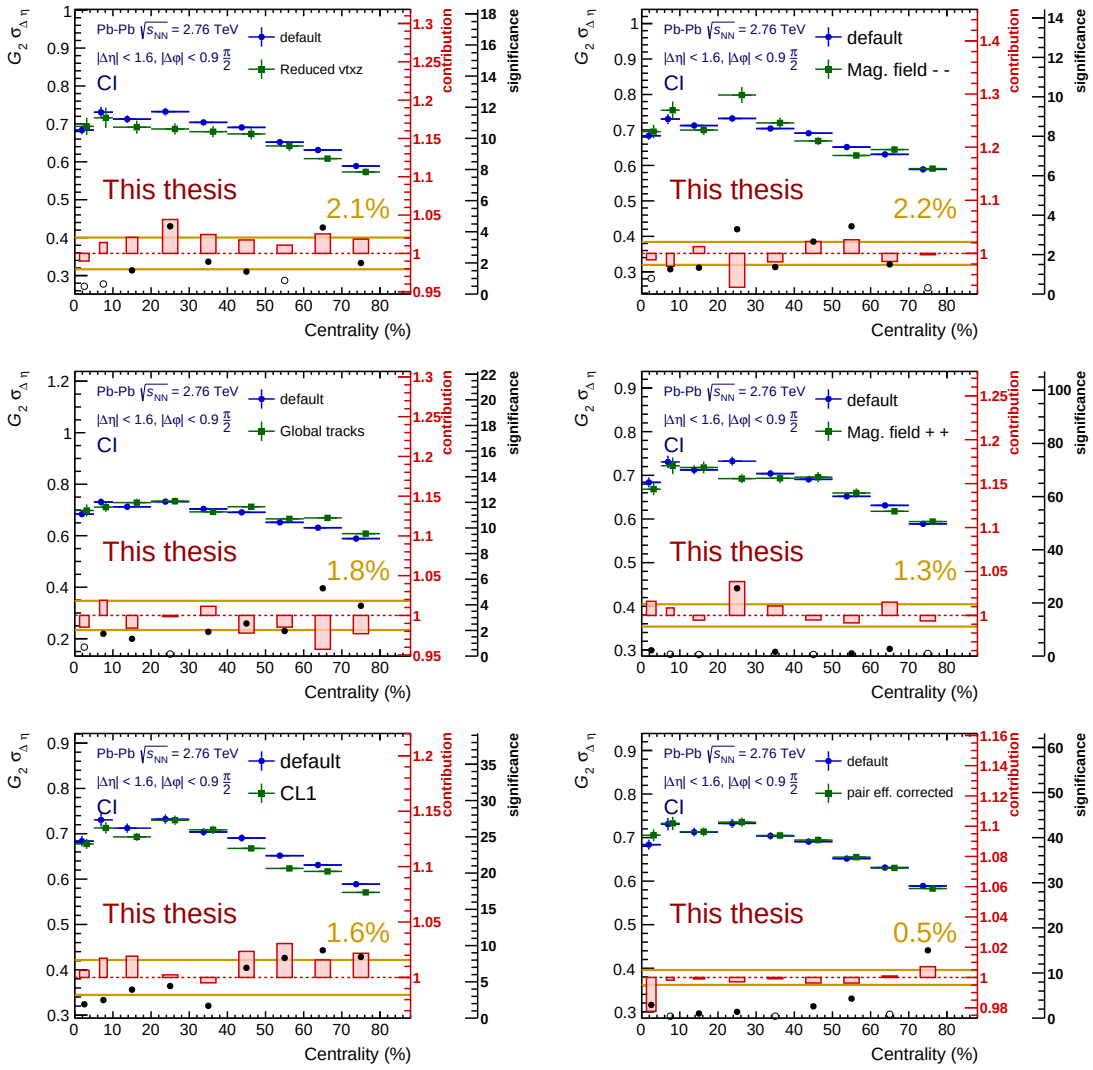

FIGURE 5.8: Analysis of the individual contribution to the systematic uncertainty for the $\Delta\eta$ evolution of the widths of the charge independent (CI) two-particle transverse momentum correlation function G_2 in Pb–Pb collisions at $\sqrt{s_{\rm NN}}$ = 2.76 TeV at ALICE. On the top row, reduced vertex acceptance (left) and magnetic field polarity $--$ tests; on the middle row, "Global" tracks (left) and magnetic field polarity ++ tests; on the bottom row, centrality estimation using CL1 information (left) and incorporation of the pair efficiency correction (right). On all panels the blue dots are the results from the default analysis while the green are the ones from the corresponding test. The red boxes and red scale represent, in percentage of the default value, the contribution to the systematic uncertainty on each centrality class, according to the criteria described at the beginning of this section 5.5.2. The black circles and the black scale most right on each panel represent the significance of the concrete contribution according to that criteria. If the circle is empty the concrete contribution is not significant (< 1) and if it is full the contribution is significant (> 1). The orange lines and the orange figure show the average value over the centrality classes that is used for its systematic uncertainty contribution.

Chapter 6

Results for Pb–Pb collisions at $\sqrt{s_{\mathrm{NN}}} = 2.76$ TeV and $\sqrt{s_{\mathrm{NN}}} = 5.02$ TeV

This chapter contains the main two-particle transverse momentum correlations results for Pb–Pb collisions at $\sqrt{s_{\mathrm{NN}}} = 2.76$ TeV and at $\sqrt{s_{\mathrm{NN}}} = 5.02$ TeV. Namely, the CI and CD track combinations of the two-particle transverse momentum correlations. They are obtained from the basic, $+-$, $-+$, $--$ and $++$, track pairs two-particle transverse momentum correlation (see sect. 5.3).

6.1 Results for Pb–Pb collisions at $\sqrt{s_{\mathrm{NN}}} = 2.76$ TeV

In this section the results for CI and CD track combinations are considered as the main results. Results for the LS and US charge combinations are incorporated in the appendix B.

6.1.1 Two-particle transverse momentum correlations

The two-particle transverse momentum correlation G_2 for Pb–Pb collisions at $\sqrt{s_{\mathrm{NN}}} = 2.76$ TeV for the CI and CD track combinations are shown in Figs. 6.1 and 6.2, respectively. They are calculated using Eq. (5.1) and the procedure described in sect. 5.3. The central bin at $(\Delta\eta, \Delta\varphi) = (0, 0)$ has been excluded because it is undercorrected. The full version of the correlation function is shown in appendix C.

The G_2^{CI} correlators shown in Fig. 6.1 feature sizable $\Delta\varphi$ modulations dominated in mid-central collisions by a strong elliptic ($\cos(2\Delta\varphi)$) component. On the near-side, $|\Delta\varphi| < \pi/2$, atop the azimuthal modulation, the G_2^{CI} correlators feature a near-side peak whose amplitude monotonically decreases from peripheral to central collisions while its longitudinal width systematically broadens. This behavior is captured with the fit model described in sect. 5.4.1. There are two structures which develop from semi-central towards most central events. On the near side two longitudinally extended lobes give place to a depletion around $(\Delta\eta, \Delta\varphi) = (0, 0)$. As was described in sect. 5.5.2 the depletion is not described by the proposed model and because that it is excluded from the fit. The two lobes structure might be consequence of the process described in sect. 2.4.8 where diffusion takes over wave propagation for the distribution of the momentum currents fluctuations. The second structure appears on the away-side, $|\Delta\varphi - \pi| < \pi/2$ where the long range correlations driven by the collective behavior get diluted in the short longitudinal reach. The strength of the dilution increases towards central events where the concavity of the away-side is clearly manifested.

For G_2^{CD} correlators, according to the way they are built described in sect. 2.4.2, all the manifestations of the collective behavior which are charge independent are absent. They affect in the same way to the US track combination as to the LS track combination so, by construction, they cancel out. As such there are no presence of flow modulation. At high collision energies, such as those achieved at the LHC, similar number of positively and negatively charged particles are produced and they show a very similar p_{T} spectra [68]. Consequently, the impact of energy-momentum conservation on the correlation function is expected to be similar for US track combination as for LS track combination so,

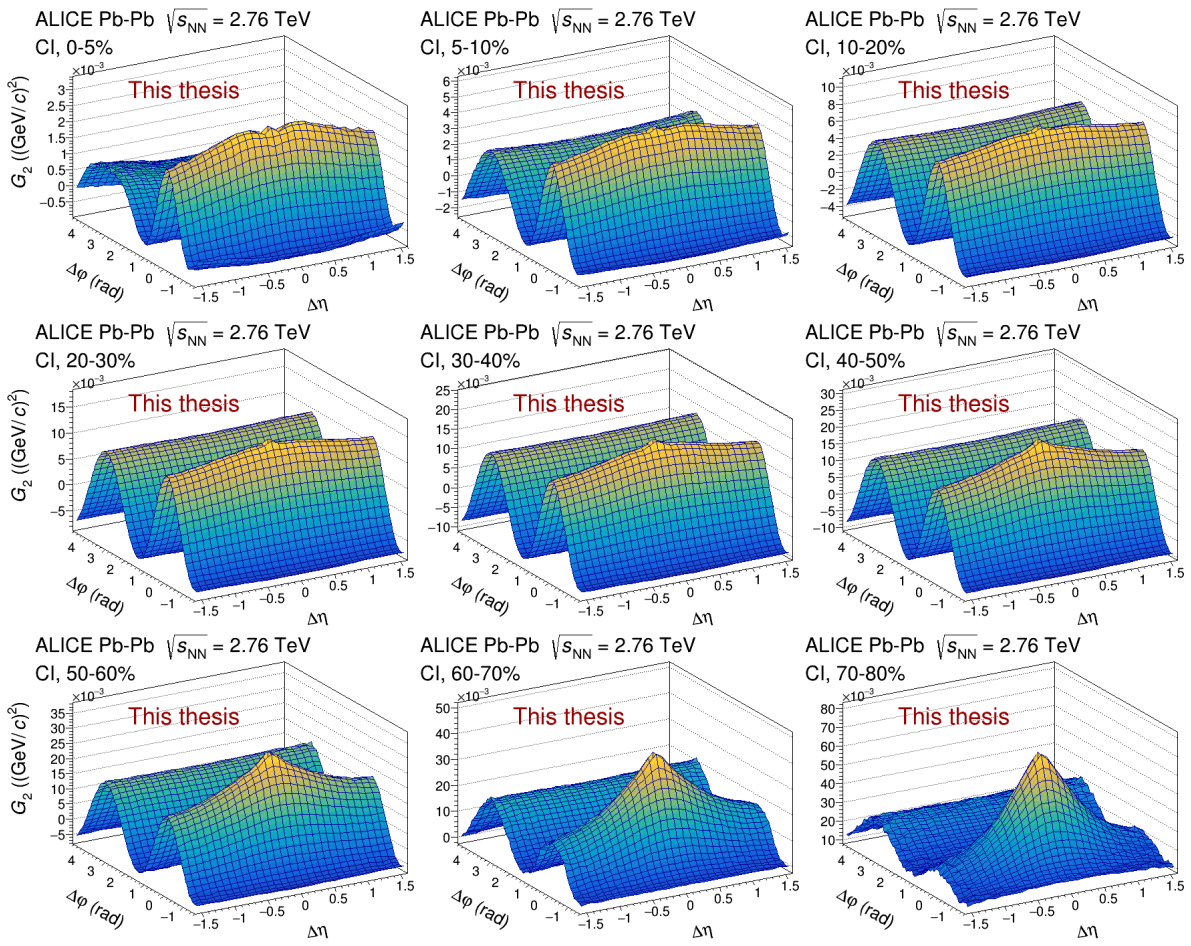

FIGURE 6.1: Charge independent (CI) two-particle transverse momentum correlation for each centrality class in Pb–Pb collisions at $\sqrt{s_{\mathrm{NN}}}$ = 2.76 TeV as measured by ALICE.

again by construction, that impact cancels out. The CD correlator is then left sensitive to charge pair creation, transverse momentum fluctuations and transport processes [69]. The G_2^{CD} correlators shown in Fig. 6.2 also feature a near-side peak whose amplitude monotonically decreases from peripheral to central collisions but whose longitudinal width systematically narrows. Again this behavior is captured with the fit model described in sect. 5.4.1. There is not clear sign of the presence or absence of the two lobes structure on the near side. On the contrary, the flatness of the away-side gives clear indication that the away-side dilution of the G_2^{CI} correlator is a charge independent effect. From semi-peripheral to peripheral collisions a plateau structure develops around a depression at $(\Delta\eta, \Delta\varphi) = (0.0)$. This structure is compatible with an excess of short range LS correlations over US whose reach increases with the inverse of the system size as happens with the HBT effect. From central to semi-central collisions where the system size stays relatively large, it is manifested as a downside spike which has been suppressed (it can be seen in the full correlation figures in the appendix C). When the system starts to shrink the excess of short range correlations enlarges and the plateau structure starts to manifest.

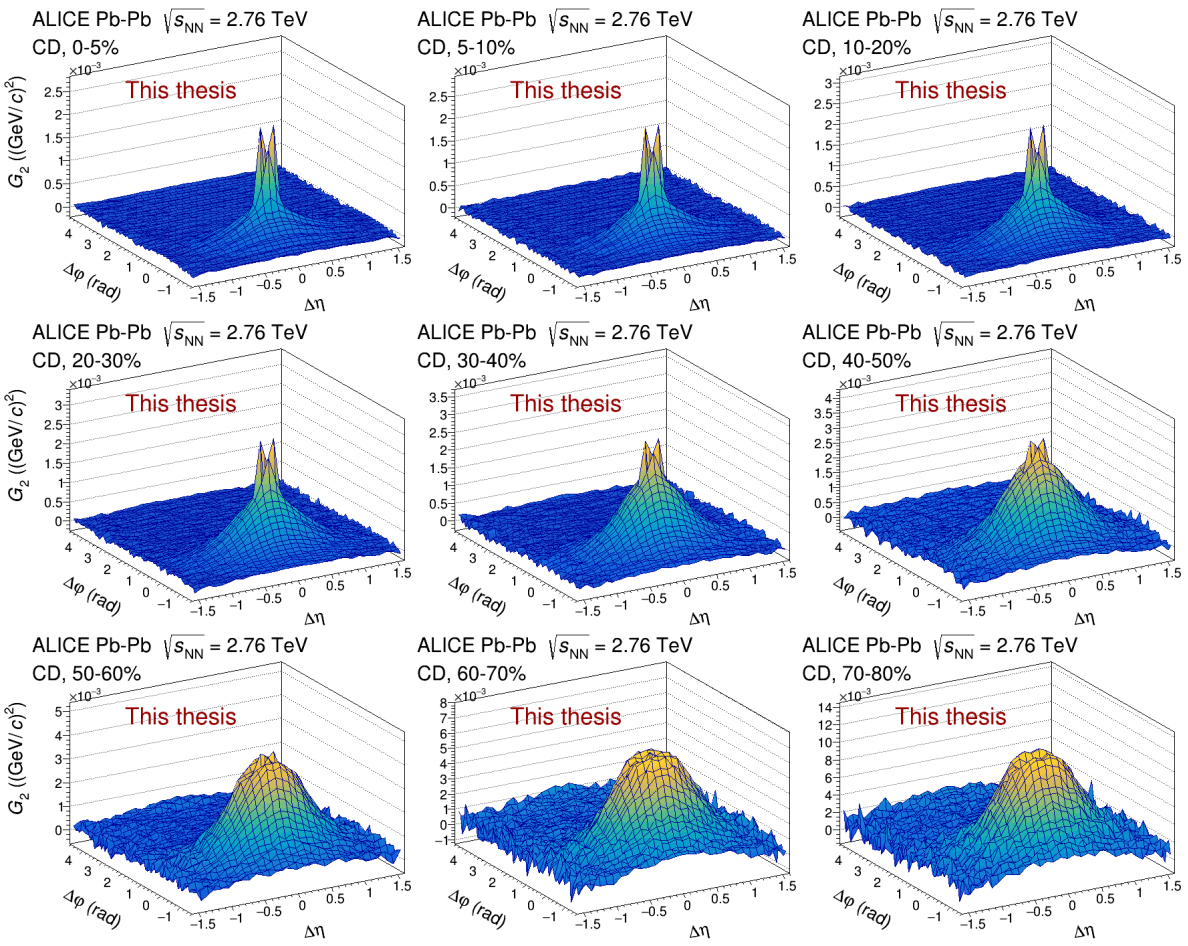

FIGURE 6.2: Charge dependent (CD) two-particle transverse momentum correlation for each centrality class in Pb–Pb collisions at $\sqrt{s_{\mathrm{NN}}}$ = 2.76 TeV as measured by ALICE.

6.1.2 Longitudinal projections

As was mentioned in sects. 2.4.5 and 2.4.6 the longitudinal evolution with the centrality of the collision of the two-particle transverse momentum correlation may show a broadening as a manifestation of the diffusion of the momentum current fluctuations due to the η/s of the medium. With the aim of better show this potential effect, the near-side, $|\Delta\varphi| < \pi/2$, longitudinal projections of two-particle transverse momentum correlation G_2 for the CI and CD track combinations are shown in Figs. 6.3 and 6.4, respectively. The projections are calculated integrating on the azimuthal range ($|\Delta\varphi| < \pi/2$) and normalizing by the number of involved azimuthal bins (31). The central bin at $(\Delta\eta, \Delta\varphi) = (0, 0)$ has been excluded because it is undercorrected. The full version of the correlation function is shown in appendix C.

The near-side longitudinal projection of the G_2^{CI} correlator in Fig. 6.3 shows the monotonic growth of the amplitude of the near-side peak from central to peripheral collisions. The collective behavior, developed along the azimuthal dimension is present just as a uniform baseline on top of which the near-side peak develops. On top of this baseline the near-side peak broadens from peripheral to central collisions. See sect. 8.2 for a quantitative description. From semi-central to central collisions the near-side peak shows a plateau consistent with the two-lobes structure shown in Fig. 6.1 and with the two modes of propagation of the momentum fluctuations described in sect. 2.4.8.

The near-side longitudinal projection of the G_2^{CD} correlator in Fig. 6.4 also shows the monotonic

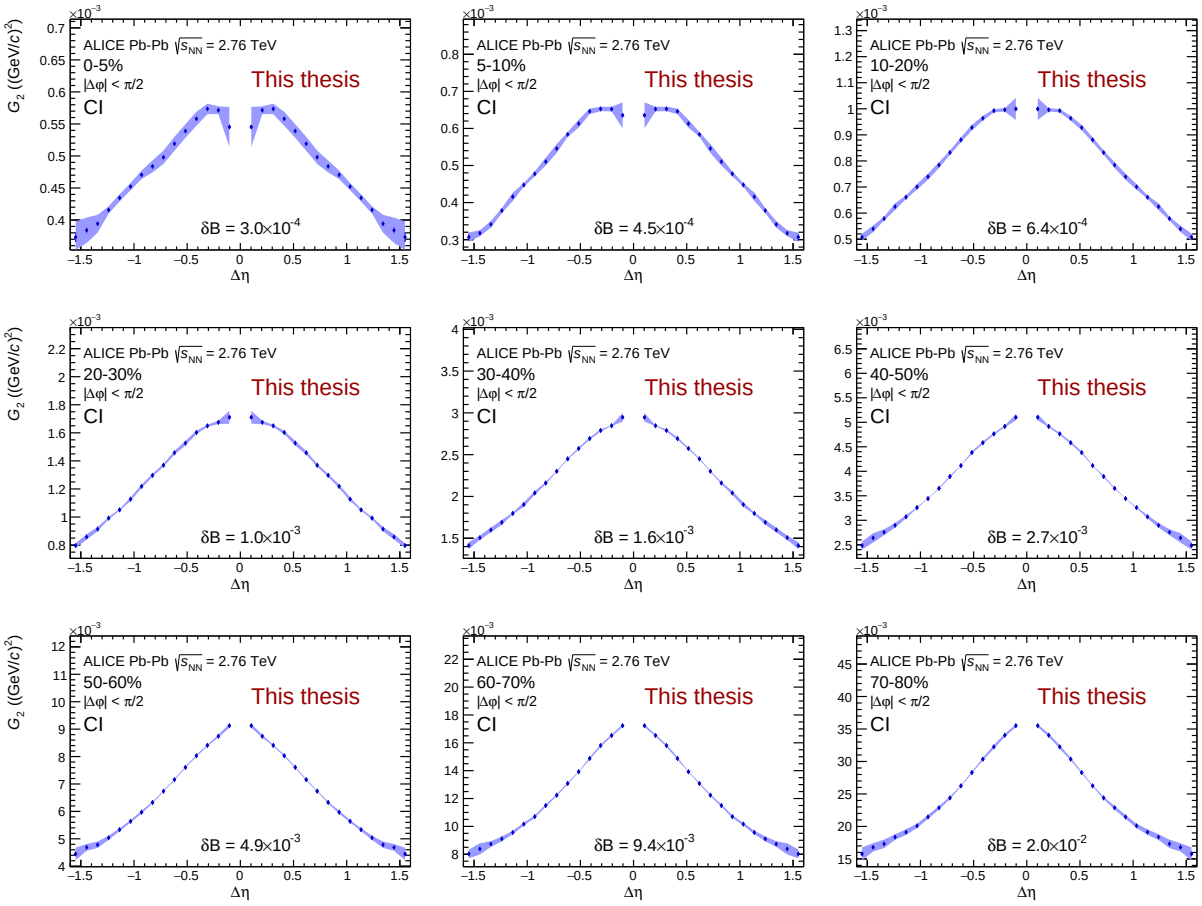

FIGURE 6.3: Near-side longitudinal projection of the charge independent (CI) two-particle transverse momentum correlation for each centrality class in Pb–Pb collisions at $\sqrt{s_{\rm NN}}$ = 2.76 TeV as measured by ALICE. Error bars represent statistical uncertainties (most of them lower than the marker size) while systematic uncertainties are represented by colored bands.

growth of the amplitude of the near-side peak from central to peripheral collisions although of lower magnitude than its CI counterpart. Here the azimuthal collective behavior is absent due to its non charge dependent nature. Consequently the baseline of the near-side peak lays at about zero. Form peripheral to central collisions the near-side peak shows a narrowing trend. See sect. 8.2 for a quantitative description. From semi-peripheral to peripheral collisions, the effect of the excess in the sort range LS correlation compatible with the HBT effect is visible in the settle down of the plateau structure.

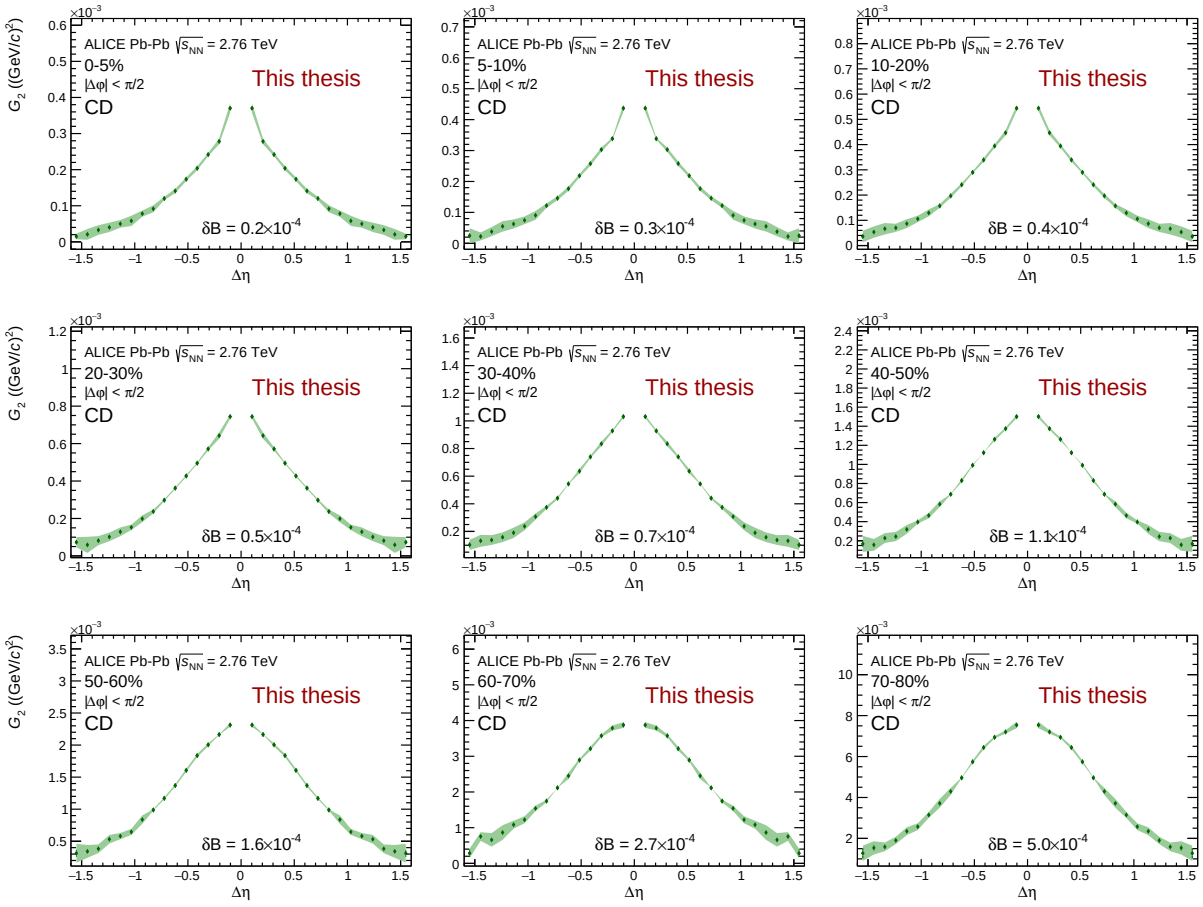

FIGURE 6.4: Near-side longitudinal projection of the charge dependent (CD) two-particle transverse momentum correlation for each centrality class in Pb–Pb collisions at $\sqrt{s_{\mathrm{NN}}}$ = 2.76 TeV as measured by ALICE. Error bars represent statistical uncertainties (most of them lower than the marker size) while systematic uncertainties are represented by colored bands.

6.1.3 Azimuthal projections

For completeness projections in the azimuthal direction are also shown. Figs. 6.5 and 6.6 show the azimuthal projections of two-particle transverse momentum correlation G_2 for the CI and CD track combinations, respectively. The projections are calculated integrating on the whole longitudinal range ($|\Delta\eta| < 1.6$) and normalizing by the number of longitudinal bins (31). The central bin at $(\Delta\eta, \Delta\varphi) = (0, 0)$ has been excluded because it is undercorrected. The full version of the correlation function is shown in appendix C.

The azimuthal projections of the $G_2^{\rm CI}$ correlator in Fig. 6.5 show the evolution with centrality of the long range collective behavior. The amplitude of the flow modulations shows the expected behavior according to the evolution of the flow coefficients, i.e. grows from central to semi-peripheral collisions where saturates to finally decrease toward more peripheral ones. From semi-central to central collisions the impact of the above mentioned short range correlation dilution on the away-side is also identifiable.

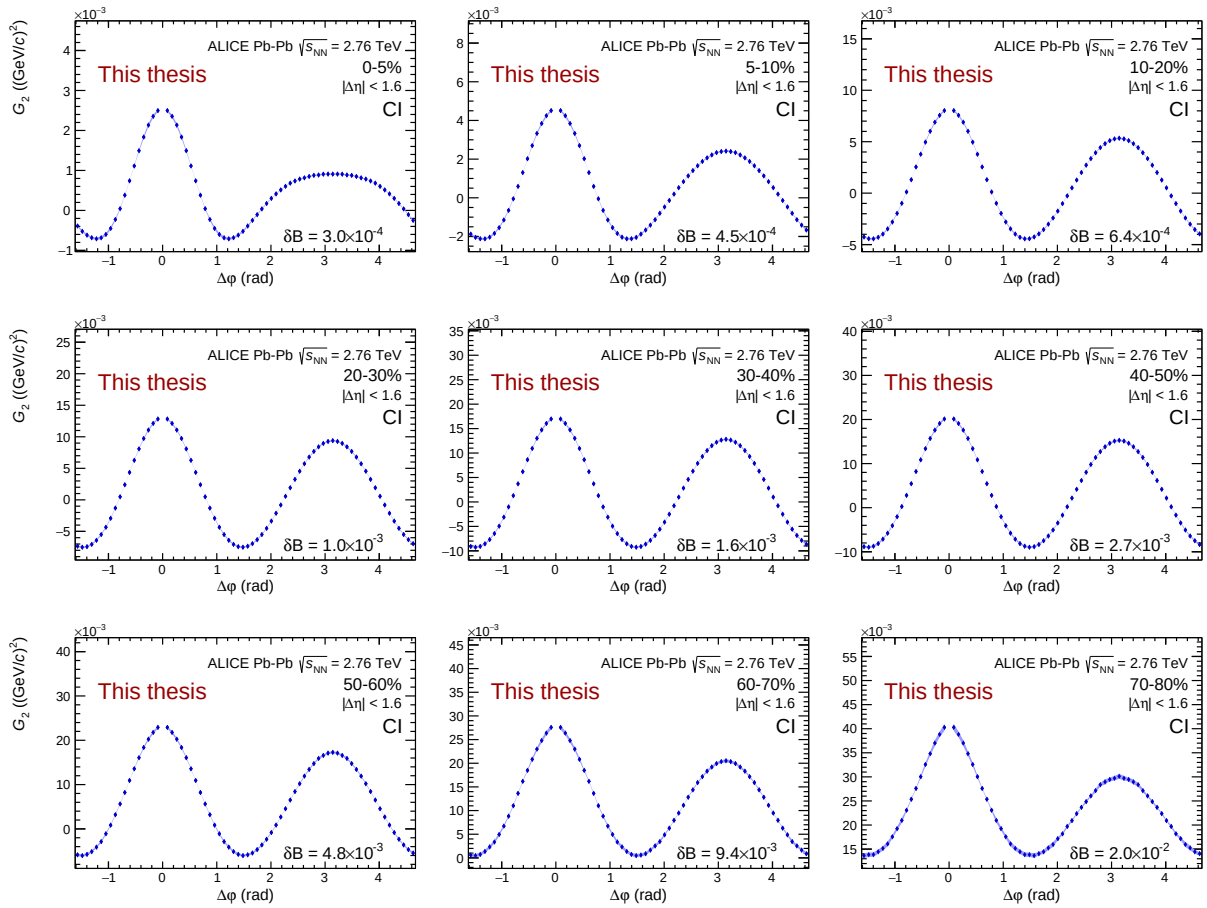

FIGURE 6.5: Azimuthal projection of the charge independent (CI) two-particle transverse momentum correlation for each centrality class in Pb–Pb collisions at $\sqrt{s_{\rm NN}}$ = 2.76 TeV as measured by ALICE. Error bars represent statistical uncertainties (most of them lower than the marker size) while systematic uncertainties are represented by colored bands.

The azimuthal projections of the $G_2^{\rm CD}$ correlator in Fig. 6.6 show the clear absence of long range collective behavior. From peripheral to central collisions the monotonic decrease of the amplitude of the near side peak is easy to track and the evidence that, azimuthally, the $G_2^{\rm CD}$ correlator also narrows from peripheral to central collisions clearly appears. The settle down of the plateau structure from

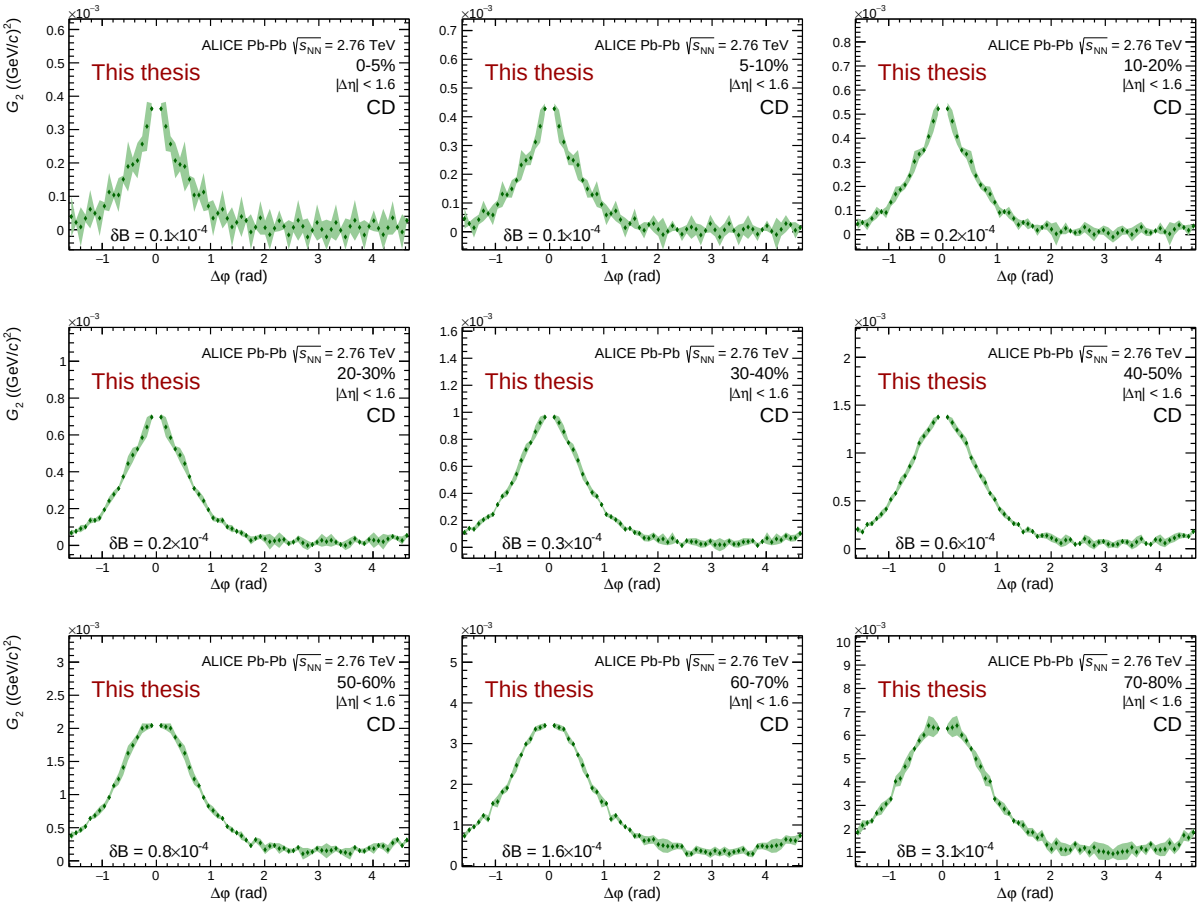

FIGURE 6.6: Azimuthal projection of the charge dependent (CD) two-particle transverse momentum correlation for each centrality class in Pb–Pb collisions at $\sqrt{s_{\rm NN}}$ = 2.76 TeV as measured by ALICE. Error bars represent statistical uncertainties (most of them lower than the marker size) while systematic uncertainties are represented by colored bands.

semi-peripheral to peripheral collisions, compatible with HBT effects, is also featured.

6.2 Results for Pb–Pb collisions at $\sqrt{s_{\rm NN}}$ = 5.02 TeV

In this section the results for CI and CD track combinations are considered as the main results. Results for the LS and US charge combinations are incorporated in the appendix B. Only statistical uncertainties are reported. Systematic tests analysis are currently ongoing and will not be available for this thesis.

6.2.1 Two-particle transverse momentum correlations

The two-particle transverse momentum correlation G_2 for Pb–Pb collisions at $\sqrt{s_{\rm NN}}$ = 5.02 TeV for the CI and CD track combinations are shown in Figs. 6.7 and 6.8, respectively. They are calculated using Eq. (5.1) and the procedure described in sect. 5.3. The central bin at $(\Delta\eta, \Delta\varphi) = (0, 0)$ has been excluded because it is undercorrected. The full version of the correlation function is shown in appendix C.

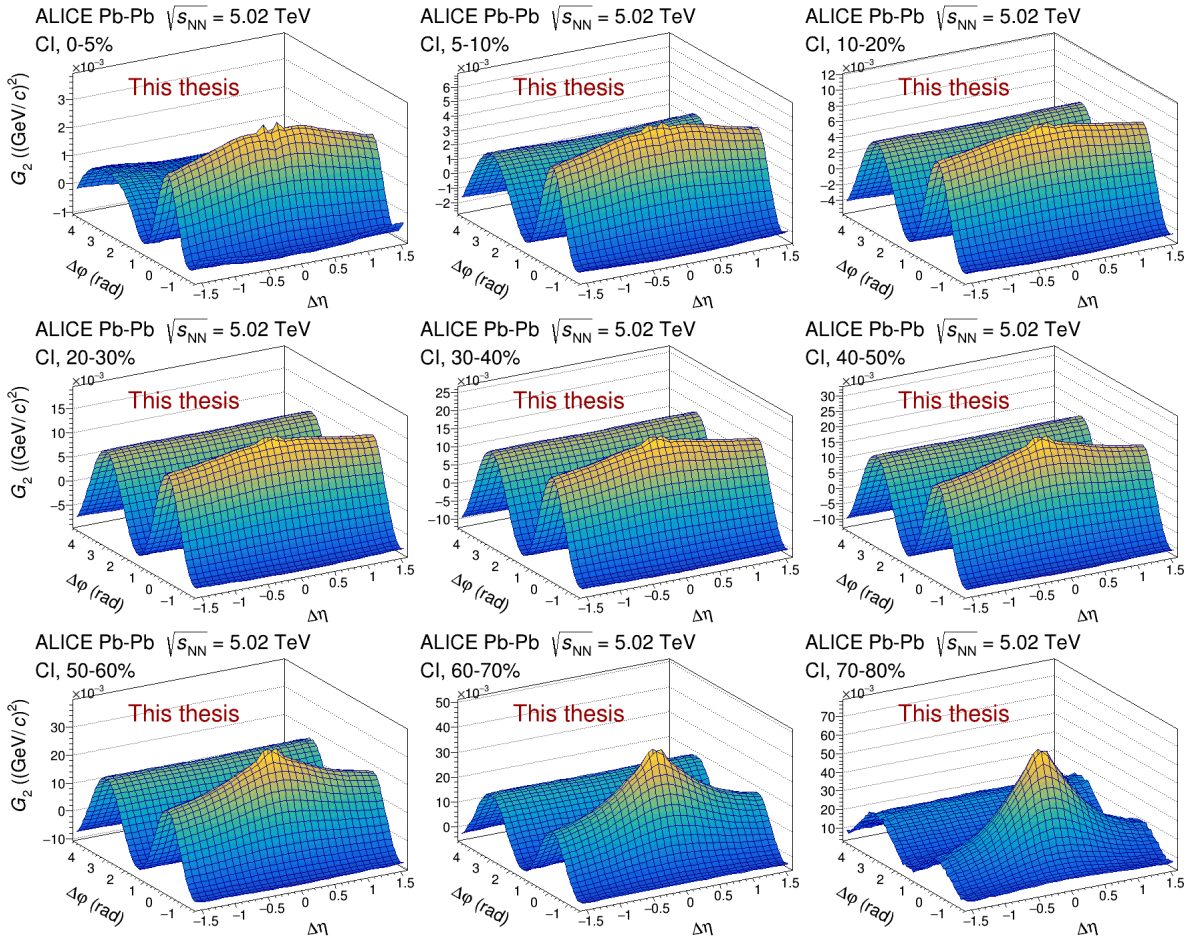

FIGURE 6.7: Charge independent (CI) two-particle transverse momentum correlation for each centrality class in Pb–Pb collisions at $\sqrt{s_{\rm NN}}$ = 5.02 TeV as measured by ALICE.

As in the case of collisions at 2.76 TeV, the $G_2^{\rm CI}$ correlators shown in Fig. 6.7 feature sizable $\Delta\varphi$ modulations dominated in mid-central collisions by a strong elliptic ($\cos(2\Delta\varphi)$) component. Similarly, on the near-side, $|\Delta\varphi| < \pi/2$, atop the azimuthal modulation, the $G_2^{\rm CI}$ correlators feature a near-side peak whose amplitude monotonically decreases from peripheral to central collisions while its longitudinal width systematically broadens. This behavior is captured with the fit model described in sect. 5.4.1. As in the case of collisions at 2.76 TeV, there are two structures which develop from semi-central towards most central events. On the near side two longitudinally extended lobes give place to a depletion around

$(\Delta\eta, \Delta\varphi) = (0, 0)$ qualitatively less deeper than fro the lower energy system. As was described in sect. 5.5.2 the depletion is not described by the proposed model and because that it is excluded from the fit. The two lobes structure might be consequence of the process described in sect. 2.4.8 where diffusion takes over wave propagation for the distribution of the momentum currents fluctuations. The second structure appears on the away-side, $|\Delta\varphi - \pi| < \pi/2$ where the long range correlations driven by the collective behavior get diluted in the short longitudinal reach. The strength of the dilution increases towards central events where the concavity of the away-side is clearly manifested.

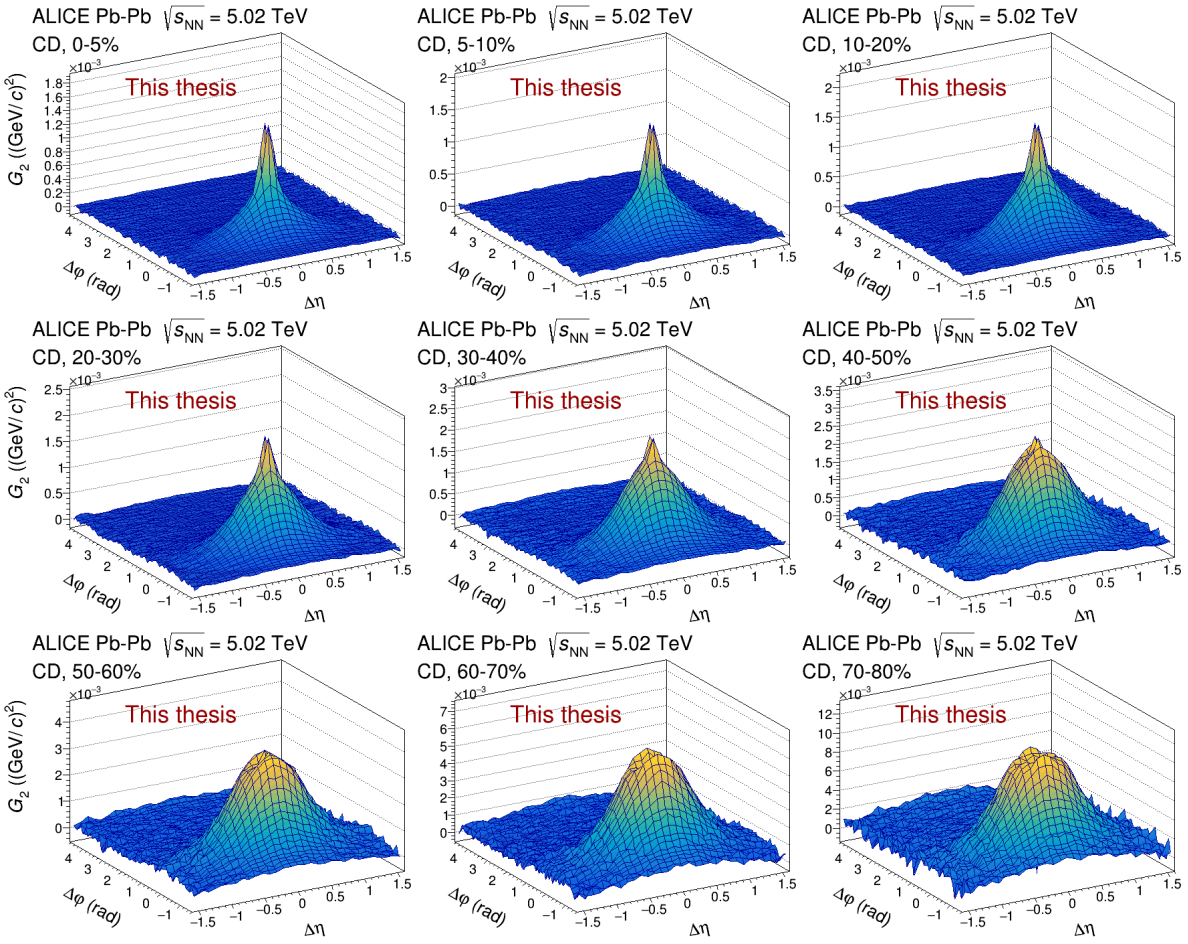

FIGURE 6.8: Charge dependent (CD) two-particle transverse momentum correlation for each centrality class in Pb–Pb collisions at $\sqrt{s_{\rm NN}}$ = 5.02 TeV as measured by ALICE.

As for collisions at 2.76 TeV, $G_2^{\rm CD}$ correlators shown in Fig. 6.8 also feature a near-side peak whose amplitude monotonically decreases from peripheral to central collisions but whose longitudinal width systematically narrows. Again this behavior is captured with the fit model described in sect. 5.4.1. As in the lower energy case, there is sign of the presence or absence of the two lobes structure on the near side, and as there, the flatness of the away-side gives indication that the away-side dilution of the $G_2^{\rm CI}$ correlator is a charge independent effect. Similarly to the lower energy system, from semi-peripheral to peripheral collisions a plateau structure develops around a depression at $(\Delta\eta, \Delta\varphi) = (0.0)$. As was suggested, this structure is compatible with an excess of short range LS correlations over US whose reach increases with the inverse of the system size as happens with the HBT effect.

6.2.2 Longitudinal projections

The near-side, $|\Delta\varphi| < \pi/2$, longitudinal projections of two-particle transverse momentum correlation G_2 for the CI and CD track combinations are shown in Figs. 6.9 and 6.10, respectively. The projections are calculated integrating on the azimuthal range ($|\Delta\varphi| < \pi/2$) and normalizing by the number of involved azimuthal bins (31). The central bin at $(\Delta\eta, \Delta\varphi) = (0, 0)$ has been excluded because it is undercorrected. The full version of the correlation function is shown in appendix C.

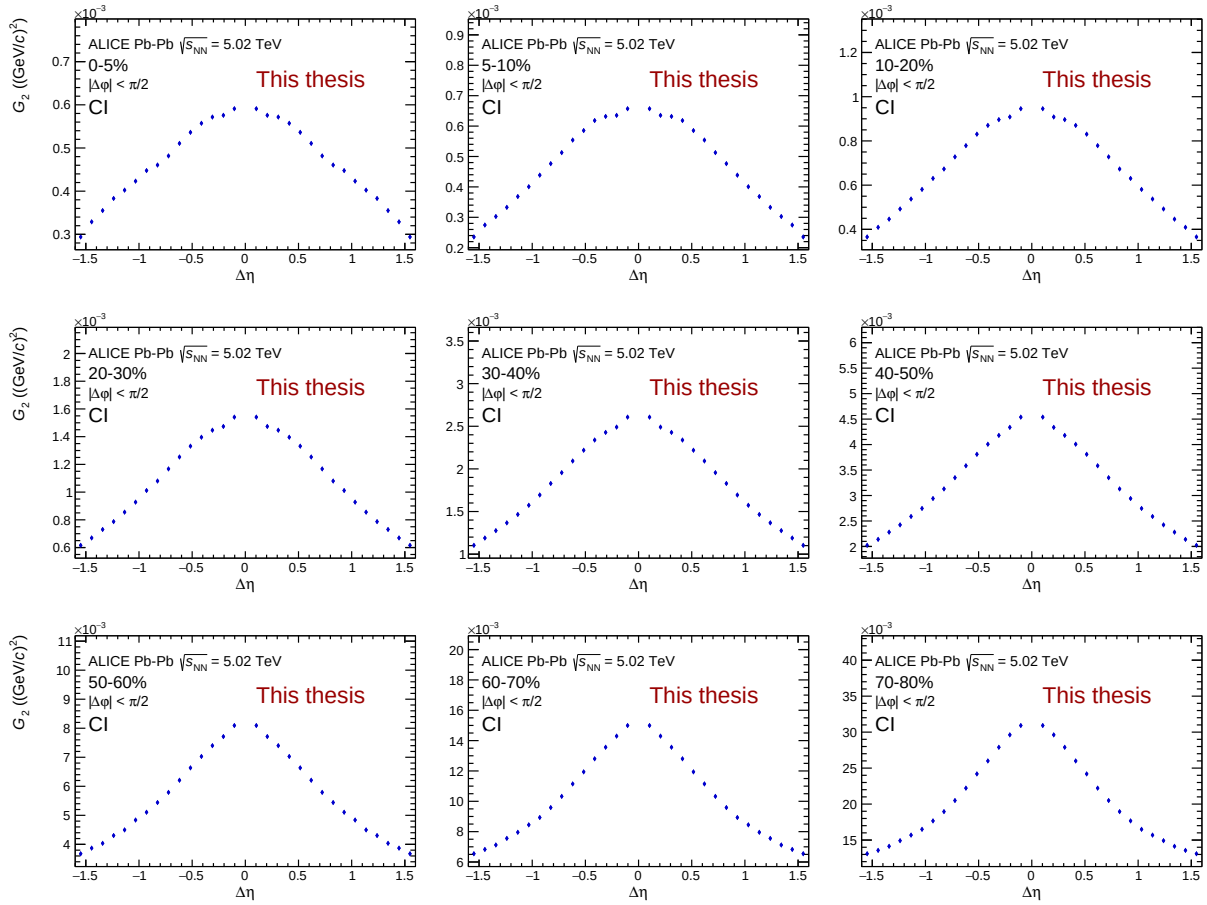

FIGURE 6.9: Near-side longitudinal projection of the charge independent (CI) two-particle transverse momentum correlation for each centrality class in Pb–Pb collisions at $\sqrt{s_{\rm NN}}$ = 5.02 TeV as measured by ALICE. Error bars represent statistical uncertainties (most of them lower than the marker size).

As for the case at 2.76 TeV the near-side longitudinal projection of the $G_2^{\rm CI}$ correlator in Fig. 6.9 shows the monotonic growth of the amplitude of the near-side peak from central to peripheral collisions. The near side peak amplitude agrees with the values shown by the lower energy system. Similarly, the collective behavior, developed along the azimuthal dimension is present just as a uniform baseline on top of which the near-side peak develops. On top of this baseline the near-side peak broadens from peripheral to central collisions. As in the collisions at 2.76 TeV case, from semi-central to central collisions the near-side peak shows a plateau consistent with the two-lobes structure shown in Fig. 6.7 and with the two modes of propagation of the momentum fluctuations described in sect. 2.4.8. But, as was previously commented the depression around $\Delta\eta = 0$ is deeper, if any, than the lowest energy case. Also, at the most central collisions the shoulders structure gets distorted pointing to remaining detector effects.

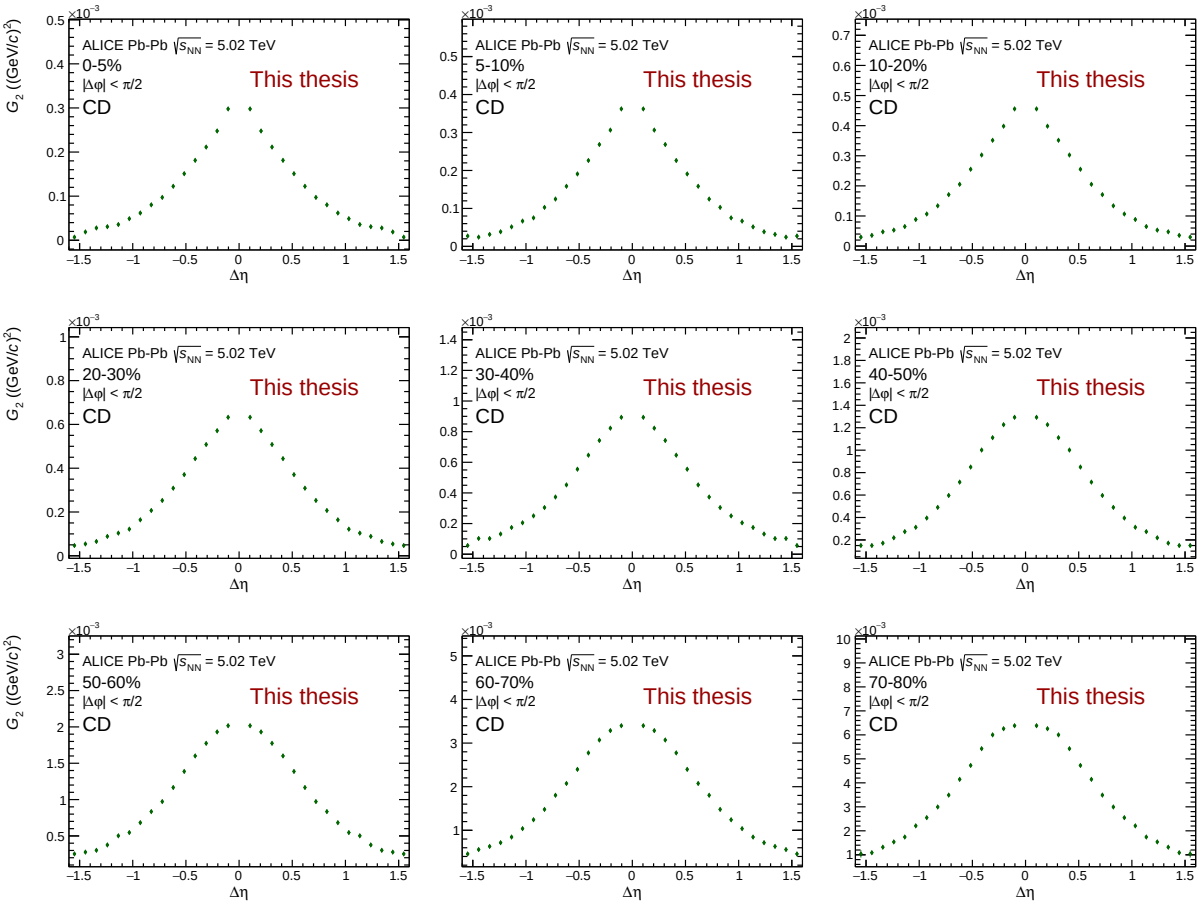

FIGURE 6.10: Near-side longitudinal projection of the charge dependent (CD) two-particle transverse momentum correlation for each centrality class in Pb–Pb collisions at $\sqrt{s_{\rm NN}}$ = 5.02 TeV as measured by ALICE. Error bars represent statistical uncertainties (most of them lower than the marker size).

As in the case of collisions at 2.76 TeV, the near-side longitudinal projections of the $G_2^{\rm CD}$ correlator in Fig. 6.10 also show the monotonic growth of the amplitude of the near-side peak from central to peripheral collisions although of lower magnitude than its CI counterpart and than its pair at lower energy. Form peripheral to central collisions the near-side peak shows a narrowing trend. From semi-peripheral to peripheral collisions, the effect of the excess in the sort range LS correlation compatible with the HBT effect is visible in the settle down of a plateau structure.

6.2.3 Azimuthal projections

Figs. 6.11 and 6.12 show the azimuthal projections of two-particle transverse momentum correlation G_2 for the CI and CD track combinations, respectively. The projections are calculated integrating on the whole longitudinal range ($|\Delta\eta| < 1.6$) and normalizing by the number of longitudinal bins (31). The central bin at $(\Delta\eta, \Delta\varphi) = (0, 0)$ has been excluded because it is undercorrected. The full version of the correlation function is shown in appendix C.

As in the case of collisions at 2.76 TeV, the azimuthal projections of the $G_2^{\rm CI}$ correlator in Fig. 6.11 show the evolution with centrality of the long range collective behavior. The amplitude of the flow modulations also shows the expected behavior according to the evolution of the flow coefficients, i.e. grows from central to semi-peripheral collisions where saturates to finally decrease toward more peripheral ones. Similarly, from semi-central to central collisions the impact of the above mentioned short range correlation dilution on the away-side is also identifiable.

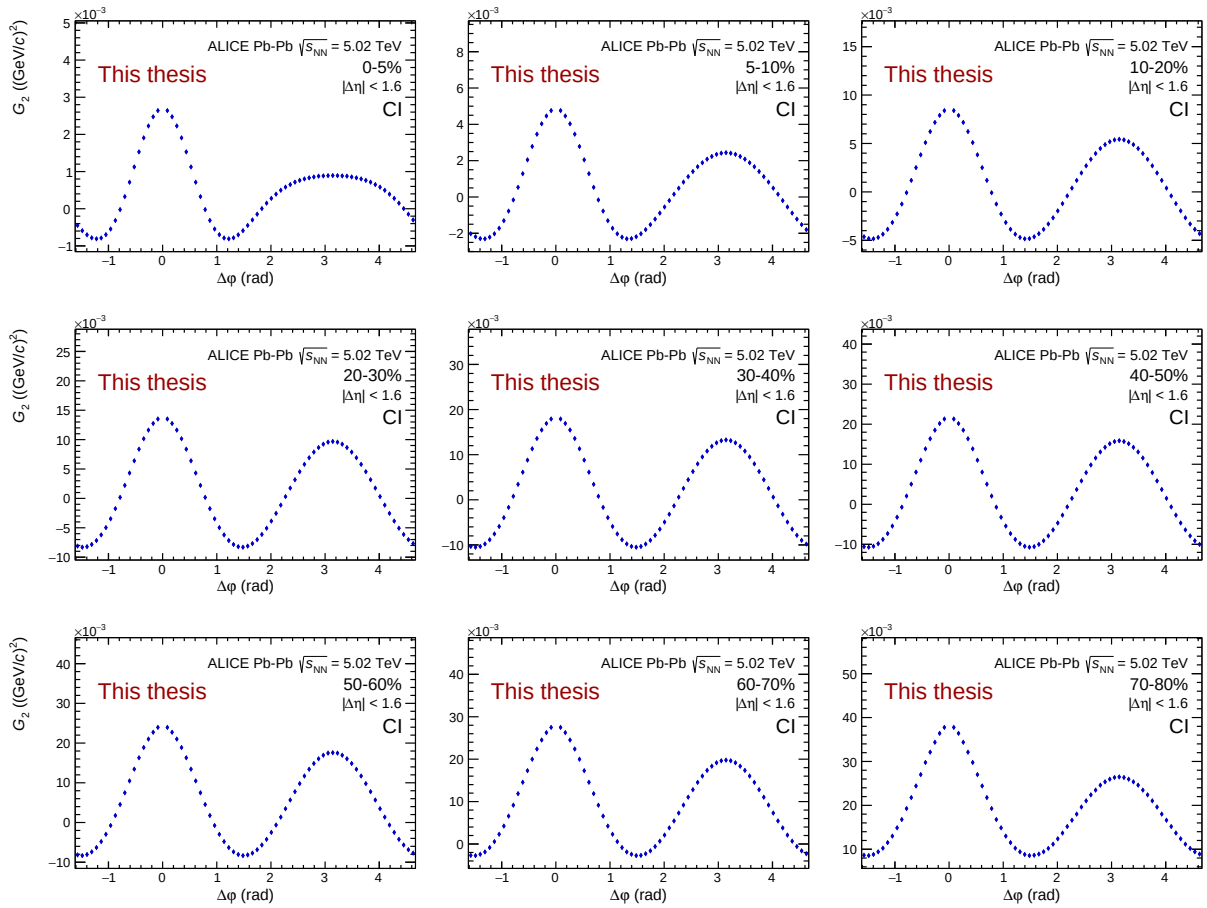

FIGURE 6.11: Azimuthal projection of the charge independent (CI) two-particle transverse momentum correlation for each centrality class in Pb–Pb collisions at $\sqrt{s_{\rm NN}}$ = 5.02 TeV as measured by ALICE. Error bars represent statistical uncertainties (most of them lower than the marker size).

The azimuthal projections of the $G_2^{\rm CD}$ correlator in Fig. 6.12 features a monotonic decrease of the amplitude of the near side peak from peripheral to central collisions as in the case of collisions at 2.76 TeV. Similarly, the $G_2^{\rm CD}$ correlator also narrows azimuthally from peripheral to central collisions. The

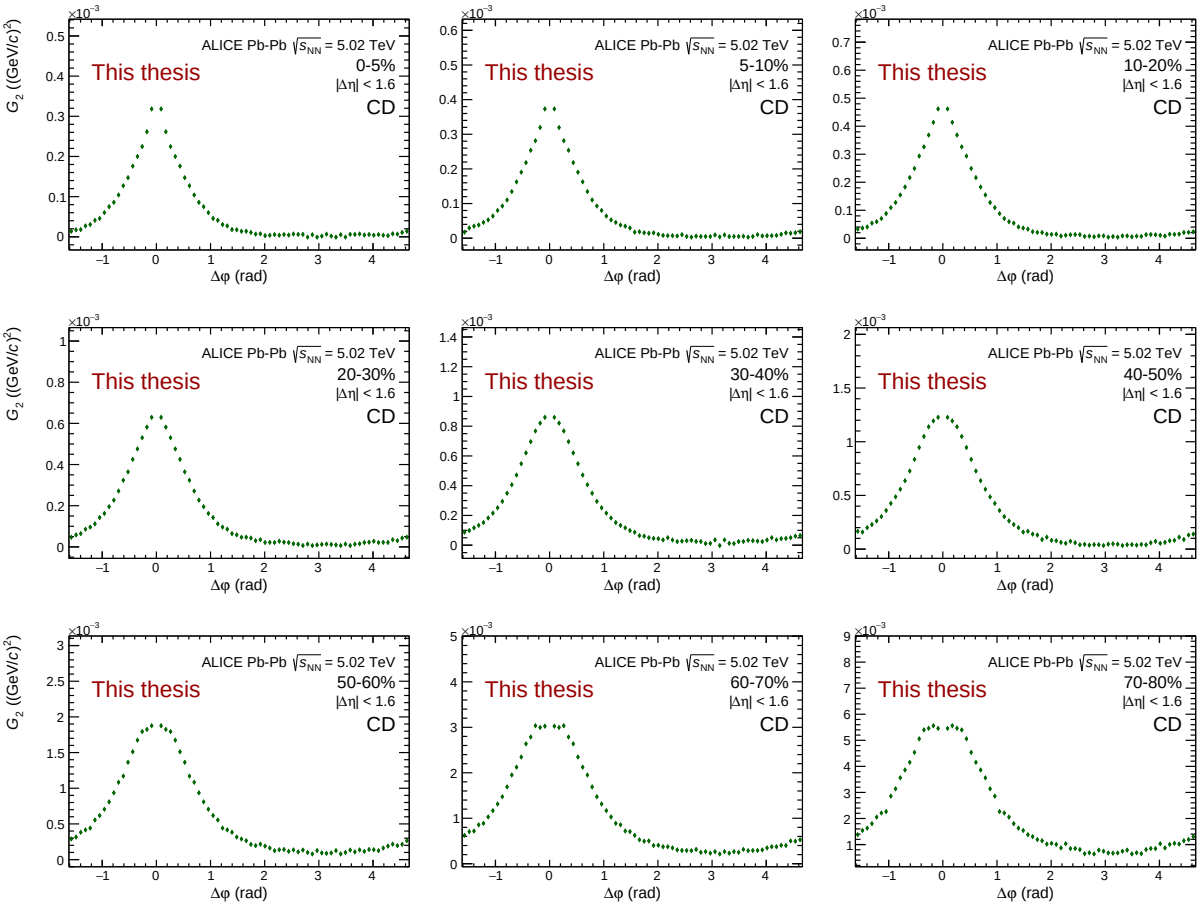

FIGURE 6.12: Azimuthal projection of the charge dependent (CD) two-particle transverse momentum correlation for each centrality class in Pb–Pb collisions at $\sqrt{s_{\rm NN}}$ = 5.02 TeV as measured by ALICE. Error bars represent statistical uncertainties (most of them lower than the marker size).

settle down of the plateau structure from semi-peripheral to peripheral collisions, compatible with HBT effects, is also featured as in the case of lower collision energy.

Chapter 7

Results for small systems: p–Pb at $\sqrt{s_{\mathrm{NN}}} = 5.02$ TeV and pp at $\sqrt{s_{\mathrm{NN}}} = 7$ TeV

This chapter contains the main two-particle transverse momentum correlation results for small systems, p–Pb pp at $\sqrt{s_{\mathrm{NN}}} = 5.02$ TeV and pp at $\sqrt{s_{\mathrm{NN}}} = 7$ TeV. Namely, the CI and CD track combinations of the two-particle transverse momentum correlations. They are obtained from the basic, $+-$, $-+$, $--$, and $++$, track pairs two-particle transverse momentum correlations (see sect. 5.3). Results for the LS and US charge combinations are incorporated in the appendix B.

7.1 p–Pb collisions at $\sqrt{s_{\mathrm{NN}}} = 5.02$ TeV results

In this section the results for CI and CD track combinations are considered as the main results. Results for the LS and US charge combinations are incorporated in the appendix B.

7.1.1 Two-particle transverse momentum correlations

The two-particle transverse momentum correlation G_2 for p–Pb collisions at $\sqrt{s_{\mathrm{NN}}} = 5.02$ TeV for the CI and CD track combinations are shown in Figs. 7.1 and 7.2, respectively. The central bin at $(\Delta\eta, \Delta\varphi) = (0, 0)$ has been excluded because it is undercorrected. The full version of the correlation function is shown in appendix C.

The G_2^{CI} correlators shown in Fig. 7.1 feature two long range correlation structures one on the away side, longitudinally flat, which monotonically decreases from low to high multiplicity collisions. A second long range structure appears on the near side atop of which the G_2^{CI} features a near side-peak whose amplitude monotonically decreases from low to high multiplicity collisions. The near side long range structure keeps its amplitude for all multiplicity classes perhaps slightly increasing from low to high multiplicity collisions and is consistently lower than the amplitude of the away side structure. Apparently the near side peak features the same shape for all multiplicity classes. Equivalent, inclusive, triggered two-particle number correlation analysis, associates the near side peak to jet like processes and part of the away side long range structure to jet recoil and momentum conservation. After subtracting the correlator for the lowest multiplicity collisions from the highest multiplicity one, a $\cos(2\Delta\varphi)$ modulation appeared with near and away long range structures with about the same amplitude [127]. So it is plausible that the near side long range correlation structure featured by G_2^{CI} reflects the presence of elliptic flow like modulation whose presence gets diminished in the away side by jet recoil effects.

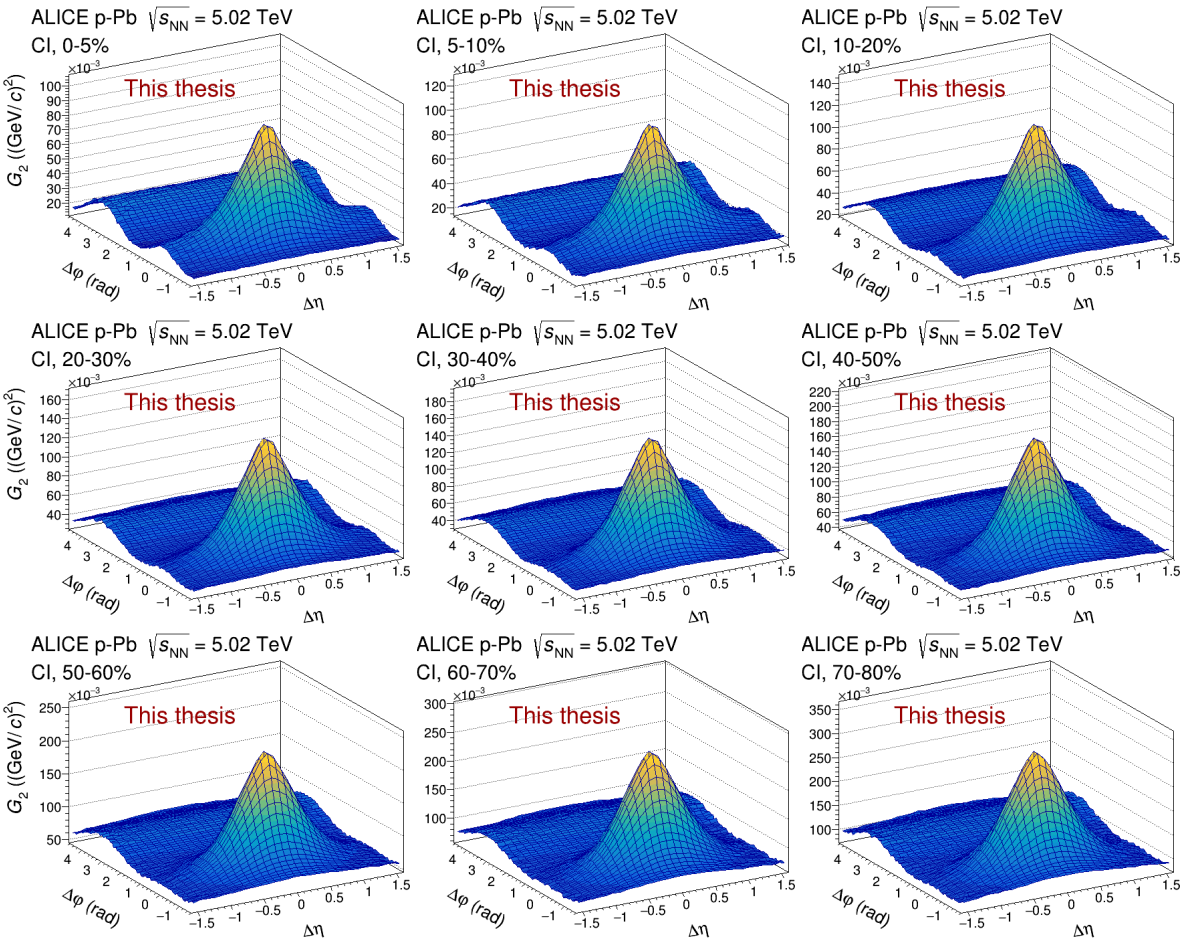

FIGURE 7.1: Charge independent (CI) two-particle transverse momentum correlation for each multiplicity class in p–Pb collisions at $\sqrt{s_{\mathrm{NN}}}$ = 5.02 TeV as measured by ALICE.

For the $G_2^{\rm CD}$ correlators there are no presence of long range structures pointing to a same magnitude effect on both US and LS track combinations. The away side presents a flat structure along multiplicity classes while the near side features a wide peak both azimuthally and longitudinally whose amplitude monotonically decreases from low to high multiplicity collisions. Qualitatively the shape of the near side peak does not change along multiplicity classes.

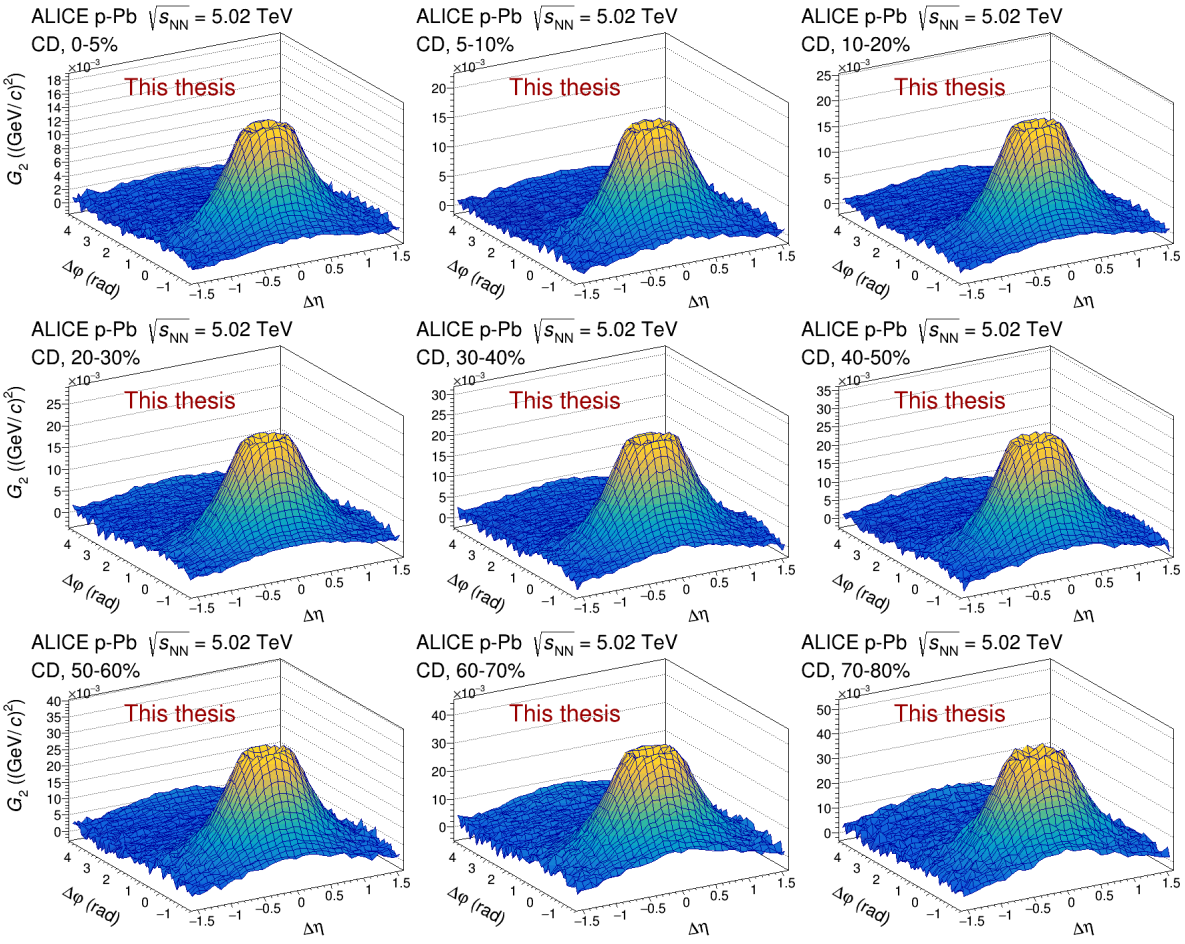

FIGURE 7.2: Charge dependent (CD) two-particle transverse momentum correlation for each multiplicity class in p–Pb collisions at $\sqrt{s_{\rm NN}}$ = 5.02 TeV as measured by ALICE.

7.1.2 Longitudinal projections

The near side, $|\Delta\varphi| < \pi/2$, longitudinal projections of two-particle transverse momentum correlation G_2 for p–Pb collisions at $\sqrt{s_{\rm NN}}$ = 5.02 TeV for the CI and CD track combinations are shown in Fig. 7.3 and 7.4, respectively. The projections are calculated integrating on the azimuthal range ($|\Delta\varphi| < \pi/2$) and normalizing by the number of involved azimuthal bins (31). The central bin at $(\Delta\eta, \Delta\varphi) = (0, 0)$ has been excluded because it is undercorrected. The full version of the correlation function is shown in appendix C.

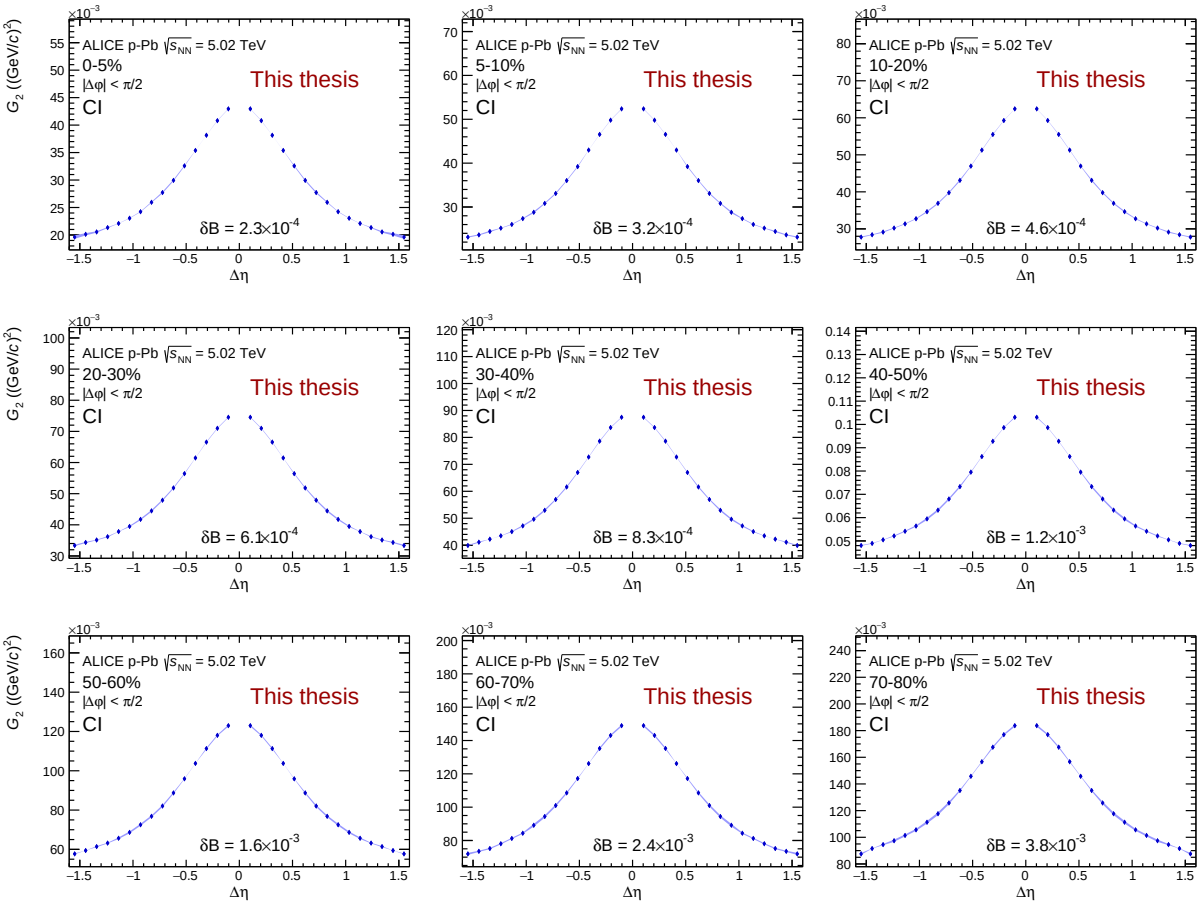

FIGURE 7.3: Longitudinal projection of the charge independent (CI) two-particle transverse momentum correlation for each multiplicity class in p–Pb collisions at $\sqrt{s_{\rm NN}}$ = 5.02 TeV as measured by ALICE.

The near-side longitudinal projection of the $G_2^{\rm CI}$ correlator in Fig. 7.3 shows the monotonic growth of the amplitude of the near side peak from high to low multiplicity collisions while its shape is kept the same along multiplicity classes.

The near-side longitudinal projection of the G_2^{CD} correlator in Fig. 7.4 also shows the monotonic growth of the amplitude of the near side peak from high to low multiplicity collisions. Its shape, which qualitatively is kept the same along multiplicity classes clearly shows a plateau structure of approximately the same longitudinal length along centrality classes. As the CI correlator does not feature such a plateau this is a charge dependent event. The strength of the LS correlator is subtracted from the US correlator so there is an excess of short range correlations in the LS correlator consistent with HBT effects.

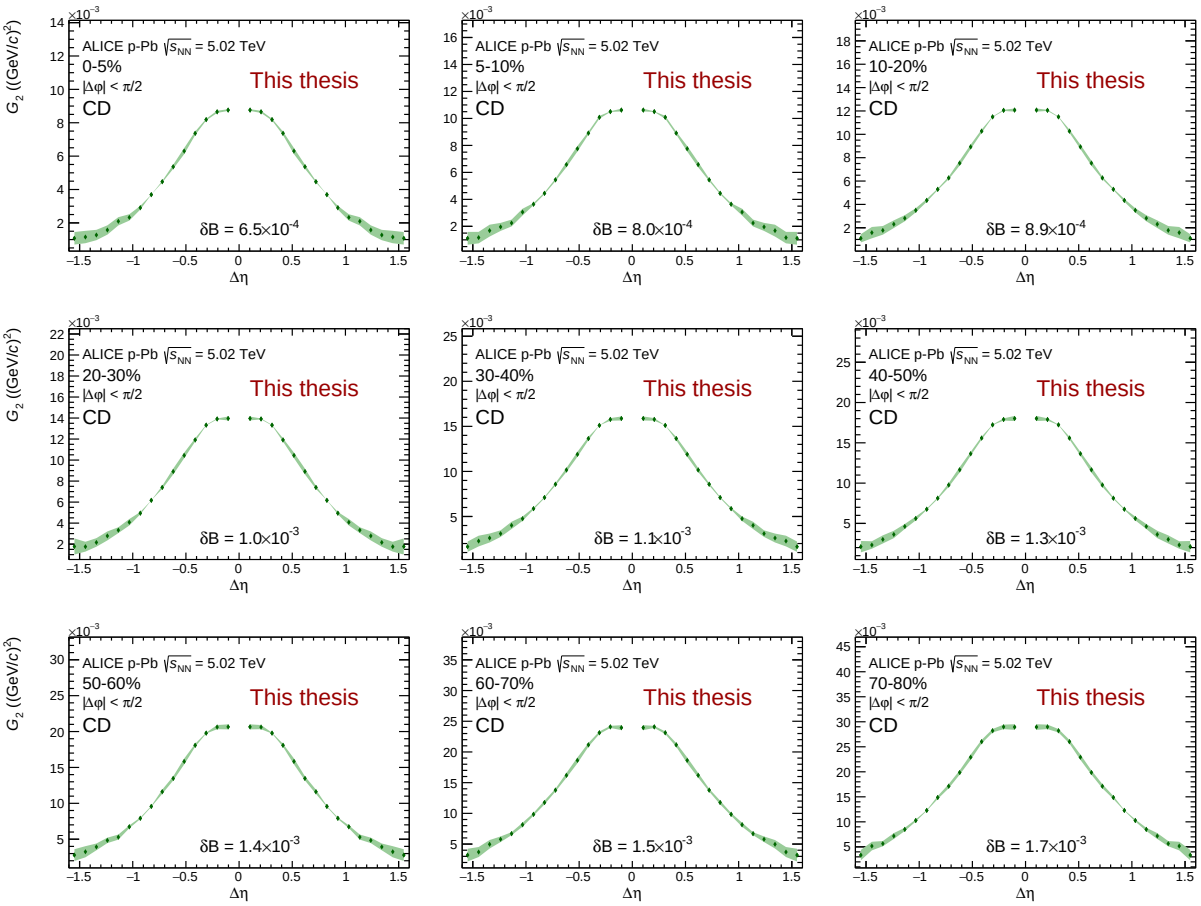

FIGURE 7.4: Longitudinal projection of the charge dependent (CD) two-particle transverse momentum correlation for each multiplicity class in p–Pb collisions at $\sqrt{s_{\mathrm{NN}}}$ = 5.02 TeV as measured by ALICE.

7.1.3 Azimuthal projections

The azimuthal projections of the two-particle transverse momentum correlation G_2 for p–Pb collisions at $\sqrt{s_{\rm NN}}$ = 5.02 TeV for the CI and CD track combinations are shown in Figs 7.5 and 7.6, respectively. The projections are calculated integrating on the whole longitudinal range ($|\Delta\eta| < 1.6$) and normalizing by the number of longitudinal bins (31). The central bin at $(\Delta\eta, \Delta\varphi) = (0, 0)$ has been excluded because it is undercorrected. The full version of the correlation function is shown in appendix C.

The azimuthal projections of the $G_2^{\rm CI}$ correlator in Fig. 7.5 show the evolution with the multiplicity of the collision of the near side peak and the away side long range structure. Both grow monotonically in amplitude from high to low multiplicity collisions with the away side structure growing at a lower pace. As was commented before, the apparent absence of the $\cos(2\Delta\varphi)$ modulation is misleading due to the jet recoil effects on the away side.

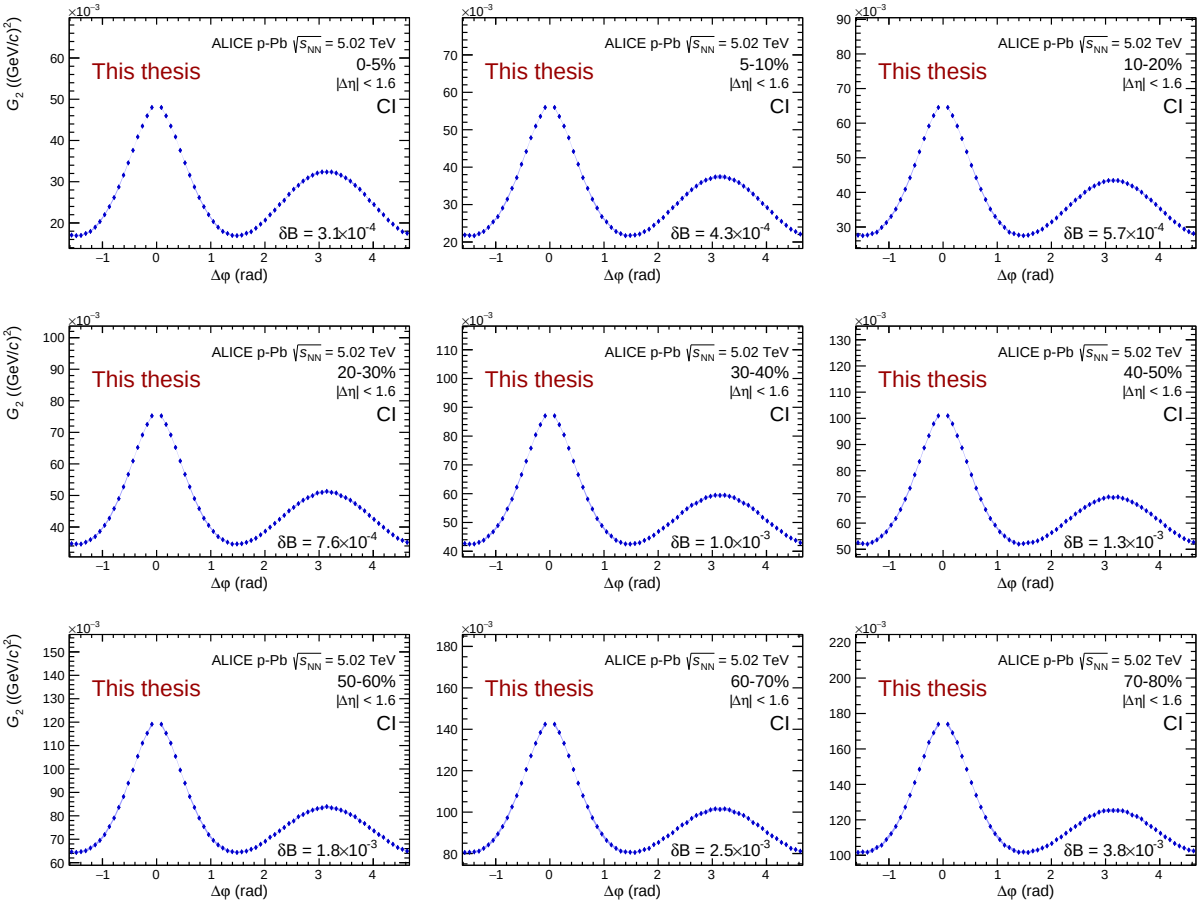

FIGURE 7.5: Azimuthal projection of the charge independent (CI) two-particle transverse momentum correlation on each multiplicity class in p–Pb collisions at $\sqrt{s_{\rm NN}}$ = 5.02 TeV as measured by ALICE.

The azimuthal projections of the G_2^{CD} correlator in Fig. 6.6 show a behavior which is consistent with that of the longitudinal projections. The near side peak amplitude grows monotonically from high to low multiplicity collisions. The plateau structure on the neighborhood of $\Delta\varphi = 0$ keeps its size along the multiplicity classes. Qualitatively the shape of the projection also remains the same along multiplicity classes.

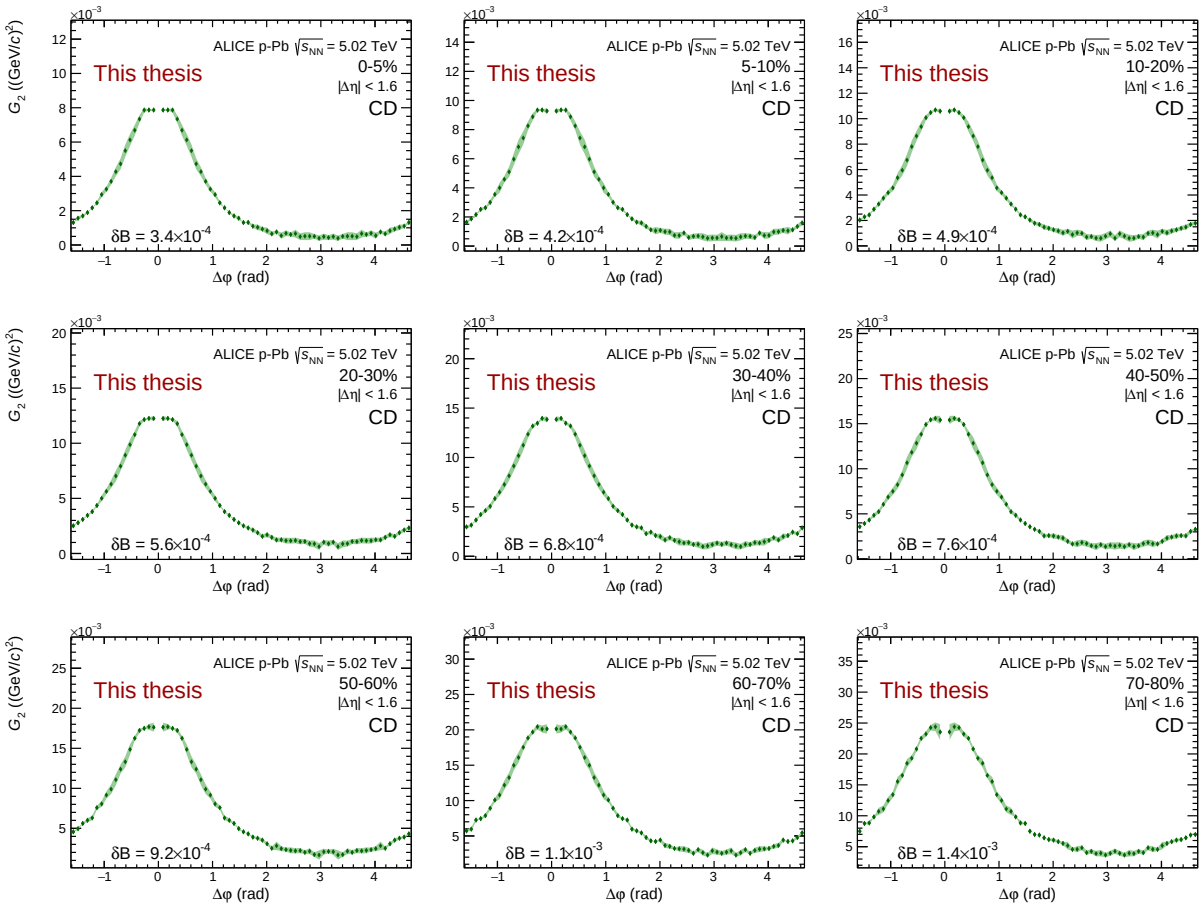

FIGURE 7.6: Azimuthal projection of the charge dependent (CD) two-particle transverse momentum correlation on each multiplicity class in p–Pb collisions at $\sqrt{s_{\mathrm{NN}}} = 5.02$ TeV as measured by ALICE.

7.2 Results for pp collisions at $\sqrt{s_{\mathrm{NN}}} = 7$ TeV

In this section the results for CI and CD track combinations are considered as the main results. Results for the LS and US charge combinations are incorporated in the appendix B.

7.2.1 Two-particle transverse momentum correlations

The two-particle transverse momentum correlation G_2 for pp collisions at $\sqrt{s_{\mathrm{NN}}} = 7$ TeV for the CI and CD track combinations are shown in Figs. 7.7 and 7.8, respectively. The central bin at $(\Delta\eta, \Delta\varphi) = (0, 0)$ has been excluded because it is undercorrected. The full version of the correlation function is shown in appendix C.

The G_2^{CI} correlators shown in Fig. 7.7 show a behavior which parallels that of the p–Pb collisions but in the near side long range structures which here is clearly absent. The long range away side structure

evolves similarly to the near side peak, the amplitude of both grows monotonically from high to medium multiplicity collisions where both saturate. Qualitatively the near side peak features the same shape along multiplicity classes.

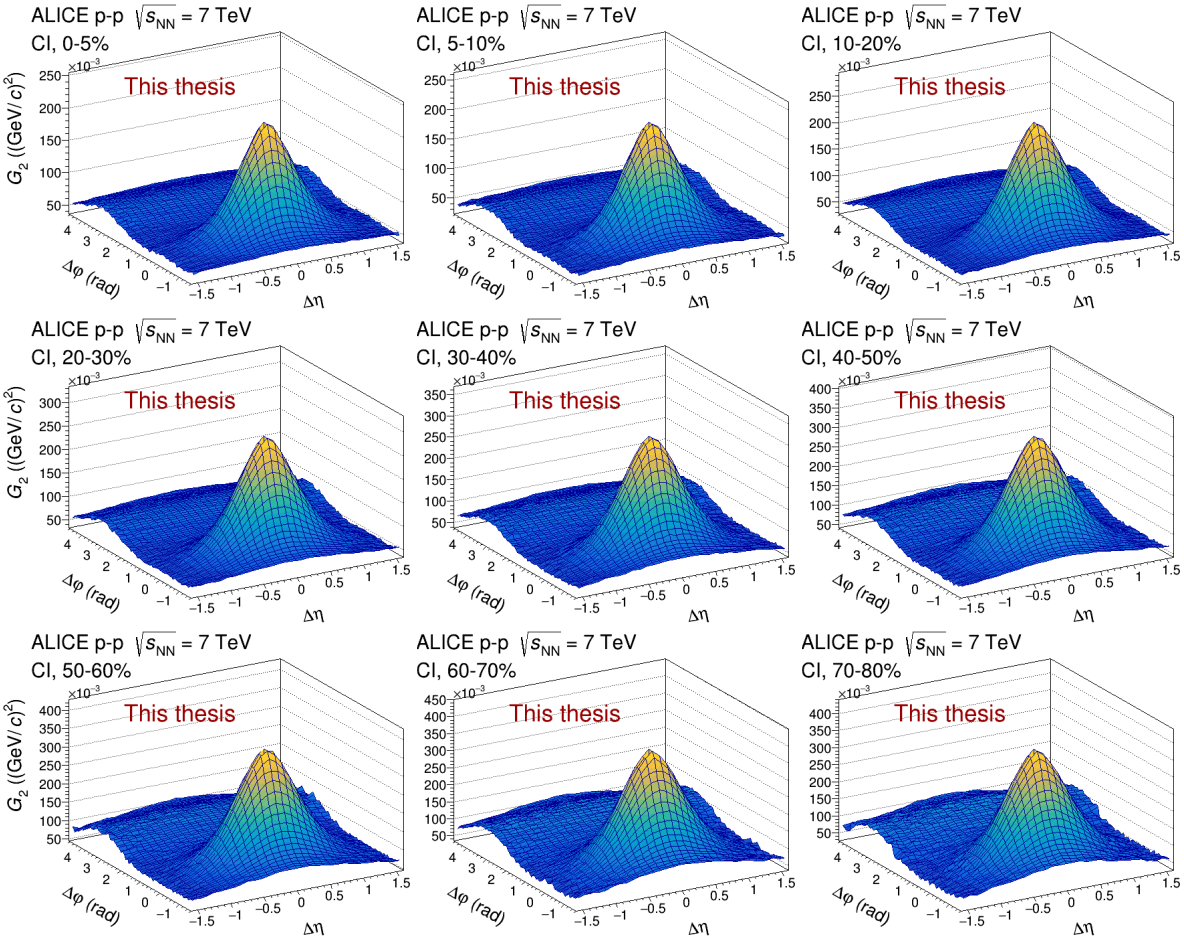

FIGURE 7.7: Charge independent (CI) two-particle transverse momentum correlation for each multiplicity class in pp collisions at $\sqrt{s_{\mathrm{NN}}}$ = 7 TeV as measured by ALICE.

For the G_2^{CD} correlators, shown in Fig. 7.8, consistently with the p–Pb results, there are not long range structures. The away side also presents a flat structure along multiplicity classes. The near side peak features a flat structure on its top with a depression on its center around $(\Delta\eta, \Delta\varphi) = (0, 0)$. The near side peak amplitude grows from high to mid multiplicity collisions where saturates. The extension of the flat structure as well as the qualitative shape of the near side peak are kept the same along multiplicity classes. The plateau structure and the depression are consistent with the HBT interpretation given for p–Pb collisions.

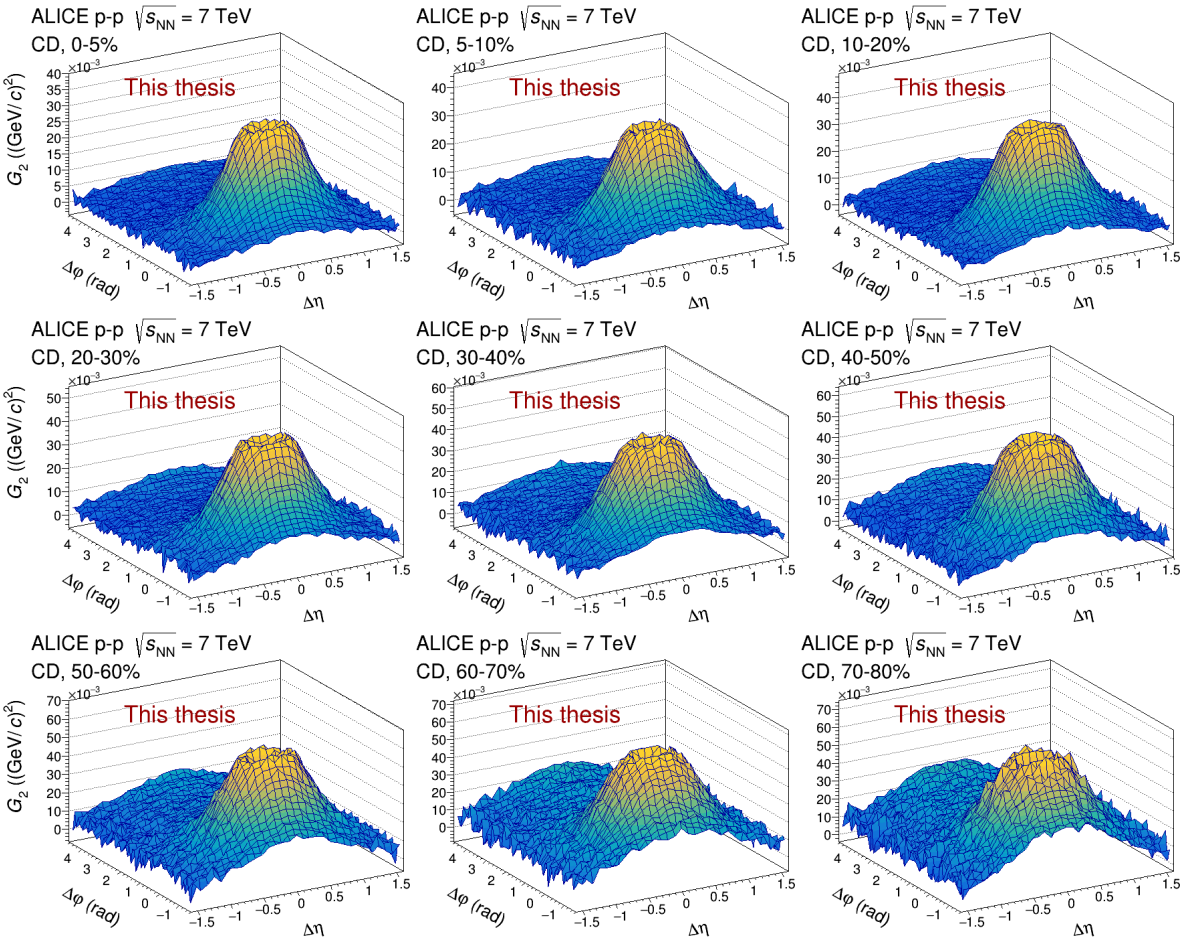

FIGURE 7.8: Charge dependent (CD) two-particle transverse momentum correlation for each multiplicity class in pp collisions at $\sqrt{s_{\mathrm{NN}}} = 7$ TeV as measured by ALICE.

7.2.2 Longitudinal projections

The near side, $|\Delta\varphi| < \pi/2$, longitudinal projection of two-particle transverse momentum correlation G_2 for pp collisions at $\sqrt{s_{\rm NN}}$ = 7 TeV for the CI and CD track combinations are shown in Figs. 7.9 and 7.10, respectively. The projections are calculated integrating on the azimuthal range ($|\Delta\varphi| < \pi/2$) and normalizing by the number of involved azimuthal bins (31). The central bin at $(\Delta\eta, \Delta\varphi) = (0, 0)$ has been excluded because it is undercorrected. The full version of the correlation function is shown in appendix C.

The near side longitudinal projection of the $G_2^{\rm CI}$ correlator in Fig. 7.9, paralleling the p–Pb results, shows a monotonic growth in the amplitude of the near side peak from high to low multiplicity collisions while its shape is kept the same along multiplicity classes.

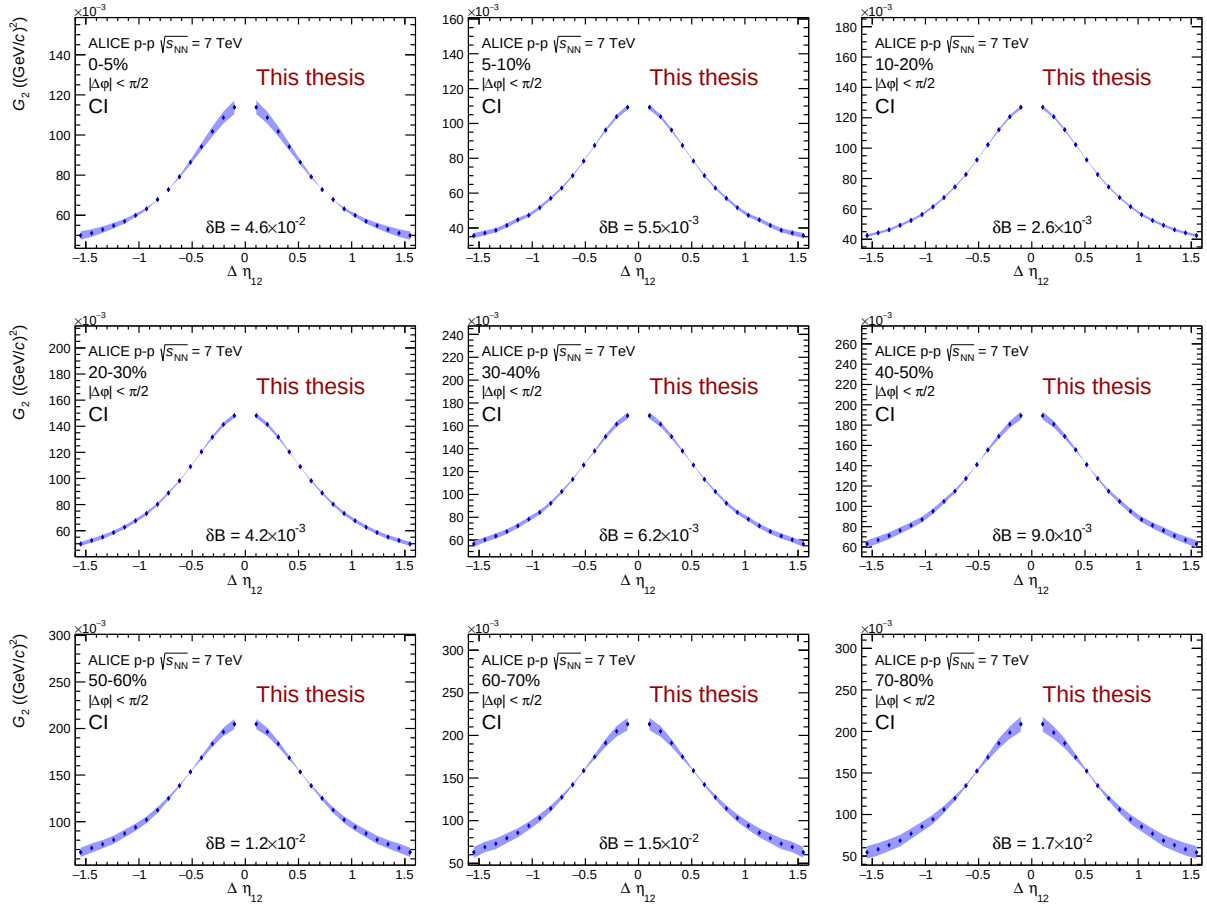

FIGURE 7.9: Longitudinal projection of the charge independent (CI) two-particle transverse momentum correlation for each multiplicity class in pp collisions at $\sqrt{s_{\rm NN}}$ = 7 TeV as measured by ALICE.

The near side longitudinal projection of the $G_2^{\rm CD}$ correlator in Fig. 7.10 shows also a similar behavior to its p–Pb counterpart. The amplitude of the near side peak grows monotonically from high to low multiplicity collisions while its shape is kept the same along multiplicity classes. The correlator projections also features a plateau structure around $\Delta\eta = 0$ which, as in the case of p–Pb collisions, is found consistent with HBT effects.

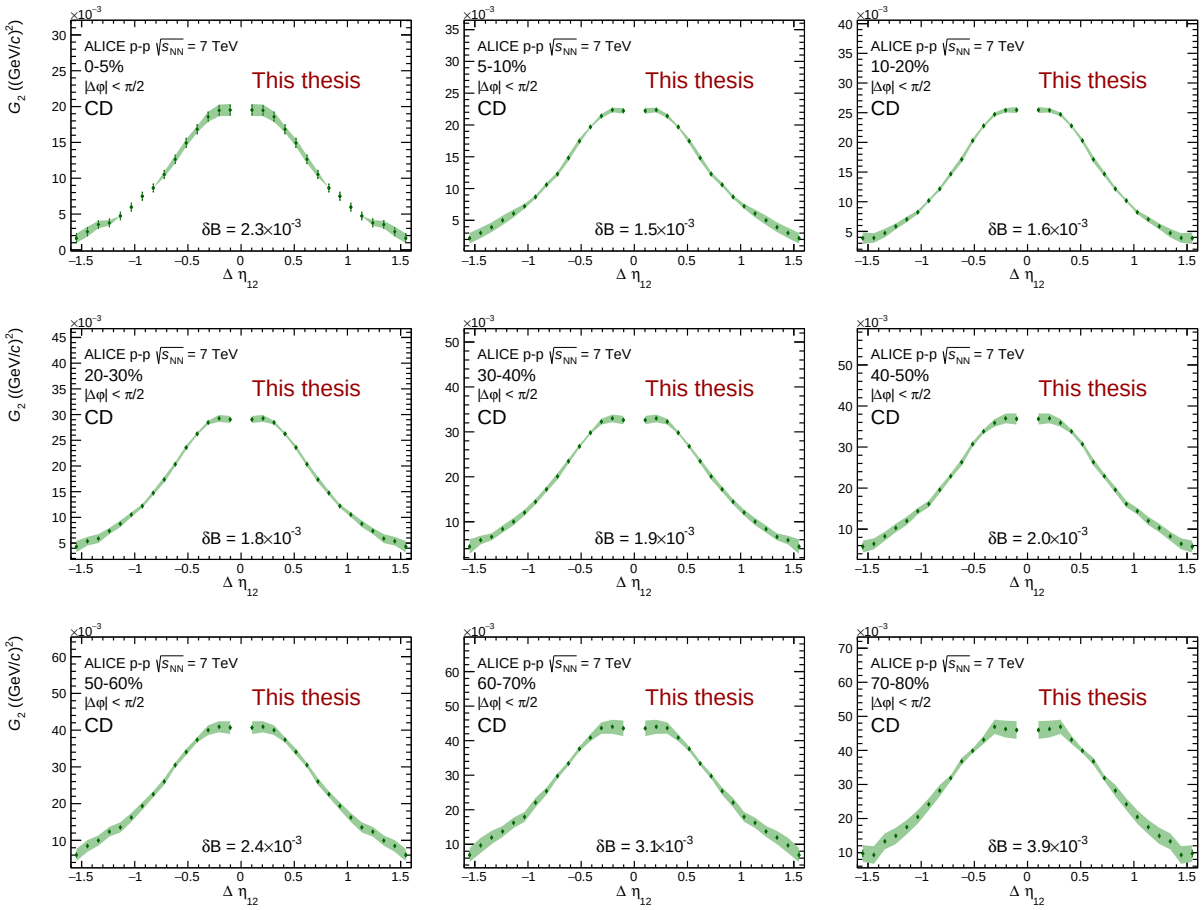

FIGURE 7.10: Longitudinal projection of the charge dependent (CD) two-particle transverse momentum correlation for each multiplicity class in pp collisions at $\sqrt{s_{\rm NN}}$ = 7 TeV as measured by ALICE.

7.2.3 Azimuthal projections

The azimuthal projections of two-particle transverse momentum correlation G_2 for pp collisions at $\sqrt{s_{\rm NN}}$ = 7 TeV for the CI and CD track combinations are shown in Figs. 7.11 and 7.12, respectively. The projections are calculated integrating on the whole longitudinal range ($|\Delta\eta| < 1.6$) and normalizing by the number of longitudinal bins (31). The central bin at $(\Delta\eta, \Delta\varphi) = (0, 0)$ has been excluded because it is undercorrected. The full version of the correlation function is shown in appendix C.

The azimuthal projections of the $G_2^{\rm CI}$ correlator in Fig. 7.11 show the evolution with the multiplicity of the collision of the near side peak and the away side long range structure. Both are consistent with the behavior shown by their p–Pb counterparts. Both growth monotonically from high to low multiplicity collisions, but in here the near side peak grows at a lower pace.

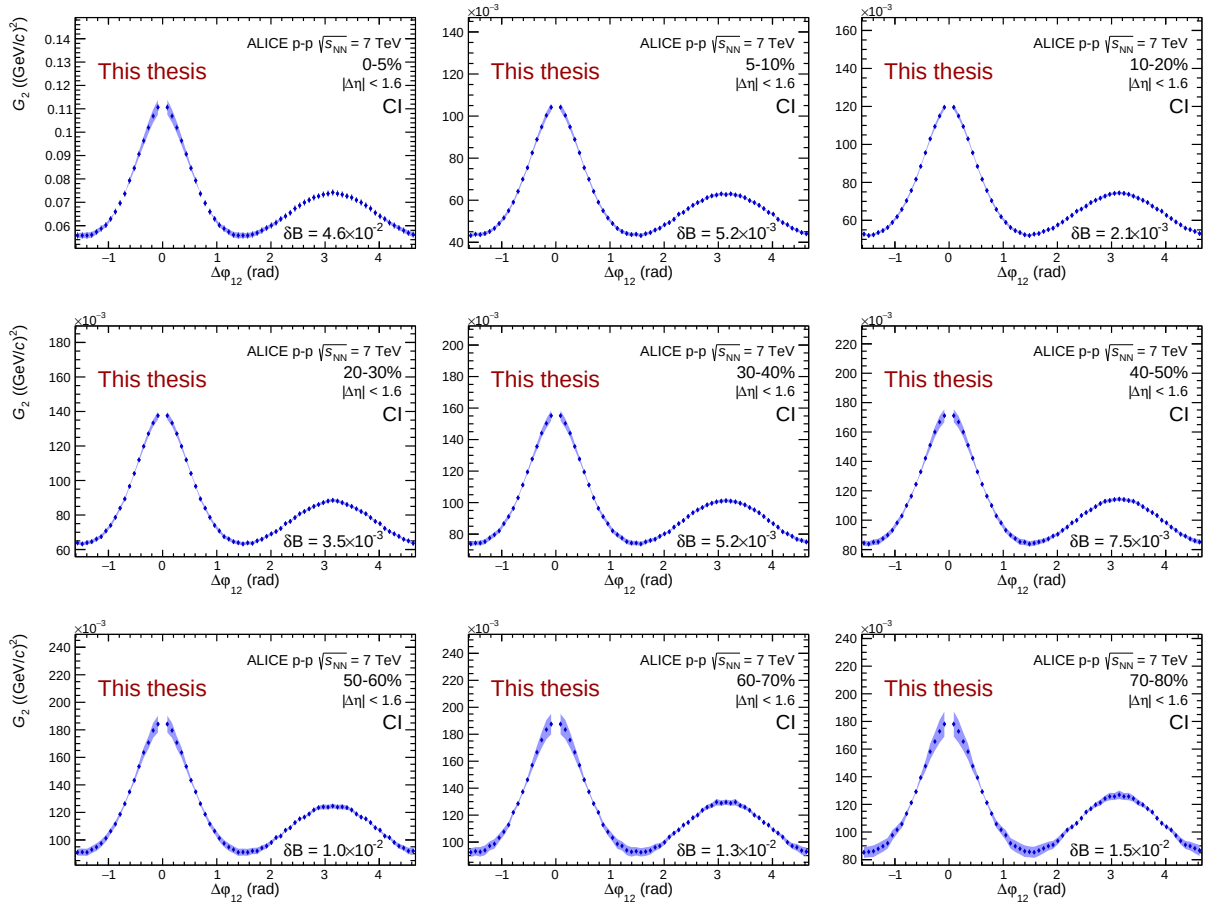

FIGURE 7.11: Azimuthal projection of the charge independent (CI) two-particle transverse momentum correlation for each multiplicity class in pp collisions at $\sqrt{s_{\rm NN}}$ = 7 TeV as measured by ALICE.

The azimuthal projections of the $G_2^{\rm CD}$ correlator in Fig. 7.12 show a consistent behavior with that of the longitudinal projections and with their p–Pb counterparts. The near side peak grows monotonically from high to low multiplicity collisions. The plateau structure keeps its extension along multiplicity classes. Qualitatively the shape of the projections also remains the same along multiplicity classes.

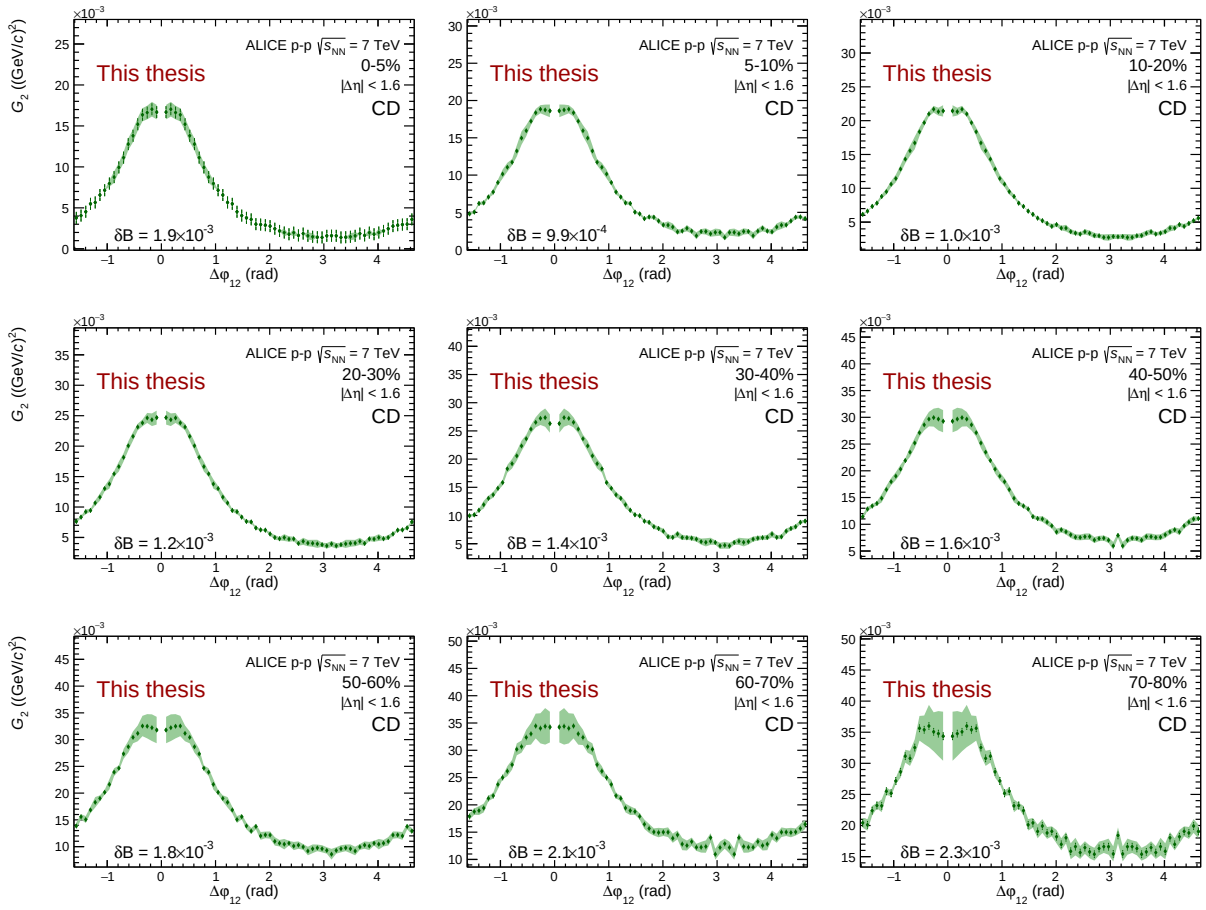

FIGURE 7.12: Azimuthal projection of the charge dependent (CD) two-particle transverse momentum correlation for each multiplicity class in pp collisions at $\sqrt{s_{\mathrm{NN}}}$ = 7 TeV as measured by ALICE.

Chapter 8

Discussion and interpretation of the results

In this chapter the main results presented for Pb–Pb collisions in chapter 6 and for small systems, pp collisions and p–Pb collisions, in chapter 7 are further elaborated and discussed.

8.1 Centrality dependence of the shape fit parameters

The full set of two-particle transverse momentum correlation functions have been parametrized following the procedure described in sect. 5.4.3 using the model in Eq. (5.48). As was described in sect. 2.4.5 the evolution of the shape of the two-particle transverse momentum correlation function contains information about the wave/diffusion process which governs the transfer of momentum fluctuations. The shape of the correlation function is parametrized by the set of parameters that models the two-dimensional generalized Gaussian according to Eq. (5.47), which is on top of the base plane and the collective behavior modeled by the Fourier expansion (Eq. 5.44). Figs. 8.1 and 8.2 show the evolution with the centrality of the collision of the parameters which conform the shape of the two-dimensional generalized Gaussian model of the two-particle transverse momentum correlation G_2^{CI} and G_2^{CD}, respectively. Statistical uncertainties are represented by vertical lines while systematic uncertainties are represented by colored boxes.

The G_2^{CI} shape parameters in Fig. 8.1 quantitatively confirm the monotonic growth from central to peripheral collisions of the amplitude of the near-side peak, on top of the collective behavior, as measured by the parameter A in Eq. (5.47). The base plane magnitude, measured by the parameter B in Eq. (5.47), also shows monotonic growing from central to peripheral collisions. The large systematic uncertainty in parameter B was already commented in sect. 5.5.2 and is linked to the combinatorial nature of the two-particle correlation background. The actual near-side peak shape is captured by the parameters γ and ω, for both dimensions, $\Delta\eta$ and $\Delta\varphi$ in Eq. (5.47). From sect. 5.4.1, when $\gamma = 2$ the near-side peak is a pure Gaussian with its $\sigma = \omega$ and when $\gamma = 1$ the near-side peak is a Laplace distribution with its $\sigma = \sqrt{2}\omega$. When $\gamma > 2$ the near-side peak starts to develop a plateau on its top, larger with the increase of γ departing from the two value. Longitudinally, G_2^{CI} shows the broadening from peripheral to central collisions in the evolution of $\omega_{\Delta\eta}$ and also in evolution of $\gamma_{\Delta\eta}$ which for semi-central to central collisions is above the Gaussian threshold starting to develop a plateau. Azimuthally, G_2^{CI} does show slight narrowing from peripheral to central in the evolution of $\omega_{\Delta\varphi}$ but at the same time this narrowing is compensated by the evolution of $\gamma_{\Delta\varphi}$ which also gets above the Gaussian threshold which would mean that a central plateau is also developed. While G_2^{CI} longitudinal features are almost directly perceived in the correlation functions and their longitudinal projections (see sects. 6.1.1 and 6.1.2), that is not the case for G_2^{CI} azimuthal features where the collective behavior is dominant in both the correlations and their projections (see sects. 6.1.1 and 6.1.3).

The G_2^{CD} shape parameters in Fig. 8.2 also confirm a smaller monotonic growth from central to peripheral collisions of the amplitude of the near-side peak, as measured by the parameter A in Eq. (5.47). The base plane magnitude, measured by the parameter B in Eq. (5.47), also shows monotonic growing

from central to peripheral collisions one order of magnitude lower than in the CI counterpart. G_2^{CD} shows strong narrowing from peripheral to central collisions both, longitudinally and azimuthally. The shape of the near side peak is below the Gaussian threshold in both dimensions and changing quickly to the Laplace distribution from peripheral to central collisions. In both dimensions ω also decreases from peripheral to central collisions strengthening the narrowing trend. In the case of G_2^{CD} longitudinal and azimuthal features are not ease to extract qualitatively from the correlation functions (see sect. 6.1.1) but they directly perceived in their projections (see sects. 6.1.2 and 6.1.3).

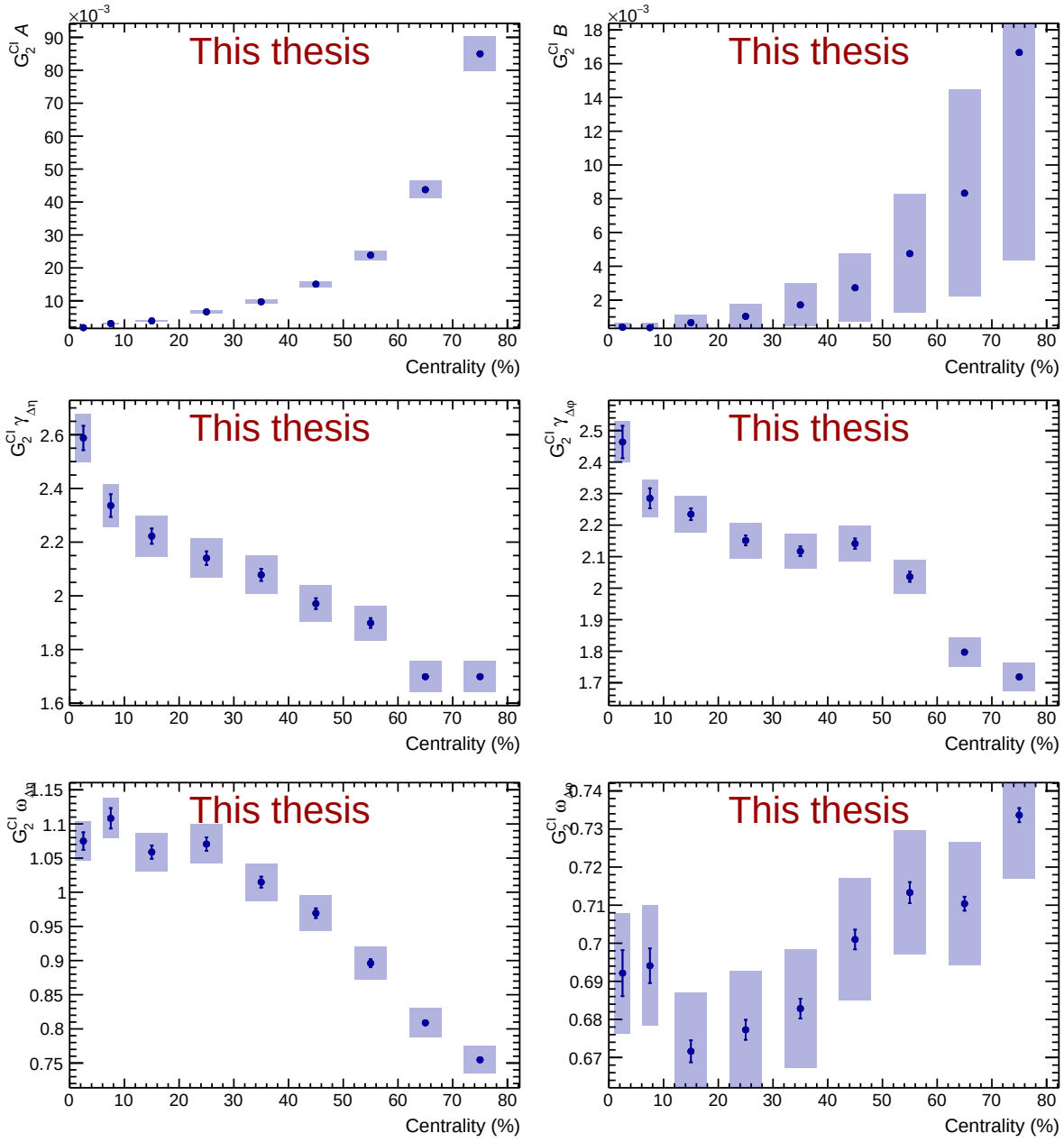

FIGURE 8.1: Centrality dependence of the two-particle transverse momentum correlation G_2^{CI} model parameters from Eq. (5.47) in Pb–Pb collisions at $\sqrt{s_{\mathrm{NN}}} = 2.76\,\mathrm{TeV}$.

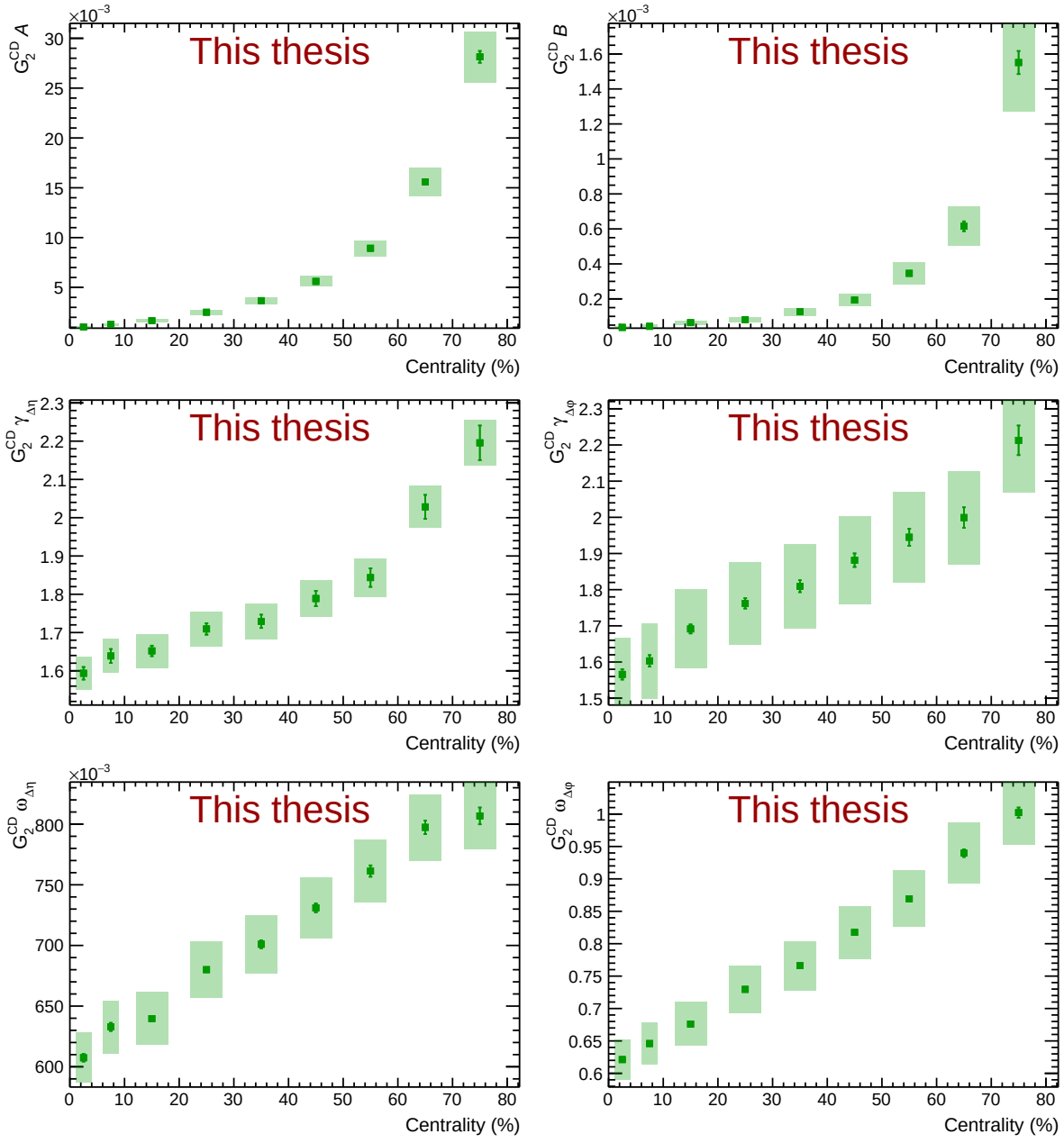

FIGURE 8.2: Centrality dependence of the two-particle transverse momentum correlation G_2^{CD} model parameters from Eq. (5.47) in Pb–Pb collisions at $\sqrt{s_{\mathrm{NN}}} = 2.76\,\mathrm{TeV}$.

8.2 Two-particle transverse momentum correlation widths evolution

The full set of two-particle transverse momentum correlation functions have been parametrized following the procedure described in sect. 5.4.3 using the model in Eq. (5.48). The longitudinal and azimuthal widths have then been extracted using Eq. (5.49).

8.2.1 Evolution with centrality

The evolution with collision centrality of the longitudinal and azimuthal widths of G_2^{CI} and G_2^{CD} correlators is shown in Fig. 8.3. The statistical uncertainties are shown as vertical lines and the

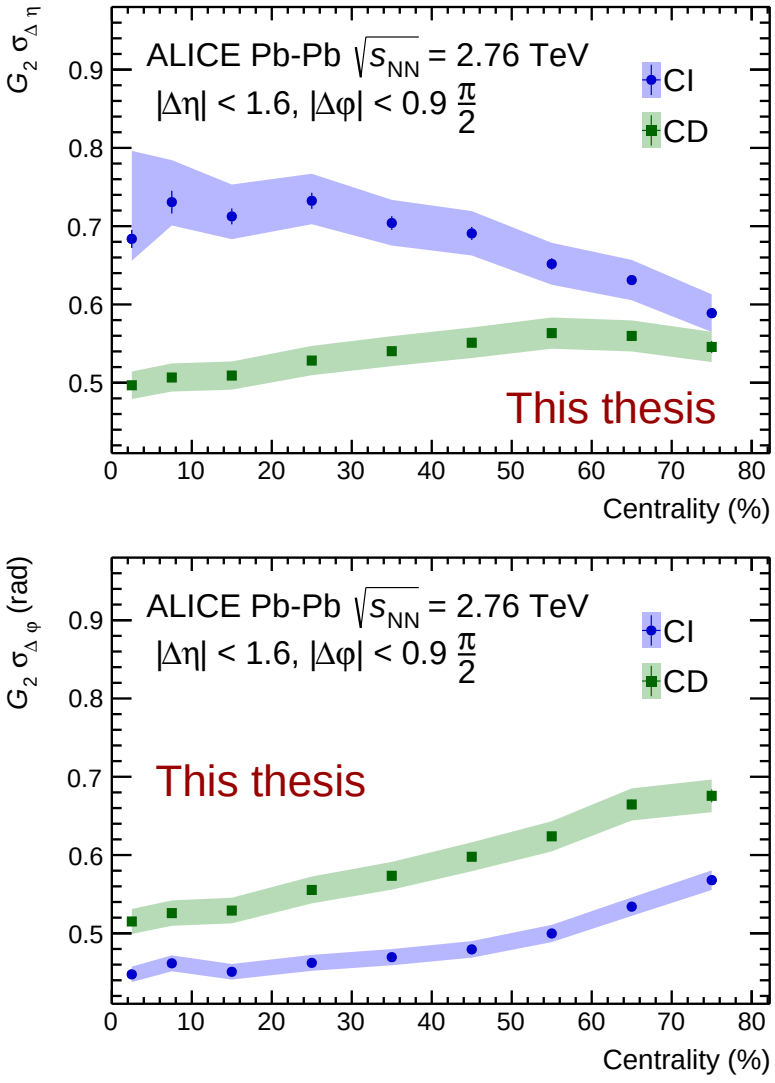

FIGURE 8.3: Evolution with collision centrality of the longitudinal (top panel) and azimuthal (bottom panel) widths of the charge independent (CI) (circles) and charge dependent (CD) (squares) two-particle transverse momentum correlations in Pb–Pb collisions at $\sqrt{s_{\mathrm{NN}}}$ = 2.76 TeV as measured by ALICE.

systematic uncertainties as colored bands. Longitudinally, G_2^{CI} broadens by about 25% from peripheral to semi-central collision, where its width saturates, while G_2^{CD} narrows by about 10% from peripheral

to central collisions. Azimuthally, both, $G_2^{\rm CI}$ and $G_2^{\rm CD}$ consistently narrow, by about 20%, although $G_2^{\rm CD}$ stays 20% wider.

These trends were already anticipated when analyzing the centrality dependence of the shape fit parameters in sect. 8.1. The narrowing trend for the $G_2^{\rm CD}$ correlator, along both dimensions, from peripheral to central collisions, was signaled by the behavior of both set of parameters γ and ω. The longitudinal broadening trend, from peripheral to central collisions, for the $G_2^{\rm CI}$ correlator, was also clearly signaled by the corresponding γ and ω, behaving consistently on that trend. For the azimuthal behavior of the $G_2^{\rm CI}$ correlator while the γ parameter showed a clear growing trend, similar to that of the longitudinal dimension, surpassing the Gaussian threshold, the behavior of the ω parameter imposed its narrowing pull. This is an interesting behavior which will get some insights comparing it with the behavior of the balance function, a two particle number correlation function.

A pair of particles of opposite charge created at a certain instant is subject to the subsequent stages of the evolution of the system. The collective behavior transforms the initial spatial correlation into correlations in the momentum space. The rescattering phase after hadronization also alters the correlation between the initial pair. The final degree of correlation is reflected in the balance function distribution which is a sensitive probe of the balancing charge distribution in momentum space [128]. It was suggested that narrow distributions corresponds to late balancing charges creation while broad distributions are associated with early balancing charges creation [129]. The balance function distribution defined as

$$B^{\alpha\beta}(\vec{p}_i^{\,\alpha},\vec{p}_j^{\,\beta}) = \frac{1}{2}\left(C^{\alpha\beta}(\vec{p}_i^{\,\alpha},\vec{p}_j^{\,\beta}) + C^{\beta\alpha}(\vec{p}_i^{\,\beta},\vec{p}_j^{\,\alpha}) - C^{\alpha\alpha}(\vec{p}_i^{\,\alpha},\vec{p}_j^{\,\alpha}) - C^{\beta\beta}(\vec{p}_i^{\,\beta},\vec{p}_j^{\,\beta})\right), \tag{8.1}$$

where $C^{\alpha\beta}(\vec{p}_i^{\,\alpha},\vec{p}_j^{\,\beta}) = \rho_2^{\alpha\beta}(\vec{p}_i^{\,\alpha},\vec{p}_j^{\,\beta})/\rho_1^{\beta}(\vec{p}_j^{\,\beta})$, is the distribution of pairs of particles, of type α emitted within a phase space bin centered at $\vec{p}_i^{\,\alpha}$ and of type β emitted within a phase space bin centered at $\vec{p}_j^{\,\beta}$, normalized by the number of particles of type β emitted within a phase space bin centered at $\vec{p}_j^{\,\beta}$, is a CD two-particle number correlation of the kind described in sect. 2.4.2. Particles α and β could come from different particle species, or be inclusive being α positive and β negative charges.

The longitudinal and azimuthal widths of the inclusive differential balance function in Pb–Pb collisions at $\sqrt{s_{\rm NN}} = 2.76$ TeV as a function of collision centrality reported by the ALICE collaboration are shown in Fig 8.4 [128]. The balance function in Eq. 8.1 was reported in angular separation, $\Delta\eta = \eta_j - \eta_i$ and $\Delta\varphi = \varphi_j - \varphi_i$. Tracks were selected within the $0.3 < p_{\rm T} < 1.5$ GeV range. The longitudinal (azimuthal) width was reported as the average $\langle\Delta\eta\rangle$ as (similar for $\langle\Delta\varphi\rangle$)

$$\langle\Delta\eta\rangle = \frac{\sum_{i=1}^{k} B^{+-}(\Delta\eta_i)\cdot\Delta\eta_i}{\sum_{i=1}^{k} B{+-}(\Delta\eta_i)} \tag{8.2}$$

where $B^{+-}(\Delta\eta_i)$ is the value of the longitudinal projection of $B{+-}(\Delta\eta,\Delta\varphi)$ for each bin $\Delta\eta_i$, with the sum running over all positive azimuthal bins k. The balance function exhibits a strong narrowing trend from peripheral to central collisions, both longitudinally and azimuthally, similar to what $G_2^{\rm CD}$ shows in Fig. 8.3. The discussion of the comparison with models is included in sect. 8.5. The longitudinal and azimuthal narrowing of the balance function are found to be consistent with a system exhibiting larger radial flow in central collisions but also whose charges are created at a later stage of the collision.

The interesting point, which connects with the previous elaboration on the G_2 widths evolution, is that this narrowing trend from peripheral to central collisions, imposed by radial flow and delayed hadronization, which is clearly also manifested by the G_2 component $G_2^{\rm CD}$ equivalent to the balance function, is also inherently present within the $G_2^{\rm CI}$ component. Evidences of which are the narrowing trend in the $\omega_{\Delta\varphi}$ parameter which, although $\gamma_{\Delta\varphi}$ could suggest a broadening trend, manages to impose an overall narrowing from peripheral to central collisions. Therefore an interplay is present on the G_2 correlation function between narrowing trends driven by radial flow and delayed hadronization and broadening trends driven by viscous evolution. The CI longitudinal broadening is able to manifest itself

from peripheral to semi-central events where saturates while the azimuthal broadening only shows a glimpse of its presence in peripheral collisions to transform in a narrowing towards central ones.

The elaboration on these aspects will continue within the next sections when comparing with STAR results and with models. But first, for being able to compare with STAR results, the evolution of the widths needs to be presented in a different way.

8.2.2 Evolution with the number of participant nucleons

As shown in sect. 2.4.6, the evolution of the longitudinal width of the G_2^{CI} two-particle transverse momentum correlator measured by STAR [77] was reported as a function of the average number of nucleons participating in the collision, $\langle N_{\mathrm{part}} \rangle$, where $\langle N_{\mathrm{part}} \rangle$ is also a measure of the collision centrality. For Pb–Pb collisions at $\sqrt{s_{\mathrm{NN}}} = 2.76$ TeV $\langle N_{\mathrm{part}} \rangle$ was calculated in [130] by the ALICE collaboration. Therefore, the longitudinal and azimuthal widths of G_2^{CI} and G_2^{CD} correlators are shown in Fig. 8.5 as a function of $\langle N_{\mathrm{part}} \rangle$.

The results of this section are the same as in the previous one just with the horizontal axis turned around because increasing in centrality mean more peripheral collisions and, as such, decreasing multiplicity. With this perspective of the evolution of the widths, the comparison with STAR results is straightforward.

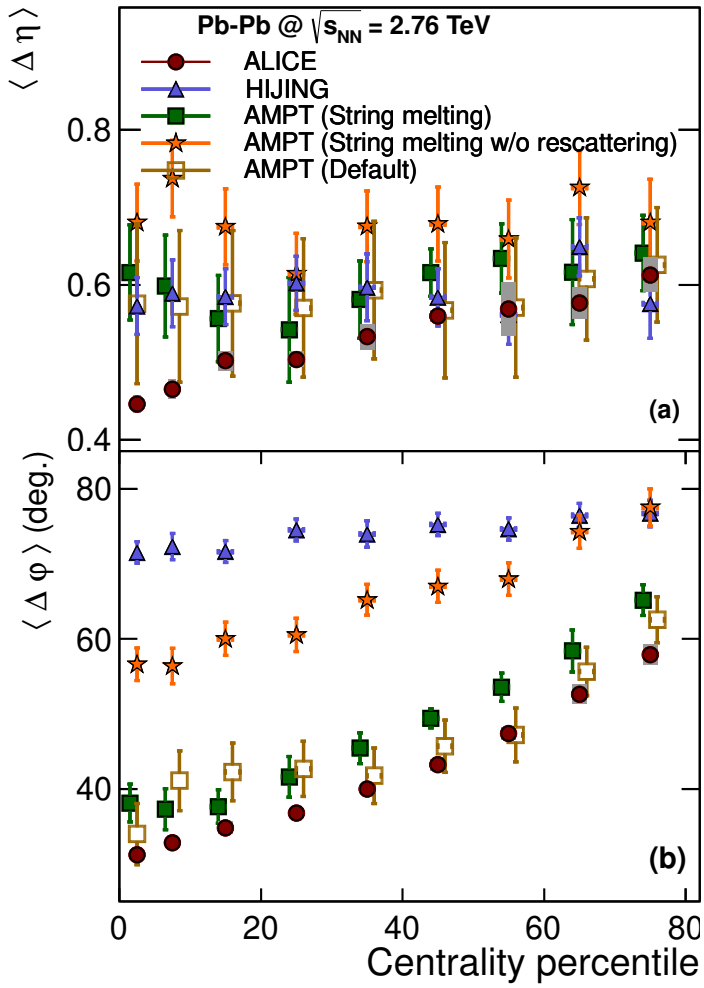

FIGURE 8.4: The centrality dependence of the widths, $\langle\Delta\eta\rangle$ and $\langle\Delta\varphi\rangle$, of the balance function B^{+-} studied in terms of the relative pseudorapidity (a) and the relative azimuthal angle (b), respectively, in Pb–Pb collisions at $\sqrt{s_{\rm NN}}$ = 2.76 TeV as measured by ALICE. The data points are compared to the predictions from HIJING, and AMPT. Error bar of each point corresponds to the statistical uncertainty. The systematic uncertainty is represented by the shaded band around each point [128].

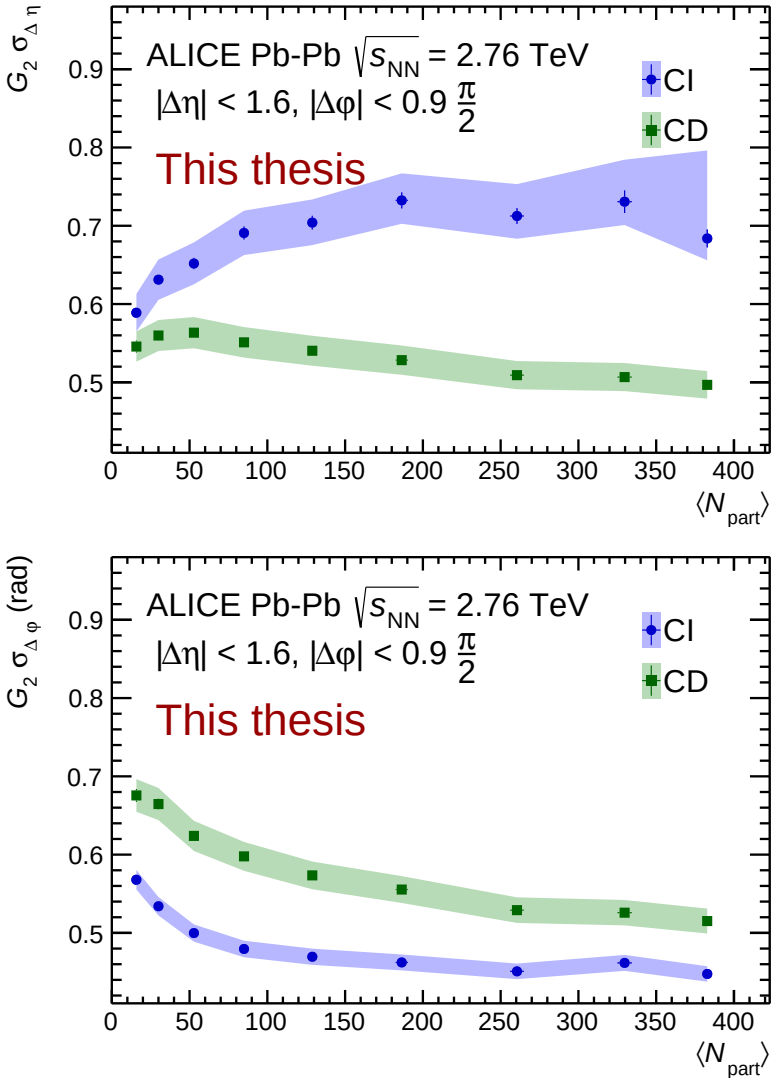

FIGURE 8.5: Longitudinal (top panel) and azimuthal (bottom panel) widths of the charge independent (CI) (circles) and charge dependent (CD) (squares) two-particle transverse momentum correlations as a function of the number of participants, $\langle N_{\rm part} \rangle$, in Pb–Pb collisions at $\sqrt{s_{\rm NN}}$ = 2.76 TeV as measured by ALICE.

8.3 Comparison with STAR results

The two-particle transverse momentum correlator G_2^{CI} and the dependence of its longitudinal width with the centrality of the collision has been only measured previously in Au–Au collisions by the STAR collaboration [77] (see sect. 2.4.6).

The longitudinal width of the two-particle transverse momentum correlator G_2^{CI} as a function of $\langle N_{\mathrm{part}} \rangle$ for Pb–Pb collisions at $\sqrt{s_{\mathrm{NN}}}$ = 2.76 TeV, reported in this PhD thesis, is directly compared in Fig. 8.6 to the results for Au–Au collisions at $\sqrt{s_{\mathrm{NN}}}$ = 200 GeV, reported by the STAR collaboration [77]. In addition, for better comparison, the widths have been also extracted using the method utilized by STAR. It consists on calculating the widths of the pseudorapidity projections as the root mean square (RMS) above a long range baseline determined using a fit to a two Gaussian components ansatz as described in sect. 2.4.6. Fig. 8.6 shows results from both methods. Additionally, the figure shows the RMS limit extracted by the STAR collaboration as also described in sect. 2.4.6.

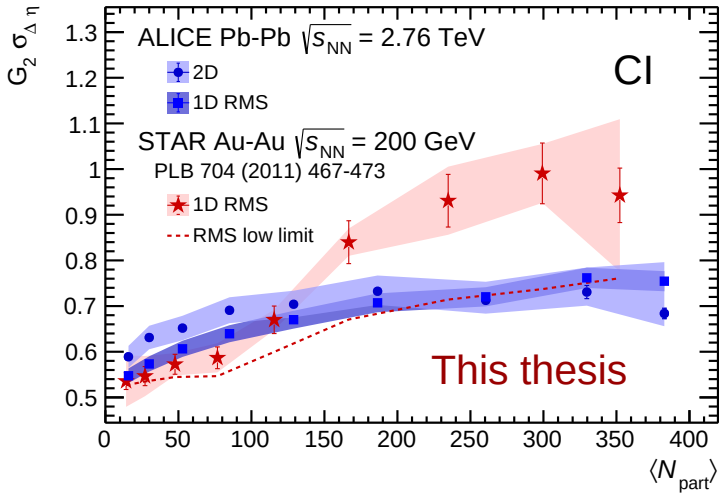

FIGURE 8.6: Longitudinal width of the charge independent (CI) two-particle transverse momentum correlation as a function of the number of participants, $\langle N_{\mathrm{part}} \rangle$, in Pb–Pb collisions at $\sqrt{s_{\mathrm{NN}}}$ = 2.76 TeV as measured by ALICE compared with the extracted from Au–Au collisions at $\sqrt{s_{\mathrm{NN}}}$ = 200 GeV at STAR [77]. ALICE data are reported as extracted from the bi-dimensional fit (2D) as described in sect. 5.4.3 and as extracted by using the same method as described in [77] (1D RMS)

With the STAR method of extracting the longitudinal widths (1D RMS in Fig. 8.6), the G_2^{CI} broadening measured in this PhD thesis amounts to 36% while that observed by STAR reaches 70% showing also a saturation level at semi-central collisions. Both results for the G_2^{CI} widths evolution are consistent with the RMS low limit estimated by STAR.

In the context of the interplay between narrowing and broadening trends, the difference in the saturation levels of the longitudinal width from low to high multiplicity collisions could be explained by the presence of stronger radial flow at LHC energies with respect to RHIC [131] while having a longer-lived QGP phase [65] with a consequence of a smaller charge pair separation at delayed hadronization [128]. But probably these differences, which will cause stronger narrowing trends at the LHC energies, will not be enough for explaining the considerable difference in the widths saturation level. Another potential contributor might come from the bigger influence from jet-like structures at the LHC with respect to RHIC resulting in more particles being emitted with small opening angles which, at the end, can be read also as a narrowing trend. The different procedures for considering the azimuthal

collective behavior and to address the shape of the correlation function could induce differences in the widths extracted. Also the difference in the acceptance on both experiments could also bias the results.

The shape of the longitudinal projection of the two-particle transverse momentum correlation for the most central events measured by STAR and shown in Fig. 2.22 differs of the equivalent measured in this thesis and shown in Fig. 6.3. The use of the generalized Gaussian as described in sect. 5.4.1 was precisely motivated for capturing the plateau shape of the correlator toward most central events. In order to discard a potential effect of the ALICE longitudinal acceptance in the longitudinal width extraction, a toy model was used to fill bidimensional histograms with sampled bidimensional generalized Gaussian of different widths. A bidimensional generalized Gaussian was then fitted to extract the longitudinal and azimuthal widths. The generated longitudinal width as a function of the measured longitudinal width for

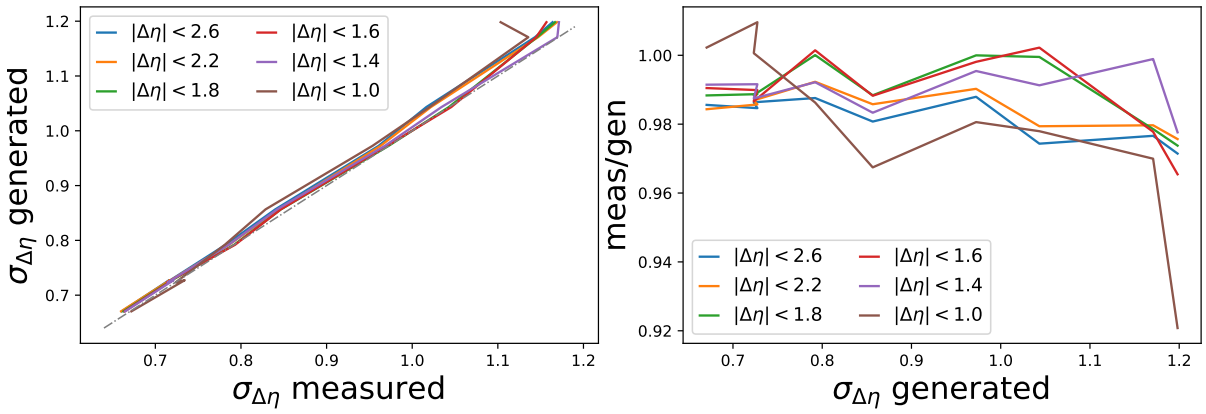

FIGURE 8.7: Left panel: generated longitudinal width vs. measured longitudinal width for different longitudinal acceptances. Right panel: relative deviation of the measured longitudinal width respect to the value used to generate the samples as a function of this value. The longitudinal acceptance used in this thesis is $|\eta| < 0.8 \rightarrow |\Delta\eta| < 1.6$.

different longitudinal acceptances is shown in the left panel of Fig. 8.7. The right panel of Fig. 8.7 shows that for the longitudinal acceptance used in this thesis, $|\eta| < 0.8 \rightarrow |\Delta\eta| < 1.6$, correlation function near side peaks described by bidimensional generalized Gaussian of up to 1.2 longitudinal width, their widths can be measured within a 2% of deviation from the generating value.

8.4 Comparison with other two-particle correlators measured by ALICE

As described in sects. 2.4.2 and 2.4.4, two-particle number correlator R_2 is sensitive to number density fluctuations, while two-particle transverse momentum correlator P_2 is sensitive to transverse momentum fluctuations, and two-particle transverse momentum correlator G_2 is sensitive to transverse momentum currents fluctuations which makes it sensitive to both, number density fluctuations and transverse momentum fluctuations. On this perspective it is of interest to compare the behavior of the three correlators. Two-particle number correlator R_2 and two-particle transverse momentum correlator P_2 have both been measured by the ALICE collaboration [132].

The longitudinal and azimuthal widths of the two-particle transverse momentum correlator G_2 are compared in Fig. 8.8 to the widths of the two-particle number correlator and transverse momentum correlator, R_2 and P_2, respectively, as a function of collision centrality for Pb–Pb collisions at $\sqrt{s_{\mathrm{NN}}} = 2.76$ TeV as measured by the ALICE collaboration [132]. The azimuthal evolution for both R_2^{CI} and P_2^{CI} was not reported and consequently that of G_2^{CI} has not been incorporated.

As shown in Fig. 8.8 the overall trends are consistent among the three correlators. For the charge dependent correlator, the behavior of G_2 mimics that of P_2 with R_2 staying apart but evolving with

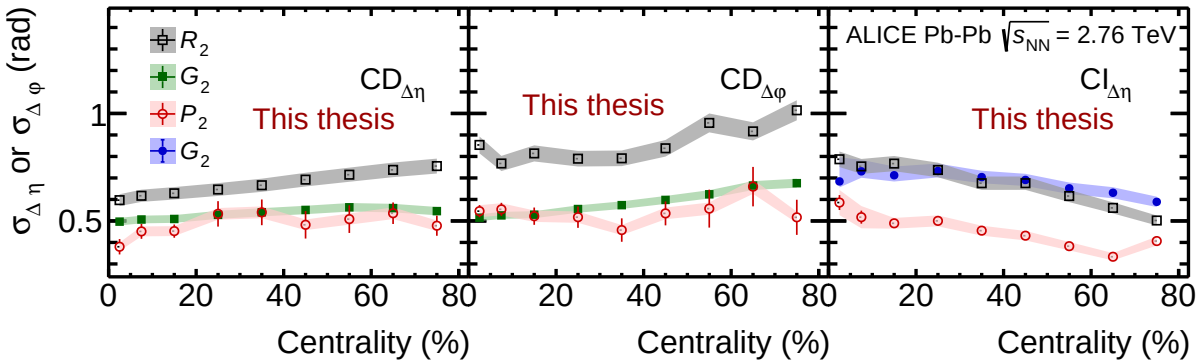

FIGURE 8.8: Left panel: collision centrality evolution of the longitudinal width of two-particle number correlator R_2^{CD} and transverse momentum correlators P_2^{CD} and G_2^{CD}; central panel; idem for the azimuthal width of R_2^{CD}, P_2^{CD} and G_2^{CD}. Right panel: collision centrality evolution of the longitudinal width of R_2^{CI}, P_2^{CI} and G_2^{CI}. Data for R_2^{CI} and P_2^{CI} from [132].

the same trend. For the charge independent correlator is P_2 which stays apart, evolving with the same trend that G_2 which mimics R_2 behavior. The energy-momentum conservation effects are canceled for the CD correlators. In this case both transverse momentum correlators behave similarly. The number correlator, which is sensitive to number density fluctuations, evolves with a similar trend but with a wider reach. The energy-momentum conservation effects are in place for the CI correlators. In this case the G_2 correlator approaches its behavior to the R_2 correlator. The number density fluctuations are more relevant for the G_2 correlator which reaches the R_2 correlator widths. The reach of the transverse momentum fluctuations decreases as shown by the P_2 correlator.

8.5 Models comparison

8.5.1 Longitudinal projections

The near side, $|\Delta\varphi| < \pi/2$, measured longitudinal projections of the two-particle transverse momentum correlations G_2^{CI} and G_2^{CD} are compared to expectations from HIJING event generator and from three flavors of the AMPT event generator (incorporating string melting, incorporating hadronic rescattering, and incorporating both, string melting and hadronic rescattering) in Figs. 8.9 and 8.10, respectively, for each centrality class in Pb–Pb collisions at $\sqrt{s_{\mathrm{NN}}} = 2.76$ TeV

The near side longitudinal projections of the two-particle transverse momentum correlation G_2^{CI} in Fig. 8.9 show a relative order when comparing data to predictions from models. Although this observation is relatively relevant due to the inherent uncertainty in the base line of the correlation function already commented in the sects. 5.5.2 and 8.1. HIJING predictions are relatively matching the behavior of data regarding qualitative shape and correlation strength, for all centrality classes except for peripheral collisions. AMPT predictions are consistently above the behavior shown by data but monotonically approaching it from peripheral to central collisions. A depletion around $\Delta\eta = 0$ with the two shoulders structure is visible from semi-peripheral to central collisions for AMPT with hadronic rescattering incorporated. In the AMPT flavor without hadronic scattering neither the depletion nor the shoulders structure are present. All the models reproduce the monotonic decrease in the near side peak amplitude shown by data.

The near side longitudinal projections of the two-particle transverse momentum correlation G_2^{CD} in Fig. 8.10 show a consistency in the model predictions which diverges from the data behavior. The near side peak of G_2^{CD} predicted from models is relatively flat with an amplitude which decreases monotonically from peripheral to central collisions, while data, although matching the amplitude trend, features a pronounced peak with always higher amplitude. The predictions from HIJING are close to the predictions from AMPT with string melting and hadronic rescattering incorporated for most centrality classes. AMPT with string melting but without hadronic rescattering predictions and AMPT without string melting but with hadronic rescattering predictions stay close for most centrality classes. HIJING longitudinal correlation strength matches AMPT when both scattering phases, the parton scattering and the hadronic rescattering, are present and fully exploited. The AMPT configuration which incorporates string melting breaks the initially produced strings into smaller pieces to also incorporate them in the partonic scattering. When only one phase of scattering is fully incorporated the correlation strength built by AMPT do not reach HIJING predictions level. As said, none of the models reach the correlation strength of data.

8.5.2 Azimuthal projections

The measured azimuthal projections of the two-particle transverse momentum correlations G_2^{CI} and G_2^{CD} are compared to expectations from HIJING event generator and from three flavors of the AMPT event generator (incorporating string melting, incorporating hadronic rescattering, and incorporating both, string melting and hadronic rescattering) in Figs. 8.11 and 8.12, respectively, for each centrality class in Pb–Pb collisions at $\sqrt{s_{\mathrm{NN}}} = 2.76$ TeV

The azimuthal projections of the two-particle transverse momentum correlation G_2^{CI} in Fig. 8.11 highlights the main differences between HIJING and AMPT models. HIJING model does not incorporate collective behavior. As potential correlation sources, HIJING incorporates jet-like effects as well as resonance decays, but not collective flow. As Fig. 8.11 shows, HIJING G_2^{CI} does not present the characteristic flow modulation featured by data and by AMPT. AMPT on its turn, takes HIJING as input and incorporates two potential sources of collectivity as described in sect. 3.11.5: partonic and hadronic rescattering. The configuration which incorporates string melting breaks the initially produced strings into smaller pieces to also incorporate them into the partonic rescattering. Consistent with the behavior exhibited by the longitudinal projections, the average value of HIJING predictions matches

that of data for all centrality classes except peripheral collisions, missing, as mentioned, the flow modulation. Also the three AMPT configurations predicted averages stay consistently above that of data but monotonically approaching it from peripheral to central collisions. The flow modulation amplitude monotonically decreases from peripheral to central collision but with AMPT predictions showing lower amplitude than data. This lower flow modulation amplitude is specially the case for the version which incorporates string melting but not hadronic rescattering, consistent with the picture of a part of the collective flow being built in that last phase in AMPT.

Consistent, as well, with the behavior exhibited by the longitudinal projections, the azimuthal projections of the two-particle transverse momentum correlation G_2^{CD} in Fig. 8.12 show coincident model predictions which diverge from data behavior. The near side peak of G_2^{CD} predicted from models feature a monotonically decreasing amplitude from peripheral to central collisions but is consistently lower than the featured by data which follows the same trend. From semi-peripheral to central collisions AMPT with string melting and hadronic rescattering incorporated predictions feature slightly stronger correlations than HIJING and the other AMPT configurations. In this case the flow modulation is excluded but what is not is the radial flow which as was described in sect.8.2 affects the CD component. The presence of both full rescattering phases generates stronger flow modulation and stronger radial flow which manifests by larger amplitude in the correlation for that AMPT configuration. None of the models exhibit the plateau featured by data from semi-peripheral to peripheral collisions compatible with HBT effects.

8.5.3 Evolution with centrality of the width in the longitudinal dimension

The dependence with collision centrality of the measured longitudinal width of the two-particle transverse momentum correlation G_2^{CI} is compared to expectations from HIJING event generator and from three flavors of the AMPT event generator (incorporating string melting, incorporating hadronic rescattering, and incorporating both, string melting and hadronic rescattering) in Fig. 8.13 for Pb–Pb collisions at $\sqrt{s_{\mathrm{NN}}}$ = 2.76 TeV. The width values are shown in the top panel while to better quantify the evolution trend, the relative width values with respect to the peripheral collisions width are shown in the bottom panel.

G_2^{CI} longitudinal width evolution with centrality is qualitative described by AMPT with string melting and hadronic rescattering incorporated although quantitatively it is around 25% wider. AMPT with hadronic rescattering incorporated and AMPT with only string melting incorporated, although qualitatively show an opposite trend to what data features, describe the width magnitude from semi-peripheral to central collisions but overestimate that of the peripheral ones. HIJING does not describe data trend. From the AMPT perspective, longitudinal broadening from peripheral to central collisions is compatible with an excess in scattering in the partonic phase, enforced by string melting, and the presence of hadronic rescattering. If one or the other is not incorporated the AMPT model predicts G_2^{CI} slight narrowing from peripheral to central collisions. The slightly narrowing trend predicted by HIJING is interesting by the fact that HIJING incorporates jet-like effects, with a basic jet quenching modeling, as well as resonances. None of them predict any longitudinal broadening on G_2^{CI}.

The dependence with collision centrality of the measured longitudinal width of the two-particle transverse momentum correlation G_2^{CD} is compared to expectations from HIJING event generator and from three flavors of the AMPT event generator (incorporating string melting, incorporating hadronic rescattering, and incorporating both, string melting and hadronic rescattering) in Fig. 8.14 for Pb–Pb collisions at $\sqrt{s_{\mathrm{NN}}}$ = 2.76 TeV. The width values are shown in the top panel while to better quantify the evolution trend, the relative width values with respect to the peripheral collisions width are shown in the bottom panel.

G_2^{CD} longitudinal width evolution with centrality is qualitatively described by HIJING. Quantitatively the widths predicted by HIJING although do not describe the data are relatively close. The fact that HIJING does not incorporate collective behavior is not significant in the context of the CD correlator,

although radial flow, which is neither incorporated by HIJING, is. The narrowing trend shown by HIJING might be expected due to mini-jets or resonance effects where particles tend to be more collimated. AMPT model predicts broadening from peripheral to central collisions, in contraposition to data trend, for the three considered configurations. The fact that AMPT with only hadronic rescattering incorporated predicts less longitudinal broadening from peripheral to central collisions, suggests that the string melting phase, which incorporates the melted strings into the partonic rescattering, originates extra longitudinal broadening for the CD correlator. Hadronic rescattering is able to compensate this broadening when considered within the CI correlator as Fig.8.13 shows. Another plausible explanation for this exaggerated broadening trend predicted by AMPT for G_2^{CD} is the violation of local charge conservation in the late hadronization scenario. As was described in sect. 8.2, local charge conservation within a late hadronization scenario causes the longitudinal width of the balance function, i.e. the CD correlator, to narrow from peripheral to central collisions. Clearly, AMPT predictions do not narrow.

8.5.4 Evolution with centrality of the width in the azimuthal dimension

The dependence with collision centrality of the measured azimuthal width of the two-particle transverse momentum correlation G_2^{CI} is compared to expectations from HIJING event generator and from three flavors of the AMPT event generator (incorporating string melting, incorporating hadronic rescattering, and incorporating both, string melting and hadronic rescattering) in Fig. 8.15 for Pb–Pb collisions at $\sqrt{s_{\mathrm{NN}}}$ = 2.76 TeV. The width values are shown in the top panel while to better quantify the evolution trend, the relative width values with respect to the peripheral collisions width are shown in the bottom panel.

G_2^{CI} azimuthal narrowing from peripheral to central collisions is qualitatively described by AMPT with string melting incorporated either with or without hadronic rescattering. The configuration with hadronic rescattering predicts a slightly wider correlator while the one without hadronic rescattering describes the correlator widths from semi-peripheral to central collisions overestimating the correlator widths for peripheral collisions. AMPT without string melting but with hadronic rescattering predicts a correlator longitudinal width independent of centrality. This behavior is consistent with AMPT building most of the radial flow in the parton rescattering phase when the strings from the initial phase are melted and incorporated to the rescattering process, with the latest phase of hadronic rescattering having no effect in the build out of radial flow. This picture is also consistent with the behavior described when analyzing the projections of the correlator in the previous sections. HIJING predicts slight narrowing from central to peripheral to central collisions, failing in describing the data, although consistent with the predicted longitudinal behavior for the G_2^{CI} correlator previously described.

The dependence with collision centrality of the measured azimuthal width of the two-particle transverse momentum correlation G_2^{CD} is compared to expectations from HIJING event generator and from three flavors of the AMPT event generator (incorporating string melting, incorporating hadronic rescattering, and incorporating both, string melting and hadronic rescattering) in Fig. 8.16 for Pb–Pb collisions at $\sqrt{s_{\mathrm{NN}}}$ = 2.76 TeV. The width values are shown in the top panel while to better quantify the evolution trend, the relative width values with respect to the peripheral collisions width are shown in the bottom panel.

G_2^{CD} azimuthal narrowing from peripheral to central collisions is qualitatively described by the four models although the correlator widths are overestimated by all of them. AMPT behaves in the opposite way as it does in the longitudinal dimension. AMPT with hadronic rescattering incorporated predicts a narrower correlator than AMPT with only string melting incorporated does. This picture is consistent with AMPT building the most part of the radial flow in the latest stage of hadronic rescattering while incorporating melted strings in the parton rescattering stage counteracts the narrowing. The qualitative behavior is then the same in both dimensions although in the longitudinal dimension the broadening trend is super imposed by the string melting effects with the hadronic rescattering counteracting it. The

slightly narrowing trend shown by HIJING is consistent with its behavior in the longitudinal dimension and attributable there to the presence of mini-jets or resonances.

The above exhaustive comparisons might help to constrain and refine the theoretical models which nourish those event generators.

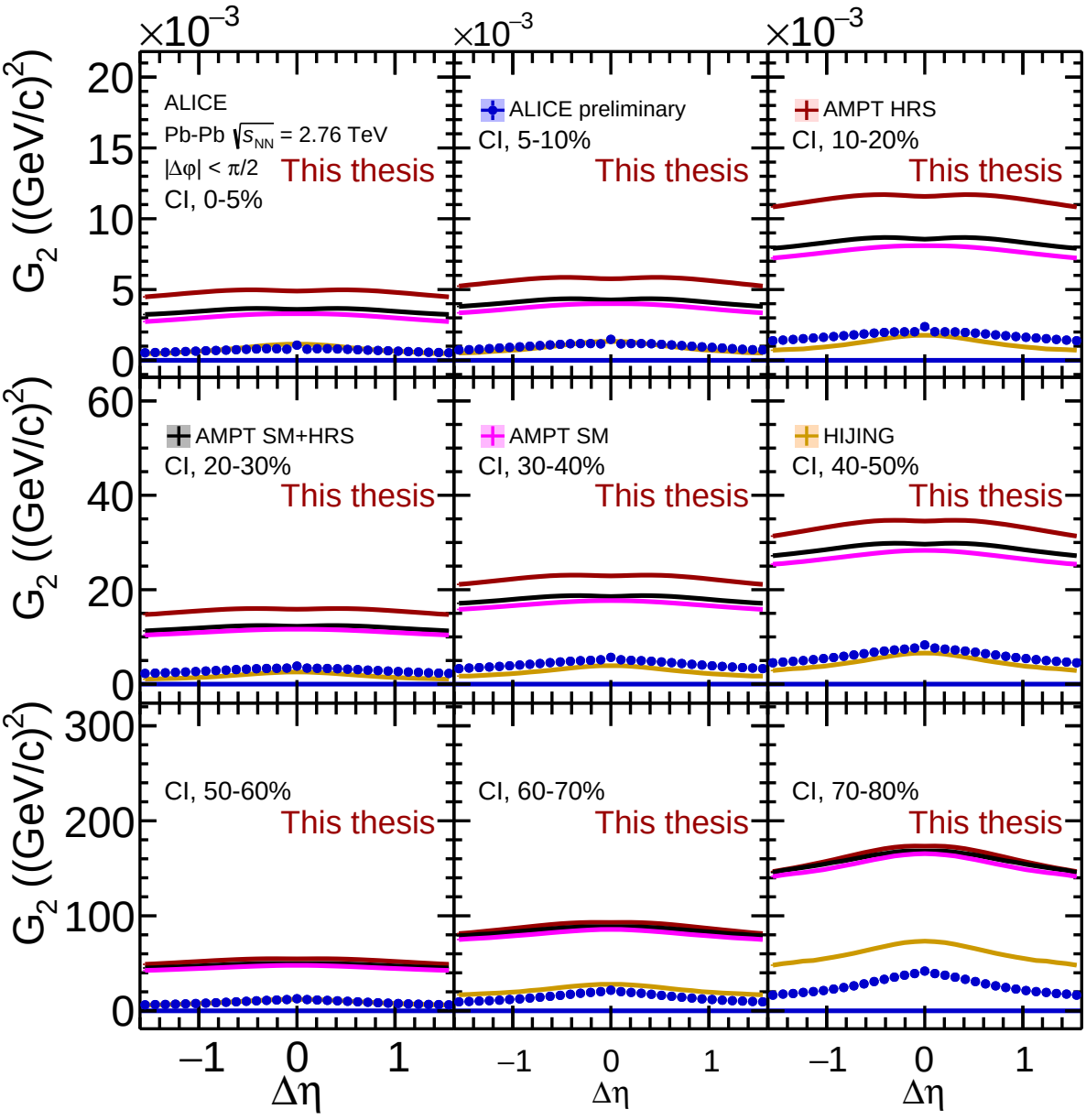

FIGURE 8.9: Near side $\Delta\eta$ projection for the charge independent (CI) two-particle transverse momentum correlation for each centrality class in Pb–Pb collisions at $\sqrt{s_{\mathrm{NN}}}$ = 2.76 TeV as measured by ALICE, compared to expectations from HIJING and three flavors of the AMPT generator, incorporating hadronic rescattering (HRS), incorporating string melting (SM), and incorporating both, hadronic rescattering and string melting (SM+HRS). For data, error bars represent statistical uncertainties (most of them lower than the marker size) while systematic uncertainties are represented by colored bands. For models, statistical uncertainties are represented by colored bands.

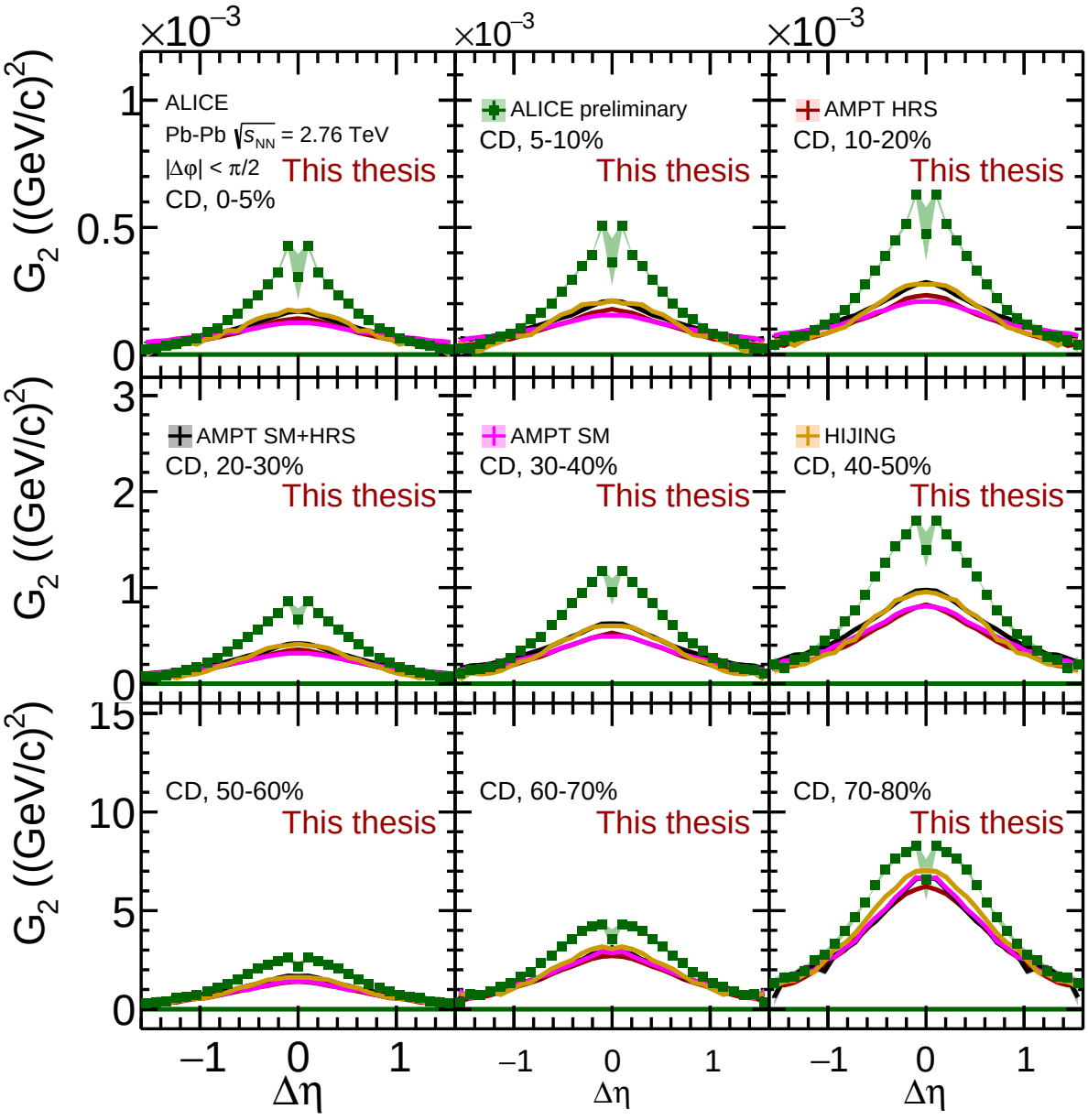

FIGURE 8.10: Near side $\Delta\eta$ projection for the charge dependent (CD) two-particle transverse momentum correlation for each centrality class in Pb–Pb collisions at $\sqrt{s_{\mathrm{NN}}}$ = 2.76 TeV as measured by ALICE, compared to expectations from HIJING and three flavors of the AMPT generator, incorporating hadronic rescattering (HRS), incorporating string melting (SM), and incorporating both, hadronic rescattering and string melting (SM+HRS). For data, error bars represent statistical uncertainties (most of them lower than the marker size) while systematic uncertainties are represented by colored bands. For models, statistical uncertainties are represented by colored bands.

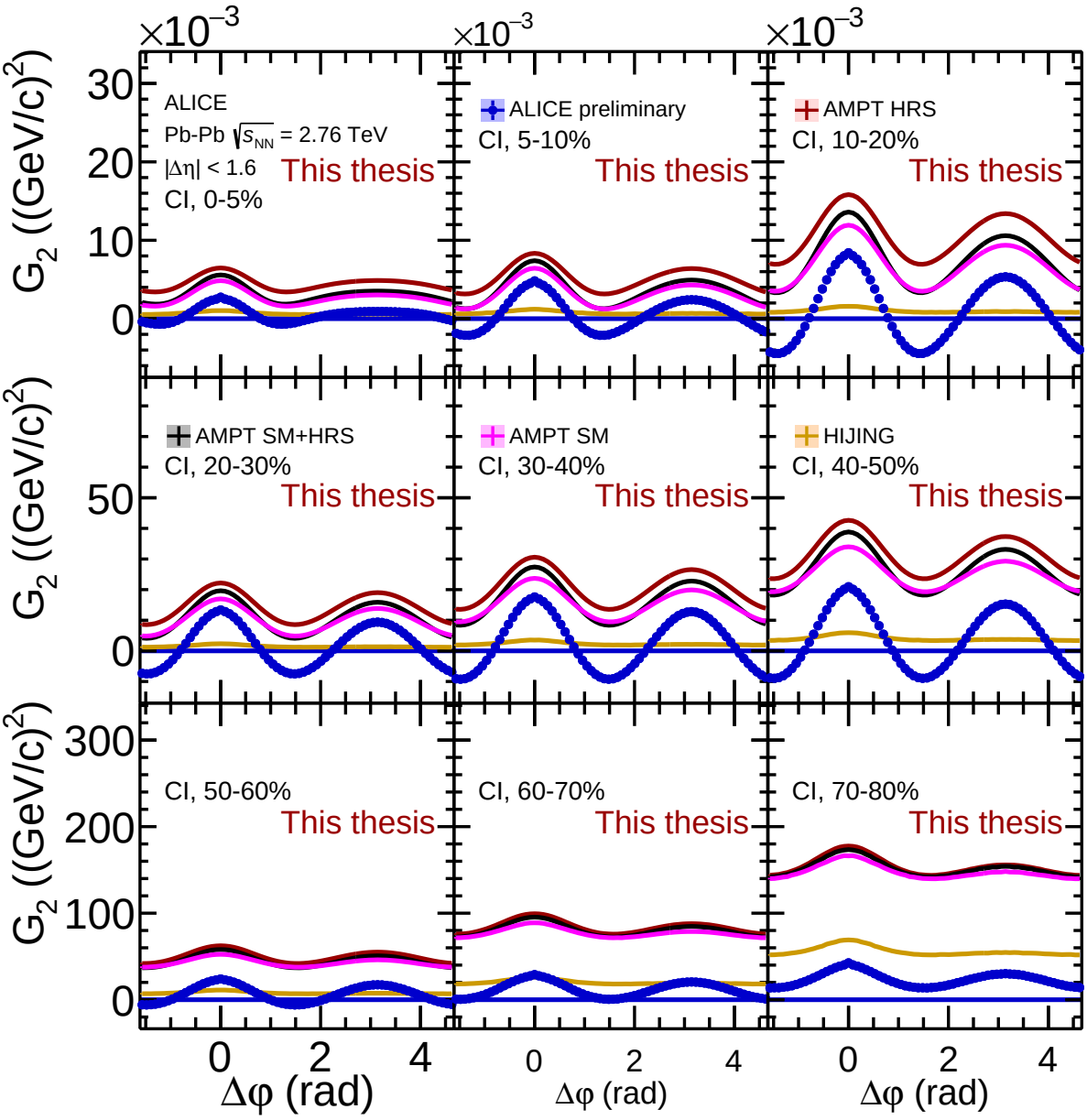

FIGURE 8.11: $\Delta\varphi$ projection for the charge independent (CI) two-particle transverse momentum correlation for each centrality class in Pb–Pb collisions at $\sqrt{s_{\rm NN}}$ = 2.76 TeV as measured by ALICE, compared to expectations from HIJING and three flavors of the AMPT generator, incorporating hadronic rescattering (HRS), incorporating string melting (SM), and incorporating both, hadronic rescattering and string melting (SM+HRS). For data, error bars represent statistical uncertainties (most of them lower than the marker size) while systematic uncertainties are represented by colored bands. For models, statistical uncertainties are represented by colored bands.

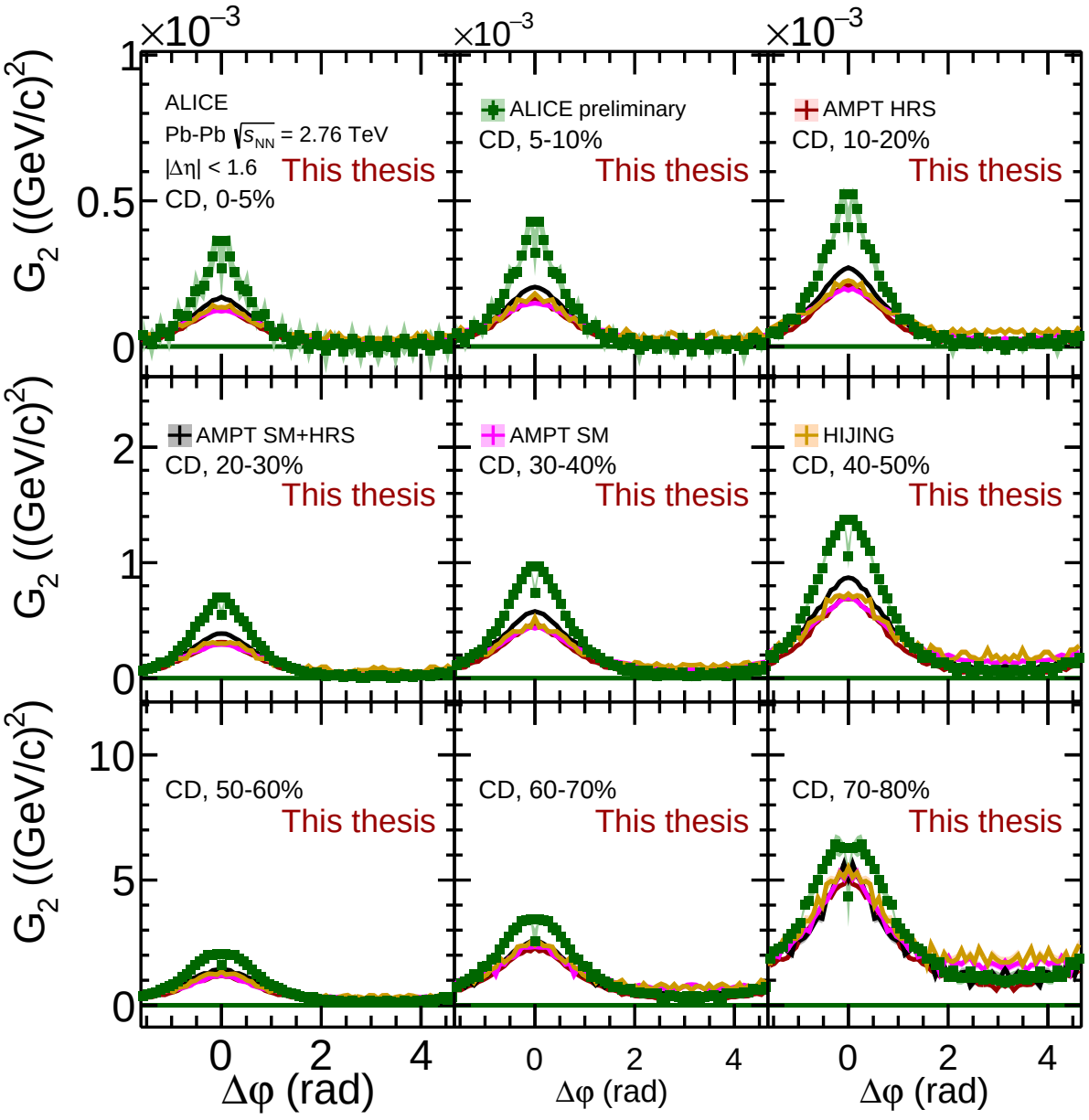

FIGURE 8.12: $\Delta\varphi$ projection for the charge dependent (CD) two-particle transverse momentum correlation for each centrality class in Pb–Pb collisions at $\sqrt{s_{\mathrm{NN}}}$ = 2.76 TeV as measured by ALICE, compared to expectations from HIJING and three flavors of the AMPT generator, incorporating hadronic rescattering (HRS), incorporating string melting (SM), and incorporating both, hadronic rescattering and string melting (SM+HRS). For data, error bars represent statistical uncertainties (most of them lower than the marker size) while systematic uncertainties are represented by colored bands. For models, statistical uncertainties are represented by colored bands.

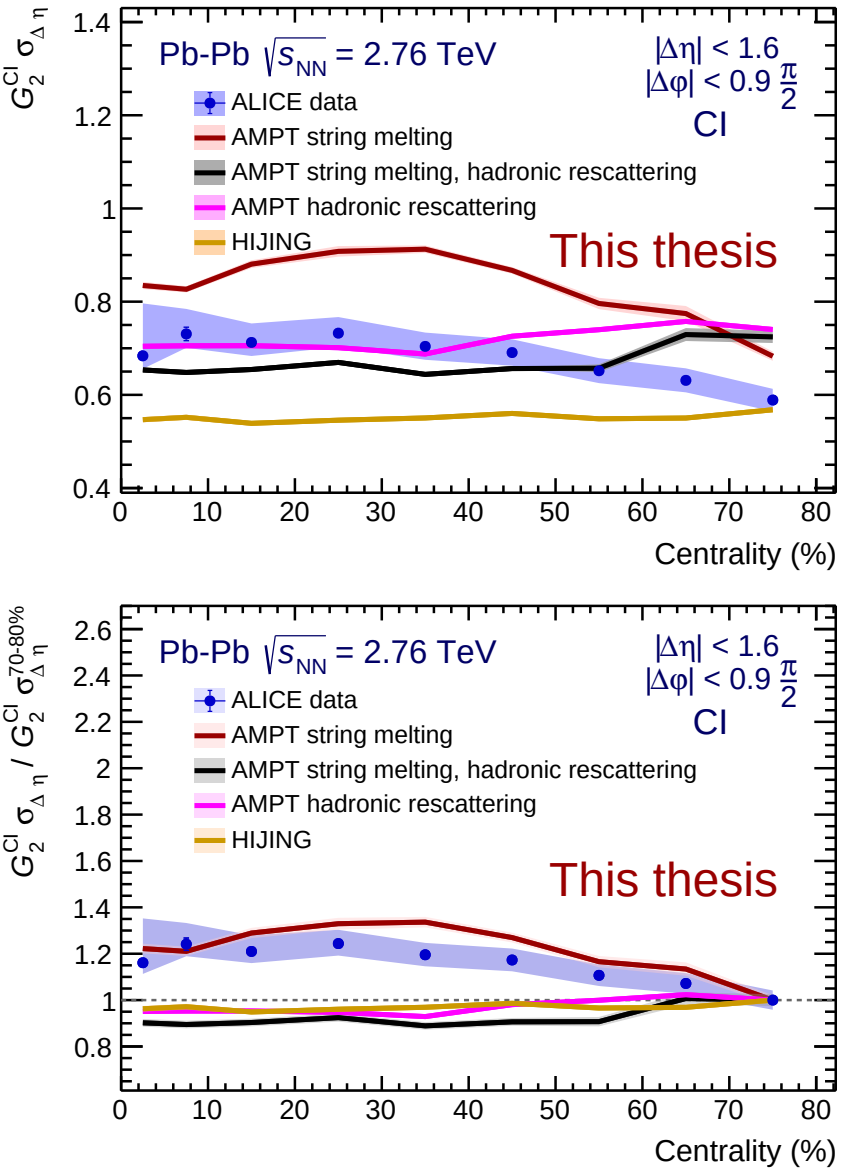

FIGURE 8.13: Evolution with centrality of the longitudinal width of the charge independent (CI) two-particle transverse momentum correlations in Pb–Pb collisions at $\sqrt{s_{NN}}$ = 2.76 TeV as measured by ALICE, compared to expectations from HIJING and from three flavors of the AMPT generator, incorporating hadronic rescattering, incorporating string melting, and incorporating both, hadronic rescattering and string melting. Top panel shows the absolute values of the widths. Bottom panel shows the relative evolution of the widths with respect to peripheral collisions. For data, error bars represent statistical uncertainties (most of them lower than the marker size) while systematic uncertainties are represented by colored bands. For models, statistical uncertainties are represented by colored bands.

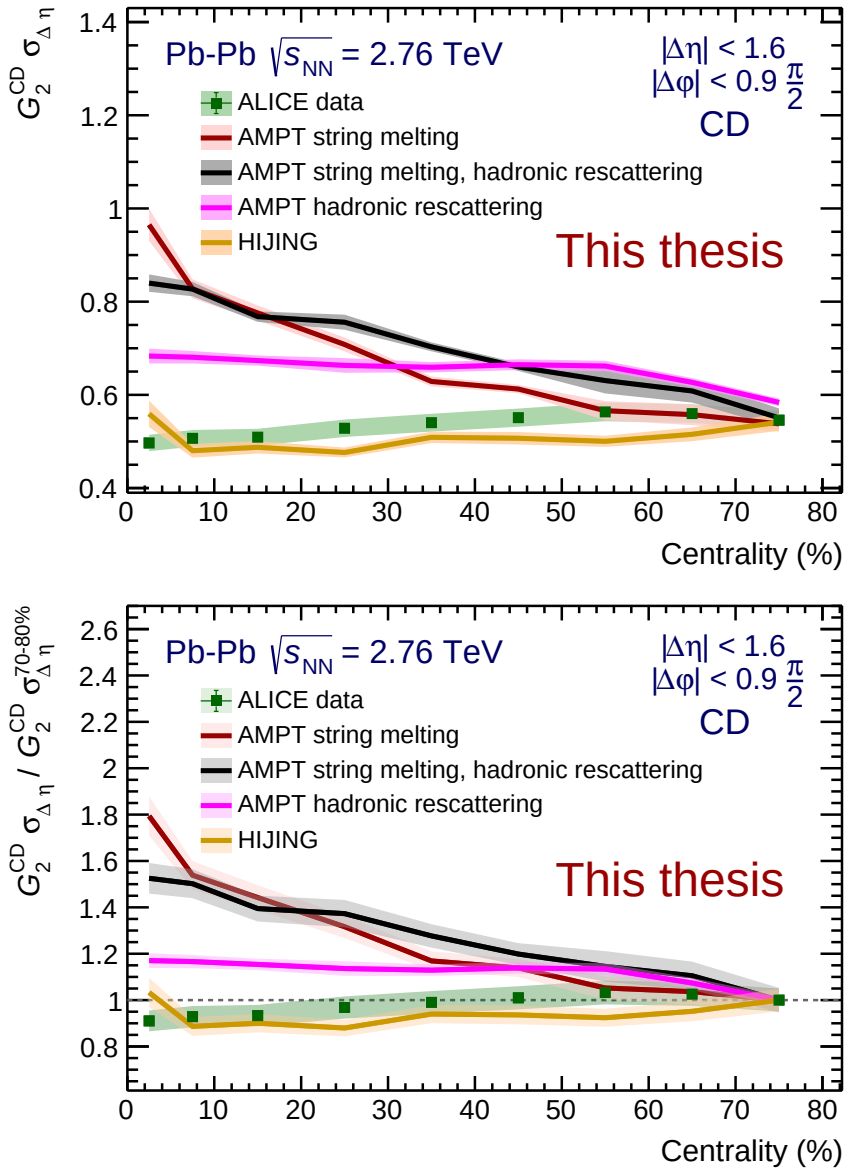

FIGURE 8.14: Evolution with centrality of the longitudinal width of the charge dependent (CD) two-particle transverse momentum correlations in Pb–Pb collisions at $\sqrt{s_{NN}}$ = 2.76 TeV as measured by ALICE, compared to expectations from HIJING and from three flavors of the AMPT generator, incorporating hadronic rescattering, incorporating string melting, and incorporating both, hadronic rescattering and string melting. Top panel shows the absolute values of the widths. Bottom panel shows the relative evolution of the widths with respect to peripheral collisions. For data, error bars represent statistical uncertainties (most of them lower than the marker size) while systematic uncertainties are represented by colored bands. For models, statistical uncertainties are represented by colored bands.

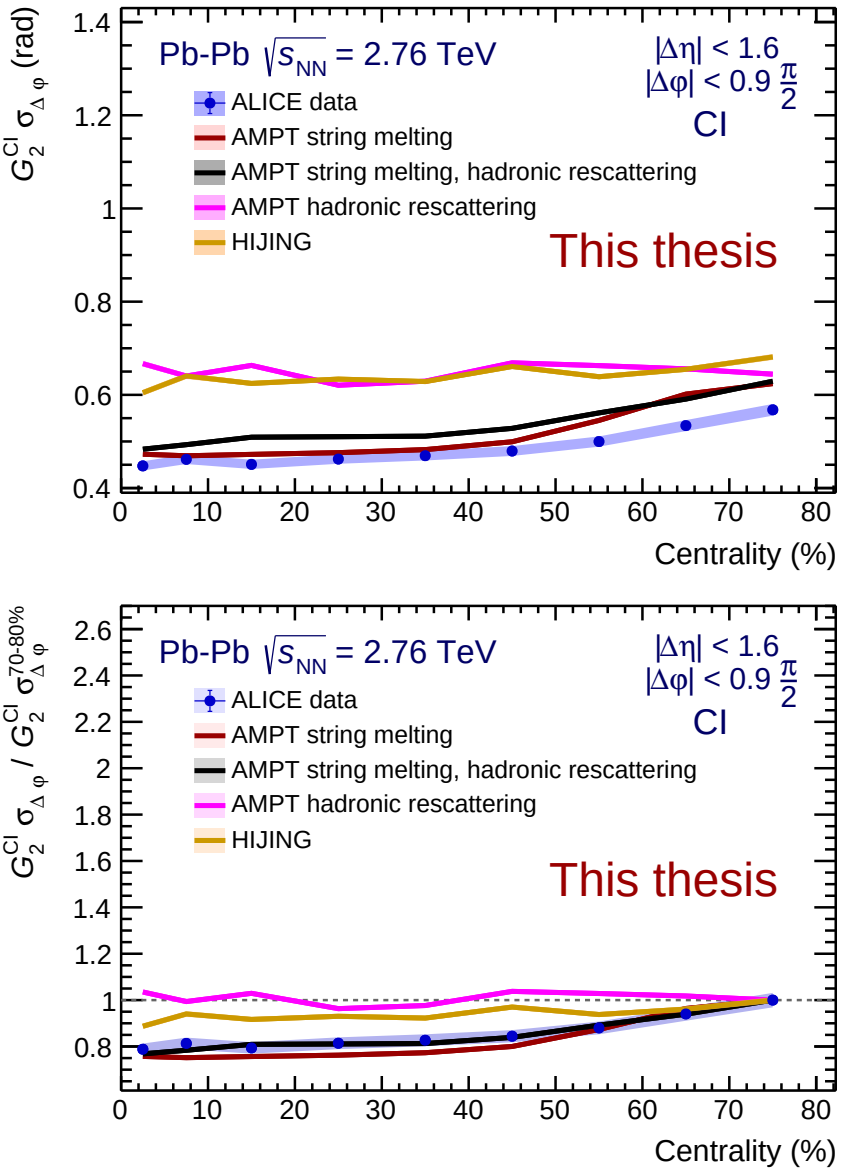

FIGURE 8.15: Evolution with centrality of the azimuthal width of the charge independent (CI) two-particle transverse momentum correlations in Pb–Pb collisions at $\sqrt{s_{NN}}$ = 2.76 TeV as measured by ALICE, compared to expectations from HIJING and from three flavors of the AMPT generator, incorporating hadronic rescattering, incorporating string melting, and incorporating both, hadronic rescattering and string melting. Top panel shows the absolute values of the widths. Bottom panel shows the relative evolution of the widths with respect to peripheral collisions. For data, error bars represent statistical uncertainties (most of them lower than the marker size) while systematic uncertainties are represented by colored bands. For models, statistical uncertainties are represented by colored bands.

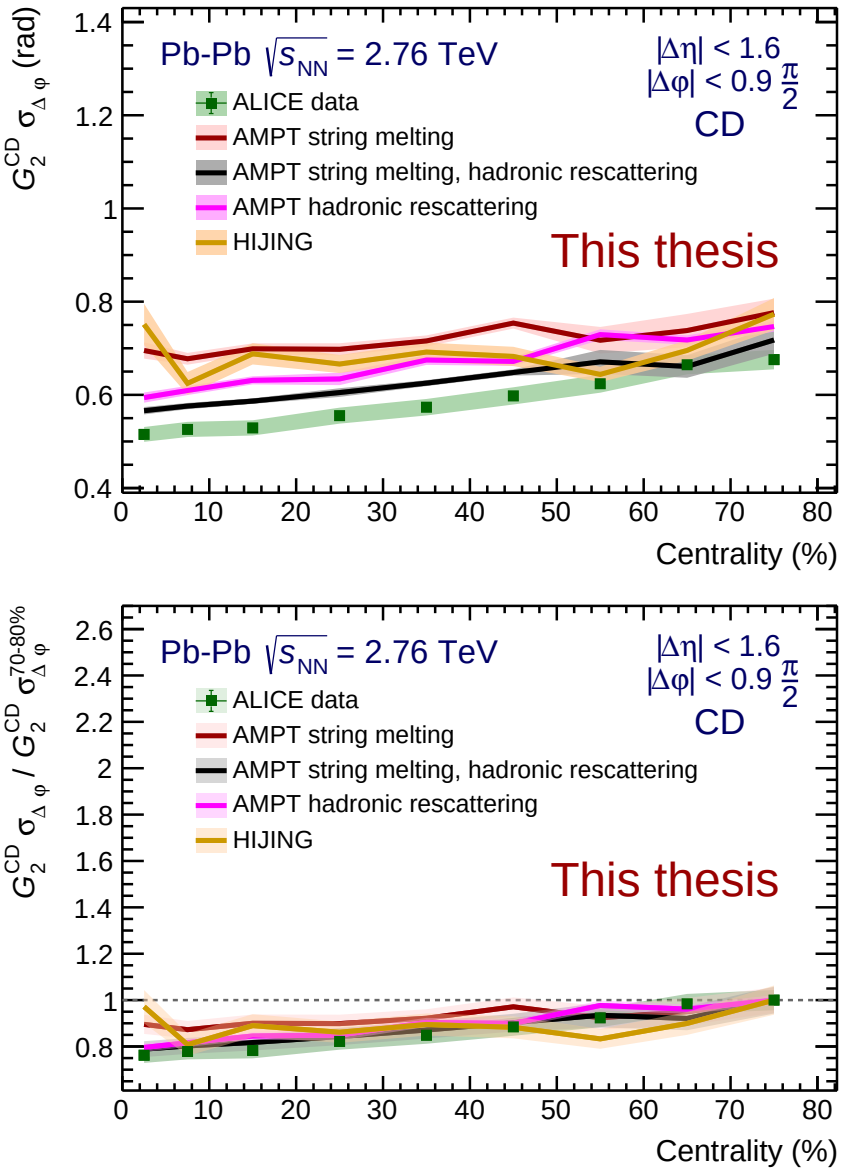

FIGURE 8.16: Evolution with centrality of the azimuthal width of the charge dependent (CD) two-particle transverse momentum correlations in Pb–Pb collisions at $\sqrt{s_{NN}}$ = 2.76 TeV as measured by ALICE, compared to expectations from HIJING and from three flavors of the AMPT generator, incorporating hadronic re-scattering, incorporating string melting, and incorporating both, hadronic rescattering and string melting. Top panel shows the absolute values of the widths. Bottom panel shows the relative evolution of the widths with respect to peripheral collisions. For data, error bars represent statistical uncertainties (most of them lower than the marker size) while systematic uncertainties are represented by colored bands. For models, statistical uncertainties are represented by colored bands.

8.6 Evolution from small systems to Pb–Pb

The usual signs of QGP formation in rHIC are the presence of jet-quenching [133] and long range collective effects [134]. Jet-quenching is the medium induced modification of a high p_{T} parton produced at the early phases of the collision. Jet-quenching manifests as a deviation from unity of p_{T} spectrum ratio to a reference obtained by scaling the measurement in pp collisions with the number of binary nucleon-nucleon collisions. Long range collective effects manifest as the azimuthal flow modulation described by the flow coefficients. Measurements at the LHC in p–Pb collisions [135] shown the absence of jet-quenching effects, at least in that way of being manifested. However, two-particle number correlations measured as a function of the relative angular separation in high multiplicity pp and p–Pb systems showed similar characteristics to the measured in Pb–Pb collisions [136]. Furthermore measurements of anisotropic flow coefficients and their cross-correlations using multi-particle cumulants in high multiplicity pp and p–Pb collisions [137, 138] indicated the presence of long range collective behavior in these systems. Although at the multiplicities selected in the pp analyses within this thesis have not shown any long range collective effects (see sect. 7.2), the p–Pb analyses have clearly shown them (see sect. 7.1). The question whether QGP is or not produced in these "small" systems is still a matter of active research.

Long range correlations are built up at early phases of the system evolution while short range correlations are build up along system evolution reflecting medium characteristics, system dynamics and particle production mechanism. Results for the G_2 two-particle transverse momentum correlators in pp and p–Pb systems have been shown in sects. 7.2 and 7.1. G_2 correlators have shown their abilities to "sense" the medium and its evolution. In this section the the evolution of the two-particle transverse momentum correlation G_2 in pp and p–Pb systems is shown compared with Pb–Pb results.

8.6.1 Longitudinal widths evolution

The longitudinal evolution of G_2^{CI} and G_2^{CD} two-particle transverse momentum correlations as a function of the average number of charged particles, $\langle N_{\mathrm{ch}} \rangle$, are shown in Fig. 8.17 for pp collisions at $\sqrt{s_{\mathrm{NN}}}$ = 7 TeV, p–Pb collisions $\sqrt{s_{\mathrm{NN}}}$ = 5.02 TeV, and Pb–Pb collisions $\sqrt{s_{\mathrm{NN}}}$ = 2.76 TeV and $\sqrt{s_{\mathrm{NN}}}$ = 5.02 TeV. In Pb–Pb collisions, the G_2^{CI} correlator clearly manifests the longitudinal broadening from low to high multiplicity collisions characteristic of a viscous medium. The multiplicity is slightly higher in Pb–Pb collisions at higher energy as expected. As was mention in sect. 7.1, the Pb–Pb at $\sqrt{s_{\mathrm{NN}}}$ = 5.02 TeV results probably are still affected by detector effects but, they show an earlier saturation compatible with slightly higher radial flow at that energies [139]. The pp and p–Pb systems evolve with constant width from low to relatively high multiplicity collisions, with the pp system showing a slight narrowing trend. The evolution of the p–Pb system is specially relevant because, at the considered multiplicities, the G_2^{CI} correlator have shown clear signs of long range collective behavior in that system. While the transition from the pp system to the p–Pb system is smooth, with similar correlator width for equivalent multiplicities, the transition from the p–Pb system to the Pb–Pb system is abrupt, although there is not so much multiplicity overlap.

In pp and p–Pb collisions, the G_2^{CD} correlator clearly shows a consistent and monotonic narrowing trend from low to relatively high multiplicity events. The width for the p–Pb collisions with higher multiplicities matches that of the most peripheral Pb–Pb collisions. But for Pb–Pb collisions there is a fundamental difference. As was described in sect. 8.2, the longitudinal evolution of the G_2^{CD} correlator manifest the interplay between the narrowing trend imposed by late hadronization and radial flow effects and the broadening trend imposed by viscous diffusion. The interplay is also shown by the Pb–Pb results at high energy showing even a bit earlier saturation consistent with stronger narrowing trend at that energy. But it is needed to wait for the evaluation of the systematic uncertainties before drawing conclusions.

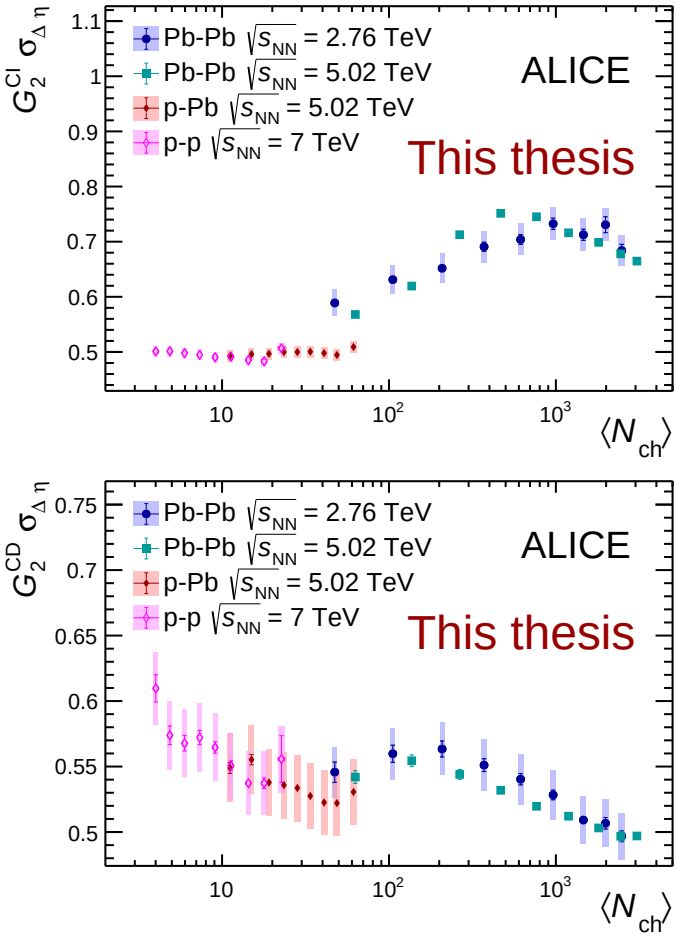

FIGURE 8.17: Longitudinal width of the two-particle transverse momentum correlation G_2^{CI} (top panel) and G_2^{CD} (bottom panel) as a function of $\langle N_{ch} \rangle$ in pp collisions at $\sqrt{s_{NN}}$ = 7 TeV, p–Pb collisions at $\sqrt{s_{NN}}$ = 5.02 TeV, Pb–Pb collisions at $\sqrt{s_{NN}}$ = 2.76 TeV, and Pb–Pb collisions at $\sqrt{s_{NN}}$ = 5.02 TeV as measured in ALICE. $\langle N_{ch} \rangle$ are the number of charged particles involved in the extraction of the correlation function after NUA and NUE corrections (see sect. 5.3). Error bars represent statistical uncertainties while systematic uncertainties are represented by colored bands. For Pb–Pb collisions at $\sqrt{s_{NN}}$ = 5.02 TeV only statistical errors are incorporated.

8.6.2 Azimuthal widths evolution

The azimuthal evolution of G_2^{CI} and G_2^{CD} two-particle transverse momentum correlations as a function of the average number of charged particles, $\langle N_{\mathrm{ch}} \rangle$, are shown in Fig. 8.18 for pp collisions at $\sqrt{s_{\mathrm{NN}}}$ = 7 TeV, p–Pb collisions $\sqrt{s_{\mathrm{NN}}}$ = 5.02 TeV, and Pb–Pb collisions $\sqrt{s_{\mathrm{NN}}}$ = 2.76 TeV and $\sqrt{s_{\mathrm{NN}}}$ = 5.02 TeV. The

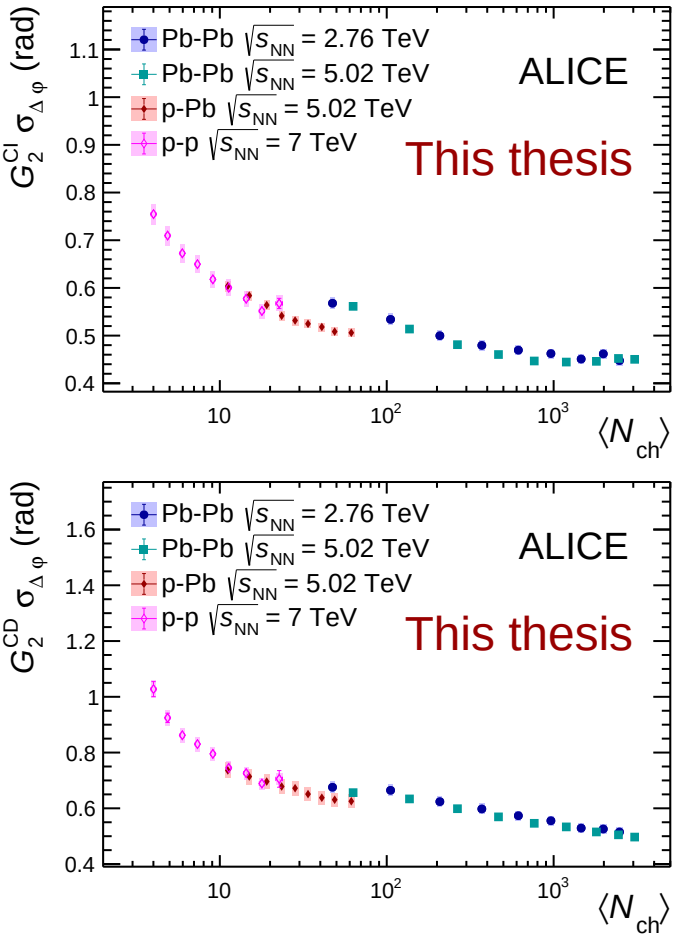

FIGURE 8.18: Azimuthal width of the two-particle transverse momentum correlation G_2^{CI} (top panel) and G_2^{CD} (bottom panel) as a function of $\langle N_{\mathrm{ch}} \rangle$ in pp collisions at $\sqrt{s_{\mathrm{NN}}}$ = 7 TeV, p–Pb collisions at $\sqrt{s_{\mathrm{NN}}}$ = 5.02 TeV, Pb–Pb collisions at $\sqrt{s_{\mathrm{NN}}}$ = 2.76 TeV, and Pb–Pb collisions at $\sqrt{s_{\mathrm{NN}}}$ = 5.02 TeV as measured by ALICE. $\langle N_{\mathrm{ch}} \rangle$ are the number of charged particles involved in the extraction of the correlation function after NUA and NUE corrections (see sect. 5.3). Error bars represent statistical uncertainties while systematic uncertainties are represented by colored bands. For Pb–Pb collisions at $\sqrt{s_{\mathrm{NN}}}$ = 5.02 TeV only statistical errors are incorporated.

overall scenario for the azimuthal dimension is a consistent narrowing trend for both correlators, G_2^{CI} and G_2^{CD}, in the four systems. This points to a possible similar underlying which drives the narrowing. As was described in sect. 8.2 radial flow is pointed out as the origin of the azimuthal narrowing in Pb–Pb collisions. If, as was described at the beginning of this section, collectivity effects are also present in pp and p–Pb systems then, it is plausible that the origin of the azimuthal narrow trend were common for pp, p–Pb and Pb–Pb systems. In pp and p–Pb collisions, both, G_2^{CI} and G_2^{CD}, correlators features a smooth width transition between them. The transition from p–Pb to Pb–Pb is not that smooth specially for the G_2^{CI} correlator where the width evolution shows a clear break, perhaps pointing to a slightly different mechanism or to additional narrowing sources. For Pb–Pb both energies show a matching not only in

the width trend evolution but in the actual width values, questioning the strength of the narrowing trend as the explanation for an early saturation of the broadening of the G_2^{CI} correlator.

The study of the small systems is necessarily incomplete without focusing specifically in the high multiplicity collisions for both, pp and p–Pb, systems.

8.7 η/s extraction

As was explained in sect. 2.4.6 η/s can be extracted directly from data using the expression [74]

$$\sigma_{\mathrm{c}}^2 - \sigma_0^2 = \frac{4}{T_{\mathrm{c}}} \frac{\eta}{s} \left(\tau_0^{-1} - \tau_{\mathrm{c,f}}^{-1} \right), \tag{8.3}$$

where σ_{c} and σ_0 stand for the longitudinal width of the two-particle correlation function (5.1) for the most central and the most peripheral collisions (σ_{p} from now on), respectively, τ_0 and $\tau_{\mathrm{c,f}}$ are formation time and freeze out time for the most central collisions, respectively, and T_{c} is the critical temperature.

For T_{c} the value of 160 MeV is adopted [140] and for τ_0 the usual value of 1 fm is used [140] while for $\tau_{\mathrm{c,f}}$ the value 10.5 fm reported by ALICE [65] is considered. The value σ_{c} can be the value already measured as the width of G_2^{CI} for the most central events. However the value of σ_{p} needs to be inferred from the measured data because the analysis reaches only 80% central collisions. In order to do that it

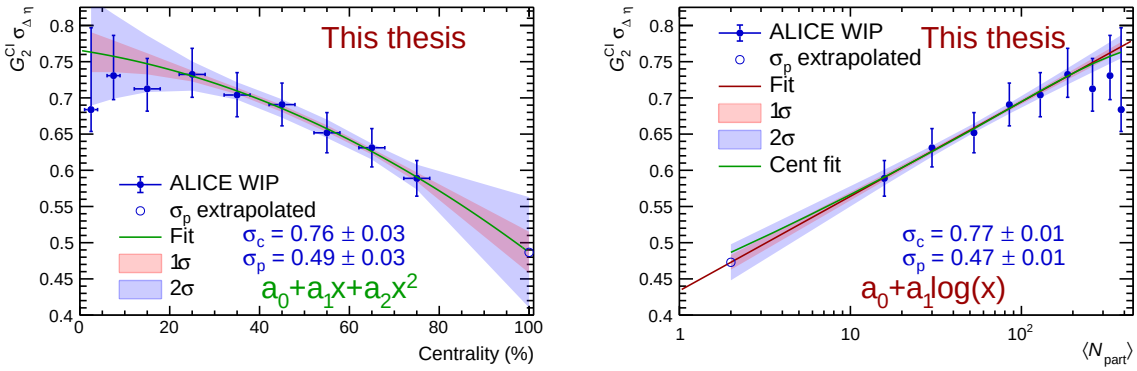

FIGURE 8.19: Fits of the evolution of the longitudinal width of G_2^{CI} with centrality (left) and with $\langle N_{\mathrm{part}} \rangle$ (right). The fit on centrality is reproduced on the right panel for compatibility check.

is relevant to highlight that the width behaves as a power law with $\langle N_{\mathrm{part}} \rangle$ for peripheral to semi-central events where it may saturate. The reason for the saturation could be system life time saturation or instrumental limitations. Due to this behavior three different methods have been considered:

1) σ_{c} and σ_{p} are extracted with the assumption that the width has a power law dependence with $\langle N_{\mathrm{part}} \rangle$ for the full centrality range

2) σ_{c} and σ_{p} are extracted with the assumption that the width has a power law dependence with $\langle N_{\mathrm{part}} \rangle$ from peripheral to semi-central collisions where it saturates

3) the evolution of the width behaves as a power law with the number of participants for peripheral to semi-central events and σ_{p} is extracted from this behavior, for σ_{c} the value extracted from data is considered

Figure 8.19 shows the evolution of the longitudinal width of the two-particle transverse momentum correlation G_2^{CI} with collision centrality and with $\langle N_{\mathrm{part}} \rangle$ using the first method. Figs. 8.20 and 8.21

show the second and third methods, respectively. With the values obtained for σ_c and σ_p from each

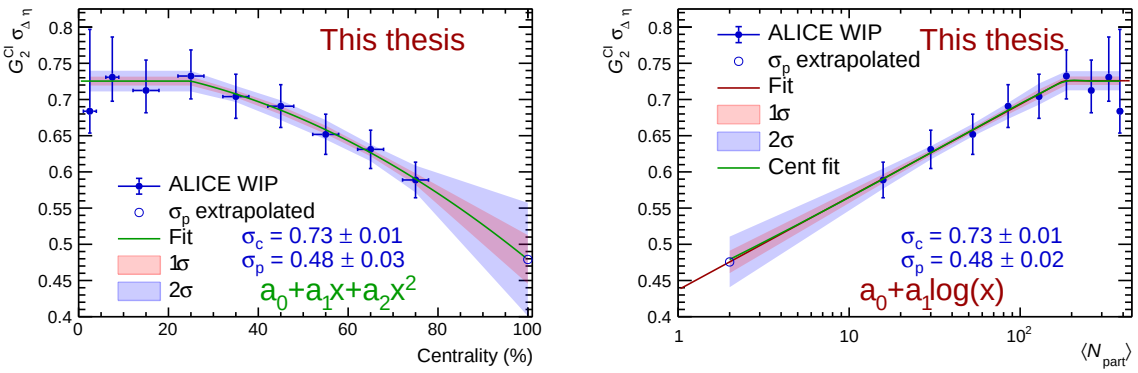

FIGURE 8.20: Fits of the evolution of the longitudinal width of G_2^{CI} with centrality (left) and with $\langle N_{\mathrm{part}} \rangle$ (right). The point where the plateau starts is an additional parameter of the fit for keeping continuity. The fit on centrality is reproduced on the right panel for compatibility check.

of the approaches, Tables 8.1 and 8.2 show the η/s values extracted using the G_2^{CI} longitudinal width evolution with centrality and with $\langle N_{\mathrm{part}} \rangle$, respectively. It is interesting to highlight that the values for the longitudinal width of the two-particle transverse momentum correlator G_2^{CI} in pp collisions, for all multiplicity classes, as shown in Fig. 8.17, match, within uncertainties, the values found in this section for σ_p. This is consistent with a picture in which the pp system is the limit of the most peripheral Pb–Pb collisions.

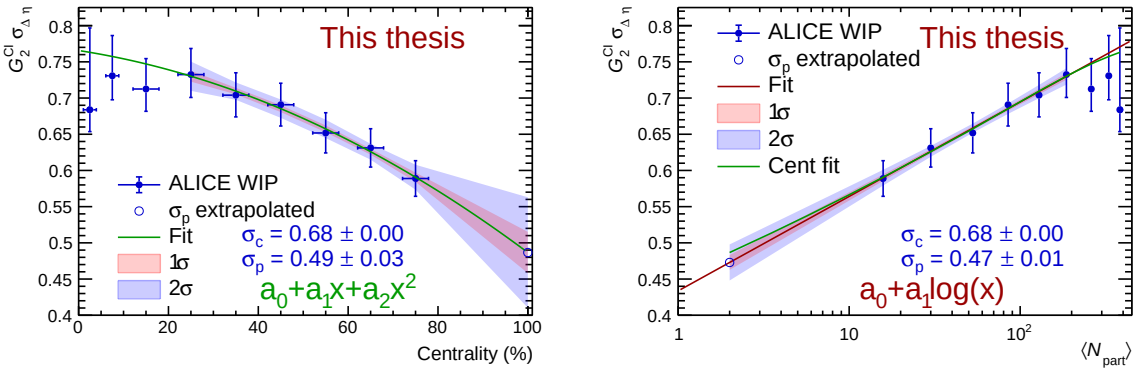

FIGURE 8.21: Fits of the evolution of the longitudinal width of G_2^{CI} with centrality (left) and with $\langle N_{\mathrm{part}} \rangle$ (right). Only the width for the most peripheral collisions is extracted from the fit, the width for the most central ones is taken as extracted from data. The fit on centrality is reproduced on the right panel for compatibility check.

An alternative way of presenting the potential η/s range extracted above, is to show the expected longitudinal width the G_2^{CI} would have if the shear viscosity over entropy density had different values given that the width of the correlator for the most peripheral events is the one above extracted. Figure 8.22 shows the expected longitudinal widths as bands over the higher multiplicity events for each of the η/s values considered.

method #	name	σ_c	σ_p	η/s
1	Logarithmic scaling	0.76 ± 0.03 (tot)	0.49 ± 0.03 (tot)	0.077 ± 0.011
2	Saturation level	0.73 ± 0.01 (tot)	0.48 ± 0.03 (tot)	0.066 ± 0.007
3	Most central events	0.68 ± 0.00 (tot)	0.49 ± 0.03 (tot)	0.052 ± 0.006

TABLE 8.1: η/s values extracted from the evolution of the longitudinal width of G_2^{CI} with centrality for each of the considered methods. The values extracted/considered for σ_c and σ_p are also shown.

method #	name	σ_c	σ_p	η/s
4	Logarithmic scaling	0.77 ± 0.01 (tot)	0.47 ± 0.01 (tot)	0.083 ± 0.003
5	Saturation level	0.73 ± 0.01 (tot)	0.48 ± 0.02 (tot)	0.067 ± 0.004
6	Most central events	0.68 ± 0.00 (tot)	0.47 ± 0.01 (tot)	0.055 ± 0.002

TABLE 8.2: η/s values extracted from the evolution of the longitudinal width of G_2^{CI} with the number of participants for each of the considered methods. The values extracted/considered for σ_c and σ_p are also shown.

The values of η/s obtained for the different methods (Tables 8.1 and 8.2) are shown in Fig. 8.23. The average among the different measurements is assigned as final value for η/s and their standard deviation as its uncertainty, therefore $\eta/s = 0.066 \pm 0.012$. For reference the theoretical limit $1/4\pi$ is also shown.

Finally the η/s value obtained in this thesis is compared in Fig. 8.24 to various calculations of η/s as a function of temperature as presented in [37]. The process which has been followed to extract η/s in this thesis, by using the method proposed in [70], only considers the value of the critical temperature. Therefore, the obtained value for η/s is an average along the whole evolution of the system. The interplay between broadening trend due to viscous effects and narrowing trend due to particle production and collective flow, also suggest the obtained η/s value as a lower limit. Both considerations put constrains and requirements on the proposed method. More work is needed from the experimental and theoretical point of view. Experimentally, for example, similar analyses from the beam energy scan (BES) at RHIC will shed light on the dependence of the width saturation level with collision energy. Theoretically, an extension to the proposed formula for η/s extraction to intermediate centrality collisions, will allow a potential temperature dependent η/s extraction. From both areas, for example, strategies for disentangle viscous effects from collective behavior and particle production mechanisms, will allow a better scenario for η/s extraction.

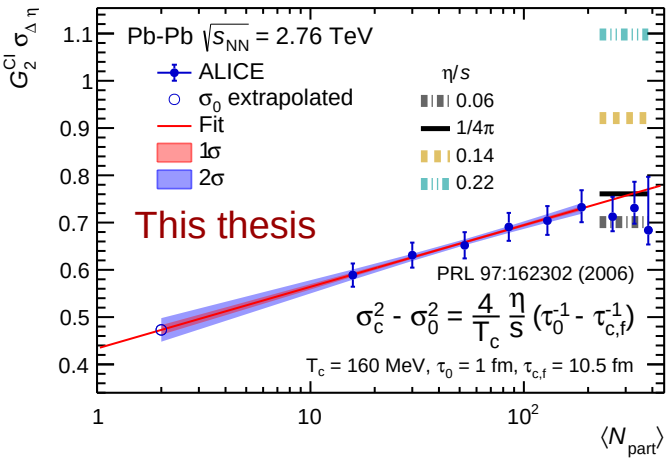

FIGURE 8.22: Expected longitudinal widths for the most central collisions of the two-particle transverse momentum correlation G_2^{CI} for different values of η/s. The extrapolated value is obtained for the most peripheral events

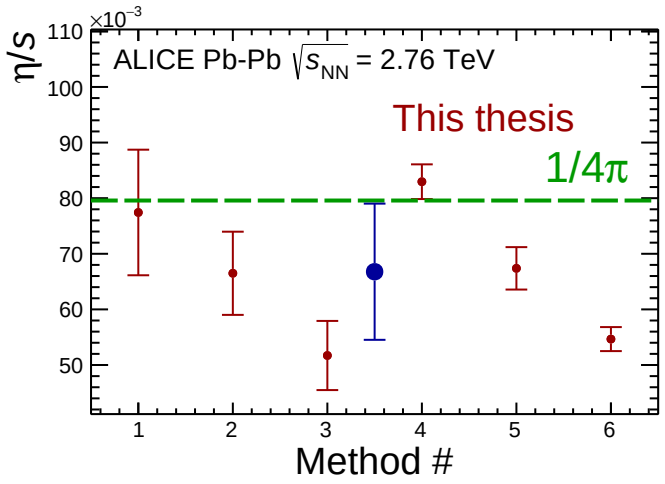

FIGURE 8.23: Values of η/s for each of the utilized methods as in Tables 8.1 and 8.2 are shown in red. The blue point is the average of all values with the error calculated as standard deviation. Horizontal dotted green line represents the theoretical KSS limit[141].

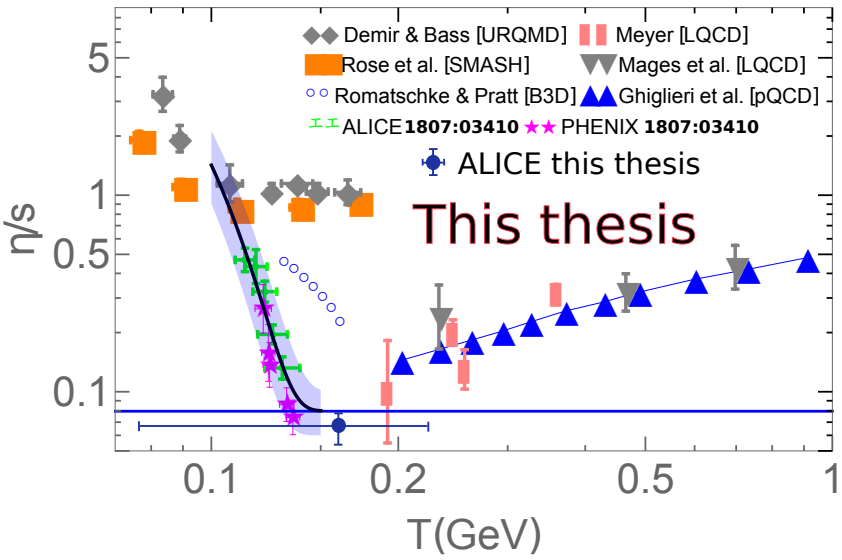

FIGURE 8.24: Comparison of the value of η/s obtained in this thesis to the values obtained for η/s as a function of temperature in [37] for ALICE and for PHENIX, and from other various calculations. The uncertainty in the temperature range is just indicative, ±80 MeV has been incorporated, to reflect the fact that the used method involves a wide evolution range. (Base figure taken from [37] incorporating the own [37] reference and the value of η/s obtained in this thesis).

Chapter 9

Conclusions

The relevance of the study of the properties of the medium created in heavy ion collisions in the huge colliders, RHIC in Brookhaven and LHC in Geneva, is evidenced mainly by two aspects. On the one hand, by the impact that their results may have in the field of development of the theories that try to understand the intimate nature of the matter. On the other hand, by the ability to mobilize gigantic investments, not only in the continuous upgrade of the existing colliders. The new facilities, planned to go into operation in the near future, such as FAIR in Darmstadt and NICA in Dubna, are born oriented to the study of the transition zone between the medium created in those collisions and the matter as it is usually known.

The medium created in relativistic heavy-ion collisions, QGP, has a set of properties which characterize it, among them the transport coefficients. The QGP transport coefficients govern the evolution of the fluctuations of the medium towards the equilibrium state. The objective of this thesis is to extract the transport coefficients of the QGP.

The success of hydrodynamic models in reproducing certain experimentally measured magnitudes in heavy-ion collisions has led to a complete generation of methods to infer the transport coefficients of QGP through hydrodynamic simulations that incorporate them as parameters. The transport coefficients of the QGP are inferred by comparing the predictions of the theoretical models with the experimental data. As such, this thesis begins with the hydrodynamic description used as a basis in most of these models. Next the different methods that have been used to infer the transport coefficients of the QGP, specifically, the specific shear viscosity, η/s, and the specific bulk viscosity, ζ/s, are introduced showing its increasing complexity and sophistication.

The use of models to infer the transport coefficients of the QGP has an inherent uncertainty associated with the model selection and with the initial conditions chosen for the start of the simulated evolution. The objective of this thesis is to extract the transport coefficients of the QGP directly from data using two-particle momentum correlations. Therefore, two-particle correlations are described from their basic concepts to the procedures for extracting the QGP transport coefficients using two-particle momentum components correlations.

This thesis describes in detail the procedure for extracting the two-particle transverse momentum correlations to which significant novel contributions have been made. The extraction of the corrections for inhomogeneities in the acceptance of the detector has been adapted to high multiplicity scenarios, large number of events and its non uniform longitudinal distribution. The fact of using Monte Carlo simulators, with their own peculiarities, to extract the detector efficiency correction, also required the adaptation of those corrections. The application of corrections for transverse momentum dependent non-uniform efficiency has been implemented for the first time in the method used. The procedure for extracting a pair detection efficiency correction and the study of its impact on the correlator is completely new. The evaluation of the impact of the width in which the centrality, or multiplicity, of the collision is measured, has been carried out using different Monte Carlo event generators. A procedure for the correction of that impact has been developed, implemented and used to produced the results reported in this thesis. The detailed analysis of the effect and the correction procedure has been published in PRC.

The evolution with the centrality of the collision of the correlator and its longitudinal and azimuthal projections for both, the charge dependent and the charge independent track combinations, presented in nine different intervals of centrality, allow to perceive the sensitivity of this correlator and the richness of nuances that its detailed analysis provides. In the case of the charge independent correlator, it is the first time that it is shown at LHC energies and has already been measured at RHIC energies. In the case of the charge dependent correlator, it is the first experimental measurement that has been performed.

The procedure for extracting the η/s of the QGP requires extracting the width of two-particle transverse momentum correlator. For doing this, and for the first time for this correlator, a two-dimensional, longitudinal and azimuthal, parametrization procedure has been used. The parametrization procedure simultaneously models the background component, inherent to two particle correlators, the collective behavior component and the component that is sensitive to in transverse momentum currents fluctuations. The width of the latter is of interest for the η/s extraction procedure.

The comparison of the evolution of the correlator, their longitudinal and azimuthal projections, and of their widths along these dimensions, with predictions of different Monte Carlo event generators, which implement different aspects of the physics of heavy-ion collisions, is also completely new and allows to put restrictions on the physics that implement these models.

From the evolution of the longitudinal width of the two-particle transverse momentum correlator, and for the first time at LHC energies, a value $\eta/s = 0.066 \pm 0.012$ has been extracted. The value is in agreement with the predictions available in the literature and close to the theoretical limit $1/4\pi$. The evolution of the longitudinal width has been compared to the results reported by STAR at RHIC energies and to the evolution of other correlators reported by ALICE at LHC energies. This comparisons allow to abound in the concrete sensitivity of the two-particle transverse momentum correlator compared to that of other two-particle correlators.

The study of the behavior of the two-particle transverse momentum correlator has been extended for the first time to the so-called small systems, where, in principle, the QGP should not have had the possibility of be constituted. For the first time, the two-particle transverse momentum correlators, their longitudinal, their azimuthal projections, and the evolution of their widths along these dimensions, are presented for proton-proton and proton-lead collisions. The result of a behavior of the longitudinal width of the two-particle transverse momentum correlator that does not depend on the multiplicity of the collision for proton-proton and proton-lead systems allows the correlator to be qualified as sensitive to the formation of the QGP.

In summary, it has been possible to extract, using the method of the evolution with the centrality of the width of the two-particle transverse momentum correlator, and for the first time for the LHC, a value of η/s that is in accordance with the values obtained using hydrodynamic models. It was shown that the two-particle transverse momentum correlator has sensitivity to establish differences between heavy-ion systems and small systems, an aspect in which other correlators have not been successful. It has also been shown how this sensitivity tests how the physics of processes in heavy-ion collisions is implemented in event generators. While the extraction of the η/s value has been completely data driven as opposed to other presented methods which rely on modeling the different system evolution phases, on predicting initial conditions and on running simulation codes, it is necessary also to say few, critical, words about the procedure used in this thesis. The first point is that the extracted η/s value is the result of the whole evolution of the system and not just of the viscous hydrodynamic phase. The second point is that the method, implicit in Eq. (2.134), attributes the longitudinal broadening of the two-particle transverse momentum correlation G_2^{CI} just to viscous effects, discarding any other effect that may influence its shape. The correlator sensitivity to medium narrowing trends has been clearly shown, which points the found value as a lower limit. The good point now is that, being a data driven method, the own data might be used to compensate for these drawbacks. Although the value found for η/s is relevant in its own and amazingly matching the values obtained by completely different methods the actual significance of this work lies on the extracted behavior of the two-particle transverse momentum

correlation and its sensitivity. The experimental measure of the two-particle transverse momentum correlators is in its dawn and the results of this thesis will contribute to give it a considerable boost.

9.1 Outlook

As part of the development of this thesis, extensive work has been done generating simulated events with event generators of different characteristics. From purely hadronic models such as UrQMD, to cascades of models such as IP-GLASMA + MUSIC + UrQMD whose chain was established from a previous IP-GLASMA + VISHNU + UrQMD one. In this context there is a substantial amount of results that require additional classification and that will allow restrictions on the models that implement these generators. The publication of the results obtained for the Pb–Pb system at $\sqrt{s_{\mathrm{NN}}}$ = 2.76 TeV are already in the process of being published in the final rounds of review of the ALICE collaboration. The publication of the proton-proton and proton-lead results as well as the detailed comparison with models, which has been presented in this thesis, is already in its early stages. The analysis of events of high multiplicity in small systems, needed to confirm whether in these systems the medium produced differs or not from that produced in small systems of conventional multiplicity, is the next step to validate the sensitivity of the two-particle transverse momentum correlation. The analysis on small systems might also provide the means for subtracting undesired contributions as narrowing or not viscous related broadening. The analysis of the two-particle correlator proposed for the extraction of the ζ/s carried out in its differential form, in relative angular separation, to make a study of its sensitivity and the applicability of the suggested extraction procedure will allow, in case of positive results, the extraction of ζ/s for the first time directly from the registered data. The suggested method for the extraction of the relaxation time of the QGP requires quantitative analysis of the correlator shape which has already been initiated in this thesis with the analysis of the parametrization of the two-particle transverse momentum correlation function.

Bibliography

[1] D. Boyanovsky *et al.*, "Phase transitions in the early and the present universe", *Ann. Rev. Nucl. Part. Sci.*, vol. 56, pp. 441–500, 2006. DOI: 10.1146/annurev.nucl.56.080805.140539. arXiv: hep-ph/0602002 [hep-ph].

[2] N. Cabibbo and G. Parisi, "Exponential Hadronic Spectrum and Quark Liberation", *Phys. Lett.*, vol. 59B, pp. 67–69, 1975. DOI: 10.1016/0370-2693(75)90158-6.

[3] C. Shen and B. Schenke, "Dynamical initialization and hydrodynamic modeling of relativistic heavy-ion collisions", *Nuclear Physics A*, vol. 982, pp. 411–414, 2019, The 27th International Conference on Ultrarelativistic Nucleus-Nucleus Collisions: Quark Matter 2018, https://indico.cern.ch/event/656452/contributions/2869808/, ISSN: 0375-9474. DOI: https://doi.org/10.1016/j.nuclphysa.2018.08.007. [Online]. Available: http://www.sciencedirect.com/science/article/pii/S0375947418301519.

[4] M. Tanabashi *et al.*, "Review of particle physics", *Phys. Rev. D*, vol. 98, p. 030 001, 3 Aug. 2018. DOI: 10.1103/PhysRevD.98.030001. [Online]. Available: https://link.aps.org/doi/10.1103/PhysRevD.98.030001.

[5] S. Ryu *et al.*, "Effects of bulk viscosity and hadronic rescattering in heavy ion collisions at energies available at the BNL Relativistic Heavy Ion Collider and at the CERN Large Hadron Collider", *Phys. Rev.*, vol. C97, no. 3, p. 034 910, 2018. DOI: 10.1103/PhysRevC.97.034910. arXiv: 1704.04216 [nucl-th].

[6] F. Cooper and G. Frye, "Single-particle distribution in the hydrodynamic and statistical thermodynamic models of multiparticle production", *Phys. Rev. D*, vol. 10, pp. 186–189, 1 Jul. 1974. DOI: 10.1103/PhysRevD.10.186. [Online]. Available: https://link.aps.org/doi/10.1103/PhysRevD.10.186.

[7] U. Heinz and R. Snellings, "Collective flow and viscosity in relativistic heavy-ion collisions", *Ann. Rev. Nucl. Part. Sci.*, vol. 63, pp. 123–151, 2013. DOI: 10.1146/annurev-nucl-102212-170540. arXiv: 1301.2826 [nucl-th].

[8] P. Romatschke, "New Developments in Relativistic Viscous Hydrodynamics", *Int. J. Mod. Phys.*, vol. E19, pp. 1–53, 2010. DOI: 10.1142/S0218301310014613. arXiv: 0902.3663 [hep-ph].

[9] L. Landau and E. Lifshitz, *Fluid mechanics*. Pergamon Press, 1959.

[10] A. Monnai, "Landau and Eckart frames for relativistic fluids in nuclear collisions", *Phys. Rev.*, vol. C100, no. 1, p. 014 901, 2019. DOI: 10.1103/PhysRevC.100.014901. arXiv: 1904.11940 [nucl-th].

[11] C. Cattaneo, "Sulla conduzione del calore", *Atti Sem. Mat. Fis. Univ. Modena*, vol. 3, pp. 83–101, 1948.

[12] I. Muller, "Zum Paradoxon der Warmeleitungstheorie", *Z. Phys.*, vol. 198, pp. 329–344, 1967. DOI: 10.1007/BF01326412.

[13] W. Israel, "Nonstationary irreversible thermodynamics: A Causal relativistic theory", *Annals Phys.*, vol. 100, pp. 310–331, 1976. DOI: 10.1016/0003-4916(76)90064-6.

[14] S. Jeon and U. Heinz, "Introduction to Hydrodynamics", *Int. J. Mod. Phys.*, vol. E24, no. 10, p. 1 530 010, 2015. DOI: 10.1142/S0218301315300106. arXiv: 1503.03931 [hep-ph].

[15] B. Abelev *et al.*, "Centrality determination of Pb-Pb collisions at $\sqrt{s_{NN}}$ = 2.76 TeV with ALICE", *Phys. Rev.*, vol. C88, no. 4, p. 044 909, 2013. DOI: 10.1103/PhysRevC.88.044909. arXiv: 1301.4361 [nucl-ex].

[16] S. Voloshin and Y. Zhang, "Flow study in relativistic nuclear collisions by Fourier expansion of Azimuthal particle distributions", *Z. Phys.*, vol. C70, pp. 665–672, 1996. DOI: 10.1007/s002880050141. arXiv: hep-ph/9407282 [hep-ph].

[17] K. Aamodt *et al.*, "Higher harmonic anisotropic flow measurements of charged particles in Pb-Pb collisions at $\sqrt{s_{NN}}$=2.76 TeV", *Phys. Rev. Lett.*, vol. 107, p. 032 301, 2011. DOI: 10.1103/PhysRevLett.107.032301. arXiv: 1105.3865 [nucl-ex].

[18] A. M. Poskanzer and S. A. Voloshin, "Methods for analyzing anisotropic flow in relativistic nuclear collisions", *Phys. Rev.*, vol. C58, pp. 1671–1678, 1998. DOI: 10.1103/PhysRevC.58.1671. arXiv: nucl-ex/9805001 [nucl-ex].

[19] I. Selyuzhenkov and S. Voloshin, "Effects of non-uniform acceptance in anisotropic flow measurement", *Phys. Rev.*, vol. C77, p. 034 904, 2008. DOI: 10.1103/PhysRevC.77.034904. arXiv: 0707.4672 [nucl-th].

[20] Victor Gonzalez for the ALICE Collaboration. (2016). QnVectorCorrection Framework, [Online]. Available: https://github.com/alisw/AliPhysics/tree/master/PWGPP/EVCHAR/FlowVectorCorrections (visited on 08/20/2019).

[21] C. Adler *et al.*, "Elliptic flow from two and four particle correlations in Au+Au collisions at s(NN)**(1/2) = 130-GeV", *Phys. Rev.*, vol. C66, p. 034 904, 2002. DOI: 10.1103/PhysRevC.66.034904. arXiv: nucl-ex/0206001 [nucl-ex].

[22] A. Bilandzic *et al.*, "Flow analysis with cumulants: Direct calculations", *Phys. Rev.*, vol. C83, p. 044 913, 2011. DOI: 10.1103/PhysRevC.83.044913. arXiv: 1010.0233 [nucl-ex].

[23] N. Borghini *et al.*, "Flow analysis from multiparticle azimuthal correlations", *Phys. Rev.*, vol. C64, p. 054 901, 2001. DOI: 10.1103/PhysRevC.64.054901. arXiv: nucl-th/0105040 [nucl-th].

[24] A. Bilandzic *et al.*, "Generic framework for anisotropic flow analyses with multiparticle azimuthal correlations", *Phys. Rev.*, vol. C89, no. 6, p. 064 904, 2014. DOI: 10.1103/PhysRevC.89.064904. arXiv: 1312.3572 [nucl-ex].

[25] E. Schnedermann *et al.*, "Thermal phenomenology of hadrons from 200-A/GeV S+S collisions", *Phys. Rev.*, vol. C48, pp. 2462–2475, 1993. DOI: 10.1103/PhysRevC.48.2462. arXiv: nucl-th/9307020 [nucl-th].

[26] B. Abelev *et al.*, "Centrality dependence of π, K, p production in Pb-Pb collisions at $\sqrt{s_{NN}}$ = 2.76 TeV", *Phys. Rev.*, vol. C88, p. 044 910, 2013. DOI: 10.1103/PhysRevC.88.044910. arXiv: 1303.0737 [hep-ex].

[27] F. Karsch *et al.*, "Universal properties of bulk viscosity near the QCD phase transition", *Phys.Lett.*, vol. B663, pp. 217–221, 2008. DOI: 10.1016/j.physletb.2008.01.080. arXiv: 0711.0914 [hep-ph].

[28] B. Alver *et al.*, "Event-by-Event Fluctuations of Azimuthal Particle Anisotropy in Au + Au Collisions at $\sqrt{s_{NN}}$ = 200 GeV", *Phys. Rev. Lett.*, vol. 104, p. 142 301, 2010. DOI: 10.1103/PhysRevLett.104.142301. arXiv: nucl-ex/0702036 [nucl-ex].

[29] J. Adams *et al.*, "Azimuthal anisotropy at RHIC: The First and fourth harmonics", *Phys. Rev. Lett.*, vol. 92, p. 062 301, 2004. DOI: 10.1103/PhysRevLett.92.062301. arXiv: nucl-ex/0310029 [nucl-ex].

[30] P. Romatschke and U. Romatschke, "Viscosity Information from Relativistic Nuclear Collisions: How Perfect is the Fluid Observed at RHIC?", *Phys. Rev. Lett.*, vol. 99, p. 172 301, 2007. DOI: 10.1103/PhysRevLett.99.172301. arXiv: 0706.1522 [nucl-th].

[31] B. Schenke *et al.*, "Anisotropic flow in $\sqrt{s}$ = 2.76 TeV Pb+Pb collisions at the LHC", *Phys. Lett.*, vol. B702, pp. 59–63, 2011. DOI: 10.1016/j.physletb.2011.06.065. arXiv: 1102.0575 [hep-ph].

[32] J.-Y. Ollitrault *et al.*, "Effect of flow fluctuations and nonflow on elliptic flow methods", *Phys. Rev.*, vol. C80, p. 014 904, 2009. DOI: 10.1103/PhysRevC.80.014904. arXiv: 0904.2315 [nucl-ex].

[33] J. Adams *et al.*, "Azimuthal anisotropy in Au+Au collisions at $\sqrt{s_{\mathrm{NN}}}$ = 200 GeV", *Phys. Rev.*, vol. C72, p. 014 904, 2005. DOI: 10.1103/PhysRevC.72.014904. arXiv: nucl-ex/0409033 [nucl-ex].

[34] B. I. Abelev *et al.*, "Systematic Measurements of Identified Particle Spectra in pp, d^+ Au and Au+Au Collisions from STAR", *Phys. Rev.*, vol. C79, p. 034 909, 2009. DOI: 10.1103/PhysRevC.79.034909. arXiv: 0808.2041 [nucl-ex].

[35] H. Song *et al.*, "200 A GeV Au+Au collisions serve a nearly perfect quark-gluon liquid", *Phys. Rev. Lett.*, vol. 106, p. 192 301, 2011, [Erratum: Phys. Rev. Lett. 109, 139904 (2012)]. DOI: 10.1103/PhysRevLett.106.192301, 10.1103/PhysRevLett.109.139904. arXiv: 1011.2783 [nucl-th].

[36] B. I. Abelev *et al.*, "Centrality dependence of charged hadron and strange hadron elliptic flow from s(NN)**(1/2) = 200-GeV Au + Au collisions", *Phys. Rev.*, vol. C77, p. 054 901, 2008. DOI: 10.1103/PhysRevC.77.054901. arXiv: 0801.3466 [nucl-ex].

[37] Z. Yang and R. J. Fries, "Extraction of the Specific Shear Viscosity of Hot Hadron Gas", 2018. arXiv: 1807.03410 [nucl-th].

[38] J. Adam *et al.*, "Centrality dependence of the nuclear modification factor of charged pions, kaons, and protons in Pb-Pb collisions at $\sqrt{s_{\mathrm{NN}}}$ = 2.76 TeV", *Phys. Rev.*, vol. C93, no. 3, p. 034 913, 2016. DOI: 10.1103/PhysRevC.93.034913. arXiv: 1506.07287 [nucl-ex].

[39] B. B. Abelev *et al.*, "Elliptic flow of identified hadrons in Pb-Pb collisions at $\sqrt{s_{\mathrm{NN}}}$ = 2.76 TeV", *JHEP*, vol. 06, p. 190, 2015. DOI: 10.1007/JHEP06(2015)190. arXiv: 1405.4632 [nucl-ex].

[40] G. S. Denicol *et al.*, "Effect of bulk viscosity on Elliptic Flow near QCD phase transition", *Phys. Rev.*, vol. C80, p. 064 901, 2009. DOI: 10.1103/PhysRevC.80.064901. arXiv: 0903.3595 [hep-ph].

[41] J. E. Bernhard *et al.*, "Applying Bayesian parameter estimation to relativistic heavy-ion collisions: simultaneous characterization of the initial state and quark-gluon plasma medium", *Phys. Rev.*, vol. C94, no. 2, p. 024 907, 2016. DOI: 10.1103/PhysRevC.94.024907. arXiv: 1605.03954 [nucl-th].

[42] J. Adam *et al.*, "Correlated event-by-event fluctuations of flow harmonics in Pb-Pb collisions at $\sqrt{s_{\mathrm{NN}}}$ = 2.76 TeV", *Phys. Rev. Lett.*, vol. 117, p. 182 301, 2016. DOI: 10.1103/PhysRevLett.117.182301. arXiv: 1604.07663 [nucl-ex].

[43] H. Niemi *et al.*, "Event-by-event fluctuations in a perturbative QCD + saturation + hydrodynamics model: Determining QCD matter shear viscosity in ultrarelativistic heavy-ion collisions", *Phys. Rev.*, vol. C93, no. 2, p. 024 907, 2016. DOI: 10.1103/PhysRevC.93.024907. arXiv: 1505.02677 [hep-ph].

[44] R. Paatelainen *et al.*, "Multiplicities and p_T spectra in ultrarelativistic heavy ion collisions from a next-to-leading order improved perturbative QCD + saturation + hydrodynamics model", *Phys. Rev.*, vol. C87, no. 4, p. 044 904, 2013. DOI: 10.1103/PhysRevC.87.044904. arXiv: 1211.0461 [hep-ph].

[45] R. Paatelainen *et al.*, "Fluid dynamics with saturated minijet initial conditions in ultrarelativistic heavy-ion collisions", *Phys. Lett.*, vol. B731, pp. 126–130, 2014. DOI: 10.1016/j.physletb.2014.02.018. arXiv: 1310.3105 [hep-ph].

[46] S. Ryu *et al.*, "The importance of the bulk viscosity of QCD in ultrarelativistic heavy-ion collisions", 2015. arXiv: 1502.01675 [nucl-th].

[47] J. Noronha-Hostler *et al.*, "Transport Coefficients of Hadronic Matter near T(c)", *Phys. Rev. Lett.*, vol. 103, p. 172 302, 2009. DOI: 10.1103/PhysRevLett.103.172302. arXiv: 0811.1571 [nucl-th].

[48] S. Chatrchyan *et al.*, "Measurement of the elliptic anisotropy of charged particles produced in PbPb collisions at $\sqrt{s_{NN}}$=2.76 TeV", *Phys. Rev.*, vol. C87, no. 1, p. 014 902, 2013. DOI: 10.1103/PhysRevC.87.014902. arXiv: 1204.1409 [nucl-ex].

[49] S. Chatrchyan *et al.*, "Measurement of higher-order harmonic azimuthal anisotropy in PbPb collisions at $\sqrt{s_{NN}}$ = 2.76 TeV", *Phys. Rev.*, vol. C89, no. 4, p. 044 906, 2014. DOI: 10.1103/PhysRevC.89.044906. arXiv: 1310.8651 [nucl-ex].

[50] J. Adam *et al.*, "Higher harmonic flow coefficients of identified hadrons in Pb-Pb collisions at $\sqrt{s_{\mathrm{NN}}}$ = 2.76 TeV", *JHEP*, vol. 09, p. 164, 2016. DOI: 10.1007/JHEP09(2016)164. arXiv: 1606.06057 [nucl-ex].

[51] B. B. Abelev *et al.*, "Multi-strange baryon production at mid-rapidity in Pb-Pb collisions at $\sqrt{s_{NN}}$ = 2.76 TeV", *Phys. Lett.*, vol. B728, pp. 216–227, 2014, [Erratum: Phys. Lett.B734,409(2014)]. DOI: 10.1016/j.physletb.2014.05.052, 10.1016/j.physletb.2013.11.048. arXiv: 1307.5543 [nucl-ex].

[52] B. B. Abelev *et al.*, "K^0_S and Λ production in Pb-Pb collisions at $\sqrt{s_{NN}}$ = 2.76 TeV", *Phys. Rev. Lett.*, vol. 111, p. 222 301, 2013. DOI: 10.1103/PhysRevLett.111.222301. arXiv: 1307.5530 [nucl-ex].

[53] J. Adam *et al.*, "Direct photon production in Pb-Pb collisions at $\sqrt{s_{\mathrm{NN}}}$ = 2.76 TeV", *Phys. Lett.*, vol. B754, pp. 235–248, 2016. DOI: 10.1016/j.physletb.2016.01.020. arXiv: 1509.07324 [nucl-ex].

[54] H. van Hees *et al.*, "Pseudo-critical enhancement of thermal photons in relativistic heavy-ion collisions?", *Nucl. Phys.*, vol. A933, pp. 256–271, 2015. DOI: 10.1016/j.nuclphysa.2014.09.009. arXiv: 1404.2846 [nucl-th].

[55] R. Chatterjee *et al.*, "Collision centrality and τ_0 dependence of the emission of thermal photons from fluctuating initial state in ideal hydrodynamic calculation", *Phys. Rev.*, vol. C85, p. 064 910, 2012. DOI: 10.1103/PhysRevC.85.064910. arXiv: 1204.2249 [nucl-th].

[56] O. Linnyk *et al.*, "Hadronic and partonic sources of direct photons in relativistic heavy-ion collisions", *Phys. Rev.*, vol. C92, no. 5, p. 054 914, 2015. DOI: 10.1103/PhysRevC.92.054914. arXiv: 1504.05699 [nucl-th].

[57] J.-F. Paquet *et al.*, "Production of photons in relativistic heavy-ion collisions", *Phys. Rev.*, vol. C93, no. 4, p. 044 906, 2016. DOI: 10.1103/PhysRevC.93.044906. arXiv: 1509.06738 [hep-ph].

[58] I. Helenius *et al.*, "Centrality dependence of inclusive prompt photon production in d+Au, Au+Au, p+Pb, and Pb+Pb collisions", *JHEP*, vol. 05, p. 030, 2013. DOI: 10.1007/JHEP05(2013)030. arXiv: 1302.5580 [hep-ph].

[59] S. Acharya *et al.*, "Direct photon elliptic flow in Pb-Pb collisions at $\sqrt{s_{\mathrm{NN}}}$ = 2.76 TeV", *Phys. Lett.*, vol. B789, pp. 308–322, 2019. DOI: 10.1016/j.physletb.2018.11.039. arXiv: 1805.04403 [nucl-ex].

[60] R. Chatterjee *et al.*, "Anisotropic flow of thermal photons at energies available at the BNL Relativistic Heavy Ion Collider and at the CERN Large Hadron Collider", *Phys. Rev.*, vol. C96, no. 1, p. 014 911, 2017. DOI: 10.1103/PhysRevC.96.014911. arXiv: 1702.02378 [nucl-th].

[61] B. Schenke *et al.*, "Fluctuating Glasma initial conditions and flow in heavy ion collisions", *Phys. Rev. Lett.*, vol. 108, p. 252 301, 2012. DOI: 10.1103/PhysRevLett.108.252301. arXiv: 1202.6646 [nucl-th].

[62] D. Lohner, "Measurement of Direct-Photon Elliptic Flow in Pb-Pb Collisions at $\sqrt{s_{NN}}$ = 2.76 TeV", *J. Phys. Conf. Ser.*, vol. 446, p. 012 028, 2013. DOI: 10.1088/1742-6596/446/1/012028. arXiv: 1212.3995 [hep-ex].

[63] D. Lohner, "Anisotropic flow of direct photons in Pb-Pb collisions at 2.76 TeV per nucleon", PhD thesis, Heidelberg U., 2013-09-16.

[64] P. Bożek, "Effect of bulk viscosity on interferometry correlations in ultrarelativistic heavy-ion collisions", *Phys. Rev.*, vol. C95, no. 5, p. 054 909, 2017. DOI: 10.1103/PhysRevC.95.054909. arXiv: 1702.01319 [nucl-th].

[65] K. Aamodt *et al.*, "Two-pion Bose-Einstein correlations in central Pb-Pb collisions at $\sqrt{s_{\mathrm{NN}}}$ = 2.76 TeV", *Phys. Lett.*, vol. B696, pp. 328–337, 2011. DOI: 10.1016/j.physletb.2010.12.053. arXiv: 1012.4035 [nucl-ex].

[66] S. Ravan *et al.*, "Correcting Correlation Function Measurements", *Phys. Rev.*, vol. C89, no. 2, p. 024 906, 2014. DOI: 10.1103/PhysRevC.89.024906. arXiv: 1311.3915 [nucl-ex].

[67] C. Pruneau *et al.*, "Methods for the study of particle production fluctuations", *Phys. Rev.*, vol. C66, p. 044 904, 2002. DOI: 10.1103/PhysRevC.66.044904. arXiv: nucl-ex/0204011 [nucl-ex].

[68] B. Abelev *et al.*, "Pion, Kaon, and Proton Production in Central Pb–Pb Collisions at $\sqrt{s_{NN}}$ = 2.76 TeV", *Phys. Rev. Lett.*, vol. 109, p. 252 301, 2012. DOI: 10.1103/PhysRevLett.109.252301. arXiv: 1208.1974 [hep-ex].

[69] S. Acharya *et al.*, "Two particle differential transverse momentum and number density correlations in p-Pb and Pb-Pb at the LHC", 2018. arXiv: 1805.04422 [nucl-ex].

[70] S. Gavin and G. Moschelli, "Viscosity and the Soft Ridge at RHIC", *J. Phys.*, vol. G35, p. 104 084, 2008. DOI: 10.1088/0954-3899/35/10/104084. arXiv: 0806.4366 [nucl-th].

[71] R. K. Pokharel, "Second Order And Fluctuating Hydrodynamic Theory Of Two-Particle Transverse Momentum Correlations In Nuclear Collisions", Wayne State University Dissertations. Paper 687, PhD thesis, Wayne State University, 2013.

[72] J. D. Bjorken, "Highly Relativistic Nucleus-Nucleus Collisions: The Central Rapidity Region", *Phys. Rev.*, vol. D27, pp. 140–151, 1983. DOI: 10.1103/PhysRevD.27.140.

[73] M. A. Aziz and S. Gavin, "Causal diffusion and the survival of charge fluctuations in nuclear collisions", *Phys. Rev.*, vol. C70, p. 034 905, 2004. DOI: 10.1103/PhysRevC.70.034905. arXiv: nucl-th/0404058 [nucl-th].

[74] S. Gavin and M. Abdel-Aziz, "Measuring Shear Viscosity Using Transverse Momentum Correlations in Relativistic Nuclear Collisions", *Phys. Rev. Lett.*, vol. 97, p. 162 302, 2006. DOI: 10.1103/PhysRevLett.97.162302. arXiv: nucl-th/0606061 [nucl-th].

[75] C. D. Zin, "Dynamic Fluctuations From Hydrodynamics And Kinetic Theory In High Energy Collisions", Wayne State University Dissertations. 1906, PhD thesis, Wayne State University, 2017.

[76] J. Adams *et al.*, "Transverse-momentum p_T correlations on (η, φ) from mean-p_T fluctuations in Au–Au collisions at $\sqrt{s_{NN}}$ = 200 GeV", *J. Phys.*, vol. G32, pp. L37–L48, 2006. DOI: 10.1088/0954-3899/32/6/L02. arXiv: nucl-ex/0509030 [nucl-ex].

[77] H. Agakishiev *et al.*, "Evolution of the differential transverse momentum correlation function with centrality in Au+Au collisions at $\sqrt{s_{NN}}$ = 200 GeV", *Phys. Lett.*, vol. B704, pp. 467–473, 2011. DOI: 10.1016/j.physletb.2011.09.075. arXiv: 1106.4334 [nucl-ex].

[78] Gonzalez, Victor, "Bulk viscosity and energy-momentum correlations in central Pb–Pb collisions at $\sqrt{s_{NN}}$ = 2.76 TeV", (To be made public), Master's thesis, Físicas, UCM, Madrid, Spain, Jun. 2015.

[79] A. Dobado *et al.*, "Bulk viscosity and energy-momentum correlations in high energy hadron collisions", *Eur. Phys. J.*, vol. C72, p. 1873, 2012. DOI: 10.1140/epjc/s10052-012-1873-9. arXiv: 1101.1801 [hep-ph].

[80] J. M. Torres-Rincon, "Hadronic Transport Coefficients from Effective Field Theories", PhD thesis, UCM, Somosaguas, New York, 2012. DOI: 10.1007/978-3-319-00425-9. arXiv: 1205.0782 [hep-ph]. [Online]. Available: http://www.springer.com/978-3-319-00424-2.

[81] S. Gavin *et al.*, "Rapidity Correlation Structure in Nuclear Collisions", *Phys. Rev.*, vol. C94, no. 2, p. 024 921, 2016. DOI: 10.1103-PhysRevC.94.024921. arXiv: 1606.02692 [nucl-th].

[82] K. Aamodt *et al.*, "The ALICE experiment at the CERN LHC", *JINST*, vol. 3, S08002, 2008. DOI: 10.1088/1748-0221/3/08/S08002.

[83] B. B. Abelev *et al.*, "Performance of the ALICE Experiment at the CERN LHC", *Int.J.Mod.Phys.*, vol. A29, p. 1 430 044, 2014. DOI: 10.1142/S0217751X14300440. arXiv: 1402.4476 [nucl-ex].

[84] *ALICE Inner Tracking System (ITS): Technical Design Report*, ser. Technical Design Report ALICE. Geneva: CERN, 1999. [Online]. Available: http://edms.cern.ch/file/398932/1.

[85] K. Aamodt *et al.*, "Alignment of the ALICE Inner Tracking System with cosmic-ray tracks", *JINST*, vol. 5, P03003, 2010. DOI: 10.1088/1748-0221/5/03/P03003. arXiv: 1001.0502 [physics.insdet].

[86] J. Alme *et al.*, "The ALICE TPC, a large 3-dimensional tracking device with fast readout for ultra-high multiplicity events", *Nuclear Instruments and Methods in Physics Research A*, vol. 622, no. 1, pp. 316–367, Oct. 2010. DOI: 10.1016/j.nima.2010.04.042. arXiv: 1001.1950 [physics.ins-det].

[87] S. Acharya *et al.*, "The ALICE Transition Radiation Detector: construction, operation, and performance", *Nucl. Instrum. Meth.*, vol. A881, pp. 88–127, 2018. DOI: 10.1016/j.nima.2017.09.028. arXiv: 1709.02743 [physics.ins-det].

[88] A. Akindinov *et al.*, "Performance of the ALICE Time-Of-Flight detector at the LHC", *Eur. Phys. J. Plus*, vol. 128, p. 44, 2013. DOI: 10.1140/epjp/i2013-13044-x.

[89] G. Volpe, "Pattern recognition and pid procedure with the alice-hmpid", *Nuclear Instruments and Methods in Physics Research Section A: Accelerators, Spectrometers, Detectors and Associated Equipment*, vol. 766, pp. 259–262, 2014, RICH2013 Proceedings of the Eighth International Workshop on Ring Imaging Cherenkov Detectors Shonan, Kanagawa, Japan, December 2-6, 2013, ISSN: 0168-9002. DOI: https://doi.org/10.1016/j.nima.2014.05.031. [Online]. Available: http://www.sciencedirect.com/science/article/pii/S0168900214005506.

[90] D. C. Zhou and the ALICE Collaboration, "PHOS, the ALICE-PHOton spectrometer", *Journal of Physics G: Nuclear and Particle Physics*, vol. 34, no. 8, S719–S723, Jul. 2007. DOI: 10.1088/0954-3899/34/8/s81. [Online]. Available: https://doi.org/10.1088%2F0954-3899%2F34%2F8%2Fs81.

[91] S. Acharya *et al.*, "Calibration of the photon spectrometer PHOS of the ALICE experiment", *JINST*, vol. 14, no. 05, P05025, 2019. DOI: 10.1088/1748-0221/14/05/P05025. arXiv: 1902.06145 [physics.ins-det].

[92] U. Abeysekara *et al.*, "ALICE EMCal Physics Performance Report", 2010. arXiv: 1008.0413 [physics.ins-det].

[93] *ALICE dimuon forward spectrometer: Technical Design Report*, ser. Technical Design Report ALICE. Geneva: CERN, 1999. [Online]. Available: https://cds.cern.ch/record/401974.

[94] P. Cortese *et al.*, *ALICE forward detectors: FMD, TO and VO: Technical Design Report*, ser. Technical Design Report ALICE. Geneva: CERN, 2004, Submitted on 10 Sep 2004. [Online]. Available: http://cds.cern.ch/record/781854.

[95] E. Abbas *et al.*, "Performance of the ALICE VZERO system", *JINST*, vol. 8, P10016, 2013. DOI: 10.1088/1748-0221/8/10/P10016. arXiv: 1306.3130 [nucl-ex].

[96] *ALICE Photon Multiplicity Detector (PMD): Technical Design Report*, ser. Technical Design Report ALICE. Geneva: CERN, 1999. [Online]. Available: http://cds.cern.ch/record/451099.

[97] M. Gallio *et al.*, *ALICE Zero-Degree Calorimeter (ZDC): Technical Design Report*, ser. Technical Design Report ALICE. Geneva: CERN, 1999. [Online]. Available: http://cds.cern.ch/record/381433.

[98] M. Ivanov *et al.*, "TPC tracking and particle identification in high-density environment", *arXiv e-prints*, physics/0306108, physics/0306108, Jun. 2003. arXiv: physics/0306108 [physics.data-an].

[99] M. Ivanov *et al.*, "Track reconstruction in high density environment", *Nucl. Instrum. Meth.*, vol. A566, pp. 70–74, 2006. DOI: 10.1016/j.nima.2006.05.029.

[100] "Centrality determination in heavy ion collisions", Aug. 2018. [Online]. Available: https://cds.cern.ch/record/2636623.

[101] M. Tanabashi *et al.*, "Review of Particle Physics", *Phys. Rev.*, vol. D98, no. 3, p. 030 001, 2018. DOI: 10.1103/PhysRevD.98.030001.

[102] J. Adam *et al.*, "Particle identification in ALICE: a Bayesian approach", *Eur. Phys. J. Plus*, vol. 131, no. 5, p. 168, 2016. DOI: 10.1140/epjp/i2016-16168-5. arXiv: 1602.01392 [physics.data-an].

[103] ALICE Collaboration. (2019). ALICE Software on GitHub, [Online]. Available: https://github.com/alisw (visited on 08/20/2019).

[104] P. Saiz *et al.*, "AliEn - ALICE environment on the GRID", *Nucl. Instrum. Meth.*, vol. A502, pp. 437–440, 2003. DOI: 10.1016/S0168-9002(03)00462-5.

[105] R. Brun and F. Rademakers, "ROOT: An object oriented data analysis framework", *Nucl. Instrum. Meth.*, vol. A389, pp. 81–86, 1997. DOI: 10.1016/S0168-9002(97)00048-X. [Online]. Available: https://root.cern.ch/ (visited on 08/21/2019).

[106] ALICE Collaboration. (2019). ALICE Software framework, [Online]. Available: https://github.com/alisw/AliRoot (visited on 08/20/2019).

[107] R. Brun *et al.*, "GEANT Detector Description and Simulation Tool", 1994. DOI: 10.17181/CERN.MUHF.DMJ1.

[108] T. Sjostrand *et al.*, "PYTHIA 6.4 Physics and Manual", *JHEP*, vol. 05, p. 026, 2006. DOI: 10.1088/1126-6708/2006/05/026. arXiv: hep-ph/0603175 [hep-ph].

[109] B. Andersson *et al.*, "Parton Fragmentation and String Dynamics", *Phys. Rept.*, vol. 97, pp. 31–145, 1983. DOI: 10.1016/0370-1573(83)90080-7.

[110] B. Andersson, "The Lund model", *Camb. Monogr. Part. Phys. Nucl. Phys. Cosmol.*, vol. 7, pp. 1–471, 1997.

[111] X.-N. Wang and M. Gyulassy, "HIJING: A monte carlo model for multiple jet production in p p, p a and a a collisions", *Phys. Rev.*, vol. D44, pp. 3501–3516, 1991. DOI: 10.1103/PhysRevD.44.3501.

[112] B. Andersson *et al.*, "A model for low-pt hadronic reactions with generalizations to hadron-nucleus and nucleus-nucleus collisions", *Nuclear Physics B*, vol. 281, no. 1, pp. 289–309, 1987, ISSN: 0550-3213. DOI: https://doi.org/10.1016/0550-3213(87)90257-4. [Online]. Available: http://www.sciencedirect.com/science/article/pii/0550321387902574.

[113] A. Capella *et al.*, "Dual parton model", *Phys. Rept.*, vol. 236, pp. 225–329, 1994. DOI: 10.1016/0370-1573(94)90064-7.

[114] Z.-W. Lin *et al.*, "A Multi-phase transport model for relativistic heavy ion collisions", *Phys. Rev.*, vol. C72, p. 064 901, 2005. DOI: 10.1103/PhysRevC.72.064901. arXiv: nucl-th/0411110 [nucl-th].

[115] B. Zhang, "ZPC 1.0.1: A Parton cascade for ultrarelativistic heavy ion collisions", *Comput. Phys. Commun.*, vol. 109, pp. 193–206, 1998. DOI: 10.1016/S0010-4655(98)00010-1. arXiv: nucl-th/9709009 [nucl-th].

[116] Z.-w. Lin and C. M. Ko, "Flavor ordering of elliptic flows at high transverse momentum", *Phys. Rev. Lett.*, vol. 89, p. 202 302, 2002. DOI: 10.1103/PhysRevLett.89.202302. arXiv: nucl-th/0207014 [nucl-th].

[117] B. Li *et al.*, "Studies of superdense hadronic matter in a relativistic transport model", *Int. J. Mod. Phys.*, vol. E10, pp. 267–352, 2001. DOI: 10.1142/S0218301301000575.

[118] J. Adams *et al.*, "The Energy dependence of p_T angular correlations inferred from mean-p_T fluctuation scale dependence in heavy ion collisions at the SPS and RHIC", *J. Phys.*, vol. G34, pp. 451–466, 2007. DOI: 10.1088/0954-3899/34/3/004. arXiv: nucl-ex/0605021 [nucl-ex].

[119] J. Adam *et al.*, "Flow dominance and factorization of transverse momentum correlations in Pb-Pb collisions at the LHC", *Phys. Rev. Lett.*, vol. 118, no. 16, p. 162 302, 2017. DOI: 10.1103/PhysRevLett.118.162302. arXiv: 1702.02665 [nucl-ex].

[120] J. Adam *et al.*, "Centrality evolution of the charged-particle pseudorapidity density over a broad pseudorapidity range in Pb-Pb collisions at $\sqrt{s_{\mathrm{NN}}} = 2.76$ TeV", *Phys. Lett.*, vol. B754, pp. 373–385, 2016. DOI: 10.1016/j.physletb.2015.12.082. arXiv: 1509.07299 [nucl-ex].

[121] B. Abelev *et al.*, "Pseudorapidity density of charged particles in p + Pb collisions at $\sqrt{s_{NN}} = 5.02$ TeV", *Phys. Rev. Lett.*, vol. 110, no. 3, p. 032 301, 2013. DOI: 10.1103/PhysRevLett.110.032301. arXiv: 1210.3615 [nucl-ex].

[122] J. L. Gramling, "Two-track resolution effects for HBT analyses in ALICE", Oct. 2011. [Online]. Available: https://cds.cern.ch/record/1419204.

[123] V. Gonzalez *et al.*, "Effect of centrality bin width corrections on two-particle number and transverse momentum differential correlation functions", *Phys. Rev.*, vol. C99, no. 3, p. 034 907, 2019. DOI: 10.1103/PhysRevC.99.034907. arXiv: 1809.04962 [physics.data-an].

[124] T. A. Trainor *et al.*, "Autocorrelations from fluctuation scale dependence by inversion", *J. Phys.*, vol. G31, pp. 809–824, 2005. DOI: 10.1088/0954-3899/31/7/023. arXiv: hep-ph/0410182 [hep-ph].

[125] J. Adam *et al.*, "Multiplicity and transverse momentum evolution of charge-dependent correlations in pp, p–Pb, and Pb–Pb collisions at the LHC", *Eur. Phys. J.*, vol. C76, no. 2, p. 86, 2016. DOI: 10.1140/epjc/s10052-016-3915-1. arXiv: 1509.07255 [nucl-ex].

[126] R. Barlow, "Systematic errors: Facts and fictions", in *Advanced Statistical Techniques in Particle Physics. Proceedings, Conference, Durham, UK, March 18-22, 2002*, 2002, pp. 134–144. arXiv: hep-ex/0207026 [hep-ex]. [Online]. Available: http://www.ippp.dur.ac.uk/Workshops/02/statistics/proceedings//barlow.pdf.

[127] B. Abelev *et al.*, "Long-range angular correlations on the near and away side in p-Pb collisions at $\sqrt{s_{NN}}$ = 5.02 TeV", *Phys. Lett.*, vol. B719, pp. 29–41, 2013. DOI: 10.1016/j.physletb.2013.01.012. arXiv: 1212.2001 [nucl-ex].

[128] B. Abelev *et al.*, "Charge correlations using the balance function in Pb-Pb collisions at $\sqrt{s_{NN}}$ = 2.76 TeV", *Phys. Lett.*, vol. B723, pp. 267–279, 2013. DOI: 10.1016/j.physletb.2013.05.039. arXiv: 1301.3756 [nucl-ex].

[129] S. A. Bass *et al.*, "Clocking hadronization in relativistic heavy ion collisions with balance functions", *Phys. Rev. Lett.*, vol. 85, pp. 2689–2692, 2000. DOI: 10.1103/PhysRevLett.85.2689. arXiv: nucl-th/0005044 [nucl-th].

[130] K. Aamodt *et al.*, "Centrality dependence of the charged-particle multiplicity density at mid-rapidity in Pb-Pb collisions at $\sqrt{s_{NN}}$ = 2.76 TeV", *Phys. Rev. Lett.*, vol. 106, p. 032 301, 2011. DOI: 10.1103/PhysRevLett.106.032301. arXiv: 1012.1657 [nucl-ex].

[131] K. Aamodt *et al.*, "Elliptic flow of charged particles in Pb-Pb collisions at 2.76 TeV", *Phys. Rev. Lett.*, vol. 105, p. 252 302, 2010. DOI: 10.1103/PhysRevLett.105.252302. arXiv: 1011.3914 [nucl-ex].

[132] P. Pujahari and C. A. Pruneau, "Two-particle differential transverse momentum and number density correlations in p-Pb and Pb-Pb collisions at LHC", Apr. 2018. [Online]. Available: https://aliceinfo.cern.ch/ArtSubmission/node/2709.

[133] U. A. Wiedemann, "Jet Quenching in Heavy Ion Collisions", pp. 521–562, 2010, [Landolt-Bornstein23,521(2010)]. DOI: 10.1007/978-3-642-01539-7_17. arXiv: 0908.2306 [hep-ph].

[134] S. A. Voloshin *et al.*, "Collective phenomena in non-central nuclear collisions", *Landolt-Bornstein*, vol. 23, pp. 293–333, 2010. DOI: 10.1007/978-3-642-01539-7_10. arXiv: 0809.2949 [nucl-ex].

[135] B. B. Abelev *et al.*, "Transverse momentum dependence of inclusive primary charged-particle production in p-Pb collisions at $\sqrt{s_{\mathrm{NN}}}$ = 5.02 TeV", *Eur. Phys. J.*, vol. C74, no. 9, p. 3054, 2014. DOI: 10.1140/epjc/s10052-014-3054-5. arXiv: 1405.2737 [nucl-ex].

[136] M. Aaboud *et al.*, "Measurements of long-range azimuthal anisotropies and associated Fourier coefficients for pp collisions at $\sqrt{s}$ = 5.02 and 13 TeV and p+Pb collisions at $\sqrt{s_{\mathrm{NN}}}$ = 5.02 TeV with the ATLAS detector", *Phys. Rev.*, vol. C96, no. 2, p. 024 908, 2017. DOI: 10.1103/PhysRevC.96.024908. arXiv: 1609.06213 [nucl-ex].

[137] M. Aaboud *et al.*, "Measurement of multi-particle azimuthal correlations in pp, p+Pb and low-multiplicity Pb+Pb collisions with the ATLAS detector", *Eur. Phys. J.*, vol. C77, no. 6, p. 428, 2017. DOI: 10.1140/epjc/s10052-017-4988-1. arXiv: 1705.04176 [hep-ex].

[138] S. Acharya *et al.*, "Investigations of anisotropic flow using multi-particle azimuthal correlations in pp, p-Pb, Xe-Xe, and Pb-Pb collisions at the LHC", 2019. arXiv: 1903.01790 [nucl-ex].

[139] N. Jacazio, "Measuring hydrodynamical expansion via the production of identified hadrons in Pb−Pb collisions with ALICE", in *53rd Rencontres de Moriond on QCD and High Energy Interactions (Moriond QCD 2018) La Thuile, Italy, March 17-24, 2018*, 2018. arXiv: 1806.07617 [nucl-ex].

[140] F. Becattini, "The Quark Gluon Plasma and relativistic heavy ion collisions in the LHC era", *J. Phys. Conf. Ser.*, vol. 527, p. 012 012, 2014. DOI: 10.1088/1742-6596/527/1/012012.

[141] P. Kovtun *et al.*, "Viscosity in strongly interacting quantum field theories from black hole physics", *Phys. Rev. Lett.*, vol. 94, p. 111 601, 2005. DOI: 10.1103/PhysRevLett.94.111601. arXiv: hep-th/0405231 [hep-th].

Appendix A

Systematic uncertainties

In this appendix the results of the systematic uncertainties tests are presented. Section A.1 covers the systematic tests on the projections of the two-particle correlation function while section A.2 does it on the their widths evolution.

A.1 Systematic uncertainties on the projections

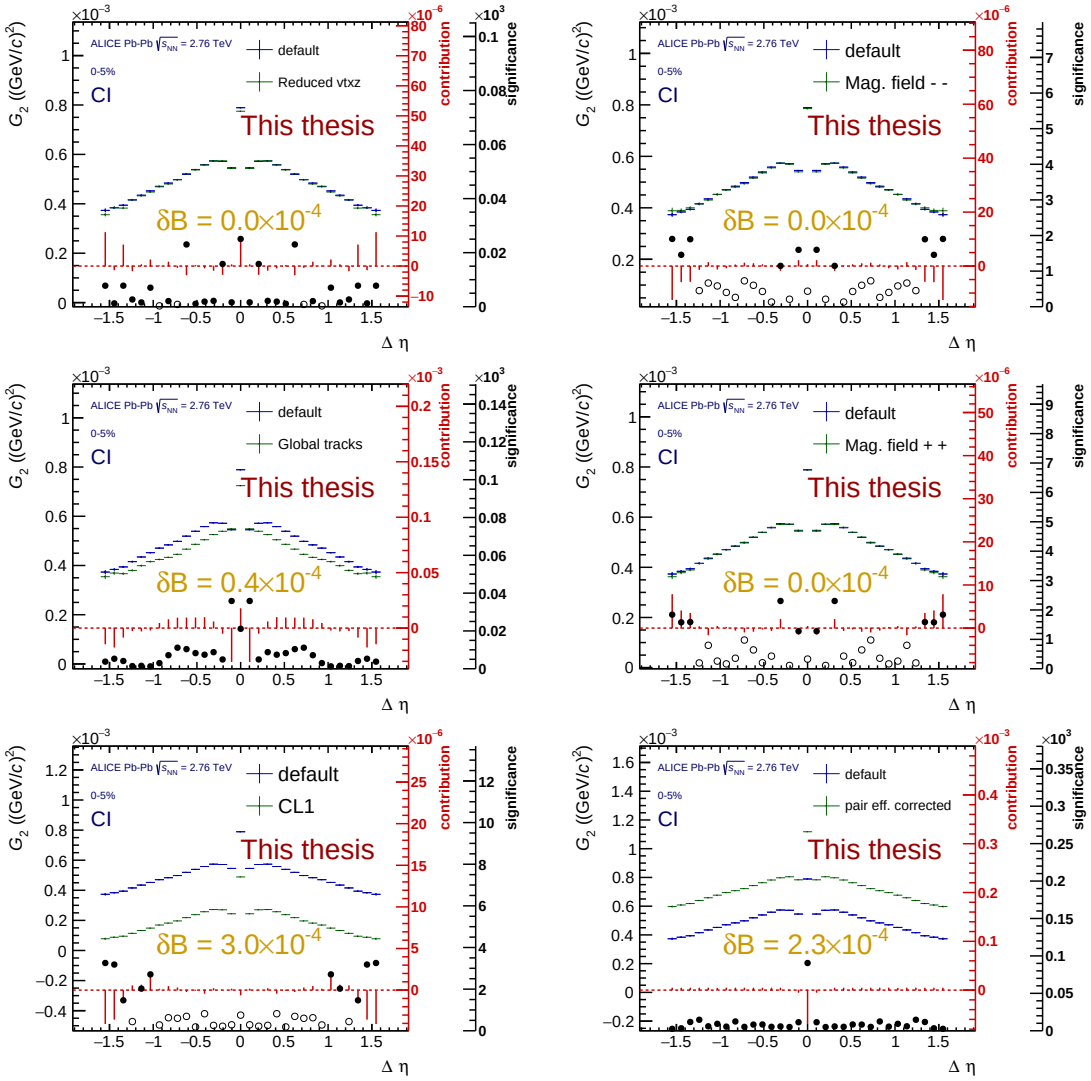

FIGURE A.1: Systematic uncertainty contribution analysis for the $\Delta\eta$ projection of the charge independent (CI) two-particle correlation function for 0–5% central Pb–Pb collisions at $\sqrt{s_{\mathrm{NN}}}$ = 2.76 TeV as measured by ALICE. On the top row, reduced vertex acceptance (left) and magnetic field polarity −− tests; on the middle row, Global tracks (left) and magnetic field polarity ++ tests; on the bottom row, centrality estimation using CL1 information (left) and incorporation of the pair efficiency correction (right). On all panels the blue points are the results from the default analysis while the green are the ones from the corresponding test (see section 5.5.2).

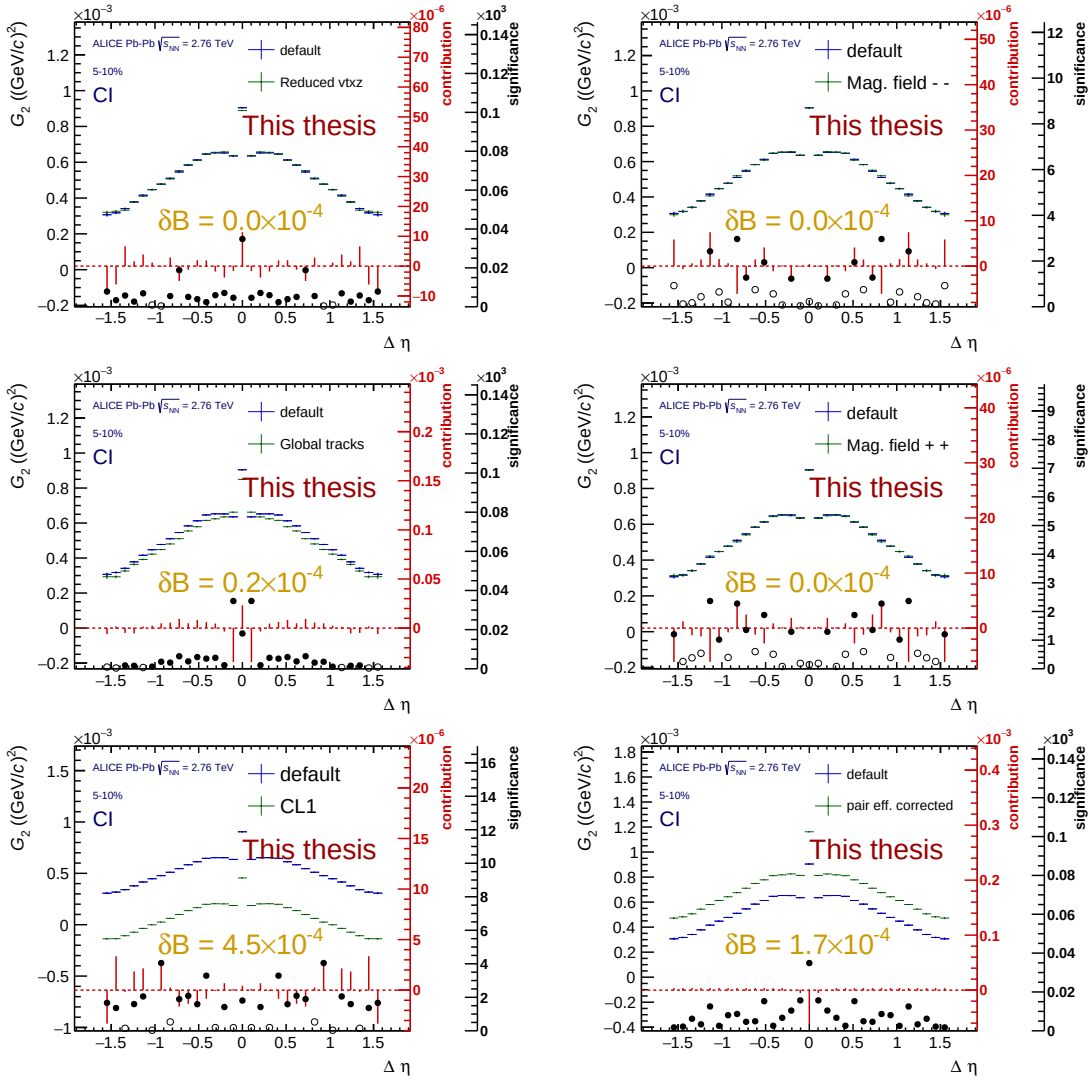

FIGURE A.2: Systematic uncertainty contribution analysis for the $\Delta\eta$ projection of the charge independent (CI) two-particle correlation function for 5–10% central Pb–Pb collisions at $\sqrt{s_{\mathrm{NN}}}$ = 2.76 TeV as measured by ALICE. On the top row, reduced vertex acceptance (left) and magnetic field polarity −− tests; on the middle row, Global tracks (left) and magnetic field polarity ++ tests; on the bottom row, centrality estimation using CL1 information (left) and incorporation of the pair efficiency correction (right). On all panels the blue points are the results from the default analysis while the green are the ones from the corresponding test (see section 5.5.2).

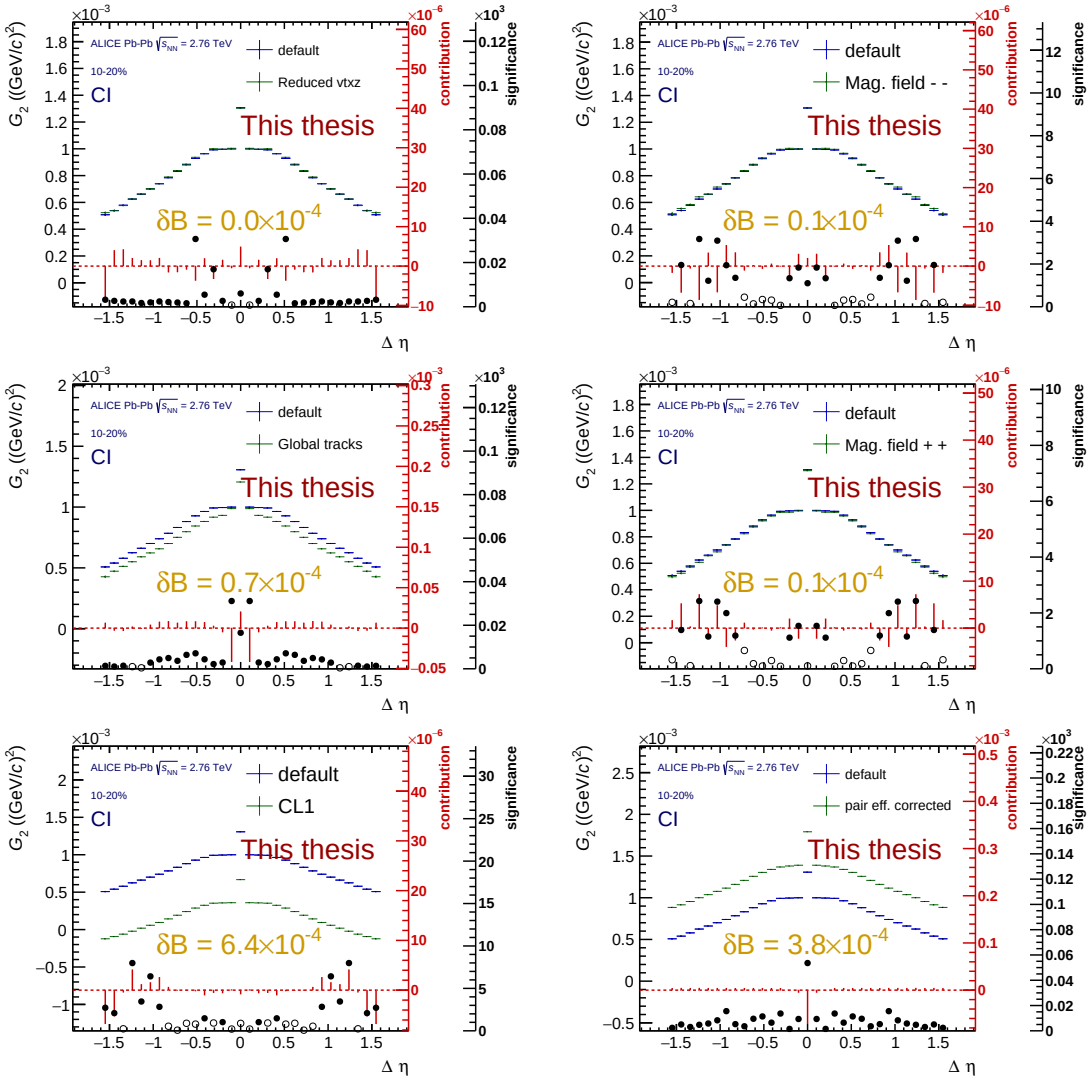

FIGURE A.3: Systematic uncertainty contribution analysis for the $\Delta\eta$ projection of the charge independent (CI) two-particle correlation function for 10–20% central Pb–Pb collisions at $\sqrt{s_{\mathrm{NN}}}$ = 2.76 TeV as measured by ALICE. On the top row, reduced vertex acceptance (left) and magnetic field polarity −− tests; on the middle row, Global tracks (left) and magnetic field polarity ++ tests; on the bottom row, centrality estimation using CL1 information (left) and incorporation of the pair efficiency correction (right). On all panels the blue points are the results from the default analysis while the green are the ones from the corresponding test (see section 5.5.2).

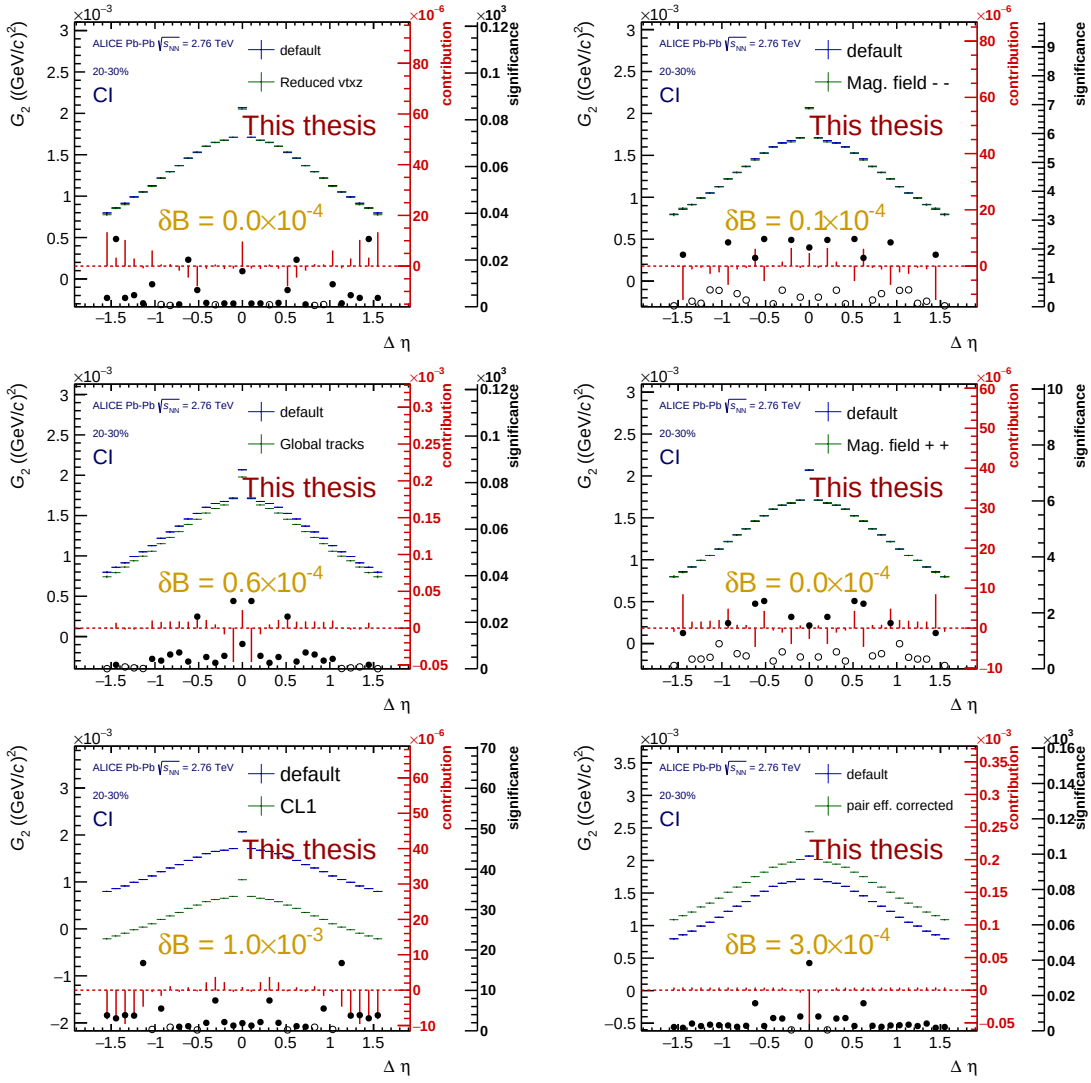

FIGURE A.4: Systematic uncertainty contribution analysis for the $\Delta\eta$ projection of the charge independent (CI) two-particle correlation function for 20–30% central Pb–Pb collisions at $\sqrt{s_{\mathrm{NN}}}$ = 2.76 TeV as measured by ALICE. On the top row, reduced vertex acceptance (left) and magnetic field polarity −− tests; on the middle row, Global tracks (left) and magnetic field polarity ++ tests; on the bottom row, centrality estimation using CL1 information (left) and incorporation of the pair efficiency correction (right). On all panels the blue points are the results from the default analysis while the green are the ones from the corresponding test (see section 5.5.2).

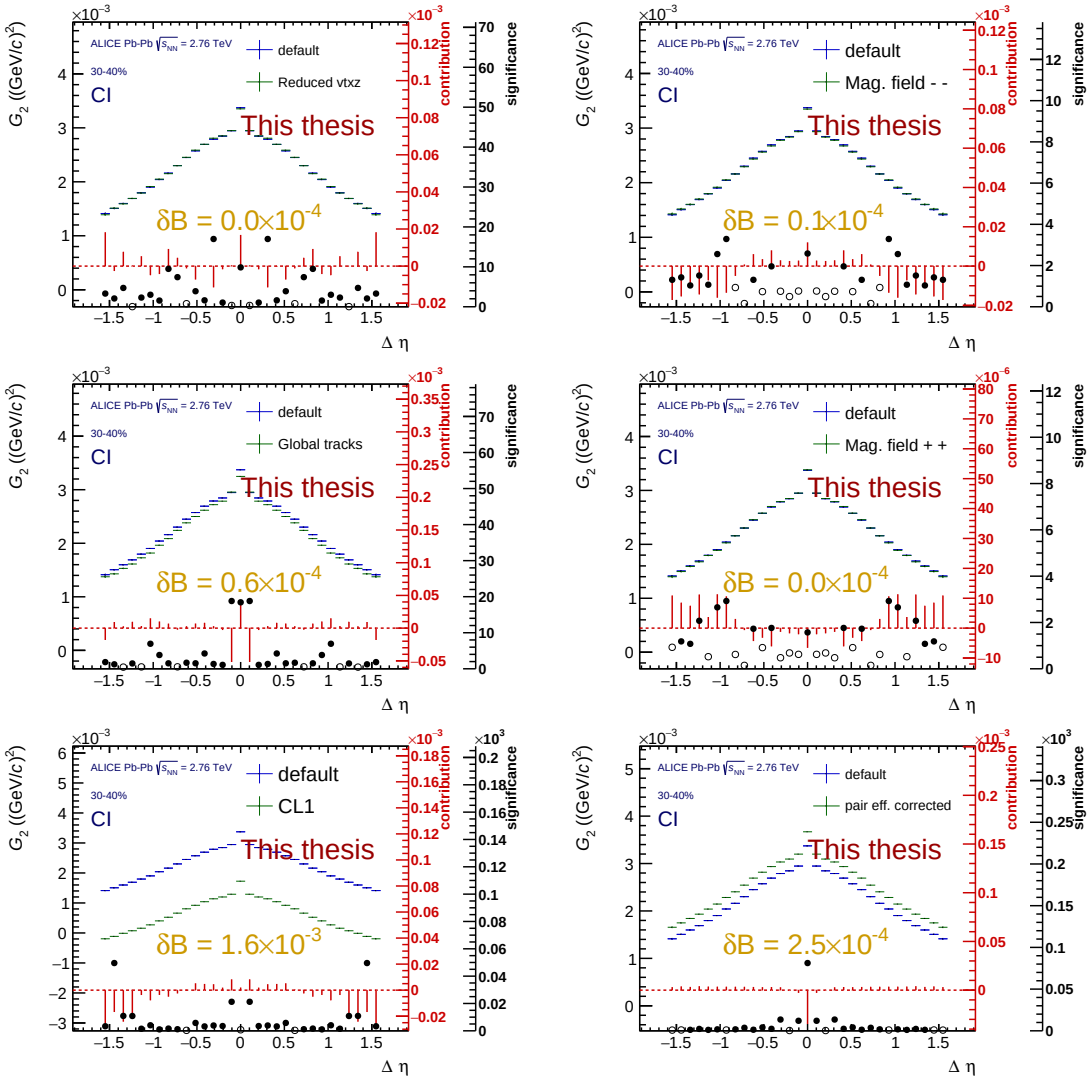

FIGURE A.5: Systematic uncertainty contribution analysis for the $\Delta\eta$ projection of the charge independent (CI) two-particle correlation function for 30–40% central Pb–Pb collisions at $\sqrt{s_{\mathrm{NN}}}$ = 2.76 TeV as measured by ALICE. On the top row, reduced vertex acceptance (left) and magnetic field polarity −− tests; on the middle row, Global tracks (left) and magnetic field polarity ++ tests; on the bottom row, centrality estimation using CL1 information (left) and incorporation of the pair efficiency correction (right). On all panels the blue points are the results from the default analysis while the green are the ones from the corresponding test (see section 5.5.2).

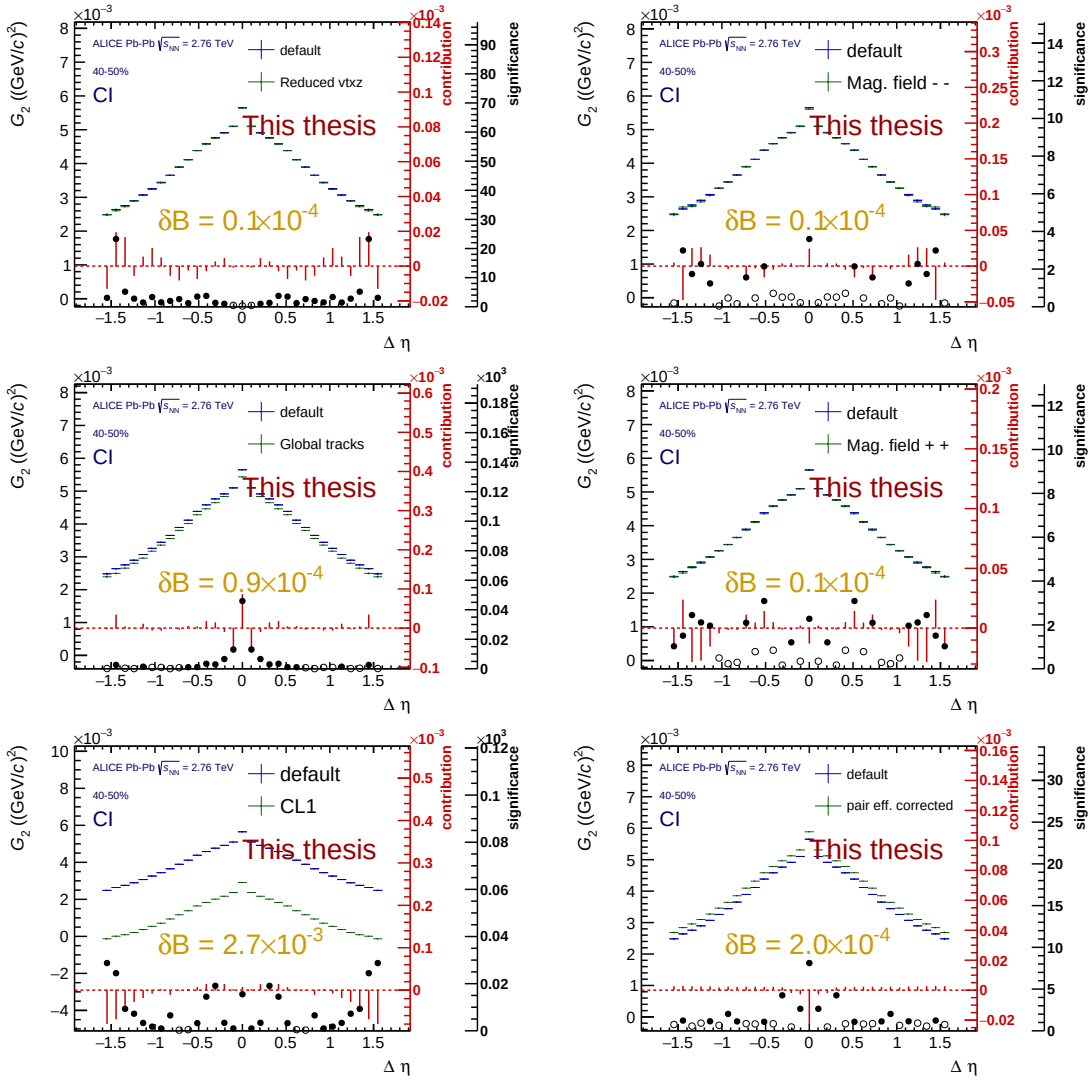

FIGURE A.6: Systematic uncertainty contribution analysis for the $\Delta\eta$ projection of the charge independent (CI) two-particle correlation function for 40–50% central Pb–Pb collisions at $\sqrt{s_{\mathrm{NN}}}$ = 2.76 TeV as measured by ALICE. On the top row, reduced vertex acceptance (left) and magnetic field polarity −− tests; on the middle row, Global tracks (left) and magnetic field polarity ++ tests; on the bottom row, centrality estimation using CL1 information (left) and incorporation of the pair efficiency correction (right). On all panels the blue points are the results from the default analysis while the green are the ones from the corresponding test (see section 5.5.2).

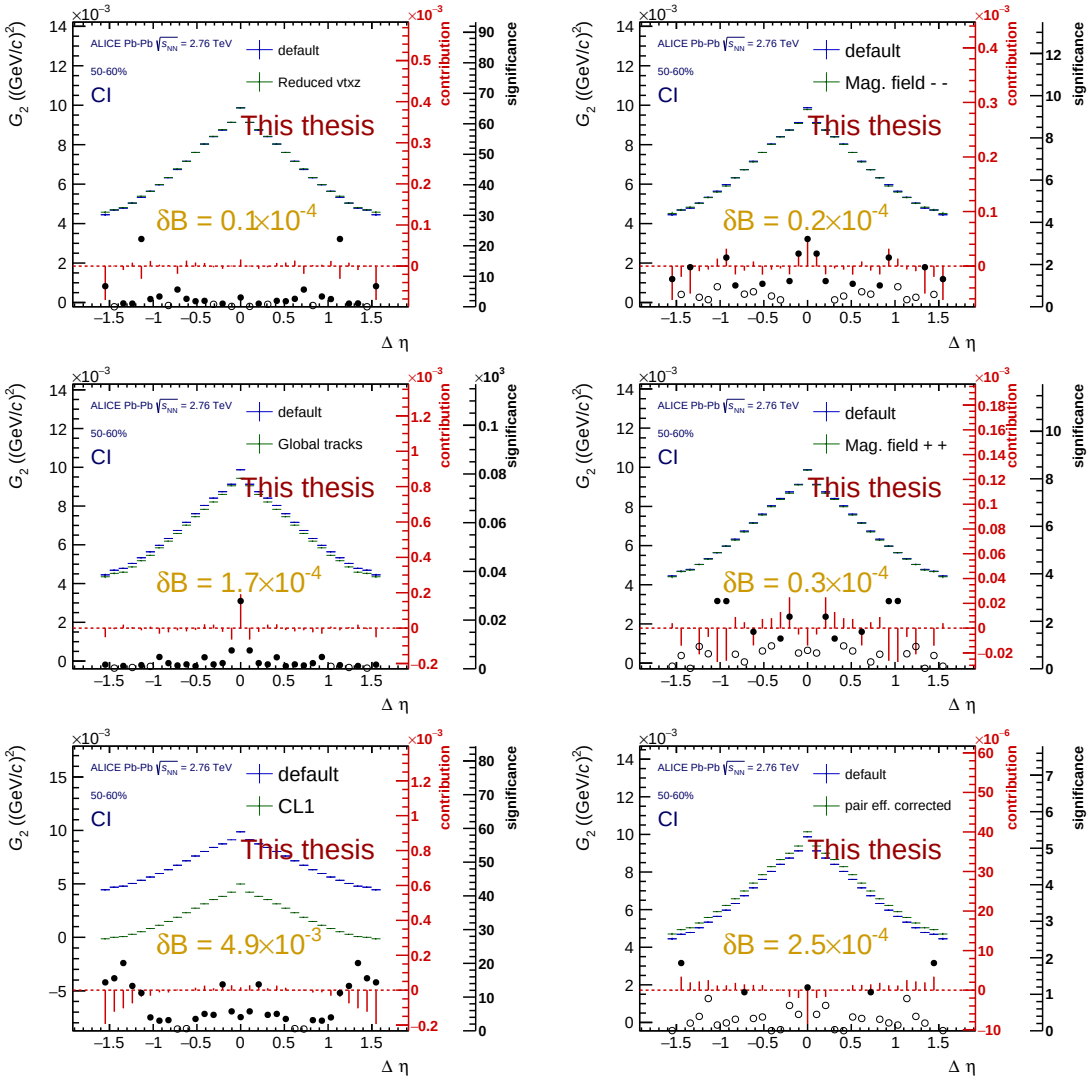

FIGURE A.7: Systematic uncertainty contribution analysis for the $\Delta\eta$ projection of the charge independent (CI) two-particle correlation function for 50–60% central Pb–Pb collisions at $\sqrt{s_{\mathrm{NN}}}$ = 2.76 TeV as measured by ALICE. On the top row, reduced vertex acceptance (left) and magnetic field polarity −− tests; on the middle row, Global tracks (left) and magnetic field polarity ++ tests; on the bottom row, centrality estimation using CL1 information (left) and incorporation of the pair efficiency correction (right). On all panels the blue points are the results from the default analysis while the green are the ones from the corresponding test (see section 5.5.2).

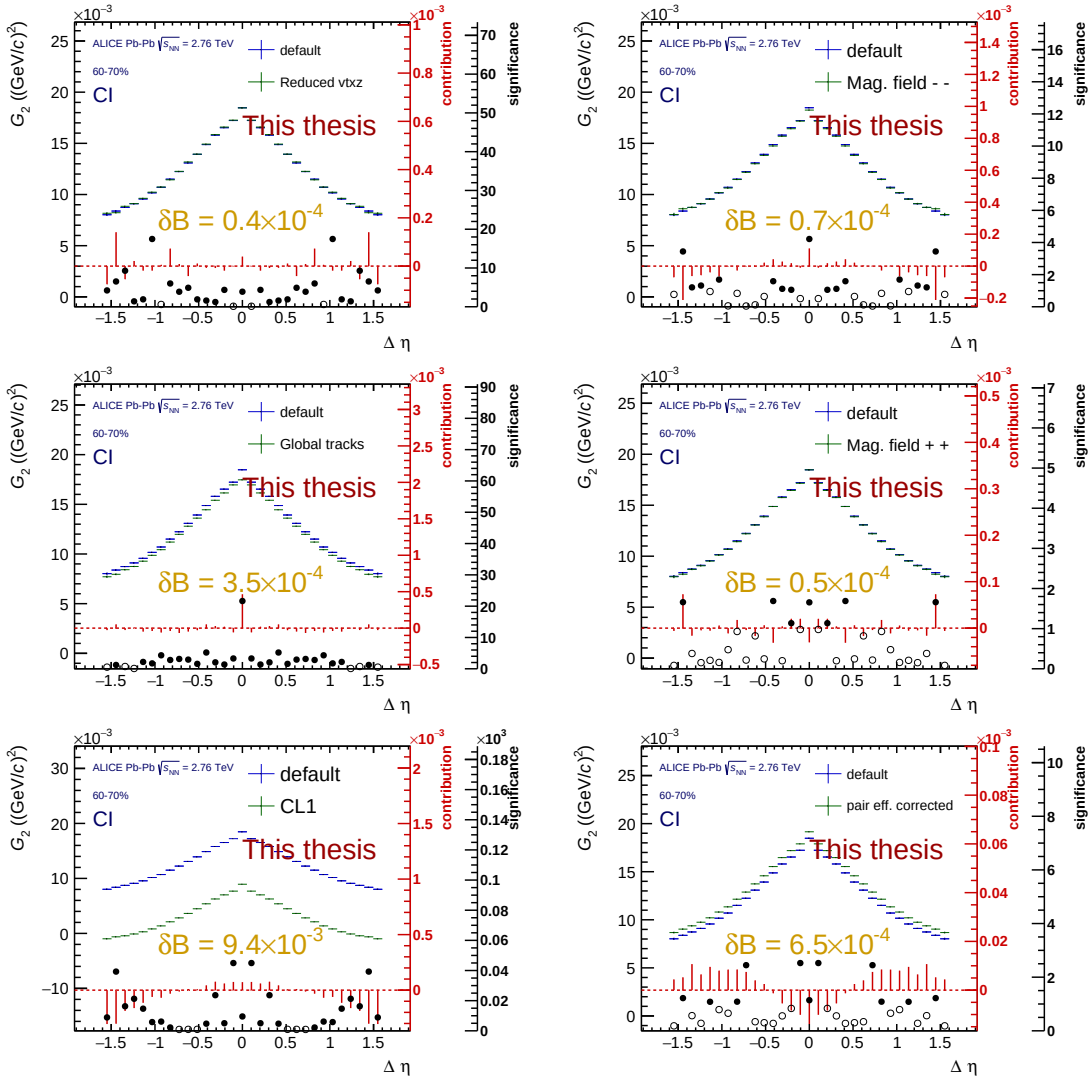

FIGURE A.8: Systematic uncertainty contribution analysis for the $\Delta\eta$ projection of the charge independent (CI) two-particle correlation function for 60–70% central Pb–Pb collisions at $\sqrt{s_{\mathrm{NN}}}$ = 2.76 TeV as measured by ALICE. On the top row, reduced vertex acceptance (left) and magnetic field polarity −− tests; on the middle row, Global tracks (left) and magnetic field polarity ++ tests; on the bottom row, centrality estimation using CL1 information (left) and incorporation of the pair efficiency correction (right). On all panels the blue points are the results from the default analysis while the green are the ones from the corresponding test (see section 5.5.2).

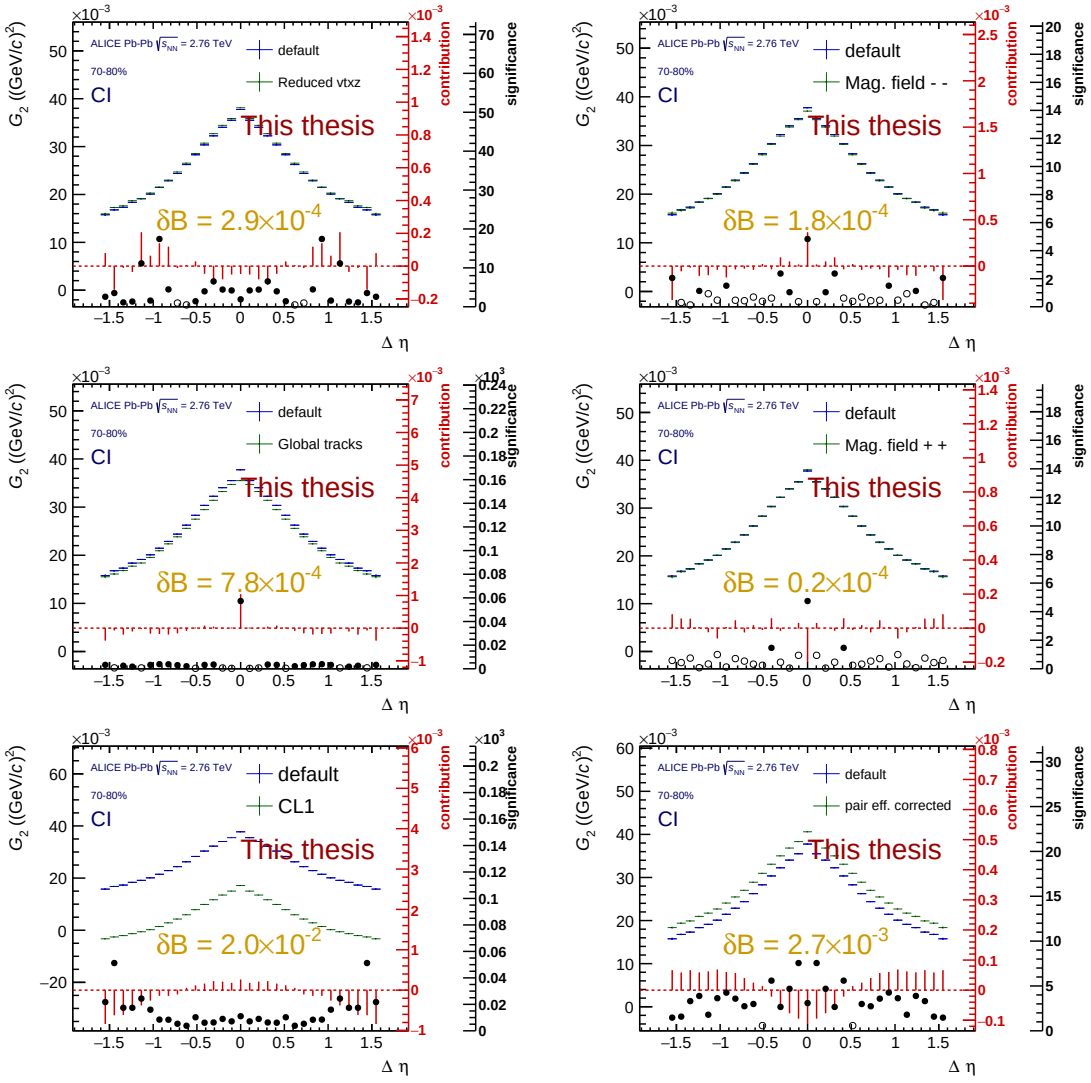

FIGURE A.9: Systematic uncertainty contribution analysis for the $\Delta\eta$ projection of the charge independent (CI) two-particle correlation function for 70–80% central Pb–Pb collisions at $\sqrt{s_{\mathrm{NN}}}$ = 2.76 TeV as measured by ALICE. On the top row, reduced vertex acceptance (left) and magnetic field polarity −− tests; on the middle row, Global tracks (left) and magnetic field polarity ++ tests; on the bottom row, centrality estimation using CL1 information (left) and incorporation of the pair efficiency correction (right). On all panels the blue points are the results from the default analysis while the green are the ones from the corresponding test (see section 5.5.2).

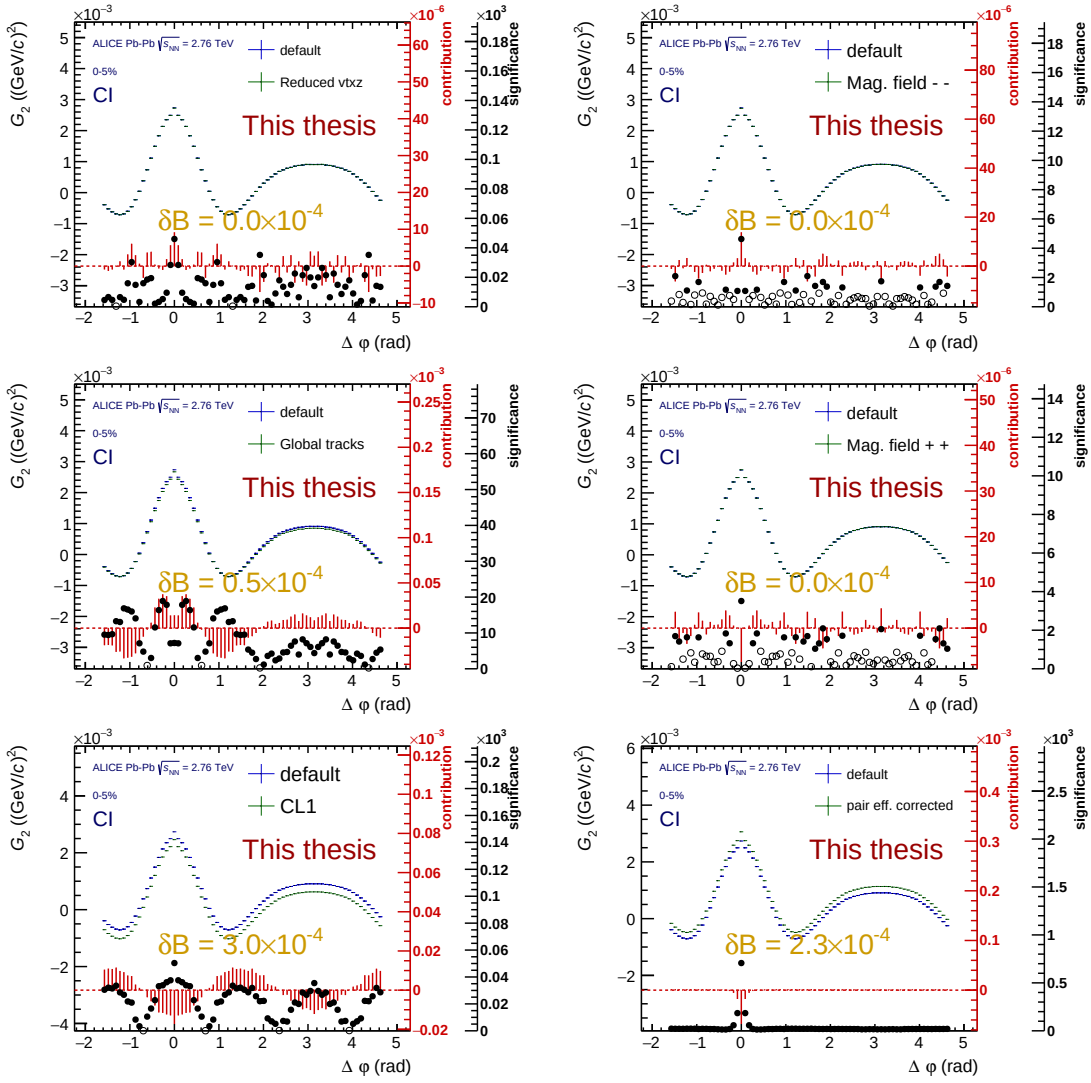

FIGURE A.10: Systematic uncertainty contribution analysis for the $\Delta\varphi$ projection of the charge independent (CI) two-particle correlation function for 0–5% central Pb–Pb collisions at $\sqrt{s_{\mathrm{NN}}}$ = 2.76 TeV as measured by ALICE. On the top row, reduced vertex acceptance (left) and magnetic field polarity −− tests; on the middle row, Global tracks (left) and magnetic field polarity ++ tests; on the bottom row, centrality estimation using CL1 information (left) and incorporation of the pair efficiency correction (right). On all panels the blue points are the results from the default analysis while the green are the ones from the corresponding test (see section 5.5.2).

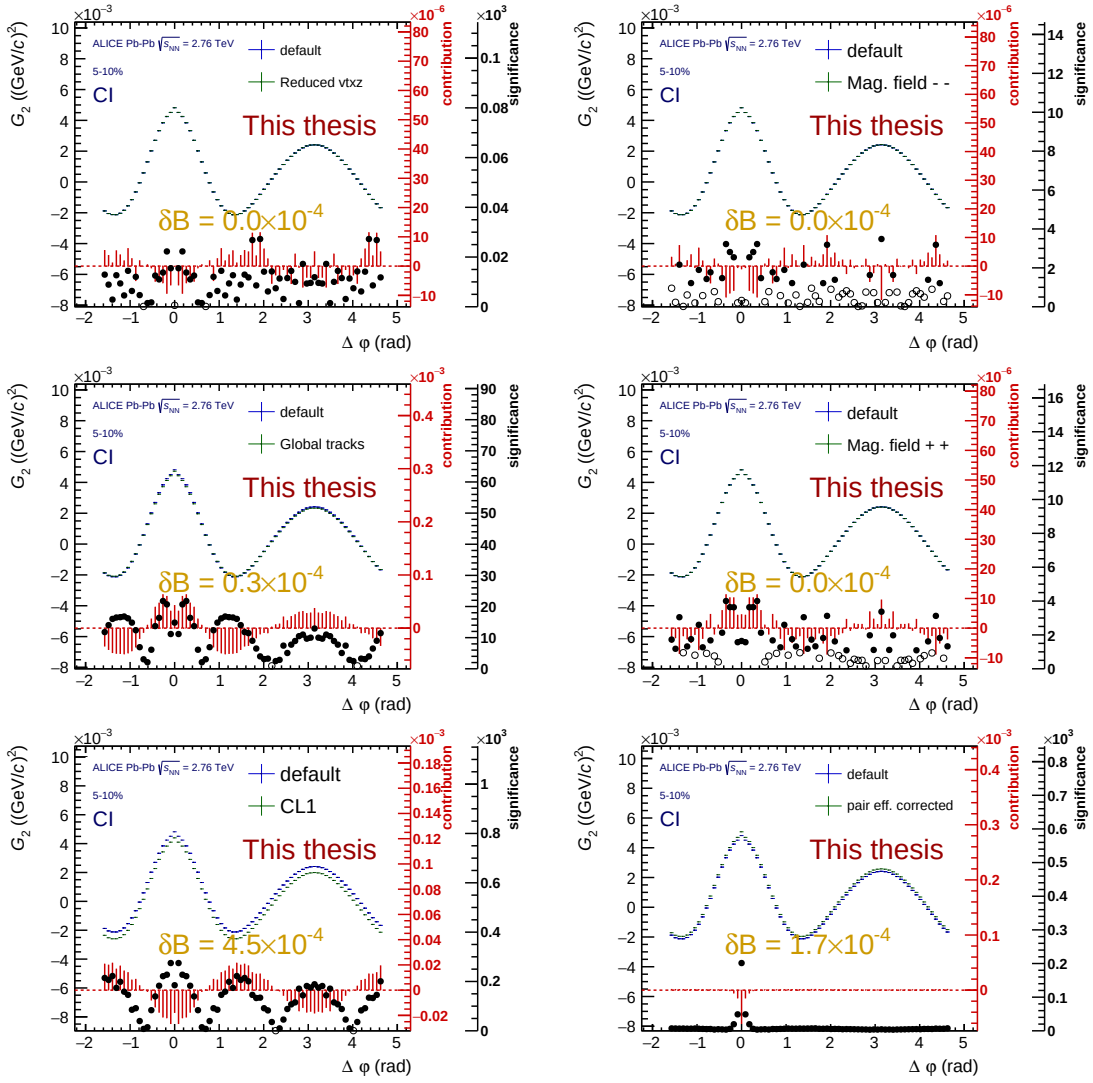

FIGURE A.11: Systematic uncertainty contribution analysis for the $\Delta\varphi$ projection of the charge independent (CI) two-particle correlation function for 5–10% central Pb–Pb collisions at $\sqrt{s_{\mathrm{NN}}}$ = 2.76 TeV as measured by ALICE. On the top row, reduced vertex acceptance (left) and magnetic field polarity −− tests; on the middle row, Global tracks (left) and magnetic field polarity ++ tests; on the bottom row, centrality estimation using CL1 information (left) and incorporation of the pair efficiency correction (right). On all panels the blue points are the results from the default analysis while the green are the ones from the corresponding test (see section 5.5.2).

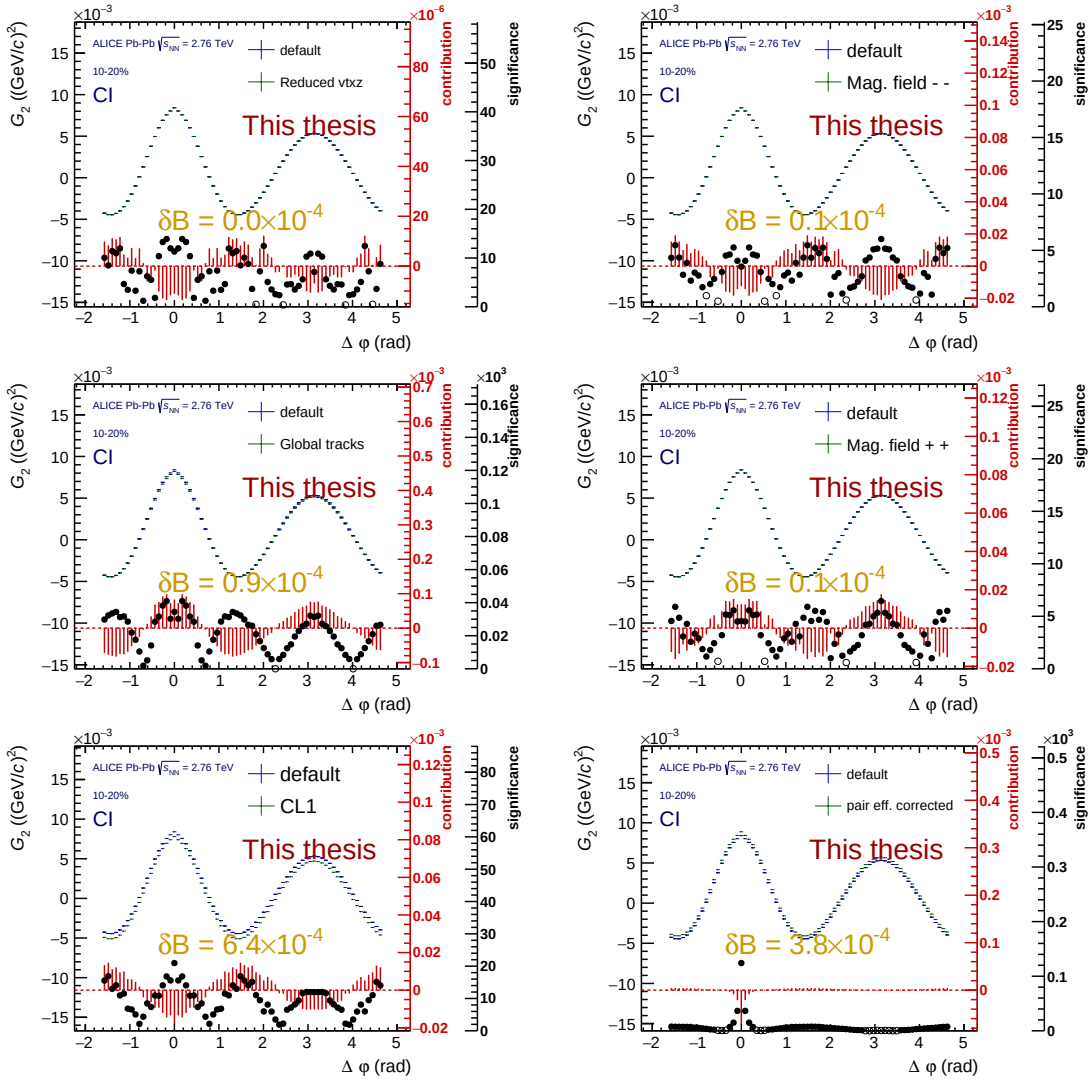

FIGURE A.12: Systematic uncertainty contribution analysis for the $\Delta\varphi$ projection of the charge independent (CI) two-particle correlation function for 10–20% central Pb–Pb collisions at $\sqrt{s_{\mathrm{NN}}}$ = 2.76 TeV as measured by ALICE. On the top row, reduced vertex acceptance (left) and magnetic field polarity −− tests; on the middle row, Global tracks (left) and magnetic field polarity ++ tests; on the bottom row, centrality estimation using CL1 information (left) and incorporation of the pair efficiency correction (right). On all panels the blue points are the results from the default analysis while the green are the ones from the corresponding test (see section 5.5.2).

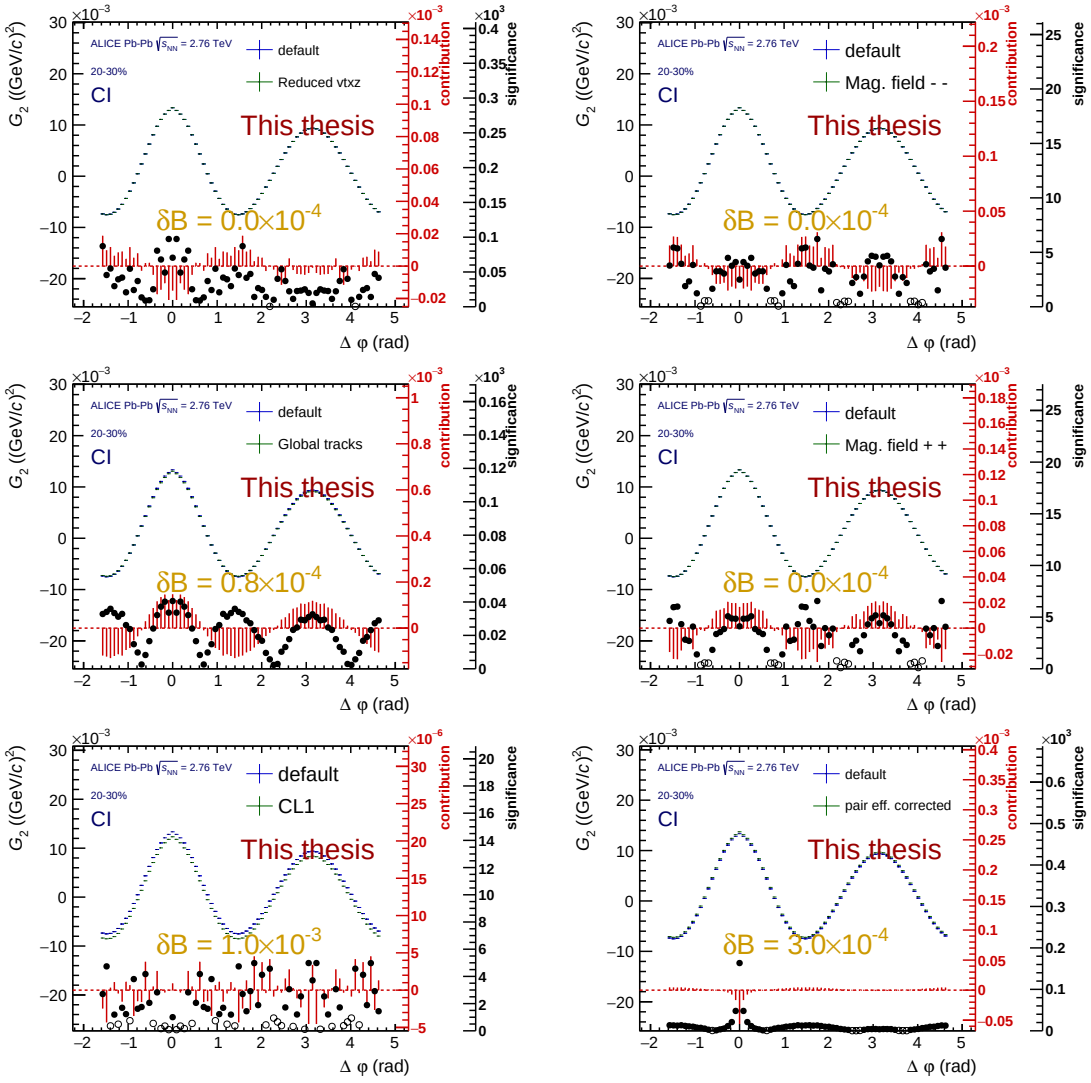

FIGURE A.13: Systematic uncertainty contribution analysis for the $\Delta\varphi$ projection of the charge independent (CI) two-particle correlation function for 20–30% central Pb–Pb collisions at $\sqrt{s_{\mathrm{NN}}}$ = 2.76 TeV as measured by ALICE. On the top row, reduced vertex acceptance (left) and magnetic field polarity −− tests; on the middle row, Global tracks (left) and magnetic field polarity ++ tests; on the bottom row, centrality estimation using CL1 information (left) and incorporation of the pair efficiency correction (right). On all panels the blue points are the results from the default analysis while the green are the ones from the corresponding test (see section 5.5.2).

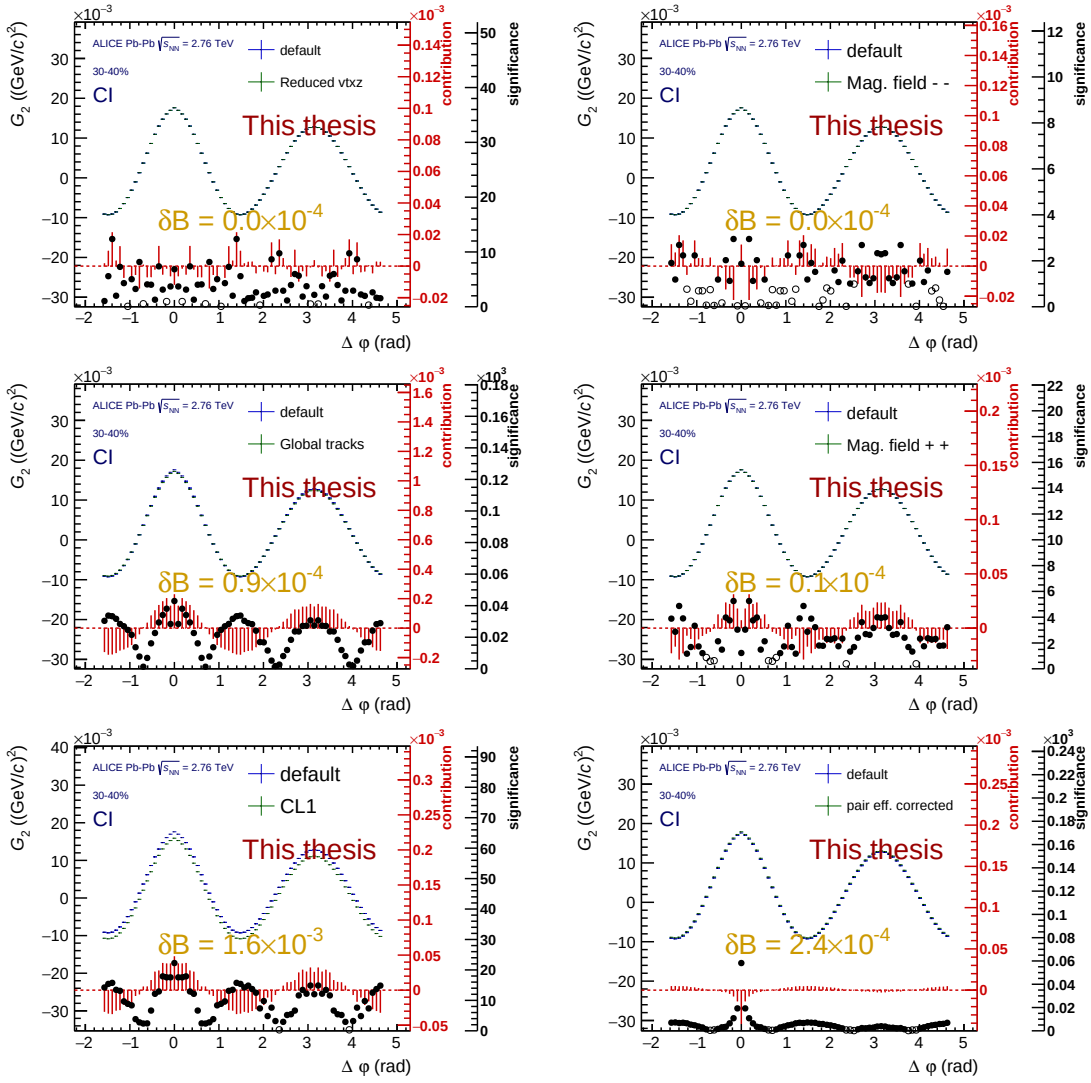

FIGURE A.14: Systematic uncertainty contribution analysis for the $\Delta\varphi$ projection of the charge independent (CI) two-particle correlation function for 30–40% central Pb–Pb collisions at $\sqrt{s_{\mathrm{NN}}}$ = 2.76 TeV as measured by ALICE. On the top row, reduced vertex acceptance (left) and magnetic field polarity −− tests; on the middle row, Global tracks (left) and magnetic field polarity ++ tests; on the bottom row, centrality estimation using CL1 information (left) and incorporation of the pair efficiency correction (right). On all panels the blue points are the results from the default analysis while the green are the ones from the corresponding test (see section 5.5.2).

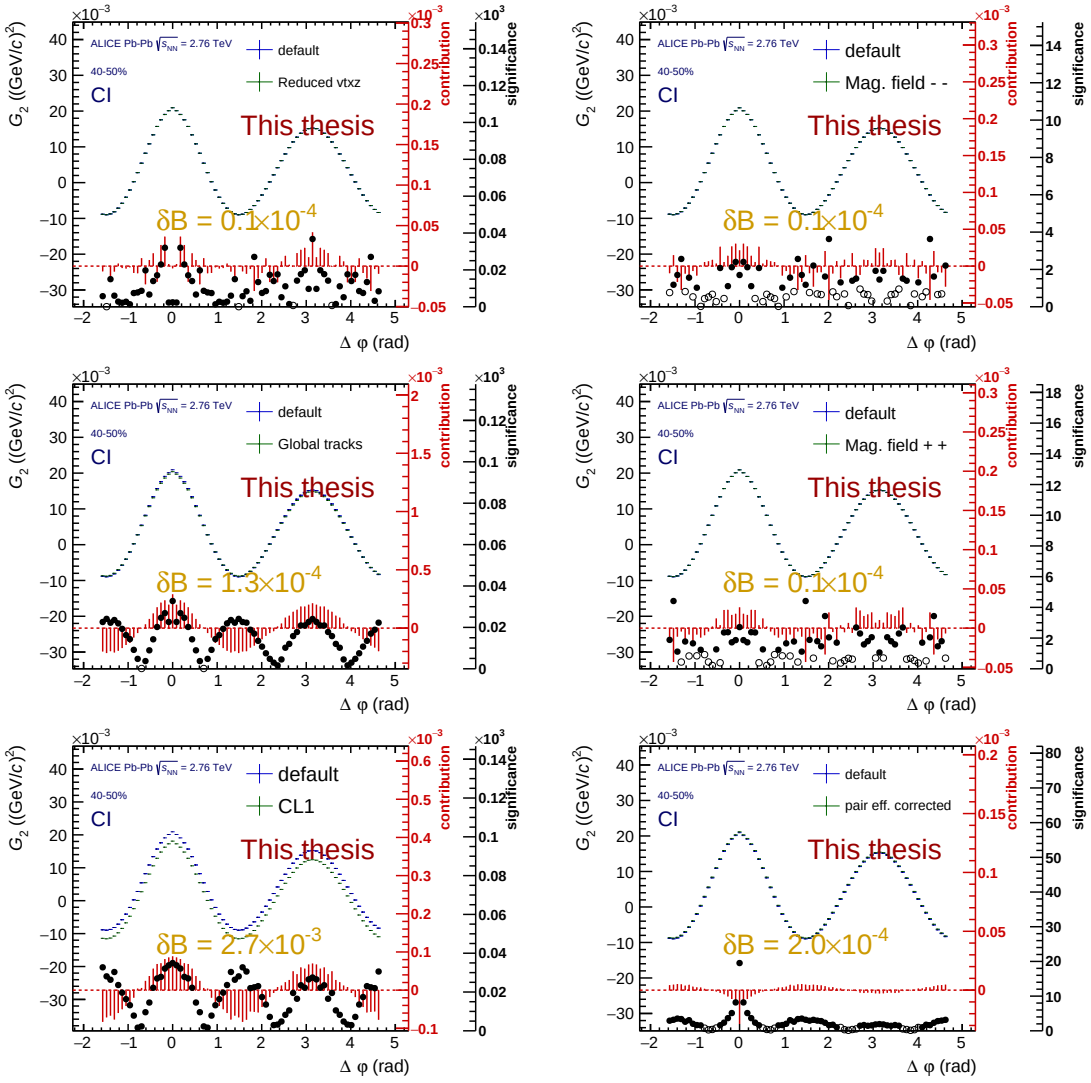

FIGURE A.15: Systematic uncertainty contribution analysis for the $\Delta\varphi$ projection of the charge independent (CI) two-particle correlation function for 40–50% central Pb–Pb collisions at $\sqrt{s_{\mathrm{NN}}}$ = 2.76 TeV as measured by ALICE. On the top row, reduced vertex acceptance (left) and magnetic field polarity −− tests; on the middle row, Global tracks (left) and magnetic field polarity ++ tests; on the bottom row, centrality estimation using CL1 information (left) and incorporation of the pair efficiency correction (right). On all panels the blue points are the results from the default analysis while the green are the ones from the corresponding test (see section 5.5.2).

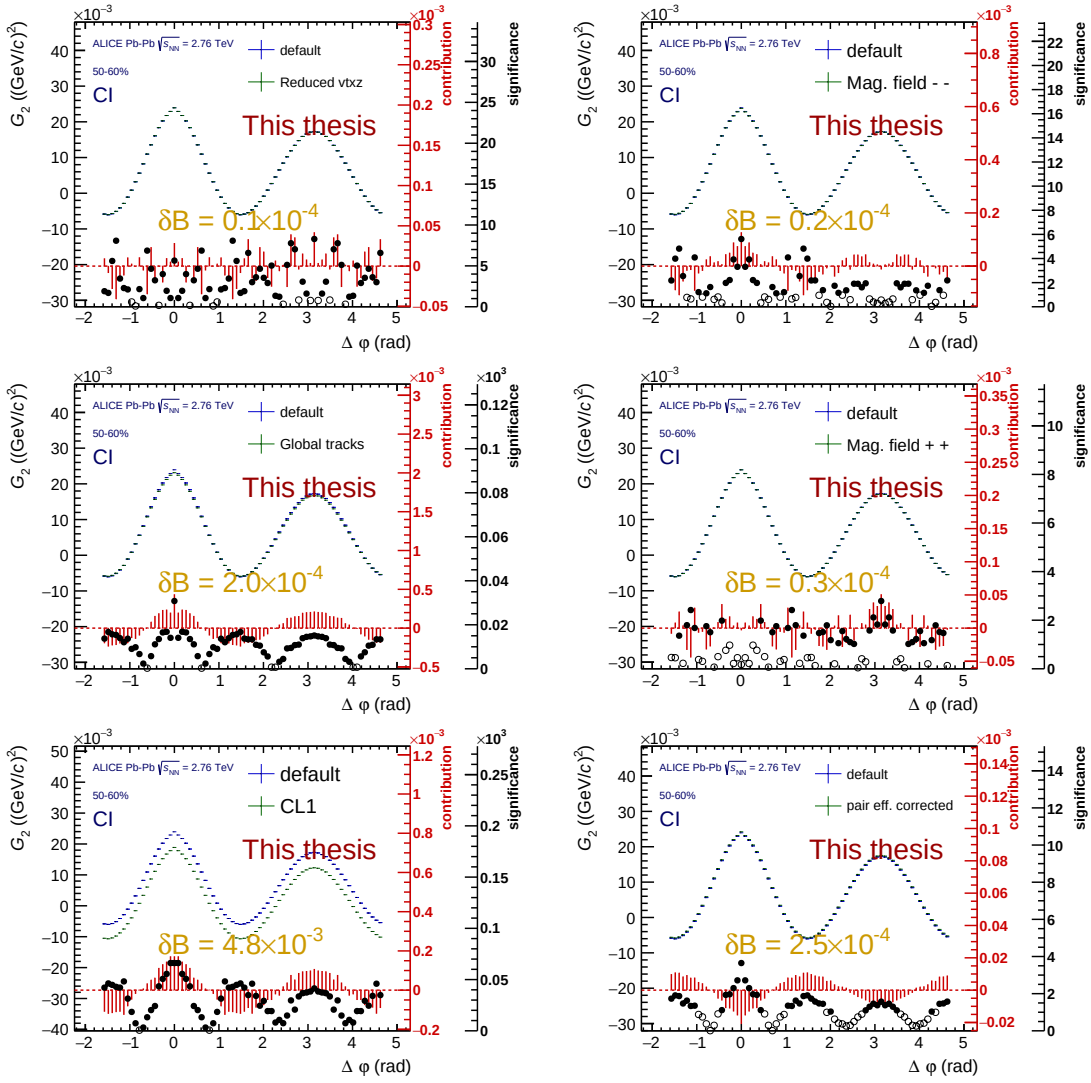

FIGURE A.16: Systematic uncertainty contribution analysis for the $\Delta\varphi$ projection of the charge independent (CI) two-particle correlation function for 50–60% central Pb–Pb collisions at $\sqrt{s_{\mathrm{NN}}}$ = 2.76 TeV as measured by ALICE. On the top row, reduced vertex acceptance (left) and magnetic field polarity −− tests; on the middle row, Global tracks (left) and magnetic field polarity ++ tests; on the bottom row, centrality estimation using CL1 information (left) and incorporation of the pair efficiency correction (right). On all panels the blue points are the results from the default analysis while the green are the ones from the corresponding test (see section 5.5.2).

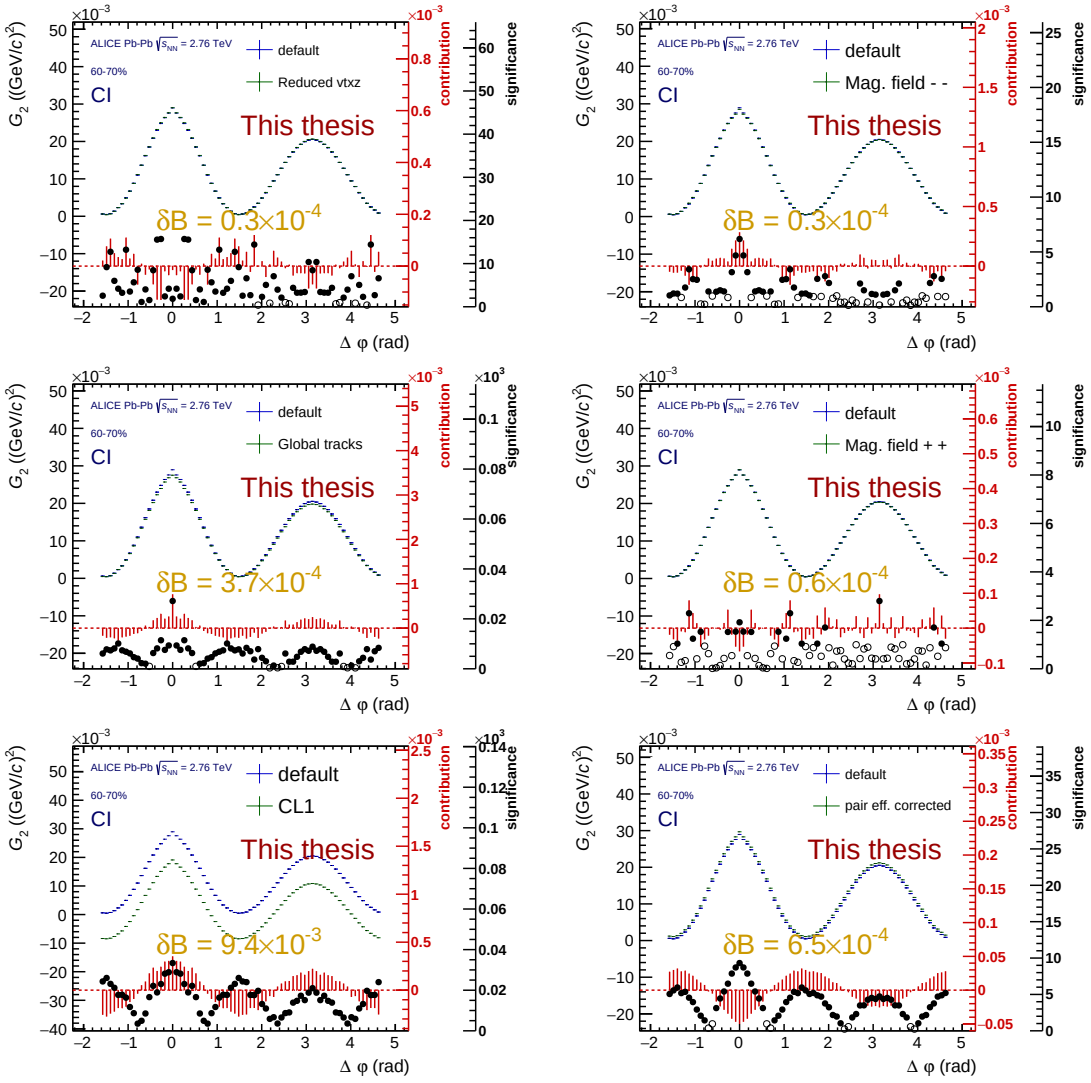

FIGURE A.17: Systematic uncertainty contribution analysis for the $\Delta\varphi$ projection of the charge independent (CI) two-particle correlation function for 60–70% central Pb–Pb collisions at $\sqrt{s_{\mathrm{NN}}}$ = 2.76 TeV as measured by ALICE. On the top row, reduced vertex acceptance (left) and magnetic field polarity −− tests; on the middle row, Global tracks (left) and magnetic field polarity ++ tests; on the bottom row, centrality estimation using CL1 information (left) and incorporation of the pair efficiency correction (right). On all panels the blue points are the results from the default analysis while the green are the ones from the corresponding test (see section 5.5.2).

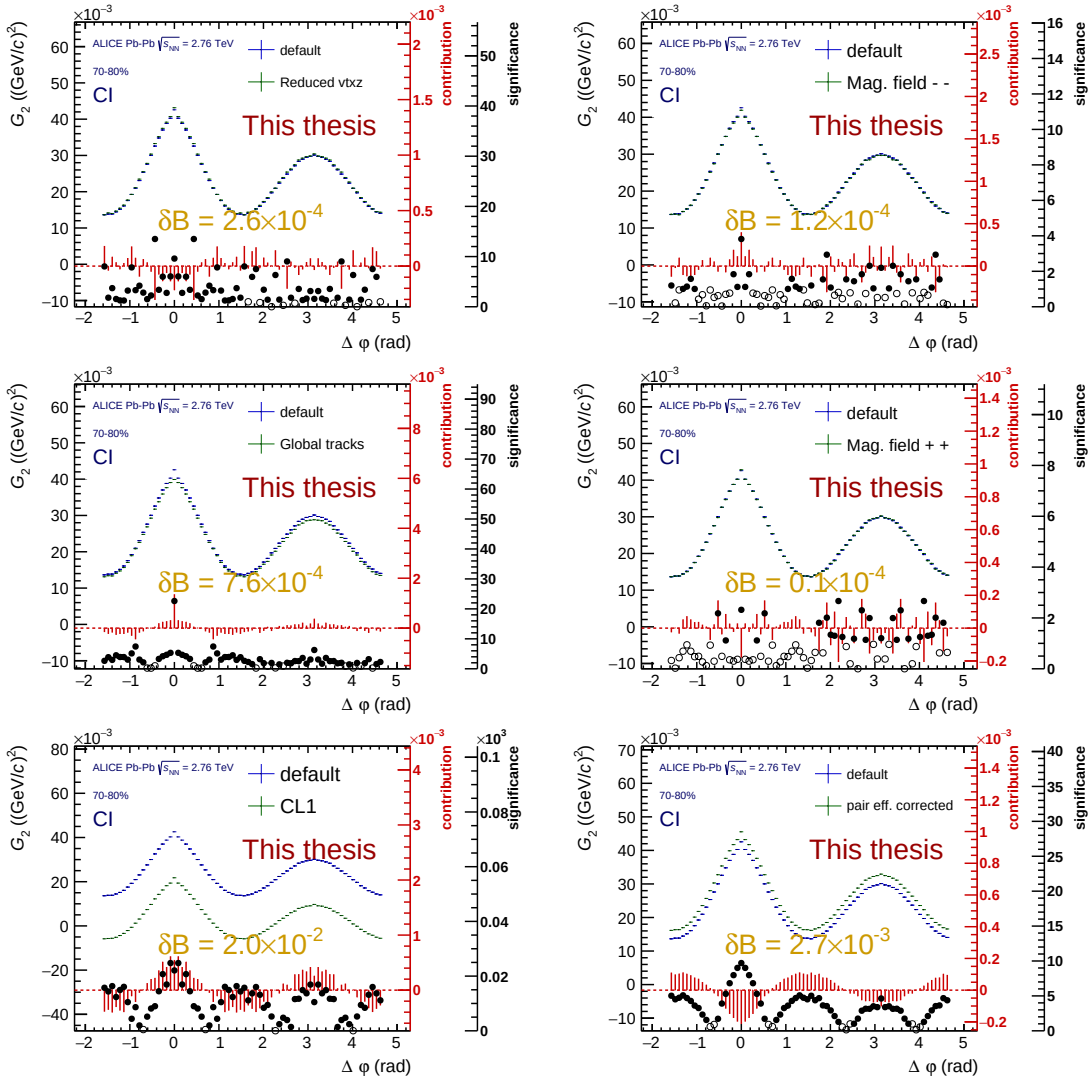

FIGURE A.18: Systematic uncertainty contribution analysis for the $\Delta\varphi$ projection of the charge independent (CI) two-particle correlation function for 70–80% central Pb–Pb collisions at $\sqrt{s_{\mathrm{NN}}}$ = 2.76 TeV as measured by ALICE. On the top row, reduced vertex acceptance (left) and magnetic field polarity −− tests; on the middle row, Global tracks (left) and magnetic field polarity ++ tests; on the bottom row, centrality estimation using CL1 information (left) and incorporation of the pair efficiency correction (right). On all panels the blue points are the results from the default analysis while the green are the ones from the corresponding test (see section 5.5.2).

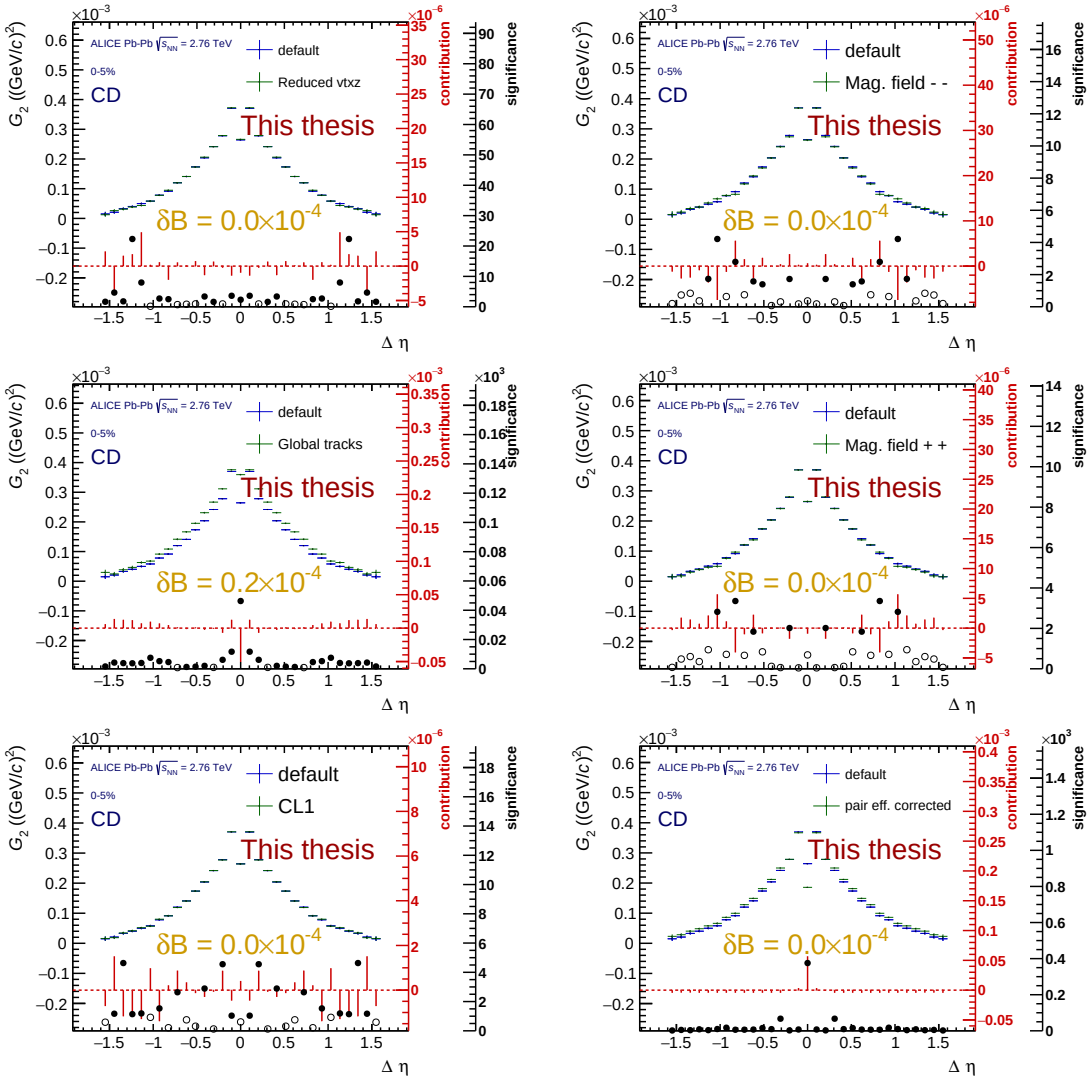

FIGURE A.19: Systematic uncertainty contribution analysis for the $\Delta\eta$ projection of the charge dependent (CD) two-particle correlation function for 0–5% central Pb–Pb collisions at $\sqrt{s_{\mathrm{NN}}}$ = 2.76 TeV as measured by ALICE. On the top row, reduced vertex acceptance (left) and magnetic field polarity −− tests; on the middle row, Global tracks (left) and magnetic field polarity ++ tests; on the bottom row, centrality estimation using CL1 information (left) and incorporation of the pair efficiency correction (right). On all panels the blue points are the results from the default analysis while the green are the ones from the corresponding test (see section 5.5.2).

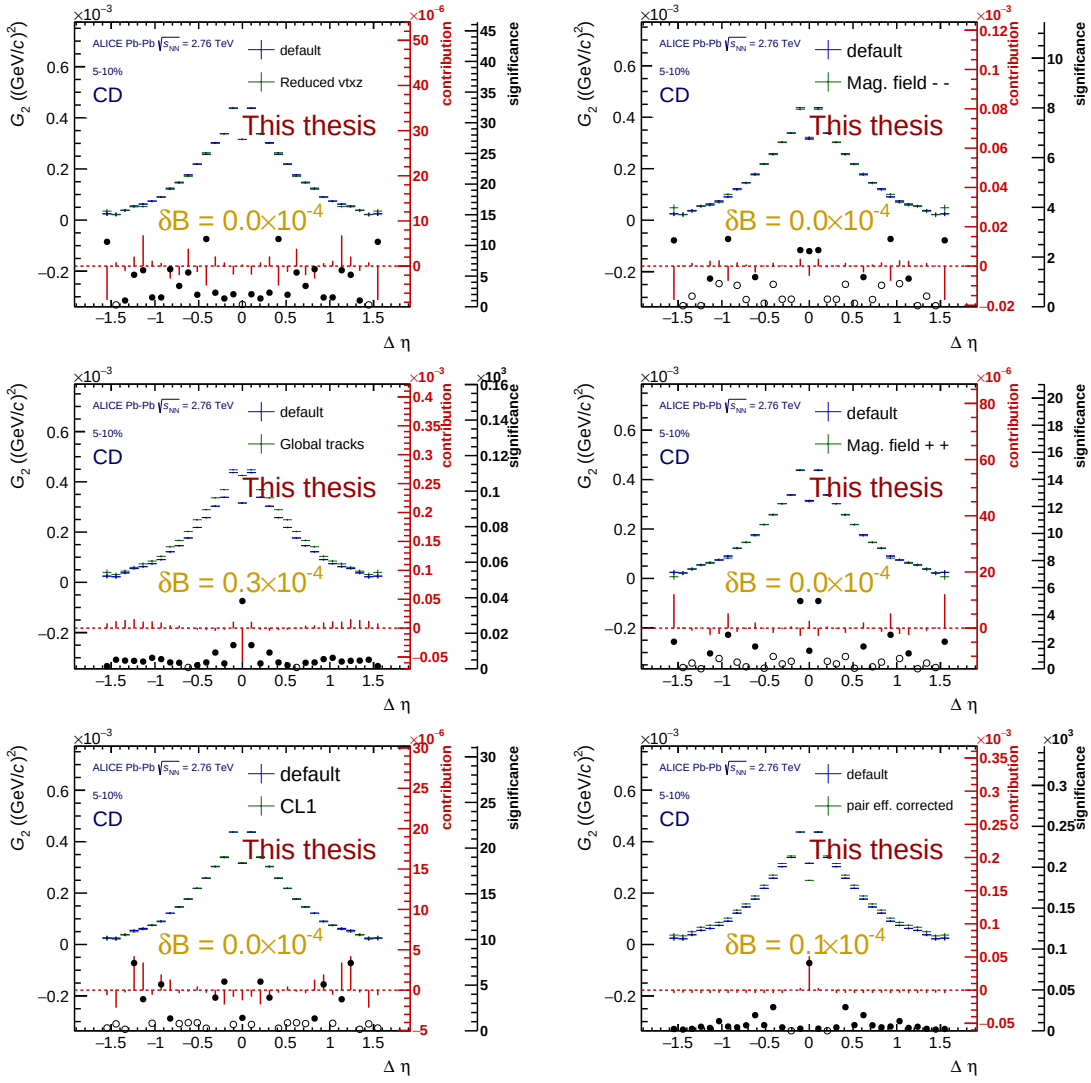

FIGURE A.20: Systematic uncertainty contribution analysis for the $\Delta\eta$ projection of the charge dependent (CD) two-particle correlation function for 5–10% central Pb–Pb collisions at $\sqrt{s_{\mathrm{NN}}}$ = 2.76 TeV as measured by ALICE. On the top row, reduced vertex acceptance (left) and magnetic field polarity −− tests; on the middle row, Global tracks (left) and magnetic field polarity ++ tests; on the bottom row, centrality estimation using CL1 information (left) and incorporation of the pair efficiency correction (right). On all panels the blue points are the results from the default analysis while the green are the ones from the corresponding test (see section 5.5.2).

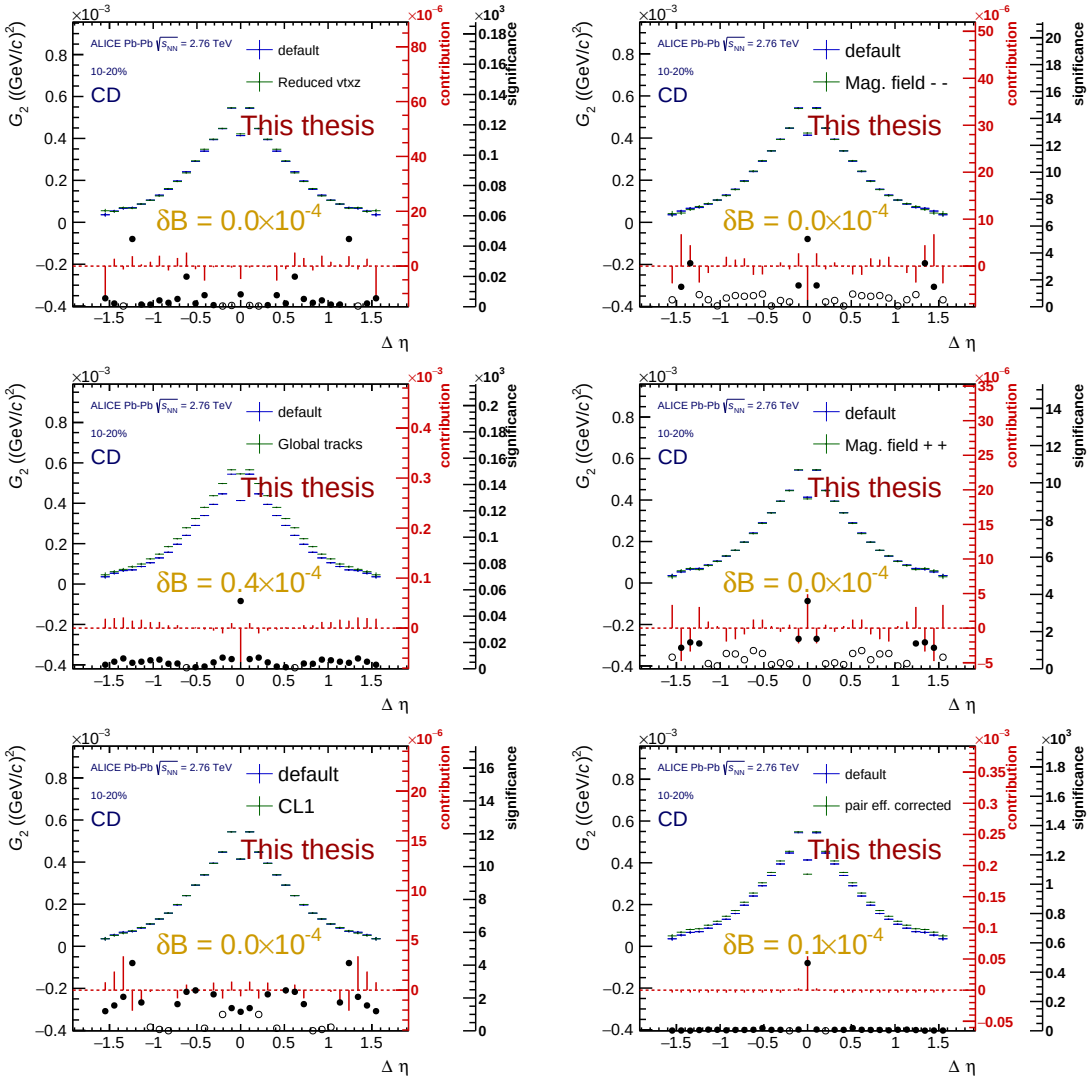

FIGURE A.21: Systematic uncertainty contribution analysis for the $\Delta\eta$ projection of the charge dependent (CD) two-particle correlation function for 10-20% central Pb–Pb collisions at $\sqrt{s_{\mathrm{NN}}}$ = 2.76 TeV as measured by ALICE. On the top row, reduced vertex acceptance (left) and magnetic field polarity −− tests; on the middle row, Global tracks (left) and magnetic field polarity ++ tests; on the bottom row, centrality estimation using CL1 information (left) and incorporation of the pair efficiency correction (right). On all panels the blue points are the results from the default analysis while the green are the ones from the corresponding test (see section 5.5.2).

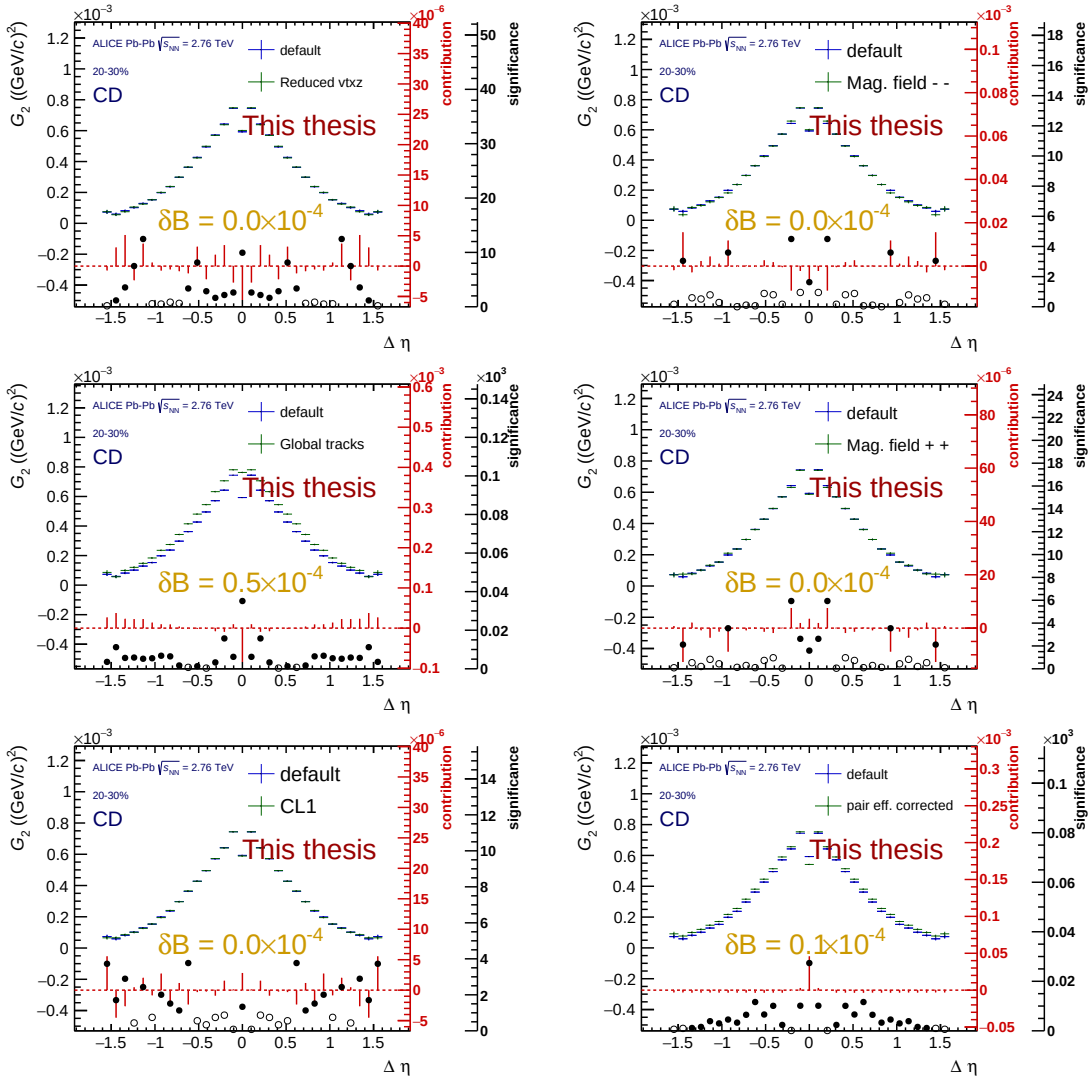

FIGURE A.22: Systematic uncertainty contribution analysis for the $\Delta\eta$ projection of the charge dependent (CD) two-particle correlation function for 20–30% central Pb–Pb collisions at $\sqrt{s_{\mathrm{NN}}}$ = 2.76 TeV as measured by ALICE. On the top row, reduced vertex acceptance (left) and magnetic field polarity −− tests; on the middle row, Global tracks (left) and magnetic field polarity ++ tests; on the bottom row, centrality estimation using CL1 information (left) and incorporation of the pair efficiency correction (right). On all panels the blue points are the results from the default analysis while the green are the ones from the corresponding test (see section 5.5.2).

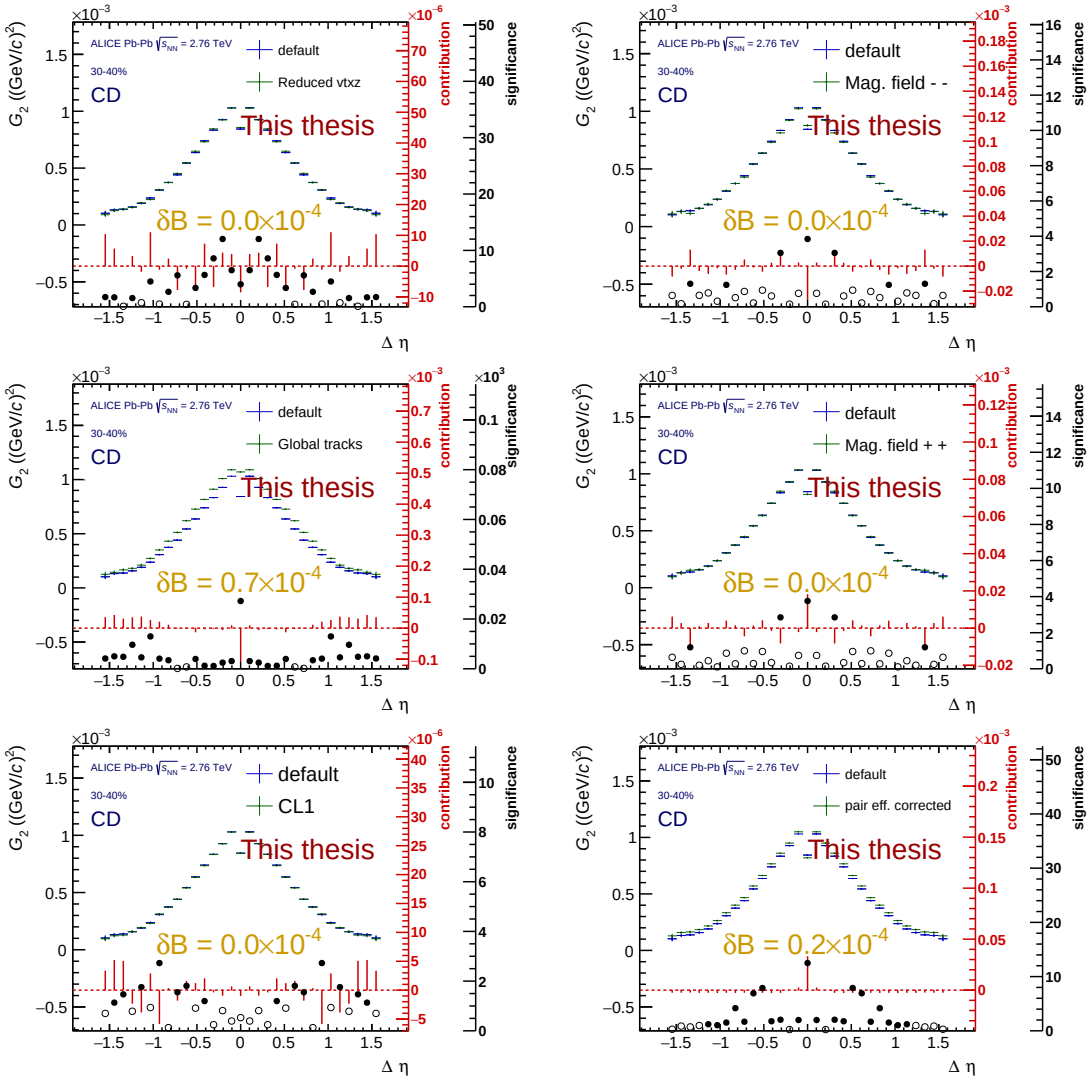

FIGURE A.23: Systematic uncertainty contribution analysis for the $\Delta\eta$ projection of the charge dependent (CD) two-particle correlation function for 30–40% central Pb–Pb collisions at $\sqrt{s_{\mathrm{NN}}}$ = 2.76 TeV as measured by ALICE. On the top row, reduced vertex acceptance (left) and magnetic field polarity −− tests; on the middle row, Global tracks (left) and magnetic field polarity ++ tests; on the bottom row, centrality estimation using CL1 information (left) and incorporation of the pair efficiency correction (right). On all panels the blue points are the results from the default analysis while the green are the ones from the corresponding test (see section 5.5.2).

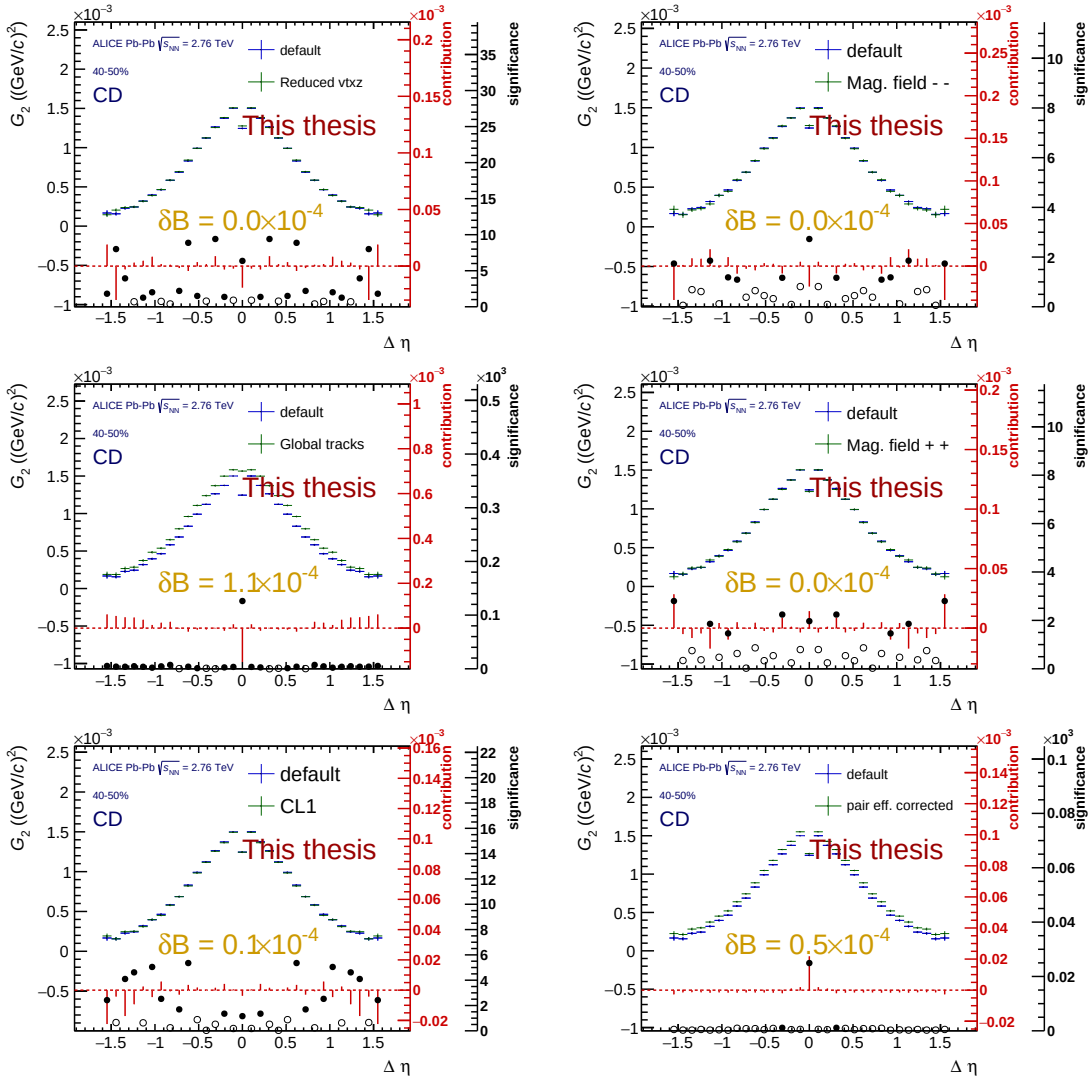

FIGURE A.24: Systematic uncertainty contribution analysis for the $\Delta\eta$ projection of the charge dependent (CD) two-particle correlation function for 40–50% central Pb–Pb collisions at $\sqrt{s_{\mathrm{NN}}}$ = 2.76 TeV as measured by ALICE. On the top row, reduced vertex acceptance (left) and magnetic field polarity −− tests; on the middle row, Global tracks (left) and magnetic field polarity ++ tests; on the bottom row, centrality estimation using CL1 information (left) and incorporation of the pair efficiency correction (right). On all panels the blue points are the results from the default analysis while the green are the ones from the corresponding test (see section 5.5.2).

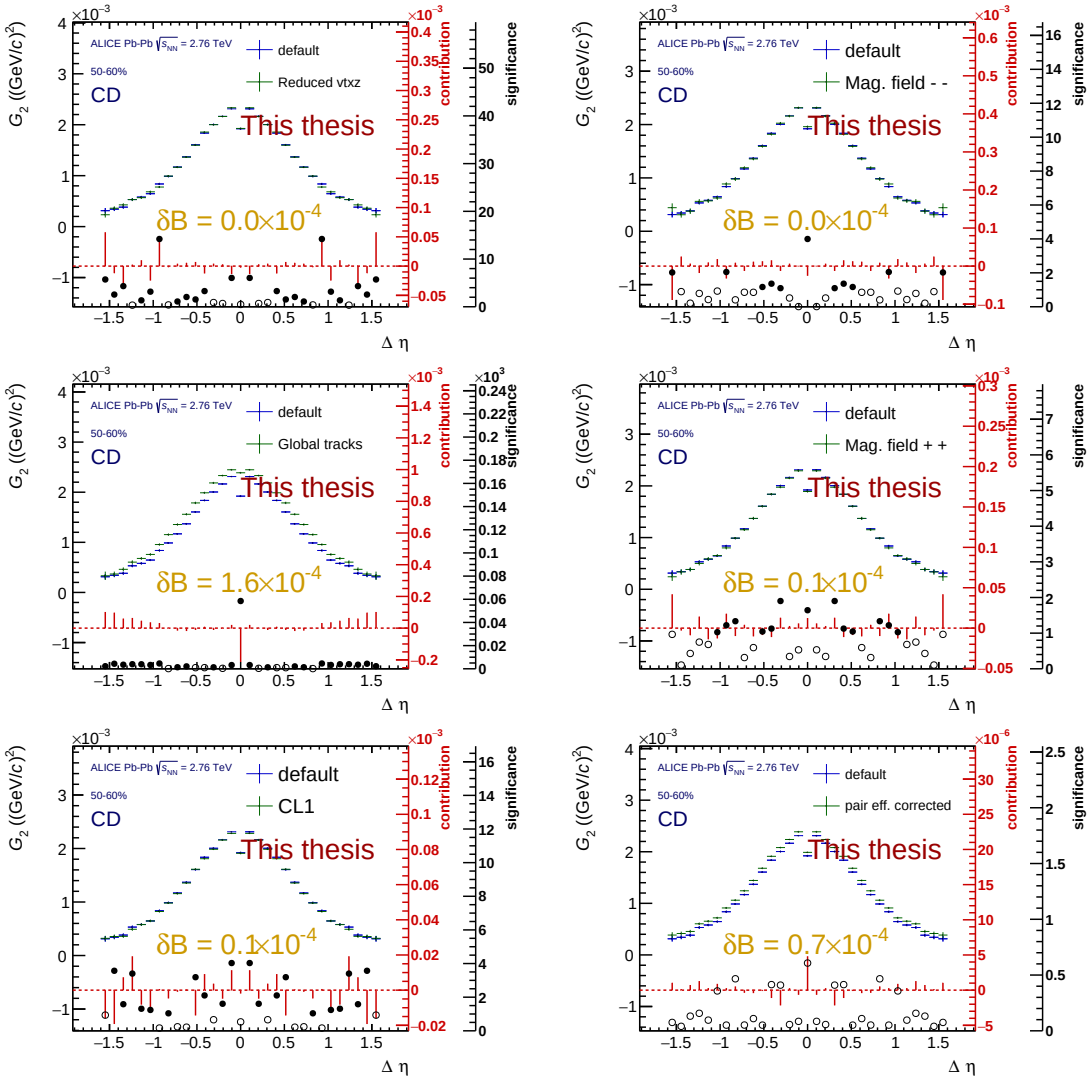

FIGURE A.25: Systematic uncertainty contribution analysis for the $\Delta\eta$ projection of the charge dependent (CD) two-particle correlation function for 50–60% central Pb–Pb collisions at $\sqrt{s_{\mathrm{NN}}}$ = 2.76 TeV as measured by ALICE. On the top row, reduced vertex acceptance (left) and magnetic field polarity −− tests; on the middle row, Global tracks (left) and magnetic field polarity ++ tests; on the bottom row, centrality estimation using CL1 information (left) and incorporation of the pair efficiency correction (right). On all panels the blue points are the results from the default analysis while the green are the ones from the corresponding test (see section 5.5.2).

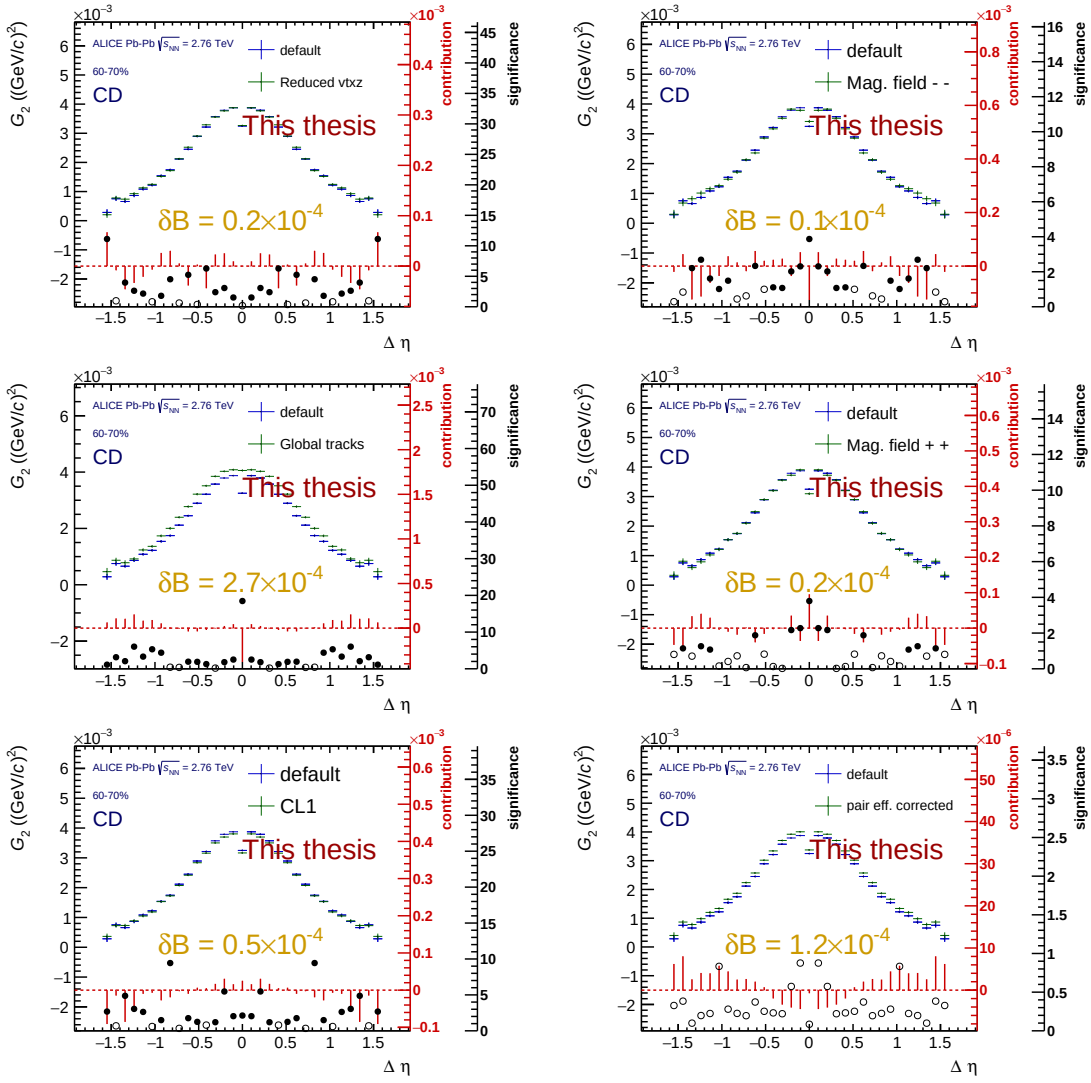

FIGURE A.26: Systematic uncertainty contribution analysis for the $\Delta\eta$ projection of the charge dependent (CD) two-particle correlation function for 60–70% central Pb–Pb collisions at $\sqrt{s_{\mathrm{NN}}}$ = 2.76 TeV as measured by ALICE. On the top row, reduced vertex acceptance (left) and magnetic field polarity −− tests; on the middle row, Global tracks (left) and magnetic field polarity ++ tests; on the bottom row, centrality estimation using CL1 information (left) and incorporation of the pair efficiency correction (right). On all panels the blue points are the results from the default analysis while the green are the ones from the corresponding test (see section 5.5.2).

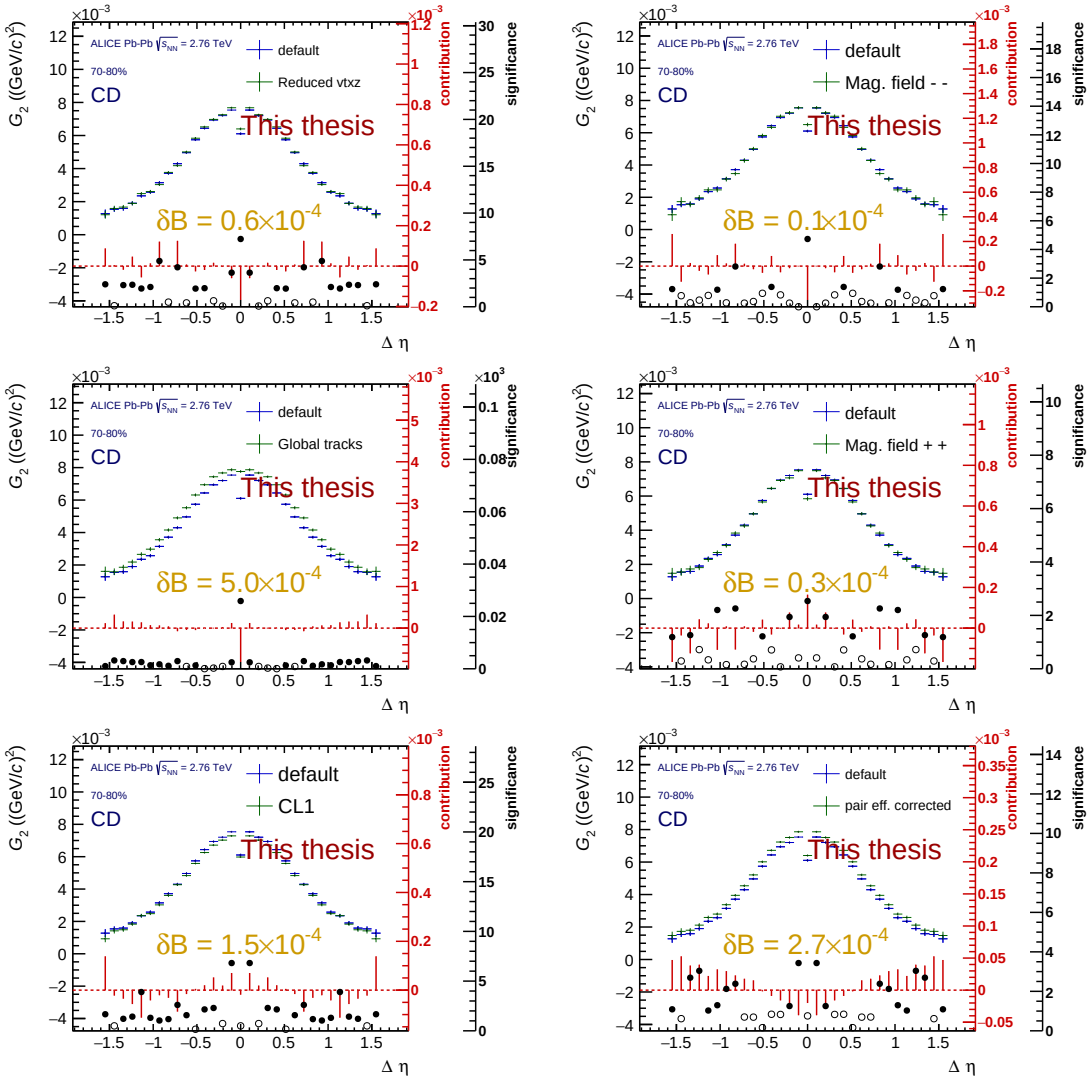

FIGURE A.27: Systematic uncertainty contribution analysis for the $\Delta\eta$ projection of the charge dependent (CD) two-particle correlation function for 70–80% central Pb–Pb collisions at $\sqrt{s_{\mathrm{NN}}}$ = 2.76 TeV as measured by ALICE. On the top row, reduced vertex acceptance (left) and magnetic field polarity −− tests; on the middle row, Global tracks (left) and magnetic field polarity ++ tests; on the bottom row, centrality estimation using CL1 information (left) and incorporation of the pair efficiency correction (right). On all panels the blue points are the results from the default analysis while the green are the ones from the corresponding test (see section 5.5.2).

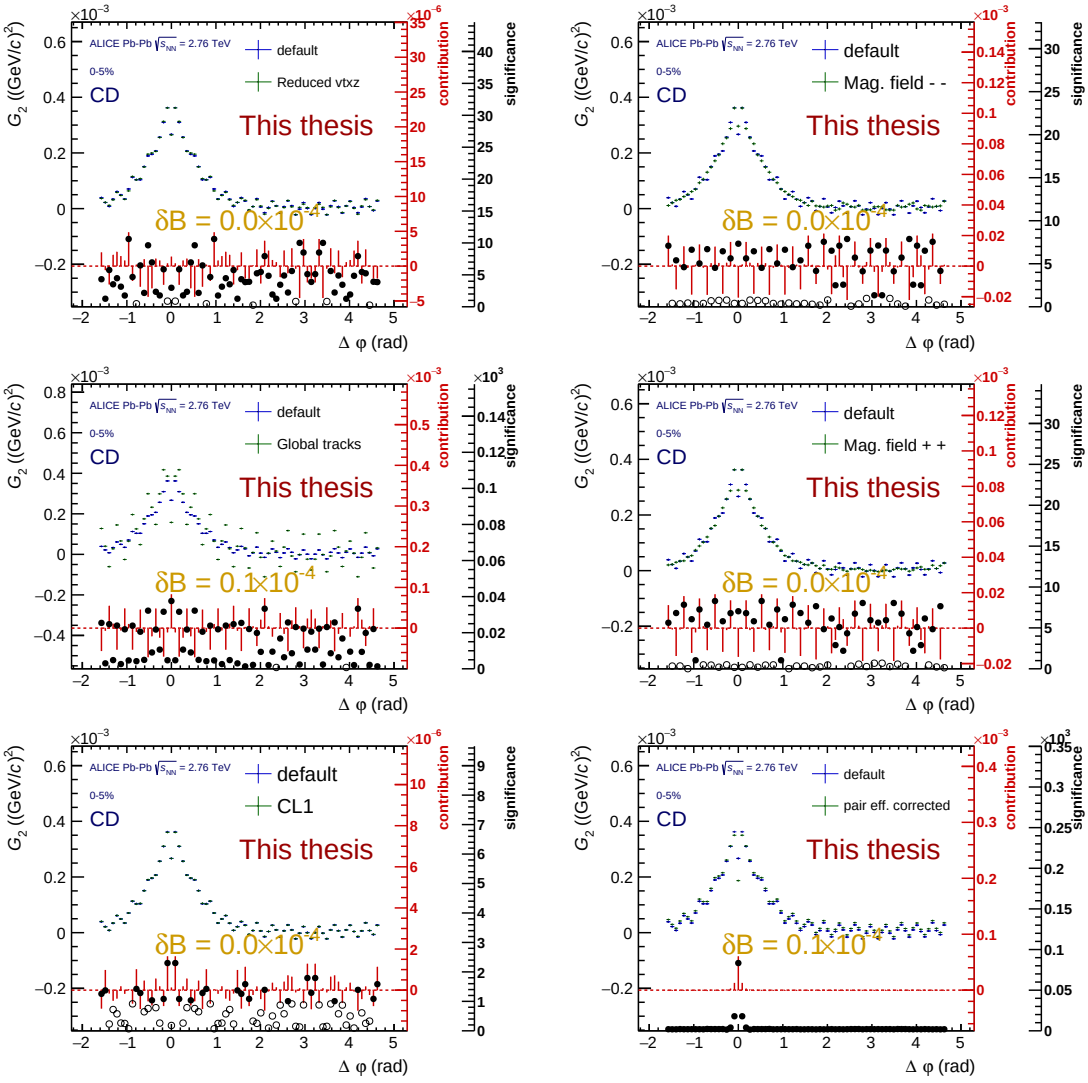

FIGURE A.28: Systematic uncertainty contribution analysis for the $\Delta\varphi$ projection of the charge dependent (CD) two-particle correlation function for 0–5% central Pb–Pb collisions at $\sqrt{s_{\mathrm{NN}}}$ = 2.76 TeV as measured by ALICE. On the top row, reduced vertex acceptance (left) and magnetic field polarity −− tests; on the middle row, Global tracks (left) and magnetic field polarity ++ tests; on the bottom row, centrality estimation using CL1 information (left) and incorporation of the pair efficiency correction (right). On all panels the blue points are the results from the default analysis while the green are the ones from the corresponding test (see section 5.5.2).

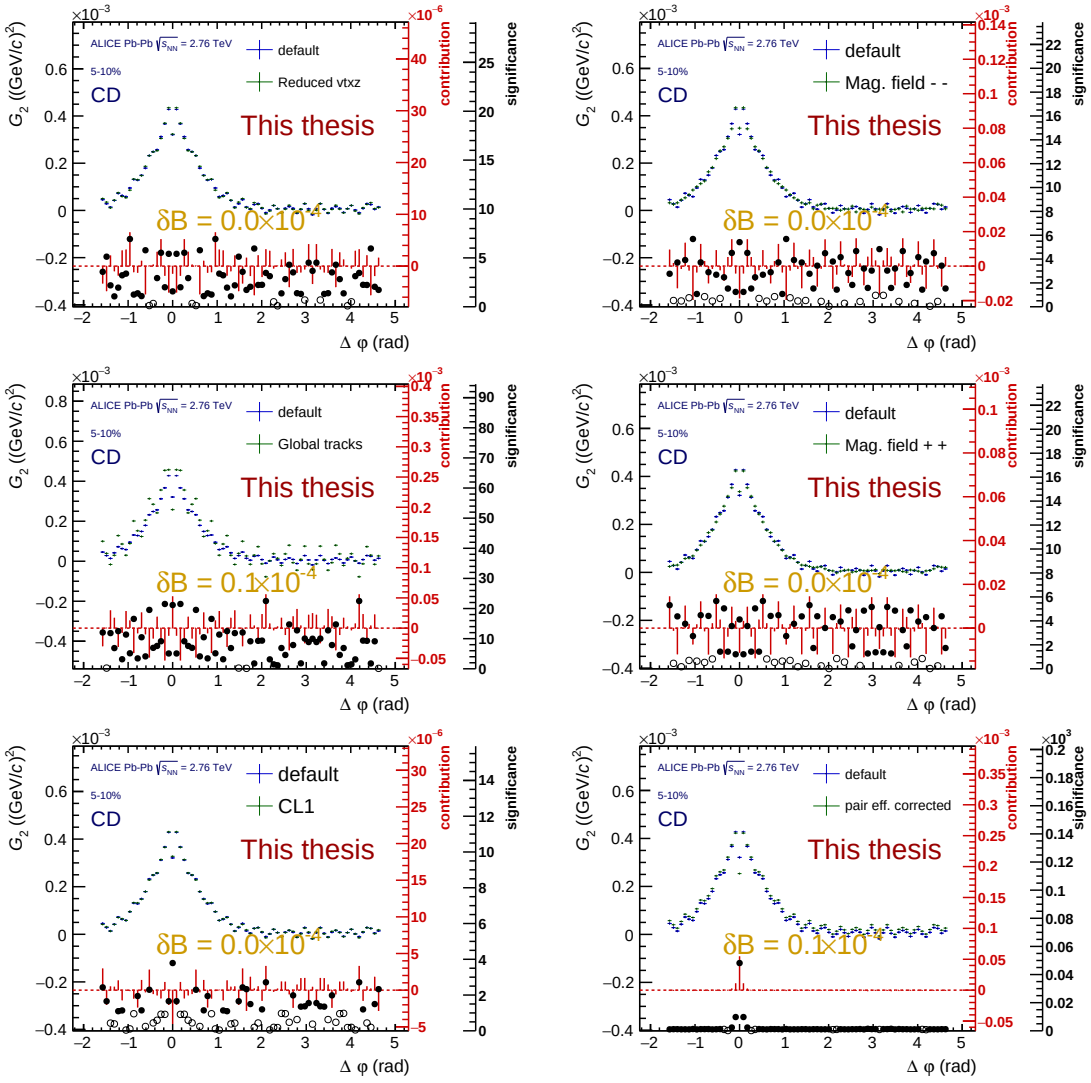

FIGURE A.29: Systematic uncertainty contribution analysis for the $\Delta\varphi$ projection of the charge dependent (CD) two-particle correlation function for 5–10% central Pb–Pb collisions at $\sqrt{s_{\mathrm{NN}}}$ = 2.76 TeV as measured by ALICE. On the top row, reduced vertex acceptance (left) and magnetic field polarity −− tests; on the middle row, Global tracks (left) and magnetic field polarity ++ tests; on the bottom row, centrality estimation using CL1 information (left) and incorporation of the pair efficiency correction (right). On all panels the blue points are the results from the default analysis while the green are the ones from the corresponding test (see section 5.5.2).

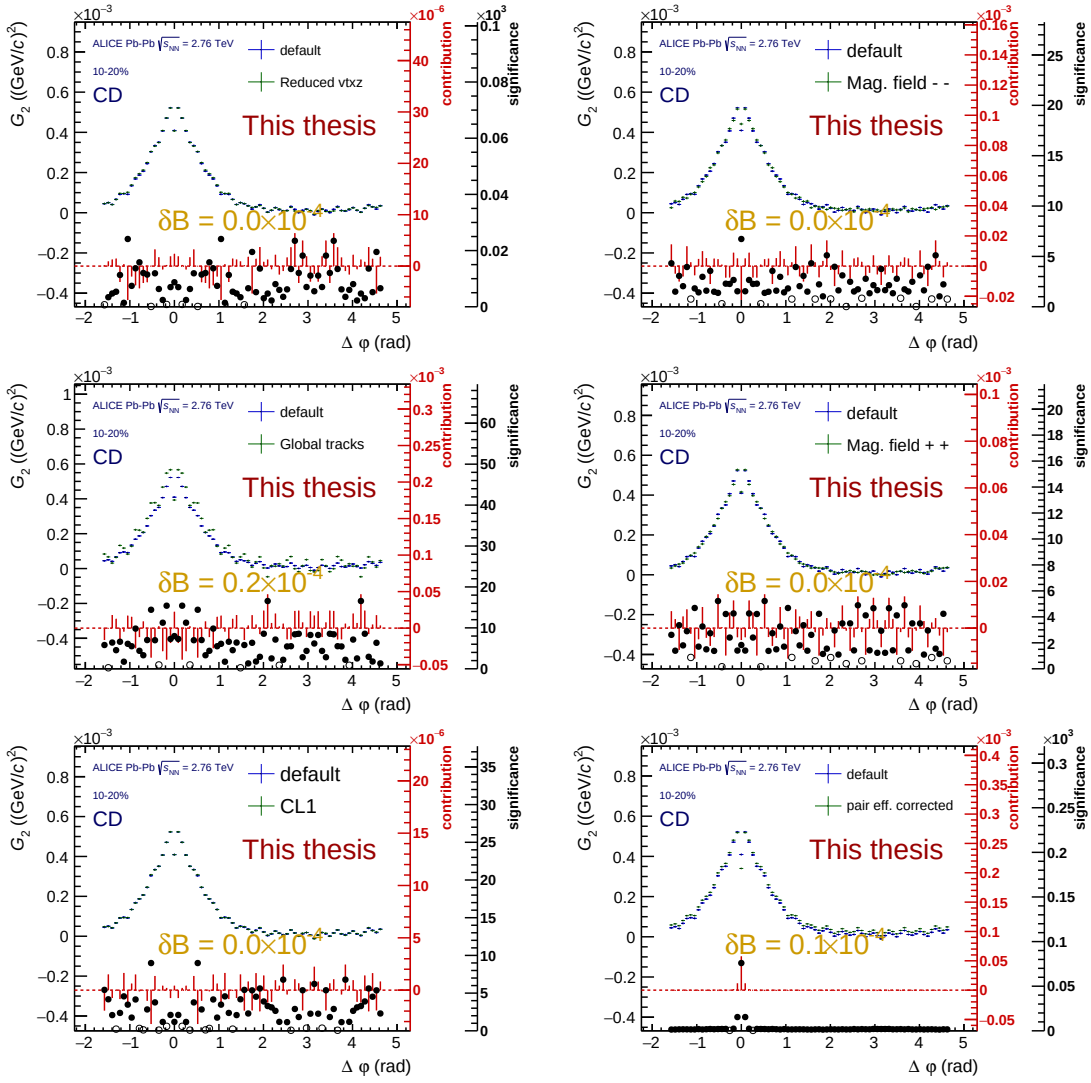

FIGURE A.30: Systematic uncertainty contribution analysis for the $\Delta\varphi$ projection of the charge dependent (CD) two-particle correlation function for 10–20% central Pb–Pb collisions at $\sqrt{s_{\mathrm{NN}}}$ = 2.76 TeV as measured by ALICE. On the top row, reduced vertex acceptance (left) and magnetic field polarity −− tests; on the middle row, Global tracks (left) and magnetic field polarity ++ tests; on the bottom row, centrality estimation using CL1 information (left) and incorporation of the pair efficiency correction (right). On all panels the blue points are the results from the default analysis while the green are the ones from the corresponding test (see section 5.5.2).

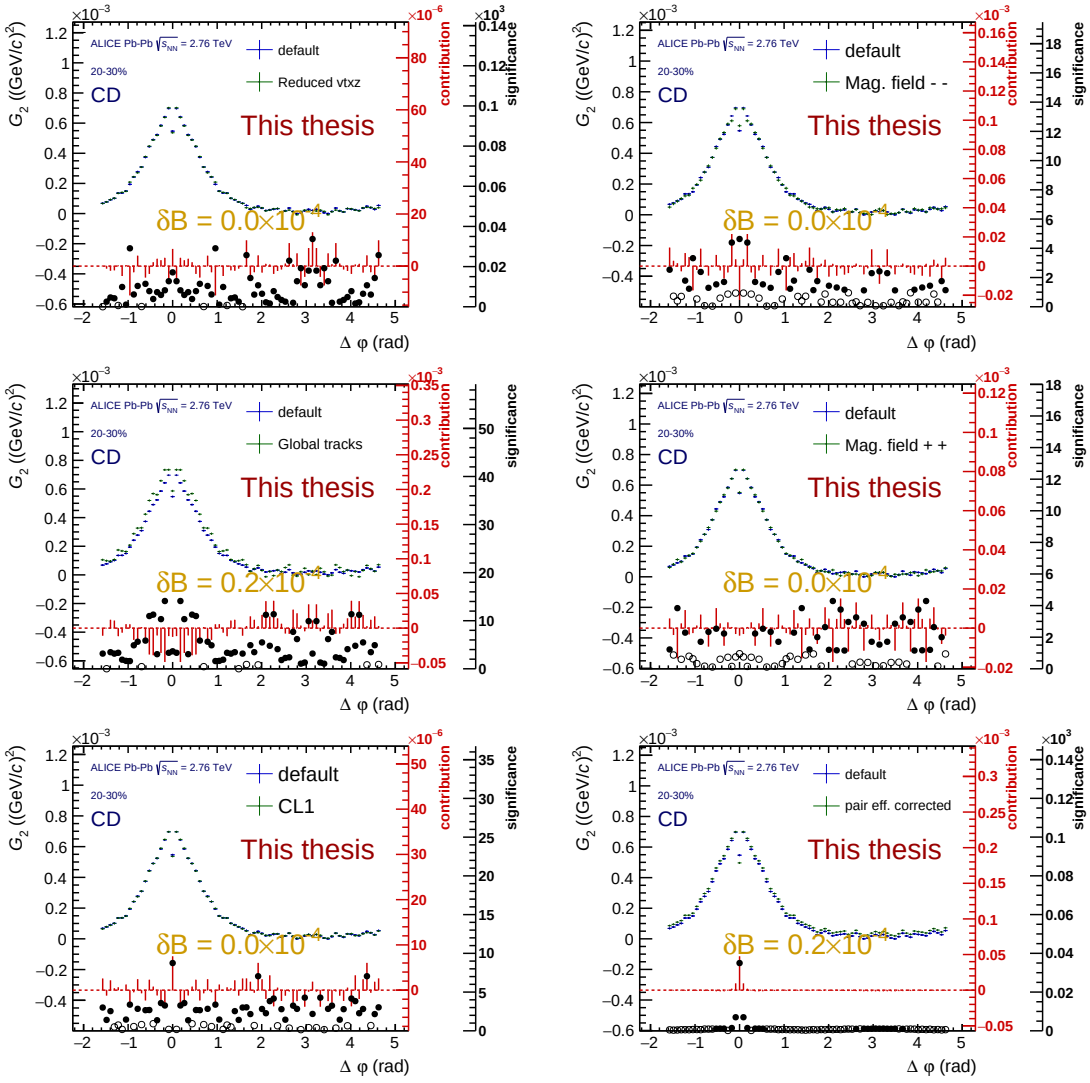

FIGURE A.31: Systematic uncertainty contribution analysis for the $\Delta\varphi$ projection of the charge dependent (CD) two-particle correlation function for 20–30% central Pb–Pb collisions at $\sqrt{s_{\mathrm{NN}}}$ = 2.76 TeV as measured by ALICE. On the top row, reduced vertex acceptance (left) and magnetic field polarity −− tests; on the middle row, Global tracks (left) and magnetic field polarity ++ tests; on the bottom row, centrality estimation using CL1 information (left) and incorporation of the pair efficiency correction (right). On all panels the blue points are the results from the default analysis while the green are the ones from the corresponding test (see section 5.5.2).

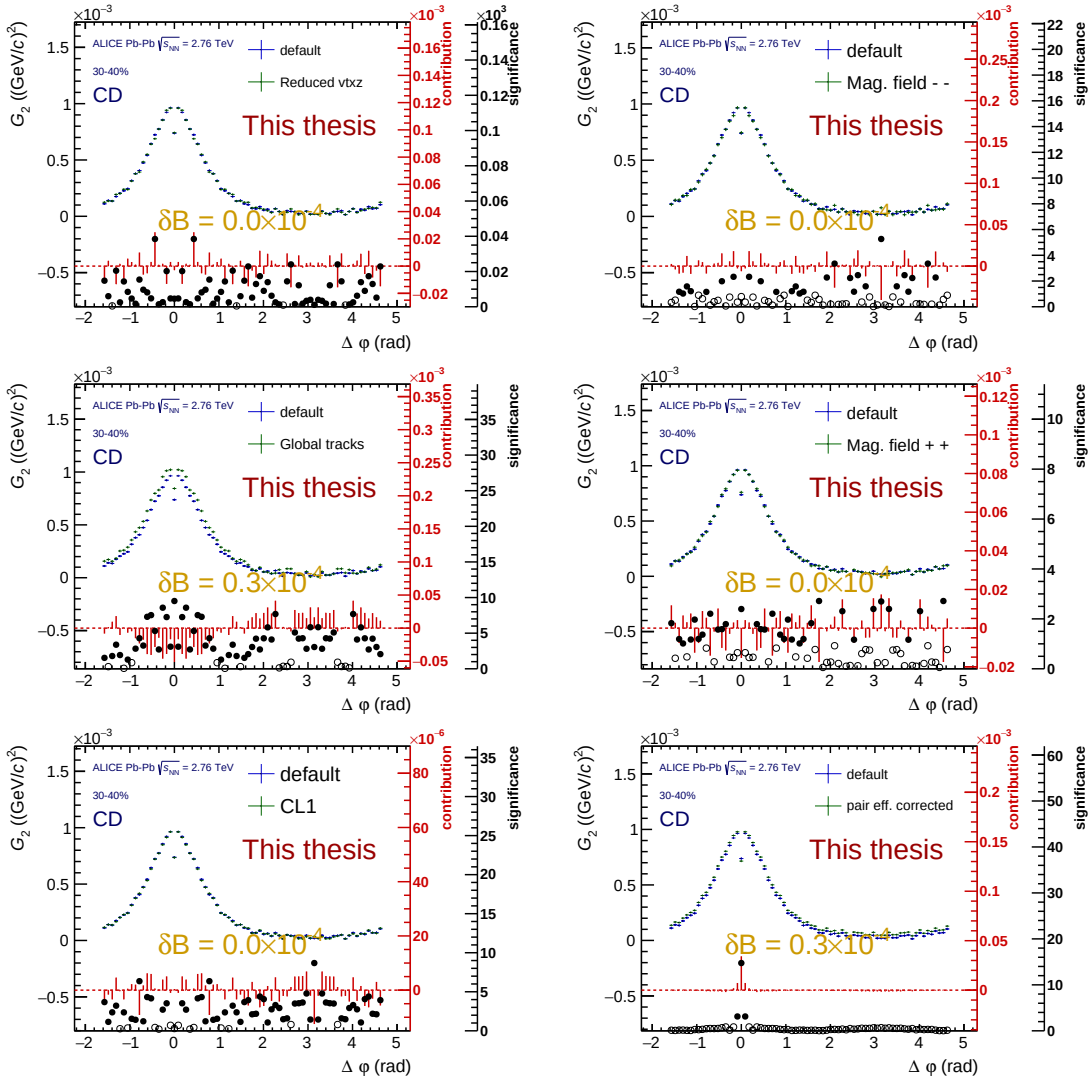

FIGURE A.32: Systematic uncertainty contribution analysis for the $\Delta\varphi$ projection of the charge dependent (CD) two-particle correlation function for 30–40% central Pb–Pb collisions at $\sqrt{s_{\mathrm{NN}}}$ = 2.76 TeV as measured by ALICE. On the top row, reduced vertex acceptance (left) and magnetic field polarity −− tests; on the middle row, Global tracks (left) and magnetic field polarity ++ tests; on the bottom row, centrality estimation using CL1 information (left) and incorporation of the pair efficiency correction (right). On all panels the blue points are the results from the default analysis while the green are the ones from the corresponding test (see section 5.5.2).

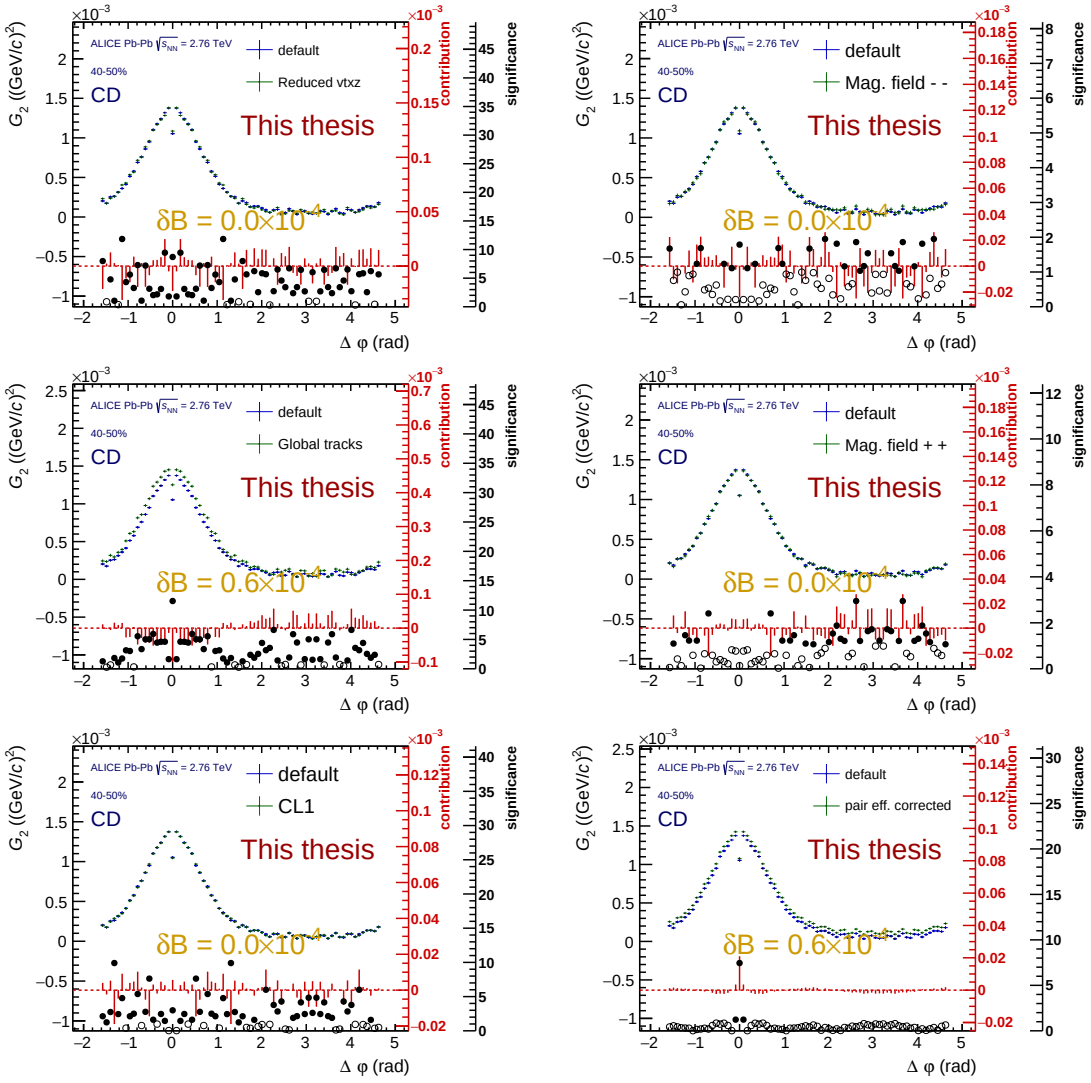

FIGURE A.33: Systematic uncertainty contribution analysis for the $\Delta\varphi$ projection of the charge dependent (CD) two-particle correlation function for 40–50% central Pb–Pb collisions at $\sqrt{s_{\rm NN}}$ = 2.76 TeV as measured by ALICE. On the top row, reduced vertex acceptance (left) and magnetic field polarity −− tests; on the middle row, Global tracks (left) and magnetic field polarity ++ tests; on the bottom row, centrality estimation using CL1 information (left) and incorporation of the pair efficiency correction (right). On all panels the blue points are the results from the default analysis while the green are the ones from the corresponding test (see section 5.5.2).

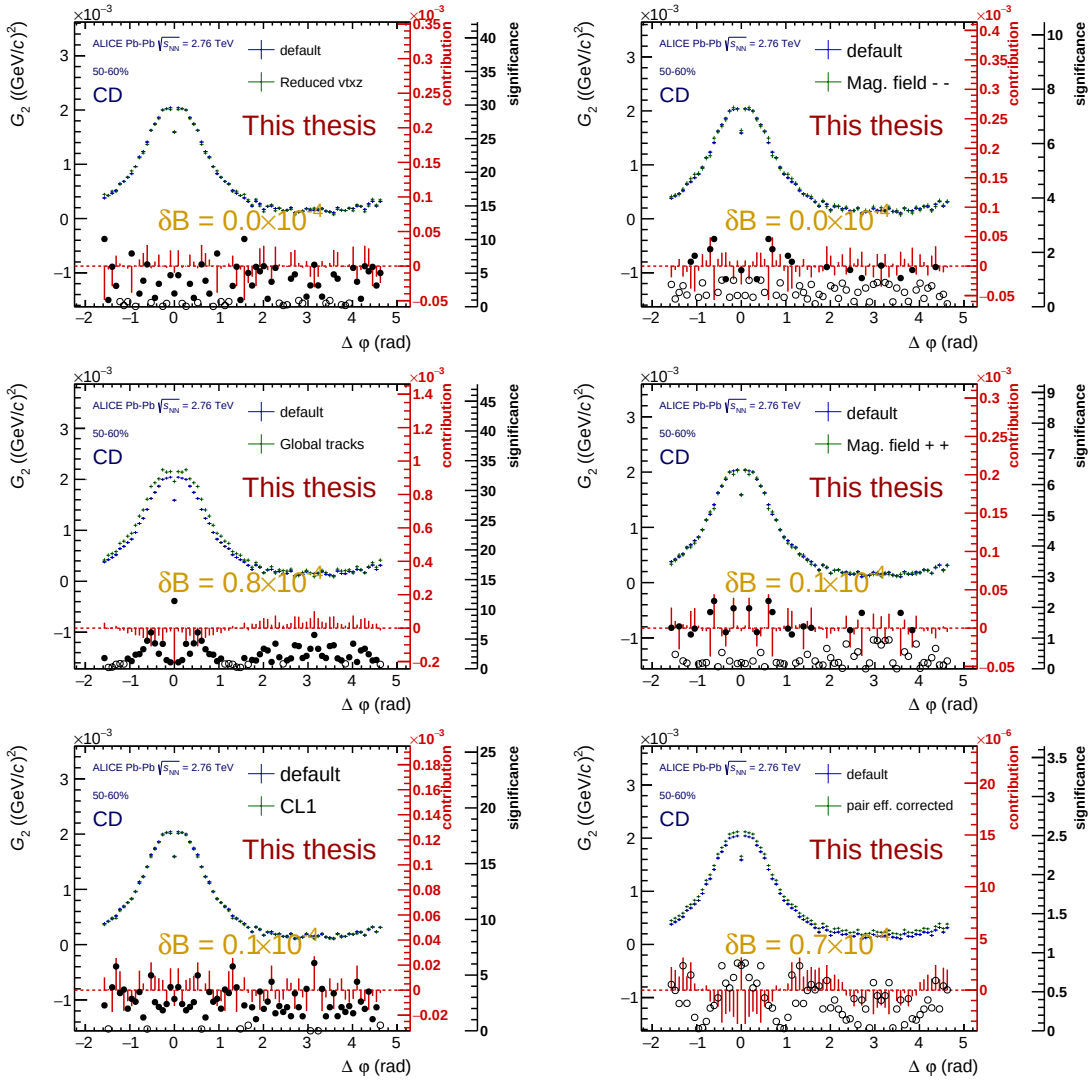

FIGURE A.34: Systematic uncertainty contribution analysis for the $\Delta\varphi$ projection of the charge dependent (CD) two-particle correlation function for 50–60% central Pb–Pb collisions at $\sqrt{s_{\mathrm{NN}}}$ = 2.76 TeV as measured by ALICE. On the top row, reduced vertex acceptance (left) and magnetic field polarity −− tests; on the middle row, Global tracks (left) and magnetic field polarity ++ tests; on the bottom row, centrality estimation using CL1 information (left) and incorporation of the pair efficiency correction (right). On all panels the blue points are the results from the default analysis while the green are the ones from the corresponding test (see section 5.5.2).

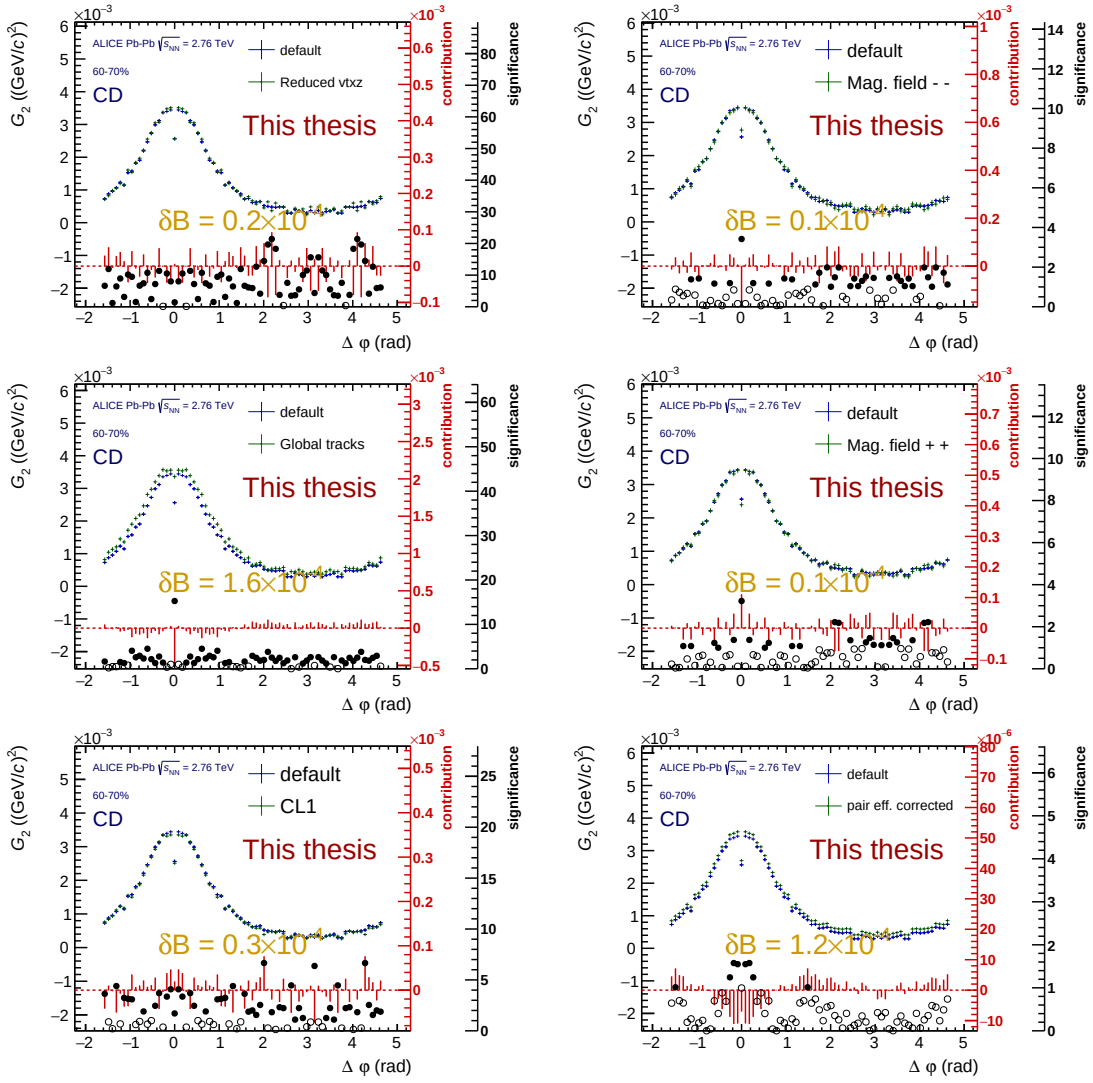

FIGURE A.35: Systematic uncertainty contribution analysis for the $\Delta\varphi$ projection of the charge dependent (CD) two-particle correlation function for 60–70% central Pb–Pb collisions at $\sqrt{s_{\mathrm{NN}}}$ = 2.76 TeV as measured by ALICE. On the top row, reduced vertex acceptance (left) and magnetic field polarity −− tests; on the middle row, Global tracks (left) and magnetic field polarity ++ tests; on the bottom row, centrality estimation using CL1 information (left) and incorporation of the pair efficiency correction (right). On all panels the blue points are the results from the default analysis while the green are the ones from the corresponding test (see section 5.5.2).

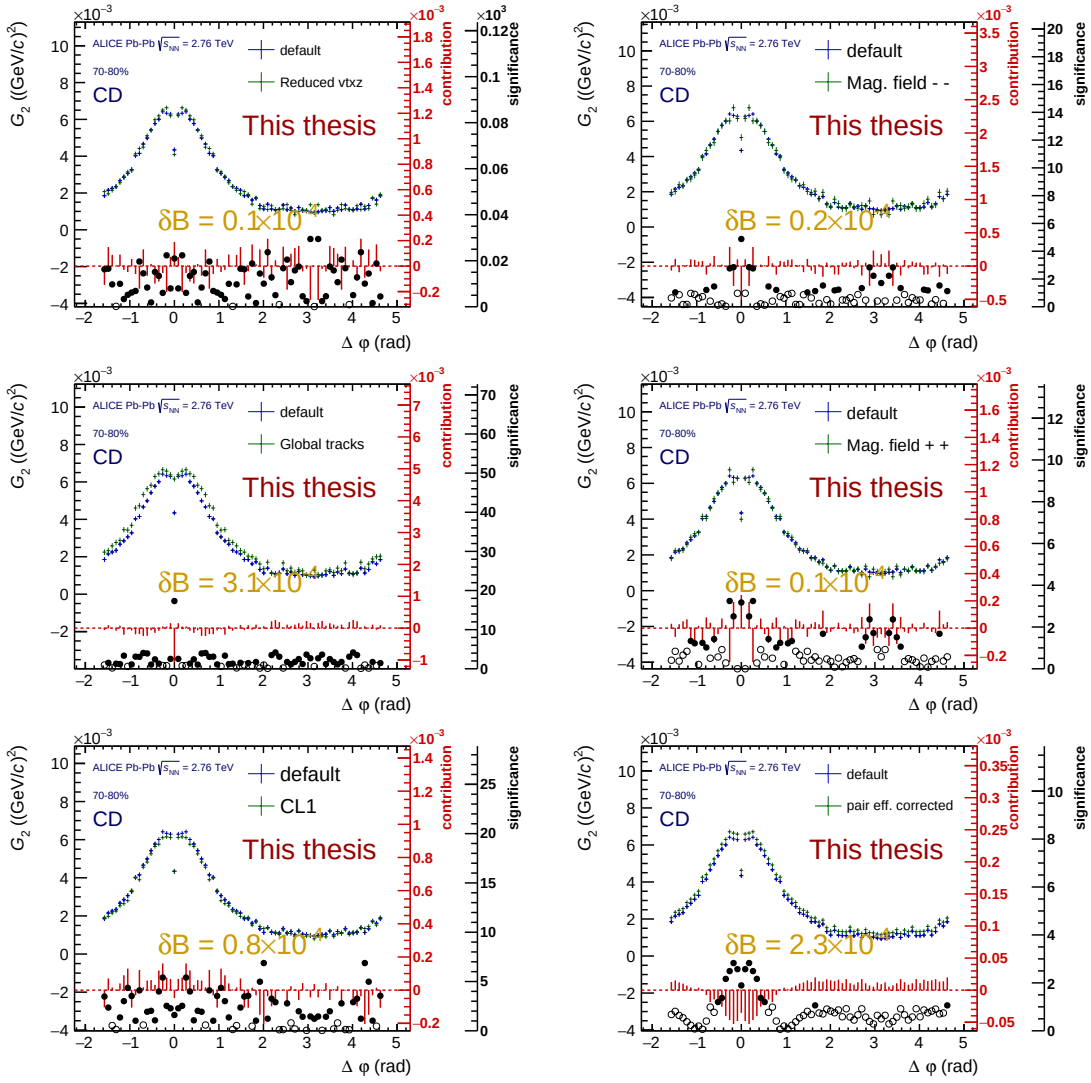

FIGURE A.36: Systematic uncertainty contribution analysis for the $\Delta\varphi$ projection of the charge dependent (CD) two-particle correlation function for 70–80% central Pb–Pb collisions at $\sqrt{s_{\mathrm{NN}}}$ = 2.76 TeV as measured by ALICE. On the top row, reduced vertex acceptance (left) and magnetic field polarity −− tests; on the middle row, Global tracks (left) and magnetic field polarity ++ tests; on the bottom row, centrality estimation using CL1 information (left) and incorporation of the pair efficiency correction (right). On all panels the blue points are the results from the default analysis while the green are the ones from the corresponding test (see section 5.5.2).

A.2 Systematic uncertainties on the widths

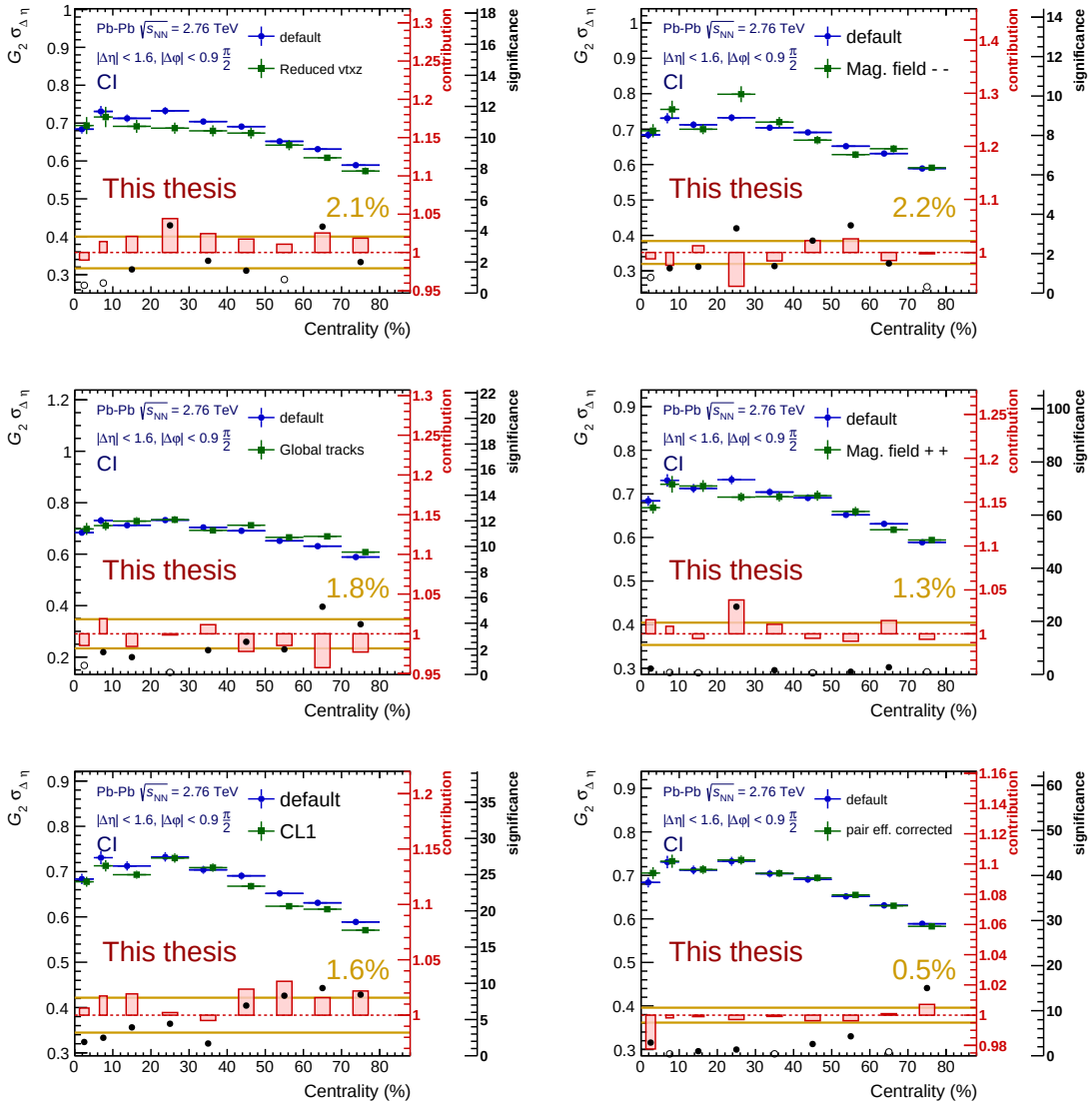

FIGURE A.37: Systematic uncertainty contribution analysis for the $\Delta\eta$ evolution of the width of the charge independent (CI) two-particle correlation function in Pb–Pb collisions at $\sqrt{s_{\mathrm{NN}}}$ = 2.76 TeV as measured by ALICE. On the top row, reduced vertex acceptance (left) and magnetic field polarity $--$ tests; on the middle row, Global tracks (left) and magnetic field polarity $++$ tests; on the bottom row, centrality estimation using CL1 information (left) and incorporation of the pair efficiency correction (right). On all panels the blue dots are the results from the default analysis while the green are the ones from the corresponding test (see section 5.5.2).

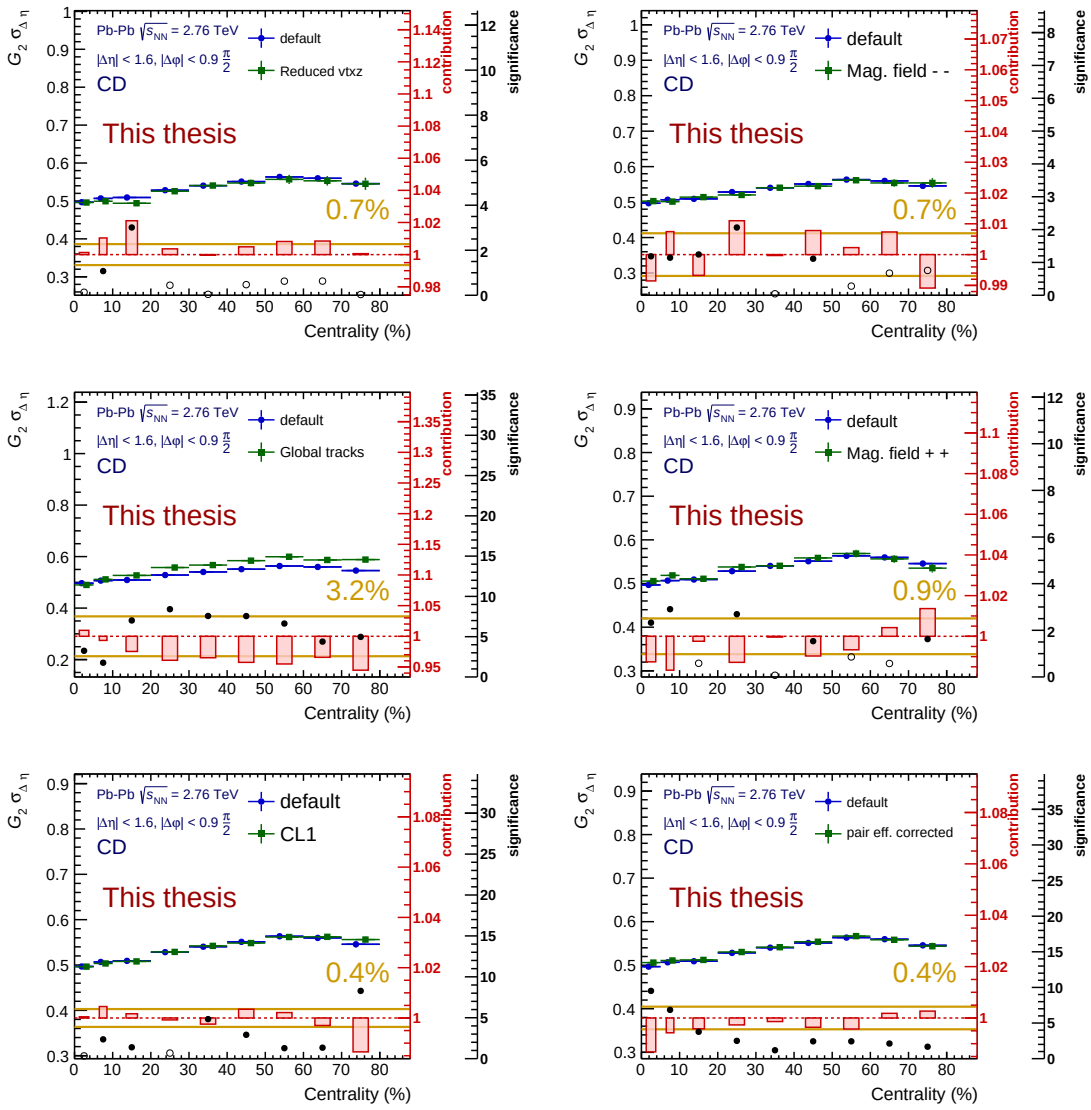

FIGURE A.38: Systematic uncertainty contribution analysis for the $\Delta\eta$ evolution of the width of the charge dependent (CD) two-particle correlation function in Pb–Pb collisions at $\sqrt{s_{\mathrm{NN}}}$ = 2.76 TeV as measured by ALICE. On the top row, reduced vertex acceptance (left) and magnetic field polarity $--$ tests; on the middle row, Global tracks (left) and magnetic field polarity $++$ tests; on the bottom row, centrality estimation using CL1 information (left) and incorporation of the pair efficiency correction (right). On all panels the blue dots are the results from the default analysis while the green are the ones from the corresponding test (see section 5.5.2).

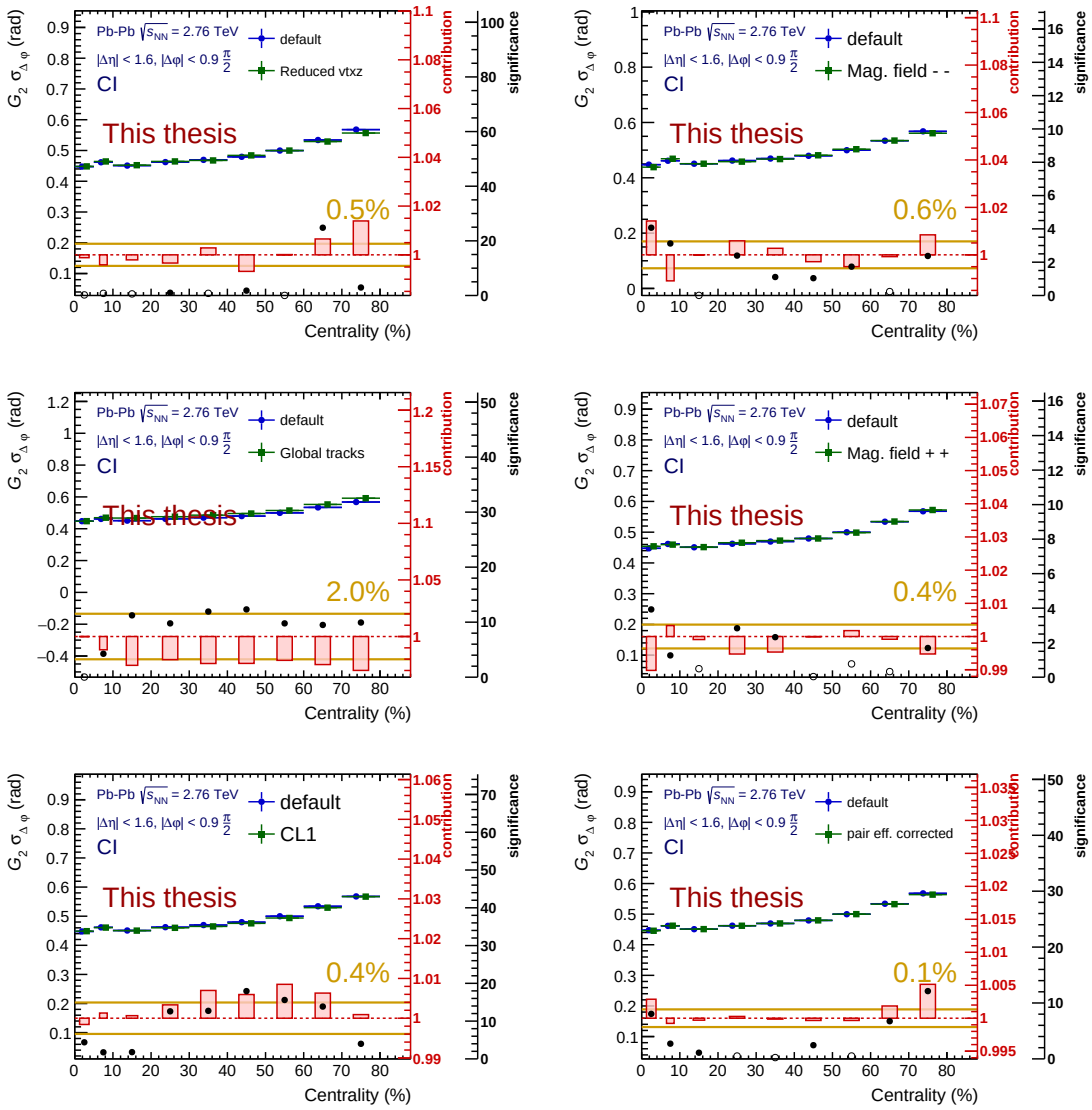

FIGURE A.39: Systematic uncertainty contribution analysis for the $\Delta\varphi$ evolution of the width of the charge independent (CI) two-particle correlation function in Pb–Pb collisions at $\sqrt{s_{\mathrm{NN}}}$ = 2.76 TeV as measured by ALICE. On the top row, reduced vertex acceptance (left) and magnetic field polarity $--$ tests; on the middle row, Global tracks (left) and magnetic field polarity ++ tests; on the bottom row, centrality estimation using CL1 information (left) and incorporation of the pair efficiency correction (right). On all panels the blue dots are the results from the default analysis while the green are the ones from the corresponding test (see section 5.5.2).

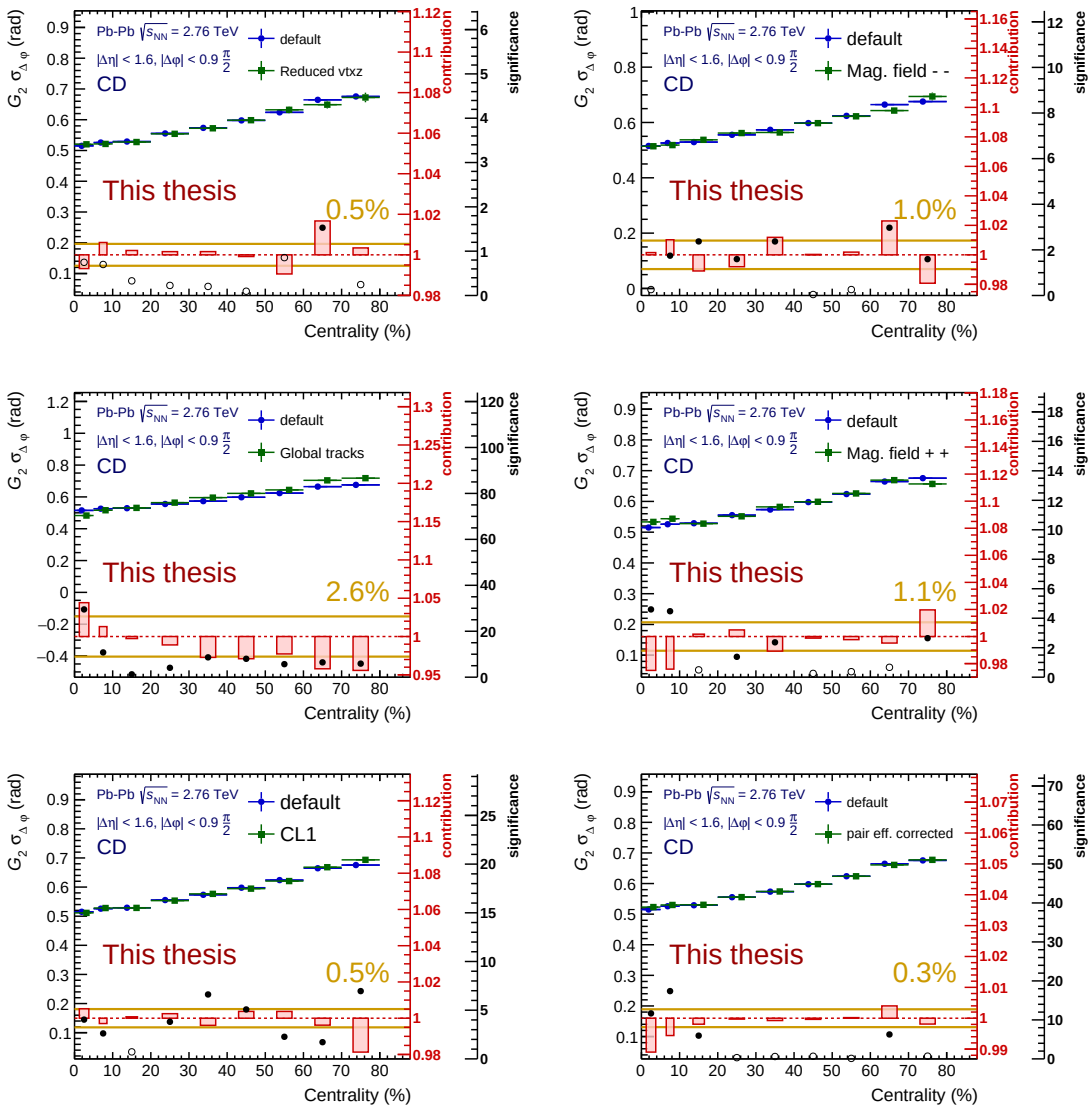

FIGURE A.40: Systematic uncertainty contribution analysis for the $\Delta\varphi$ evolution of the width of the charge dependent (CD) two-particle correlation function in Pb–Pb collisions at $\sqrt{s_{\mathrm{NN}}}$ = 2.76 TeV as measured by ALICE. On the top row, reduced vertex acceptance (left) and magnetic field polarity $--$ tests; on the middle row, Global tracks (left) and magnetic field polarity $++$ tests; on the bottom row, centrality estimation using CL1 information (left) and incorporation of the pair efficiency correction (right). On all panels the blue dots are the results from the default analysis while the green are the ones from the corresponding test (see section 5.5.2).

Appendix B

Results for US and LS track combinations

B.1 Pb–Pb at $\sqrt{s_{\mathrm{NN}}} = 2.76$ TeV results

B.1.1 Two-particle transverse momentum correlations

Figures B.1 and B.2 show the two-particle transverse momentum correlation G_2 for the US and LS track combinations, respectively. The central bin at $(\Delta\eta, \Delta\varphi) = (0, 0)$ has been excluded because it is undercorrected. The full version of the correlation function is shown in appendix C.

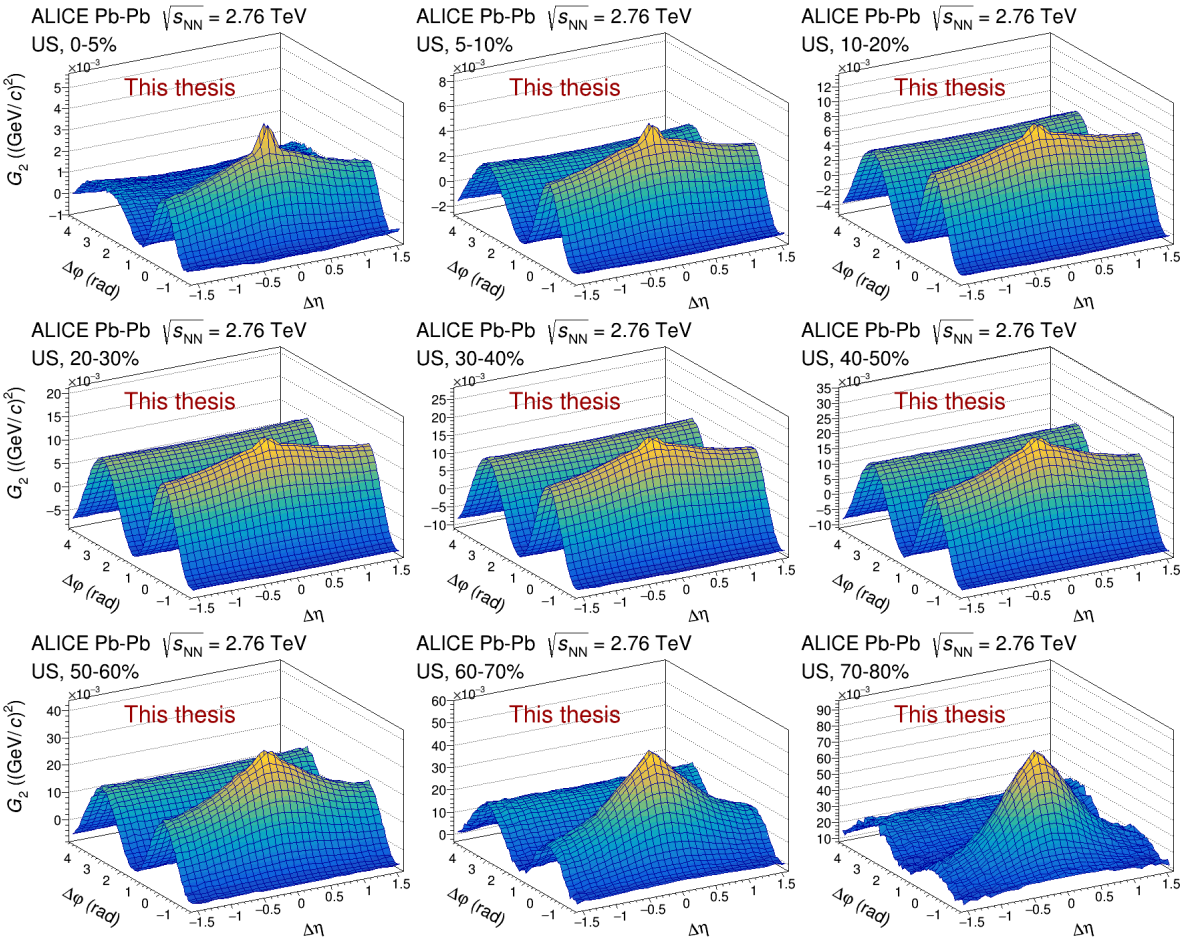

FIGURE B.1: Unlike sign (US) two-particle transverse momentum correlation in Pb–Pb collisions at $\sqrt{s_{\mathrm{NN}}} = 2.76$ TeV as measured by ALICE.

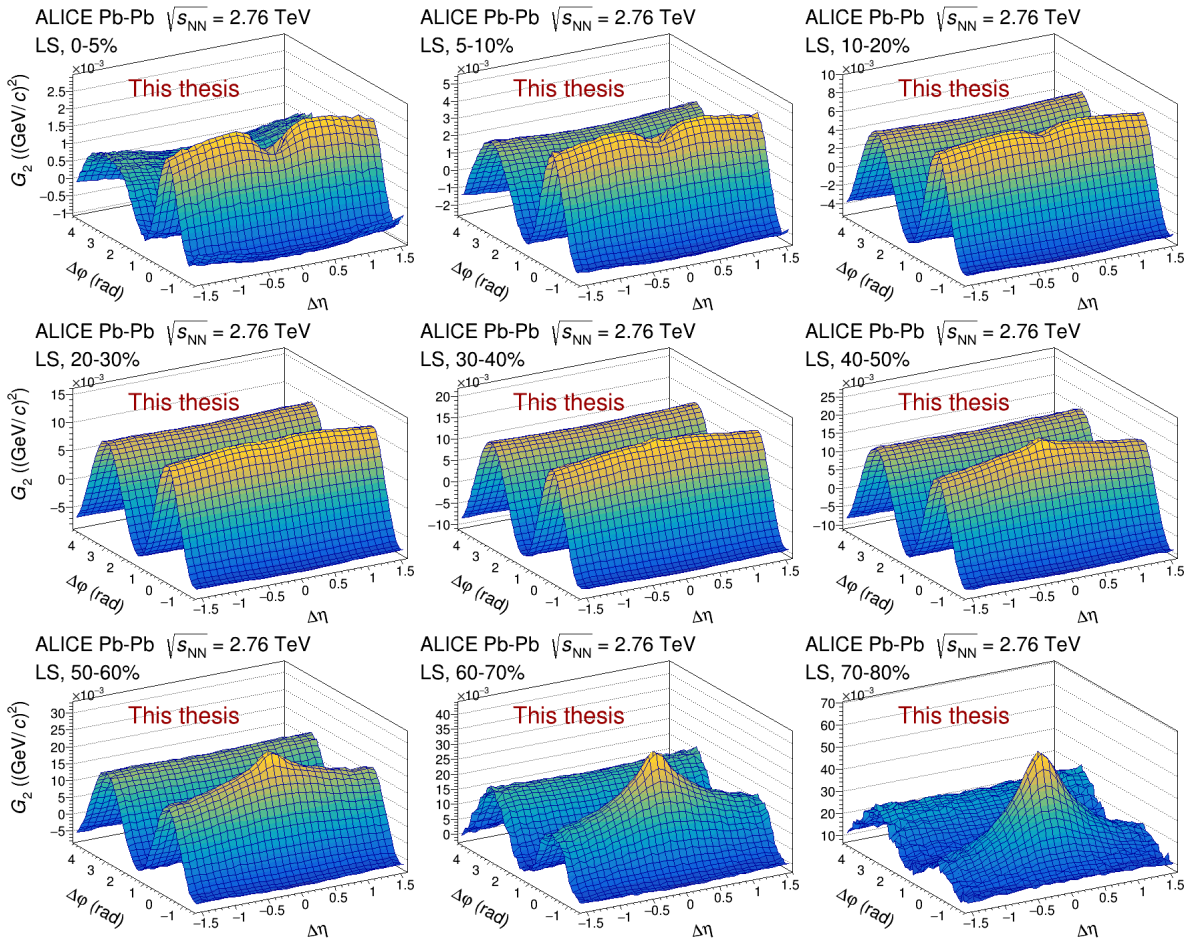

FIGURE B.2: Like sign (LS) two-particle transverse momentum correlation in Pb–Pb collisions at $\sqrt{s_{\mathrm{NN}}}$ = 2.76 TeV as measured by ALICE.

B.1.2 Longitudinal projections

Figures B.3 and B.4 show the longitudinal projection of two-particle transverse momentum correlation G_2 for the US and LS track combinations, respectively. The central bin at $(\Delta\eta, \Delta\varphi) = (0, 0)$ has been excluded because it is undercorrected. The full version of the correlation function is shown in appendix C.

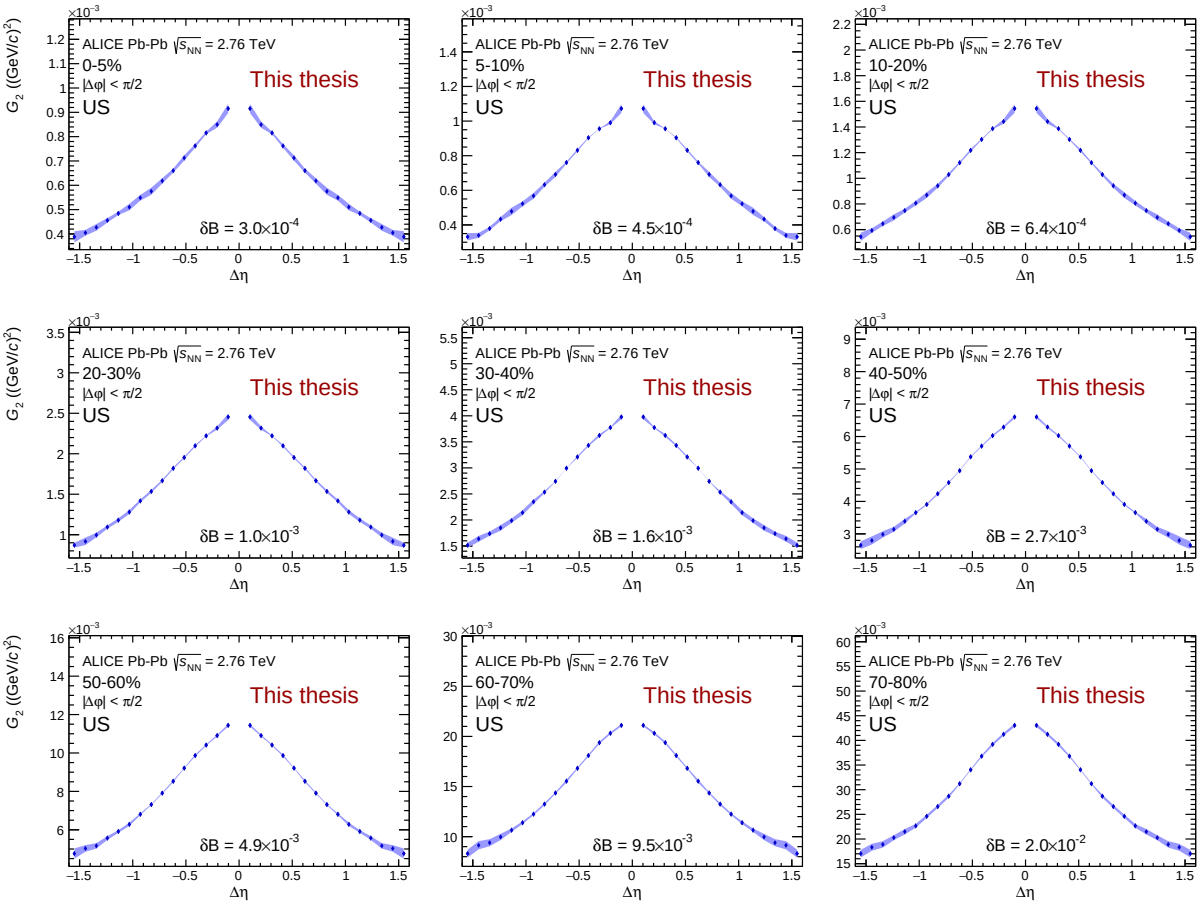

FIGURE B.3: Longitudinal projection of the unlike sign (US) two-particle transverse momentum correlation in Pb–Pb collisions at $\sqrt{s_{\mathrm{NN}}}$ = 2.76 TeV as measured by ALICE.

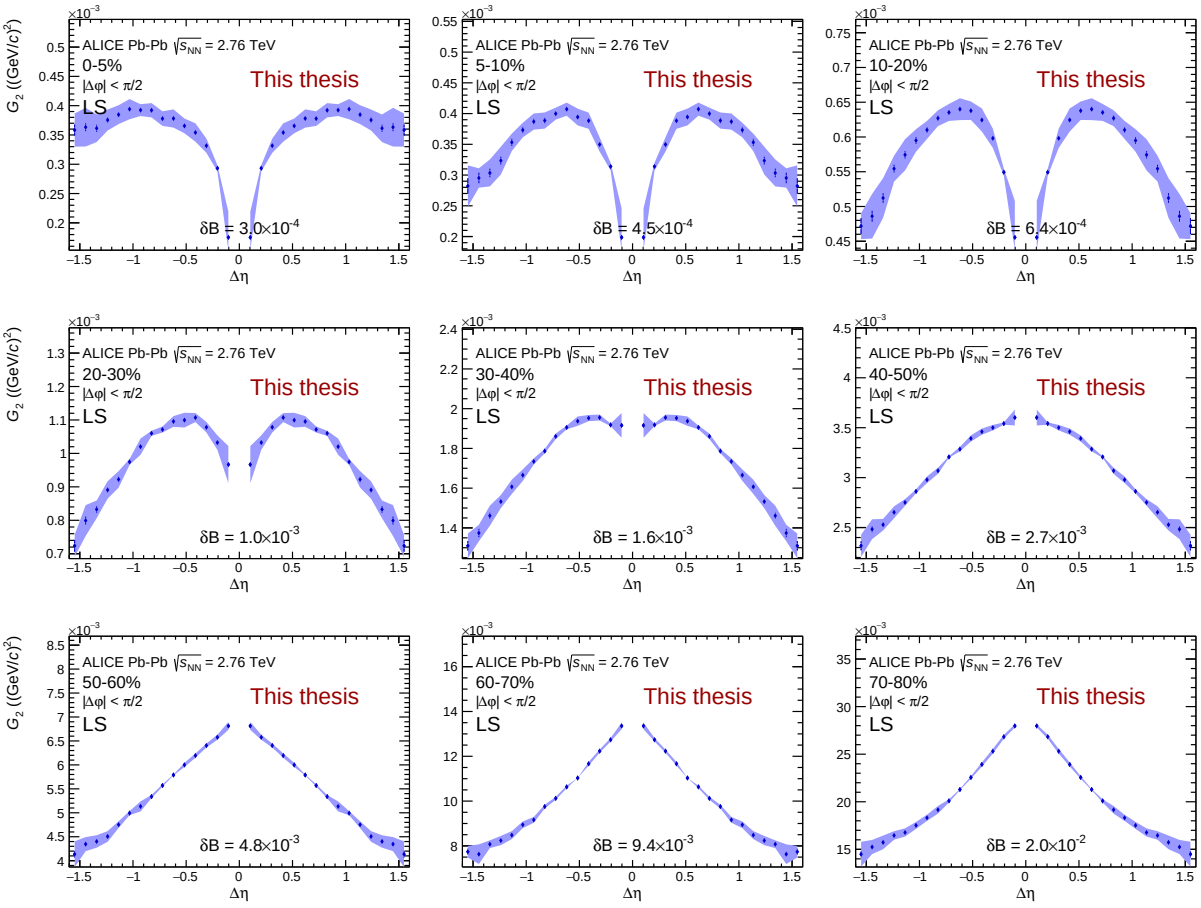

FIGURE B.4: Longitudinal projection of the like sign (LS) two-particle transverse momentum correlation in Pb–Pb collisions at $\sqrt{s_{\mathrm{NN}}}$ = 2.76 TeV as measured by ALICE.

B.1.3 Azimuthal projections

Figures B.5 and B.6 show the azimuthal projections of two-particle transverse momentum correlation G_2 for the US and LS track combinations, respectively. The central bin at $(\Delta\eta, \Delta\varphi) = (0, 0)$ has been excluded because it is undercorrected. The full version of the correlation function is shown in appendix C.

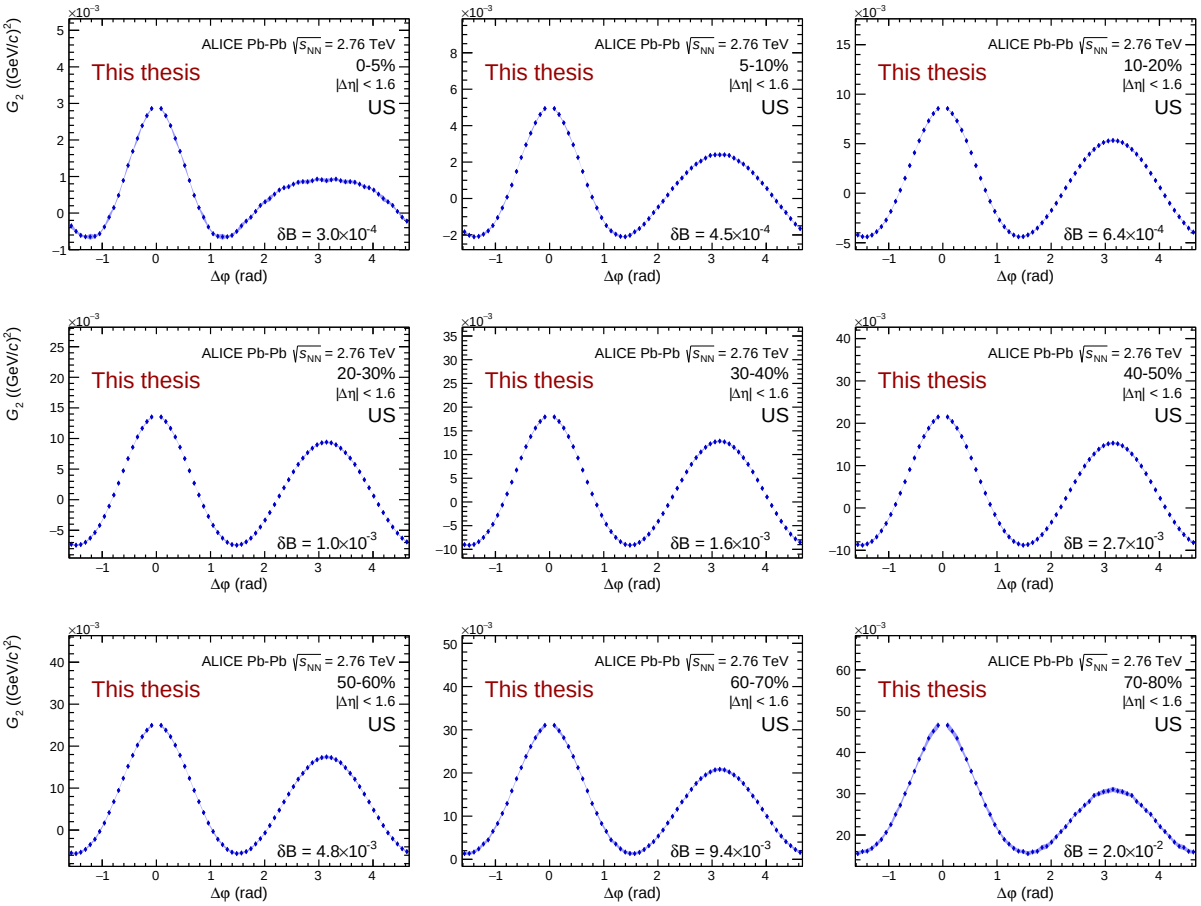

FIGURE B.5: Azimuthal projection of the unlike sign (US) two-particle transverse momentum correlation in Pb–Pb collisions at $\sqrt{s_{\mathrm{NN}}}$ = 2.76 TeV as measured by ALICE.

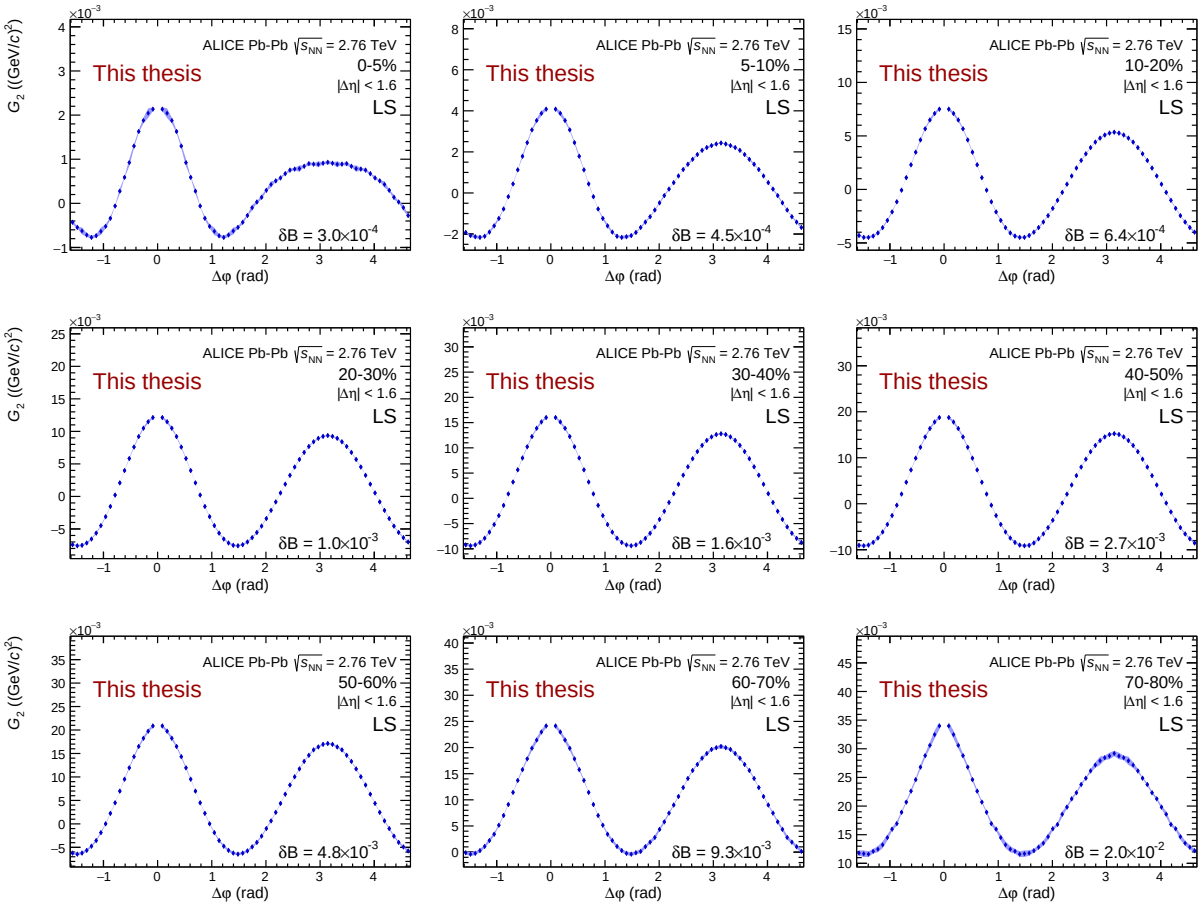

FIGURE B.6: Azimuthal projection of the like sign (LS) two-particle transverse momentum correlation in Pb–Pb collisions at $\sqrt{s_{\mathrm{NN}}} = 2.76$ TeV as measured by ALICE.

B.2 Pb–Pb at $\sqrt{s_{\mathrm{NN}}}$ = 5.02 TeV results

B.2.1 Two-particle transverse momentum correlations

Figures B.7 and B.8 show the two-particle transverse momentum correlation G_2 for the US and LS track combinations, respectively. The central bin at $(\Delta\eta, \Delta\varphi) = (0, 0)$ has been excluded because it is undercorrected. The full version of the correlation function is shown in appendix C.

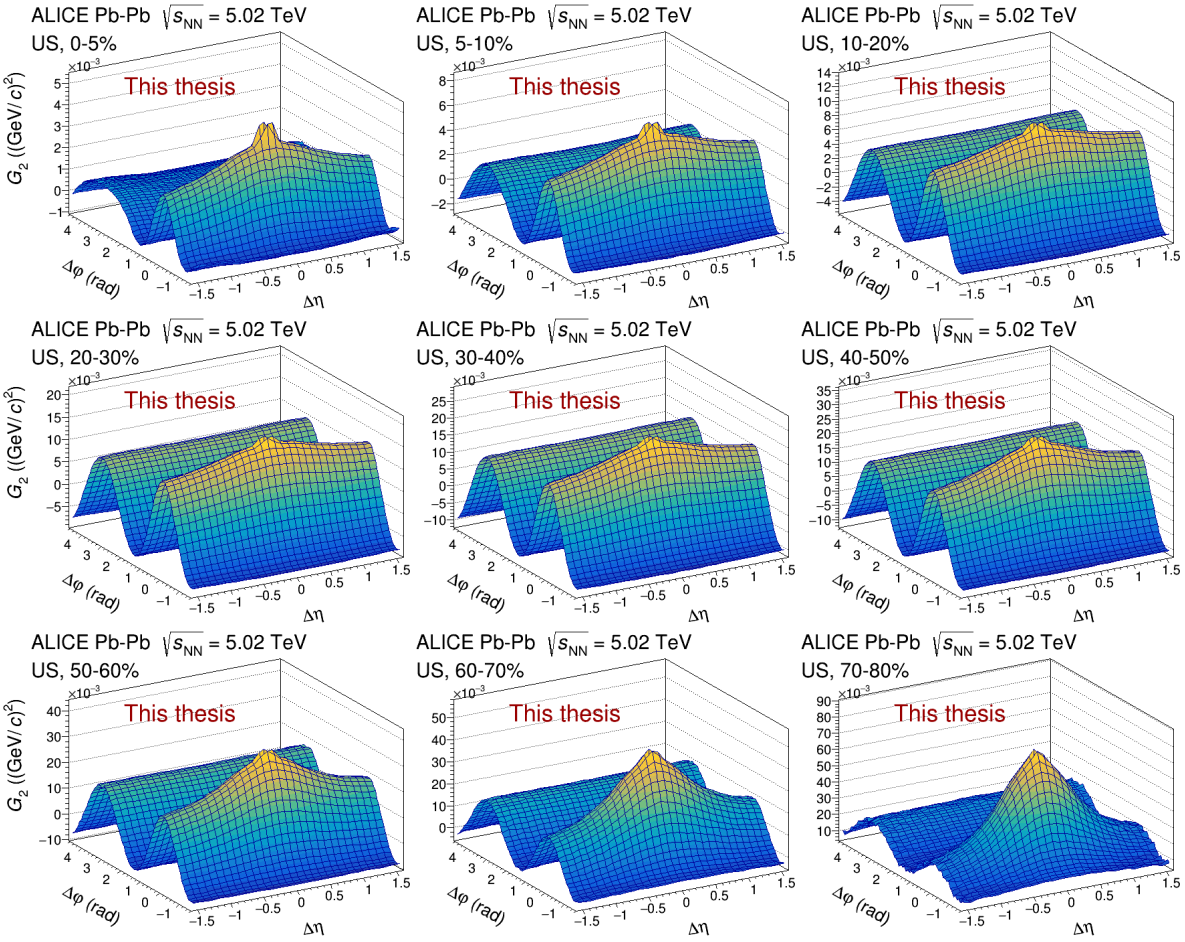

FIGURE B.7: Unlike sign (US) two-particle transverse momentum correlation in Pb–Pb collisions at $\sqrt{s_{\mathrm{NN}}}$ = 5.02 TeV as measured by ALICE.

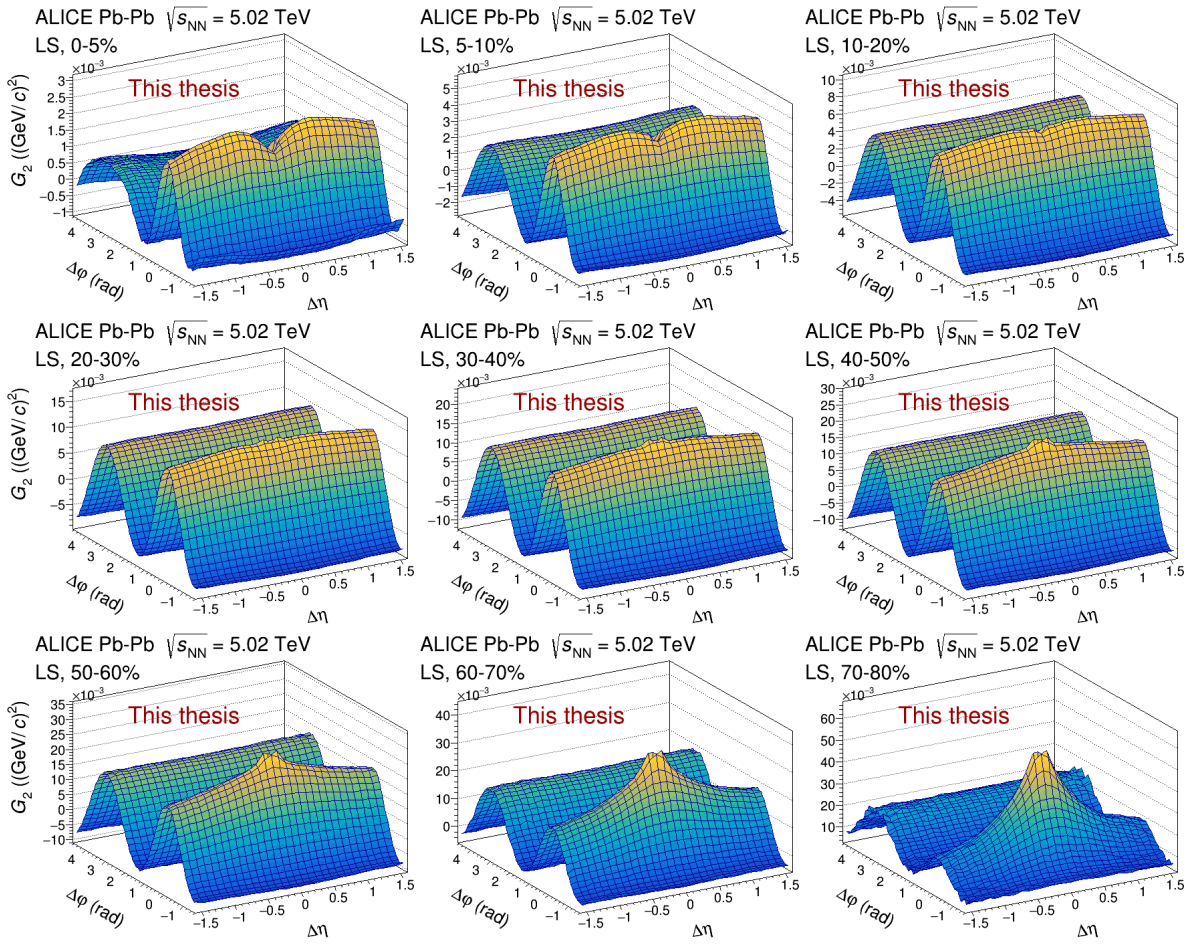

FIGURE B.8: Like sign (LS) two-particle transverse momentum correlation in Pb–Pb collisions at $\sqrt{s_{\mathrm{NN}}}$ = 5.02 TeV as measured by ALICE.

B.2.2 Longitudinal projections

Figures B.9 and B.10 show the longitudinal projection of two-particle transverse momentum correlation G_2 for the US and LS track combinations, respectively. The central bin at $(\Delta\eta, \Delta\varphi) = (0, 0)$ has been excluded because it is undercorrected. The full version of the correlation function is shown in appendix C.

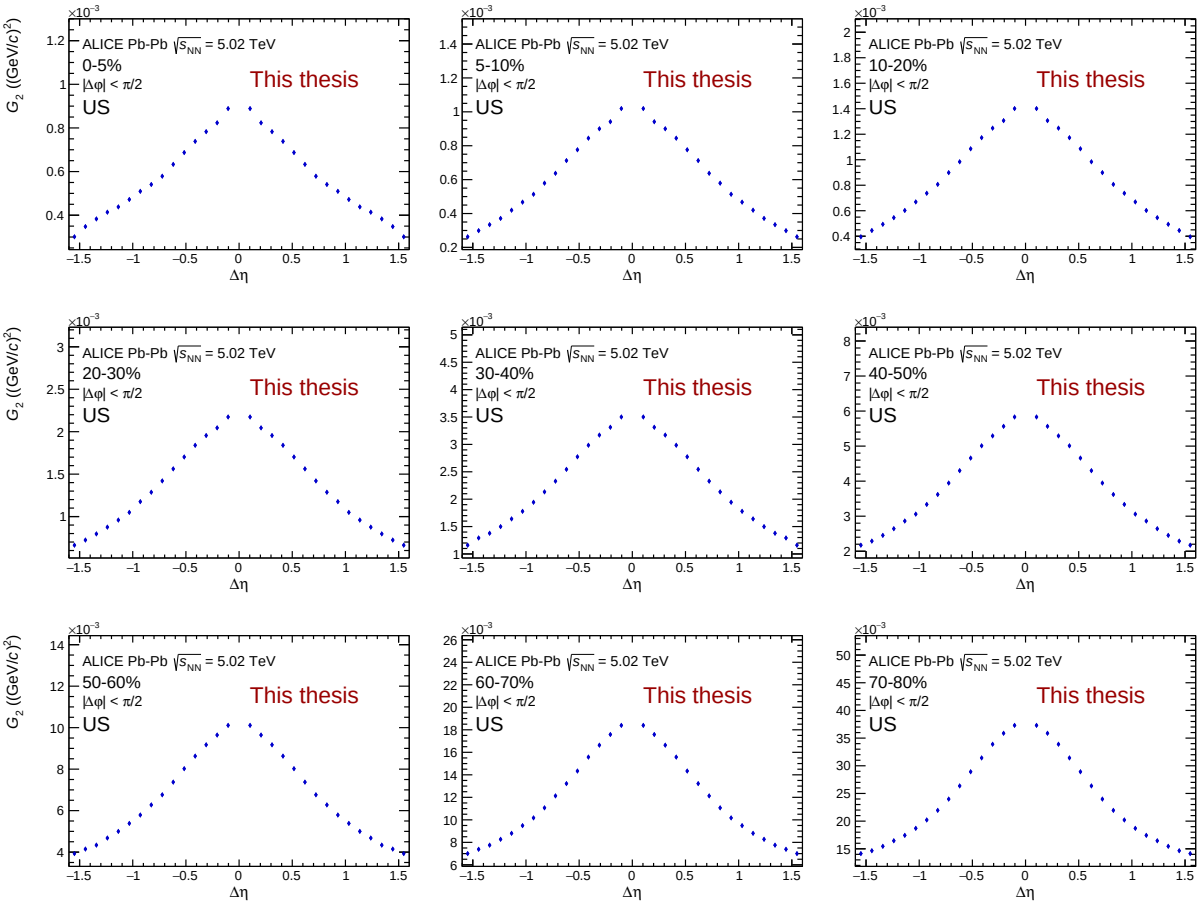

FIGURE B.9: Longitudinal projection of the unlike sign (US) two-particle transverse momentum correlation in Pb–Pb collisions at $\sqrt{s_{\mathrm{NN}}}$ = 5.02 TeV as measured by ALICE.

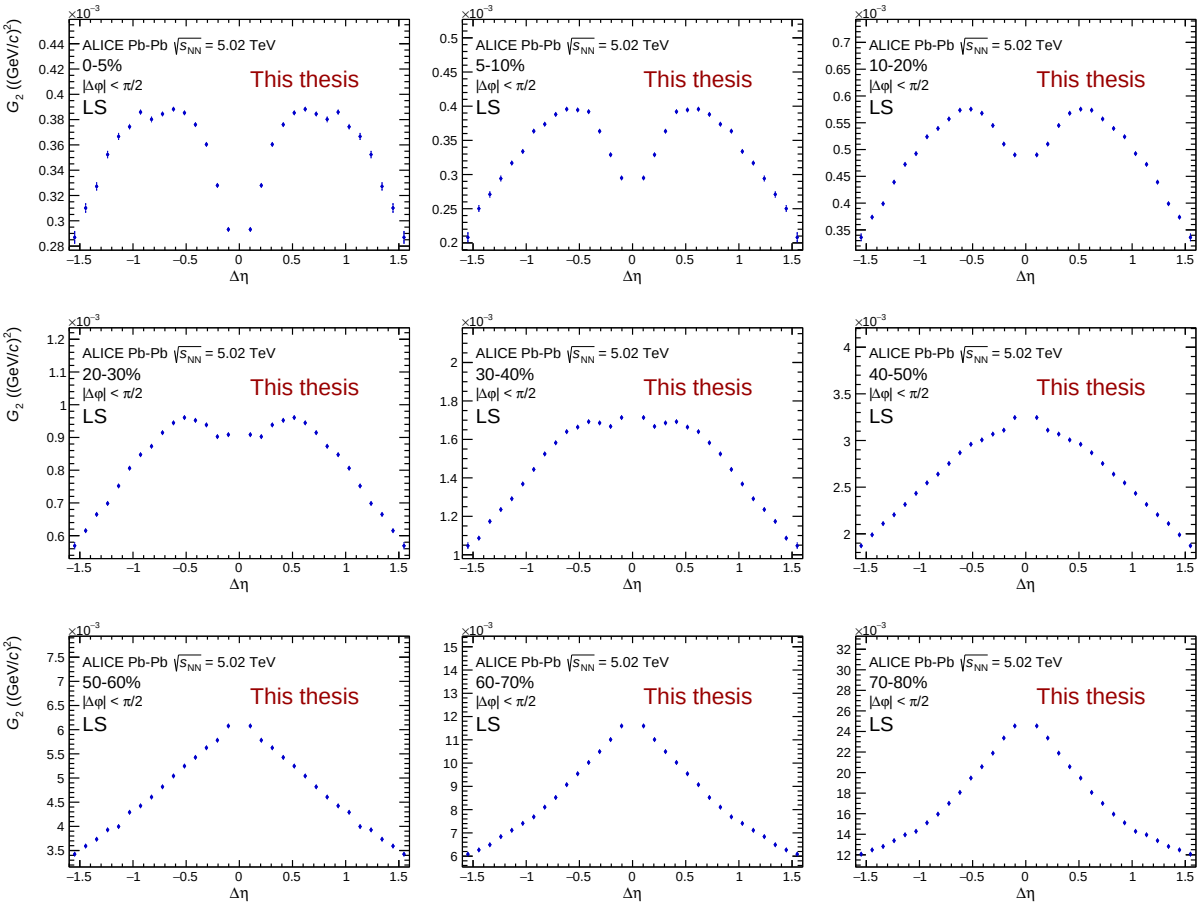

FIGURE B.10: Longitudinal projection of the like sign (LS) two-particle transverse momentum correlation in Pb–Pb collisions at $\sqrt{s_{\mathrm{NN}}}$ = 5.02 TeV as measured by ALICE.

B.2.3 Azimuthal projections

Figures B.11 and B.12 show the azimuthal projections of two-particle transverse momentum correlation G_2 for the US and LS track combinations, respectively. The central bin at $(\Delta\eta, \Delta\varphi) = (0, 0)$ has been excluded because it is undercorrected. The full version of the correlation function is shown in appendix C.

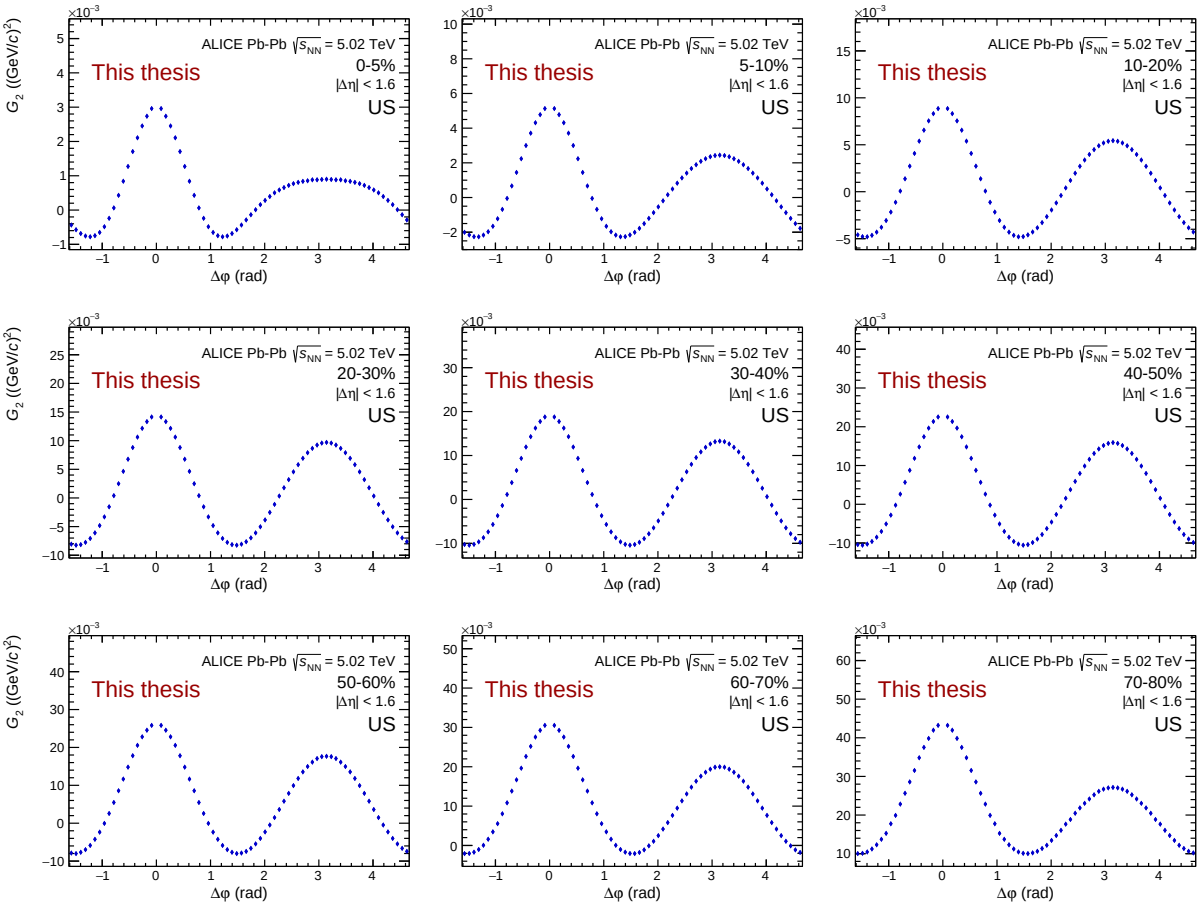

FIGURE B.11: Azimuthal projection of the unlike sign (US) two-particle transverse momentum correlation in Pb–Pb collisions at $\sqrt{s_{\mathrm{NN}}}$ = 5.02 TeV as measured by ALICE.

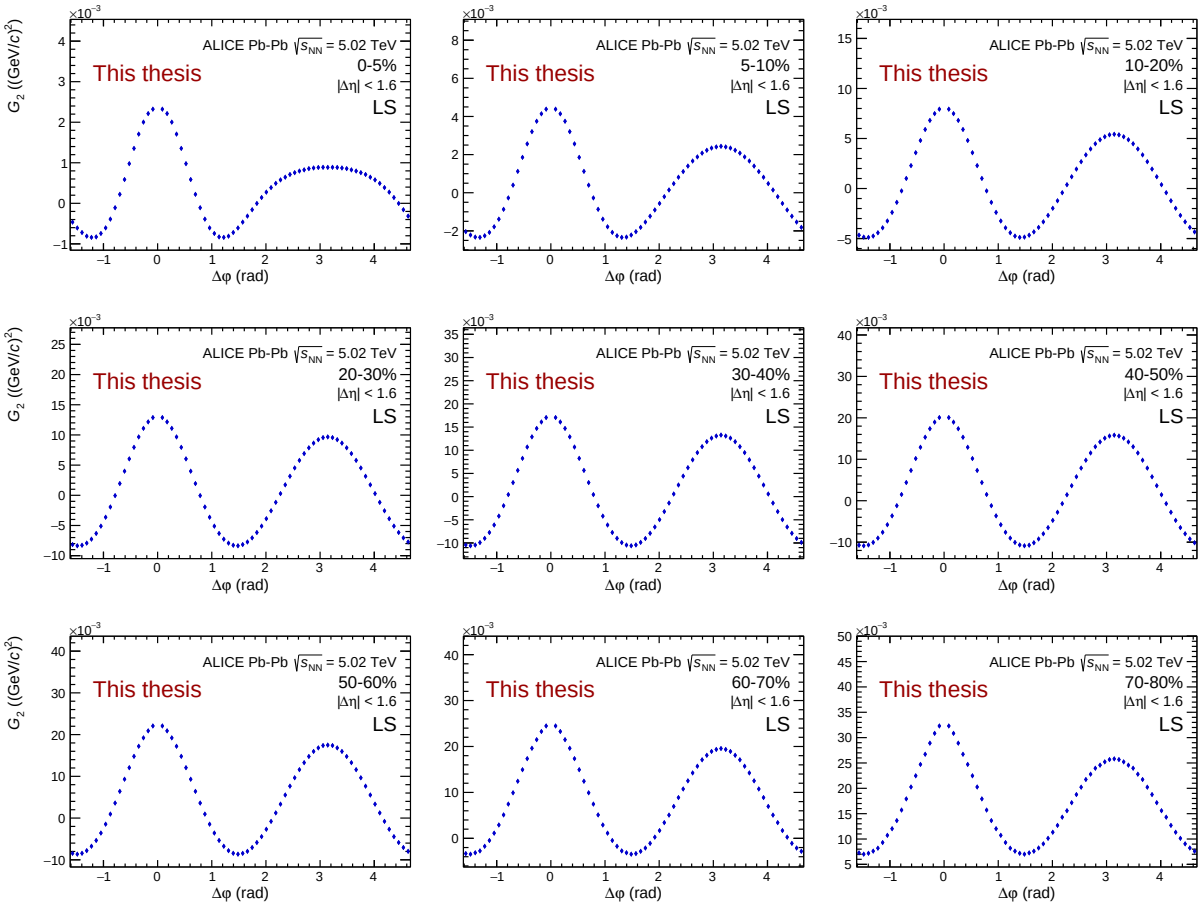

FIGURE B.12: Azimuthal projection of the like sign (LS) two-particle transverse momentum correlation in Pb–Pb collisions at $\sqrt{s_{\mathrm{NN}}} = 5.02$ TeV as measured by ALICE.

B.3 p–Pb at $\sqrt{s_{\mathrm{NN}}}$ = 5.02 TeV results

B.3.1 Two-particle transverse momentum correlations

Figures B.13 and B.14 show the two-particle transverse momentum correlation G_2 for the US and LS track combinations, respectively. The central bin at $(\Delta\eta, \Delta\varphi) = (0, 0)$ has been excluded because it is undercorrected. The full version of the correlation function is shown in appendix C.

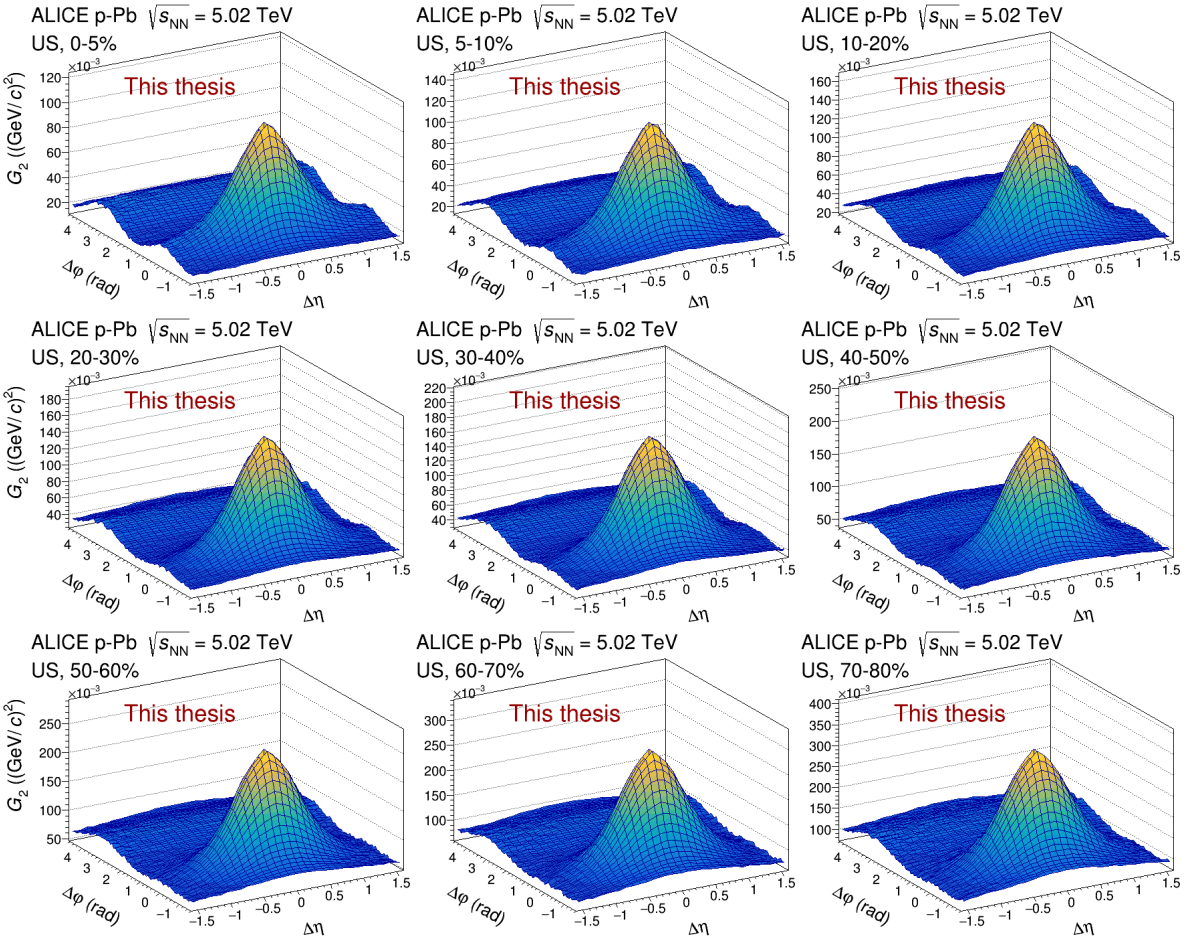

FIGURE B.13: Unlike sign (US) two-particle transverse momentum correlation in p–Pb collisions at $\sqrt{s_{\mathrm{NN}}}$ = 5.02 TeV as measured by ALICE.

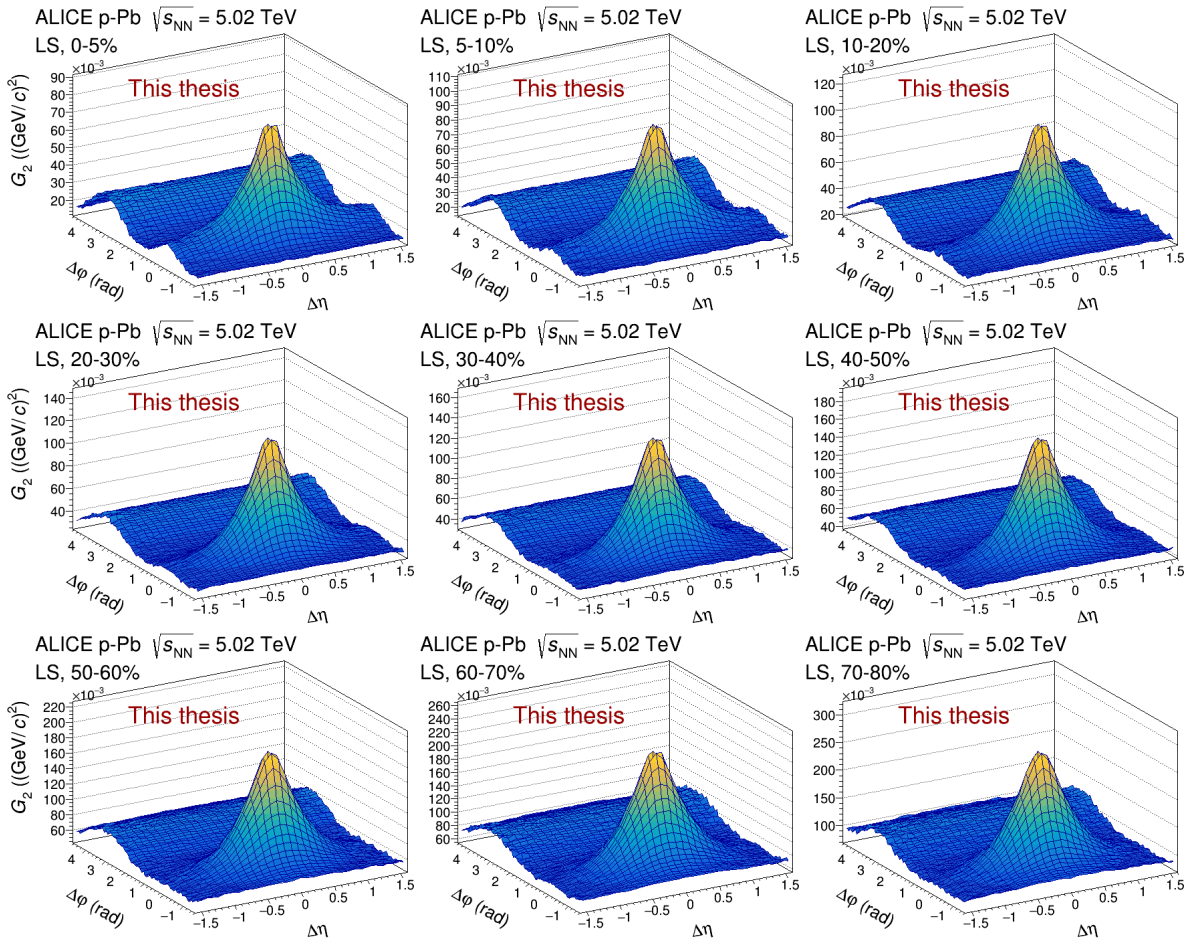

FIGURE B.14: Like sign (LS) two-particle transverse momentum correlation in p–Pb collisions at $\sqrt{s_{NN}}$ = 5.02 TeV as measured by ALICE.

B.3.2 Longitudinal projections

Figures B.15 and B.16 show the longitudinal projection of two-particle transverse momentum correlation G_2 for the US and LS track combinations, respectively. The central bin at $(\Delta\eta, \Delta\varphi) = (0, 0)$ has been excluded because it is undercorrected. The full version of the correlation function is shown in appendix C.

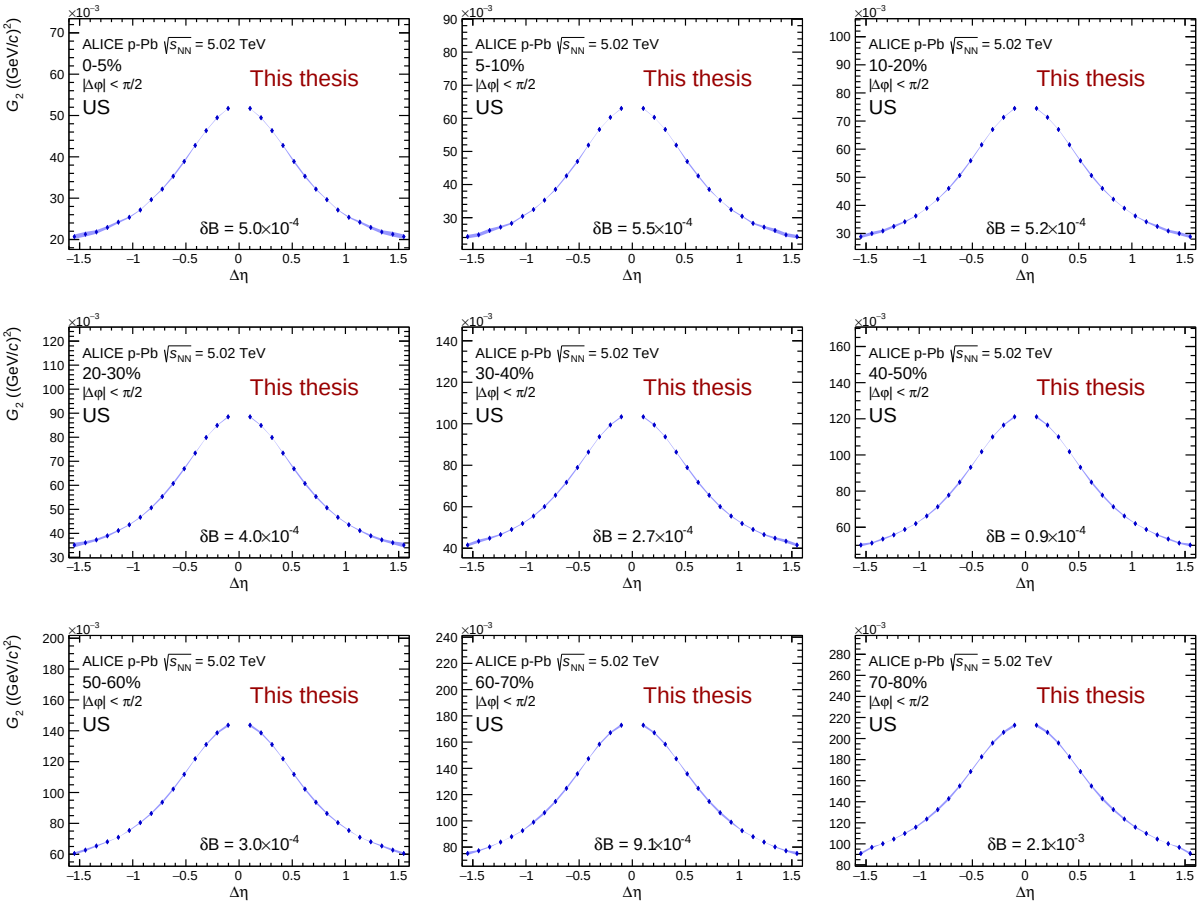

FIGURE B.15: Longitudinal projection of the unlike sign (US) two-particle transverse momentum correlation in p–Pb collisions at $\sqrt{s_{\mathrm{NN}}}$ = 5.02 TeV as measured by ALICE.

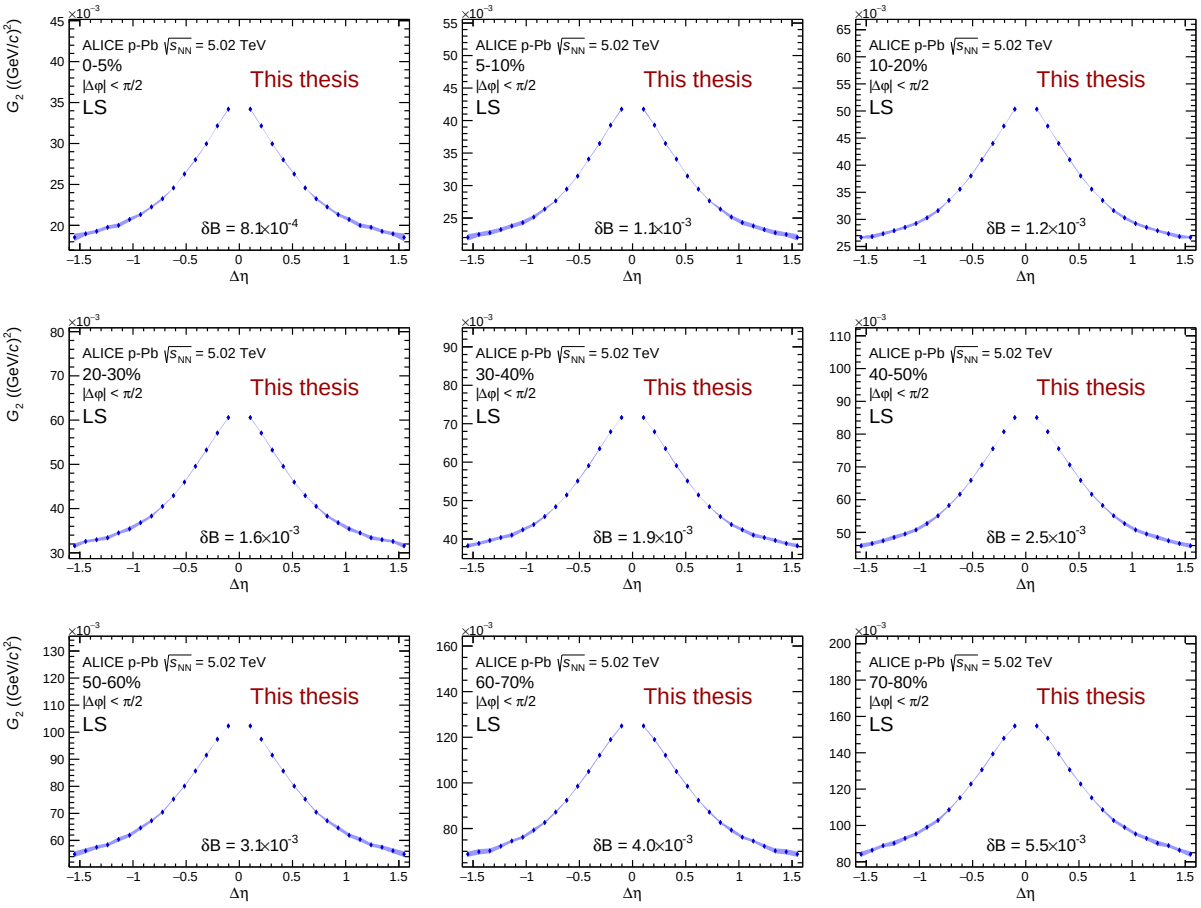

FIGURE B.16: Longitudinal projection of the like sign (LS) two-particle transverse momentum correlation in p–Pb collisions at $\sqrt{s_{\mathrm{NN}}}$ = 5.02 TeV as measured by ALICE.

B.3.3 Azimuthal projections

Figures B.17 and B.18 show the azimuthal projections of two-particle transverse momentum correlation G_2 for the US and LS track combinations, respectively. The central bin at $(\Delta\eta, \Delta\varphi) = (0, 0)$ has been excluded because it is undercorrected. The full version of the correlation function is shown in appendix C.

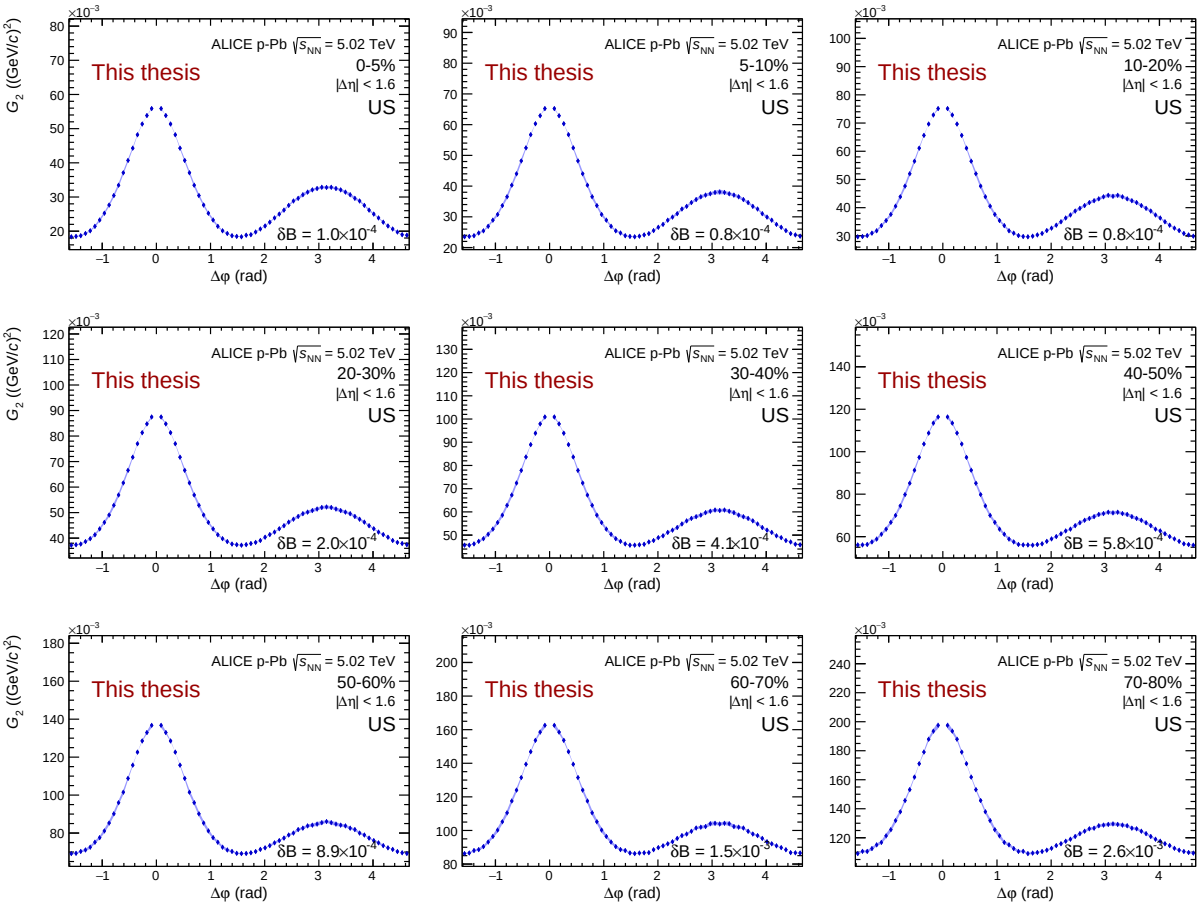

FIGURE B.17: Azimuthal projection of the unlike sign (US) two-particle transverse momentum correlation in p–Pb collisions at $\sqrt{s_{\mathrm{NN}}}$ = 5.02 TeV as measured by ALICE.

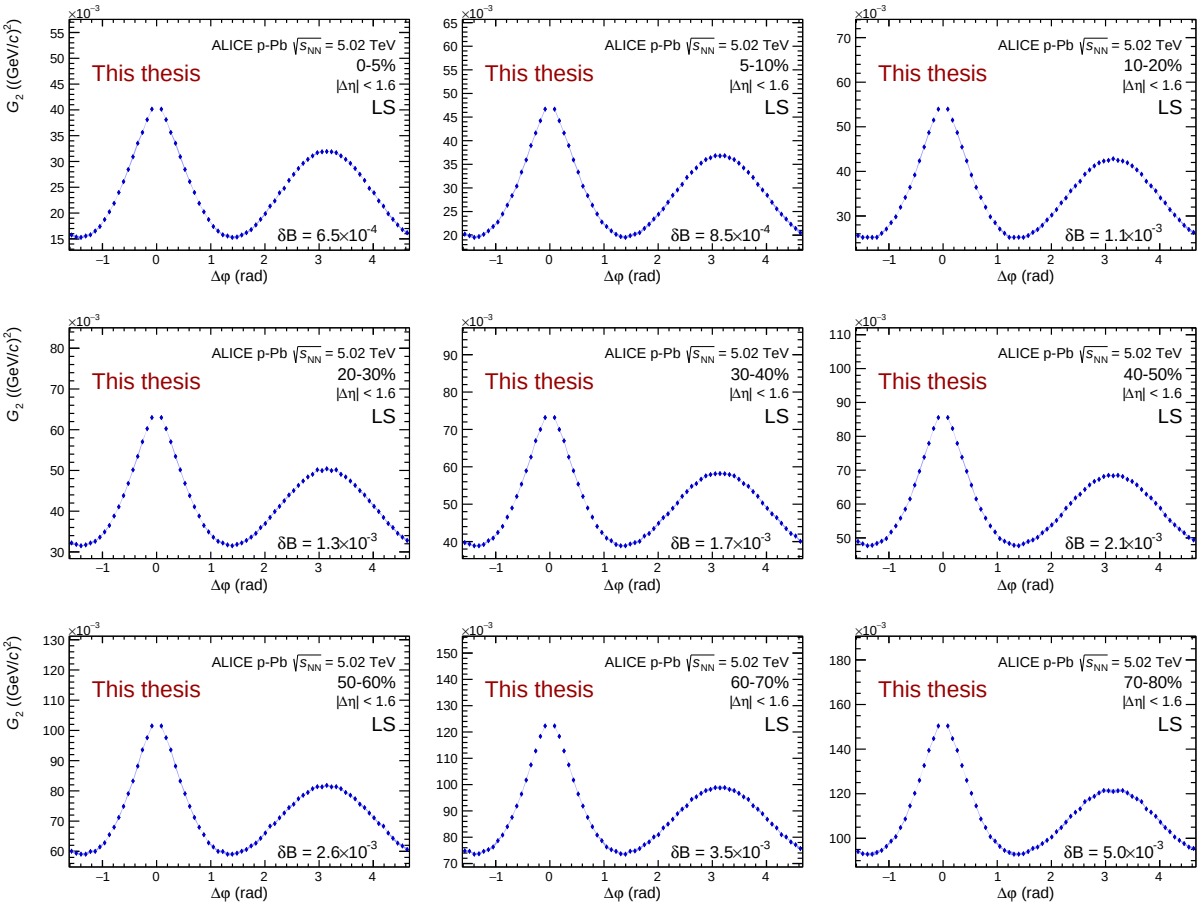

FIGURE B.18: Azimuthal projection of the like sign (LS) two-particle transverse momentum correlation in p–Pb collisions at $\sqrt{s_{\mathrm{NN}}}$ = 5.02 TeV as measured by ALICE.

B.4 pp at $\sqrt{s_{\mathrm{NN}}}$ = 7 TeV results

B.4.1 Two-particle transverse momentum correlations

Figures B.19 and B.20 show the two-particle transverse momentum correlation G_2 for the US and LS track combinations, respectively. The central bin at $(\Delta\eta, \Delta\varphi) = (0, 0)$ has been excluded because it is undercorrected. The full version of the correlation function is shown in appendix C.

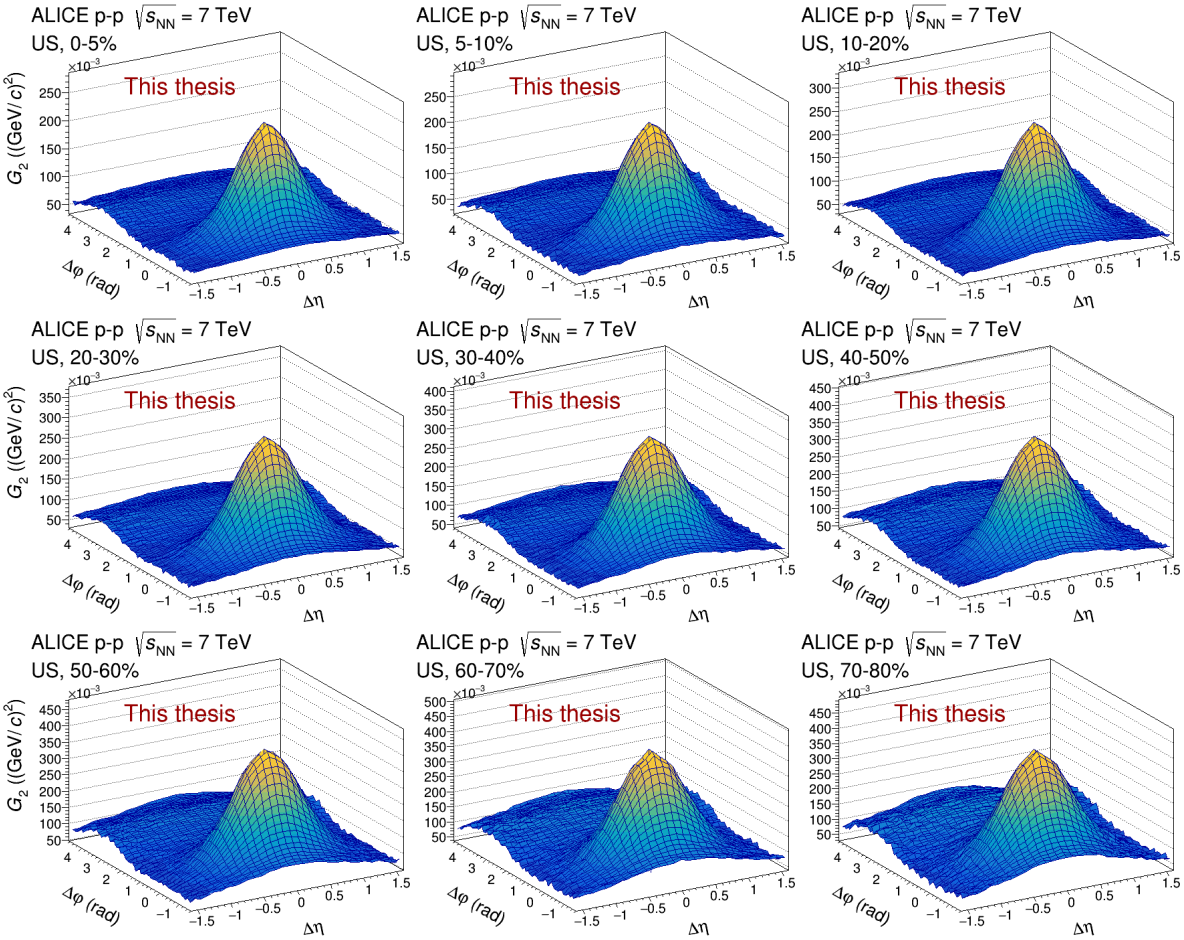

FIGURE B.19: Unlike sign (US) two-particle transverse momentum correlation in pp collisions at $\sqrt{s_{\mathrm{NN}}}$ = 7 TeV as measured by ALICE.

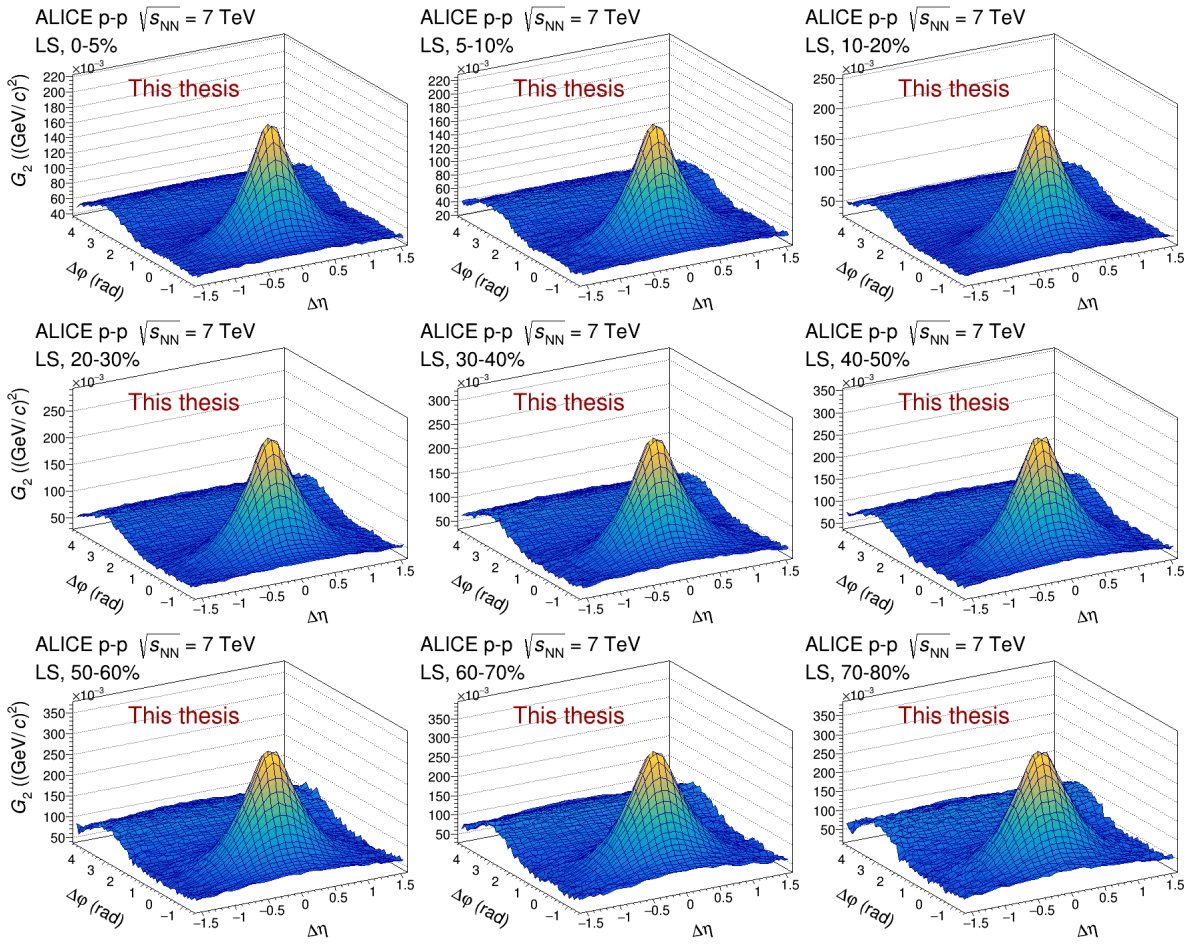

FIGURE B.20: Like sign (LS) two-particle transverse momentum correlation in pp collisions at $\sqrt{s_{NN}}$ = 7 TeV as measured by ALICE.

B.4.2 Longitudinal projections

Figures B.21 and B.22 show the longitudinal projection of two-particle transverse momentum correlation G_2 for the US and LS track combinations, respectively. The central bin at $(\Delta\eta, \Delta\varphi) = (0, 0)$ has been excluded because it is undercorrected. The full version of the correlation function is shown in appendix C.

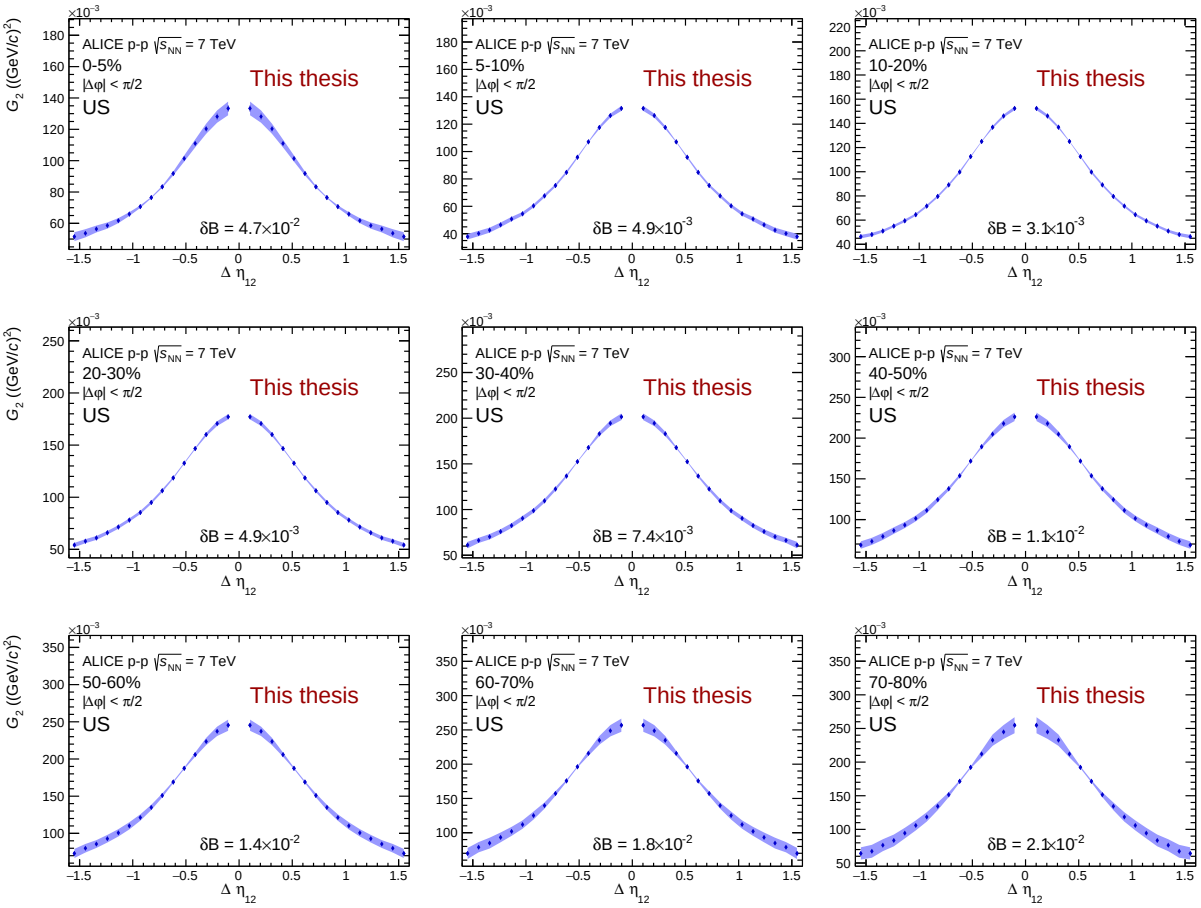

FIGURE B.21: Longitudinal projection of the unlike sign (US) two-particle transverse momentum correlation in pp collisions at $\sqrt{s_{\mathrm{NN}}}$ = 7 TeV as measured by ALICE.

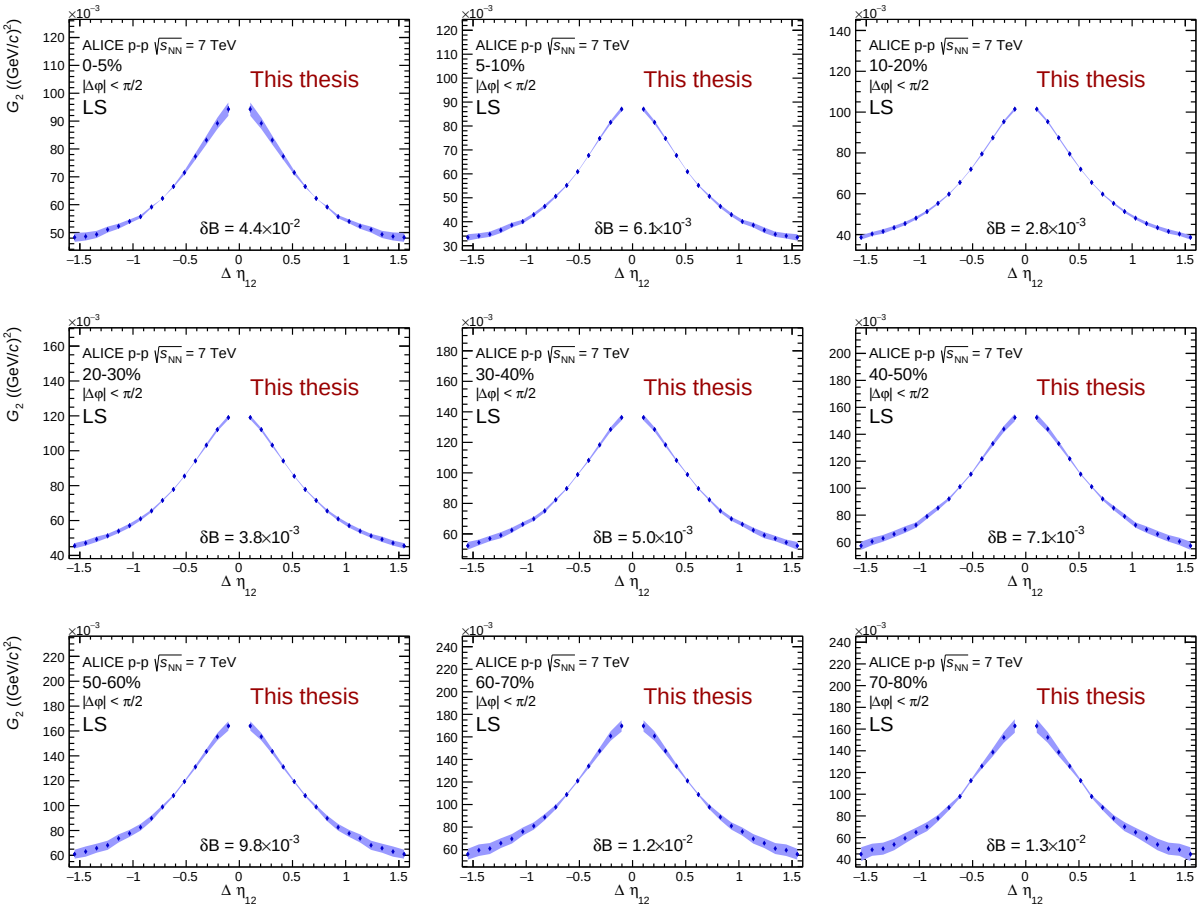

FIGURE B.22: Longitudinal projection of the like sign (LS) two-particle transverse momentum correlation in pp collisions at $\sqrt{s_{\mathrm{NN}}}$ = 7 TeV as measured by ALICE.

B.4.3 Azimuthal projections

Figures B.23 and B.24 show the azimuthal projections of two-particle transverse momentum correlation G_2 for the US and LS track combinations, respectively. The central bin at $(\Delta\eta, \Delta\varphi) = (0, 0)$ has been excluded because it is undercorrected. The full version of the correlation function is shown in appendix C.

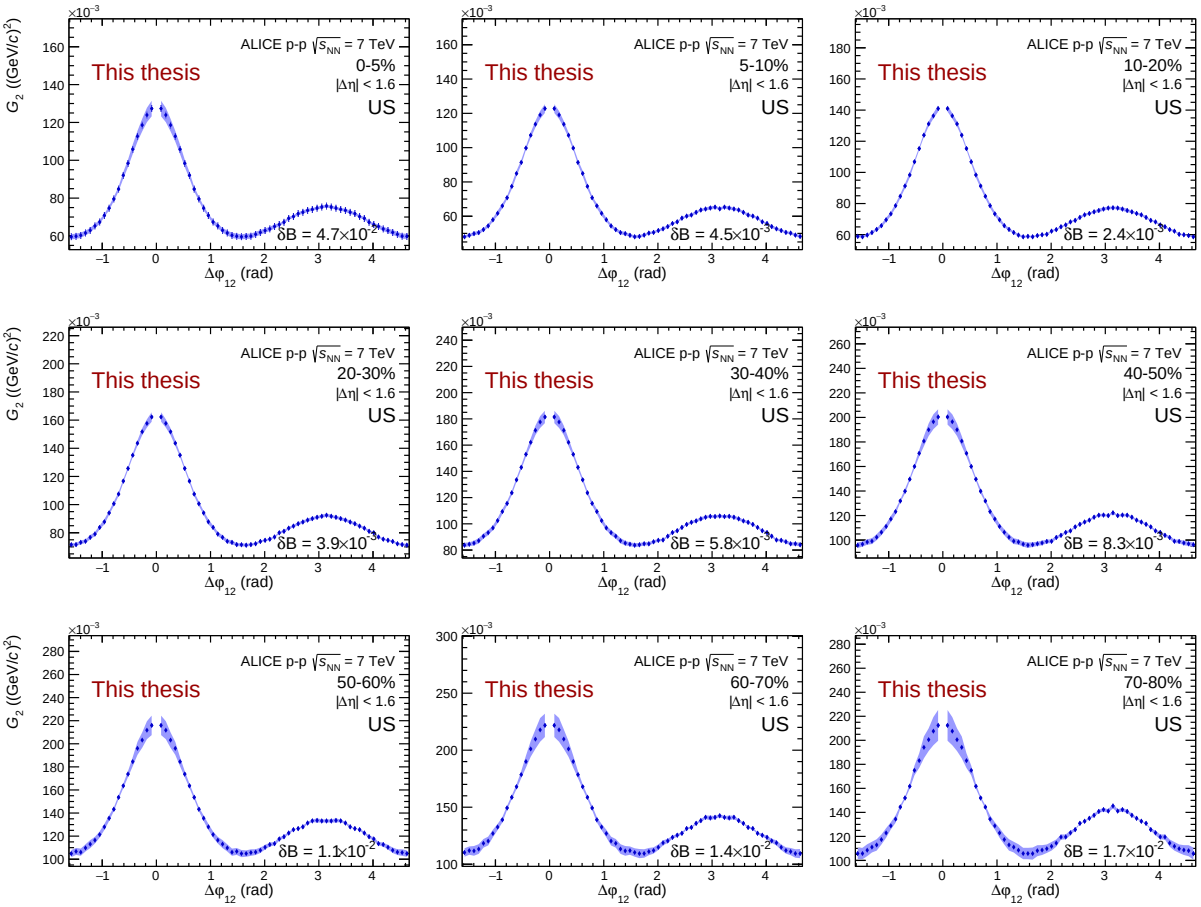

FIGURE B.23: Azimuthal projection of the unlike sign (US) two-particle transverse momentum correlation in pp collisions at $\sqrt{s_{\mathrm{NN}}}$ = 7 TeV as measured by ALICE.

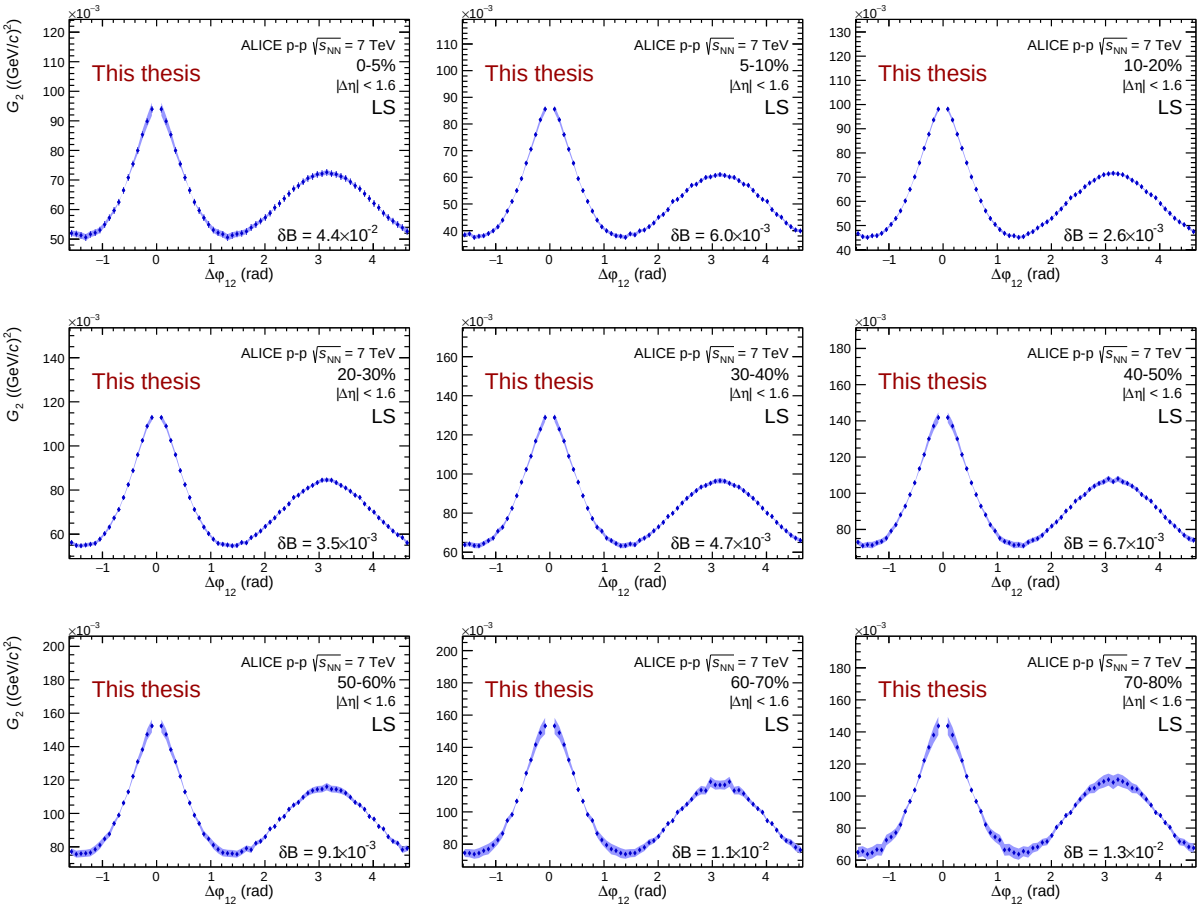

FIGURE B.24: Azimuthal projection of the like sign (LS) two-particle transverse momentum correlation in pp collisions at $\sqrt{s_{\mathrm{NN}}}$ = 7 TeV as measured by ALICE.

Appendix C

Results for CI, CD, US, and LS track combinations including the central bin

C.1 Pb–Pb at $\sqrt{s_{\mathrm{NN}}}$ = 2.76 TeV results

C.1.1 Two-particle transverse momentum correlations

Figures C.1, C.2, C.3, and C.4 show the two-particle transverse momentum correlation G_2 for the CI, CD, US and LS track combinations, respectively.

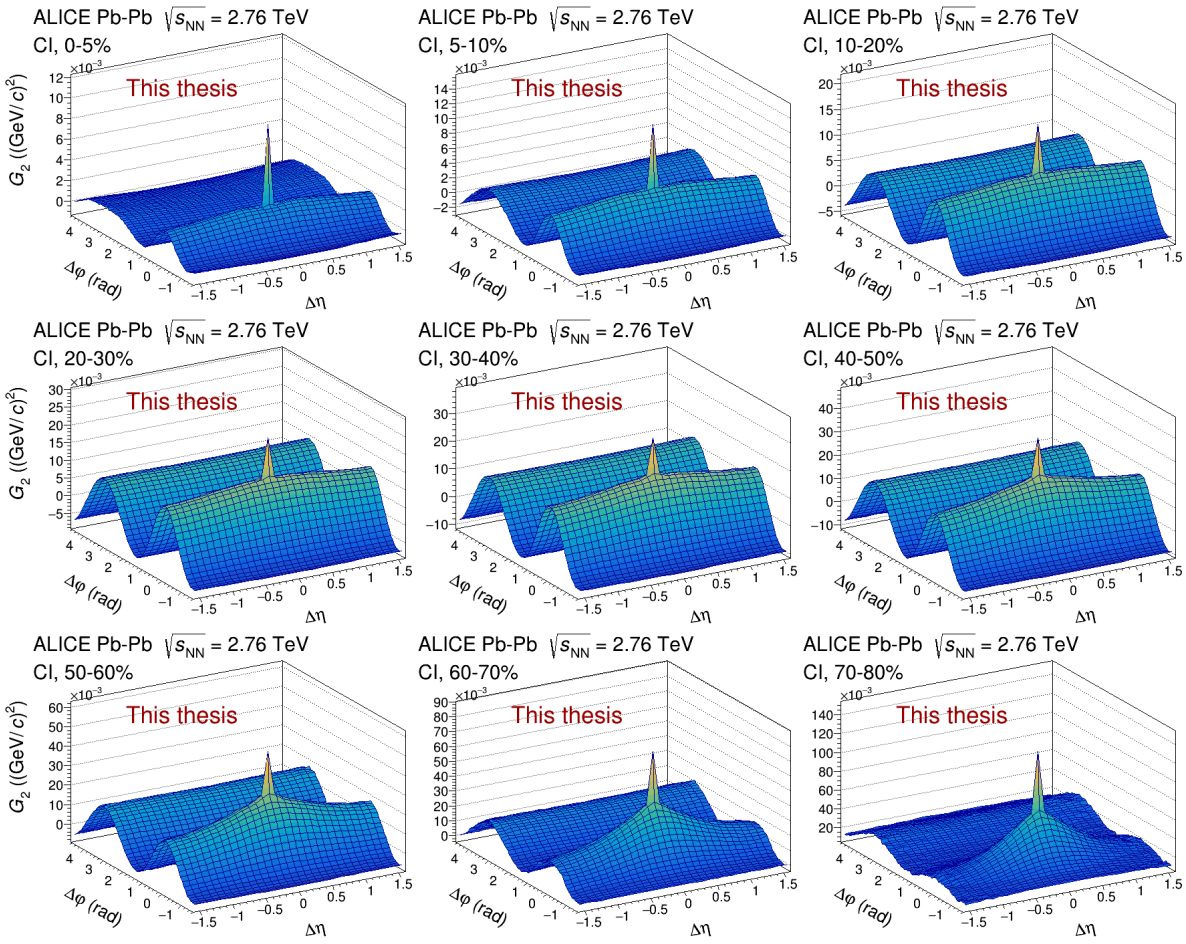

FIGURE C.1: Charge independent (CI) two-particle transverse momentum correlation in Pb–Pb collisions at $\sqrt{s_{\mathrm{NN}}}$ = 2.76 TeV as measured by ALICE.

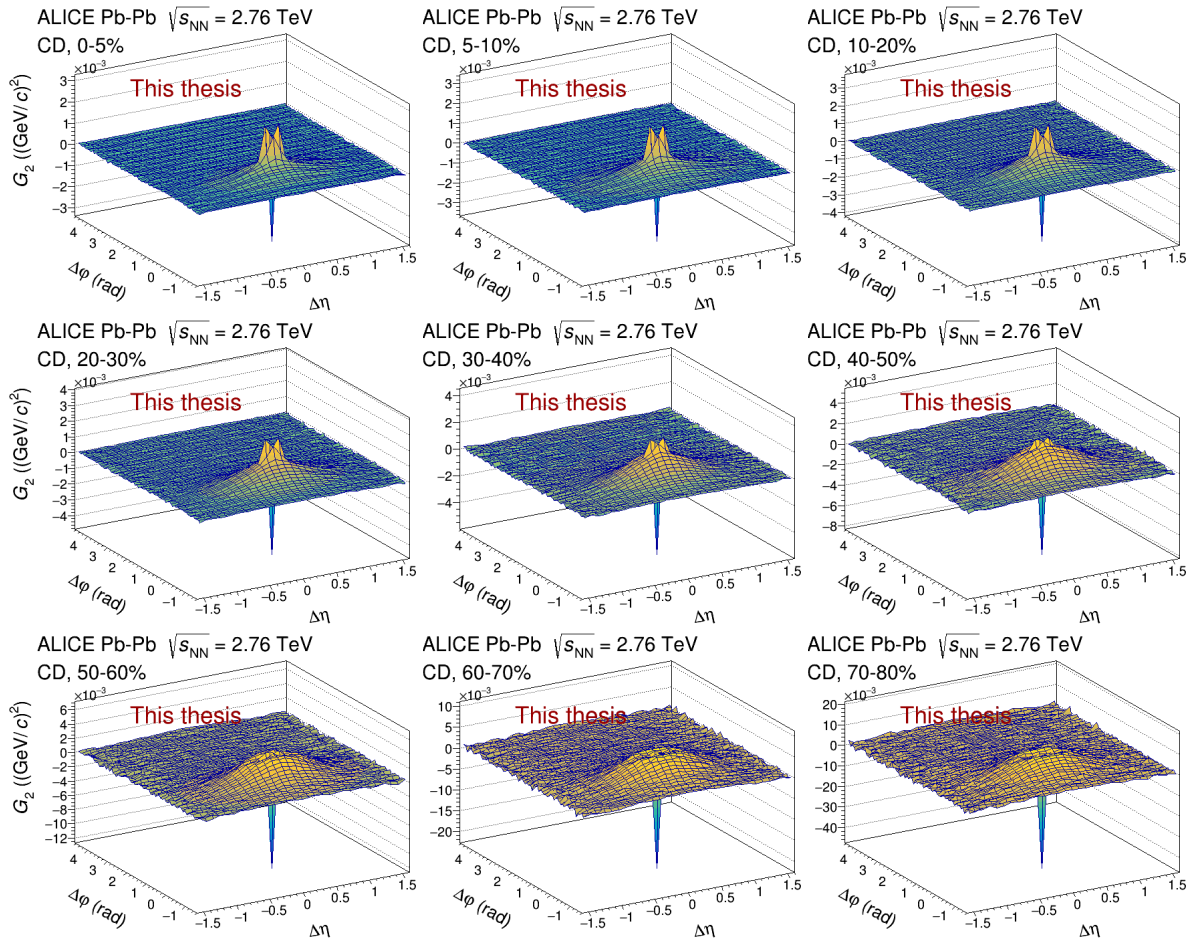

FIGURE C.2: Charge dependent (CD) two-particle transverse momentum correlation in Pb–Pb collisions at $\sqrt{s_{NN}}$ = 2.76 TeV as measured by ALICE.

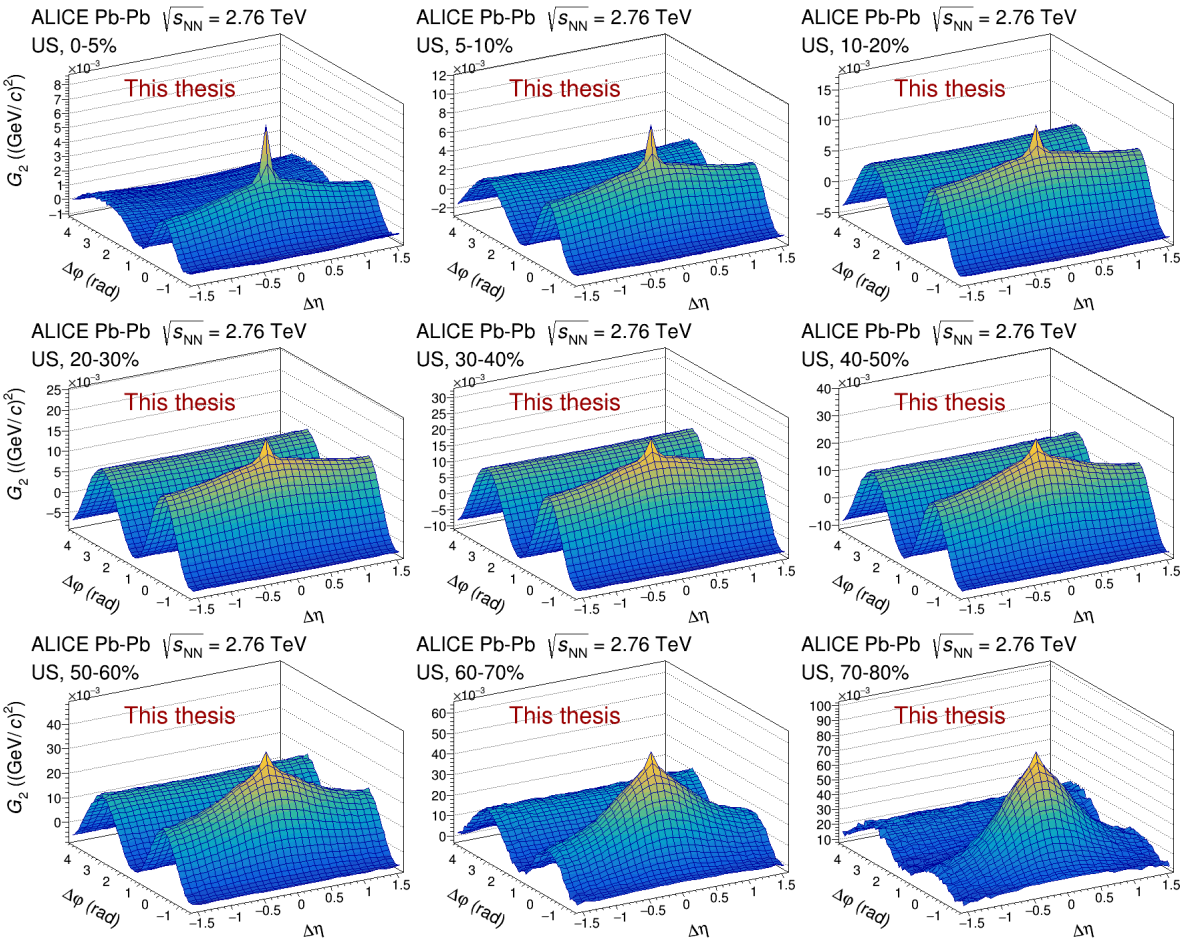

FIGURE C.3: Unlike sign (US) two-particle transverse momentum correlation in Pb–Pb collisions at $\sqrt{s_{\mathrm{NN}}}$ = 2.76 TeV as measured by ALICE.

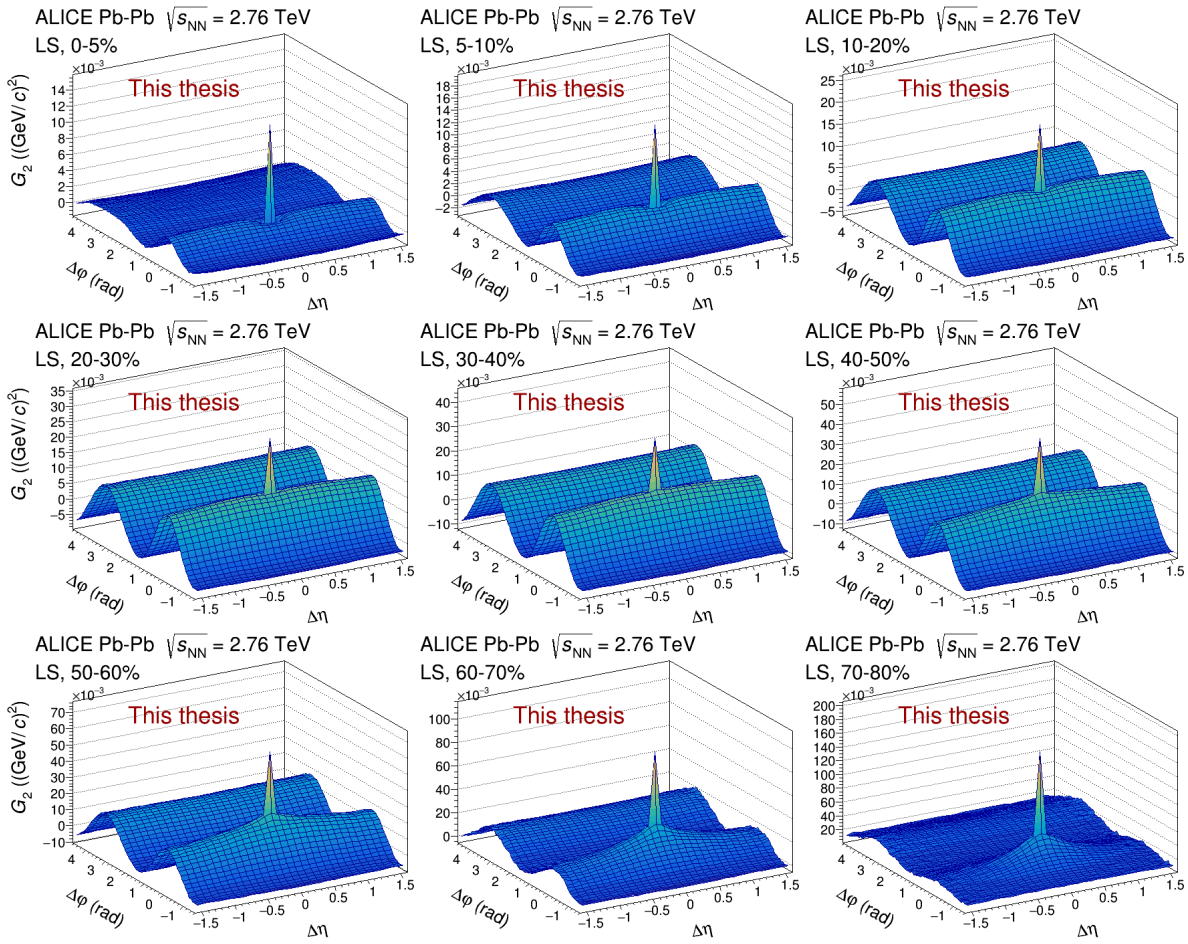

FIGURE C.4: Like sign (LS) two-particle transverse momentum correlation in Pb–Pb collisions at $\sqrt{s_{\mathrm{NN}}}$ = 2.76 TeV as measured by ALICE.

C.1.2 Longitudinal projections

Figures C.5, C.6, C.7, and C.8 show the longitudinal projection of two-particle transverse momentum correlation G_2 for the CI, CD, US, and LS track combinations, respectively.

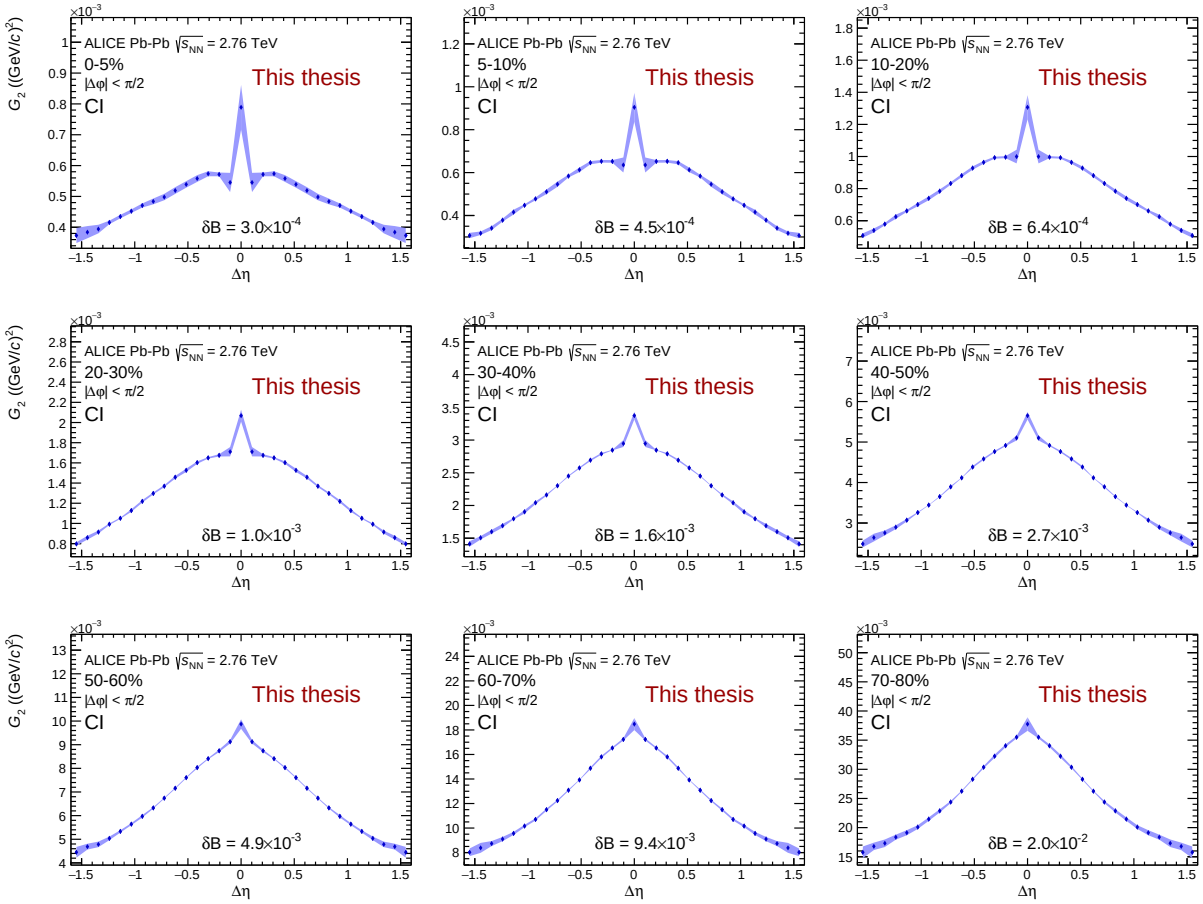

FIGURE C.5: Longitudinal projection of the charge independent (CI) two-particle transverse momentum correlation in Pb–Pb collisions at $\sqrt{s_{\mathrm{NN}}}$ = 2.76 TeV as measured by ALICE.

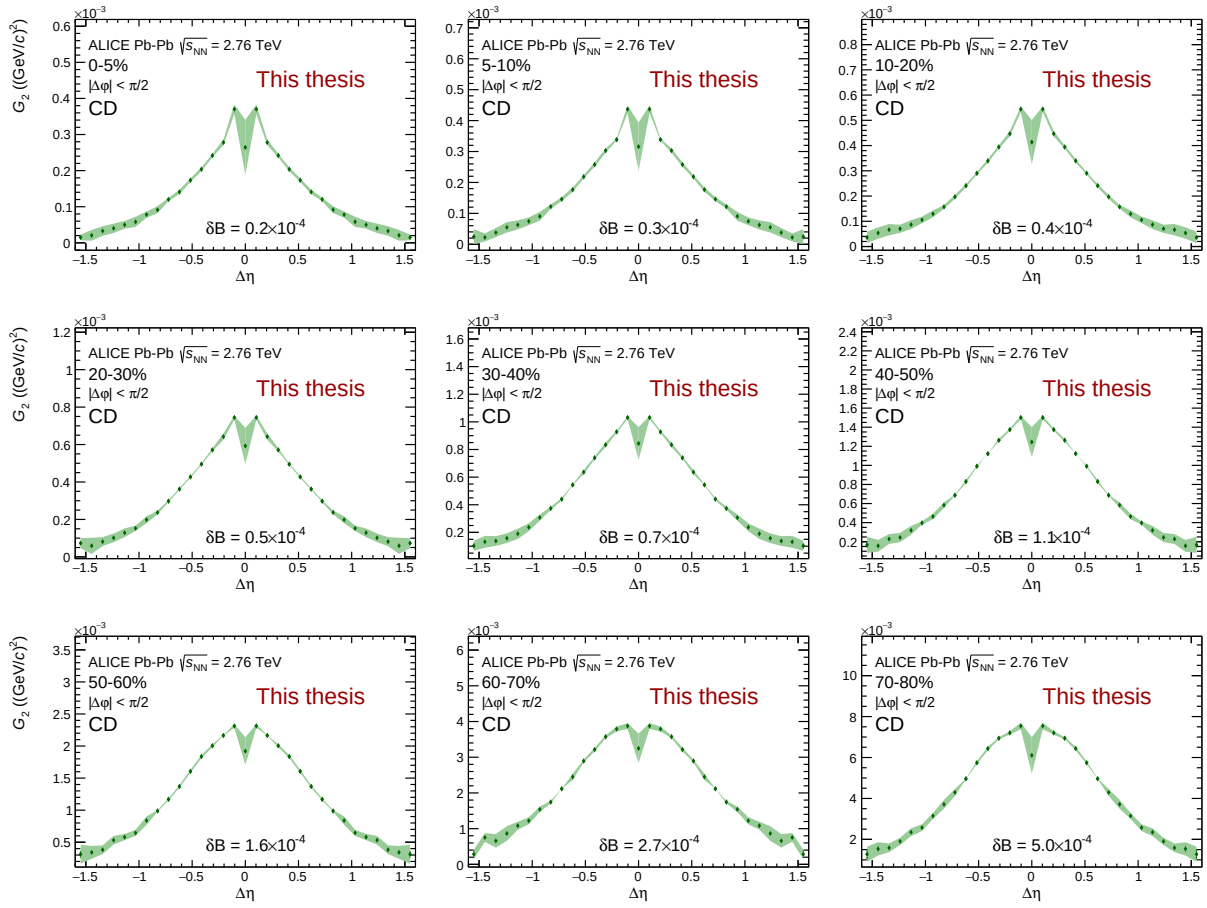

FIGURE C.6: Longitudinal projection of the charge dependent (CD) two-particle transverse momentum correlation in Pb–Pb collisions at $\sqrt{s_{\mathrm{NN}}}$ = 2.76 TeV as measured by ALICE.

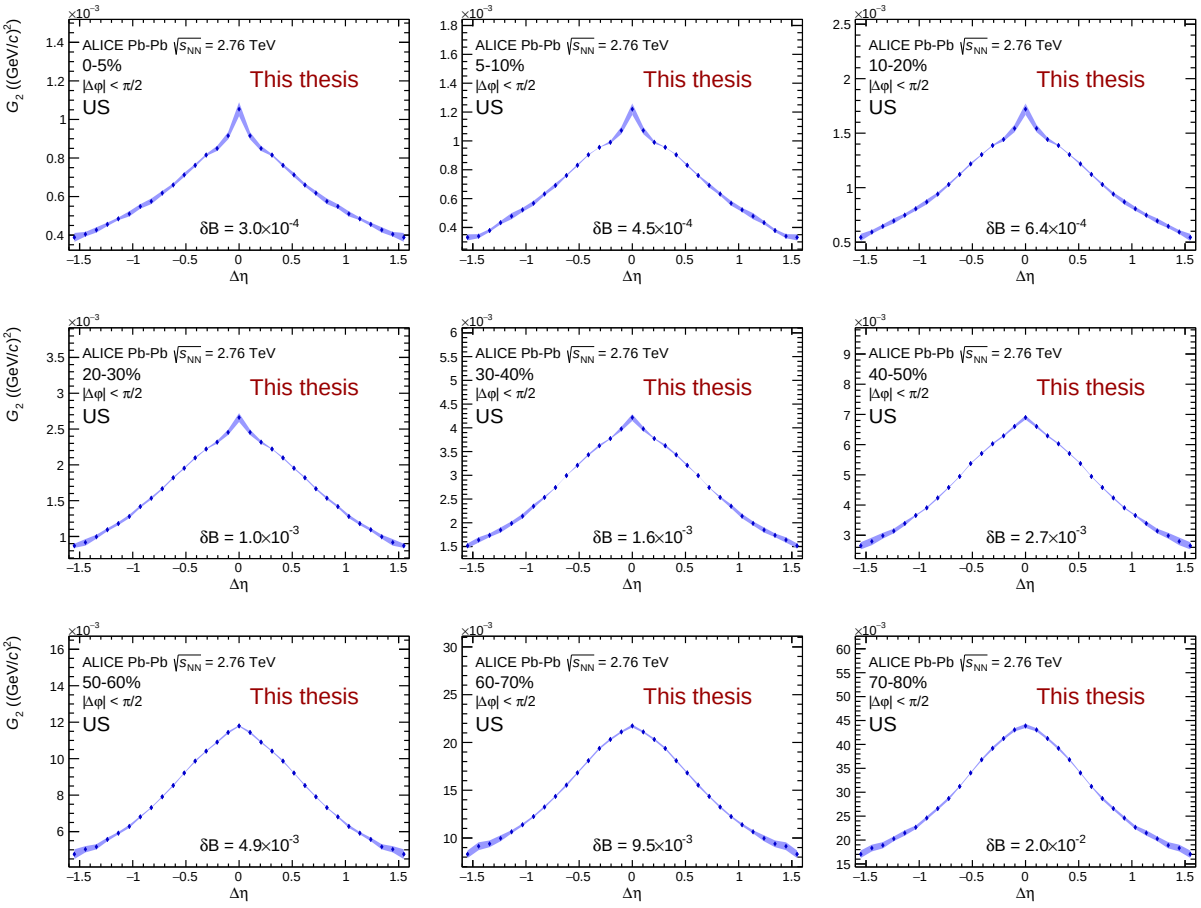

FIGURE C.7: Longitudinal projection of the unlike sign (US) two-particle transverse momentum correlation in Pb–Pb collisions at $\sqrt{s_{\mathrm{NN}}}$ = 2.76 TeV as measured by ALICE.

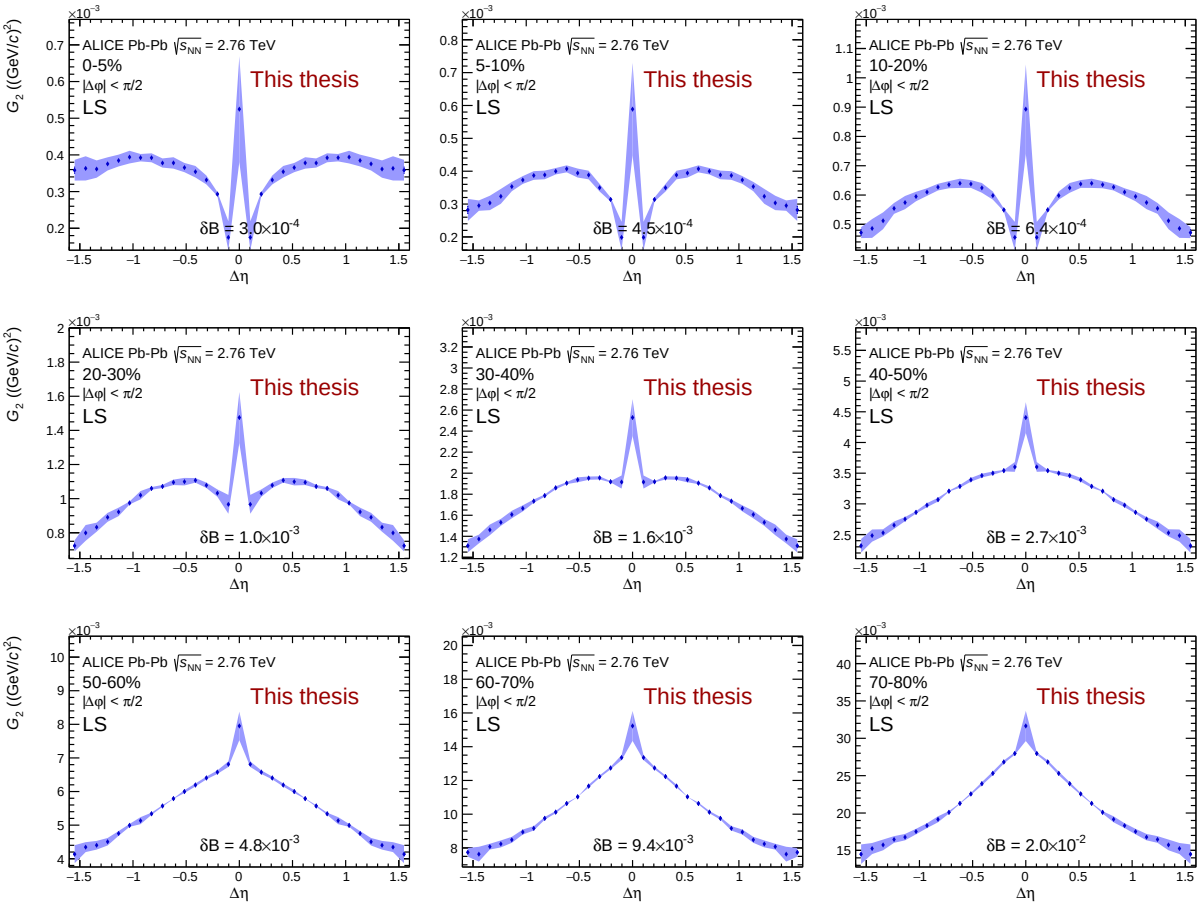

FIGURE C.8: Longitudinal projection of the like sign (LS) two-particle transverse momentum correlation in Pb–Pb collisions at $\sqrt{s_{\mathrm{NN}}}$ = 2.76 TeV as measured by ALICE.

C.1.3 Azimuthal projections

Figures C.9, C.10, C.11, and C.12 show the azimuthal projections of two-particle transverse momentum correlation G_2 for the CI, CD, US, and LS track combinations, respectively.

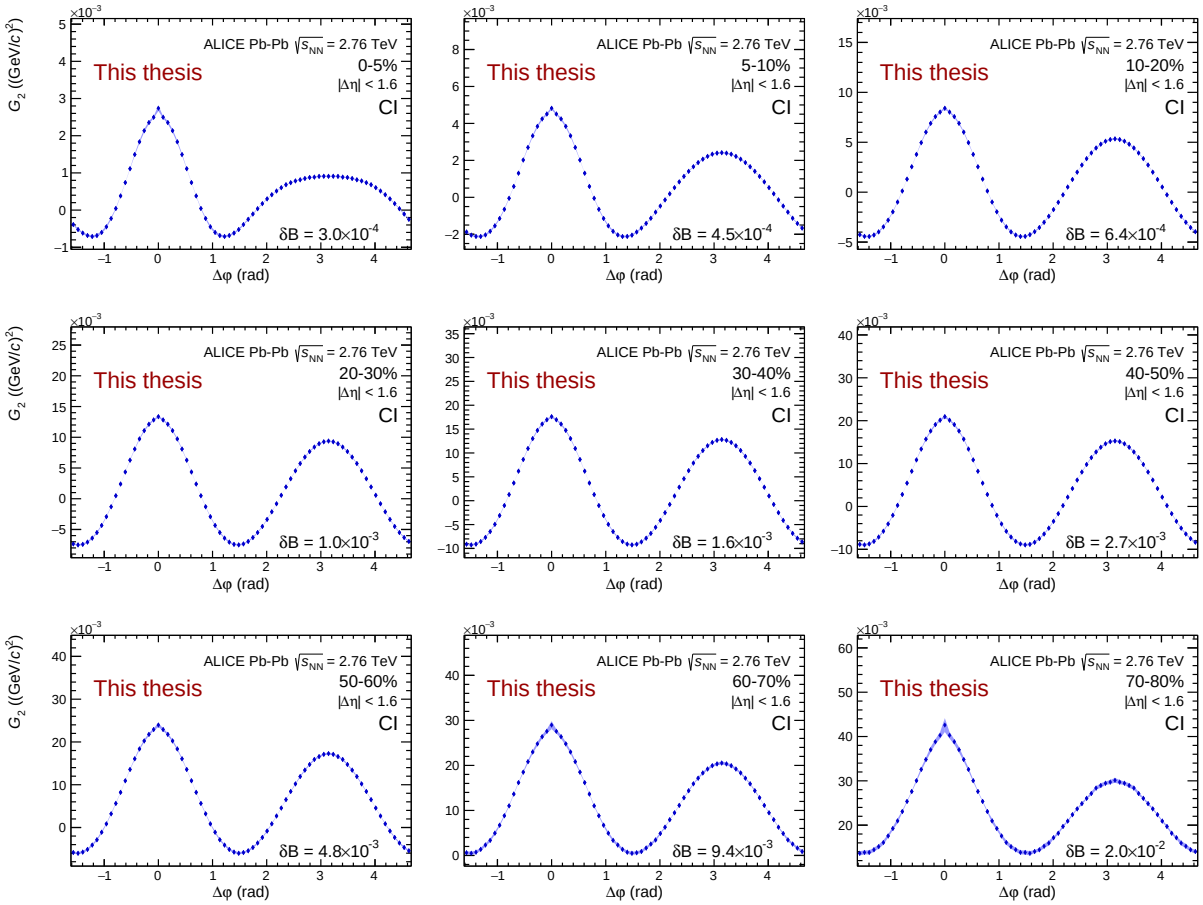

FIGURE C.9: Azimuthal projection of the charge independent (CI) two-particle transverse momentum correlation in Pb–Pb collisions at $\sqrt{s_{\mathrm{NN}}}$ = 2.76 TeV as measured by ALICE.

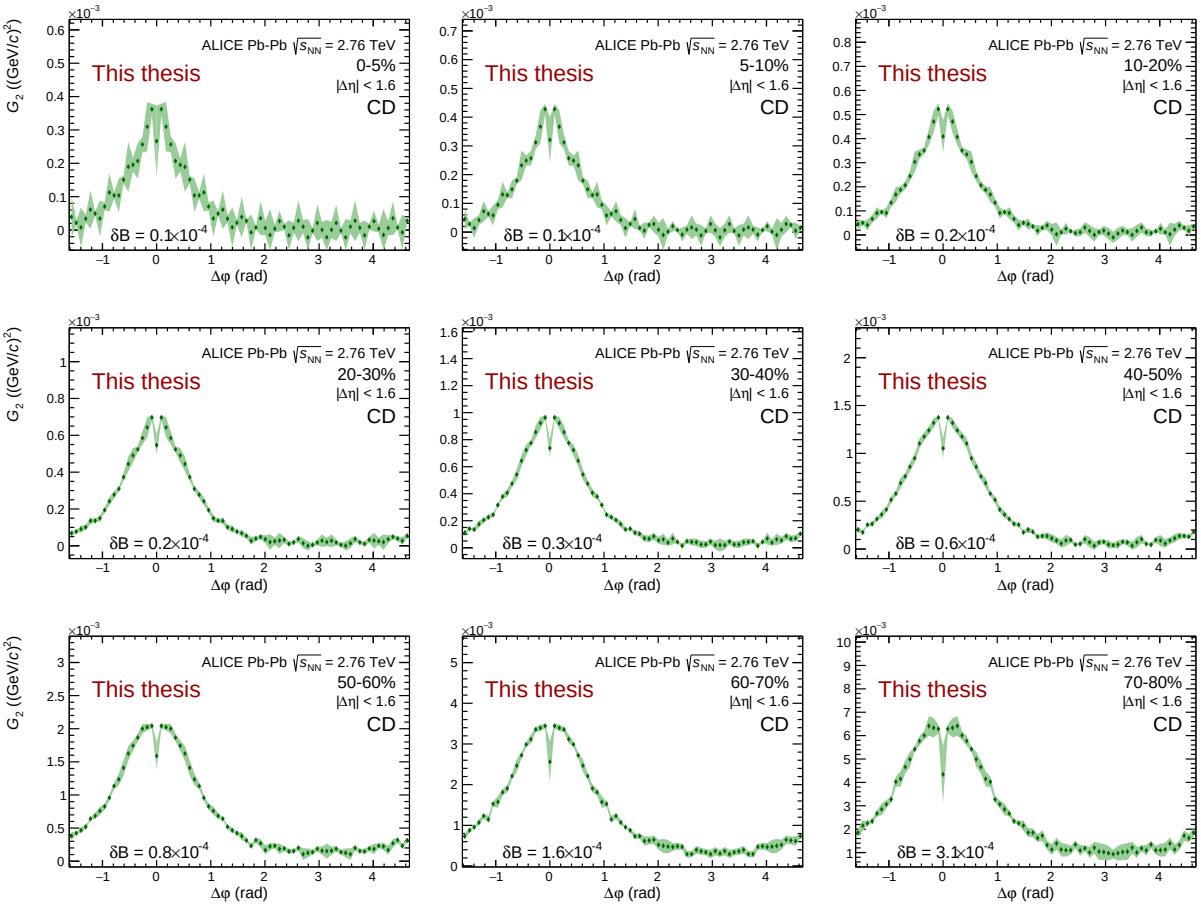

FIGURE C.10: Azimuthal projection of the charge dependent (CD) two-particle transverse momentum correlation in PbPb collisions at $\sqrt{s_{\mathrm{NN}}} = 2.76$ TeV as measured by ALICE.

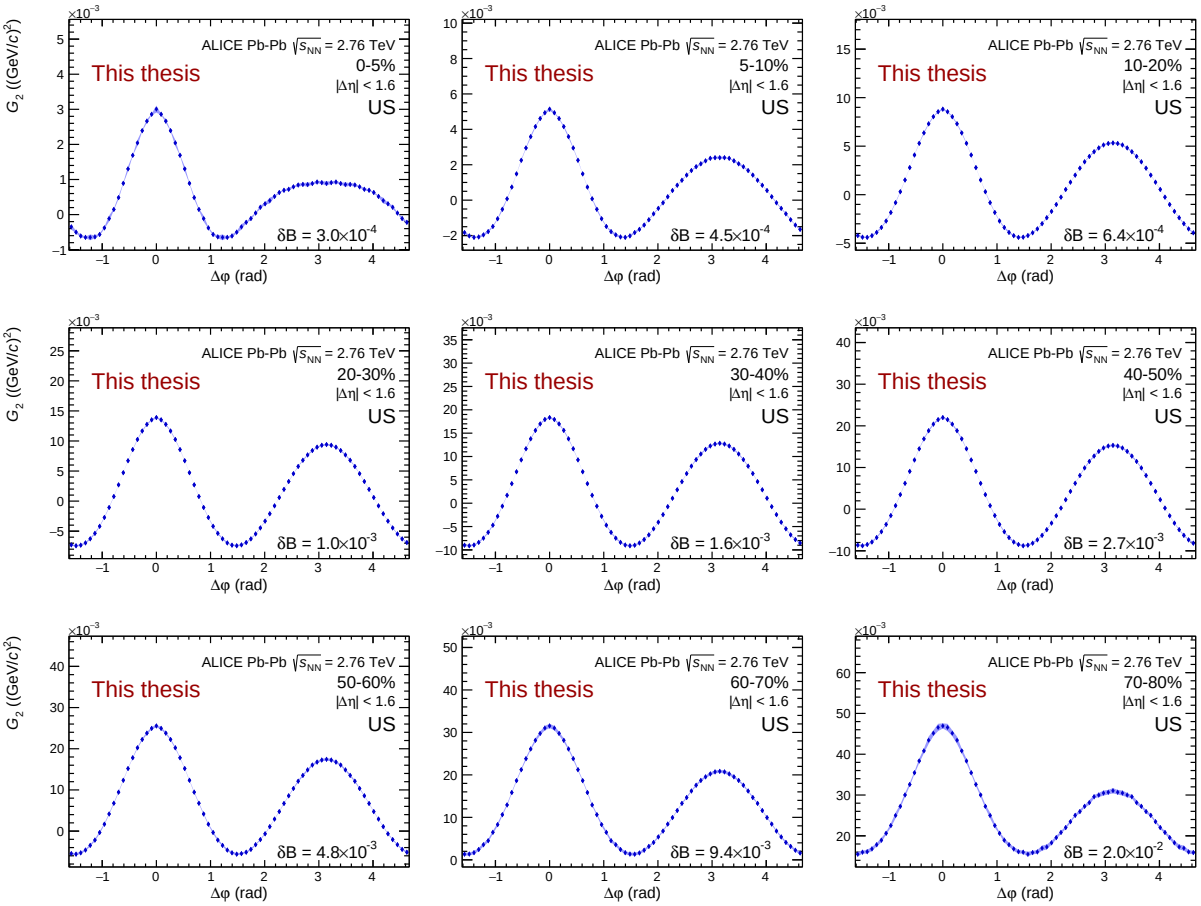

FIGURE C.11: Azimuthal projection of the unlike sign (US) two-particle transverse momentum correlation in Pb–Pb collisions at $\sqrt{s_{\mathrm{NN}}}$ = 2.76 TeV as measured by ALICE.

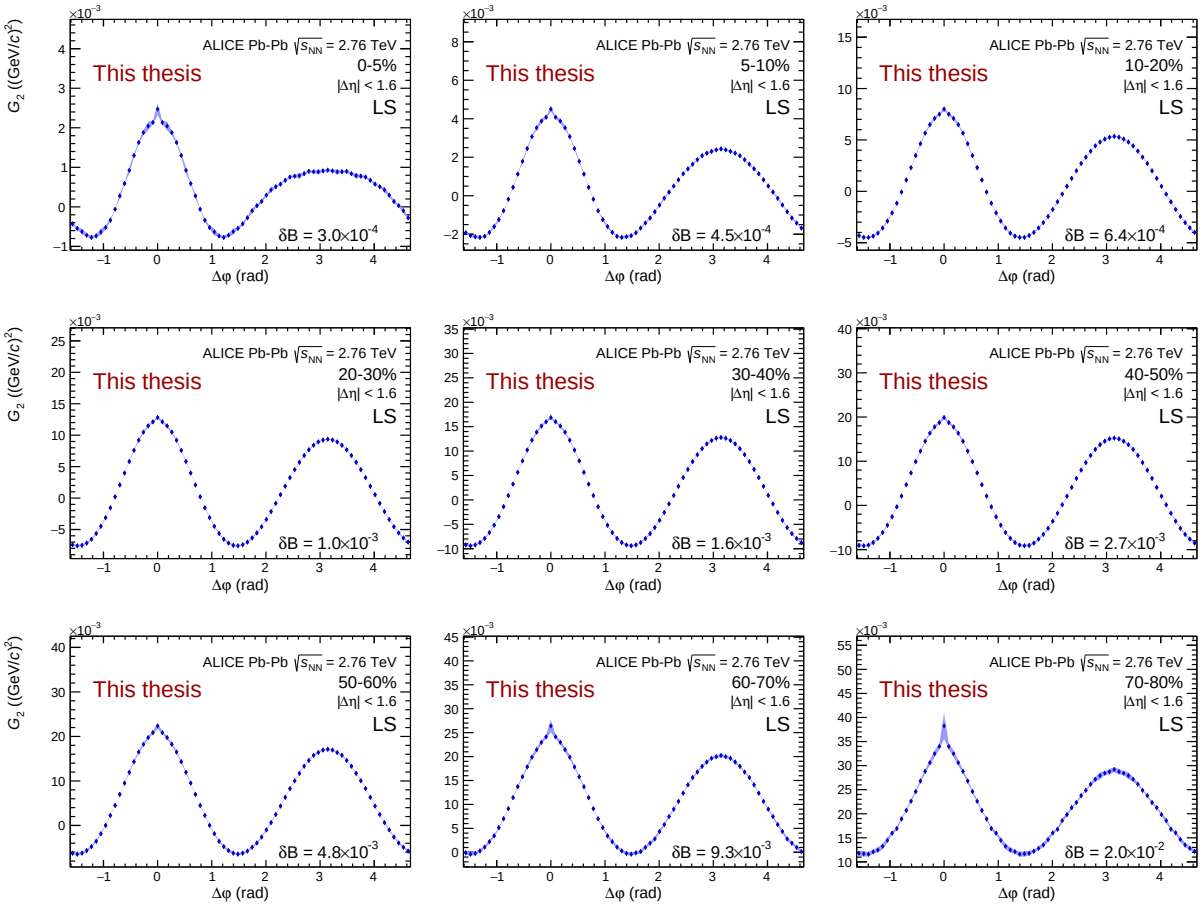

FIGURE C.12: Azimuthal projection of the like sign (LS) two-particle transverse momentum correlation in PbPb collisions at $\sqrt{s_{\mathrm{NN}}}$ = 2.76 TeV as measured by ALICE.

C.2 Pb–Pb at $\sqrt{s_{\mathrm{NN}}}$ = 5.02 TeV results

C.2.1 Two-particle transverse momentum correlations

Figures C.13, C.14, C.15, and C.16 show the two-particle transverse momentum correlation G_2 for the CI, CD, US and LS track combinations, respectively.

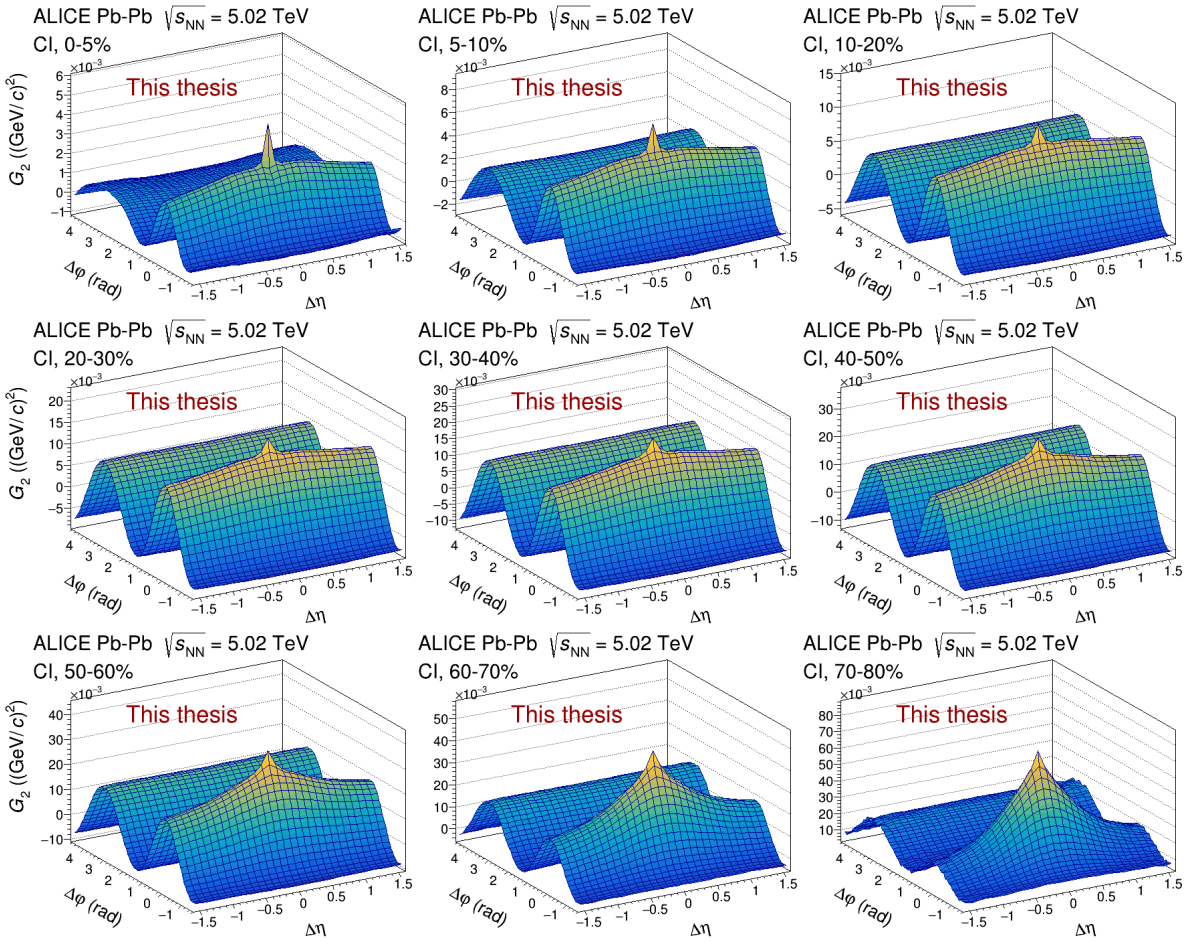

FIGURE C.13: Charge independent (CI) two-particle transverse momentum correlation in Pb–Pb collisions at $\sqrt{s_{\mathrm{NN}}}$ = 5.02 TeV as measured by ALICE.

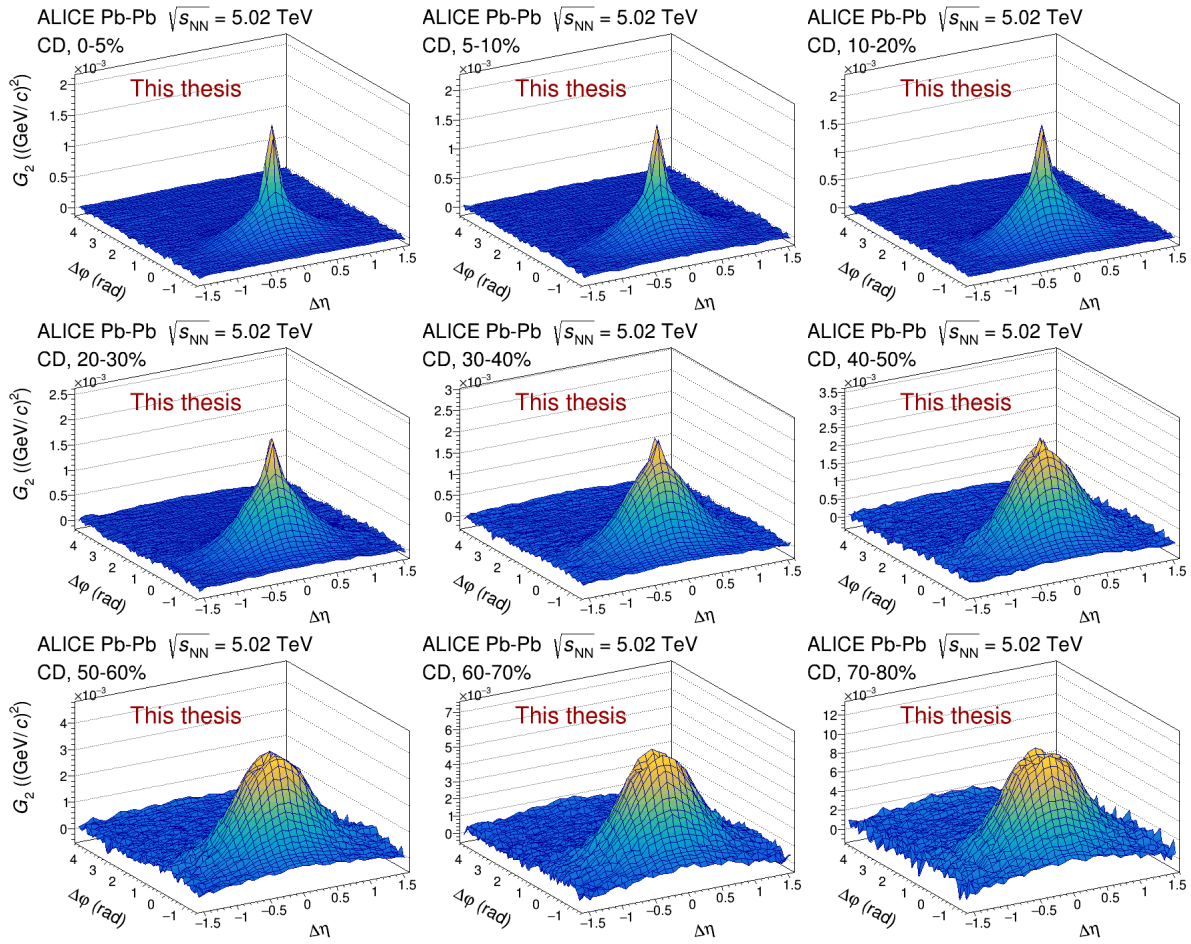

FIGURE C.14: Charge dependent (CD) two-particle transverse momentum correlation in Pb–Pb collisions at $\sqrt{s_{NN}}$ = 5.02 TeV as measured by ALICE.

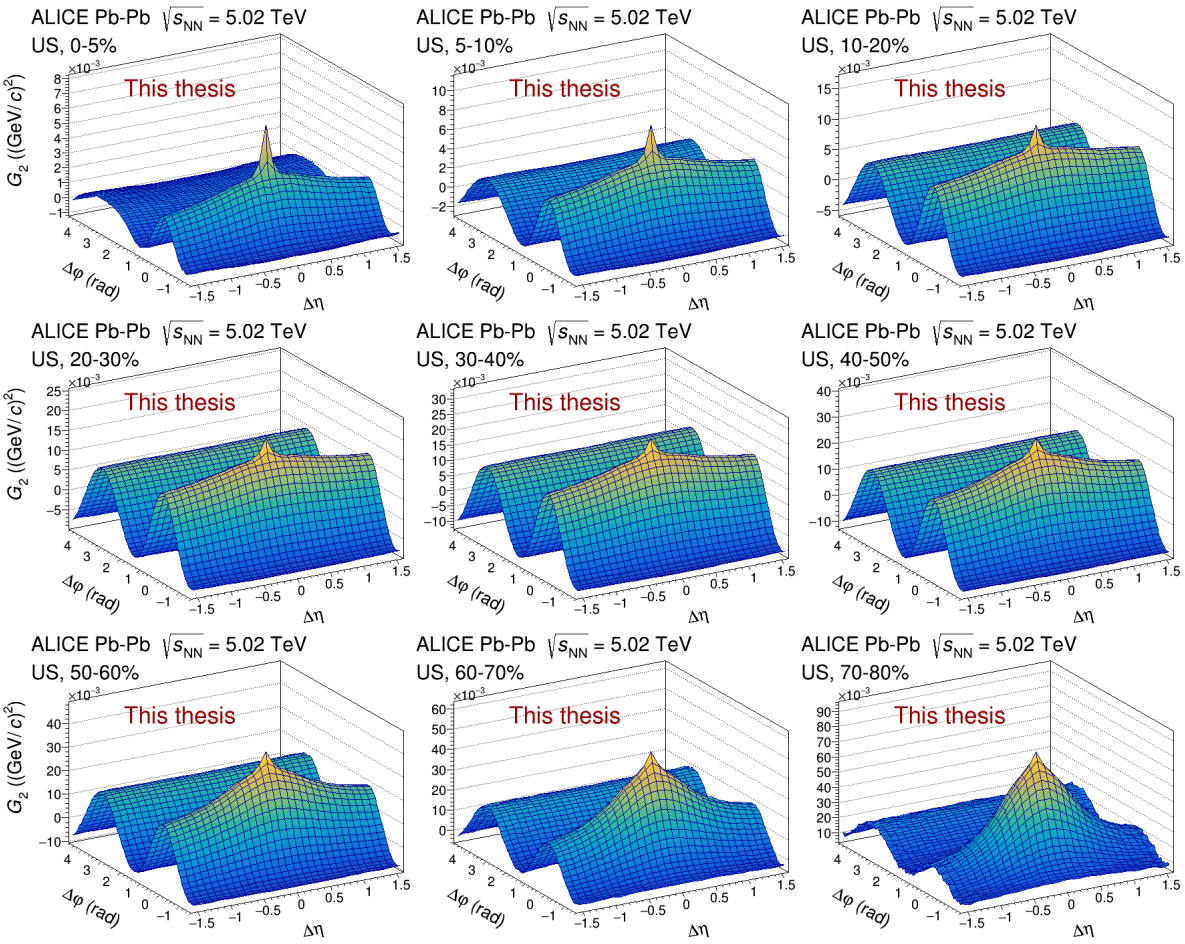

FIGURE C.15: Unlike sign (US) two-particle transverse momentum correlation in Pb–Pb collisions at $\sqrt{s_{\mathrm{NN}}}$ = 5.02 TeV as measured by ALICE.

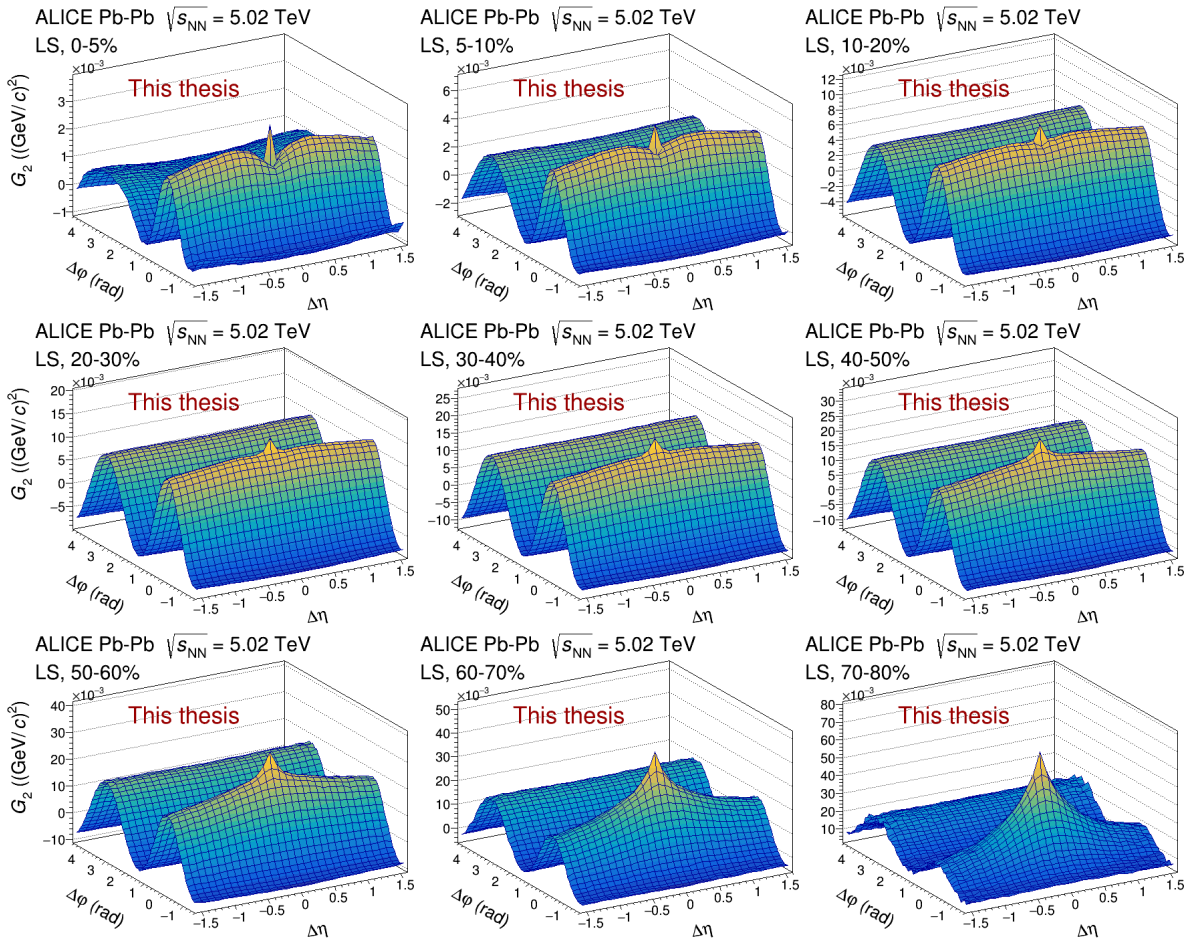

FIGURE C.16: Like sign (LS) two-particle transverse momentum correlation in Pb–Pb collisions at $\sqrt{s_{NN}}$ = 5.02 TeV as measured by ALICE.

C.2.2 Longitudinal projections

Figures C.17, C.18, C.19, and C.20 show the longitudinal projection of two-particle transverse momentum correlation G_2 for the CI, CD, US, and LS track combinations, respectively.

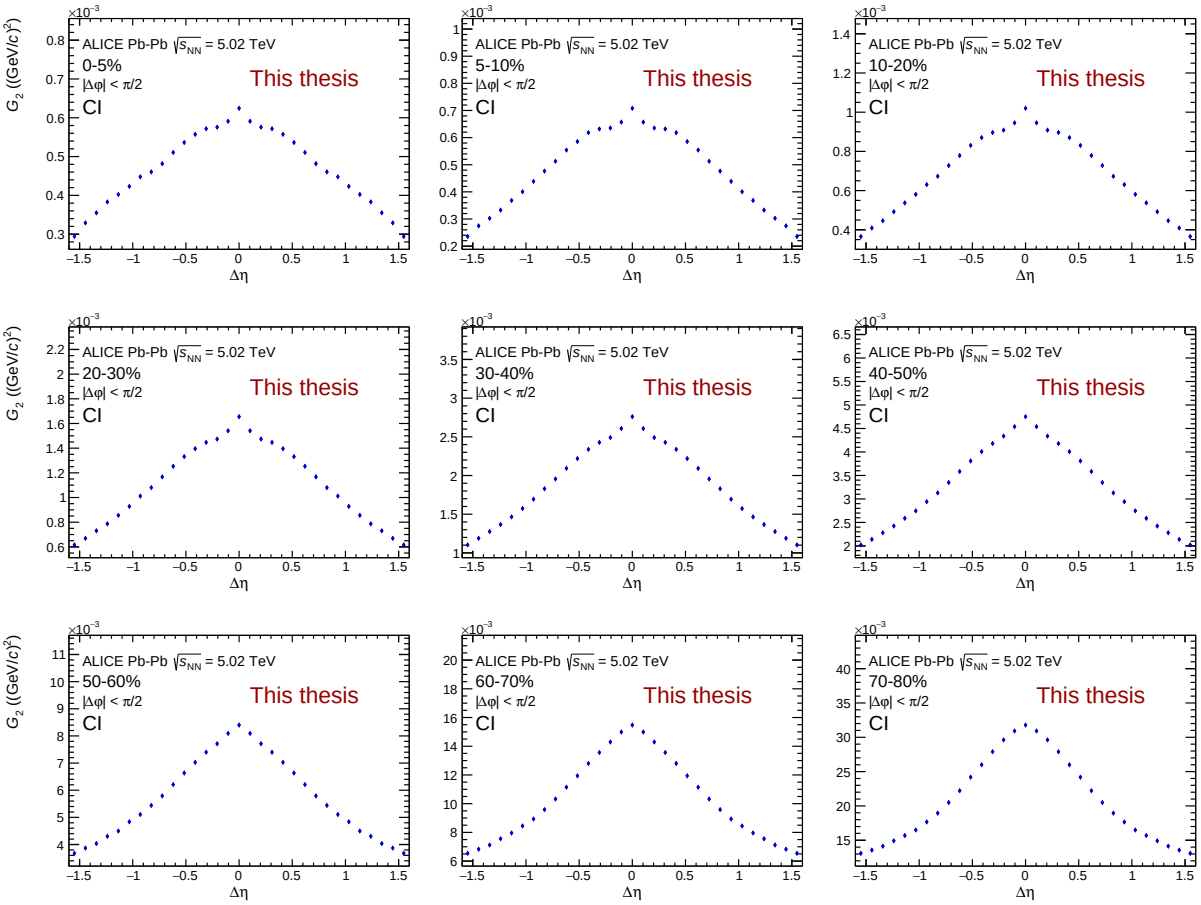

FIGURE C.17: Longitudinal projection of the charge independent (CI) two-particle transverse momentum correlation in Pb–Pb collisions at $\sqrt{s_{\mathrm{NN}}}$ = 5.02 TeV as measured by ALICE.

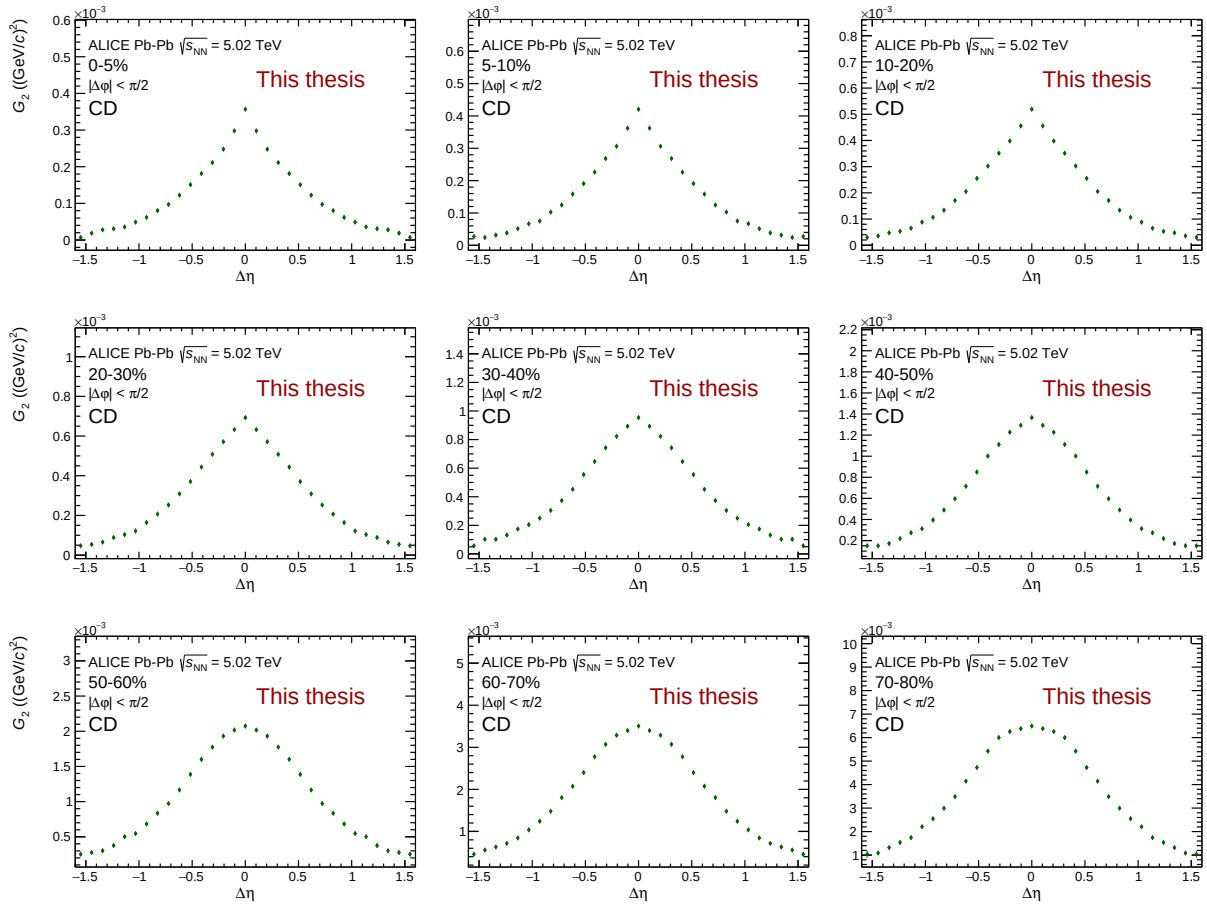

FIGURE C.18: Longitudinal projection of the charge dependent (CD) two-particle transverse momentum correlation in Pb–Pb collisions at $\sqrt{s_{\mathrm{NN}}}$ = 5.02 TeV as measured by ALICE.

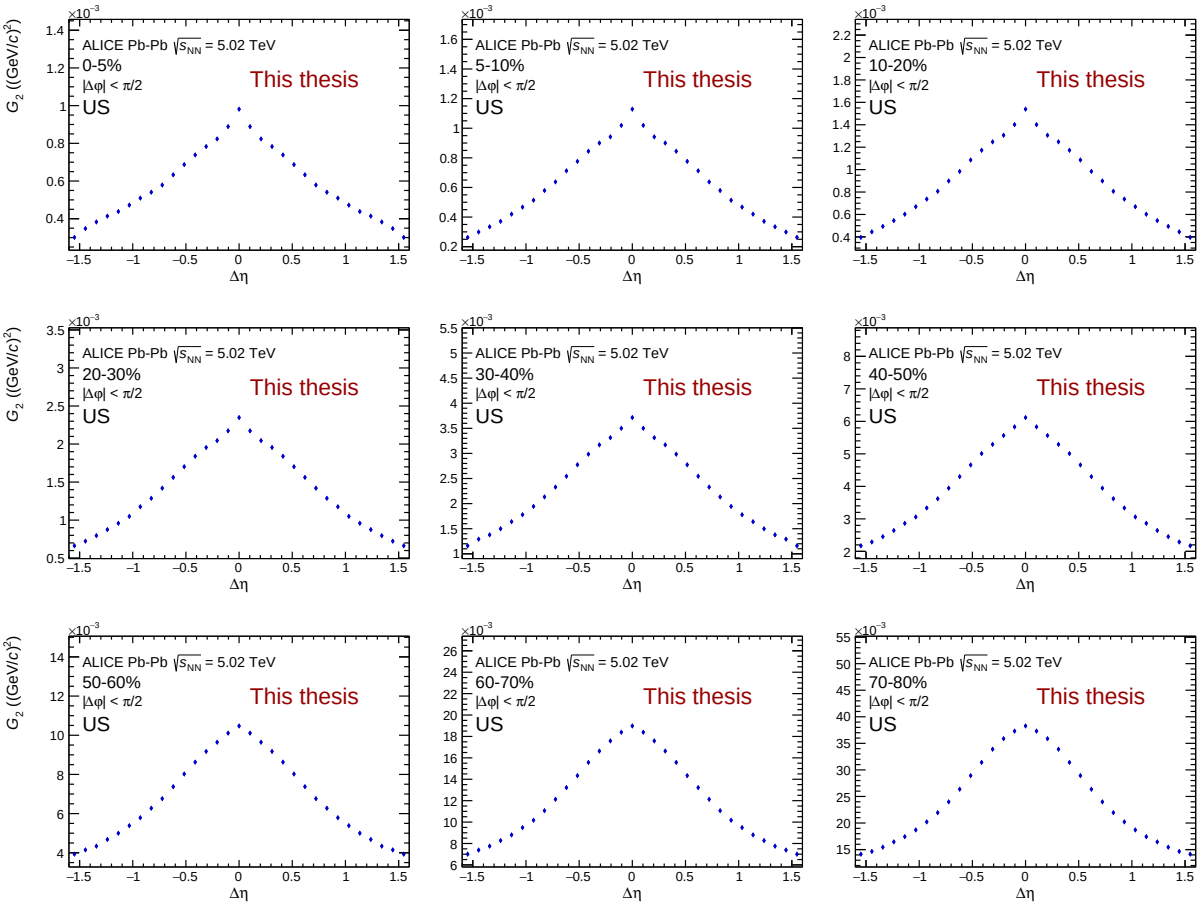

FIGURE C.19: Longitudinal projection of the unlike sign (US) two-particle transverse momentum correlation in Pb–Pb collisions at $\sqrt{s_{\mathrm{NN}}}$ = 5.02 TeV as measured by ALICE.

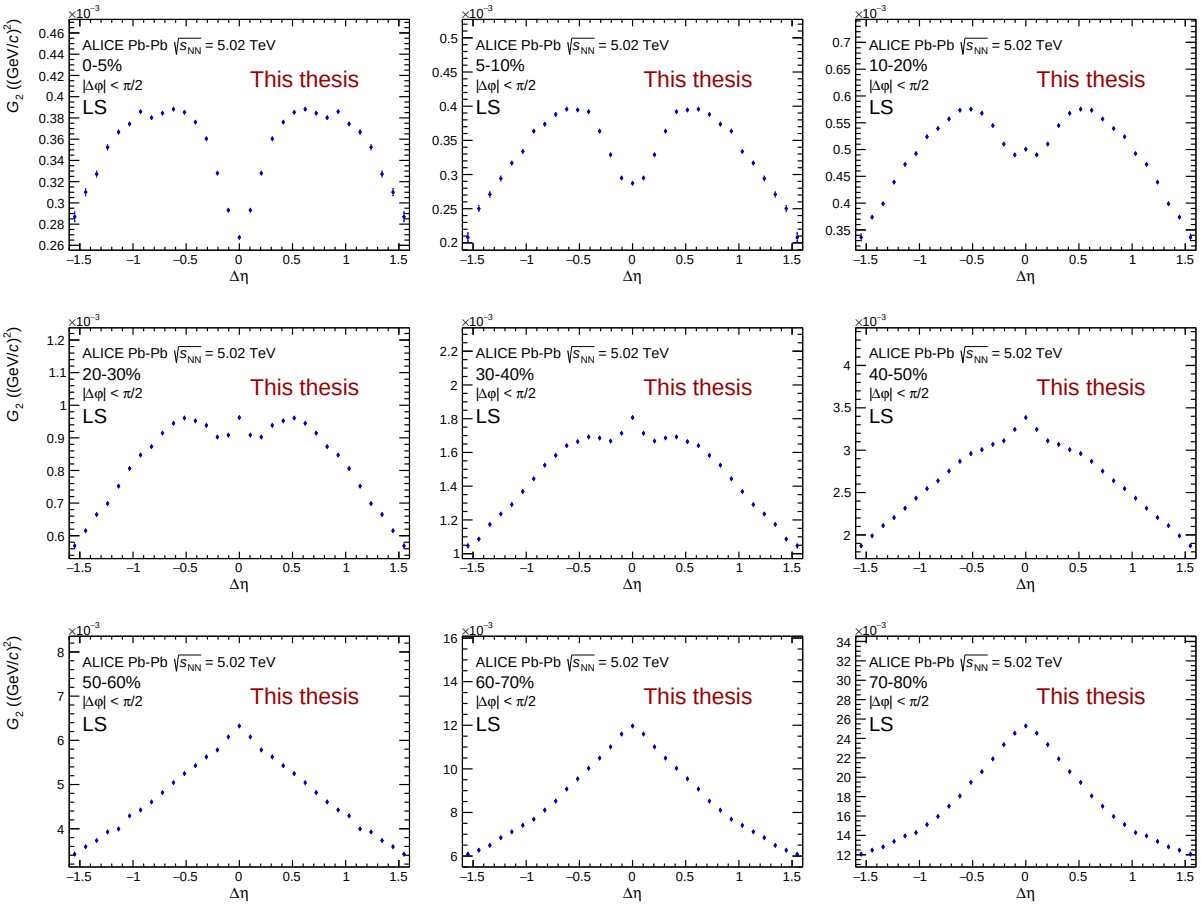

FIGURE C.20: Longitudinal projection of the like sign (LS) two-particle transverse momentum correlation in Pb–Pb collisions at $\sqrt{s_{\mathrm{NN}}}$ = 5.02 TeV as measured by ALICE.

C.2.3 Azimuthal projections

Figures C.21, C.22, C.23, and C.24 show the azimuthal projections of two-particle transverse momentum correlation G_2 for the CI, CD, US, and LS track combinations, respectively.

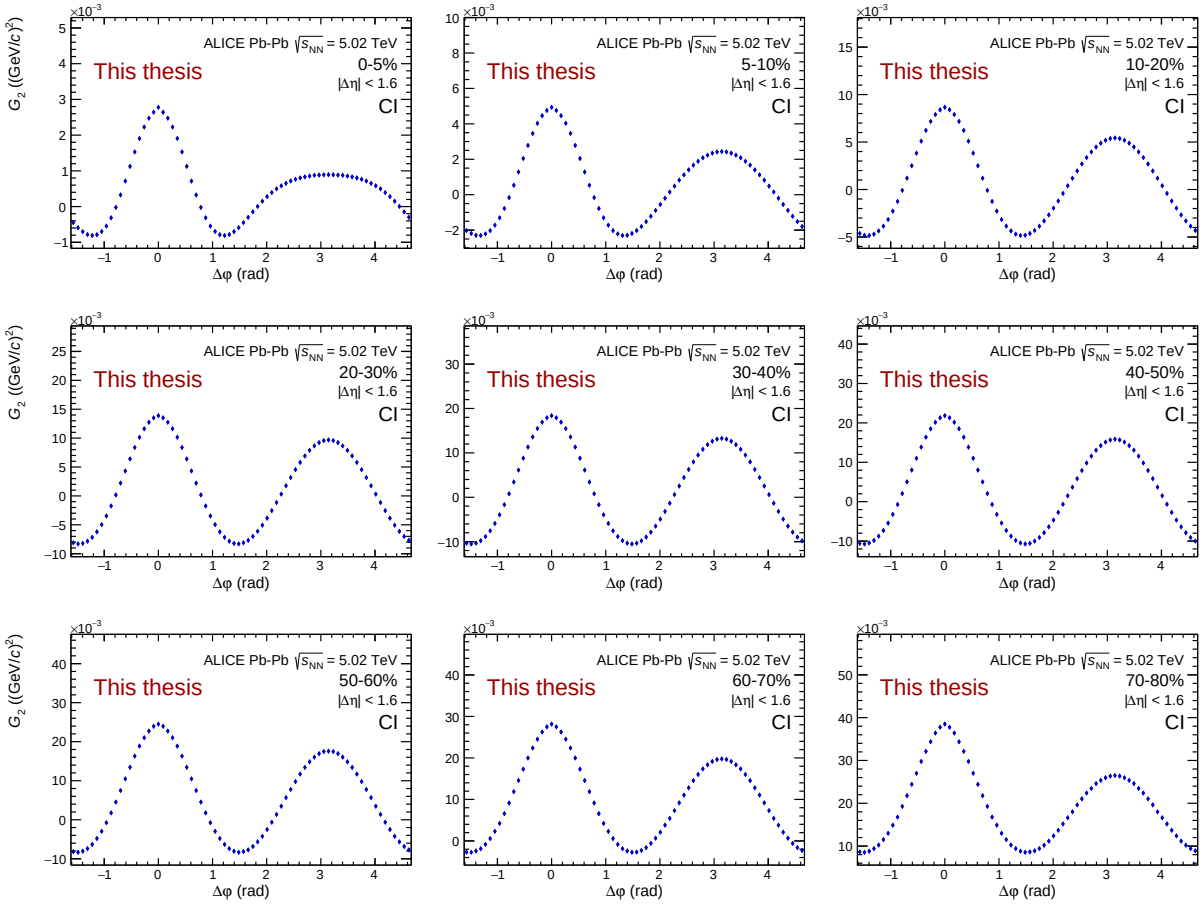

FIGURE C.21: Azimuthal projection of the charge independent (CI) two-particle transverse momentum correlation in Pb–Pb collisions at $\sqrt{s_{\rm NN}}$ = 5.02 TeV as measured by ALICE.

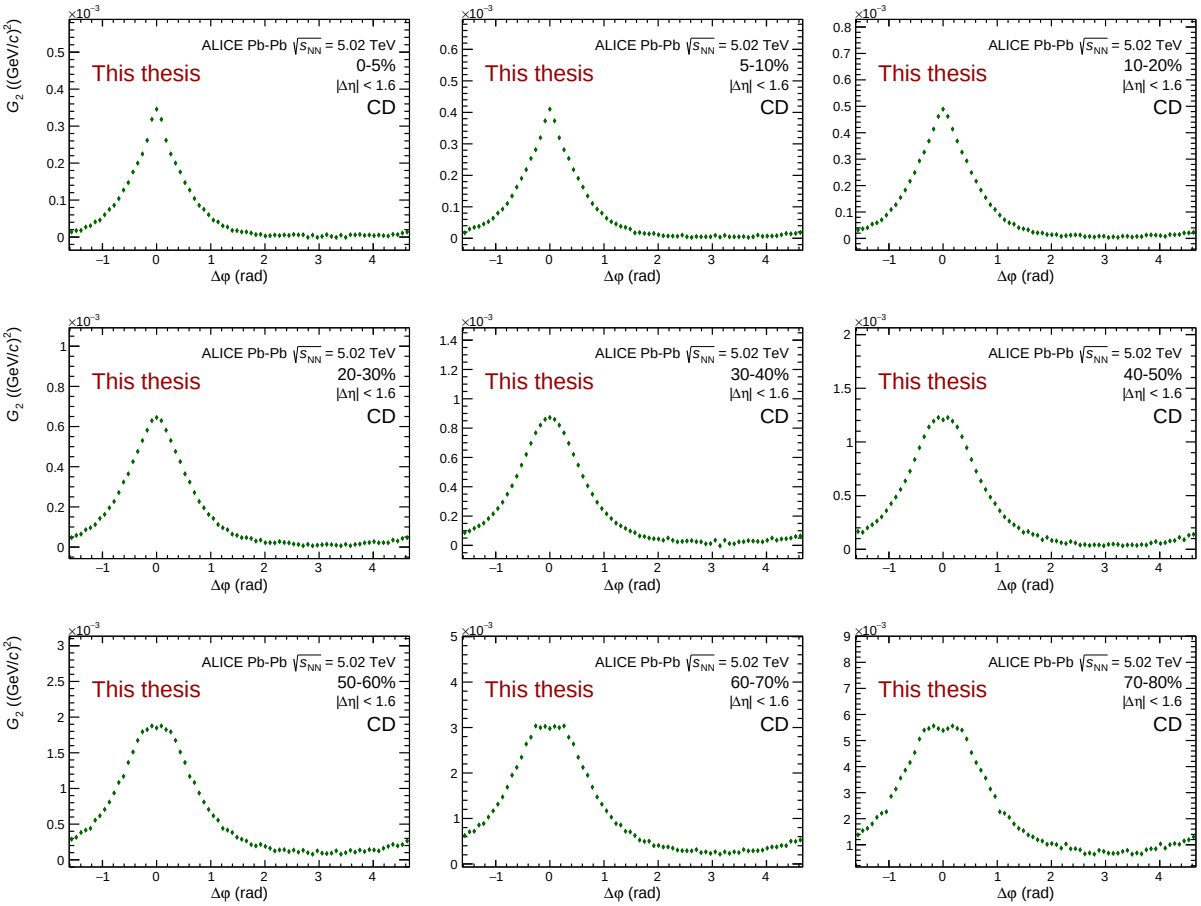

FIGURE C.22: Azimuthal projection of the charge dependent (CD) two-particle transverse momentum correlation in PbPb collisions at $\sqrt{s_{\mathrm{NN}}} = 5.02$ TeV as measured by ALICE.

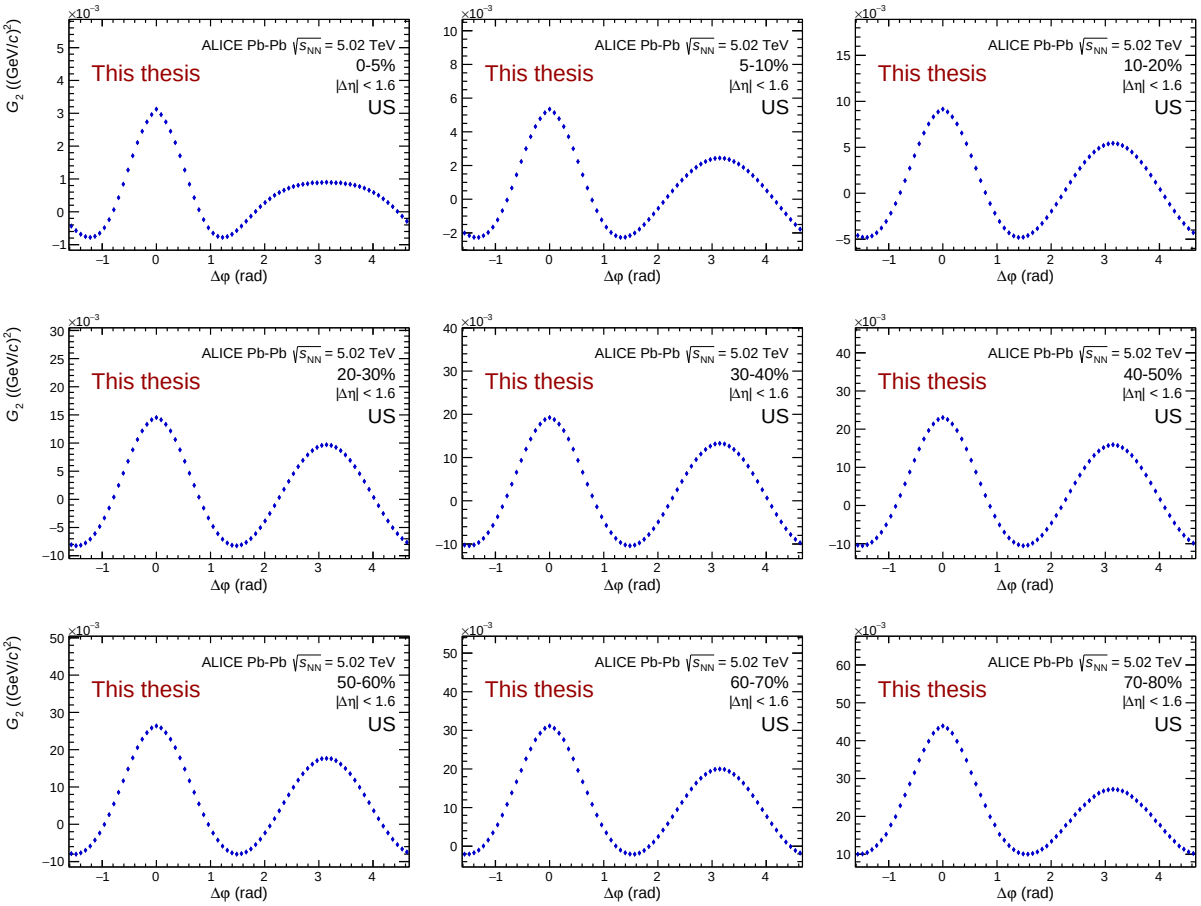

FIGURE C.23: Azimuthal projection of the unlike sign (US) two-particle transverse momentum correlation in Pb–Pb collisions at $\sqrt{s_{\mathrm{NN}}}$ = 5.02 TeV as measured by ALICE.

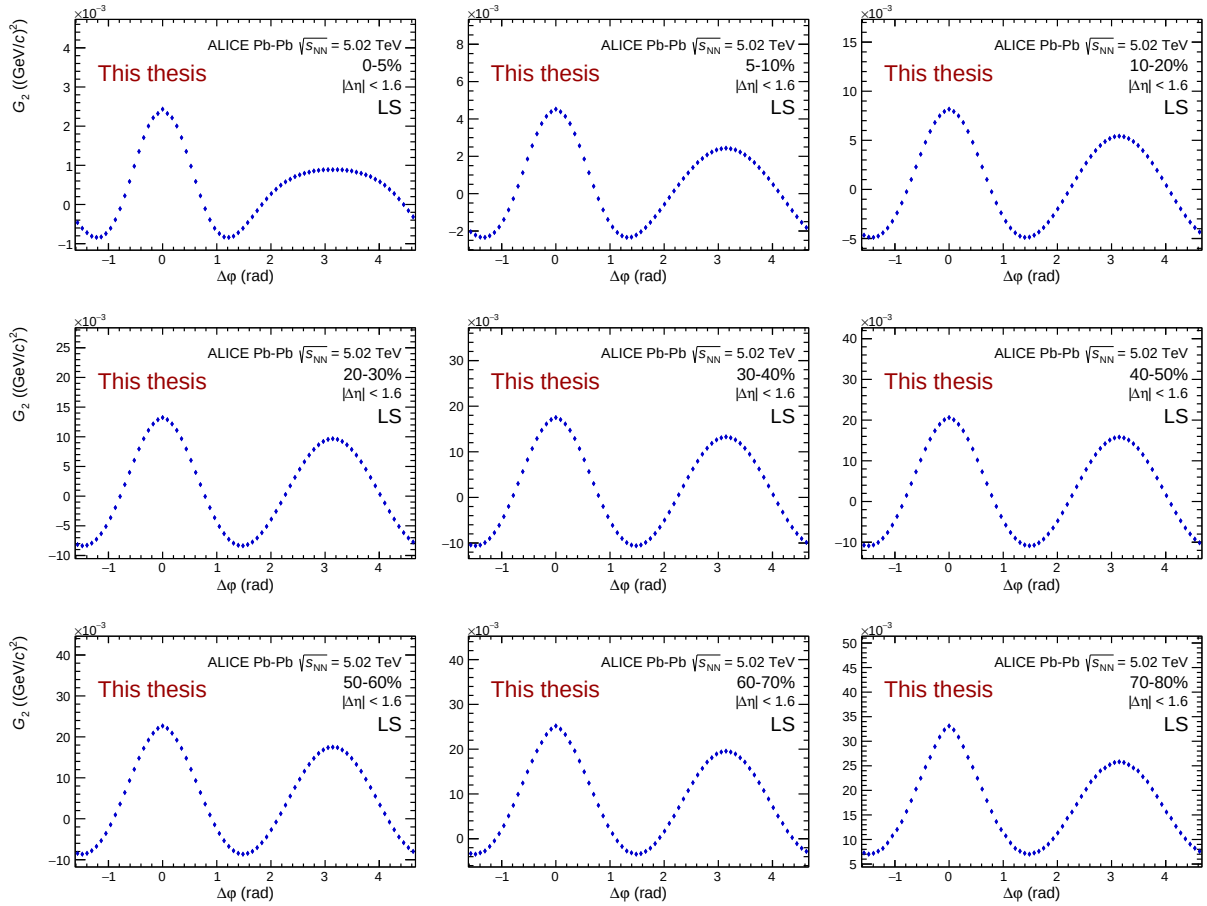

FIGURE C.24: Azimuthal projection of the like sign (LS) two-particle transverse momentum correlation in PbPb collisions at $\sqrt{s_{\mathrm{NN}}}$ = 5.02 TeV as measured by ALICE.

C.3 p–Pb at $\sqrt{s_{\mathrm{NN}}}$ = 5.02 TeV results

C.3.1 Two-particle transverse momentum correlations

Figures C.25, C.26, C.27, and C.28 show the two-particle transverse momentum correlation G_2 for the CI, CD, US and LS track combinations, respectively.

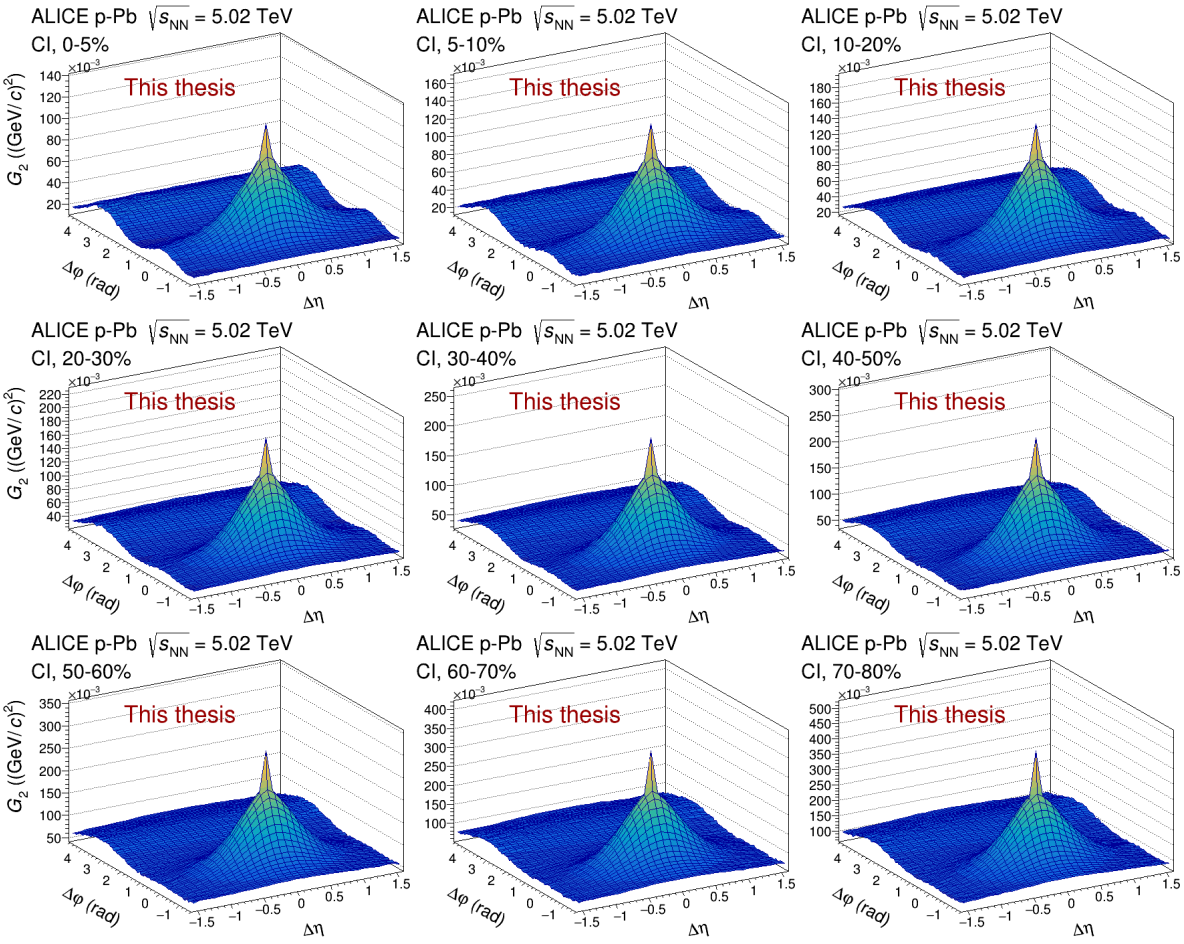

FIGURE C.25: Charge independent (CI) two-particle transverse momentum correlation in p–Pb collisions at $\sqrt{s_{\mathrm{NN}}}$ = 5.02 TeV as measured by ALICE.

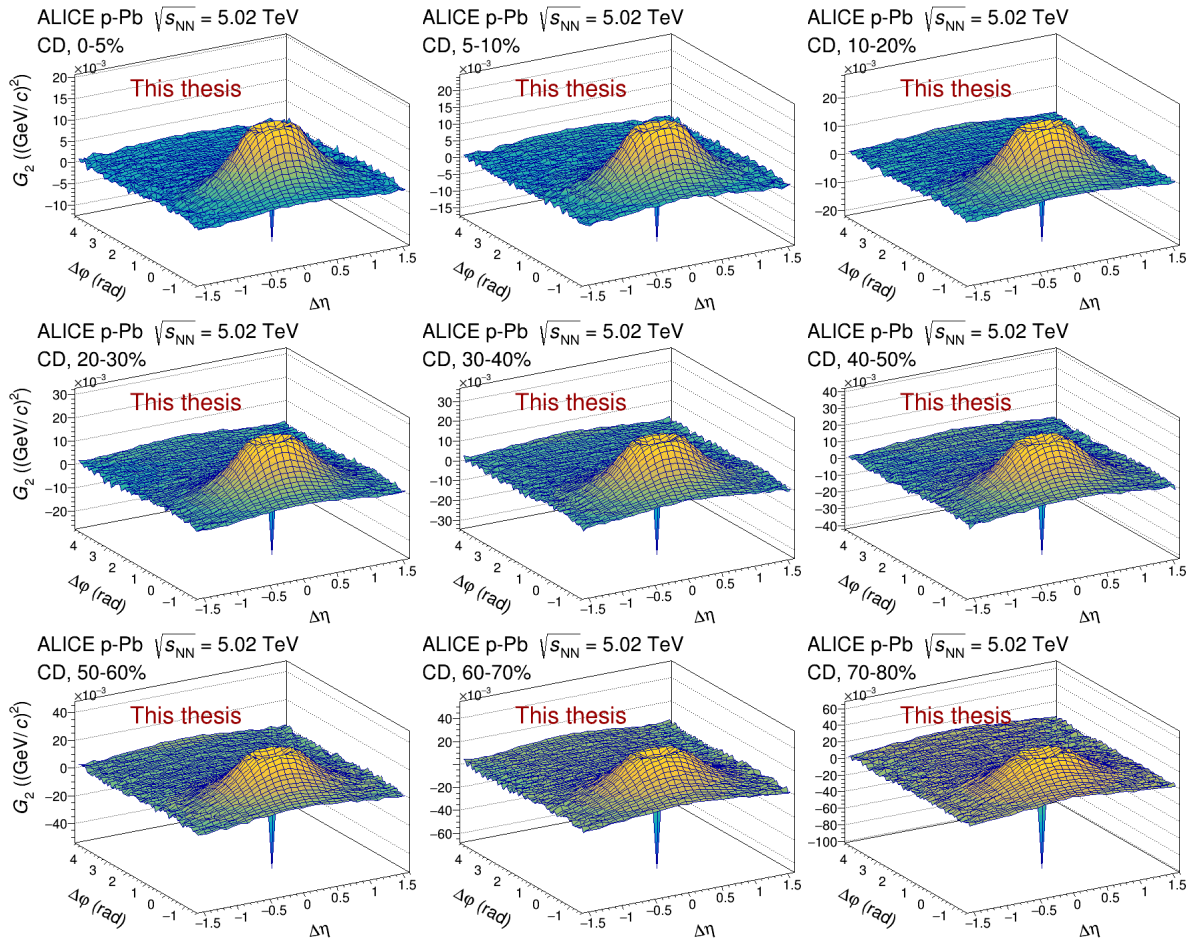

FIGURE C.26: Charge dependent (CD) two-particle transverse momentum correlation in p–Pb collisions at $\sqrt{s_{NN}}$ = 5.02 TeV as measured by ALICE.

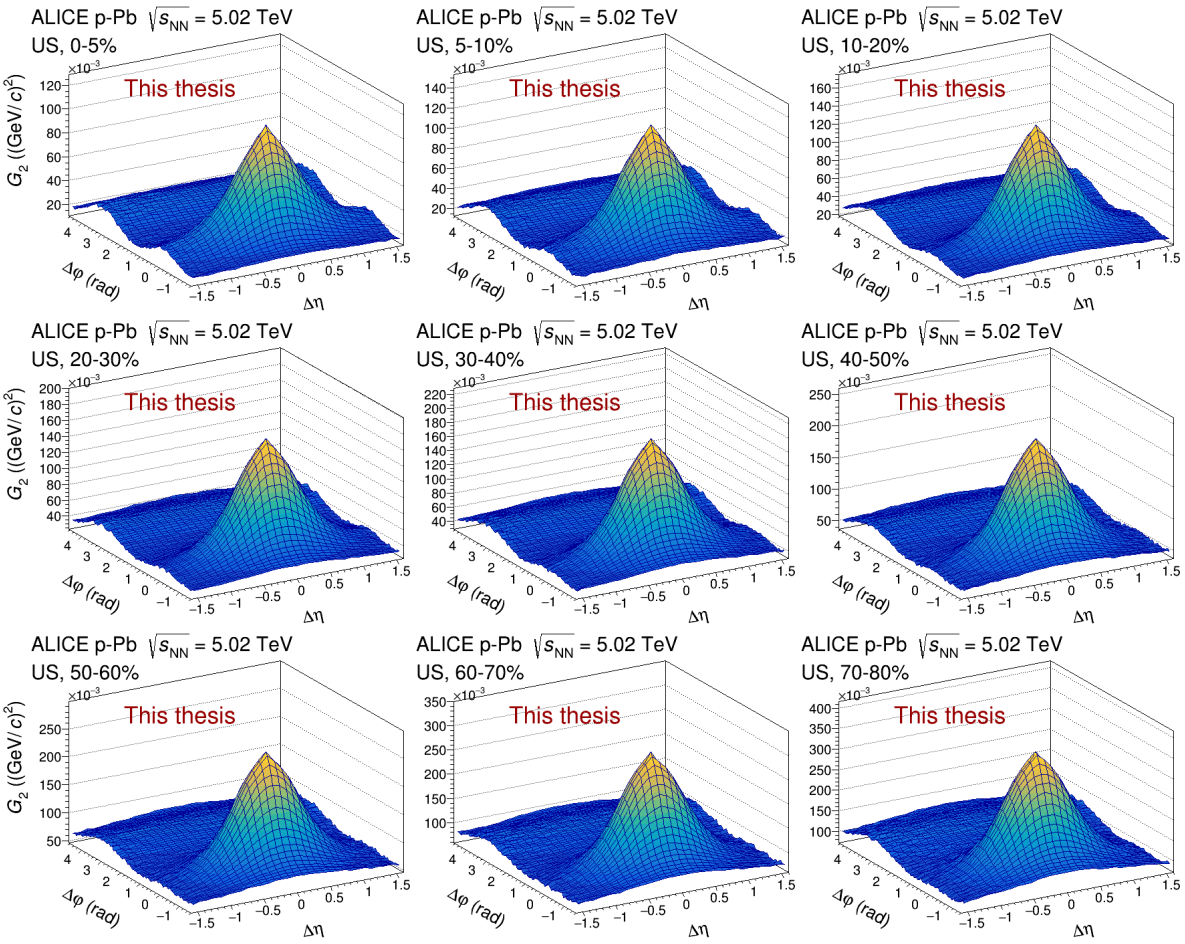

FIGURE C.27: Unlike sign (US) two-particle transverse momentum correlation in p–Pb collisions at $\sqrt{s_{\mathrm{NN}}}$ = 5.02 TeV as measured by ALICE.

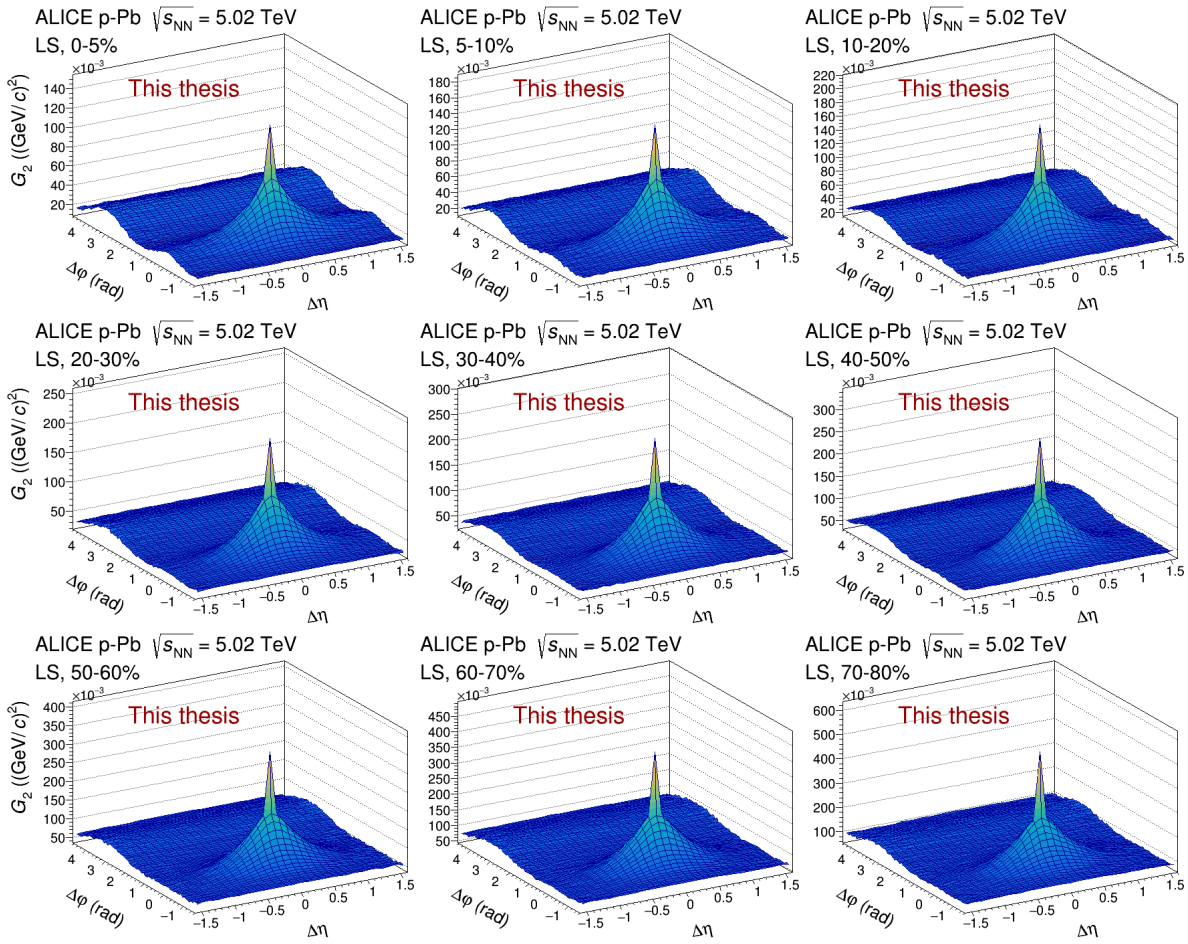

FIGURE C.28: Like sign (LS) two-particle transverse momentum correlation in p–Pb collisions at $\sqrt{s_{NN}}$ = 5.02 TeV as measured by ALICE.

C.3.2 Longitudinal projections

Figures C.29, C.30, C.31, and C.32 show the longitudinal projection of two-particle transverse momentum correlation G_2 for the CI, CD, US, and LS track combinations, respectively.

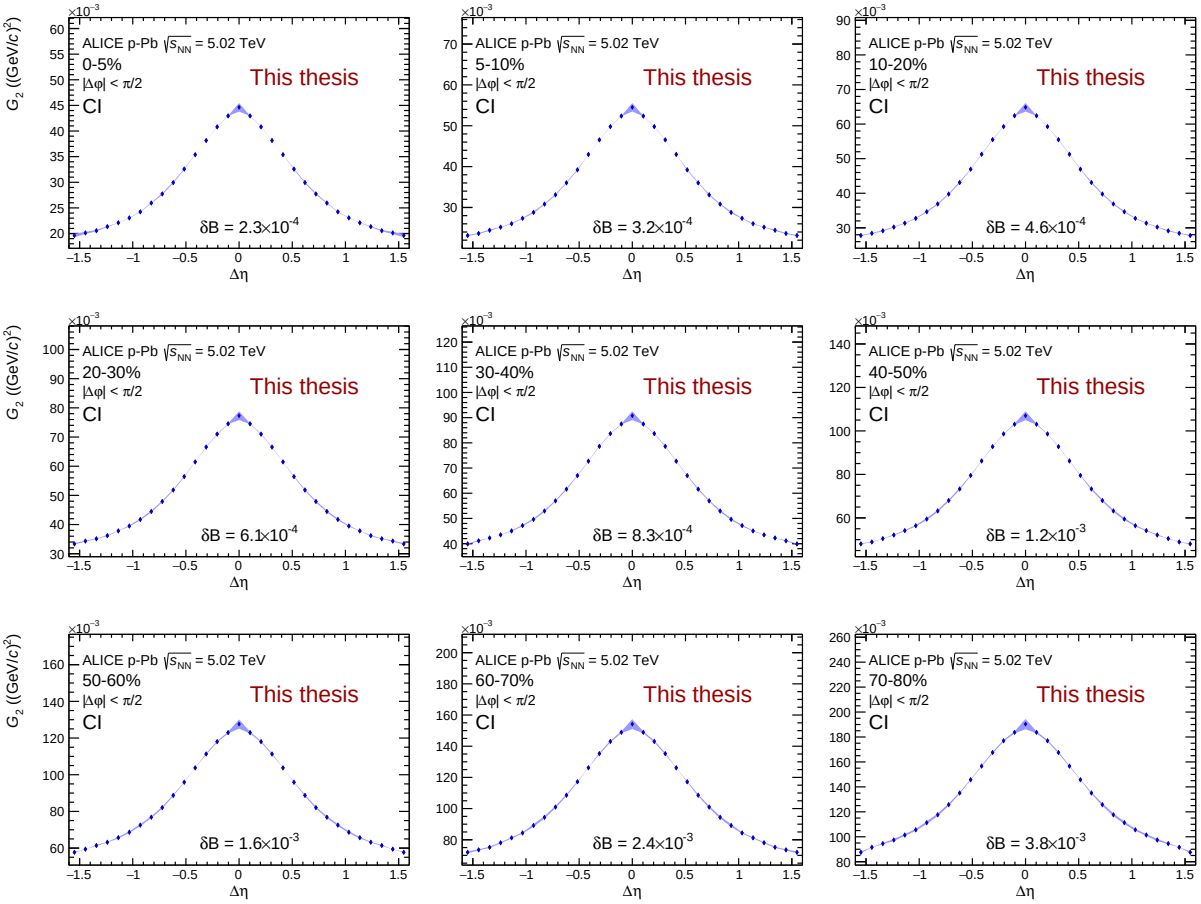

FIGURE C.29: Longitudinal projection of the charge independent (CI) two-particle transverse momentu correlation in p–Pb collisions at $\sqrt{s_{\mathrm{NN}}}$ = 5.02 TeV as measured by ALICE.

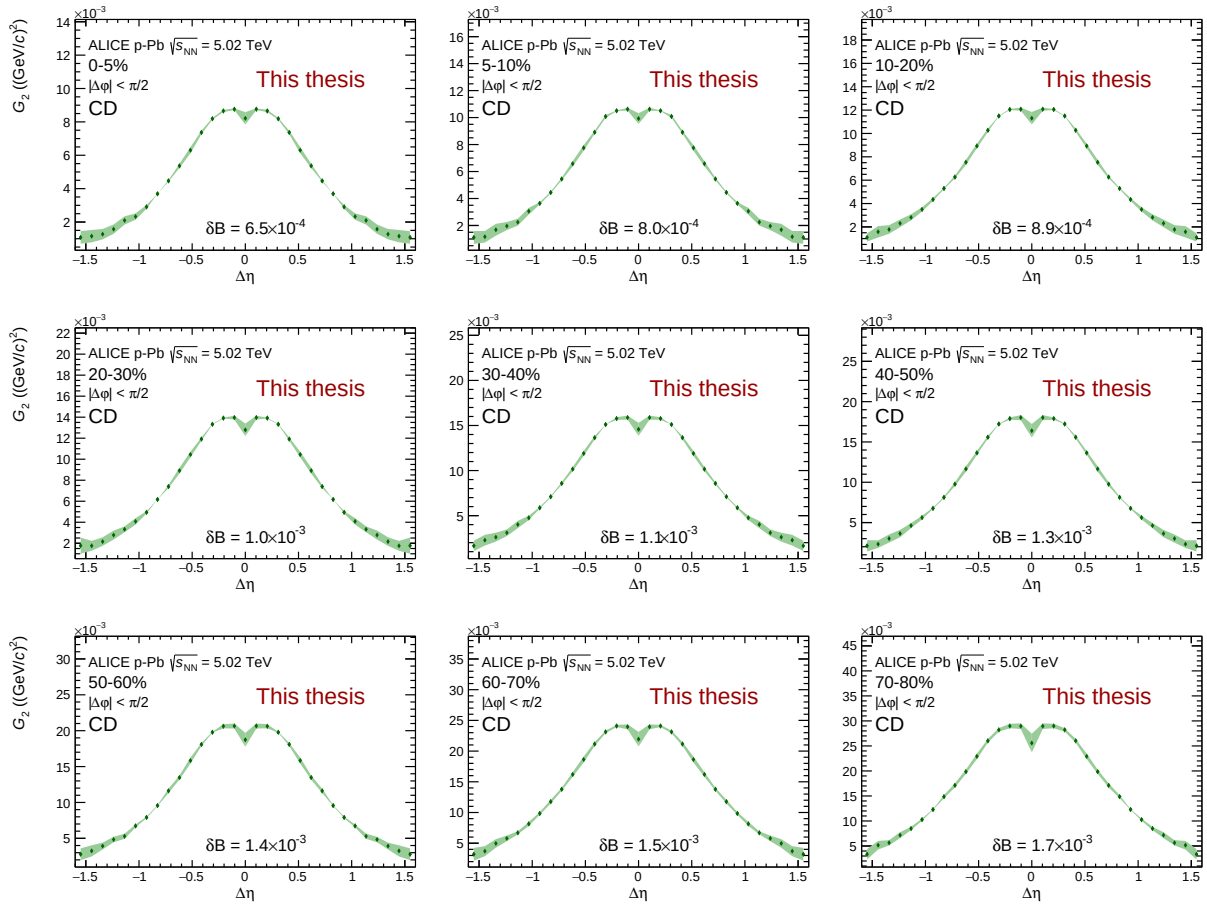

FIGURE C.30: Longitudinal projection of the charge dependent (CD) two-particle transverse momentum correlation in p–Pb collisions at $\sqrt{s_{\mathrm{NN}}}$ = 5.02 TeV as measured by ALICE.

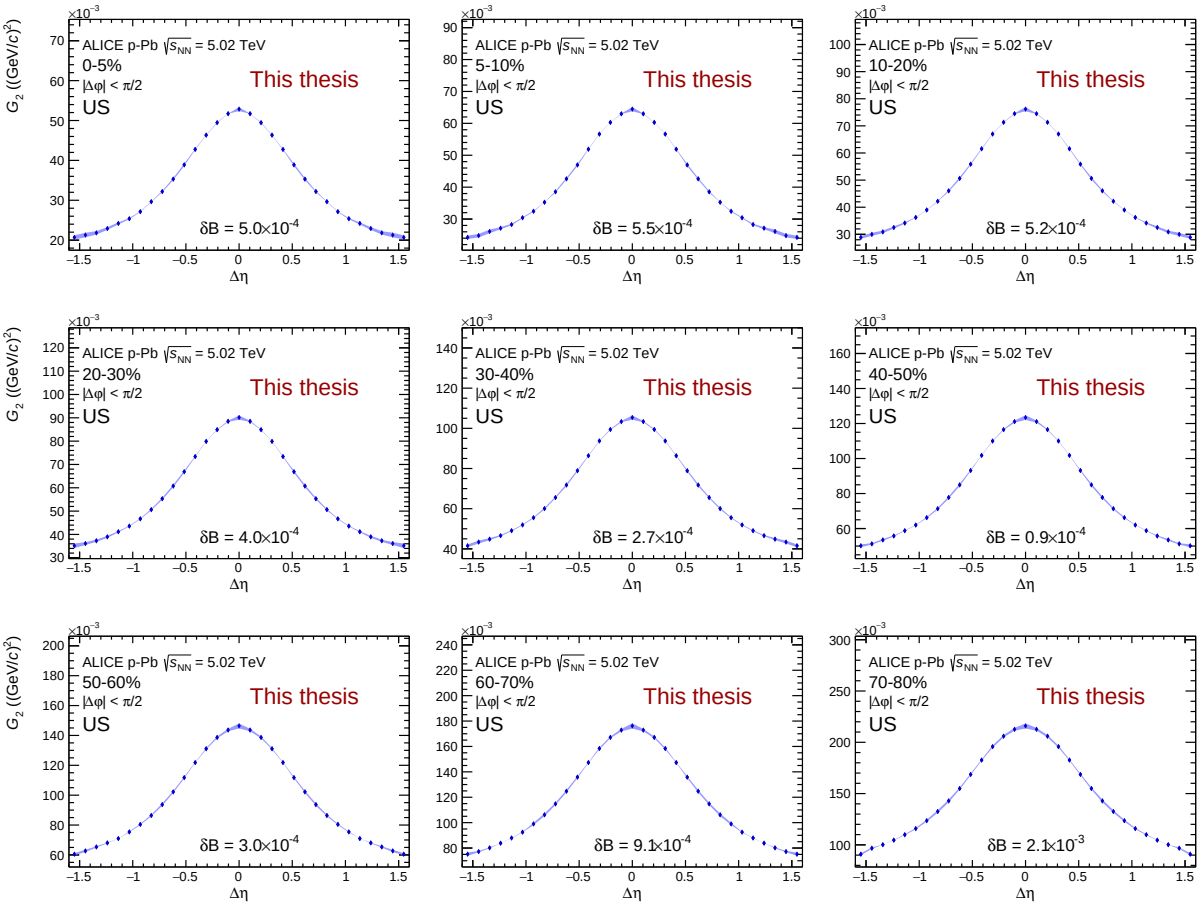

FIGURE C.31: Longitudinal projection of the unlike sign (US) two-particle transverse momentum correlation in p–Pb collisions at $\sqrt{s_{\mathrm{NN}}}$ = 5.02 TeV as measured by ALICE.

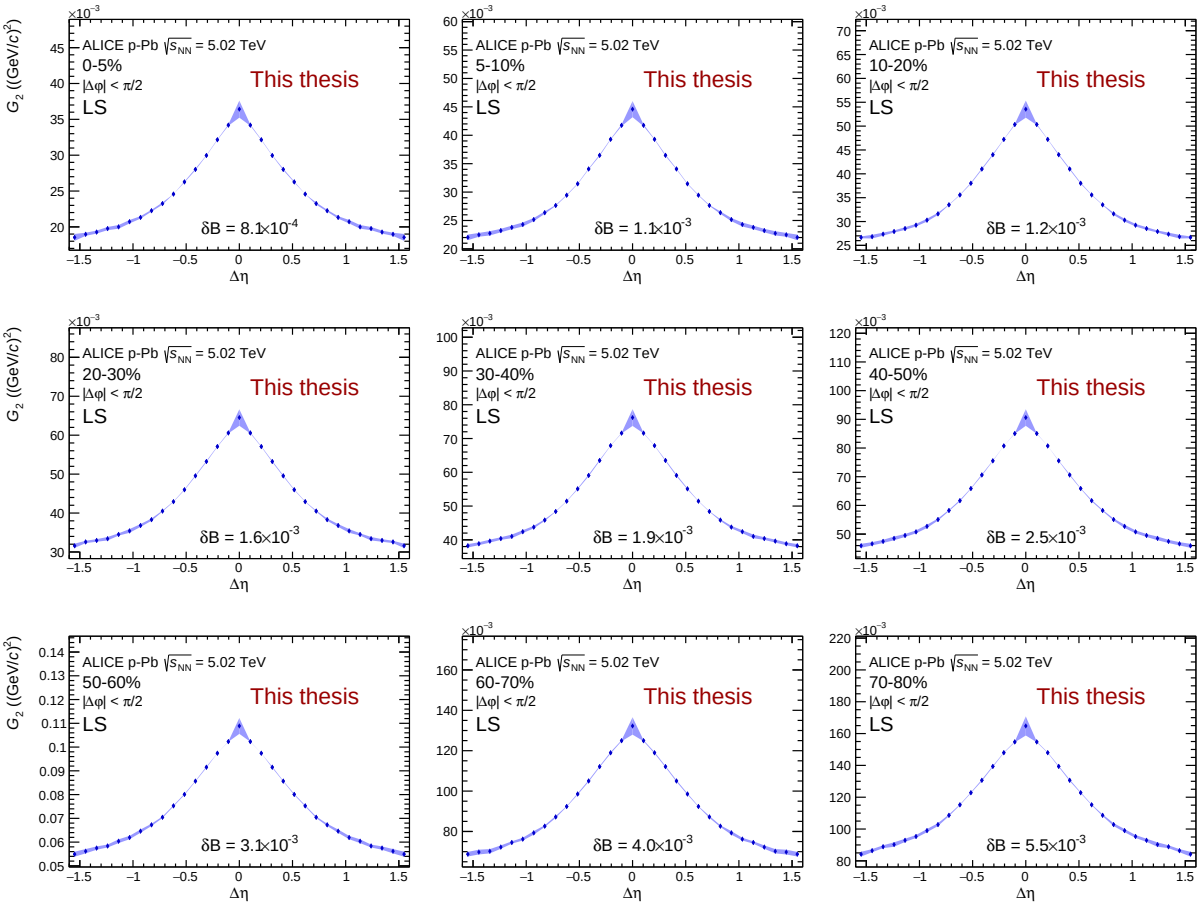

FIGURE C.32: Longitudinal projection of the like sign (LS) two-particle transverse momentum correlation in p–Pb collisions at $\sqrt{s_{\mathrm{NN}}}$ = 5.02 TeV as measured by ALICE.

C.3.3 Azimuthal projections

Figures C.33, C.34, C.35, and C.36 show the azimuthal projections of two-particle transverse momentum correlation G_2 for the CI, CD, US, and LS track combinations, respectively.

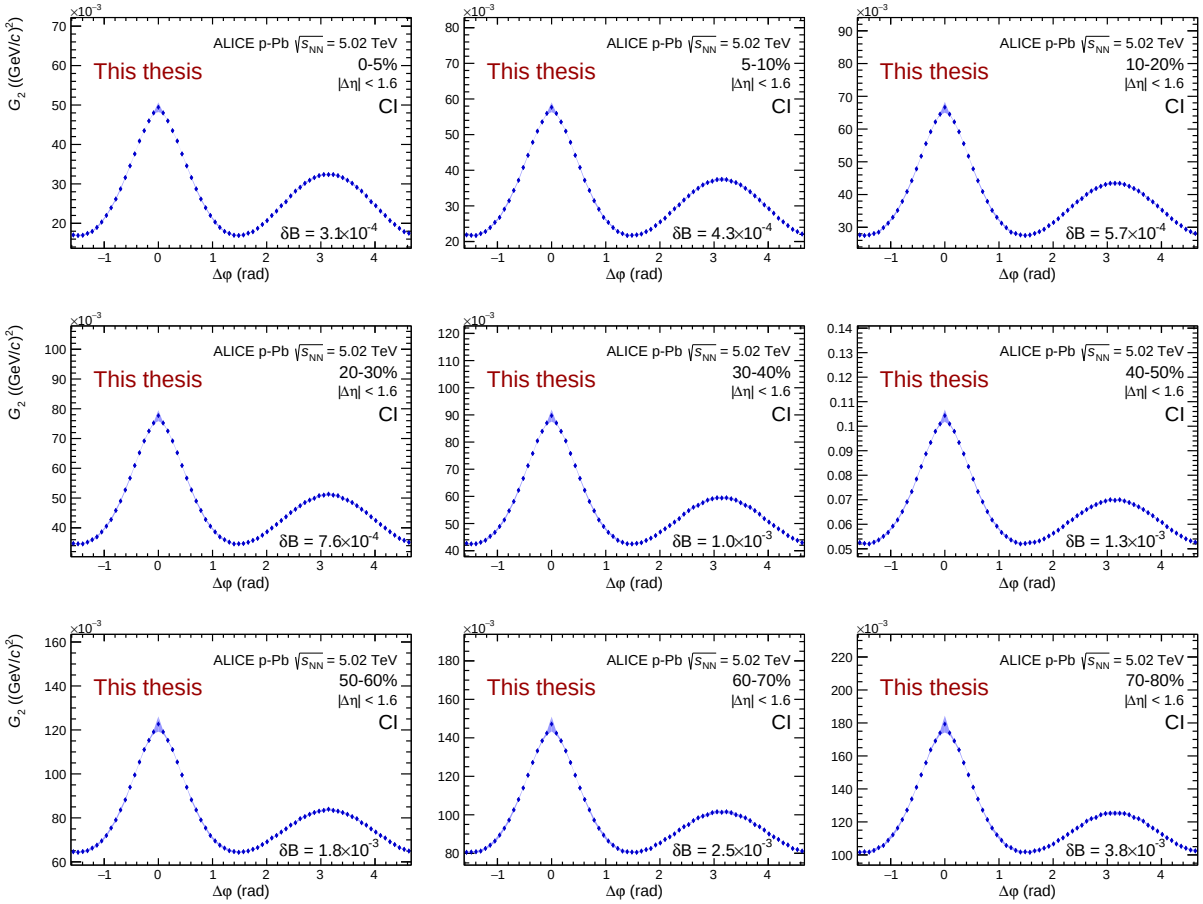

FIGURE C.33: Azimuthal projection of the charge independent (CI) two-particle transverse momentum correlation in p–Pb collisions at $\sqrt{s_{\mathrm{NN}}}$ = 5.02 TeV as measured by ALICE.

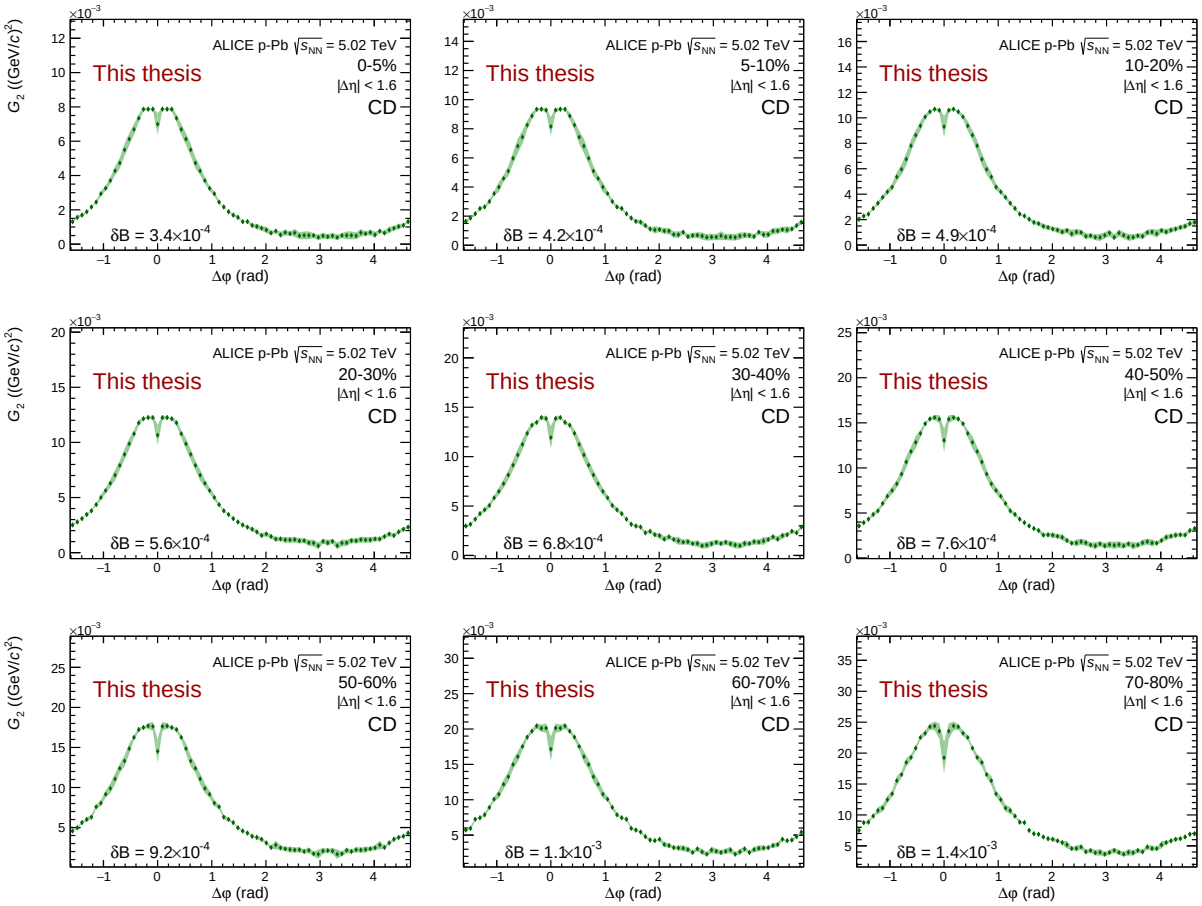

FIGURE C.34: Azimuthal projection of the charge dependent (CD) two-particle transverse momentum correlation in p–Pb collisions at $\sqrt{s_{\mathrm{NN}}} = 5.02$ TeV as measured by ALICE.

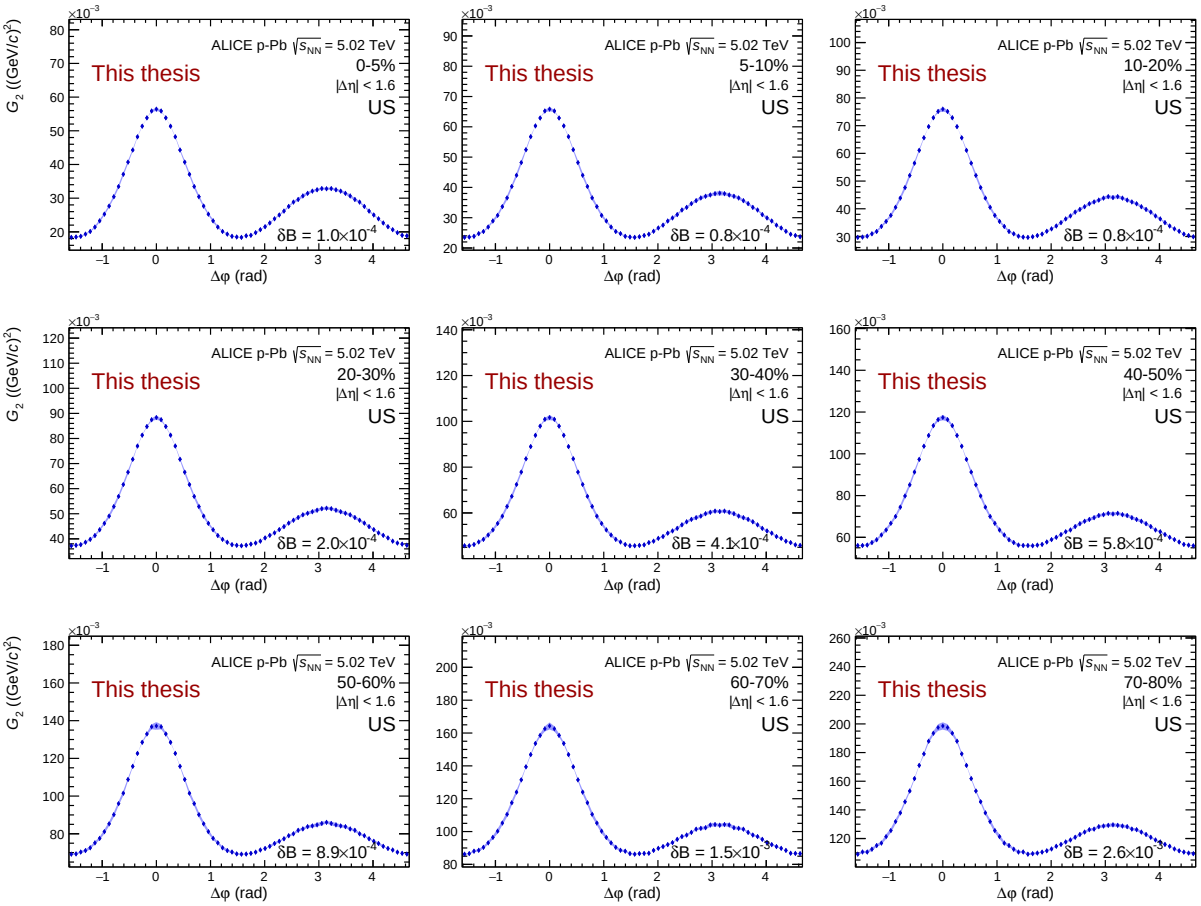

FIGURE C.35: Azimuthal projection of the unlike sign (US) two-particle transverse momentum correlation in p–Pb collisions at $\sqrt{s_{\mathrm{NN}}}$ = 5.02 TeV as measured by ALICE.

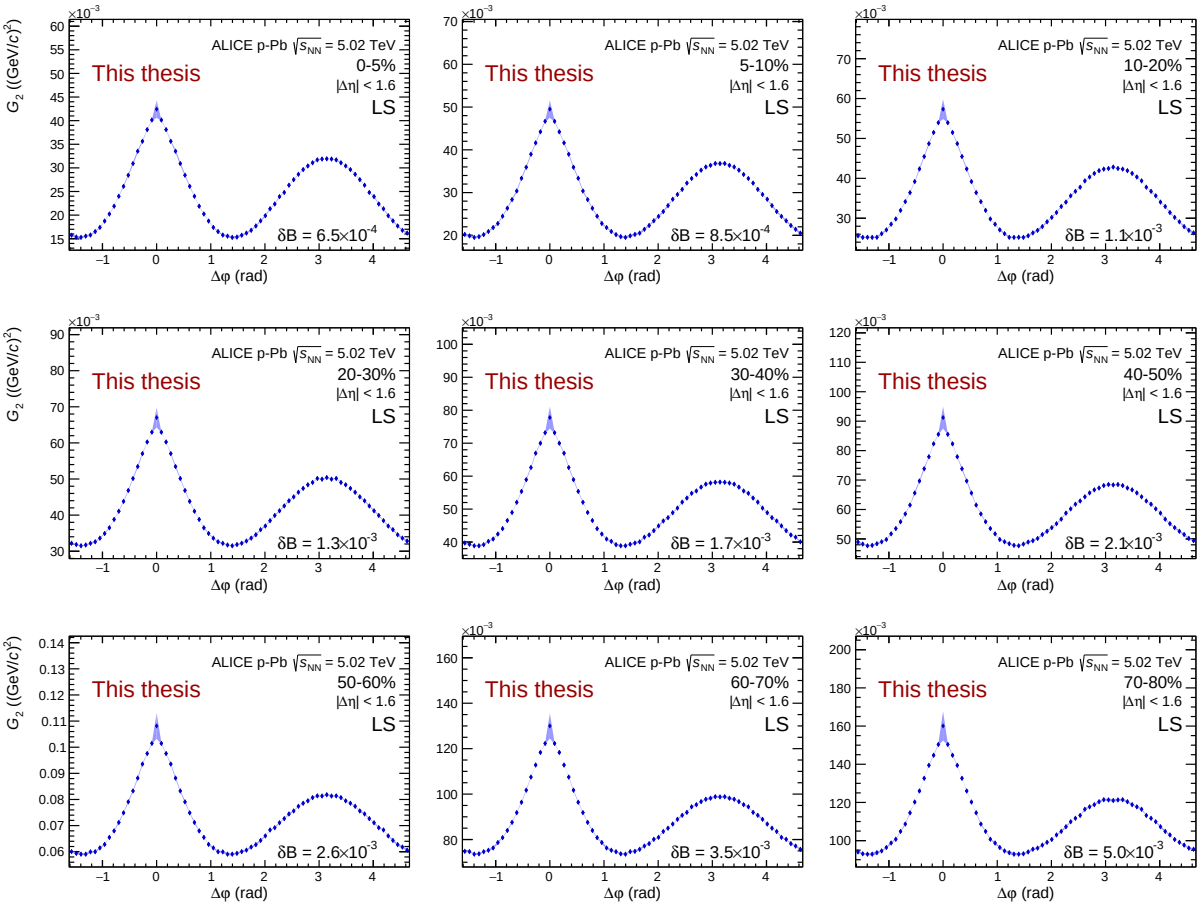

FIGURE C.36: Azimuthal projection of the like sign (LS) two-particle transverse momentum correlation in p–Pb collisions at $\sqrt{s_{\mathrm{NN}}}$ = 5.02 TeV as measured by ALICE.

C.4 pp at $\sqrt{s_{\mathrm{NN}}}$ = 7 TeV results

C.4.1 Two-particle transverse momentum correlations

Figures C.37, C.38, C.39, and C.40 show the two-particle transverse momentum correlation G_2 for the CI, CD, US and LS track combinations, respectively.

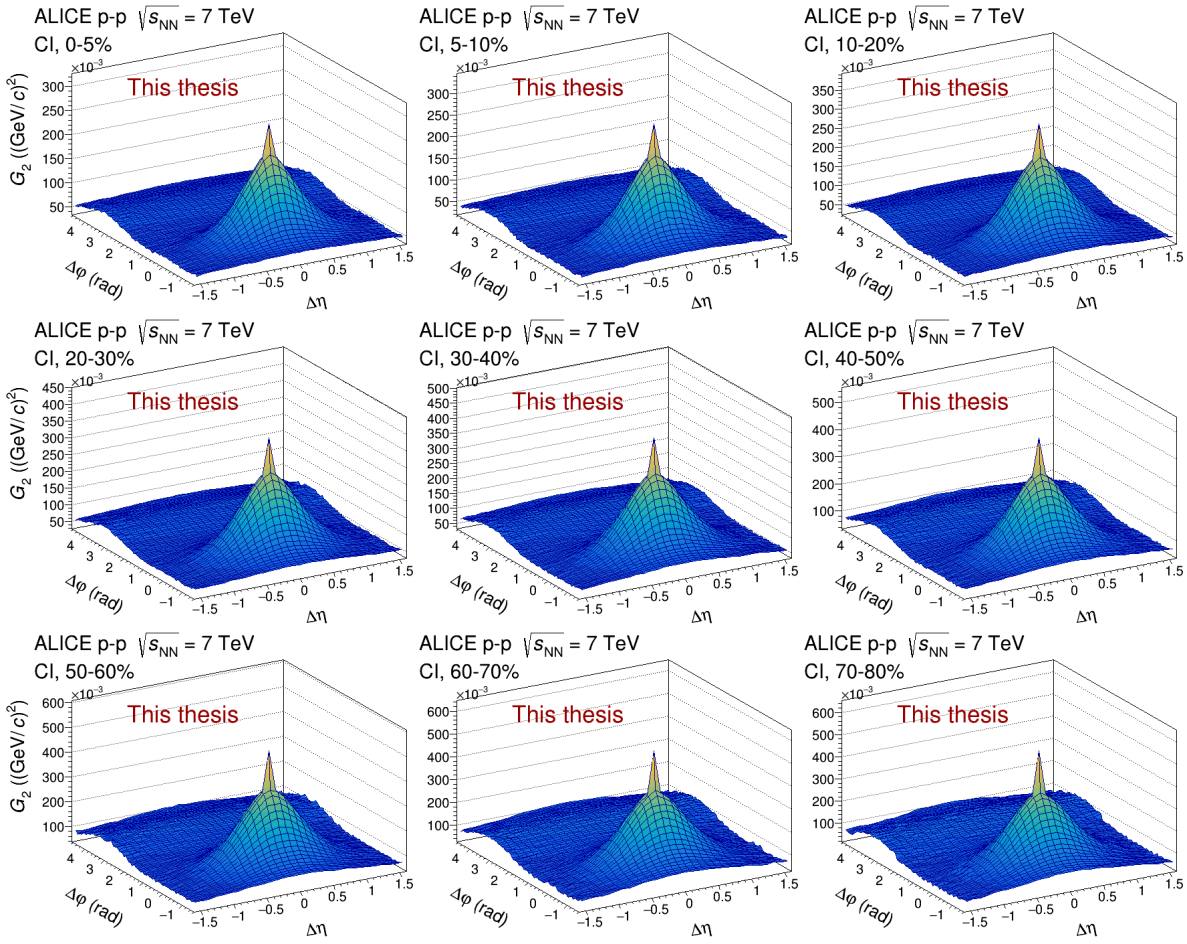

FIGURE C.37: Charge independent (CI) two-particle transverse momentum correlation in pp collisions at $\sqrt{s_{\mathrm{NN}}}$ = 7 TeV as measured by ALICE.

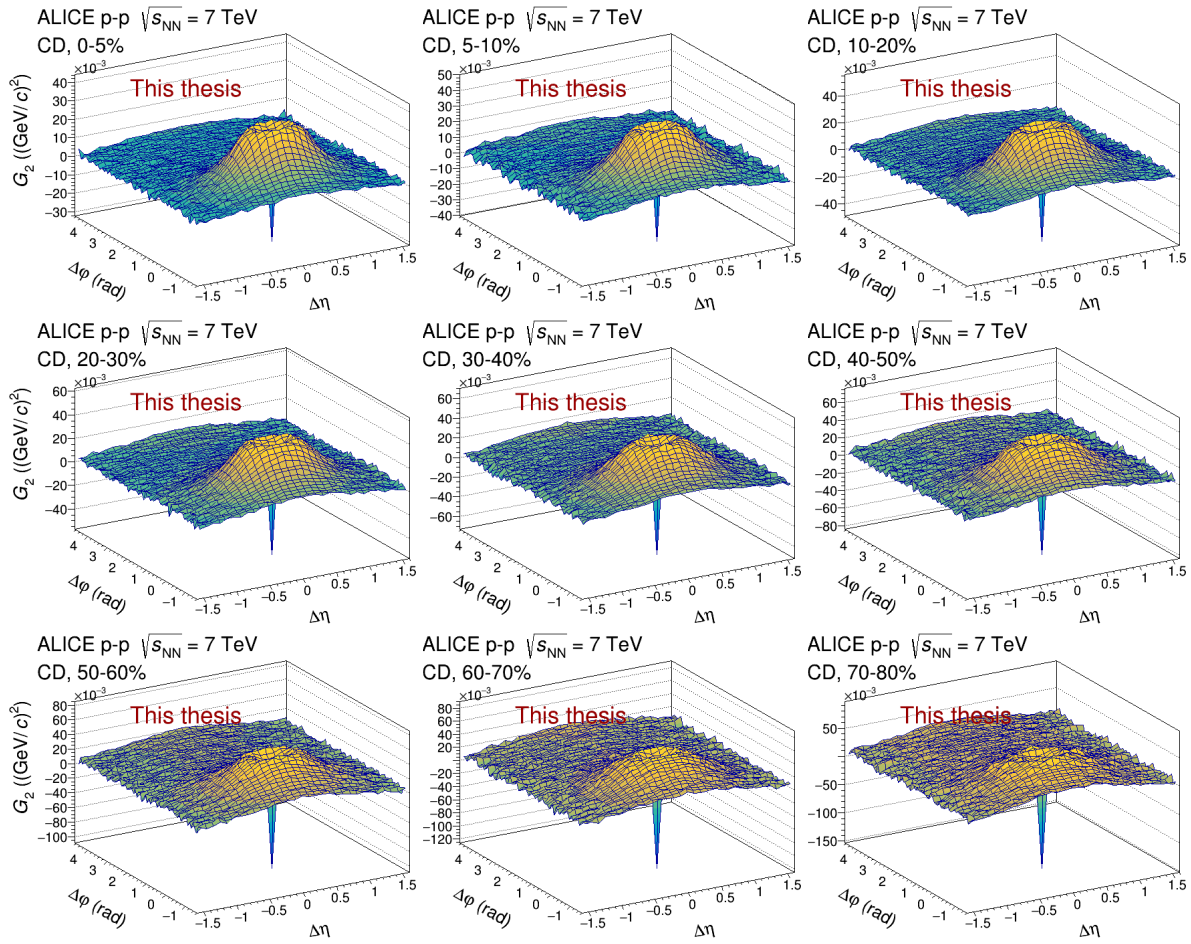

FIGURE C.38: Charge dependent (CD) two-particle transverse momentum correlation in pp collisions at $\sqrt{s_{NN}}$ = 7 TeV as measured by ALICE.

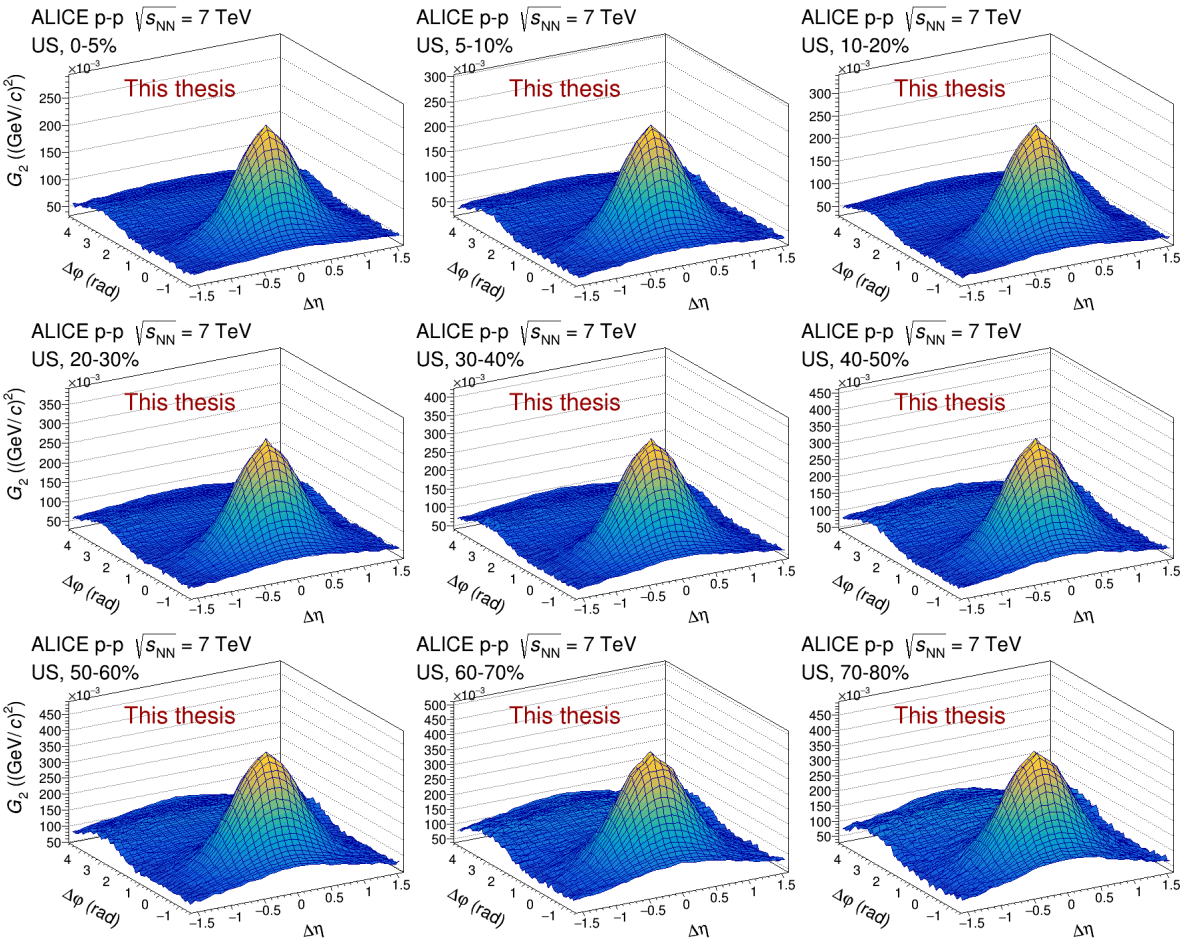

FIGURE C.39: Unlike sign (US) two-particle transverse momentum correlation in pp collisions at $\sqrt{s_{\mathrm{NN}}}$ = 7 TeV as measured by ALICE.

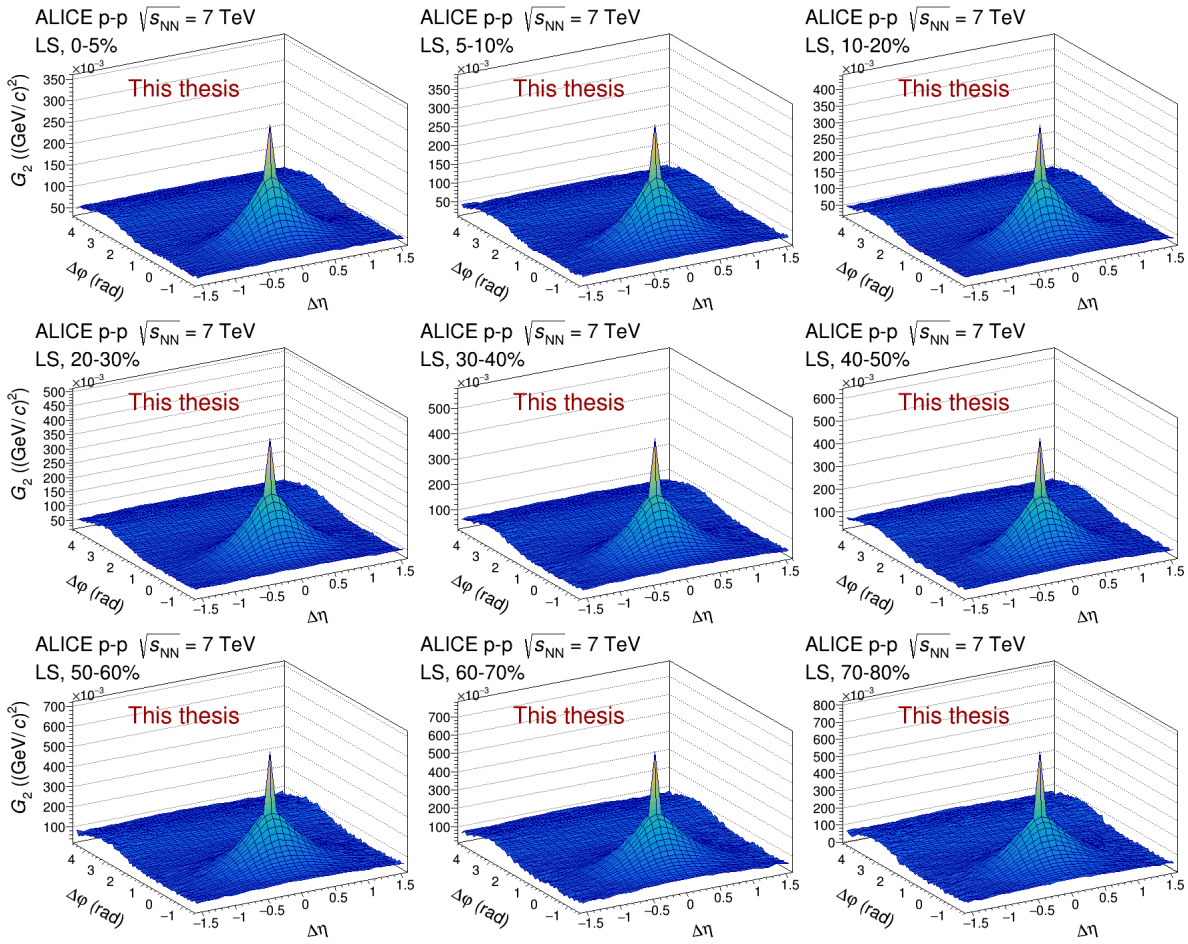

FIGURE C.40: Like sign (LS) two-particle transverse momentum correlation in pp collisions at $\sqrt{s_{NN}}$ = 7 TeV as measured by ALICE.

C.4.2 Longitudinal projections

Figures C.41, C.42, C.43, and C.44 show the longitudinal projection of two-particle transverse momentum correlation G_2 for the CI, CD, US, and LS track combinations, respectively.

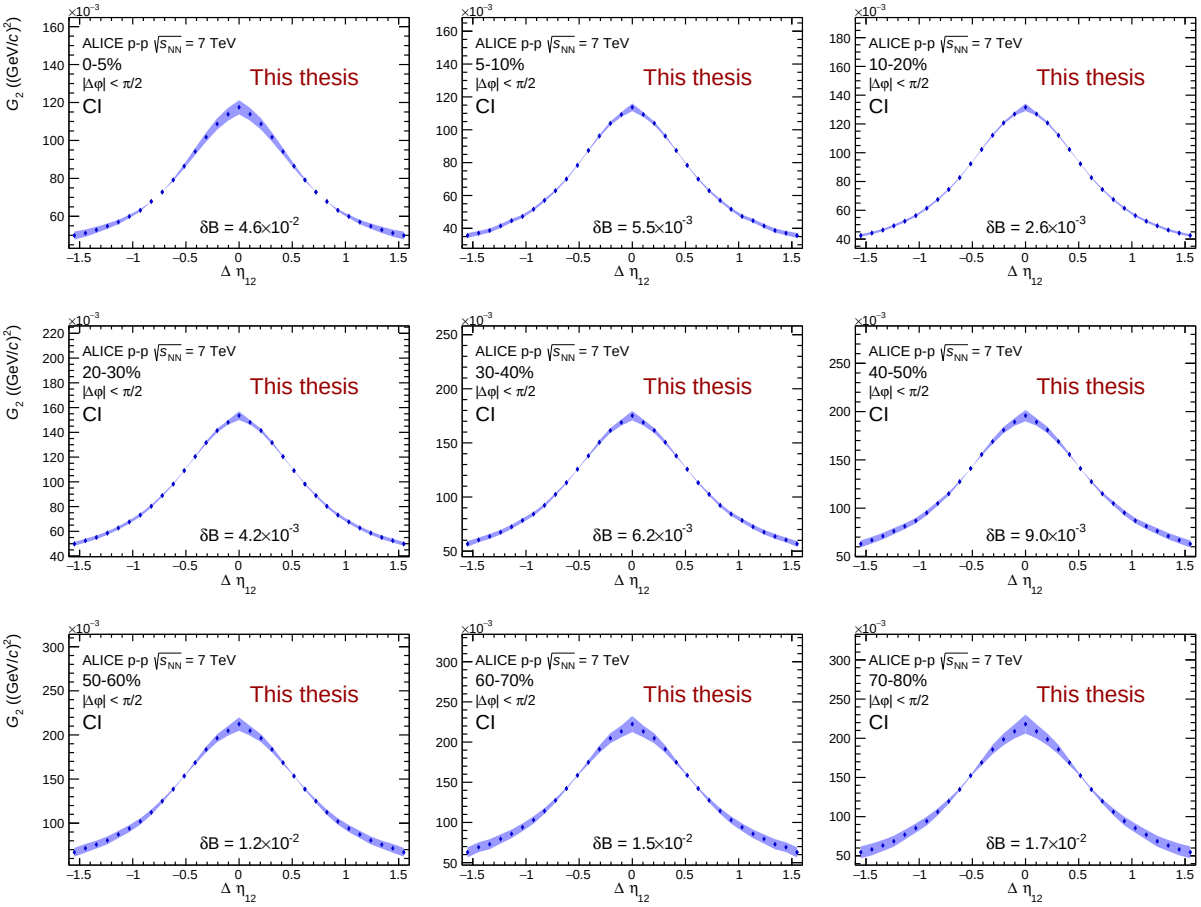

FIGURE C.41: Longitudinal projection of the charge independent (CI) two-particle transverse momentum correlation in pp collisions at $\sqrt{s_{\rm NN}}$ = 7 TeV as measured by ALICE.

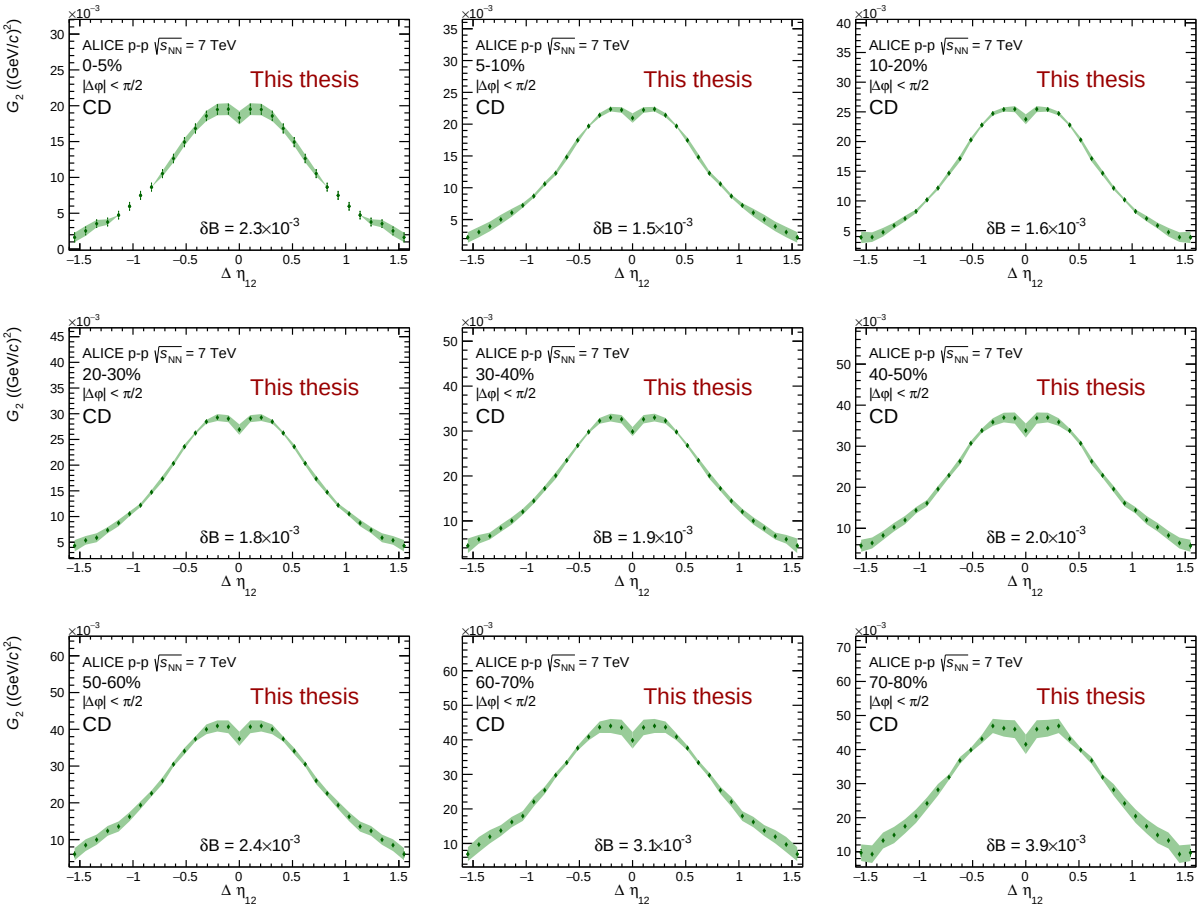

FIGURE C.42: Longitudinal projection of the charge dependent (CD) two-particle transverse momentum correlation in pp collisions at $\sqrt{s_{\mathrm{NN}}}$ = 7 TeV as measured by ALICE.

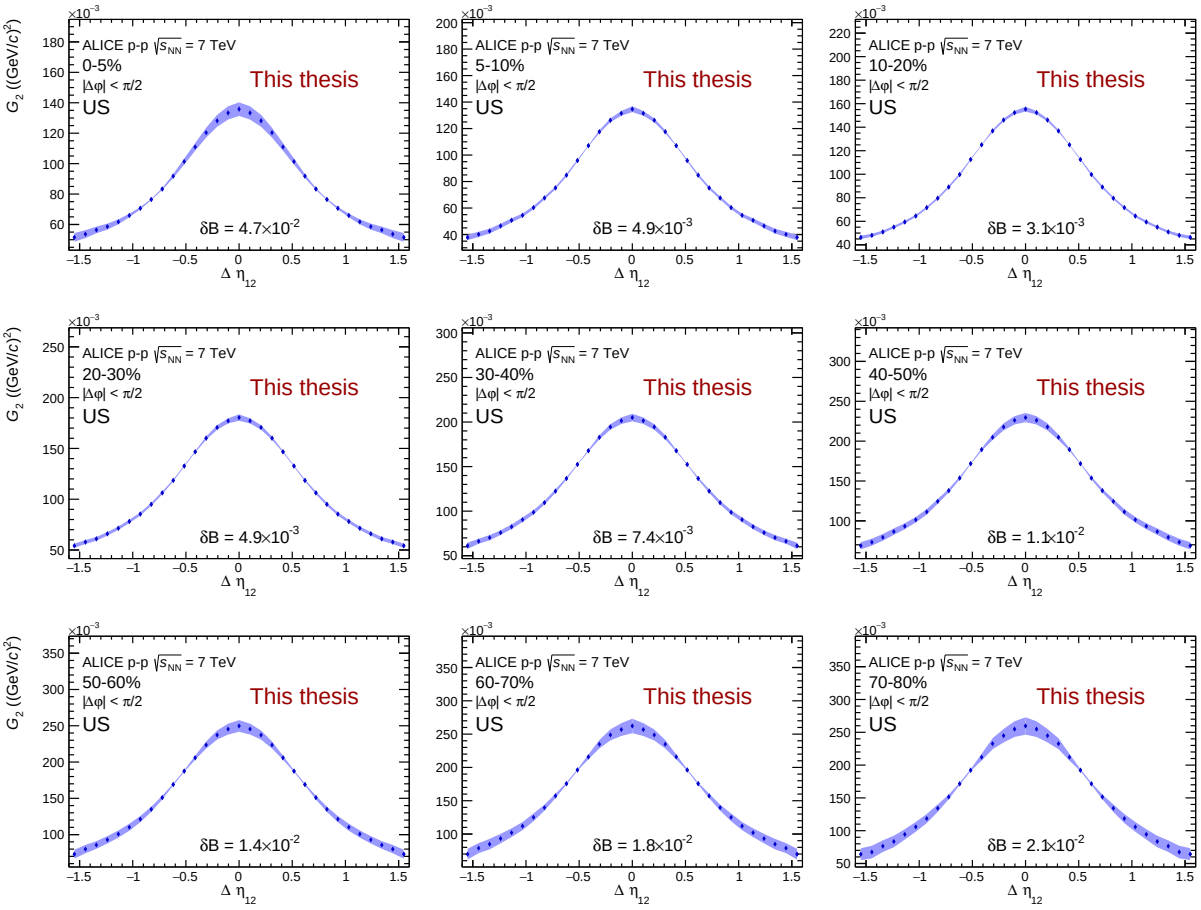

FIGURE C.43: Longitudinal projection of the unlike sign (US) two-particle transverse momentum correlation in pp collisions at $\sqrt{s_{\rm NN}}$ = 7 TeV as measured by ALICE.

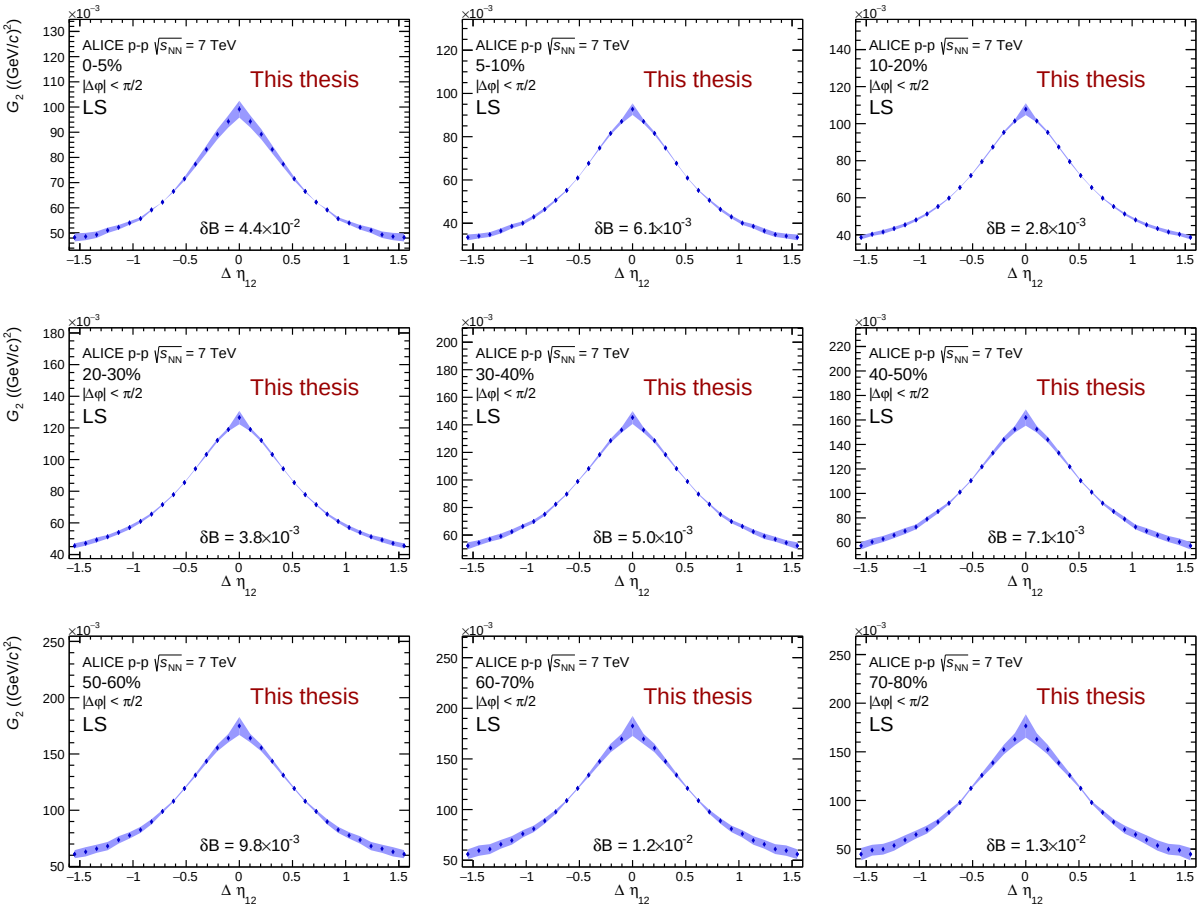

FIGURE C.44: Longitudinal projection of the like sign (LS) two-particle transverse momentum correlation in pp collisions at $\sqrt{s_{\mathrm{NN}}}$ = 7 TeV as measured by ALICE.

C.4.3 Azimuthal projections

Figures C.45, C.46, C.47, and C.48 show the azimuthal projections of two-particle transverse momentum correlation G_2 for the CI, CD, US, and LS track combinations, respectively.

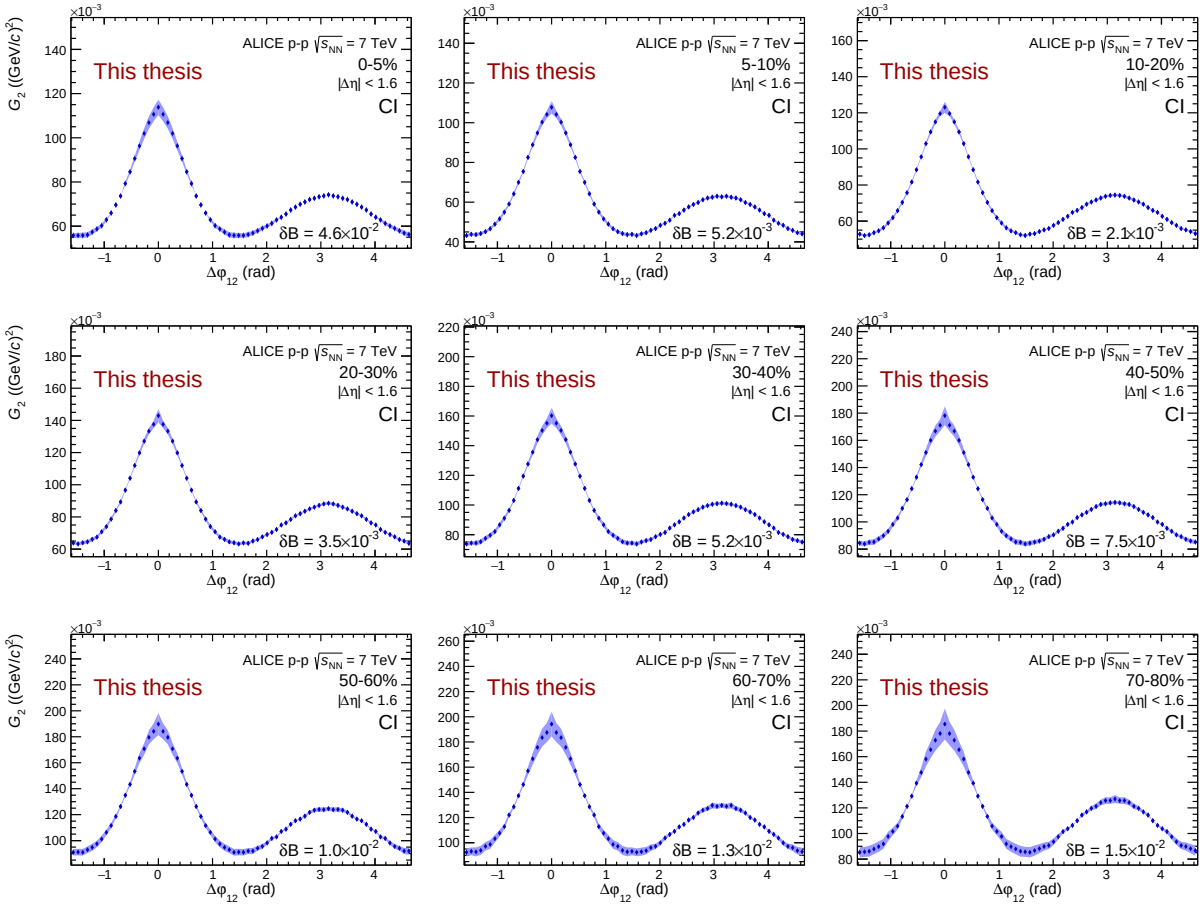

FIGURE C.45: Azimuthal projection of the charge independent (CI) two-particle transverse momentum correlation in pp collisions at $\sqrt{s_{\mathrm{NN}}}$ = 7 TeV as measured by ALICE.

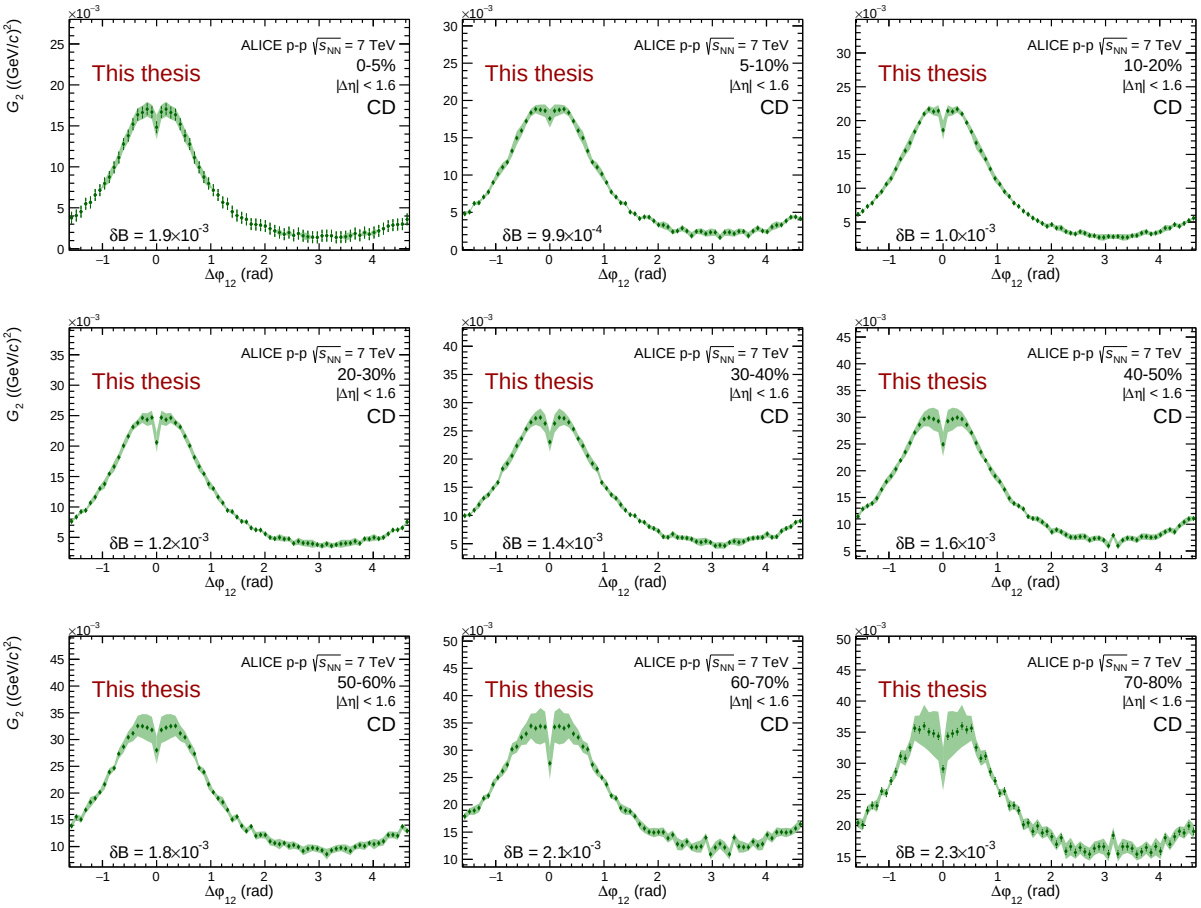

FIGURE C.46: Azimuthal projection of the charge dependent (CD) two-particle transverse momentum correlation in pp collisions at $\sqrt{s_{\mathrm{NN}}}$ = 7 TeV as measured by ALICE.

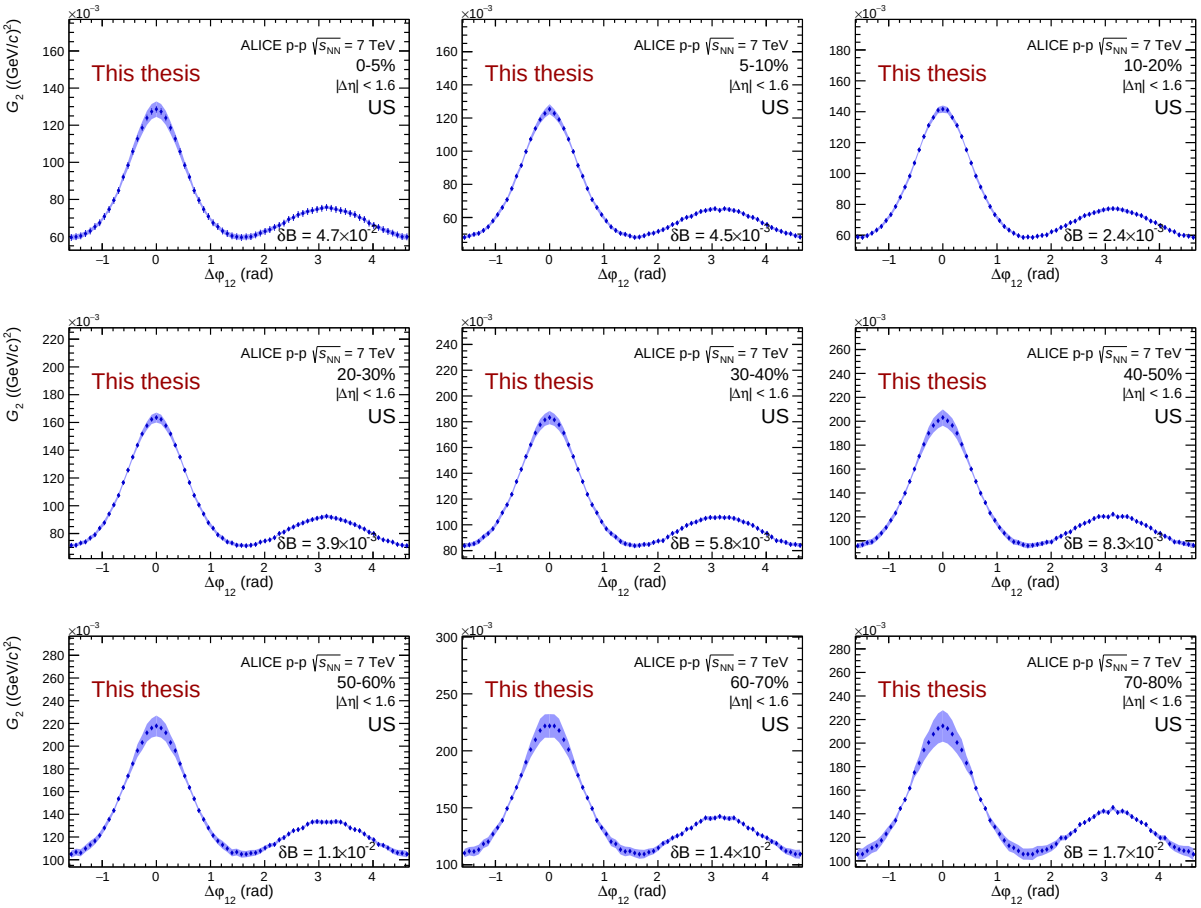

FIGURE C.47: Azimuthal projection of the unlike sign (US) two-particle transverse momentum correlation in pp collisions at $\sqrt{s_{\rm NN}}$ = 7 TeV as measured by ALICE.

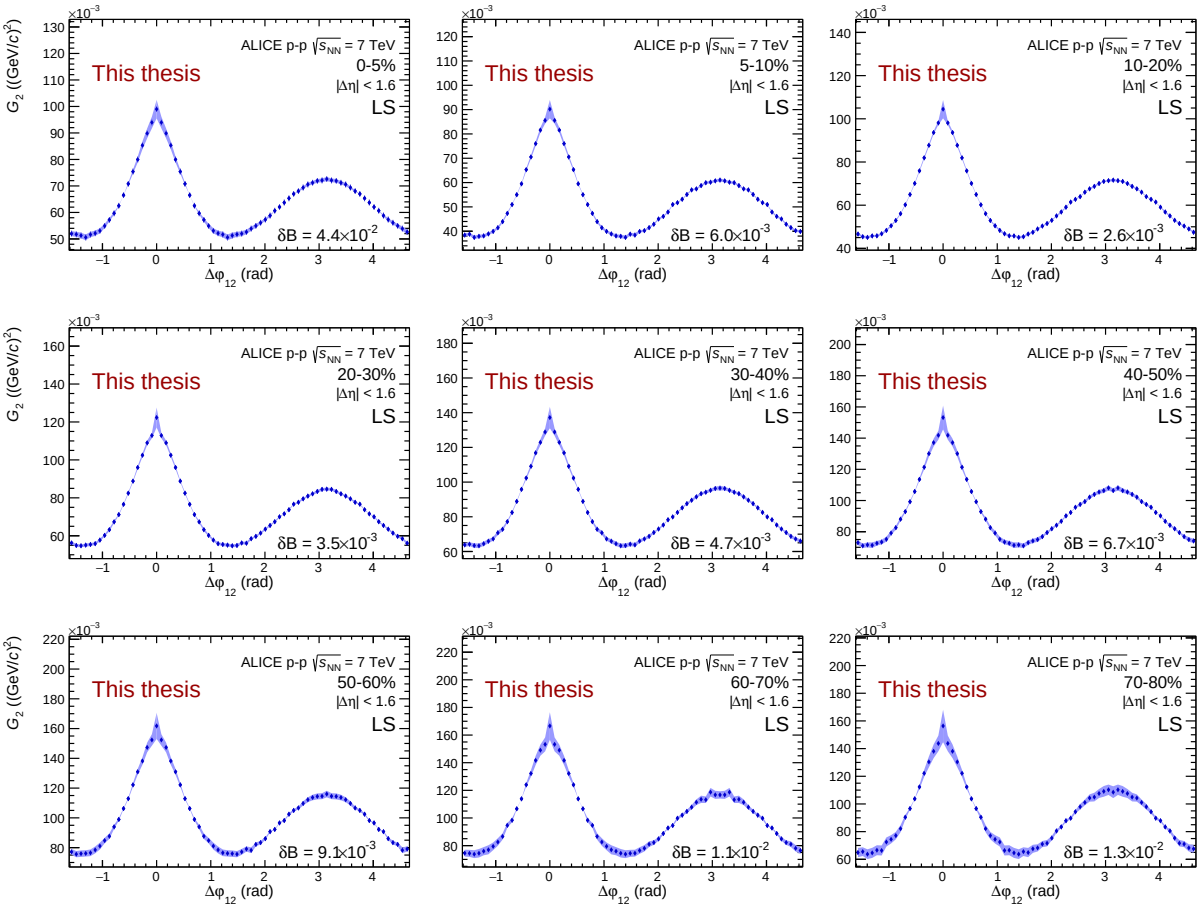

FIGURE C.48: Azimuthal projection of the like sign (LS) two-particle transverse momentum correlation in pp collisions at $\sqrt{s_{\mathrm{NN}}}$ = 7 TeV as measured by ALICE.